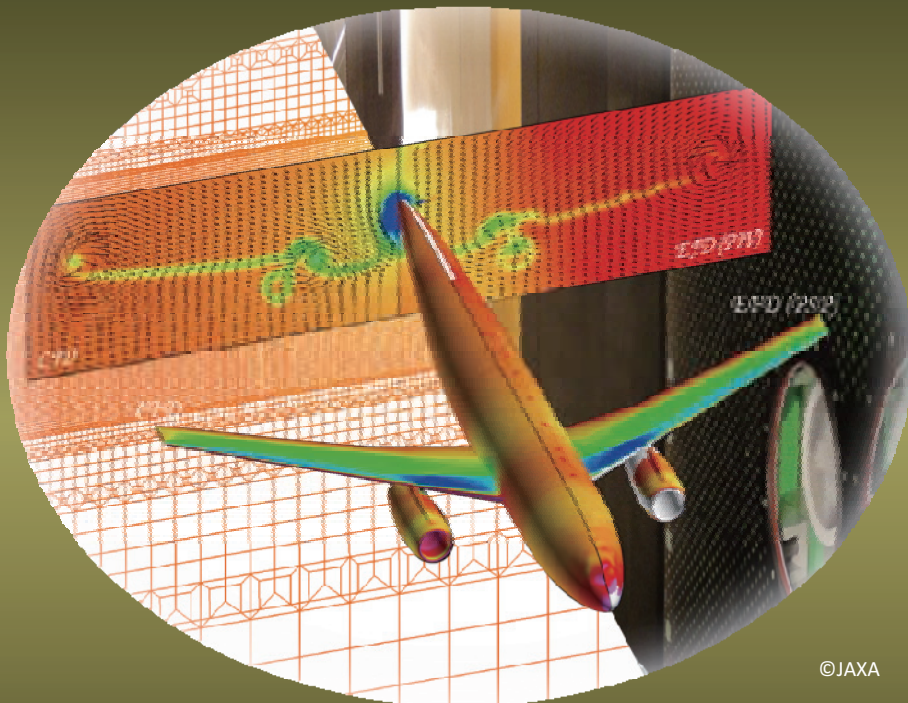TOHOKU UNIVERSITY

JAXA

Integration 2012

5th Symposium on Integrating CFD and Experiments in Aerodynamics

©JAXA

October 3-5, 2012
JAXA Chofu Aerospace Center
Tokyo, JAPAN

http://integration2012.jaxa.jp

General Co-Chairs

Shigeru Obayashi, Tohoku University
Shigeya Watanabe, Japan Aerospace Exploration Agency (JAXA)

International Scientific Panel

Ken Badcock, University of Liverpool
Russell Cummings, United States Air Force Academy
Kevin Knowles, Cranfield University
Shigeru Obayashi, Tohoku University
Philippe Planquart, von Karman Institute
Patrick Rambaud, von Karman Institute
Alistair Saddington, Cranfield University
Shigeya Watanabe, JAXA

Local Scientific Committee

Keisuke Asai, Tohoku University
Takayuki Ito, Ochanomizu University
Takeshi Ito, JAXA
Masahiro Kanazaki, Tokyo Metropolitan University
Hiromitsu Kawazoe, Tottori University
Yuichi Matsuo, JAXA
Shigeru Obayashi, Tohoku University
Akihiro Sasoh, Nagoya University
Keisuke Sawada, Tohoku University
Kojiro Suzuki, University of Tokyo
Makoto Tsubokura, Hokkaido University
Shigeya Watanabe, JAXA
Kazuomi Yamamoto, JAXA
Kenji Yoshida, JAXA

Local Organizing Committee

Hideaki Aiso, Chair, JAXA
Kentaro Imagawa, JAXA
Shigeru Kuchi-Ishi, JAXA
Hiroyuki Kato, JAXA
Keiichi Murakami, JAXA
Toshiyuki Suzuki, JAXA
Kanako Yasue, JAXA

Integration 2012

5th Symposium on Integrating CFD and Experiments in Aerodynamics

3rd to 5th October, 2012
JAXA Chofu Aerospace Center, Tokyo, JAPAN

Technical Session Program

Wednesday, Octorber 3, 2012

Time	Session	Page
8:30-16:00	**Registration**	
9:30	**Opening Ceremony**	
9:45	**Invited Lecture 1 chaired by Kenji Yoshida (JAXA, Japan)**	1
	IL1, EFD/CFD for MRJ Development	
	Ichiro Maeda, Keita Hatanaka (Mitsubishi Aircraft Co., Japan)	
	Session 1: Digital/Analog-Hybrid Wind Tunnel (DAHWIN) chaired by Kenji Yoshida (JAXA, Japan)	
10:30	**1-1, DAHWIN - Digital/Analog-Hybrid Wind Tunnel**	13
	Shigeya Watanabe, Shigeru Kuchi-Ishi, Keiichi Murakami, Atsushi Hashimoto, Hiroyuki Kato, Tatsuya Yamashita, Kanako Yasue, Kentaro Imagawa (JAXA, Japan), Hideji Saiki, Jyun Ogino (Ryoyu Systems Co., Ltd., Japan)	
11:00	**1-2, Development of Digital Wind Tunnel as a Subsystem of JAXA Digital/Analog Hybrid Wind Tunnel**	29
	Keiichi Murakami, Atsushi Hashimoto (JAXA, Japan), Manabu Hishida (Ryoyu Systems Co., Ltd., Japan), Paulus R. Lahur (Research Center of Computational Mechanics, Inc., Japan), Akira Kunieda (CEC Ltd., Japan), Shigeya Watanabe (JAXA, Japan)	
11:30	**Poster Presentations chaired by Kenji Yoshida (JAXA, Japan)**	
12:00	**Lunch & Poster Session**	
14:00	**Invited Lecture 2** chaired by Shigeru Obayashi (Tohoku University, Japan)	37
	IL2, Overview of Activities in Stochastic Data Assimilation for Applications in Aerodynamics	
	Richard Dwight (Delft University of Technology, Netherlands)	
	Session 2: Data Assimilation-1 chaired by Shigeru Obayashi (Tohoku University, Japan)	
14:45	**2-1, Using Proper Orthogonal Decomposition Methods for Comparing CFD Results to Experimental Measurements**	55
	Thomas Andrianne, Amandine Guissart, Greg Dimitriadis, Vincent Terrapon (University of Liege, Belgium)	
15:15	**Coffee Break**	
	Session 3: Wind Tunnel Application chaired by Shigeya Watanabe (JAXA, Japan)	
15:45	**3-1, Experience in the application of numerical methods to TsAGI's wind-tunnel testing techniques**	67
	S. L. Chernyshev, V. Ya. Neyland, S. M. Bosnyakov, S. A. Glazkov, A. R. Gorbushin, I. A. Kursakov, V. V. Vlasenko (TsAGI, Russian Federation)	
16:15	**3-2, A Methodology to Derive Wind Tunnel Wall Corrections from RANS Simulations**	83
	Jean-Luc Hantrais-Gervois, Jean-François Piat (ONERA, France)	
16:45	**3-3, Wall Interference Analysis by Whole Wind Tunnel CFD**	103
	Atsushi Hashimoto, Masataka Kohzai (JAXA, Japan)	
17:15	**3-4, Prediction of the Aerodynamic Effect of Model Deformation during Transonic Wind Tunnel Tests**	115
	Sylvain Mouton, Marianne Lyonnet, Yves Le Sant (ONERA, France)	
17:45		
18:00-20:00	**Reception (Exhibition Hall, JAXA CAC)**	

Thursday, Octorber 4, 2012

9:00-16:00	**Registration**	
9:30	**Invited Lecture 3 chaired by Shigeru Kuchi-Ishi (JAXA, Japan)**	**131**
	IL3, InfoSymbiotics - The power of Dynamic Data Driven Applications Systems (DDDAS)	
	Frederica Darema (Air Force Office of Scientific Research, United States of America)	
10:15	**Coffee Break**	
	Session 4: Aeroacoustics chaired by Yuichi Matsuo (JAXA, Japan)	
10:45	**4-1, Numerical Noise Prediction of a generic Flap Configuration**	**157**
	Lilla Kapa-Koloszar, Patrick Rambaud, Philippe Planquart, Christophe Schram(VKI, Belgium)	
11:15	**4-2, Computational Efforts in Designing Experiment for High-Lift Aeroacoustics**	**167**
	Mitsuhiro Murayama, Yuzuru Yokokawa, Kazuomi Yamamoto, Kazuhisa Amemiya (JAXA, Japan), Kentaro Tanaka, Tohru Hirai (Ryoyu Systems. Co. Ltd., Japan),	
11:45	**4-3, Integrating CFD, CAA, and Experiments towards Benchmark Datasets for Airframe Noise Problems**	**183**
	Meelan Choudhari (NASA, United States of America), Kazuomi Yamamoto (JAXA, Japan)	
12:15	**Lunch**	
13:15	**Invited Lecture 4** chaired by Tomoyuki Higuchi (Institute of Statistical Mathematics, Japan)	**191**
	IL4, Integration of CFD and EFD for Analysis of Complex Real Flows	
	Toshiyuki Hayase (Tohoku University, Japan)	
	Session 5: Data Assimilation-2 chaired by Tomoyuki Higuchi (Institute of Statistical Mathematics, Japan)	
14:00	**5-1, Sensitivity Analysis of Unsteady Flow Fields and Numerical Experiments for Optimal Measurement**	**209**
	Takashi Misaka (DLR, Germany), Shigeru Obayashi (Tohoku University, Japan)	
14:30	**5-2, Application of the Measurement Integrated Simulation Method to Compressible Fluid Problems**	**217**
	Kentaro Imagawa, Kanako Yasue, Shigeru Kuchi-Ishi (JAXA, Japan)	
15:00	**5-3, Toward the Development of Measurement Integrated Simulation**	**229**
	Hiroshi Kato, Shigeru Obayashi (Tohoku University, Japan)	
15:30	**Coffee Break**	
	Session 6: Modeling/Flow Control/Wind Turbine chaired by Hiromitsu Kawazoe (Tottori University, Japan)	
16:00	**6-1, A Variable Fidelity Response Surface Approach towards Integration of CFD and EFD**	**243**
	Wataru Yamazaki (Nagaoka University of Technology, Japan), Shigeru Kuchi-Ishi (JAXA, Japan)	
16:30	**6-2, Requirements for Computer Generated Aerodynamic Models for Aircraft Stability and Control Analysis**	
	A. McCracken, U. Akram, A. Da Ronch, K.J. BadcockKenneth Badcock (University of Liverpool, United Kingdom)	
17:00	**6-3, A Study on the Performance of Fluidic Thrust Vector Control Utilizing Supersonic Coanda Effects**	**253**
	MyungJun Song, SangHun Yoon (Korea Aerospace University, Republic of Korea), HongBeen Chang (Agency for Defense Development, Republic of Korea), YongHo Cho (Micro Friend, Inc, Republic of Korea), Yeol Lee (Korea Aerospace University, Republic of Korea)	
17:30	**6-4, Measurements of Counter Flow Region in Averaged Wake-Velocity-Field of a Small Straight-Bladed Vertical Axis Wind Turbine**	**263**
	Yutaka Hara, Takahiro Suzuki, Hirofumi Kamon (Tottori University, Japan)	
18:00		
19:00-21:30	**Banquet (KICHIJOJI PARK CAFE, Kichijoji Tokyu INN 1F)**	

Friday, Octorber 5, 2012

8:30-10:00	**Registration**	
9:00	**Invited Lecture 5** chaired by Kojiro Suzuki (The University of Tokyo, Japan)	**271**
	IL5, CFD for Aerodynamic Flight Performance Prediction: From Irrational Exuberance to Sobering Reality	
	Pradeep Raj (Virginia Tech, United States of America)	
9:45	**Coffee Break**	
	Session 7: Supersonic/Hypersonic Flow chaired by Keisuke Sawada (Tohoku University, Japan)	
10:15	**7-1, A Combined Study on Shock Diffraction**	**279**
	Mark Kenneth Quinn, Konstantinos Kontis (University of Manchester, United Kingdom)	
10:45	**7-2, Wind Tunnel and CFD Studies on Production of Prebiotic Materials in Hypersonic Flow around Extraterrestrial Entry Object**	**295**
	Kojiro Suzuki, Yasumasa Watanabe (The University of Tokyo, Japan)	
11:15	**7-3, Experimental and Numerical Study on Shock Layer Radiation for Planetary Entry Flights**	**307**
	Gouji Yamada, Shota Ago, Yuto Kubo, Takashi Matsuno, Hiromitsu Kawazoe (Tottori University, Japan)	
11:45	**7-4, Numerical Study on Anomalous Heating over Apollo CM Test Model in Free-Piston Shock Tunnel HIEST**	**317**
	Tomoaki Ishihara, Yousuke Ogino, Naofumi Ohnishi, Keisuke Sawada (Tohoku University, Japan), Hideyuki Tanno (JAXA, Japan)	
12:15-14:30	**Lunch (Jindaiji, Suijin-en)**	
14:30-16:45	**Technical Tours (JAXA CAC)**	
16:45-17:00	**Closing Ceremony**	

Poster Session:

P1, Visualization of Unsteady Behavior of Shock Waves around Supersonic Intake installed in Shock Tunnel — **327**
Naruaki Tanaka, Toshiharu Mizukaki (Tokai University, Japan)

P2, Experimental investigation of initial shear-layer effect on the pressure oscillation in supersonic cavity — **335**
Takaya Ozaki, Shinji Maruyama (Kyushu University, Japan), Hatsuki Kakuno (Nippon Steel Engineering Co., Ltd., Japan), Taro Handa (Kyushu University, Japan)

P3, Aerodynamic Characteristics of a Delta Wing with Arc Camber for Mars Exploration — **343**
Takao Unoguchi, Shogo Aoyama, Hiroshi Suemura, Gouji Yamada, Takashi Matsuno (Tottori University, Japan), Shigeru Obayashi (Tohoku University, Japan), Hiromitsu Kawazoe (Tottori University, Japan)

P4, CFD Calculation of Airfoil Characteristics for Performance Prediction of Vertical Axis Wind Turbine — **353**
Naoko Inoue, Kana Tanaka, Yutaka Hara, Takahiro Sumi (Tottori University, Japan)

P5, Multi-objective Optimization of Airfoil of Mars Exploration Aircraft using Evolutionary Algorithm — **361**
Gaku Sasaki (Kyusyu Institute of Technology, Japan), Tomoaki Tatsukawa, Taku Nonomura (JAXA, Japan), Koichi Yonemoto (Kyusyu Institute of Technology, Japan), Akira Oyama (JAXA, Japan), Takaaki Matsumoto, Tomohiro Narumi (Kyusyu Institute of Technology, Japan)

P6, Bow-shock instability around an Edged Ballistic Object in a Low-Gamma Gas — **367**
Yosuke Sato (Tohoku University, Japan), Kanako Yasue (JAXA, Japan), Takamasa Kikuchi, Kiyonobu Ohtani, Naofumi Ohnishi (Tohoku University, Japan)

P7, A Study on Pressure Variation of a Rotor Blade Tip using PSP — **375**
Kidong Kim (University of Science and Technology, Republic of Korea), Kijung Kwon (KARI, Republic of Korea)

P8, Assessment of some experimental and processing factors for background oriented schlieren measurements — **385**
Ardian B. Gojani, Shigeru Obayashi (Tohoku University, Japan)

P9, Dynamic Wind-Tunnel Testing of a Delta Wing Using a Multi-Degree-of-Freedom Robotic Manipulator — **397**
Tatsuya Hara, Daiju Numata, Keisuke Asai, Takahumi Ito, Xin Jiang (Tohoku University, Japan)

P10, Integration between Measurements and Particle Simulations for Hypersonic Rarefied Flows — **407**
Takashi Ozawa, Toshiyuki Suzuki, Kazuhisa Fujita (JAXA, Japan)

P11, Experimental Data Reconstruction Using CFD Results Based on Proper Orthogonal Decomposition — **417**
Kanako Yasue, Shigeru Kuchi-Ishi, Shigeya Watanabe (JAXA, Japan)

P12, Drag and Lift Estimation from 3-D Velocity Field Data Measured by Multi-Plane Stereo PIV — **425**
Hiroyuki Kato (JAXA, Japan), Kisa Matsushima (University of Toyama, Japan), Makoto Ueno, Shunsuke Koike, Shigeya Watanabe (JAXA, Japan)
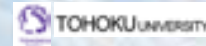
EFD/CFD for MRJ Development

Integration 2012

2012/10/03

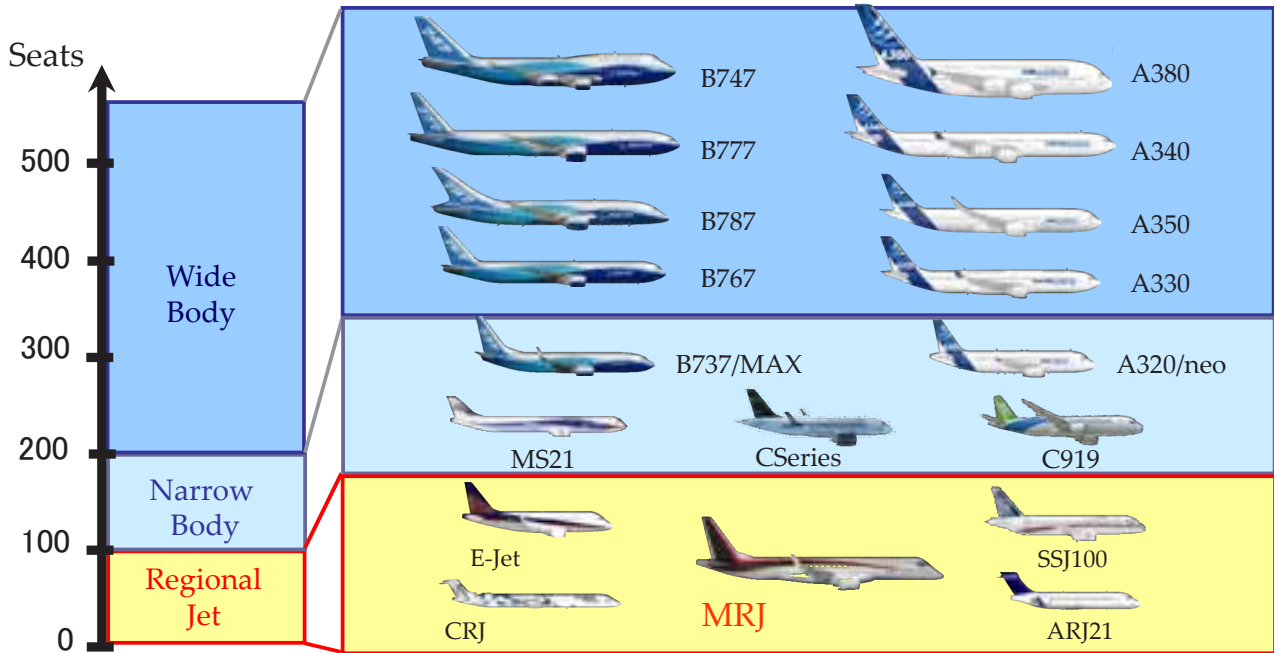### Mitsubishi Aircraft Corporation

Ichiro Maeda

MITSUBISHI AIRCRAFT CORPORATION   MITSUBISHI AIRCRAFT CORP. PROPRIETARY   NA231103 NC   1/

1. Introduction of MRJ

2. EFD/CFD for MRJ Development

3. Future prospect on EFD and CFD

MITSUBISHI AIRCRAFT CORPORATION   MITSUBISHI AIRCRAFT CORP. PROPRIETARY   NA231103 NC   2/

Commercial Jet Market

- More than 28,000 airplanes to be delivered in the next 20 years
- Fierce competition with five regional jet makers

Seats

500

400

300

200

100

0

Wide Body

Narrow Body

Regional Jet

B747   A380
B777   A340
B787   A350
B767   A330

B737/MAX   A320/neo

MS21   CSeries   C919

E-Jet   SSJ100
CRJ   MRJ   ARJ21

Vision and Key Features

【Vision】

- Apply advanced mainline jet technology to regional jet and create the standard for next-generation regional jet.
- Offer unprecedented values for environment, passengers, and airlines.

Environment
Lowest Fuel Burn, Noise, Emissions
■Game-Changing Engine
■Advanced Aerodynamics

Passengers
Most Comfortable Cabin
■Passenger-Oriented Cabin
■New Slim Seat

Airlines
Most Efficient Aircraft
■Game-Changing Engine
■Advanced Aerodynamics
■Human-Centered Flight Deck
■Composite Structure

Key Features
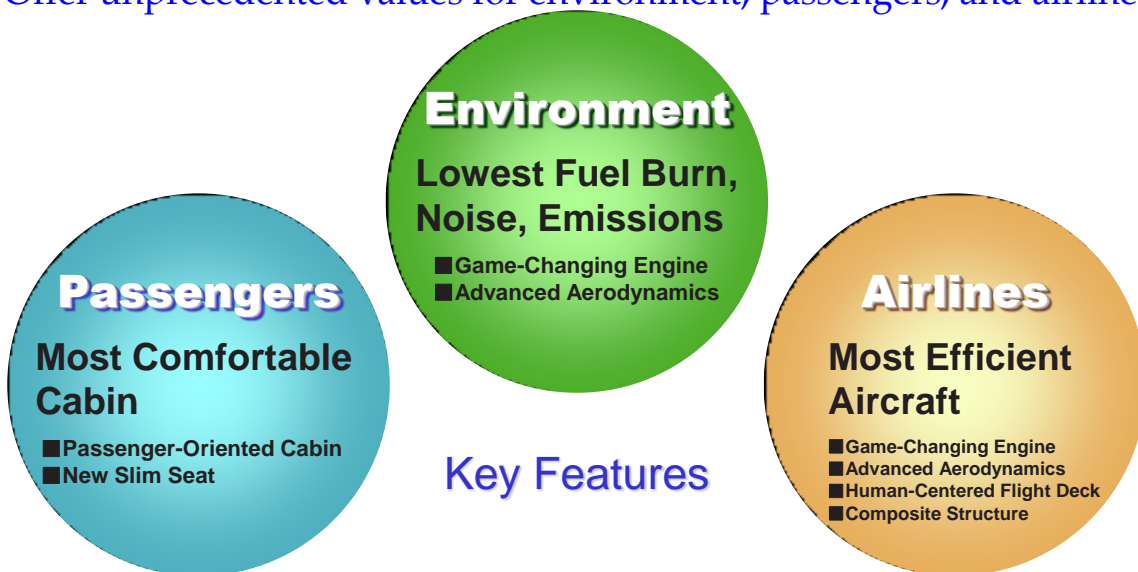
MRJ Family

- Three models to cover global market needs
- High commonality for airline economics
  pilot type rating, engines, maintenance program and spare parts

MRJ100X (Plan)
100 seats
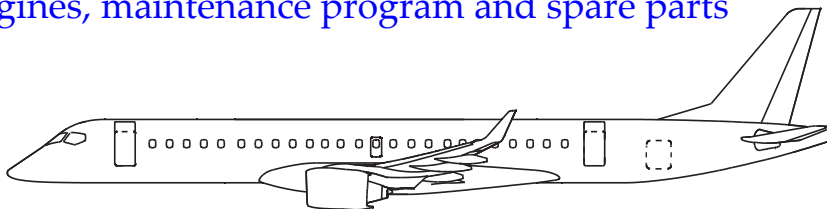
MRJ90
92 seats
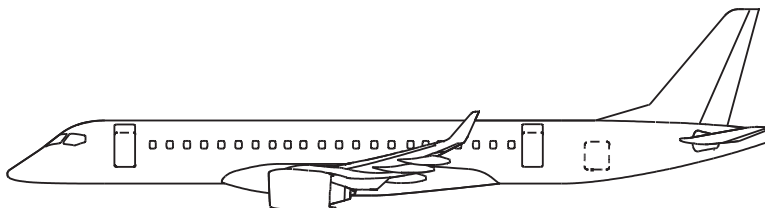
MRJ70
78 seats
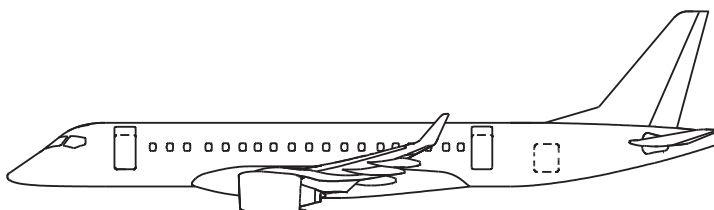
General Arrangement - MRJ90

- Designed for fuel efficiency without compromising cabin comfort

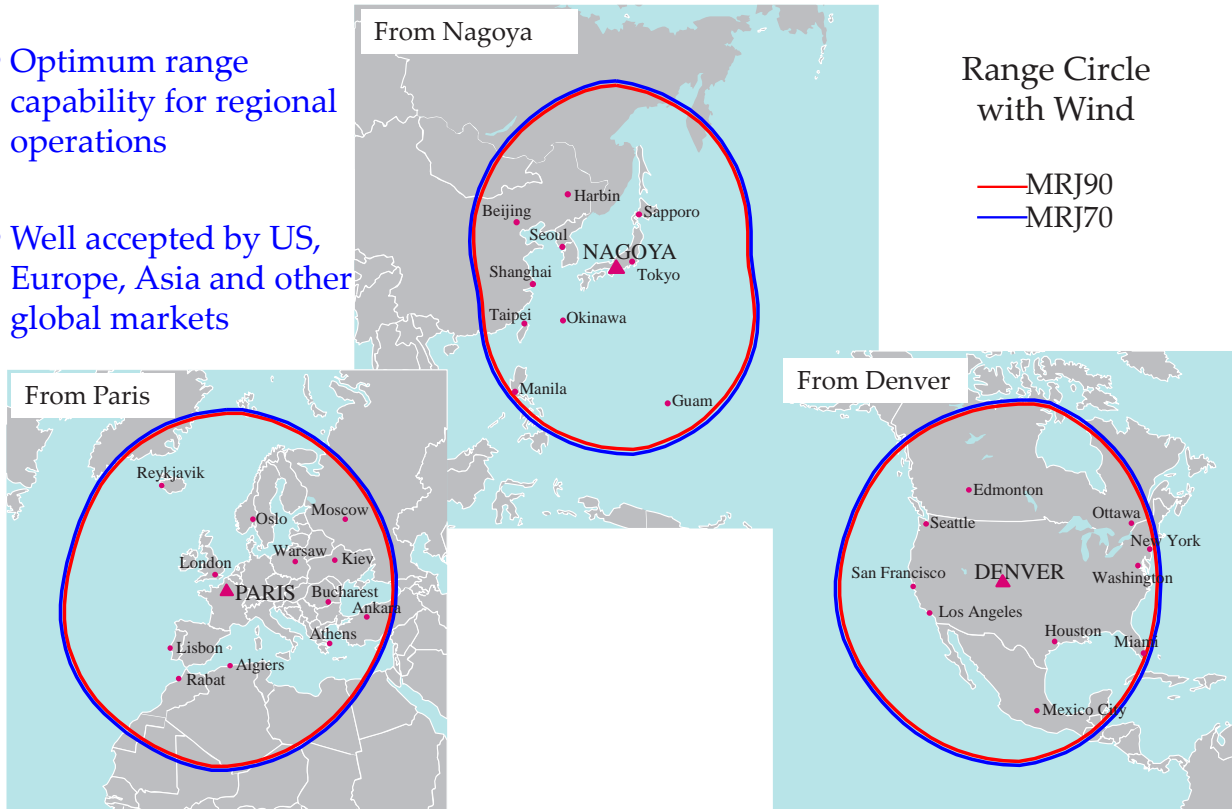- High aspect ratio wing with winglets, small diameter fuselage, and innovative GTF engine
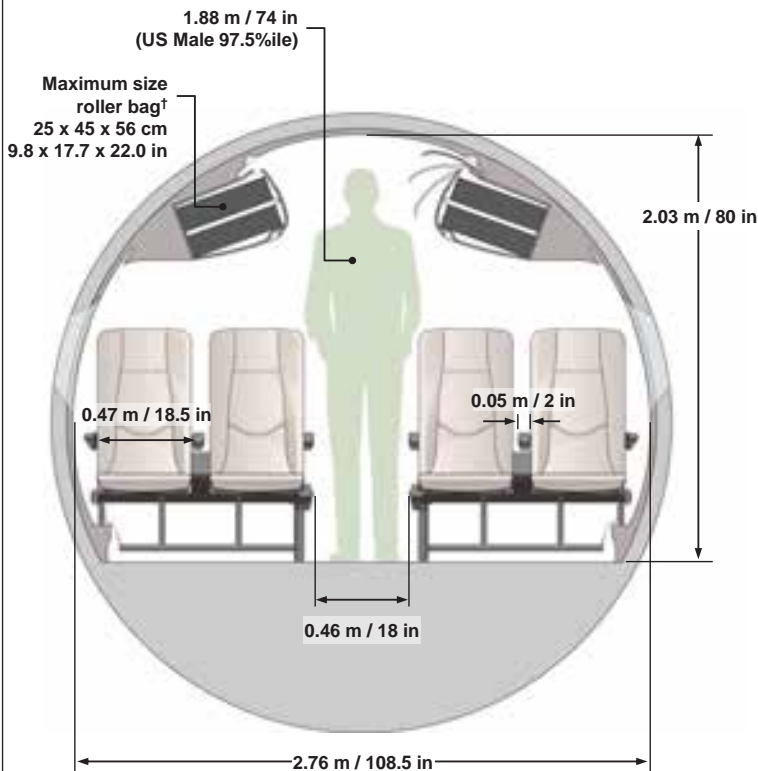
GTF: Geared Turbo Fan

11.0 m / 36.2 ft

29.2 m / 95.9 ft

35.8 m / 117.4 ft

10.5 m / 34.4 ft

5.3 m / 17.5 ft

14.0 m / 45.9 ft
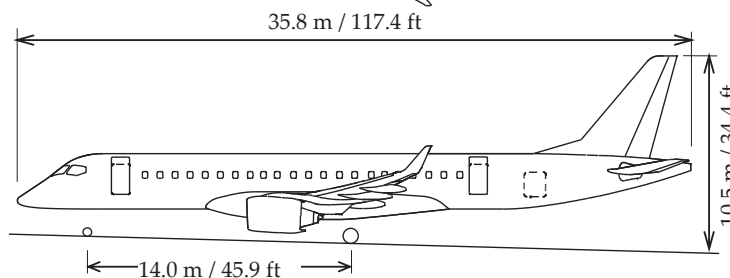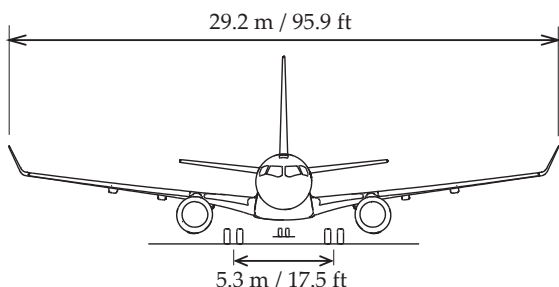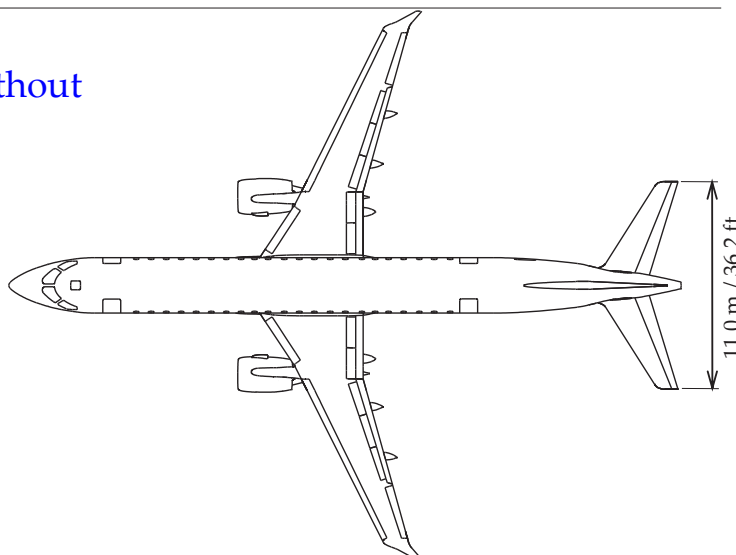
Range Capability

- Optimum range capability for regional operations

- Well accepted by US, Europe, Asia and other global markets

From Nagoya

Range Circle with Wind
— MRJ90
— MRJ70

Harbin
Beijing
Sapporo
Seoul
NAGOYA
Shanghai
Tokyo
Taipei
Okinawa
Manila
Guam

From Paris

Reykjavik
Oslo   Moscow
Warsaw   Kiev
London
PARIS
Bucharest
Ankara
Lisbon
Athens
Algiers
Rabat

From Denver

Edmonton
Seattle
Ottawa
New York
San Francisco
DENVER
Washington
Los Angeles
Houston
Miami
Mexico City

MITSUBISHI AIRCRAFT CORPORATION   MITSUBISHI AIRCRAFT CORP. PROPRIETARY   NA231103 NC   7/

Passengers – Most Comfortable Cabin

1.88 m / 74 in
(US Male 97.5%ile)

Maximum size roller bag†
25 x 45 x 56 cm
9.8 x 17.7 x 22.0 in

2.03 m / 80 in

0.47 m / 18.5 in

0.05 m / 2 in

0.46 m / 18 in

2.76 m / 108.5 in

Mainline jet comfort

- **Same seat width as 787 with 8 abreast**

MRJ	18.5 in
787 (8abreast)	18.5 in
787 (9abreast)	17.2 in
EMB170/190	18.25 in
CRJ	17.3 in

- **Ample head & foot clearance at the seat**

- **Large overhead bin**

† IATA-recommended maximum size bag

MITSUBISHI AIRCRAFT CORPORATION   MITSUBISHI AIRCRAFT CORP. PROPRIETARY   NA231103 NC   8/

Environment – Lowest Noise

- Advanced aerodynamics and GTF engine for low noise
- MRJ90 noise area reduced by 40%

Current RJ

| 85 dBA |
| 80 dBA |
| 75 dBA |
| 70 dBA |
| —— Flight Path |

MRJ90

| 85 dBA |
| 80 dBA |
| 75 dBA |
| 70 dBA |
| —— Flight Path |
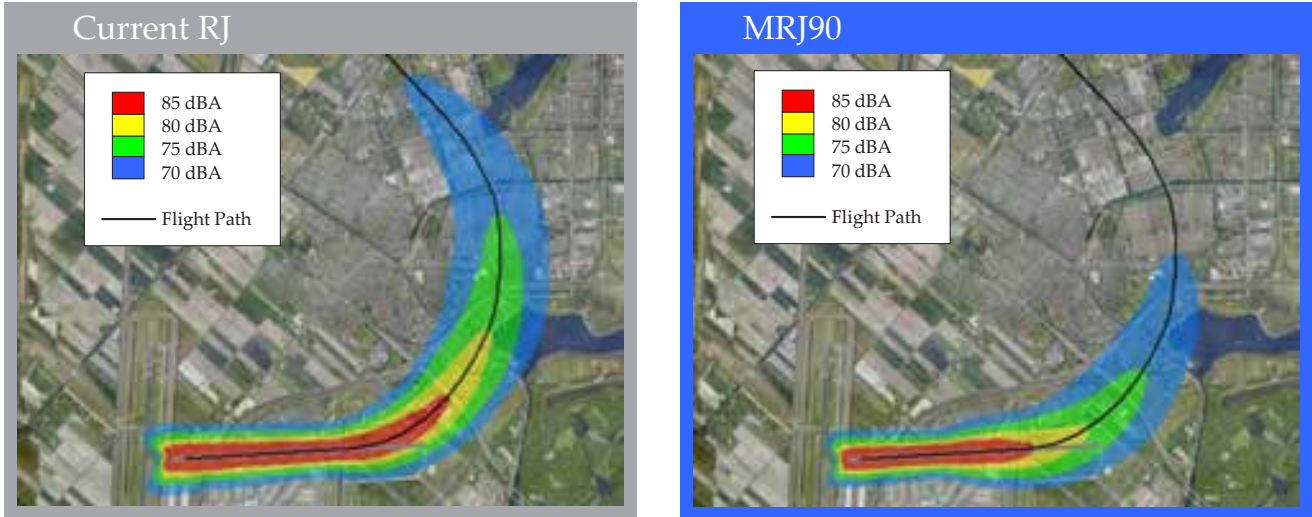
* Mitsubishi Aircraft Estimation at Schiphol Airport (AMS)

Environment – Lowest Emission

- Advanced aerodynamics and GTF engine for low fuel burn
- Significantly Lower Fuel Burn & CO_2 Emissions

CO_2 emission (%)

More than 20%

= CO_2 Reduced by More than 4,000 t./ year / a/c

Current RJ

MRJ90
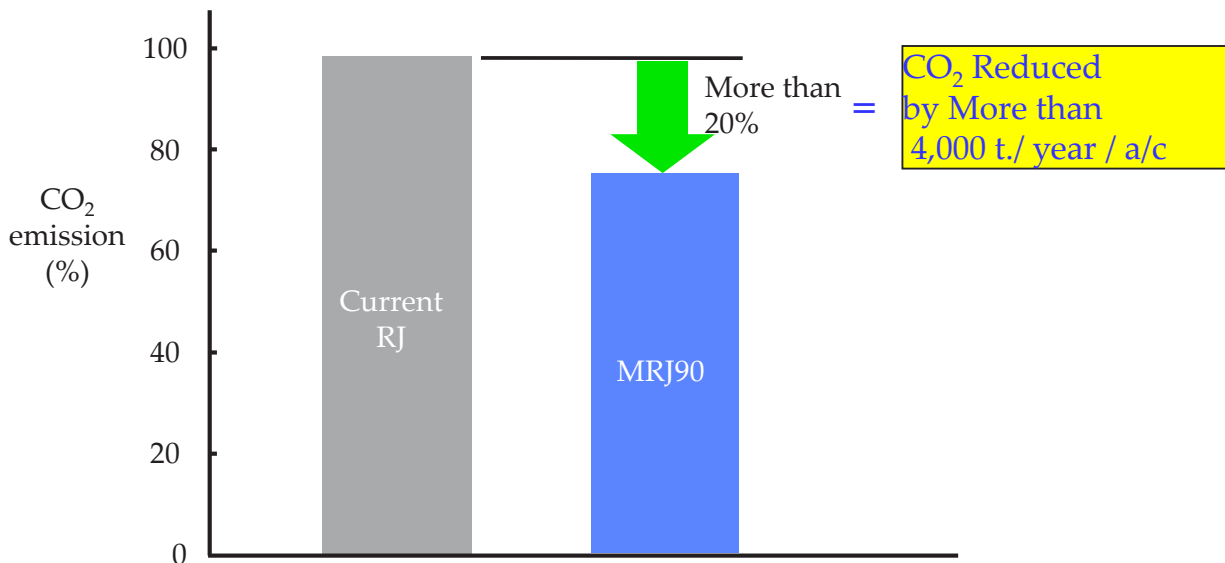
*Mitsubishi Aircraft estimation, 500nm Trip, 2,200 cycle/year, Fuel price 3$/USG

Milestones and Events

Metal Cut Ceremony
Sep./2010

Last Bolt Ceremony
Mar./2011

First Rivetting
April/2011

First Engine to Test
May/2011

Paris Airshow
June/2011

Iron Bird
Dec./2011

Farnborough Airshow
July/2012

EFD/CFD for MRJ Development : outline

Aerodynamic characteristics will be validated by flight test.
  Aerodynamic design : designed by CFD and evaluated by EFD
  Aerodynamic data   : estimated by EFD interpolated or corrected with CFD
  Noise prediction   : investigated/estimated/evaluated by EFD and CFD

EFD application
  ・Wind tunnel tests (examples)
  ・Flow visualizations by advanced optical measurements
  ・Noise source survey at low speed wind tunnel

CFD application
  ・CFD technology
  ・Simulation for all configurations
  ・Aerodynamic design based on MDO
  ・Equipment installation design for ADS and ECS
  ・Investigation for noise generation and propagation

EFD for MRJ Development　: Wind Tunnel Tests
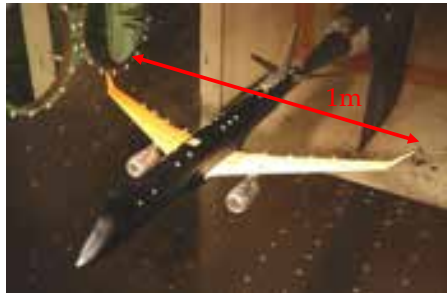
High speed wind tunnel test@
JAXA 2m × 2m TWT
JAXA/MHI collaborative work

Ground effect test@
MHI 2m LWT
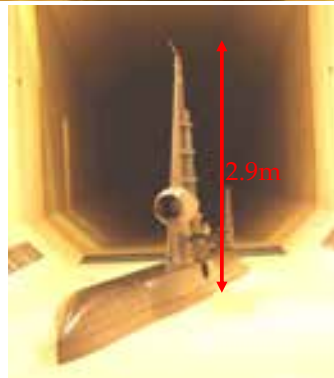
20% half span model@
JAXA 6.5m × 5.5m LWT
JAXA/MHI collaborative work
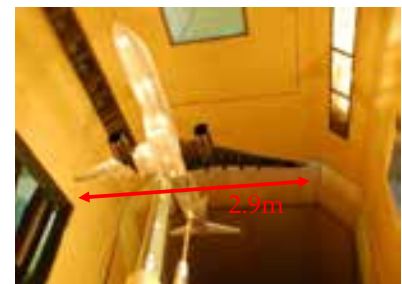
10% full span model@
JAXA 6.5m × 5.5m LWT
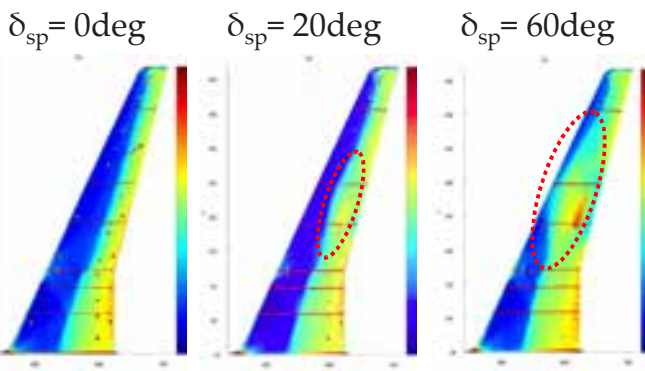JAXA/MHI collaborative work

MITSUBISHI AIRCRAFT CORPORATION　　　MITSUBISHI AIRCRAFT CORP. PROPRIETARY　　　NA231103 NC　　13/
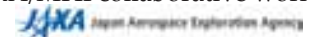
EFD for MRJ Development : Flow Visualization

Advanced optical measurement technologies（JAXA/MHI collaborative work）

・PSP（Pressure Sensitive Paint）： aerodynamic load estimation.
・PIV（Particle Image Velocimetry ）： evaluation of chine design.

δ_{sp}= 0deg　　　δ_{sp}= 20deg　　　δ_{sp}= 60deg　　　with Chine　　　w/o Chine

CFD　　PSP
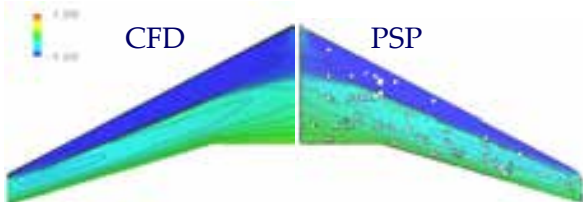
Wing Pressure Distribution at Cruise condition
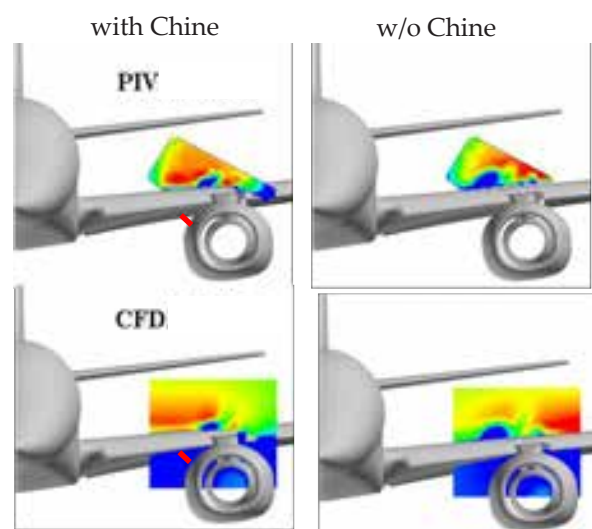
Velocity distribution around the wing-pylon
junction (PIV)@High AoA of HLD cfg.

MITSUBISHI AIRCRAFT CORPORATION　　　MITSUBISHI AIRCRAFT CORP. PROPRIETARY　　　NA231103 NC　　14/

EFD for MRJ Development : Noise prediction

Noise source survey (JAXA/MHI collaborative work)

・Evaluate aerodynamic properties and noise level simultaneously.

・Understand where the noise comes from.

JAXA 6.5m x 5.5m LWT
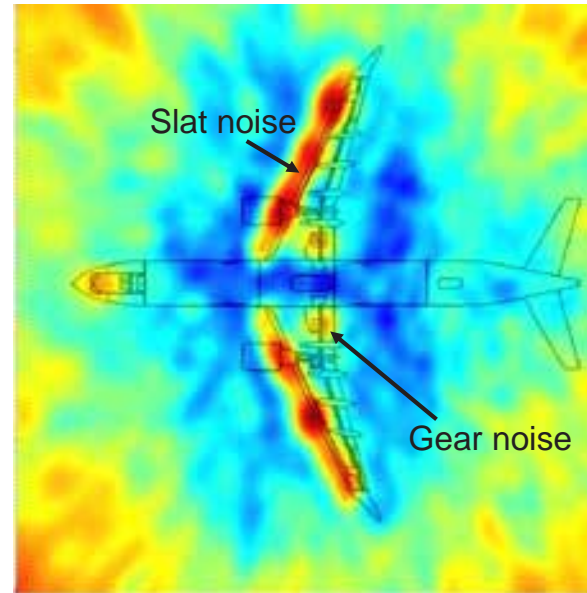
Noise visualization for HLD cfg.

MITSUBISHI AIRCRAFT CORPORATION   MITSUBISHI AIRCRAFT CORP. PROPRIETARY   NA231103 NC   15/

CFD for MRJ Development : CFD Technology

Apply CFD technology developed by collaborative work with Tohoku Univ. and JAXA
⇒ Over 100,000 CPU hours calculation!

- CFD Tool for Complex Geometry (Collaborative work with Tohoku Univ.)
    - Unstructured Mesh : TAS (Tohoku Univ. Aerodynamics Simulation)
    - Cartesian Mesh   : BCM (Building-Cube Method)

- Parallel Computing with Supercomputers (JSS, Cyber Science Center)
    Collaborative work with JAXA and Tohoku Univ.
    - Standard Steady Calculations : Aerodynamic Design etc.
   - Large Scale Unsteady Calculations : Noise and Flutter Analysis

TAS

BCM

MITSUBISHI AIRCRAFT CORPORATION   MITSUBISHI AIRCRAFT CORP. PROPRIETARY   NA231103 NC   16/
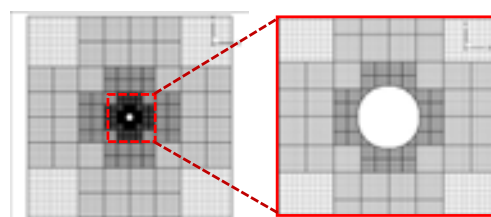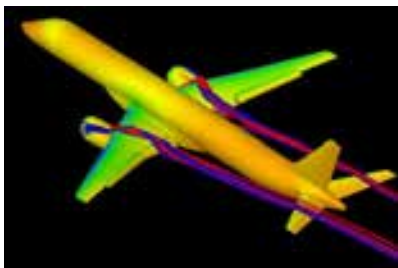
CFD for MRJ Development : All Configurations MRJ

Data productivity criteria for practical aircraft design : more than 1 case/day.

- Simulate all configurations of aircraft operation in a practical time.
- Apply to thrust reverser design to improve design efficiency and reduce risks before flight test.

Cruise

Take-off   Landing

Braking

Spoilers
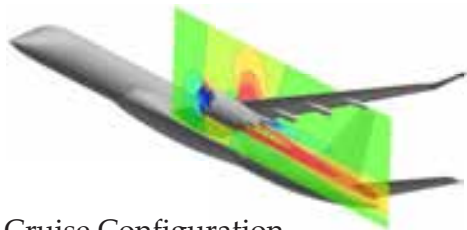
Cruise Configuration
7.5 million mesh points 10 cases/day

Ground

Take-off/Landing Configurations
10 million mesh points, 3 cases/day
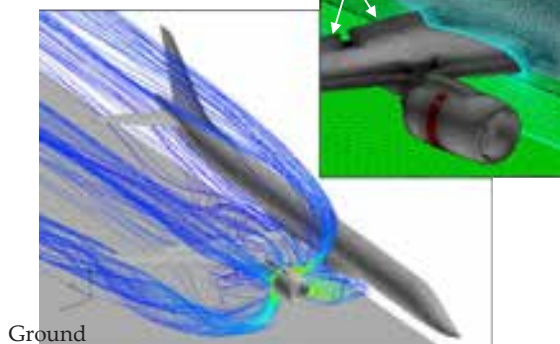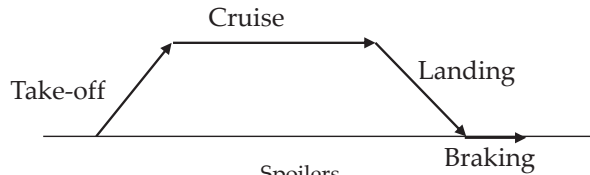
Braking with Thrust Reverser
15 million mesh points, 1 case/day

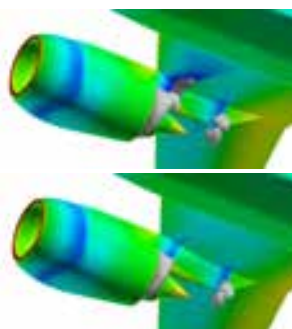# CFD for MRJ Development : Aerodynamic Design MRJ

MDO (Multidisciplinary Design Optimization) developed by Tohoku Univ.

- Apply to aerodynamic designs of wing/engine configuration and winglet
- Optimize aerodynamics (drag, lift) and structure (size, weight) simultaneously under constraints from design requirements.
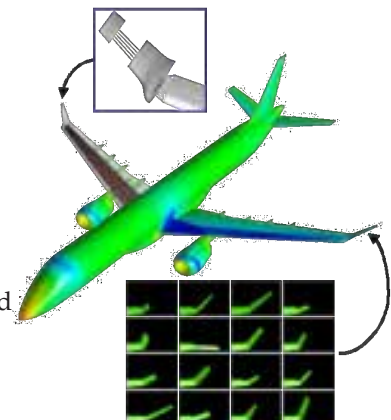

Wing CFD mesh

Engine CFD mesh

Wing FEM model

Engine FEM model
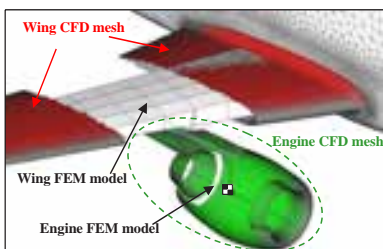
Initial

Optimized

Design of Wing/Engine Configuration

Winglet Design

CFD : Aerodynamic characteristics and aerodynamic load
FEM : Internal forces and displacement of structure

TOHOKU UNIVERSITY

CFD for MRJ Development : High fidelity simulation

MRJ

**Toward CFD for "Actual aircraft", instead of aero "Aircraft model"**

- Protuberance drag, conventionally estimated with hand-book method.
- Location of ADS, conventionally defined at WT and FT.
- Performance of air inlet/outlet for ECS, APU, ventilation etc.

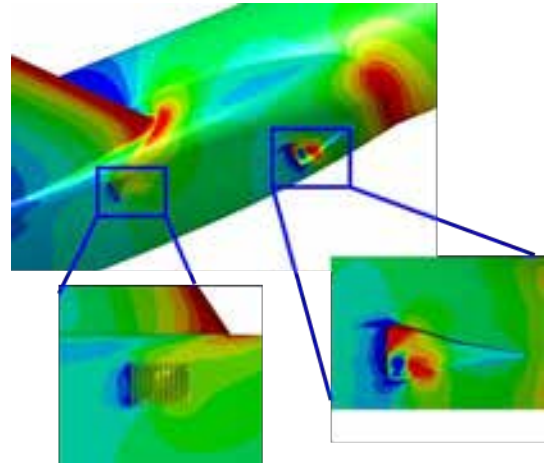|		
CD	=0.0300	:Total Drag of Airplane （about 1/10 of Car）
ΔCD	=10^{-4}(1count)	:Low-Drag Design
ΔCD	=10^{-6}	:Drag of a Sensor

Miscellaneous drag = 5% of CD!!!
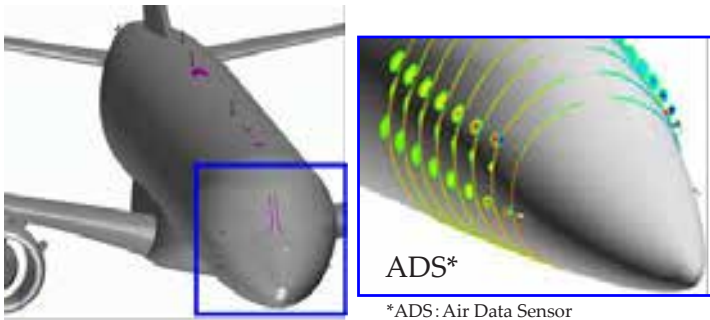
ADS*

*ADS：Air Data Sensor

Evaluation of Small-size Equipments

Performance Evaluation of Inlet/Outlet of ECS* ram air flow

*ECS：Environment Control System

MITSUBISHI AIRCRAFT CORPORATION   MITSUBISHI AIRCRAFT CORP. PROPRIETARY   NA231103 NC   19/

# CFD for MRJ Development : Noise prediction

MRJ

Noise prediction and Low-noise design by collaborative work with JAXA and Tohoku Univ.

- Investigation of noise source and prediction of airframe noise with acoustic analysis for community noise
- Prediction of engine noise propagation into cabin for passenger noise
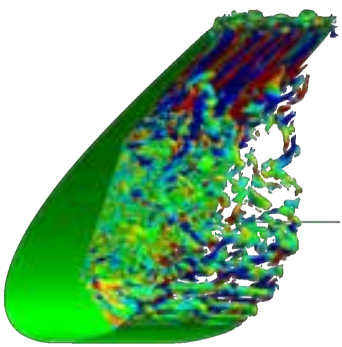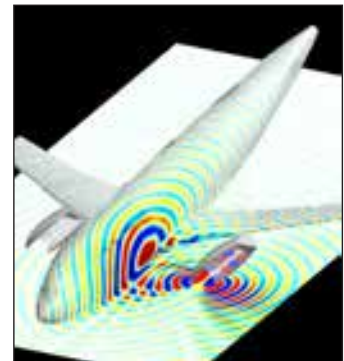

LES* for Slat Noise
（Courtesy of JAXA）

*LES：Large Eddy Simulation
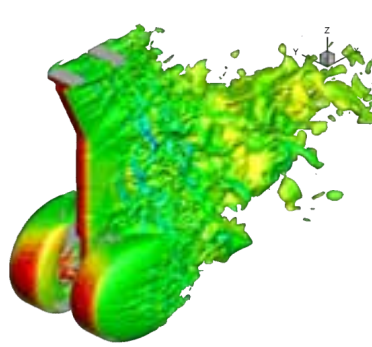
BCM*/LES for Landing Gear Noise
（Collaboration with Tohoku Univ.）

*BCM：Building-Cube Method

LEE* for Fan Noise Propagation to Cabin
（Courtesy of JAXA）

*LEE：Linearized Euler Equation

JAXA Japan Aerospace Exploration Agency   TOHOKU UNIVERSITY

MITSUBISHI AIRCRAFT CORPORATION   MITSUBISHI AIRCRAFT CORP. PROPRIETARY   NA231103 NC   20/

Future prospect on EFD and CFD

Issues to be improved :

EFD
  ・Lead time for test model preparation : design/manufacturing
  ・Data productivity : per day/per test run
  ・Accuracy of measurement : drag
  ・Compensation for the effects due to flow condition differences ： Re/facility etc.
CFD
  ・Lead time for calculation model preparation : geometry/grid generation
  ・Data productivity : hardware, algorithm

Further application :

EFD
  ・Extension to flight test : optical measurement/noise source survey
  ・Unsteady measurement : PSP for buffet
CFD
  ・Integration of multi-flow field : internal/external flow of equipment
  ・Unsteady simulation : dynamic stability/noise prediction

MITSUBISHI AIRCRAFT CORPORATION   MITSUBISHI AIRCRAFT CORP. PROPRIETARY   NA231103 NC   21/

Flying into the future.

Mitsubishi Regional Jet, a new concept from Japan
for the skies of the world.

http://www.mrj-japan.com/

MITSUBISHI AIRCRAFT CORPORATION   MITSUBISHI AIRCRAFT CORP. PROPRIETARY   NA231103 NC   22/

DAHWIN - Digital/Analog-Hybrid Wind Tunnel

Shigeya Watanabe
Shigeru Kuchi-ishi
Keiichi Murakami
Atsushi Hashimoto
Hiroyuki Kato
Tatsuya Yamashita
Kanako Yasue
Kentaro Imagawa

Japan Aerospace Exploration Agency (JAXA)
Chofu, Tokyo 182-8522
 Japan
watanabe.shigeya@jaxa.jp

 Hideji Saiki
 Jyun Ogino

Ryoyu Systems Co., Ltd.
Nagoya, Aichi 464-0075
Japan
jyun_ogino@mail.ryoyu.co.jp

Abstract

The development of 'Digital/Analog-Hybrid WINd tunnel (DAHWIN),' which is an innovative system integrating CFD (Computational Fluid Dynamics) with EFD (Experimental Fluid Dynamics), is presented. The aim of the system is to improve efficiency, accuracy, and reliability of aerodynamic characteristics evaluation in aerospace vehicle developments through mutual support between EFD and CFD. DAHWIN is constructed based on two large facilities, JAXA 2m x 2m Transonic Wind Tunnel for EFD and JAXA Supercomputer System for CFD. The function of this system consists of optimization of test planning, an accurate correction of the wind tunnel wall and support interaction effects, the most probable aerodynamic characteristics estimation based on both EFD and CFD data, and so forth. Key technical challenges in the system development, such as an automatic grid generator, high-speed CFD solver, and a high-speed data processing technique for image measurement data, are addressed. Some preliminary applications of DAHWIN to practical wind tunnel tests showed the usefulness and reliability of DAHWIN.

Key words: EFD, CFD, Wind Tunnel, Database, Data Fusion

Introduction

In order to evaluate aerodynamic characteristics of aircraft and aerospace vehicles, experimental techniques using wind tunnels (experimental fluid dynamics: EFD) were mainly employed as well as theoretical methods till 1970's. However, since then, computational fluid dynamics (CFD) has been gaining its importance in the aerodynamic prediction with significant advances of CFD techniques and processing speed of computers. At present, it could be addressed that the importance of CFD in aerodynamic design is comparable to that of EFD.

On the other hand, still now, EFD and CFD are usually conducted separately by different groups of experts with relatively weak interaction and collaboration. This situation in the aerodynamic characteristics prediction indicates that as the next step, synergy of EFD/CFD integration is expected to improve the prediction techniques further.

Researches aiming at such real integration of the two techniques do not seem to be matured so far while some trials have been reported with certain degree of success at laboratory condition [1-2]. In particular, practical applications of EFD/CFD integration in industrial aerospace development are very few except the system called ViDI (Virtual Diagnostics Interface System) developed by NASA Langley Research Center [3]. Although the ViDI system was originally developed to aid pretest design of optical fluid diagnostic techniques such as Pressure-Sensitive Paint (PSP), it has the capability of real time comparisons of experimental results with pretest CFD calculations using 3-D graphic feature called Live View 3D. However, the comparisons are done without the EFD/CFD integration only when CFD data are available from users.

Towards the development of future innovative aerodynamic prediction technologies, Japan Aerospace Exploration Agency (JAXA), is developing a practical EFD/CFD integration system called the Digital/Analog Hybrid WINd tunnel (DAHWIN), where 'Digital' and 'Analog' denote CFD and EFD (or wind tunnel), respectively. The aim of this system is to improve effectiveness, accuracy, and reliability of wind tunnel tests by jointly utilizing CFD as well as some advanced techniques for the EFD/CFD integration. Furthermore, this system is to be used for reliable and accurate prediction of aerodynamic characteristics at real flight condition, based on both ground-based EFD and CFD.

This paper presents the system concept of DAHWIN and technical challenges which should be overcome in the development of this system. Also, described are details of the subsystems and individual technical issues such as a common data format applied to both EFD and CFD data, real-time comparison between wind tunnel test data and pretest CFD data, and so forth. Since the development of DAHWIN is at the final stage, its function, effectiveness, and reliability are being evaluated through applications to some real wind tunnel tests of both aircraft and a space vehicle. The findings in the evaluations are presented, mentioning future upgrades of the system.

Technical Issues in EFD and CFD

For describing the motivation of development of DAHWIN, technical issues in both EFD and CFD, which should be overcome, are surveyed below.

Individual issues in EFD and CFD

EFD using wind tunnels has problems to be solved, such as 1) the compensation of effects due to some differences between flight and wind tunnel test conditions, especially Reynolds number effect, 2) limited flow properties which can be measured by usual measurement techniques, 3) relatively long lead time before a wind tunnel test campaign including model manufacturing and measurement apparatus development, and so forth.

On the other hand, technical issues of CFD include 1) improvement of reliability of calculation results, especially in complex flow cases with turbulence, boundary layer transition, separation, and chemical reaction, 2) relatively long computational time for high-fidelity analysis even using state-of-the-art supercomputers, and 3) difficult, time-consuming grid generation around complex configuration.

In order to solve the remaining tough technical problems described above, some break-through technologies using advanced EFD/CFD integration techniques should be innovated.

Issues in comparison between EFD and CFD

The advancement of CFD has been relying on rigorous comparisons with comparative experimental results for improving accuracy and evaluating applicable range of CFD in terms of flow conditions and model configurations. However, such comparisons are usually conducted by only one side, that is, EFD or CFD side, without a mutual collaboration between both sides. Therefore, it is common that the comparisons are affected by slight discrepancies in flow conditions, model attitude, and model geometry, which are caused by uncertainty of wind tunnel flow condition setting, deflection of balance and sting, and model deformation due to aerodynamic load in wind tunnel tests. In some cases, the experimental data reductions neglect aerodynamic interference

effects caused by the wind tunnel wall and model support system. On the other hand, a grid for CFD may not take the wall and support into account. Also, in general, it is difficult to match boundary layer transition location between EFD and CFD. Such various discrepancies encountered in the EFD/CFD comparisons make it difficult to identify problems existing in the CFD technique applied, disturbing the advancement of CFD. To overcome this undesirable situation, a platform which always guarantees the EFD/CFD comparisons at an identical condition is definitely required.

Issues in terms of time-span difference

In general, the time period required for the wind tunnel test model design and manufacturing is long while CFD needs less time for the grid generation as pre-processing. It should be noted that the grid generation time could be significant when many model configurations with various deflections of aerodynamic surfaces have to be treated. On contrary, the computational time required for high fidelity CFD at a flow condition is much longer than data acquisition time for a test point in a wind tunnel test. In addition, recent image-based measurement techniques employed in wind tunnel tests need a relatively long time for the data reduction of huge volume of image data. These differences in time-span between EFD and CFD pose a serious problem when both EFD and CFD should be conducted in a concurrent manner. Therefore, it is needed to shorten the model manufacturing time, the data reduction time of the image-based measurement methods, and the time for the grid generation and high-fidelity calculation of CFD for the concurrent collaboration.

System Concept of DAHWIN

Objectives

The objectives to develop DAHWIN are to comprehensively solve the issues mentioned above by effectively utilizing both EFD and CFD capabilities, resulting in the reduction of design time, cost, and risk and the improvement of design data accuracy and reliability in the aircraft and aerospace vehicle development. In particular, near-term targets are to apply this system to the developments of Japanese regional jet, MRJ (Mitsubishi Regional Jet), which is under development towards the first flight. Also, it is expected that this innovative system promotes the advancement of the CFD technology, leading to acquiring competitiveness of Japan in the design of aircraft against the other foreign countries. Furthermore, it could be possible that DAHWIN will become a typical system of the integration of experiments and numerical simulations, facilitating creation of similar systems in the other technical fields, such as structure, engine, material, chemistry, medicine, biology, and so forth.

Users and functions of the system

We are expecting aerospace engineers as well as researchers as users of DAHWIN. The aerospace engineers of the heavy industries consist of experimental specialists who work near the wind tunnel itself and aerodynamic designers who usually stay at the office of their company far from the wind tunnel. For the designers at remote locations, nearly real-time data transfer capability is incorporated in this system.

Firstly, the system is applied to JAXA 2 m x 2 m Transonic Wind Tunnel (JAXA TWT1) since needs of the industrial users are higher than those to the other JAXA's wind tunnels covering different speed ranges. Another reason why this tunnel was chosen is that CFD calculation is relatively easy at cruise condition of transport-type aircraft with a simple configuration since the flow is attached to the vehicle with no large separations in contrast to the low-speed flow around a high-lift configuration at stall condition with significant separations. For the next step of the system development, the present system will be applied to the other tunnels such as JAXA 1 m x 1 m Supersonic Wind Tunnel (JAXA SWT1) and 6.5 m x 5.5 m Low-speed Wind Tunnel (JAXA LWT1) in future.

Based on the survey of the technical challenges in the previous chapter and the requirements from the users of the wind tunnels and CFD, the functions of the hybrid wind tunnel were specified as follows:

- ✓ Test planning optimization using pretest CFD calculations in the point of view of the improvement of efficiency as well as the reduction of risk in wind tunnel tests.
- ✓ CAD-based wind tunnel test setting simulation for facilitating the planning of optical aerodynamic measurements before wind tunnel tests.
- ✓ Accurate corrections of aerodynamic interferences due to the wind tunnel wall and model support system using CFD to improve the accuracy and reliability of wind tunnel test data towards the aerodynamic characteristics prediction at real flight condition.

✓ Most probable data estimation using both wind tunnel and CFD data considering each error level and reliability.
✓ Nearly real-time visualization and comparison of EFD/CFD data and its transfer to allow the remote users the wind tunnel data evaluation in a timely manner, called 'Virtual participation in wind tunnel test.'
✓ Accelerated data processing of the optical flow measurement techniques such as PIV (Particle Image Velocimetry), PSP (Pressure-Sensitive Paint), and model deformation measurement.
✓ Refinement and optimization of the CFD parameters like turbulence model and grid.
✓ Establishment of a database which consists of EFD and CFD data at perfectly identical condition in order to facilitate improvement of CFD technology.

For enabling the functions shown above, a fast CFD solver in conjunction with an automatic grid generation tool should be developed for the 'digital' wind tunnel as one of major subsystems of DARWIN.

System concept

Figure 1 shows the system concept of DAHWIN to realize the functions described in the previous section. After defining a wind tunnel test model geometry in the course of the vehicle configuration design, the 'digital' wind tunnel, the right hand side of the figure, conducts pretest CFD calculations in two cases, that is, a test model alone and a configuration including both test model and wind tunnel with a model support system. Then, the CFD results in both cases are transferred to the 'analog' wind tunnel, that is, the conventional wind tunnel shown in the left-hand side of the figure. The CFD data are utilized for the optimization of the test planning and model design. Also, the effects of wall and sting interferences can be corrected using the CFD data with and without wall and sting. In the wind tunnel test phase, optical aerodynamic measurement data as well as ordinary measurement data are reduced in a nearly real-time fashion, which are transferred to the remote users as well as the users working at the wind tunnel. The wind tunnel data including the model deformation are sent back to the digital wind tunnel for a revised, detailed CFD analysis for the CFD parameter optimizations, taking the model deformation data into account. At the finish of the wind tunnel test as well as the revised CFD calculations, we can obtain both EFD and CFD data at an identical condition in terms of flow and boundary conditions. Finally, the two data are combined into the most probable aerodynamic characteristics data by using data assimilation (or fusion) techniques, which are stored in the EFD/CFD–combined database.

As shown in Fig. 2, the initial goal of the operation time sequence of the hybrid wind tunnel is that one or two months prior to the start of a wind tunnel test campaign, the pretest CFD is started and the final whole data after the data assimilation are handed to the user about two weeks after finishing the wind tunnel test. In future, the time after the completion of wind tunnel test should be shorten to several days to reduce the aerodynamic design time. It was suggested that this goal can be almost attained through preliminary applications of DAHWIN as presented in one of following chapters.
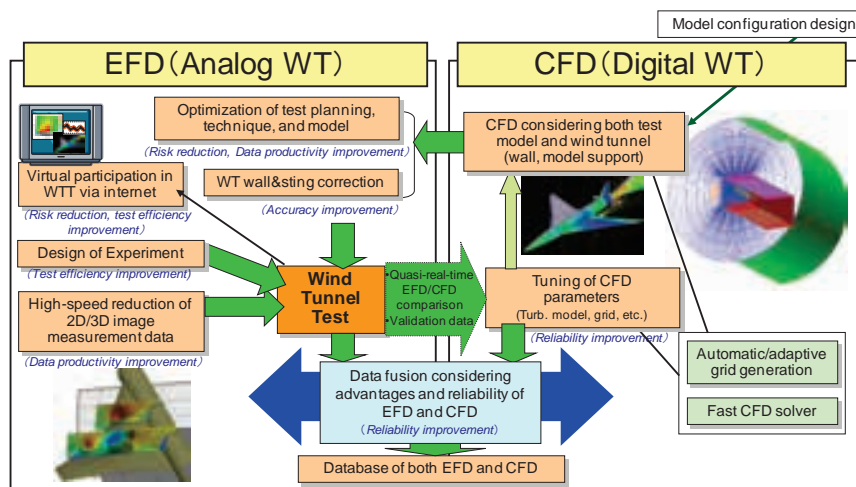

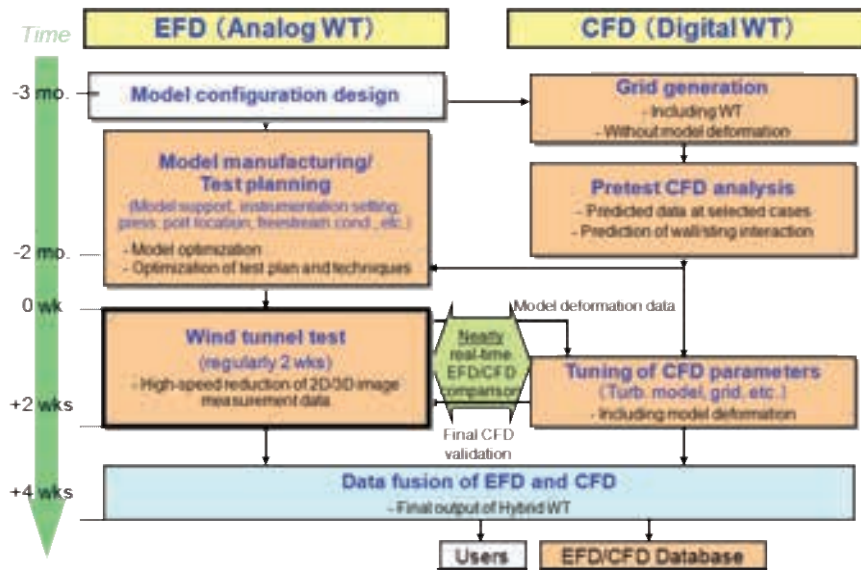**Figure 1 System concept of the Digital/Analog-Hybrid Wind Tunnel (DAHWIN).**

Figure 2 Operation sequence of DAHWIN.

System architecture

Figure 3 presents the system architecture of the hybrid wind tunnel. This system consists of seven servers (web, control, visualization, CAD, SAN, backup, and wind tunnel (WT) servers) and a data storage with SAS and SATA hard disk drives which are connected with each other through 1 Gigabit-Ethernet. The users as well as system administrators have access to this system through the web server. This architecture might be changed or upgraded till the completion of the DAHWIN development through future evaluations of the system in order to keep system reliability and to increase customer satisfaction.
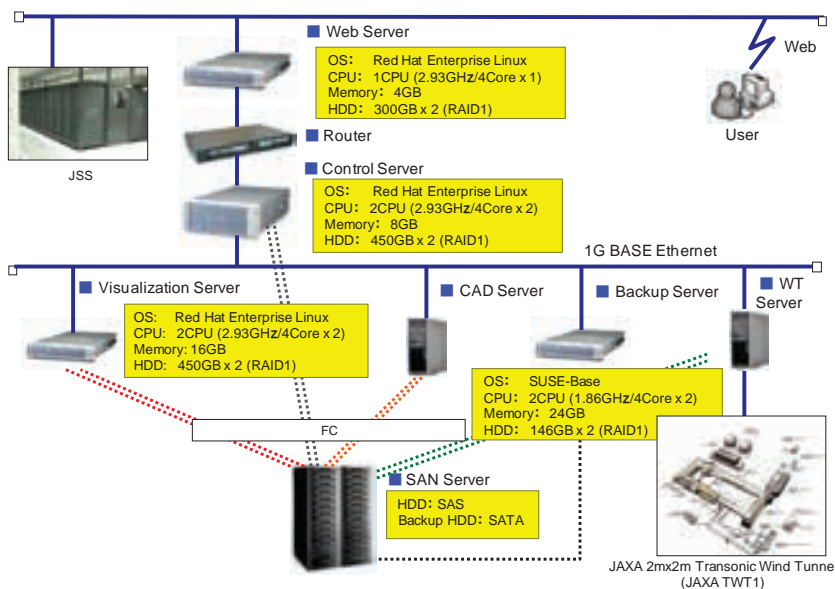

Figure 3 System architecture of DAHWIN.

For the CFD calculations, the supercomputer for the common use in JAXA, JAXA Supercomputer System (JSS), is used as the main hardware of the digital wind tunnel. On the other hand, as the main hardware of the analog wind tunnel, JAXA TWT1 with its data acquisition/processing system is used in conjunction with stand-alone optical measurement systems like PSP, PIV, and model deformation measurement to conduct wind tunnel tests.

First, the EFD/CFD data produced by the analog and digital wind tunnels are converted into a common data format HDF5 (Hierarchical Data Format), which was adopted to facilitate the comparison between original EFD and CFD data with different data format. Next, after the data format conversion, the data are stored in the SAS data storage while the metadata are extracted from the original data and then stored in the database (DB) in the data storage for search purpose. Also, the converted data are sent to the visualization server for displaying the EFD data in comparison with the corresponding pretest CFD data which are automatically chosen in an easy and correct way through database search based on model name, flow conditions, model attitude, and so forth. This integrated visualization feature helps the wind tunnel user to evaluate the validity of wind tunnel data at real-time basis and to understand the overall flowfield which cannot be measured in conventional wind tunnel tests.

The CAD server is used for the wind tunnel test setting simulation [4] before wind tunnel tests and other purposes. Figure 4 shows an example of pretest check of camera field of view and interference between wind tunnel and optical measurement instruments. This feature is useful to reduce time for design of wind tunnel model and optical measurement setup and risk of invalid setting, possibly eliminating an onsite check using real instruments.
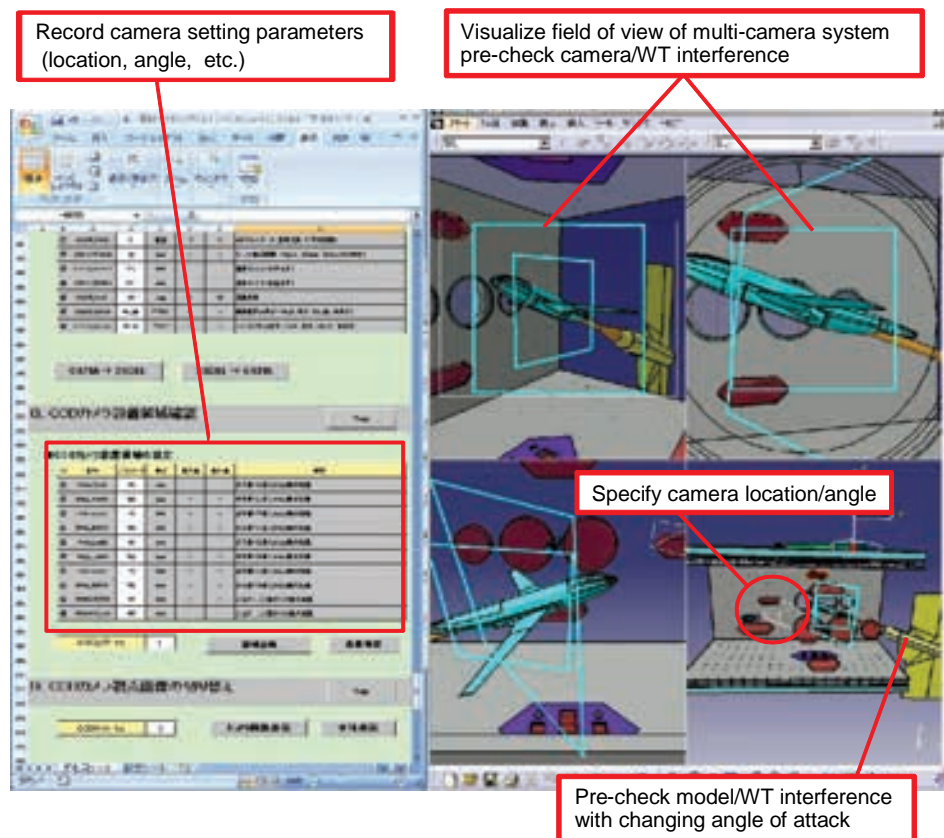

Figure 4 CAD-based wind tunnel test setting simulation.

Key Challenges in Development of DAHWIN

Fast CFD solver with automatic grid generator
For the development of the digital wind tunnel, both features of high-speed performance and high degree of accuracy must be accomplished simultaneously for realizing the timely use of DAHWIN and the high-fidelity wind tunnel data corrections. Mainly, a newly-developed fast CFD solver called FaSTAR (FaST Aerodynamic Routine) for unstructured grid [5] is used in combination with an automatic unstructured grid generator, HexaGrid, using the Cartesian grid generation technique [6-7]. In addition, an unstructured-grid Navier-Stokes solver called TAS (Tohoku University Aerodynamic Simulation) [8], which has been applied to some real aircraft developments such as MRJ, can be used with the user interface being improved as a backup in case that reliability is more emphasized than calculation speed.

Using HexaGrid, it is possible to generate a grid with twelve million cells automatically within an hour by a 64-bit PC around a generic civil transport configuration named NASA CRM as shown in Fig. 5. The generator can densely gather the grid into the regions where a fine grid is needed, such as around the model surface and wing trailing edge. The generated grid has a quality similar to that by the grid generator MEGG3D [9] originally developed for TAS while the number of grid points is comparable between the newly generated grid and the TAS grid by MEGG3D. Difference in drag coefficient between TAS results using the two different grids explained above is about 5 counts ($\Delta CD = 0.0005$) [10], indicating reasonable quality of the grid by HexaGrid for this type of a simple wing-body combination.

An example of grid generation including a wind tunnel model, a model support, and wind tunnel walls is presented in Fig. 6. This result shows that HexaGrid has an ability to automatically generate this type of grid required for the wind tunnel wall/support interference correction based on CFD.

Considering the use of the new CFD solver, FaSTAR, in the pretest CFD calculations, target of its calculation speed performance was set to an hour per case for a grid with ten million cells using a hundred CPUs of JSS. Accuracy of drag coefficient should be less than 10 counts to be used for an industrial vehicle development. Governing equation of FaSTAR can be chosen from Euler and Reynolds-Averaged Navier Stokes (RANS). As turbulence model, Spalart-Allmaras, SST models or so were implemented with their important variations. Although the FaSTAR is still under development at present, its preliminary version has been completed as a RANS solver with two convergence acceleration techniques, that is, the multi-grid technique and GMRES. The preliminary application of FaSTAR to NASA CRM model showed that the difference in drag coefficient between the results FaSTAR and TAS is around 8 counts [10], illustrating acceptable accuracy of this new solver. Incorporating two convergence acceleration techniques shown above has realized four times faster calculation than before, illustrating that the target of calculation speed was accomplished.
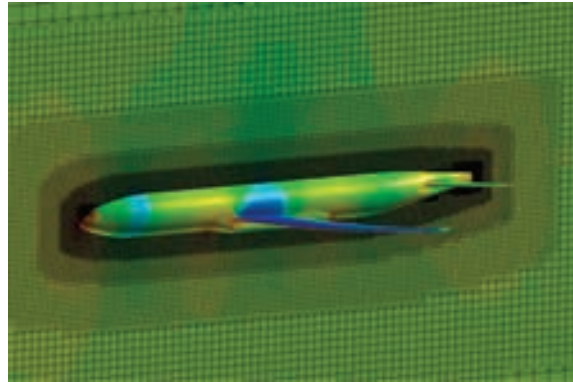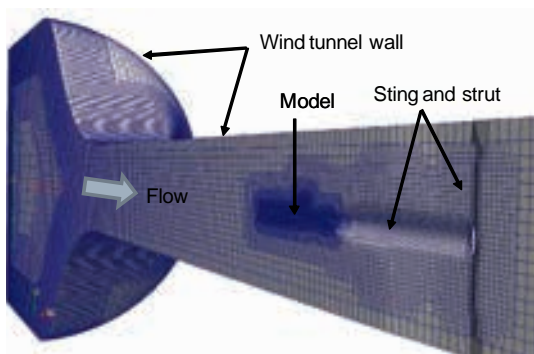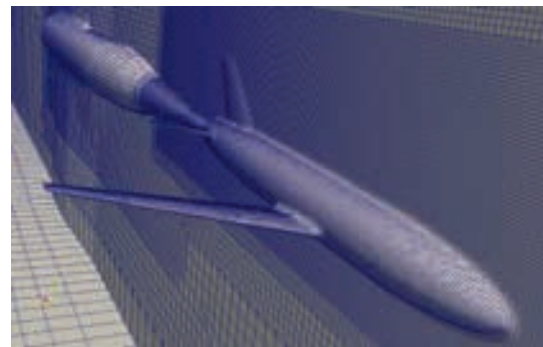

Figure 5 Grid for NASA CRM model generated by HexaGrid (cell number: 12 millions).

(a) Grid covering flow path of JAXA TWT1.   (b) Grid around model and sting.

Figure 6 An example of automatically generated grid around a generic transport model (ONERA-M5) inside JAXA 2m x 2m Transonic Wind Tunnel (JAXA TWT1).

Using the Digital Wind Tunnel, it is possible to count the aerodynamic coefficients of each part of a model, which are constructed from STL data of fuselage, wing, nacelle, pylon, model support, and so on. Therefore, users can examine the influence of each part on aerodynamic characteristics in the pretest CFD calculations.

Before manufacturing a wind tunnel test model and support stings, the digital wind tunnel can be used to evaluate the effects of the configuration of model support on the flowfield around the model. An example of grid generation including two different types of model support, that is, blade-type sting and straight sting, is shown in Fig. 7. Also, corresponding RANS calculation results of pressure distribution (Cp map) on surfaces of the model and sting are shown in Fig. 8. The results of grid generation suggest the robustness of HexaGrid (Fig. 7) while the results of the RANS calculations clearly indicate the model support effect which is seen on the model surface pressure distribution near the junction of the model and support (Fig. 8). Based on these results, the users can choose the best configuration of model support sting without manufacturing several different stings to check the effects of the support configuration during wind tunnel tests. It is significant that this feature of the digital wind tunnel allows aerospace vehicle manufacturers to reduce time and cost for wind tunnel tests during vehicle developments.
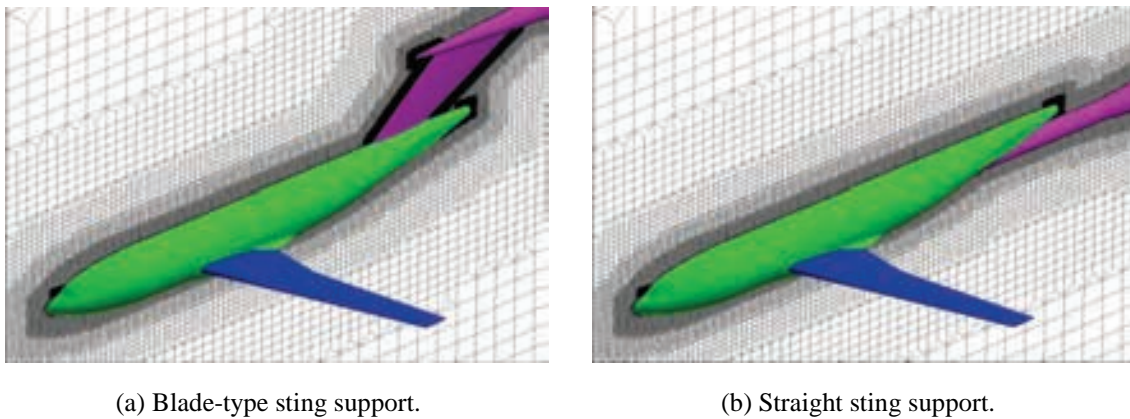

| (a) Blade-type sting support. | (b) Straight sting support. |

Figure 7 An example of automatically generated grid including two different model supports around the DLR F6-FX2B model.

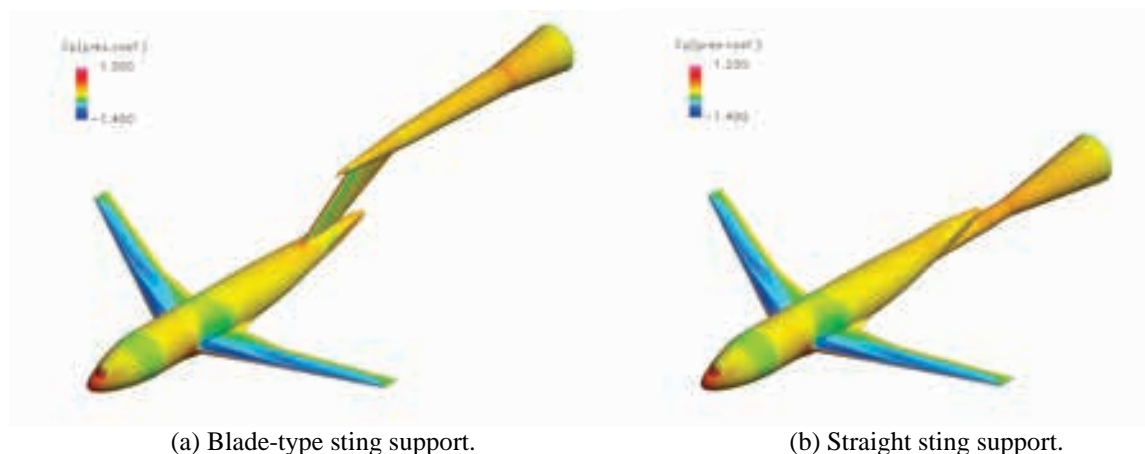| (a) Blade-type sting support. | (b) Straight sting support. |

Figure 8 Calculation results of pressure distribution (Cp) on surfaces of the DLR F6-FX2B model.

A newly-developed feature of the digital wind tunnel is the fluid/structure interaction analysis. As described above, the wind tunnel model is deformed by aerodynamic forces acting on the model during a wind tunnel run. As shown in Fig. 9, in this interaction analysis, firstly, a CFD analysis using FaSTAR is conducted for an original configuration with no deformation. Secondly, the surface pressure distribution data obtained by CFD are used to calculate the model deformation by a structure analysis using NASTRAN, which has been widely used in the field of structure analysis. In this structure analysis, the model is assumed to be solid, ignoring the

structure inside the model. Thirdly, based on the model deformation data, the CFD grid on the model surface and in flow field is deformed. Then this loop is repeated until a converged result in terms of both pressure distribution and model deformation is acquired. An example of this analysis for a deformed aircraft wing shown in Fig. 9 indicates that two or three loops of analysis are enough to reach a converged result. Using this feature, we can obtain the pretest CFD data which roughly reflect the model deformation, so the comparison of the pretest CFD data with wind tunnel test data during a wind tunnel test becomes more accurate and reliable, decreasing the need of a further detailed CFD analysis which reflects the model deformation measurement data. In future, a test model will be manufactured, considering the model deformation at wind tunnel test so as to form the real flight configuration under the aerodynamic load at wind tunnel test.
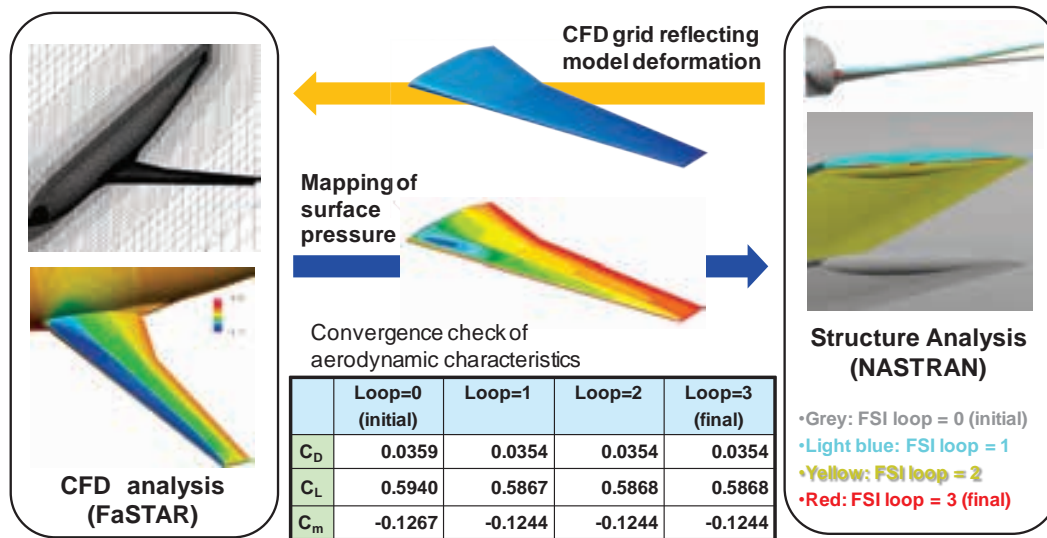

CFD grid reflecting model deformation

Mapping of surface pressure

Convergence check of aerodynamic characteristics

	Loop=0 (initial)	Loop=1	Loop=2	Loop=3 (final)
C_D	0.0359	0.0354	0.0354	0.0354
C_L	0.5940	0.5867	0.5868	0.5868
C_m	-0.1267	-0.1244	-0.1244	-0.1244

CFD analysis (FaSTAR)

Structure Analysis (NASTRAN)

•Grey: FSI loop = 0 (initial)
•Light blue: FSI loop = 1
•Yellow: FSI loop = 2
•Red: FSI loop = 3 (final)

Figure 9 Procedure of fluid/structure interaction analysis.

Acceleration of optical measurement image data processing

Among many types of flow diagnostics in wind tunnels, PIV is one of the measurement techniques which need heavy data processing. Therefore, the acceleration of the PIV data reduction was included in the development of DAHWIN, which is one of key challenges in the improvement of the analog wind tunnel. As shown in Fig. 10, the data processing for a thousand of velocity vector maps usually takes several hours using a PC cluster with eight CPUs while the processing time depends on the choice of data processing algorithm. The goal of the process acceleration in the hybrid wind tunnel is to reduce the processing time by more than one order, resulting in several to ten minutes for the same data processing. As the result, the time needed for PIV becomes not so far from the time for conventional measurement like force balance or pressure measurement, enabling the nearly real-time comparison between the PIV data and corresponding pretest CFD data. To achieve this need, we chose Cell/B. E. as accelerator based on a preliminary evaluation. The system developed with two Cell/B. E. boards resulted in 25 times faster data processing than that of the original data processing system using a PC cluster with eight CPUs [11]. This result means that the goal of processing time less than ten minutes was attained using this accelerator.

Also, acceleration of data processing of PSP measurement [12-13] is being pursued since it is impossible to conduct the processing in a quasi-real-time manner. To overcome this problem, some manual processes such as the detection of position markers on a wind tunnel model surface have to be replaced by new automatic processes.

Model deformation measurement technique using stereo view of position markers on a test model with two cameras was also modified for automation. Similar to PSP, a manual process for finding markers on camera images was successfully automated in order to realize quasi-real-time data reduction.
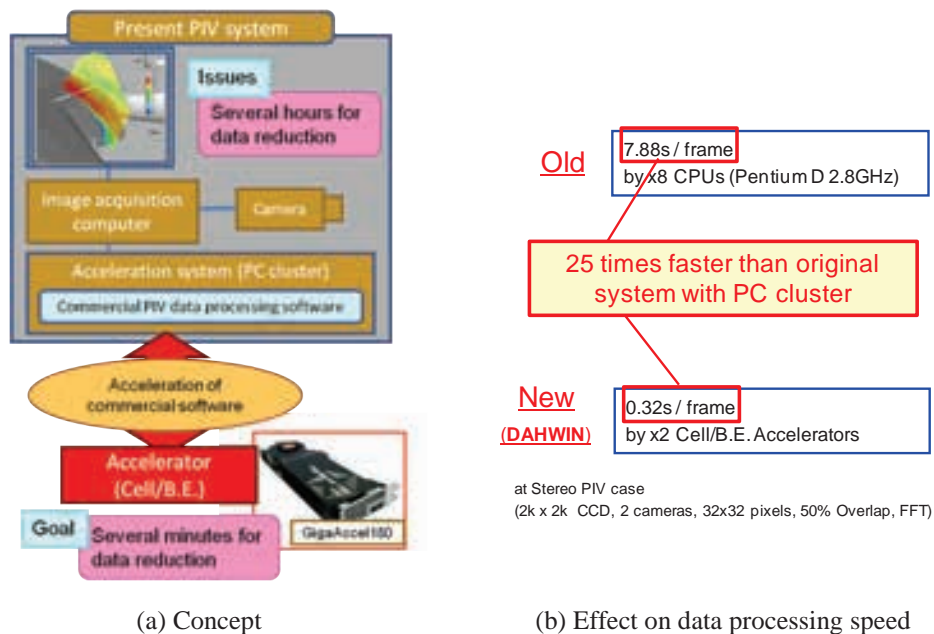
(a) Concept   (b) Effect on data processing speed

Figure 10 Acceleration of the PIV data processing via accelerator.

Examples of Preliminary Applications of DAHWIN

DAHWIN at the final development stage was applied to a series of wind tunnel tests performed at JAXA TWT1 in order to evaluate the usefulness and reliability of the system and find technical items for further improvements towards the complete system. The results are outlined below.

Civil transport-type model test

Firstly, DAHWIN was applied to the wind tunnel test using a civil transport-type standard model (DLR-F6) [14] as shown in Fig. 11. In this test, optical measurement data of PSP and PIV were obtained as well as six-component aerodynamic force and moment and pointwise pressure data. A total of 42 pretest CFD cases (a maximum cell number of 24 millions) were arranged and performed within two weeks. The force/pressure port data obtained by the measurement apparatus were sent to the system and immediately plotted together with the pretest CFD data as seen in Fig. 11 (c). The pretest CFD datasets that have the same flow properties as those in experimental conditions are automatically chosen by the data search function in the database. Real time comparison of the experimental data with the pretest CFD data enables to check the validity of the measurement data during the test period and to rearrange the plan of the subsequent test cases. The comparison of data acquired by PSP and PIV with CFD data is also possible during testing. By the speed-up of the data reduction as described in the previous chapter, these processed data can be obtained within ten minutes after the measurement. As depicted in Fig. 11 (d), by comparing the PSP data with CFD, we can qualitatively check the degree of measurement error and notice significant problems of the measurement techniques as well as the CFD calculations.

Reentry capsule configuration test

DAHWIN was also applied to a wind tunnel test for a reentry capsule configuration (Fig. 12 (a)) which was conducted as a part of conceptual design of a future space transportation system. Pretest CFD computations of 174 cases (a maximum cell number of 9 millions) were performed within two weeks (Fig. 12 (b)). Computations including a model support system were also made to correct the support interaction effect on the wind tunnel data. At the present system, this was simply done by adding the difference of CFD aerodynamic coefficient data between with and without the support system to the test data. Figure 12 (c) is an example of drag polar plot displayed on the monitoring screen. In this case, it seems that the effect of support interaction was reasonably corrected, using the pretest CFD data. Although in the past, wind tunnel data correction was usually made after the completion of wind tunnel test, it can be made during the test by using DAHWIN. This means that we can readily examine wind tunnel test data without the sting interaction effect.

In this test, CFD calculations with different turbulence models were conducted using the fast CFD solver for the cases where the disagreement between wind tunnel test data and CFD data was intolerable. This application of DAHWIN illustrates that it is possible to evaluate the wind tunnel data in comparison with different CFD data in a concurrent manner.
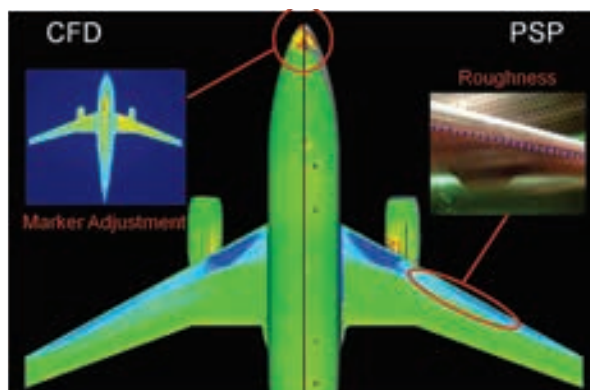

(a) DLR-F6 model mounted in the test section of JAXA TWT1.

(b) Display setting for operation (balance, pressure sensor, PIV, PSP compared with CFD).
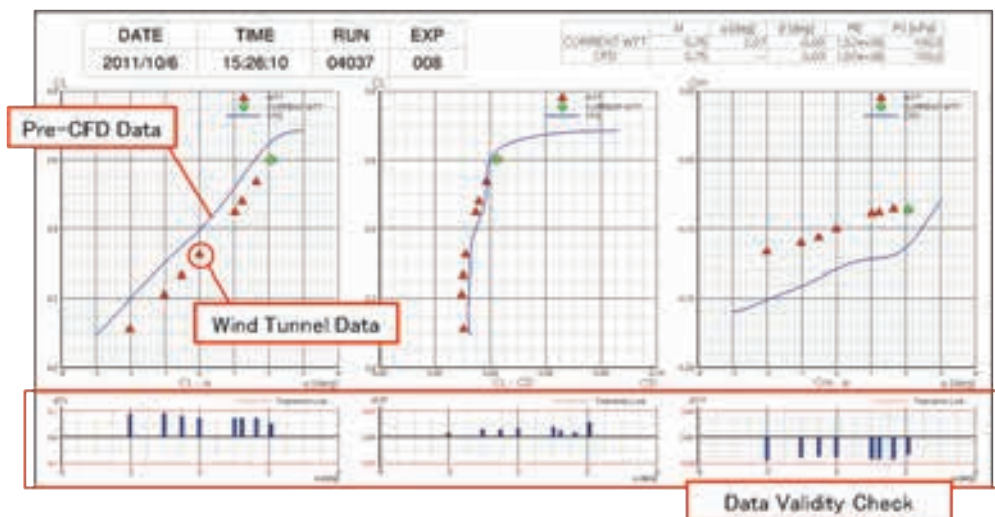
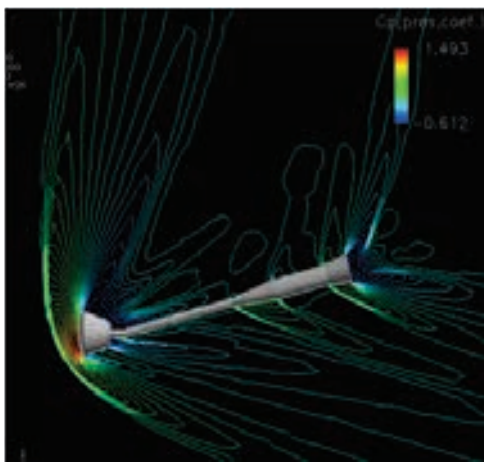(c) Balance measurement monitoring screen (EFD and CFD with difference (Δ)).

(d) Comparison of pressure distribution by EFD (PSP) and CFD and error sources of PSP measurement.
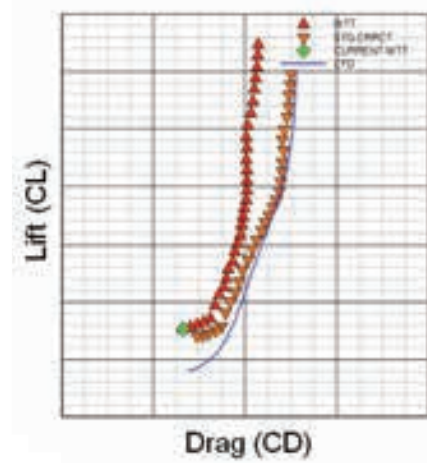
Figure 11 DLR-F6 configuration tests at JAXA TWT1.

(a) Capsule model in JAXA TWT1.

(b) Pretest CFD results including model support system.

(c) Drag polar plots (comparison between WT data with/without support interference correction).

Figure 12 Reentry capsule configuration tests at JAXA TWT1.

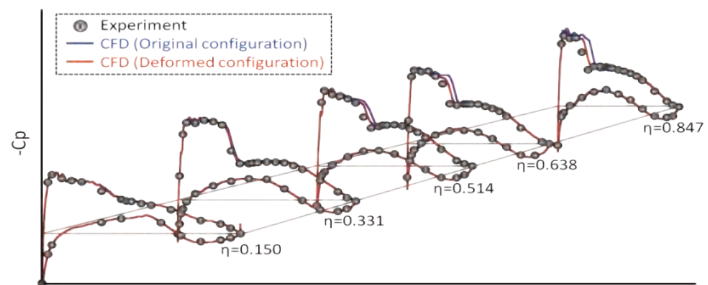## High-fidelity CFD using measurement data

Figure 13 shows an example of the high-fidelity computation using measurement data. Here, high-fidelity computation means that the CFD condition was rearranged so that it becomes almost identical to the experimental condition. In this case, CFD was performed, considering the effect of model deformation caused by aerodynamic load during wind tunnel testing. The model deformation measurement was made using stereo photogrammetry technique with markers located on wind tunnel model (Fig. 13 (a)) [15]. The information of the marker displacement is then used to deform the CFD model surface mesh by applying a simple deformation law with a polynomial approximation (Fig. 13 (b)). The volume mesh for the deformed configuration was obtained by modifying that of the original configuration using the surface influence method. The details of the numerical technique can be found in Ref. 16. As can be confirmed in Fig. 13 (c), the CFD pressure distribution on the main wing shows better agreement with the wind tunnel data when the effect of deformation is taken into account in CFD. The process of the present analysis (measurement data acquisition, surface/volume mesh deformation, and CFD execution) can be made automatically in the system if measurement data as well as pretest CFD data are available. In the complete system of DAHWIN, we will incorporate other conditions which should be matched between wind tunnel test and CFD, such as boundary layer transition location, to realize ideal EFD/CFD comparison under a perfectly matched condition.
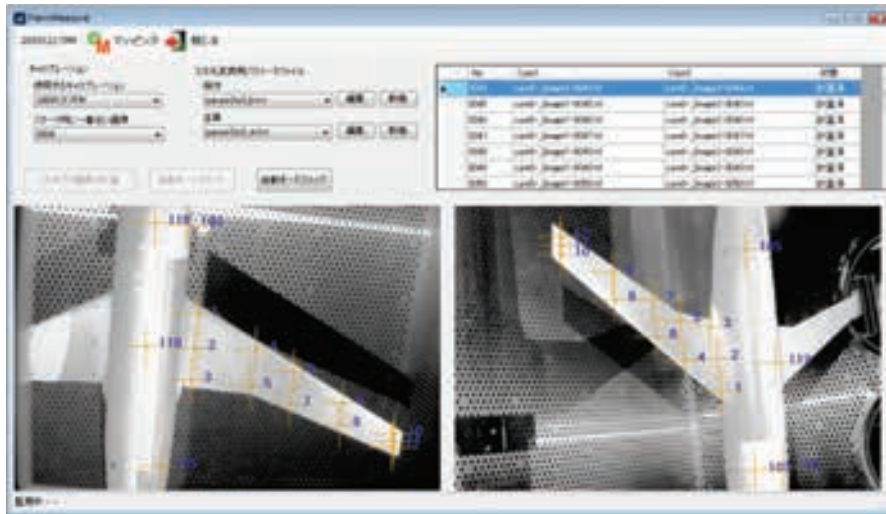
(a) GUI of model deformation measurement system.
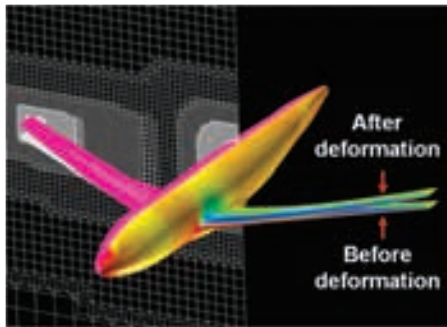
(b) CFD model geometry before/after
the deformation.

(c) Comparison of chord-wise static pressure distribution at
five spanwise locations on the main wing.

Figure 13 High-fidelity CFD using model deformation measurement data.

Concluding Remarks

The system concept and development status of the Digital/Analog Hybrid Wind Tunnel (DAHWIN) were presented, whose aim is to improve both EFD and CFD technologies by integrating CFD with EFD, resulting in a significant improvement in efficiency and accuracy of the aerodynamic design of aircraft and aerospace vehicles. At present, the system is at the final development stage, conducting evaluations in some actual wind tunnel test campaigns. The results of the preliminary evaluations showed that the system can be used effectively in industrial-type wind tunnel tests while suggesting various further improvements mainly to increase reliability.

Although the final goal of this type of system is to predict aerodynamic characteristics at the real flight conditions, the present system is mainly focusing on the wind tunnel test conditions since this is a prototype system for future advanced system. As the first step towards the final goal, ability of Reynolds number effect prediction by CFD is evaluated in a limited range of Reynolds number at JAXA TWT1. Then, the CFD solver will be tested in comparison with wind tunnel test results at real flight Reynolds number at a high Reynolds number transonic wind tunnel such as NTF (National Transonic Facility) of NASA and ETW (European Transonic Windtunnel) to confirm the ability of CFD to predict real flight aerodynamic characteristics. Utilizing available flight test data as well as newly acquired data for comparison with various wind tunnel and CFD data is also under consideration.

As mentioned earlier, the EFD/CFD integration technology has not been matured yet, so it is important for the rapid progress in the technology that many researchers and engineers of all types get together to solve various

technical challenges. Advanced techniques of the EFD/CFD integration, which will be developed through such cooperation, should be incorporated into DAHWIN in order to add extra values to this system.

Acknowledgements

References

[1] Hayase, T., Nisugi, K., and Shirai, A.: Numerical Realization for Analysis of Real Flows by Integrating Computation and Measurement. *Int. J. for Numerical Methods in Fluids* 47, pp. 543-559, 2005.

[2] Crowther, W. J, et al.: A Grid Enabled Wind Tunnel Test System (GEWiTTS): Towards Real Time Integration of CFD and Experiment. In Proc. 2nd Symposium on Integrating CFD and Experiments in Aerodynamics, 2005.

[3] Schwartz, R. J. and Fleming, G. A.: Virtual Diagnostics Interface: Real Time Comparison of Experimental Data and CFD Predictions for a NASA Ares I-Like Vehicle. In Proc. ICIASF 07, R56, 2007.

[4] Ogino, J., et al.: EFD Setting Simulation on Hybrid Wind Tunnel. In Proc. 42nd Fluid Dynamics Conference/Aerospace Numerical Simulation Symposium 2010, JSASS-2010-2079-F/A, 2010 (in Japanese).

[5] Hashimoto, A., Murakami, K., et al.: Toward the Fastest Unstructured CFD Code 'FaSTAR.' AIAA-2012-1075, 2012.

[6] Hashimoto, A., et al.: Drag Prediction on NASA CRM Using Automatic Hexahedra Grid Generation. AIAA Paper 2010-1417, 2010.

[7] Hashimoto, A., et al.: Validation of Fully Automatic Grid Generation Method on Aircraft Drag Prediction. AIAA-2010-4669, 2010.

[8] Nakahashi, K., Ito, Y., and Togashi, F.: Some Challenges of Realistic Flow Simulations by Unstructured Grid CFD. *Int. J. Numerical Methods in Fluids* 43(6-7), 2003.

[9] Ito, Y., et al.: Unstructured Mesh Generation Using MEGG3D - Mixed-Element Grid Generator in Three Dimensions. In Proc. the International Conf. on Numerical Geometry, Grid Generation and Scientific Computing (NUMGRID2008), pp. 5-11, 2008.

[10] Aoyama, T., et al.: Digital Wind Tunnel Consisting of Automatic Grid Generation Tool and Fast CFD Solver on Work Flow System. In Proc. 42nd Fluid Dynamics Conference/Aerospace Numerical Simulation Symposium 2010, JSASS-2010-2080-F/A, 2010 (in Japanese).

[11] Tomita, A., et al.: Quasi-Real Time Data Processing of Stereoscopic PIV using Cell/B. E. In Proc. 42nd Fluid Dynamics Conf., 2010 (in Japanese).

[12] Kurita, M., Mitsuo, K., Nakakita, K., Watanabe, S.: Multi-Camera Pressure-Sensitive Paint Measurement. AIAA-2010-4797, 2010.

[13] Kurita, M., Nakakita, K., Mitsuo, K., Watanabe, S.: Temperature Correction of Pressure-Sensitive Paint for Industrial Wind Tunnel Testing. *J. Aircraft* 43(5), pp. 1499-1505, 2006.

[14] Laflin, K. R., Vassberg, J. C., Wahls, R. A., Morrison, J. H., Brodersen, O., Rakowitz, M., Tinoco, E. N., and Godard, J.: Summary of Data from the Second AIAA CFD Drag Prediction Workshop. AIAA Paper

2004-0555, 2004.

[15] Kato, H., et al.: Model deformation measurement for wind tunnel tests using photogrammetry by makers. In Proc. 48th Aircraft Symposium. JSASS-2010-5032, 2010 (in Japanese).

[16] Yasue, K., Kuchi-ishi, S., Hashimoto, A., Murakami, K., Kato, H., Nakakita, K., Watanabe, S., and Hishida, M.: High-Fidelity CFD Simulation of a Wind Tunnel Model Using Model Deformation Data. In Proc. 15th International Forum on Aeroelasticity and Structural Dynamics, 2011.

Development of Digital Wind Tunnel as a Subsystem of JAXA Digital/Analog Hybrid Wind Tunnel

Keiichi Murakami[1]
Atsushi Hashimoto[1]
Manabu Hishida[2]
Paulus R. Lahur[3]
Akira Kunieda[4]
Shigeya Watanabe[5]

1) Numerical Analysis Group, Aerospace Research and Development Directorate
Japan Aerospace Explosion Agency (JAXA)
7-44-1, Jinndaiji Higashi-machi, Chofu-shi, Tokyo, 182-8522
Japan
murakami.keiichi@jaxa.jp
hashimoto.atsushi@jaxa.jp

2) Numerical Analysis Group, Aerospace Technology Dept., Engineering Solution Div.
Ryoyu Systems Co., Ltd.
6-19 Oye-cho, Minato-Ku, Nagoya, 455-0024
Japan
MANABU_HISHIDA@mail.ryoyu.co.jp

3) Meshing Technical Development Dept.
Research Center of Computational Mechanics, Inc. (RCCM)
Togoshi NI-Bldg., 1-7-1, Togoshi, Shinagawa-ku, Tokyo, 142-0041
Japan
lahur@oi.rccm.co.jp

4) Systems Div. 2, Systems Development Services Unit 2
Computer Engineering & Consulting, Ltd. (CEC)
Shirakawa 8th Bldg., 1-10-29, Marunouchi, Naka-ku, Nagoya, 460-0002
Japan
cecakira@chofu.jaxa.jp

5) Wind Tunnel Technology Center, Aerospace Research and Development Directorate
Japan Aerospace Explosion Agency (JAXA)
7-44-1, Jinndaiji Higashi-machi, Chofu-shi, Tokyo, 182-8522
Japan
watanabe.shigeya@jaxa.jp

Abstract

Japan Aerospace Exploration Agency (JAXA) is developing a practical Experimental Fluid Dynamics and Computational Fluid Dynamics (EFD/CFD) integration system called the Digital/Analog Hybrid Wind Tunnel (DAHWIN), where 'Digital' and 'Analog' denote CFD and EFD (or wind tunnel), respectively. The aim of this system is to improve effectiveness, accuracy, and reliability of wind tunnel tests by jointly utilizing CFD as well

as some advanced techniques for the EFD/CFD integration. For the development of the Digital Wind Tunnel (DWT), both features of high-speed performance and high degree of accuracy must be accomplished simultaneously for realizing the timely use of the DAHWIN system and high-fidelity wind tunnel data corrections. In this paper, several functions of the DWT and a newly-developed fast CFD routine for the DWT are introduced.

Key words: digital wind tunnel, computational fluid dynamics

Introduction

One of the main features of the Digital/Analog Hybrid Wind Tunnel [1] named DAHWIN is quasi real-time visualization of CFD and wind tunnel data during the test, so that we can immediately check the measured data comparing with the CFD result. The CFD data is prepared in advance before the testing and huge parametric study of Mach number and angle of attack is necessary. Therefore, we need a fast CFD tools to improve the productivity to integrate the CFD and EFD.

During wind tunnel test campaign, approximately 200 aerodynamic data are obtained every day. The campaign continues for 8 days in general. Therefore, the total 1600 data are obtained in one campaign. Since it is difficult to carry out CFD for all cases with the current high performance computer technologies, we set our target as 1/5 data of them. If we carry out the CFD in 20 days, the required speed is approximately one hour per case. In order to achieve one hour computation time per case, we have newly developed a fast CFD codes.

For the CFD side, the goal is to reduce the simulation cycle time to the order of hours as mentioned above. The essential technique to achieve this is through automatic grid generation. Automatic grid generation is a great improvement over manual grid generation in terms of ease-of-use and time consumed. A process that used to take weeks can be drastically reduced to an hour. Another important goal is the level of solution accuracy. It has to be sufficient enough to predict drag. This capability has been satisfactorily demonstrated in our participation in the 4th Drag Prediction Workshop (DPW4) [2-4], in which participants submitted their computation on a standard transonic aircraft model.

These automatic grid generation and CFD tools are installed into the DWT as a subsystem of the DAHWIN, and are called from several functions of DWT. The aerodynamic coefficients obtained by CFD are stored in the database of DAHWIN with the same format of wind tunnel test data to establish EFD and CFD database.

Installed CFD tools

For the development of the DWT, both features of high-speed performance and high degree of accuracy must be accomplished simultaneously in order to realize the timely use of the hybrid wind tunnel system and the high-fidelity wind tunnel data corrections. Mainly, a newly-developed fast CFD solver called FaSTAR (FaST Aerodynamic Routine) [5] for unstructured grid is installed in combination with an automatic unstructured grid generator, HexaGrid [6], using the Cartesian grid generation technique.

The grid made by HexaGrid is a hybrid between Cartesian grid and prismatic grid, where the Cartesian grid fills the far-field region and the prismatic grid fills the region around solid surface to resolve boundary layer flow. Cartesian grid was chosen due to its speed in filling computational domain, owing to the fact that it does not follow body surface, a property known as non-body-fitted. HexaGrid uses body surface data in STL (Stereo Lithography) format, which describes the surface as a set of triangles, and achieves grid generation that is tolerant to defects in STL representation. This brings us closer to full automation of the whole simulation process, and may reduce the order of simulation time to a few hours. Using HexaGrid, it is possible to generate a grid with twelve million cells automatically within an hour by a 64-bit PC around a generic civil transport configuration named NASA CRM as shown in Fig. 1.

FaSTAR consists of three parts: pre-processor, flow solver, and post-processor. The pre-processor implements a conversion of grid data format, a decomposition of calculation domain, a computation of cell volume and face area, and a reordering with Cuthill-Mackee. The flow solver compute flows, and the post-process make data for visualization. Governing equation of FaSTAR can be chosen from Euler and RANS. As turbulence model, Spalart-Allmaras, SST models or so were implemented. Accuracy of drag coefficient should be less than 10 counts (1 count means 0.0001 of aerodynamic coefficient) to be used for an industrial vehicle development. The portion of pre-process is relatively high in this code, and this is designed for efficient joint development and maintenance purpose.

Considering the use of the new CFD solver, FaSTAR, in the pretest CFD calculations, target of its calculation speed performance was set to an hour per case for a grid with ten million cells using a hundred CPUs of JAXA Supercomputer System (JSS). Although the FaSTAR is under development at present, its preliminary version has been completed as a RANS solver with two convergence acceleration techniques, that is, the multi-grid technique and GMRES. Incorporating two convergence acceleration techniques will be realized four times faster calculation than before, indicating that the target of calculation speed was accomplished.

For verification and validation of FaSTAR, we carry out several test computations. As preliminary test, the one-dimensional shock tube problems (Sod's problems) are solved. Then, the laminar and turbulent boundary layers are computed. These computational results are found to agree well with theoretical solutions. Since FaSTAR is used for comparison of aerodynamic coefficients with wind tunnel data, accuracy of aerodynamic prediction is important. Therefore, the accuracy of drag prediction with FaSTAR is validated by the DPW4 benchmark problems. The computation result of Cp distribution on the surface of NASA CRM with FaSTAR is shown in Fig. 1. Although we employ the hexahedra-based grid generated with HexaGrid, the computed drag coefficients generally agree with other results [5].
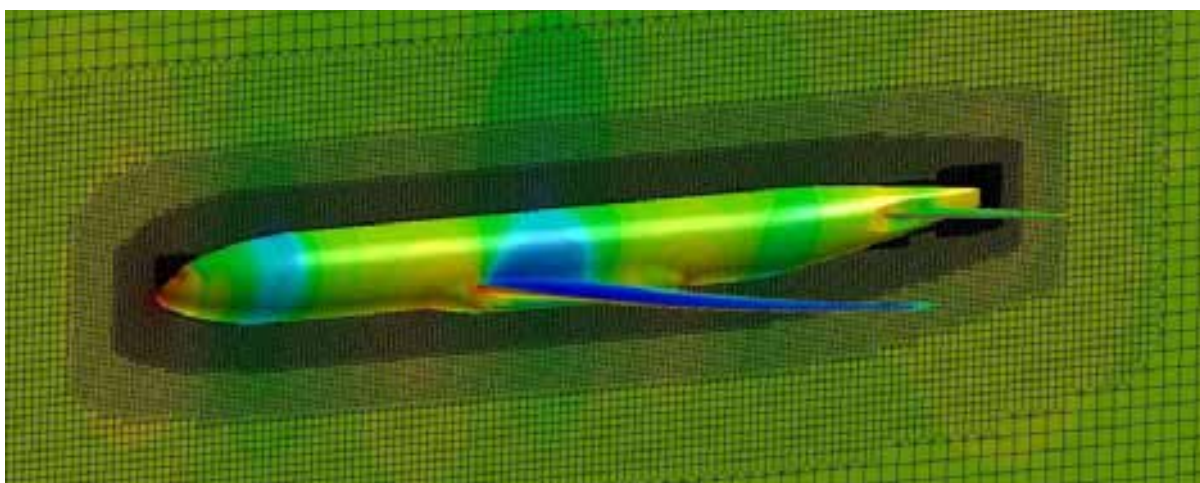

Figure 1. Computational grid and result of Cp distribution for NASA CRM.

Parametric CFD

The main function of DWT is a parametric CFD function, which is constructed from automatic workflow of grid generation, CFD calculation on JSS, and storing the results to database. The pretest CFD calculations are performed for the preparation of wind tunnel test with wind tunnel flow conditions of different Mach number, Reynolds number, and angle of attack. The number of pretest CFD cases is supposed to 20 percent of wind tunnel test cases. The results of pretest parametric CFD is used to improve the efficiency as well as the reduction of risk in wind tunnel tests, to make a real time comparison of the experimental data of force/pressure ports data with that of CFD data for checking the validity of the measurement data during the test period, to correct the support interference effect of the wind tunnel data, and so on. The results of pressure distribution on the surface of wind tunnel model by CFD are also compared with that obtained from Pressure-Sensitive Paint (PSP) measurement. In addition, the results of flow vector around the model are compared with that obtained from Particle Image Velocimetry (PIV) measurement.

Using the DWT, it is possible to count the aerodynamic coefficients of each part of a model, which are constructed from STL data of fuselage, wing, nacelle, pylon, model support and so on. Therefore, users can examine the influence of model supports on each part in the pretest CFD calculations. Before manufacturing wind tunnel test models and supports, the DWT can be used to evaluate the effects of the configuration of model support on the flow field around the model. An example of grid generation including two different types of model support, that is, blade-type sting and straight sting, is shown in Fig. 2. Also, corresponding RANS calculation results of Cp map on surfaces of the model and sting are shown in Fig. 3. The results on grid generation suggest the robustness of HexaGrid while the results of the RANS calculations clearly indicate the model support effect which is seen on the model surface pressure distribution near the junction of the model and

support. Based on these results, the users can choose the best configuration of model support sting without manufacturing several different stings to check the effects of the support configuration during wind tunnel tests.
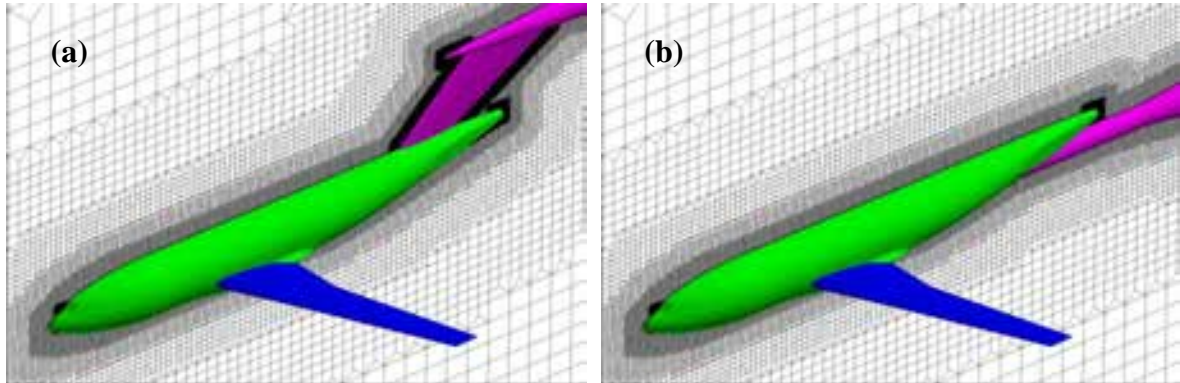

Figure 2. Examples of automatically generated grid including two different model support around the DLR F6-FX2B model; (a) Blade-type sting support, (b) Straight sting support.
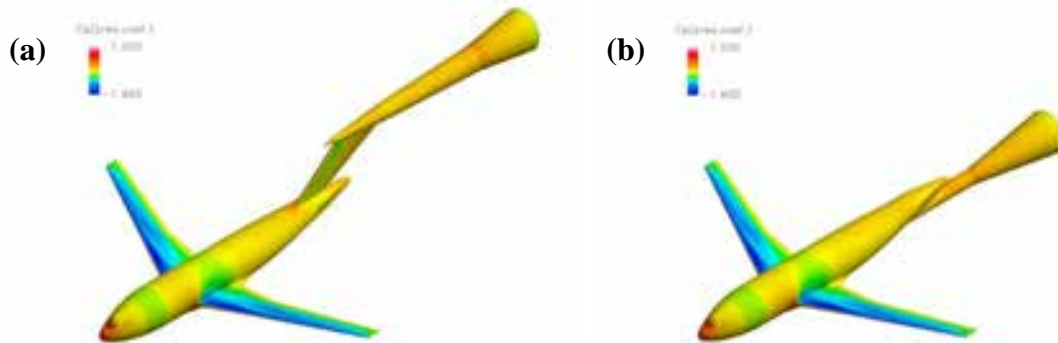

Figure 3. Calculation results of Cp map on surfaces of the DLR F6-FX2B model; (a) Blade-type sting support, (b) Straight sting support.

Static Model Deformation

During a wind tunnel test, a part of model such as a wing is deformed under the circumstances. The deformation of wing affects the aerodynamic coefficients, and causes the difference between EFD data and CFD calculations. It is possible to take a model deformation into account to CFD calculations using the Static Model Deformation Function of DWT. Users need to obtain displacement data of a deformed model, which are measured at dispersed points on wing surface during wind tunnel test. This function has an algorism of whole wing deformation with displacement data at discrete points, which is called Z44 model and installed as a default. In addition, the Surface Influence (SI) method is installed as a default algorism of grid deformation on the assumption that a degree of wing deformation is small. The SI method is one of algebraic schemes for fast grid deformation, and has good prospects of high performance of DWT because of high parallelization ability and easier implementation.

Figure 4 shows an example of the model deformation computation using measurement data. Model deformation measurements were made using stereo photogrammetry with markers as shown in Fig.4 (a). The information for the marker displacement is then used to deform the CFD model surface and volume mesh (Fig. 4(b)). The detail of the numerical technique can be found in [7]. As can be confirmed in Fig. 4 (c), the pressure distribution of CFD shows closer values compared to wind tunnel data if the effect of deformation is taken into account. The process of the present analysis (measurement data acquisition, surface/ volume mesh deformation, and CFD execution) can be made automatically through the DWT system if both measurement/pretest CFD data are available.
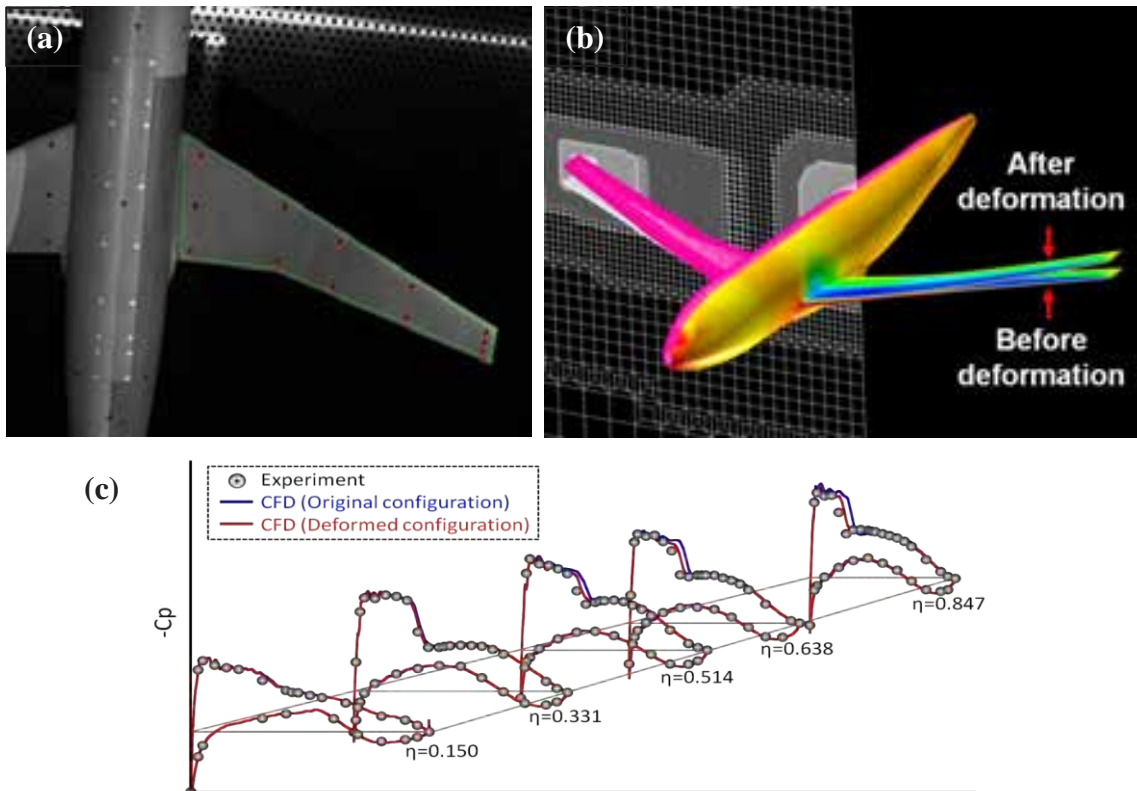
Figure 4. Model deformation computation using measurement data; (a) markers for stereo photogrammetry, (b) CFD model geometry before/after the deformation, (c) comparison of chord-wise static pressure distribution.

Fluid-Structure Interaction

The DWT has a function of Fluid-Structure Interaction (FSI) analysis, which can analyze a static aeroelasticity of the main wing. In the present FSI function, a user needs to input the unstructured mesh data for the structural analysis of wing, which is generated by PATRAN for example. The mesh for structural analysis is, in general, different from that for CFD, and the former is coarse in comparison with the later. An appropriate data converter is, therefore, made in order to map the pressure distributions on wing surface, which is obtained by CFD calculation, on the mesh for structural analysis. The structural analysis is executed to deform the wing shape by static load distribution, which is converted from converged CFD calculation result. The NASTARN is used for the structural analysis. The loop of FSI analysis is performed until the degree of deformation and the change on aerodynamic coefficients become small.

Figures 5-7 show an example of FSI calculation. Computational conditions are Mach number of M=0.75, angle of attack of 1 degree, and Reynolds number of Re=1.5×10^{6}. SA turbulence model is employed as turbulence model. It is assumed that the physical properties of a solid wing are Young's modulus of 208GPa and Poisson's ratio of 0.27, which are the same as that of wind tunnel test model. Figure 5 (a) shows the Cp distributions on wing surface mesh of CFD calculation. Figure 5 (b) shows the mesh and static load mapping for structural calculation. It is also assumed that the wing is only deformable part. In this example, the static balance is achieved after that the FSI loop is iterated three times as shown in Fig. 6 and Table 1. Here, Cp plots on wing cross section of non-deformed and deformed cases are compared in Fig. 7. In Fig. 7, the experimental data are also plotted with solid circle. The close section is located at 0.638% and 0.847% of wing span length. The computational Cp distribution becomes closer to experimental results by considering the wing deformation. The influence of wing deformation on Cp distribution is, however, very small in this example. The reason of that is the assumption of solid wing, which has no laying pipes for pressure measurement ports. The inside structure of wind tunnel test model is more complicate, and does not have simple solid wing. The assumption of solid wing makes the structural model inflexible rather than the actual wind tunnel test model.
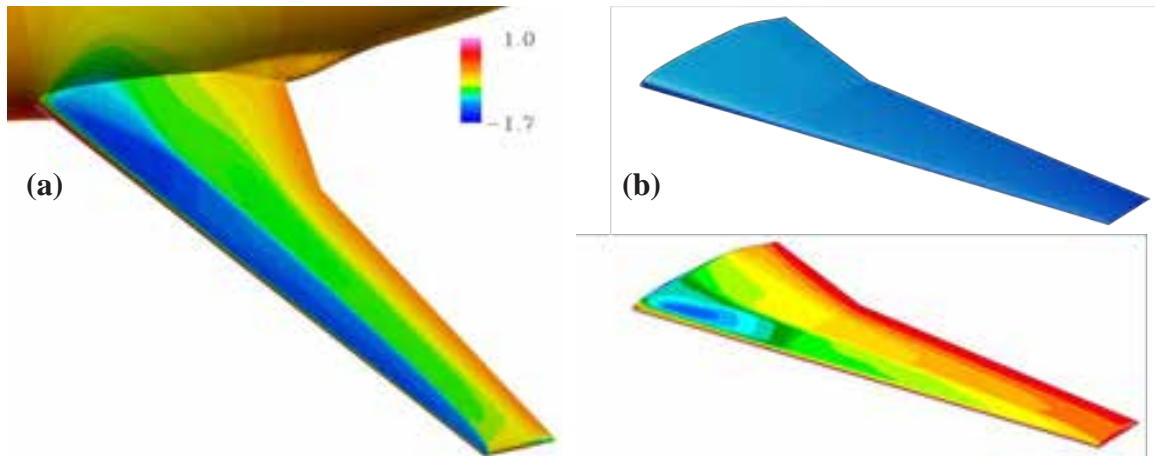
Figure 5. Cp and static load distributions on wing surface; (a) Cp, (b) static load
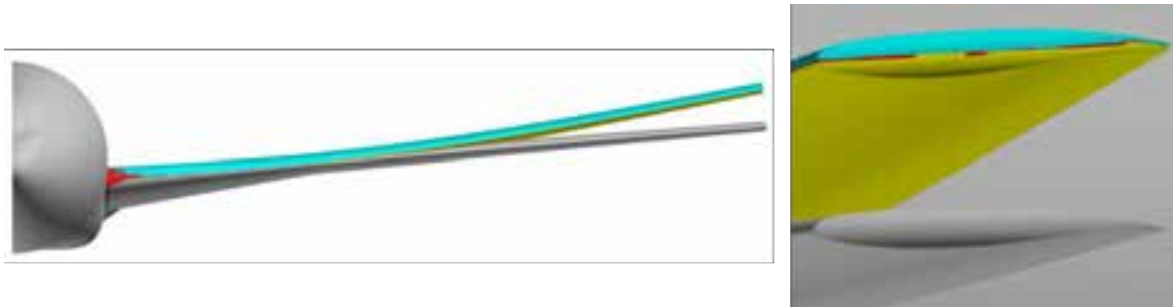

Figure 6. Wing deformation by FSI loop.

Table 1. Aerodynamic coefficient of each FSI loop.

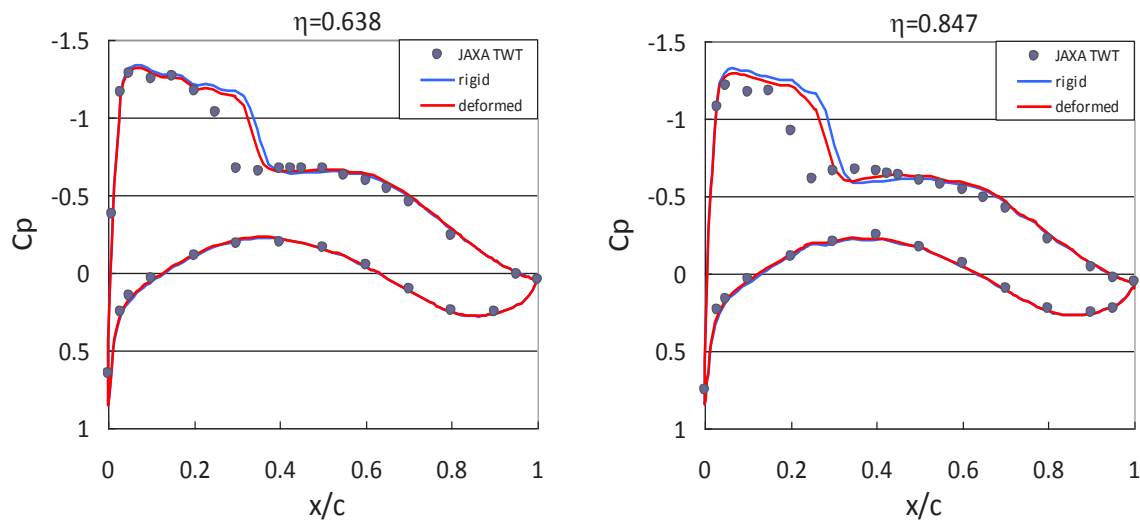| FSI Loop No.	0 (Original)	1	2	3 (Converged)
C_D	0.0359	0.0354	0.0354	0.0354
C_L	0.5940	0.5867	0.5868	0.5868
C_m	-0.1267	-0.1244	-0.1244	-0.1244

Figure 7. Cp plots of wing cross sections.

Summary

The CFD tools, which are installed into the DWT, were presented. The functions of parametric CFD, measured static model deformation, and fluid-structure interaction calculation were also presented. We are improving these tools and functions day by day toward to the completion of DAHWIN system, which is scheduled on the end of this fiscal year.

The future works on CFD tools are modeling of roughness on the wing surface, structural calculation parameters, and porous wall of wind tunnel, for example. These modeling will close computation aerodynamic coefficients to experimental that. Although the EFD/CFD integration technology has not been matured, we believe that a fast and accurate CFD code accelerates the integration of them.

References

[1] S. Watanabe, S. Kuchi-ishi, K. Murakami, A. Hashimoto, H. Kato, T. Yamashita, K. Yasue, K. Imagawa, and K. Nakakita: Development Status of a Prototype System for EFD/CFD Integration, 47th Applied Aerodynamics Symposium, FP54-2012, 2012.

[2] A. Hashimoto, K. Murakami, T. Aoyama, and P. R. Lahur: Lift and Drag Prediction Using Automatic Hexahedra Grid Generation Method, AIAA paper 2009-1365, 2009.

[3] A. Hashimoto, K. Murakami, T. Aoyama, K. Yamamoto, M. Murayama, and P. R. Lahur: Drag Prediction on NASA CRM using Automatic Hexahedra Grid Generation, AIAA Paper 2010-1417, 2010.

[4] A. Hashimoto, P. R. Lahur, K. Murakami, and T. Aoyama: Validation of fully automatic grid generation method on aircraft drag prediction. AIAA Paper 2010-4669, 2010.

[5] A. Hashimoto, K. Ishiko, M. Hishida, K. Murakami, P. R. Lahur, M. Sakashita, and T. Aoyama: Toward the Fastest Unstructured CFD Code 'FaSTAR.' AIAA Paper 2012-1075, 2012.

[6] P. R. Lahur: Automatic Hexahedra Grid Generation Method for Component-based Surface Geometry, AIAA paper 2005-5242, 2005.

[7] K. Yasue, S. Kuchi-ishi, A. Hashimoto, K. Murakami, H. Kato, K. Nakakita, S. Watanabe, and M. Hishida: High-Fidelity CFD Simulation of a Wind Tunnel Model Using Model Deformation Data, Proceedings of 15th International Forum on Aeroelasticity and Structural Dynamics, 2010.

Overview of Activities in Stochastic Data Assimilation for Applications in Aerodynamics

Richard P. Dwight
Jouke H.S. de Baar
Andrea Sciacchitano
Mustafa Percin
Hester Bijl
Fulvio Scarano

Aerodynamics Section, Faculty of Aerospace Engineering,
TU Delft, 2600 GB Delft, The Netherlands.
r.p.dwight@tudelft.nl
https://aerodynamics.lr.tudelft.nl/~rdwight

Abstract

In this conspectus paper we present a brief summary of a variety of recent activities in data assimilation performed at the Aerodynamics Section of the TU Delft. We hope to demonstrate a few of the exciting possibilities for combining experimental data and numerical models, improving the capability of both. Our activities are bound by a common theme of combining experimental wind-tunnel measurements and CFD simulations in order to (i) improve fidelity of experimental data, (ii) obtain estimates of unmeasured quantities, (iii) estimate modeling error and parametric uncertainty in simulation. The methodologies we use depends strongly on the application, but all have Bayesian inference at their root with some statistical model representing the relation between measurement and simulation. Bayesian statistics offers a coherent and flexible framework for describing solutions of the ill-posed problems that arise in this analysis of data, but new numerical methods are needed to find these solutions efficiently.

Key words: Bayesian inference, uncertainty quantification, data assimilation, aerodynamics, CFD, particle image velocimetry, model inadequacy, Kriging.

Introduction

This paper is intended primarily as an overview of some recent activities of the data assimilation group at the Aerodynamics Section, TU Delft. For technical details see our papers cited throughout. All work has a foundation Bayesian inference. In three sections we discuss three distinct methodologies and applications:

1. Reducing uncertainty in aeroelastic flutter boundaries.
2. Kriging interpolation of stereo-PIV data with a local error estimate.
3. Navier-Stokes simulation in gappy PIV data.

In addition to the activities described in this document, we are also working on at this time (September 2012):

1. Calibration of RANS turbulence models, with a view to obtaining estimates of model inadequacy.
2. Multi-level statistical models for estimating structural variability (Dwight et al., 2012).
3. Kalman smoothing for filling gaps and increasing time resolution of PIV data.
4. Least-squares FEM solutions to the problem of integrating PIV data and CFD solvers (Dwight, 2010).

1. Reducing Uncertainty in Aeroelastic Flutter Boundaries[1]

In this section we compute the uncertainty in dynamic stability boundaries in an aeroelastic system (flutter) due to uncertainties in structural parameters. For moderate levels of structural uncertainty (±5%) we observe extremely high levels of uncertainty in the flutter altitude (±3500 ft) for a model wing. This is a consequence of both high sensitivity of the stability boundary to individual structural parameters, and the cumulative effect of many parameters. We conclude that the predictive capability of our aeroelastic analysis is fundamentally limited by our incomplete knowledge of the structure, more so than by discretization error or modeling inadequacy. To address this limitation we assume measurements of the aeroelastic response at sub-critical altitudes are available, such data as might be gathered from flight-tests. Using Bayesian inference we deduce updated uncertainties for structural parameters and the flutter altitude. Using very small amounts of data we see the introduction of a covariance relationship into the structural parameters and a substantial reduction in flutter boundary uncertainty. In this framework we study the informativeness of sub-critical eigenvalue measurements for the flutter altitude with respect to two parameters: measurement accuracy, and proximity of the measurement to the flutter altitude.

Motivation and Methodology

Flight flutter tests entail cost and risk, whereas computational methods may not accurately predict the flutter boundary (Lind and Brenner, 1997). As such there is a history in aeroelasticity of combining limited flight-test data at sub-critical speeds, with simplified fluid-structure models to predict the flutter envelope, either deterministically (Zimmerman and Weissenburger, 1964) or stochastically (Khalil et al., 2010).

Stochastic approaches arise from the acknowledgement that both estimates of structural parameters and experimental measurements are imprecise. Epistemic uncertainty in the former arises from airframe material and manufacturing variability, as well as wear over varying service histories of aircraft. Recent work has shown that small uncertainties in a large number of structural parameters can result in dramatic uncertainties in the aeroelastic response (Pettit and Beran, 2006; Witteveen et al., 2007) in particular the flutter boundary (Marques et al., 2010). Our goal in this section is to *reduce* the epistemic uncertainty in both parameters and response using experimental observations of stability eigenvalues of the system at non-flutter conditions. In contrast to previous studies of model updating in aeroelasticity, our model is a high-fidelity fluid-structure interaction (FSI) solver, with a finite-volume compressible Euler solver for the fluid part - which makes the method applicable to the transonic regime. Furthermore since the stand-alone model (without data) is predictive and accurate, we expect the amount of flight-test data required to update the model to be low, and the calibrated model to have broad validity. These benefits justify the extra computational work involved resulting from the high cost of the FSI simulation.

The two main components of the statistical analysis are: 1) propagating specified structural parameter uncertainty through the FSI simulation to obtain estimates of flutter boundary uncertainty, and 2) using experimental data to update estimates of structural uncertainty in the model. The former is accomplished with non-intrusive uncertainty quantification (UQ) techniques (Xiu and Karniadakis, 2002), in particular probabilistic collocation (Loeven, 2010). For the latter we construct a statistical model relating the output of the simulation to the experimental observations, and solve it within the Bayesian framework. There are several benefits to this stochastic approach: the inherent ill-posedness of the inverse problem is treated naturally without need for regularization terms, noise in the experimental observations can be readily accounted for, as can prior information on the structure (Kennedy and O'Hagan, 2001).

Flutter Prediction with an Eigenvalue Solver

The unsteady fluid-structure system consisting of an elastic wing in high-speed flow, is approximated by coupling the compressible Euler equations to a structural model for the wing - with surface forces and displacements interpolated between the fluid mesh and the structural model. The flow discretization is based on the University of Liverpool's parallel multiblock solver - a cell-centered finite-volume code, operating on

---

[1] From: R.P. Dwight, S. Marques, H. Bijl, K.J. Badcock (2011). Reducing Uncertainty in Aeroelastic Flutter Boundaries using Experimental Data. *International Forum on Aeroelasticity and Structural Dynamics*, Paris, IFASD-2011-71.

curvilinear body-fitted meshes.   The structural discretization uses a finite-element model, analyzed with MSC.Nastran. The coupling approach used is described in Woodgate et al. (2005). For the Goland wing we consider throughout this section the coarse aerodynamic grid, and structural model are depicted in Figure 1.

In order to estimate the stability properties of the aeroelastic system, we could integrate the discrete system forward in time for each parameter-set and condition of interest - but this is computationally expensive. Instead we perform a linear stability analysis of the coupled discrete system (Marques et al., 2010) about a stationary solution. This involves a linearization of the full non-linear coupled solver, resulting in a Jacobian matrix containing both fluid, structure and cross-terms. Finding the eigenvalues of this matrix directly is intractable - therefore the system is factored using the Schur complement, resulting in a non-linear eigenvalue problem with of the size of the number of structural parameters. By parameterizing the structure using the leading-order mode-shapes only, this number is kept small and the eigenvalue problem is solved rapidly with a Newton iteration. A typical result (for the Goland wing) is shown in Figure 2 (left). Eigenvalues associated with the first 4 structural modes are plotted, and it can be seen that at a certain altitude two modes interact, leading to one mode going unstable (real-part of eigenvalue greater than zero). To get a rough estimate of the influence of discretization error in the fluid the calculation is repeated on a much finer fluid mesh. The altitude at which flutter occurs is only very slightly changed.

Aerodynamic model
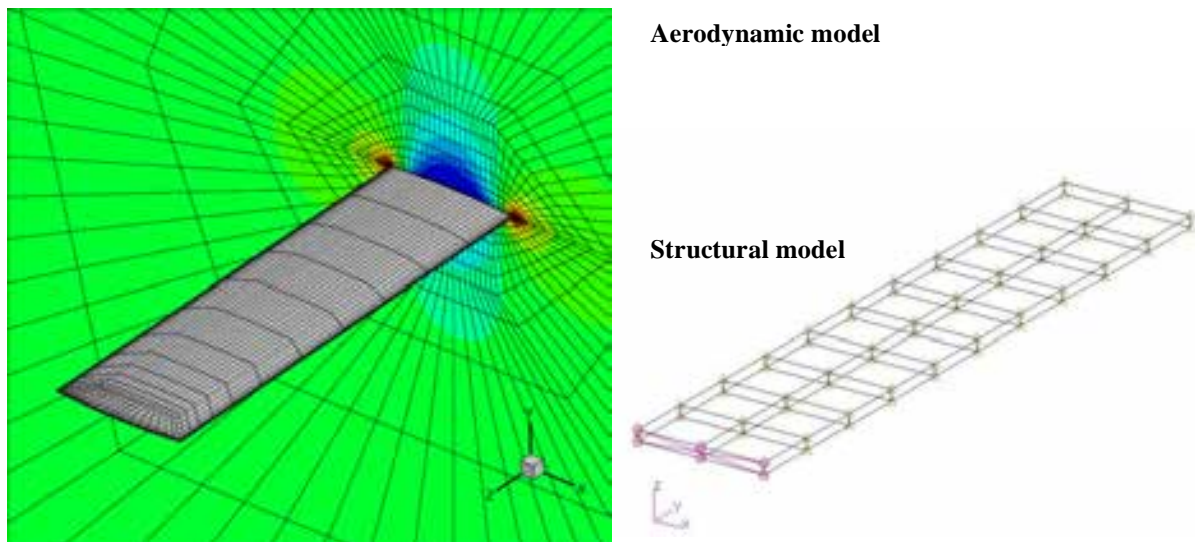
Structural model

Figure 1: Goland wing with coarse aerodynamic grid (left); eigenvalues of four dominant aeroelastic modes, for aerodynamics on fine and coarse grids (right).

Probabilistic collocation for uncertainty propagation

Now we consider the case in which the wing structure is imperfectly known. Consulting with aero-structure experts, a preliminary best-guess of ±5% variability in any given structural model parameter was made. In a precursory sensitivity analysis with linear aerodynamics, of the 31 structural parameters in the model, only 7 were identified as having a substantial influence on flutter. These 7 are treated stochastically (as uniform distributions) in the following, and the influence of the remaining parameters is neglected.

Probabilistic collocation (PC), see e.g. Loeven (2010), is a means of computing statistics of the output of a computational model, given pdfs on the model's input parameters. The method uses a polynomial expansion based on Lagrange polynomials to approximate the response of the model in the uncertain parameter space. Gaussian quadrature weighted by the pdf of the uncertain input is applied to compute the mean, variance, and higher moments of the output. By choosing the support points and Gauss rule appropriately, it is possible to achieve decoupling of the equations for different parameter values (collocation), and a higher-order approximation of the mean and variance of the output (spectral convergence). Multidimensional rules are build via tensor products of 1d rules - with cost exponential in the dimension. By Monte-Carlo sampling the polynomial response, approximate pdfs of output quantities can also be rapidly obtained.

We apply PC with a quadratic approximation in each of the 7 uncertain directions (i.e. PC(2)), requiring $3^7 = 2187$ evaluations of the simulation code. This is feasible thanks to the low cost of the Schur-eigenvalue code. The output for PC(2) is plotted in Figure 2 (right). The main subfigure shows the real part of the eigenvalue of the first aeroelastic mode (responsible for flutter), plotted as a function of altitude, as in Figure 2 (left). The multiple lines of varying thickness represent the uncertainty in this value caused by the specified structural uncertainty. The "truth" has a probability of 1/2 of lying to the right of the $P = 1/2$ line, a probability of 1/3 of lying to the right of the $P = 1/3$ line, etc. The histogram to the right approximates the pdf of the real eigenvalue at the red vertical line in the main subfigure (not the marginal pdf over altitude!). Similarly the histogram below approximate the pdf of the flutter altitude (i.e. the pdf of $Re(\lambda) = 0$), from which the probability of flutter can be quickly evaluated. Flutter is certain for an altitude < 6,000 ft, and guaranteed not to occur for an altitude > 14,000 ft, under the assumption that structural uncertainty is the dominant source. Clearly the predictive capability of the analysis is primarily limited by structural uncertainty and not discretization error. The conclusion that (under the relatively mild uncertainties on the structure) it is not possible to state the flutter altitude within 8000 ft is dismaying - this result is so broad as to be useless. Further this will remain true no matter how good the numerical code, and can only be reduced by experimental measurements of the structure, or some other aspect of the system.
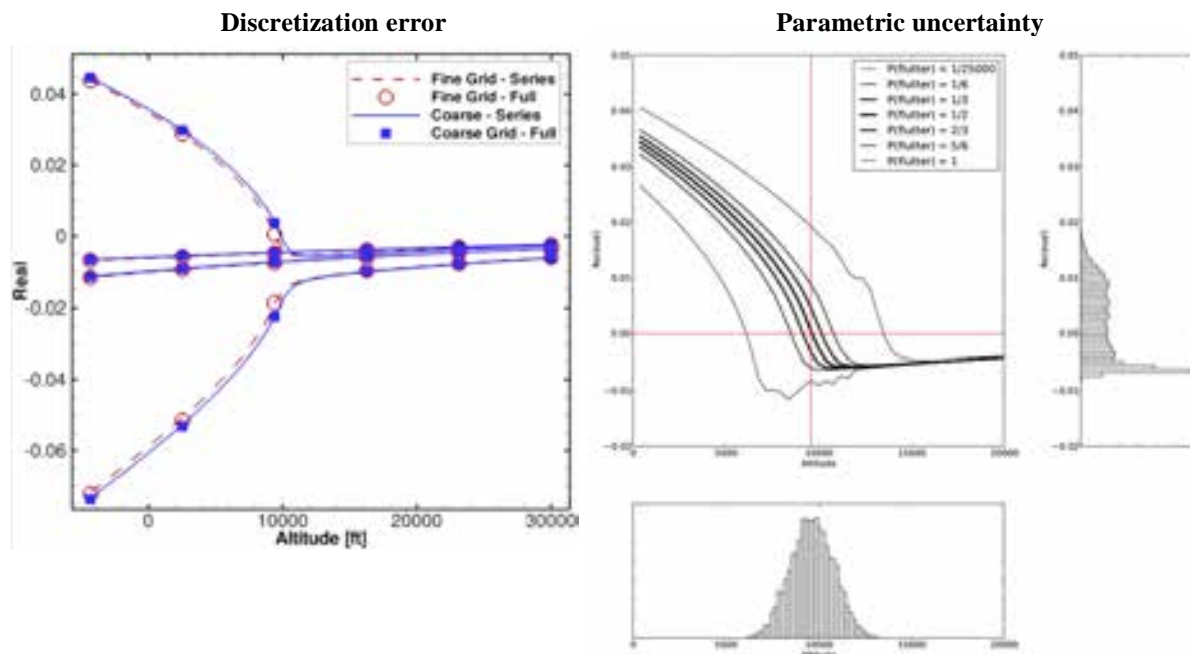

Figure 2: Eigenvalues of four dominant aeroelastic modes, for aerodynamics on fine and coarse grids (left); uncertainty in single unstable eigenvalue due to structural uncertainty (right). The lower pdf displays the probability of flutter boundary occurring at a given altitude.

Bayesian updating of structural uncertainty

Flight tests are one source of information commonly used to determine flutter altitude. Let us assume that an experiment has been performed using a Goland wing, and eigenvalues of the system at pre-flutter conditions are measured with a certain accuracy σ_d. Measurements at- or beyond flutter conditions are to be avoided lest the model be damaged (or the aircraft in a real flight-test). No experimental eigenvalue data currently exists for the Goland wing test-case, therefore to demonstrate the method artificial data is generated using simulation with added noise (a ``twin problem'' in the terminology of inverse problems).

Updating parameters in the presence of measurement data is known variously as model parameter estimation, model calibration, and system identification, and is accomplished in a stochastic setting using Bayes' theorem. Two good introductory books on the subject are Tarantola (2004) and Gelman et al. (2004). The first step is to

define a prior: a probability distribution on the structural parameters encoding all information which is known about the parameters prior to observing the data, with pdf $\rho_0(\alpha)$.

The second step is to describe the relationship between the model and the data, this is the *statistical model*. Let the vector of observed quantities be denoted d (the data). Let $H(w, \alpha)$ be an *observation operator*, which takes a model state w and parameter vector α, and returns the model's approximation of the observed quantities d. The model state $w(\alpha)$ satisfies the model equation:

$$R(w, \alpha) = 0.$$

Under the assumptions: (i) that the noise in the measurements d is known and described by the random variable ε, and (ii) that there is no modeling error (for the correct choice of α), then the model and data are related as:

$$d = H(w, \alpha) + \varepsilon \quad \text{s.t.} \quad R(w, \alpha) = 0.$$

Given which the probability of observing data d given parameters α (the likelihood) is

$$\rho(d|\alpha) := \rho_\varepsilon\big(d - H(w, \alpha)\big),$$

where $\rho_\varepsilon(.)$ is the pdf of ε. For a prior and a likelihood, Bayes' theorem gives an explicit expression for the *posterior*, the probability of parameters given the observed data:

$$\rho(\alpha|d) \propto \rho(d|\alpha)\rho_0(\alpha),$$

where the constant of proportionality (independent of α) is not usually of interest. In the Bayesian framework this posterior is regarded as the answer to the question: What is known about α?, and is therefore the updated estimate of the parameters. If we require a deterministic estimate of α - rather than the probabilistic posterior - then a reasonable choice is the most-likely value of α, the maximum *a posteriori* estimate (MAP estimate):

$$\alpha_{MAP} := \arg\max_\alpha \rho(\alpha|d).$$

Reducing uncertainty for the Goland wing

The procedure of the previous subsection is applied to the Goland wing test-case. We assume measurement data at 5 different accuracies, and at 5 distances from the "true" flutter point. This is intended to simulate flight-tests with differing measurement capabilities, and that are allowed only to approach flutter at different distances. In each case only a single complex eigenvalue is measured. In reality more data would be available, though we can only exploit that data which our model predicts. Once updated distributions on the structural parameters are estimated, those distributions can be propagated through the Schur-eigenvalue code to obtain updated (and hopefully narrower) distributions on the flutter altitude.

The posterior distributions on flutter altitude for calibrations using each of the 25 pieces of data are plotted in Figure 3. The prior is the same ±5% uniform distributions on each parameter used in the UQ study. Immediately clear is that, in many cases, the level of uncertainty in flutter is reduced over the level present in the pure UQ study summarized in Figure 2 (right). Furthermore as the accuracy of the measurements increases, and the proximity to the flutter point decreases, more specific information about the true flutter altitude is identified. This is expected, but this study gives us quantitative information on how much we know about the flutter altitude given the data. For example at $\sigma_d = 0.002$ and a distance from flutter of 3400 ft, the posterior distribution looks almost identical to the prior, with a likely range of flutter altitude between 6000 and 13000 ft, indicating that data of that quality says very little about flutter. At the other extreme, with an accuracy of $\sigma_d = 0.0001$ and a distance from flutter of 600 ft, the true flutter altitude is identified in a very narrow band of less than 150 ft.

However in all cases, given the high-dimensional input parameter space (the 7 structural parameters) and the small quantity of added data (a single complex number), true values of individual structural parameters are only broadly identified. Nevertheless, thanks to the fact that the stability eigenvalue data is closely related to the

quantity of interest (the flutter altitude), the latter can be identified narrowly by the procedure, and the large uncertainty present in the original analysis is substantially reduced.
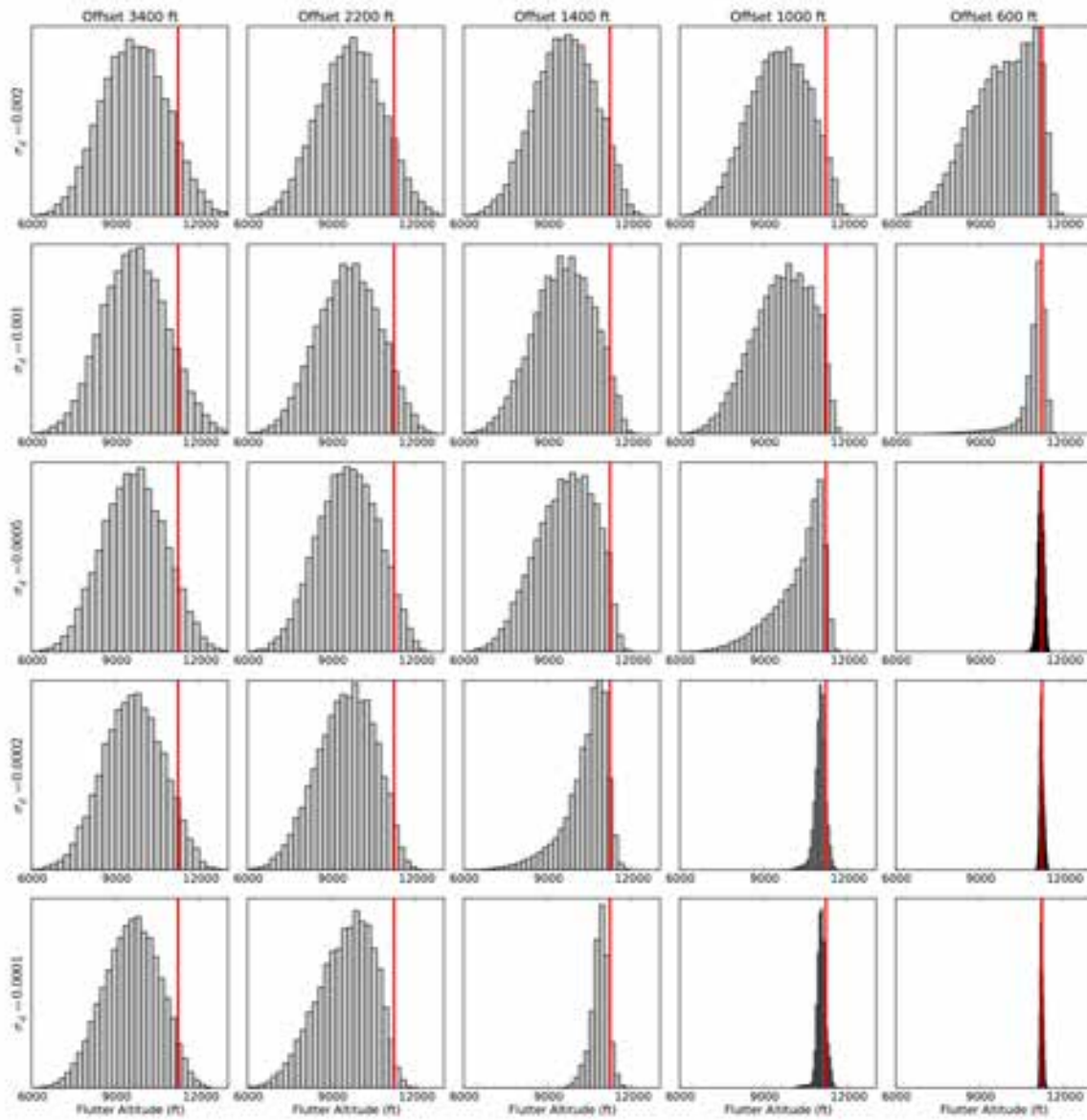

Figure 3: Dependence of posterior pdf of flutter altitude on distance of eigenvalue measurement from the flutter point (decreasing left-to-right), and accuracy of the measurement (increasing top-to-bottom). Vertical red line is the "truth".

2. Kriging Regression of PIV Data using a Local Error Estimate[2]

Postprocessing Particle-Image Velocimetry (PIV) data is a challenging task. We introduce a method based on a interpolation method with origins in Bayesian statistics. Thanks to its stochastic heritage Kriging is able to incorporate estimates of noise in the data, and beliefs about the smoothness of the response. We apply Kriging to two purposes: interpolation of low-resolution data (from multiple planes), and improved estimates of velocity fields from poor quality images. In both cases Kriging is seen to provide substantial advantages over the best existing methods.

Gaussian Process Regression using Local Error Estimates

Usually, the post-processing of PIV data includes several steps, such as outlier detection, outlier replacement, smoothing, and in some cases interpolation to a finer grid. Each of these steps can involve different techniques, for example one might replace outliers by linear interpolation and increase the resolution with cubic spline interpolation. The Kriging predictor enables a different approach, it can provide a single-step prediction of the flow field at any (existing or new) set of grid-points and generally acts as a regressor - although in most cases the Kriging predictor is set to act as an exact interpolator.

Given the data $U_{PIV} = (u_{PIV}, v_{PIV})$, the Kriging predictor for the flow field U is given by (Wikle and Berliner, 2007):

$$E(U|U_{PIV}) = \mu + PH'(R + HPH')^{-1}(U_{PIV} - H\mu), \tag{2.1}$$

where the observation matrix H selects the PIV data locations $X_{PIV} = HX$ from the complete set of locations X. For large domains we can reduce the computational cost by generating a sparse covariance matrix P, through approximation of the commenly used Gaussian covariance function with a spline.

The mean μ and variance σ^2 of the flow are estimated from the statistical mean and standard deviation of the PIV data. The correlation range can be found from a Maximum Likelihood Estimate (Mardia et al., 1989) optimization, however in the following we use a Frequency-domain Sample Variogram optimization to reduce computational cost (de Baar et al., 2011; de Baar et al., 2012). In (2.1) usually $R = 0$, such that Kriging is an exact interpolator, although a small $R = \upsilon I$ might be implemented for reasons of numerical stability, with υ of the order of the square-root of machine precision.

From a Bayesian perspective, we can introduce some amount of regression by choosing (Wikle and Berliner, 2007):

$$R = \varepsilon_0^2 I,$$

where ε_0 is an estimate of the observation error, which is assumed to be globally constant, and R is the error matrix. This can be interpreted as smoothing of the data, however from the Bayesian perspective the objective is not to smooth the data but to arrive at the most optimal prediction of the true flow. For Kriging with global error prediction presented here (Kriging GE), we use 32-fold random cross validation to estimate which value of ε_0 gives an optimal interpolation (Witten et al., 2011).

However in many cases we have an estimate of the velocity error per interrogation window (i.e. local). The same Bayesian perspective allows us to choose (Wikle and Berliner, 2007):

$$R = \text{diag}(\varepsilon_i^2),$$

where we now interpret ε_i as a vector of local observation errors. Substituting this expression for R into (2.1) results in a Kriging predictor with local error estimate (Kriging LE).

---

[2] From: J.H.S. de Baar, M. Percin, R.P. Dwight, B.W. van Oudheusden, H. Bijl, "Kriging regression of PIV data using a local error estimate", Experiments in Fluids (in preparation).

The question remains how to estimate the local observation error ε_i. This is a fundamental and long-standing problem in PIV, and a variety of rough estimates have been developed and are used, that are accurate to differing degrees depending on the source of the error. Ultimately, the user providing the PIV data might also quantify the accuracy of that data. Fortunately the Kriging predictor is fairly robust to inaccurate estimates of noise levels. In the we use the following simple model to estimate velocity error:

$$\varepsilon_i \;=\; \frac{c}{SNR_i - SNR_{min}}$$

where SNR_i is the signal-to-noise ratio in the interrogation window i, and where the choice of SNR_{min} results from the expertise of the PIV experimenter. We use 32-fold random cross-validation to estimate which value of c gives the optimal interpolation.

Study of the Method for Synthetic Data

In this section we simulate PIV processing of synthetic images, interpolate the results to a finer grid using both conventional and new methods, and finally we perform a parametric investigation of the effect of bad seeding and reflections on the accuracy of the interpolation. This approach enables us to quantify the improved accuracy of an interpolation technique that employs a local error estimate of the PIV data. We consider the two dimensional incompressible flow (which we regard as "truth") given by:

$$u(x,y) \;=\; \sin(2\pi x)\cos(2\pi y),$$
$$v(x,y) \;=\; -\cos(2\pi x)\sin(2\pi y),$$

on the domain $x = [0,1]$ and $y = [0,1]$, which is visible on the right in Figure 4. From this flow we create synthetic image pairs with random seeding, Gaussian noise, reflection, 256x256 pixels, and 256 greyscale color-depth. A typical image is shown on the left in Figure 4.
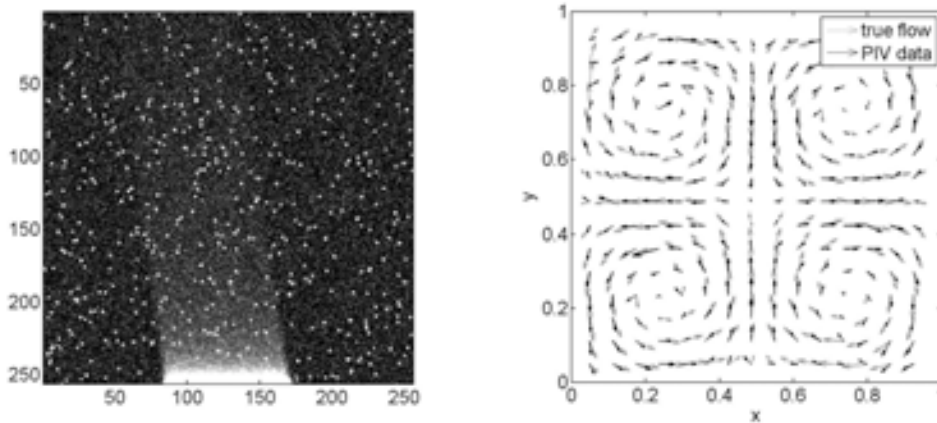

Figure 4: Synthetic PIV image with seeding, noise, and reflection (left), reconstruction of the synthetic flow-field with PIV (right).

We apply the Matlab PIV Toolbox MPIV (Mori, 2009) to reconstruct the flow field, using a recursive correlation algorithm with a final interrogation window size of 16x16 pixels and three point subpixel fitting. Black arrows in Figure 4 show a typical reconstruction of the flow field. In this process we deliberately introduce several sources of error - such as noise, reflection, low image resolution, and low PIV data resolution - as a result of which we find a local offset of the PIV data with respect to the true flow, an example of which is visible in Figure 4. MPIV provides two different signal-to-noise ratio, of which we use the Peak-to-Mean ratio - that the ratio of the correlation peak height to the average correlation value in the fitting domain.

The next step is to interpolate the PIV data to a finer grid of 10^4 random grid-points. We compare the Root Mean Squared Error (RMSE) accuracy of three interpolation methods. For cubic spline interpolation the data is passed through the MPIV median filter, while both Kriging methods use the raw data directly. We perform a

parametric study to quantify the effect of poor image quality on the accuracy of the interpolation. The first parameter we change is the seeding. Figure 5 (left) illustrates the effect of poor seeding on the RMSE accuracy of the three different interpolation methods. For underseeding we observe a dramatic increase of the cubic spline interpolation error. For Kriging GE this effect is less dramatic, while for Kriging LE we see only a very minor effect on the accuracy. This result is seen to be insensitive to the particular error estimate used.
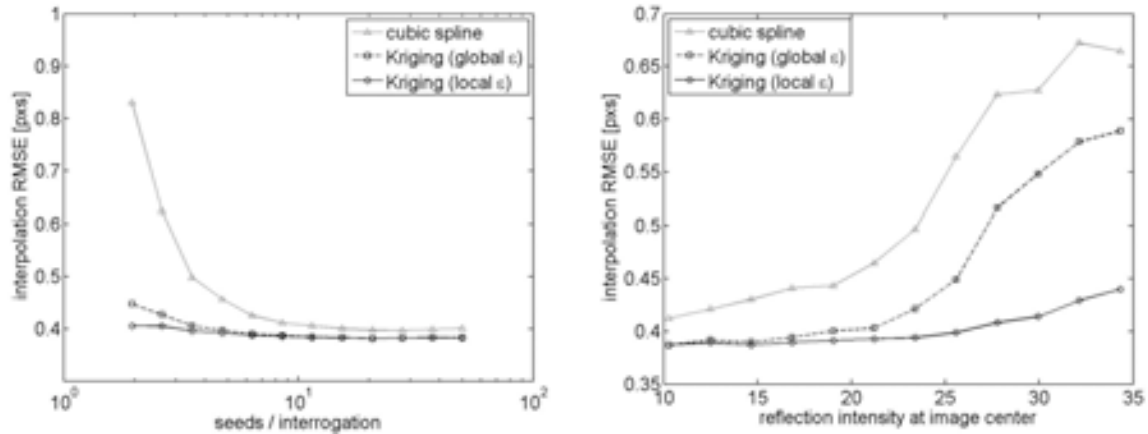
Figure 5: RMS error in predicted velocity field for three different interpolation techniques. As a function of seeding density (left), as a function of reflection intensity (right).

The second parameter we increase is the intensity of the reflection. This leads to a region of poor image quality, resulting in a low SNR and therefore a high value of the local error estimate. This region of high estimated error roughly corresponds to the region where we observe a large offset of the PIV data with respect to the true flow. The resulting interpolation accuracies are given in Figure 5 (right). Again, we see a dramatic increase of the cubic spline interpolation error, while the Kriging LE interpolation error remains much smaller. The reason for this is that in poor images the local offset is correlated with the local SNR. This relation is modeled by Kriging LE which results in an improved accuracy, as is illustrated by Figure 5 (right).

Application: Interpolation of Stereo PIV Data of the DelFly II MAV

In this section, we implement the Kriging interpolation technique using local error estimate in the interpolation of the experimental data acquired via Stereoscopic Particle Image Velocimetry (Stereo-PIV) technique. The time-resolved PIV measurements were performed in the wake of the flapping-wing Micro Air Vehicle (MAV) `DelFly' II (Figure 6 (left)) in forward flight configuration, the experimental setup is shown in Figure 6 (right). Three-component velocity fields were obtained at several spanwise planes in the wake of the flapping wings and at a high framing rate to allow a reconstruction of the three-dimensional wake structure throughout the flapping cycle. The wake reconstruction was performed by interpolating between the measurement planes.

Experiments were performed for a large variety of parameters, i.e. flapping frequency, free-stream velocity, angle of attack and tail configuration. However, as the matter of interest is the performance of Kriging interpolation technique using local error estimate based on the Signal to Noise Ratio (SNR) of the PIV data, only some representative cases are represented and discussed in this paper. Before starting the discussion of the results, it is necessary to underline some important points regarding to interpretation of the results. First, it should be noted that only one half of the wake is visualized (the wake, however, is assumed to be nominally symmetrical) and that the region in the vicinity of the tail masked during PIV processing due to intensive reflection underneath and lack of illumination above the tail.

Results are shown in Figure 7, in which isocontours of the z-component of the vorticity are plotted. Accuracy of derivatives such as vorticity are naturally more sensitive to the quality of interpolation. Two prominent counter-rotating vortices are visible in Figure 7, corresponding to tip vortices from the upper and lower wing respectively. We compare the effectiveness of cubic-spline interpolation and Kriging GE (results for Kriging LE are currently being worked on, and are expected to be even better). There is no longer any "truth" velocity field, so the methods must be evaluated by reference to possible and plausible physical behaviour. In the cubic

spline reconstruction (top left), as well as the two main vortices we see a large quantity of spurious vorticity packets that are apparently non-physical and a result of (i) the large distance between measurement planes with respect to the in-plane resolution, (ii) the mismatch of fluctuations in the planes (which were measured at the same flapping phase but at different times), and (iii) the cubic spline not accounting for noise in the velocity vectors. In contrast in the Kriging interpolation (bottom left), the reconstruction is substantially smoother and spurious oscillations are reduced, such that we might examine the remaining vorticity blobs more closely, with a stronger belief that they may represent true flow features. The iso-plot (left) shows the complete flow domain.

By the robustness of its interpolation, and the ability to handle completely unstructured (point-cloud) data, error estimates, and derivative information natively, Kriging has provided a flexible means of analyzing the DelFly II data set that was possible only in a limited fashion before.
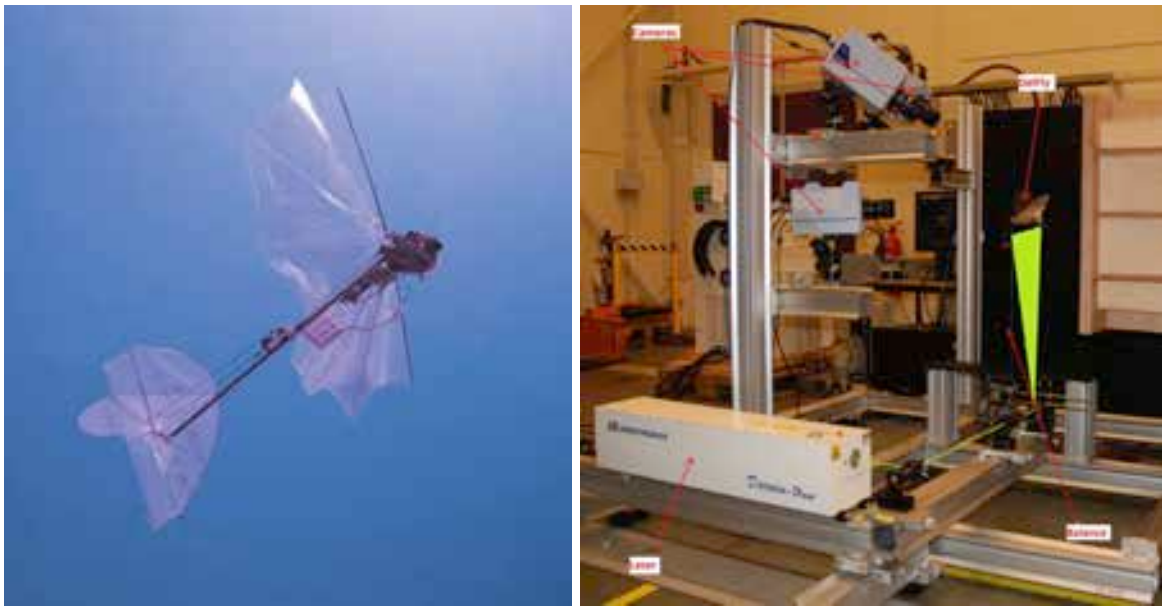

Figure 6: DelFly II in flight (left), the stereo PIV setup, open-jet nozzle visible on the extreme right (right).
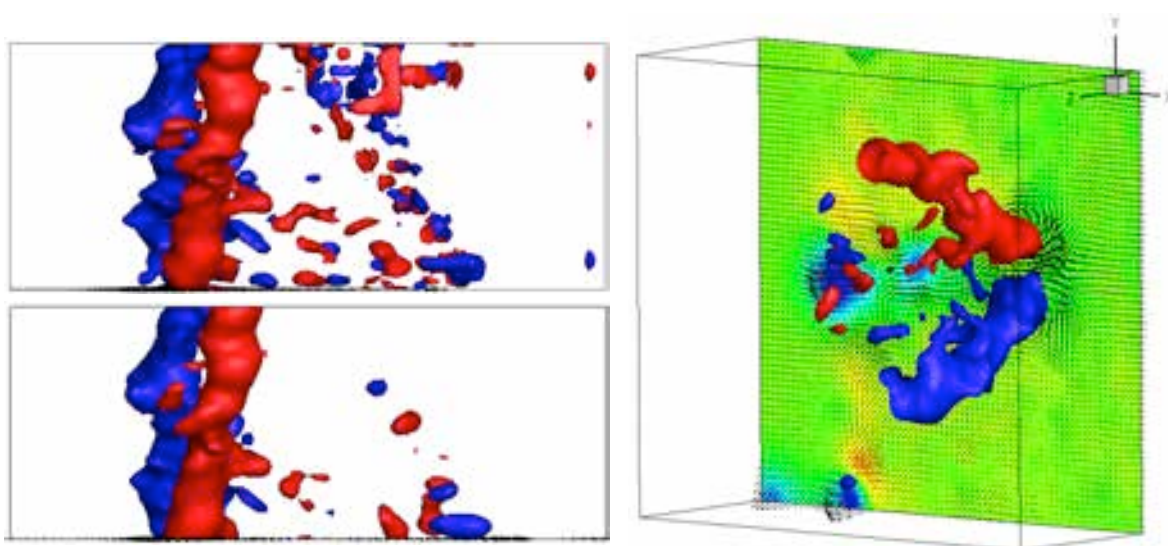

Figure 7: Vorticity fields. Top left: cubic spline interpolation, plan view. Bottom left: Kriging GE interpolation. Right: Kriging GE interpolation, perspective view with example velocity plane.

3. Navier-Stokes Simulation in Gappy PIV Data[3]

PIV measurements are often affected by gaps, i.e. regions where no information regarding the velocity field is obtained. The gaps occur in areas where the particle image displacement cannot be evaluated. There are a wide variety of reasons for this: 1) absence of seeding particles due to inhomogeneous tracer dispersion or due to the centrifugal forces acting in vortices and wakes of high-speed flows (Schrijer and Walpot, 2010, Bitter et al., 2010); in this case the gaps occur irregularly in space and time; 2) laser light reflections from the surface of objects, which lead to corrupted tracer particle images; 3) shadows due to the presence of objects in the light path; 4) inaccessible regions for the imaging system.

The treatment of gaps in PIV data has received little attention. Generally considered as a byproduct of the vector validation problem, (detection and replacement of false vectors, see Westerweel, 1994 for instance) several data refill procedures have been proposed by practitioners. In essence, data refill procedures are nothing more than spatial interpolation or regression of neighbouring vectors. Several choices for the basis function are proposed, the lowest-order being bilinear interpolation of the known values at the boundary of the gaps. Gunes and Rist (2008) proposed to employ the Kriging method for stereoscopic data reconstruction. Ventura and Karniadakis (2004) investigated the possibility of using proper orthogonal decomposition (POD) for reconstructing flow fields from gappy data. The aforementioned methods can only reconstruct a monotonic velocity field or at most a field with a single peak inside the gap (a half wave).

The main idea behind the present method is to use the full governing equations of the flow to predict the velocity distribution inside the gap, in order to reduce the error associated with the data refill procedure. We employ a numerical solution of the 2d incompressible Navier-Stokes equations to estimate the velocity field within the gap, using a staggered-grid finite volume solver, with time-varying Dirichlet boundary conditions imposed using the velocity provided by the PIV data. Unusually for data assimilation problems the PDE is well-posed with these boundary conditions; in particular, boundary conditions on the pressure are not required. Therefore assuming complete knowledge of BCs and belief in high accuracy of the experimental data, no stochastic approach is necessary - and we proceed deterministically with a standard NS solve. The initial condition on the velocity in the gap is unknown, but has a diminishing effect on the solution over time provided that information is convected out of the gap; therefore it is sufficient to specify any initial condition consistent with the boundary conditions at time zero, and integrate sufficiently far forward in time.

Numerical solution method

Considering a measurement domain with a gap Ω where no velocity is measured, the velocity field in Ω is computed by solving the unsteady Navier-Stokes equations, which in non-dimensional form read:

Conservation of mass:
$$\boldsymbol{\nabla} \cdot \boldsymbol{V} = 0 ; \tag{3.1}$$

Conservation of momentum:
$$\frac{\partial \boldsymbol{V}}{\partial t} + \boldsymbol{\nabla} p = \boldsymbol{R} , \tag{3.2}$$

where the following units are chosen: velocity: V_{ref}; length: L; density ρ_{ref}, pressure: $\rho_{ref} V_{ref}^2$. The vector $\boldsymbol{R} = [Ru \; Rv]^{\mathrm{T}}$ contains the contributions of advection and diffusion and is given by:

$$\boldsymbol{R} = \boldsymbol{\nabla} \cdot \left[-\boldsymbol{V} \otimes \boldsymbol{V} + \frac{1}{Re} \left(\boldsymbol{\nabla} \boldsymbol{V} + \boldsymbol{\nabla} \boldsymbol{V}^T \right) \right], \tag{3.3}$$

with $Re = \rho_{ref} V_{ref} L / \mu$ the Reynolds number, and μ the coefficient of dynamic viscosity. To solve the Navier-Stokes equations in Ω, a finite volume method is employed using a Cartesian staggered grid (Welch et al., 1966). Following the approach by Veldman (1990), the continuity and momentum equations are combined to reformulate the problem as a Poisson equation for pressure, which in the discrete form reads:

$$D_h^{\Omega} G_h \, p^{n+1} = D_h^{\Omega} \left(\frac{1}{\delta t} V_h^n + R_h^n \right) + \frac{1}{\delta t} D_h^{\partial \Omega} V_h^{n+1}, \qquad (3.4)$$

where h represents the mesh spacing, D_h^{Ω} and $D_h^{\partial \Omega}$ are the discrete divergence operators at the points of the volume mesh and boundary mesh respectively, G_h is the discrete gradient operator, δt is the temporal step and n indexes the time level. Finally V_h, p and R_h are discrete quantities corresponding to V, p and R. Employing a central discretization for both convective and diffusive terms, equation (3.4) written out in full reads:

$$\frac{p_{i+1,j}^{n+1} - 2p_{i,j}^{n+1} + p_{i-1,j}^{n+1}}{h_x^2} + \frac{p_{i,j+1}^{n+1} - 2p_{i,j}^{n+1} + p_{i,j-1}^{n+1}}{h_y^2} = \frac{1}{\delta t} \left(\frac{u_{i+1/2,j}^n - u_{i-1/2,j}^n}{h_x} + \frac{v_{i,j+1/2}^n - v_{i,j-1/2}^n}{h_y} \right) +$$

$$+ \frac{Ru_{i+1/2,j}^n - Ru_{i-1/2,j}^n}{h_x} + \frac{Rv_{i,j+1/2}^n - Rv_{i,j-1/2}^n}{h_y} \qquad , \quad (3.5)$$

with i and j representing the position of a generic cell inside the domain and u and v the horizontal and vertical velocity components respectively. Finally the update is made via:

$$V_h^{n+1} = V_h^n + \delta t R_h^n - \delta t G_h \, p^{n+1}, \qquad (3.6)$$

The pressure values computed from equation (3.5) guarantee that the velocity components obtained by solving (3.6) satisfy the incompressibility constraint (3.1).

Critically for this approach, (3.4) and (3.6) can be solved imposing boundary conditions *only* on the velocity and not on the pressure (Ferziger and Peric, 2002). The boundary conditions on V are provided at discrete time instants by the PIV measurements and are imposed as Dirichlet conditions. In order for the numerical scheme to be stable, the spacing h of the computational mesh and the time step δt are selected according to the conditions proposed by Ferziger and Peric (2002) for the linear convection-diffusion equation. To fulfill those conditions, δt often needs to be smaller than the time interval Δt between PIV recordings. Therefore, the velocity boundary conditions at intermediate time instants are computed through interpolation in time of the PIV velocity data. The time interpolation for the boundary conditions is based on the advection model proposed by Scarano and Moore (2011).

Application: Treatment of Shadow Regions

The technique is applied to an experiment in air of a rod-airfoil configuration. A cylindrical rod of 6 mm diameter is mounted 10.2 cm upstream of a NACA 0012 airfoil, having a chord of 10 cm and placed at zero angle of attack. The airfoil is made out of Plexiglas in order to be transparent to the laser light. The nominal free-stream velocity is set to 15 m/s, yielding Reynolds numbers of 6,000 and 100,000 with respect to the rod diameter and the airfoil chord respectively. The temporal separation between laser pulses is 50 µs, while the acquisition frequency is 2,700 Hz. The field of view size is 164×83 mm, imaged by 1939×1024 pixels. A thorough description of the experiment is reported in Lorenzoni et al., 2009.

The illumination is directed from the bottom of the field of view upwards, tilted clockwise by 11 degrees. According to Snell's law (Born and Wolf, 1999), when a light ray passes from air (refractive index $n_1 = 1.000$) to Plexiglas (refractive index $n_2 = 1.488$), it undergoes a deflection that depends on the angle between the incident ray and the normal to the interface. The deflection is negligible in the central part of the airfoil, where the incident and refracted rays are roughly parallel to the normal to the interface. In contrast, where the airfoil curvature is larger, i.e. at the leading and trailing edges, the refraction becomes so strong that non-illuminated regions are generated above the airfoil, see Figure 8.

For both the shadow regions A and B, above the leading and the trailing edge respectively, the numerical simulation is conducted in rectangular domains, indicated by the dashed lines in Figure 9. The first region, Ω_A is composed by 112×88 cells, corresponding to 56×44 PIV grid nodes, while Ω_B is composed by 62×100 cells, which correspond to 31×50 PIV grid nodes. The region containing measurement data inside the numerical domains serves as the buffer region B. Both numerical domains Ω_A and Ω_B exhibit a central region where no

PIV data is present and two lateral regions where particle image velocimetry vectors have been measured; the numerical solution is calculated in the entirety of the rectangular domains, but it is retained only in the central regions. At the unknown boundaries, the boundary conditions are computed as a linear interpolation of the measured PIV velocity data. Figure 9 shows an example of reconstructed instantaneous velocity fields. In both the shadow regions, the velocity components computed with the Navier-Stokes solver exhibit good agreement with the surrounding experimental data.
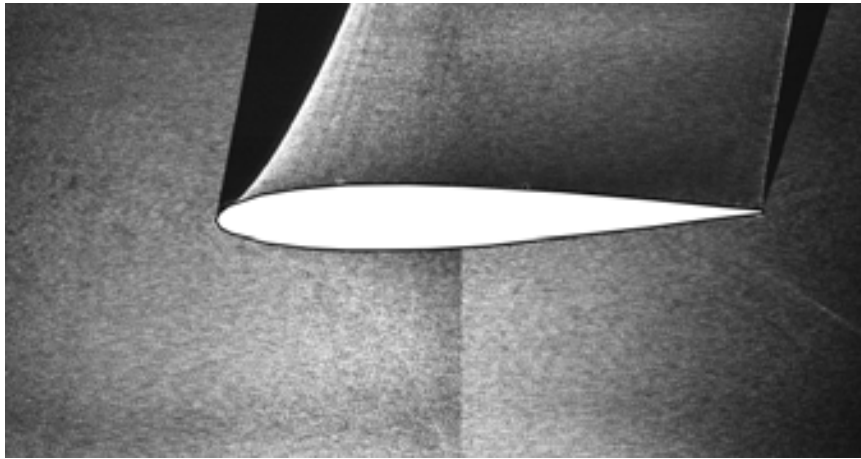
Figure 8: Double-frame recording of particle images on a transparent NACA 0012 airfoil (laser light directed from below) in the wake of a rod (outside the field of view).
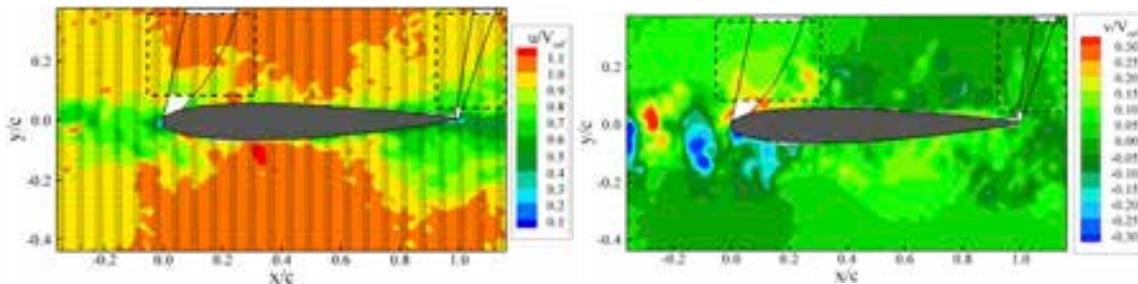
Figure 9: Instantaneous reconstructed velocity fields. Left: horizontal velocity component; right: vertical velocity component.

The added value of the present technique with respect to interpolation approaches is evident when small flow structures need to be reconstructed in the shadow region. In Figure 10, the motion of two vortices a and b is illustrated. At time $t = 0$, vortex a has a single core while vortex b has two distinct cores; both the vortices are on the left of the shadow region. The two vortices are adverted downstream by the flow and pass through the shadow region, where the velocity is calculated via the numerical simulation. The proposed filling approach allows tracking the vortices within the shadow region and estimating the distance between them within 5% accuracy. However, modulation effects are noticed which have two main consequences: reducing the peak vorticity up to 50% of the original value and merging the two cores of vortex b in a single-core vortex (see Figure 10). Downstream of the shadow region, the vorticity is measured from PIV data: the peak vorticity is recovered and the two cores of vortex b become distinct again.
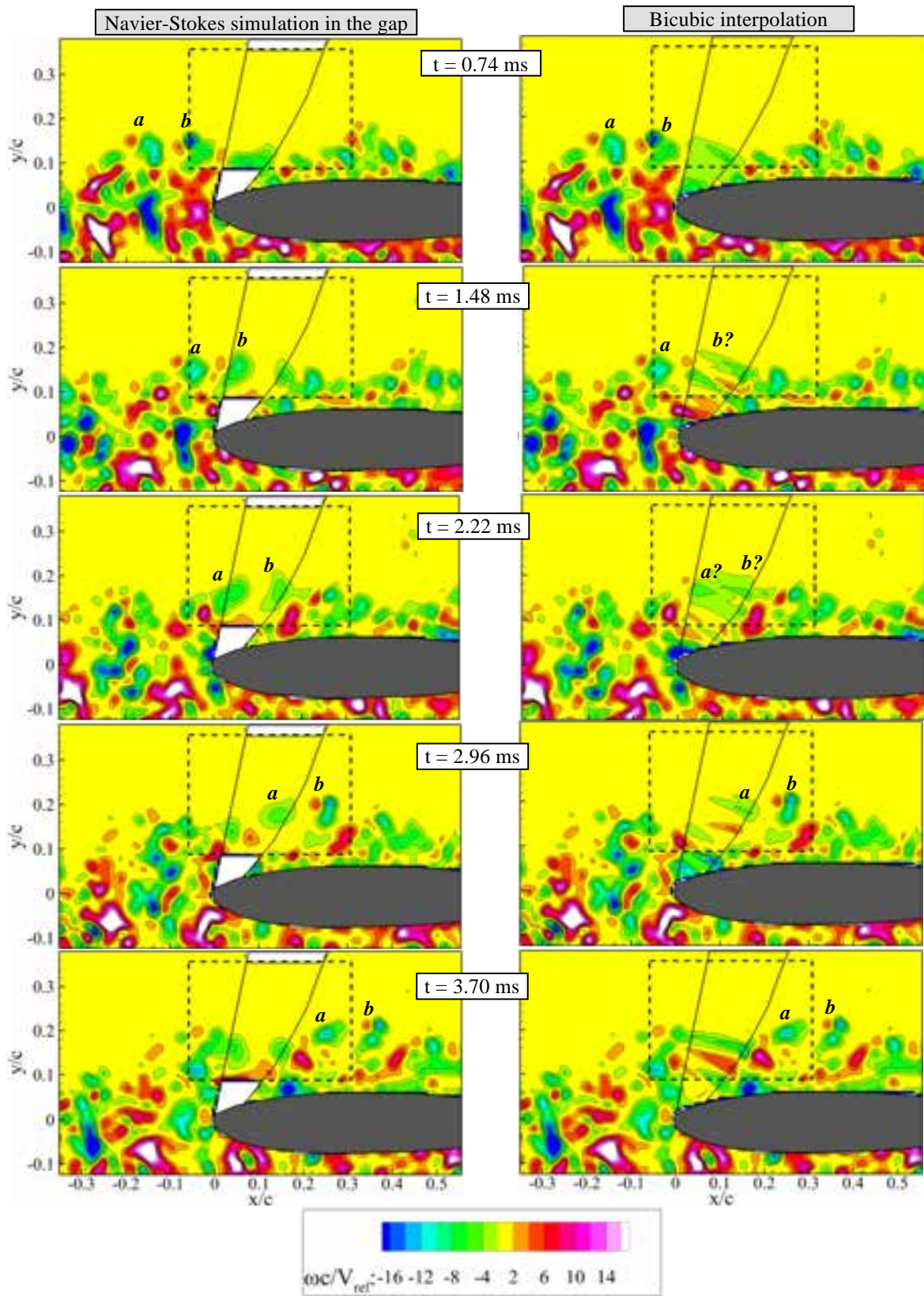
Figure 10: Vorticity contours showing the convection of two vortices *a* and *b* through the shadow region. Left: reconstruction through the Navier-Stokes solver; right: reconstruction through a bicubic interpolation of the velocity boundary values.

Conclusions and Further Work

In all engineering tasks use is made of both experimental data and simulation. We have shown how these may be combined in a variety of situations with Bayesian inference, assisted with appropriate numerical algorithms, to give results that are more complete and/or accurate than either simulation or experiment alone. The existence of Bayes as a unifying framework allows sharing of methods and implementations across widely varying application domains. We are firm believers in the use of Bayesian statistics for exploiting modern high-fidelity CFD solvers and rich data provided by modern experimental methods.

In each of the applications discussed work is ongoing, in order:

1. The main limitation of the current study was the use of manufactured data, which allowed us to assume that model inadequacy was negligible, and gave us exact knowledge of the experimental noise. Next steps are application to aeroelastic wind-tunnel tests, where a more complete statistical model will be necessary.

2. There are a number of directions in which Kriging PIV interpolation can be developed. Algorithms used to identify window displacements in PIV are usually iterative, with an initial low-quality velocity field being used to inform window distortion in a second step. Kriging is ideal for reconstructing this initial velocity field from noisy velocity vectors, and could help improve the efficiency and stability of these algorithms. We would also like to incorporate physical information into the interpolation via the covariance structure - this will allow the imposition of known properties like zero divergence or conservation, and improve the quality of results with bigger gaps (Dwight, 2010).

3. The gappy PIV technique relies on velocities being measured at all boundaries of a gap - which is an unusual situation, not even satisfied by our rod-aerofoil test-case. Compensating with interpolation at the boundary will not always be feasible, or give acceptable results. Similarly the velocity data must be accurate everywhere on the boundary. The method also relies on the assumption of incompressibility, without which velocity-only BCs lead to an ill-posed problem. Even worse if we desire to increase time resolution with this method, there is no way to match the numerical solution to measured data after a given time. All these issues can be resolved by also treating this problem stochastically. In this case a non-linear Kalman filter is an appropriate stochastic method, which may be derived from Bayesian statistics, Wickle and Berliner (2007). We are investigating the Ensemble Kalman Filter (EnKF) and Ensemble Optimal Interpolation (EnOI), Evensen (2003). Uncertainities in ICs, BCs and the model will be reflected in the solution.

References

[1] de Baar, J.H.S., Dwight, R.P. and Bijl, H. (2011). Fast maximum likelihood estimate of the Kriging correlation range in the frequency domain. In *IAMG Conference Salzburg*.

[2] de Baar, J.H.S., Dwight, R.P. and Bijl, H. (2012). Speeding up kriging: fast estimation of Kriging hyperparameters in the frequency-domain. *To be submitted*.

[3] de Baar, J.H.S, Percin, M., Dwight, R.P., van Oudheusden, B.W. and Bijl, H. (2012). Kriging regression of PIV data using a local error estimate. *Experiments in Fluids* (in preparation).

[4] Bitter, M., Scharnowski, S., Hain, R. and Kaehler, C.J. (2010). High-repetition rate PIV investigations on a generic rocket model in sub- and supersonic flows. *Exp. Fluids* 50:1019-30.

[5] Born, M. and Wolf, E. (1999). Principles of optics. *Cambridge university press*, Cambridge, U.K.

[6] Dwight, R.P. (2010). Bayesian inference for data assimilation using Least-Squares Finite Element methods. *IOP Series: Materials Science and Engineering,* Vol. 10 (1), pp. 222-232, doi:10.1088/1757-899X/10/1/012224, 2010.

[7] Dwight, R.P., Haddad-Khodaparast, H. and Mottershead, J.E. (2012). Identifying Structural Variability using Bayesian Inference. *Proc. Uncertainty in Structural Dynamics (ISMA/USD)*.

[8]   Dwight, R.P., Marques, S., Bijl, H. and Badcock, K.J. (2011). Reducing Uncertainty in Aeroelastic Flutter Boundaries using Experimental Data. *International Forum on Aeroelasticity and Structural Dynamics*, Paris, IFASD-2011-71.

[9]   Evensen, G. (2003). The Ensemble Kalman Filter: Theoretical formulation and practical implementation. *Ocean Dynamics* 53(4), pp. 343-367.

[10] Ferziger, J.H. and Peric, M. (2002). Computational methods for fluid dynamics. *Springer*.

[11] Gelman, A., Carlin, J.B., Stern, H.S., and Rubin, D.B. (2004). Bayesian Data Analysis. *CRC Press*.

[12] Gunes, H. and Rist, U. (2008). On the use of kriging for enhanced data reconstruction in a separated transitional flat-plate boundary layer. *Physics of Fluids* 20, 104109.

[13] Kennedy, M. and O'Hagan, A. (2001). Bayesian calibration of computer models (with discussion). *Journal of the Royal Statistical Society*, Series B., 63, 425–464.

[14] Khalil, M., Sarkar, A., and Poirel, D. (2010). Application of Bayesian inference to the flutter margin method: New developments. *ASME Conference Proceedings*, 2010(54518), 1143–1151. doi:10.1115/FEDSM- ICNMM2010-30041.

[15] Lind, R. and Brenner, M. (1997). Robust flutter margins of an F/A-18 aircraft from aeroelastic flight data. *Journal of Guidance, Control and Dynamics*, 20(3), 597–604.

[16] Loeven, G. (2010). Efficient Uncertainty Quantification in Computational Fluid Dynamics. Ph.D. thesis, TU Delft, Department of Aerodynamics.

[17] Lorenzoni, V., Tuinstra, M., Moore, P.D. and Scarano, F. (2009). Aeroacoustic analysis of a rod-airfoil flow by means of time-resolved PIV. *15th AIAA/CEAS Aeroacoustic Conference* (30th AIAA Aeroacoustic Conference), Miami, Florida, May 11-13.

[18] Mardia, K.V. and Marshall, R.J. (1984). Maximum likelihood estimation of models for residual covariance in spatial regression. *Biometrika,* vol. 71, no. 1, pp. 135–146.

[19] Marques, S., Badcock, K., Khodaparast, H., et al. (2010). Transonic aeroelastic stability predictions under the influence of structural variability. *Journal of Aircraft*, 47(4), 1229–1239.

[20] Mori, N. (2009). MPIV. *http://www.oceanwave.jp/softwares/mpiv*.

[21] Pettit, C. L. and Beran, P. S. (2006). Spectral and multiresolution wiener expansions of oscillatory stochastic processes. *Journal of Sound and Vibration*, 294(4–5), 752–779.

[22] Scarano, F. and Moore, P.D. (2011). An advection-based model to increase the temporal resolution of PIV time series. *Exp Fluids*, DOI 10.1007/s00348-011-1158-3.

[23] Schrijer, F.F.J. and Walpot, L.M.G.F.M. (2010). Experimental investigation of the supersonic wake of a reentry capsule. *Proc. AIAA 2010-1251, 48th AIAA Aerospace Sciences Meeting (Orlando, FL)*.

[24] Sciacchitano, A., Dwight, R.P. and Scarano, F. (2012). Navier-Stokes Simulations in Gappy PIV Data. *Experiments in Fluids*, DOI: 10.1007/s00348

[25] Tarantola, A. (2004). Inverse Problem Theory and Methods for Model Parameter Estimation. *Society for Industrial and Applied Mathematics.*

[26] Veldman, A.E.P. (1990). "Missing" boundary conditions? Discretize first, substitute next, and combine later. *SIAM J. Sci. Stat. Comput.* 11, 82-91.

[27] Venturi, D. and Karniadakis, G.E.M. (2004). Gappy data and reconstruction procedures for flow past a cylinder. *J. Fluid Mech*. vol. 509 pp. 315-336.

[28] Welch, J.E., Harlow, F.H., Shannon, J.P. and Daly, B.J. (1966). The MAC method, a computing technique for solving viscous incompressible, transient fluid-flow problems involving free surfaces. *Report LA-3425, Los Alamos Research Laboratories*, Los Alamos, NM.

[29] Westerweeel, J. (1994). Efficient detection of spurious vectors in particle image velocimetry data. *Exp. Fluids* 16:236-247.

[30] Wikle, C.K. and Berliner, L.M. (2007). A Bayesian tutorial for data assimilation. *Physica D: Nonlinear Phenomena,* vol. 230, no. 1-2, pp. 1–16.

[31] Witten, I.H., Frank, E. and Hall, M. (2011). Data Mining: Practical Machine Learning Tools and Techniques. *3rd Edition. Morgan Kaufmann.*

[32] Witteveen, J., Sarkar, S., and Bijl, H. (2007). Modeling physical uncertainties in dynamic stall induced fluid- structure interaction of turbine blades using arbitrary polynomial chaos. *Computers and Structures*, 85, 866–878.

[33] Woodgate, M., Badcock, K., Rampurawala, A., et al. (2005). Aeroelastic calculations for the Hawk aircraft using the Euler equations. *Journal of Aircraft*, 42(4), 1005–1012.

[34] Xiu, D. and Karniadakis, G. (2002). The Wiener-Askey polynomial chaos for stochastic differential equations. *SIAM J. Sci. Comput.*, 24(2), 619–644.

[35] Zimmerman, N. and Weissenburger, J. (1964). Prediction of flutter onset speed based on flight testing at subcritical speeds. *Journal of Aircraft*, 1(4), 190–202.

Using Proper Orthogonal Decomposition Methods for Comparing CFD Results to Experimental Measurements

T. Andrianne
A. Guissart
V. Terrapon
G. Dimitriadis

University of Liège
Liège, 4000
Belgium
t.andrianne@ulg.ac.be

Abstract

This work presents a method for quantitative comparison of numerical results to experimental measurements. It is based on the concept of Proper Orthogonal Decomposition. This technique is selected in order to compare the unsteady aerodynamic flows around static and oscillating bodies obtained from wind tunnel testing and numerical simulations. Two dimensional Time-resolved Particle Image Velocimetry measurements are carried-out on the upper surface a 4:1 rectangular cylinder. Simulations are performed using unsteady Reynolds-Averaged Navier-Stokes and an unsteady Discrete Vortex Method. It is demonstrated that the proposed technique is a good preliminary step for comparing the main characteristics of unsteady aerodynamic data.

Key words: unsteady aerodynamics, proper orthogonal decomposition, particle image velocimetry, CFD

Introduction

Over the last decades, our understanding of complex aerodynamic flows has been strongly intensified. The effect of small turbulent structures in unsteady flow-fields can now be taken into account in large computational models [1]. On the other hand, experimental analysis also became more advanced, especially with the Time-resolved Particle Image Velocimetry (Tr-PIV) technique [2], which allows the measurement of highly unsteady phenomena occurring at small and large scales in the flow-field around a body [3], [4]. In parallel to these exciting evolutions, the need for reliable comparison techniques of the resulting numerical and experimental data is also becoming more important.
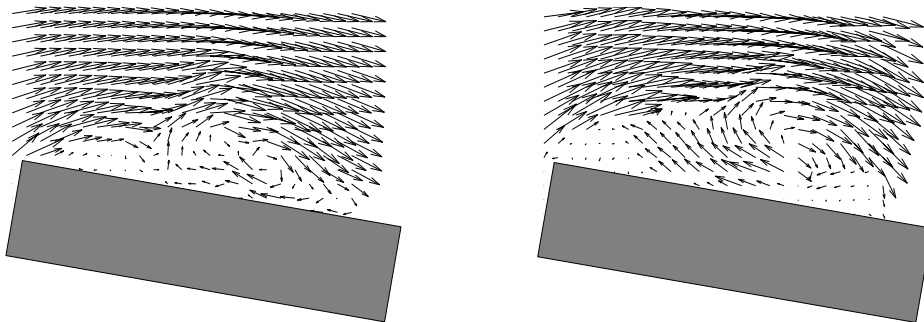

Figure 1: Snapshots of the velocity fields over an oscillating 4:1 rectangular cylinder Experiments (left), Simulations (right)

Figure 1 shows two instantaneous snapshots of the velocity fields on the upper surface of a rectangle which undergoes pitching oscillations around its geometric center. The snapshots are measured and simulated when the rectangle reaches the maximum pitch angle of the upstroke motion. Despite the relative resemblance of these two snapshots, it is not practical to repeat this comparison for all the simulation and experimental observations (300 snapshots in this case). Furthermore, because of the measurement noise present in the Tr-PIV data, it is vain to try to compare the absolute value of the velocity components at all the location of the grid points of the observation window.

It is proposed to use the Proper Orthogonal Decomposition (POD) technique in order to extract the main characteristics of the simulated and measured velocity fields and to facilitate the comparison.

This paper first presents the basic properties of the POD technique when applied on unsteady velocity fields u(x,y,t) and v(x,y,t). The use of the Modal Assurance Criterion (MAC) is also introduced in this section. Then the approach is applied to two applications, dealing with a 2D bluff body in a subsonic flow-field. In particular, a rectangular cylinder characterized by an aspect ratio *c/d* equal to 4 is chosen. This specific aspect ratio leads to interesting flow separation and re-attachment on its surface. Hence, it constitutes a good test case for the validation of the proposed comparison technique.

The two applications concern the analysis of the unsteady flow-field on the upper surface of the rectangle when it is:
1.   statically set at an angle of attack equal to 5°,
2.   oscillating in pitch around its mid-chord point at an imposed frequency and amplitude.

For each application, Tr-PIV measurements and numerical simulations, using Discrete Vortex Method (DVM), are performed. In the case of the static rectangle, Reynolds-Averaged Navier-Stokes (RANS) simulations are additionally carried out using OpenFOAM. The main characteristics of both numerical models are described and results about for quantities such as aerodynamic force coefficients and Strouhal number are presented. Finally, we focus on the comparison between numerical and experimental unsteady flow velocities using the POD technique.

Proper Orthogonal Decomposition

The POD approach consists in calculating a set of proper orthogonal functions in order to decompose the signal with the objective to capture the maximum amount of energy. The 2D unsteady flow-fields u(x,y,t) and v(x,y,t) can be expressed as

$$u(x,y,t) = \sum_{i=1}^{M} q_i(t)\, \Phi_{u,i}(x,y) \qquad \text{and} \qquad v(x,y,t) = \sum_{i=1}^{M} q_i(t)\, \Phi_{v,i}(x,y)$$

where M denotes the number of time instances. $\Phi_{u,i}(x,y)$ and $\Phi_{v,i}(x,y)$ are the POD modes, which only depend on the spatial coordinates (x,y). The generalized coordinates $q_i(t)$ represent the time dependence of the velocity field. The main advantage of POD is that no a priori knowledge about the data is needed. More details on the implementation of the POD technique can be found in reference [5].

The objective of the method is to apply the POD technique to the numerical results and experimental measurements, and to compare its outputs. In this paper, the quantitative comparison of the spatial patterns, the POD modes, is carried on using the Modal Assurance Criterion (MAC) [6]. The concept of MAC is commonly used in the field of structural dynamics in order to compare the mode shapes obtained from experimental modal analysis to the ones computed from finite elements models [7].

The value of the MAC is defined for each experimental (EXP) and numerical (NUM) couple of POD modes $(\Phi_i^{EXP}, \Phi_j^{NUM})$ by

$$MAC(\Phi_i^{EXP}, \Phi_j^{NUM}) = \left(\frac{\Phi_i^{EXP} \cdot \Phi_j^{NUM}}{\left\| \Phi_i^{EXP} \right\| \left\| \Phi_j^{NUM} \right\|} \right)^2$$

The value of $MAC(\Phi_i^{EXP}, \Phi_j^{NUM})$ varies between 1 and 0, depending if the ith experimental POD mode Φ_i^{EXP} is equivalent, or not, to the jth numerical POD mode Φ_j^{NUM}.

Unsteady flow around a static body

The first application concerns the modelisation of the unsteady flow around the rectangle at an angle of attack of 5°. The Reynolds number, based on the chord of the rectangle is equal to $Re = 10^5$.

As stated in the introduction, two numerical tools are used for simulating the flow around the rectangle. They are presented concisely below.

DVM model

The DVM model is based on the Lagrangian approach, which consists in shedding vortex particles on the surface of the rectangle and to track them individually at each time step [8]. Several studies have demonstrated that the DVM technique is well suited for simulating the unsteady flow-field around bluff structures (see for example [9] or [10]). This is due to the large separation and re-attachment of the flow-field around the sharp edges of the bluff body. Furthermore, the DVM tool is very interesting in terms of numerical cost, because it adds vortex particles where more details are required, i.e. in the vicinity of the upper surface of the body. The regions of the fluid domain not affect by the presence of the body are not taken into account (no vortex particles). This natural refinement of DVM avoids over-refined zones such as the boundary layer around the body that are necessary in CFD based methods.

The number of panels discretizing the geometry of the rectangle is set to 350. The time step is chosen as $dt = 0.1 \, c / V_\infty$, where c is the chord of the rectangle and V_∞ is the free-stream velocity of the incoming flow-field. The detailed description of the implementation can be found in Ref. [9].

Unsteady Reynolds-Averaged Navier-Stokes (RANS) simulations

Two-dimensional unsteady RANS simulations are also performed one the same case using the open source CFD code OpenFOAM[1], which is based on the finite volume method for unstructured meshes. For the purpose of this study, the transient solver for incompressible flows pisoFoam based on the PISO algorithm [11] is used.
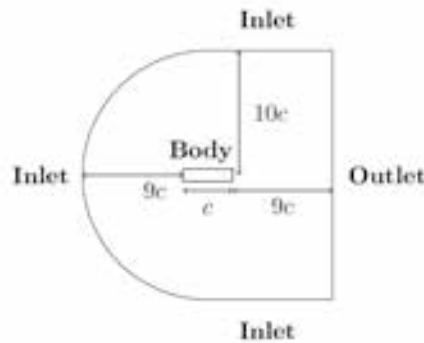

Figure 2: Computational domain for the RANS simulations

---

[1] www.openfoam.com
[2] http://geuz.org/gmsh/

The dimensions corresponding to computational domain are represented in Figure 2. The hexahedral mesh, created with GMSH[2], is divided into two regions as shown in Figure 3. In order to have an adequate resolution and accuracy in the critical flow regions, in particular where flow separation is expected, a fine structured mesh is used in the vicinity of the rectangle and in its wake (see the detailed view in Figure 3).

Because no wall-function is used, the first mesh point away from the rectangle surface is set such that y+≈1, where the + exponent indicates wall units, for most of the cells around the rectangle. A grid convergence analysis on four different meshes (i.e., with around 310 000 , 140 000, 80 000 and 36 000 cells, respectively) has shown that the solution is grid-independent. The following results were obtained on the 140 000 cells mesh, the computation on the finest one being too slow.
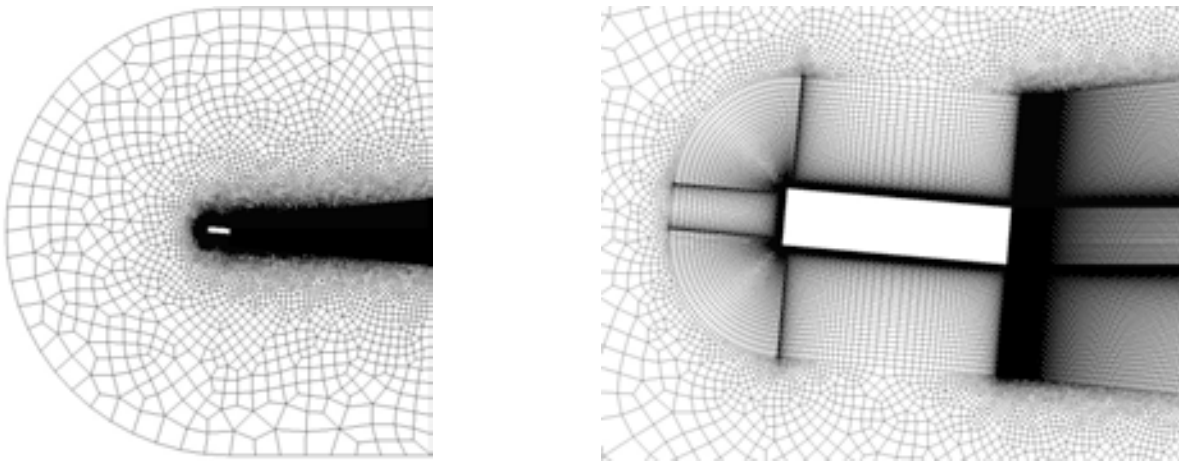
Figure 3: Computational mesh for the RANS simulations: entire computational domain (left) and detailed view of the regions close to the rectangle (right)

To close the RANS equations, the Menter k-ω SST model [11] is employed, as it is known to be better to predict flow separations than the standard k-ε model and to be less sensitive to free-stream turbulence than the standard k-ω model [13].

The backward Euler scheme is used to advance the equations in time. In order to capture accurately the smallest time scales of the flow and to ensure numerical stability, the time step is chose to be 10^{-4}. This corresponds to a CFL of about 0.9 and 18 000 times steps per shedding period.

At the boundary surface, the no-slip condition is imposed for the velocity, a homogeneous Neumann condition for pressure, and Dirichlet conditions for the turbulent scalars. At the inlet, the free-stream velocity ant turbulent scalars are imposed. The latters correspond to the wind-tunnel free-stream turbulence intensity of 0.15% [9].
For the pressure, a zero-gradient boundary condition is set. Finally, the outlet corresponds to a zero-gradient for the velocity and turbulent scalars, while the pressure is enforced.

Preliminary analysis

On the basis of the two numerical tools presented above, the following global quantities are computed: the mean aerodynamic force coefficients C_L, C_D and the Strouhal number, defined by $St = f\, d / V_\infty$, where f is the shedding frequency and d is the thickness of the rectangle. These results are summarized in Table 1 for the two numerical simulations, together with experimental results from the literature [14] and previous works of the authors [9].

---

[2] http://geuz.org/gmsh/

Table 1: Mean aerodynamic lift and drag coefficients and Strouhal number for the flow around a rectangle of aspect ratio of 4 at 5° angle of attack and Re=10^5.

	C_L	C_D	*St*
DVM	0,56	0,32	0,143
Unsteady RANS	0,83	0,45	0,136
Experiments	0,53	0,45	0,152

It is observed from this table that the two numerical tools are not capable to predict accurately the values of C_L, C_D and *St*. The lift coefficient and the Strouhal number are well estimated by the DVM code but the drag coefficient is too small in comparison with experiments. On the other hand, RANS accurately predict the drag coefficient but the lift coefficient is over-estimated. The error on the Strouhal number is acceptable. Note that eddy viscosity models are know to be inaccurate for separated flows.

Up to this point, the main characteristics of the two numerical tools have been presented, together with some basic global results. It is proposed to push further the understanding of the unsteady phenomena taking place around the rectangle by analyzing the flow-field on its upper surface.

POD analysis

The unsteady flow-field is measured and computed on the upper surface of the cylinder, on a mesh of 25 by 13 points as shown by crosses in Figure 4. In this figure, the rectangle is shown in gray and the flow comes from the left of the image.
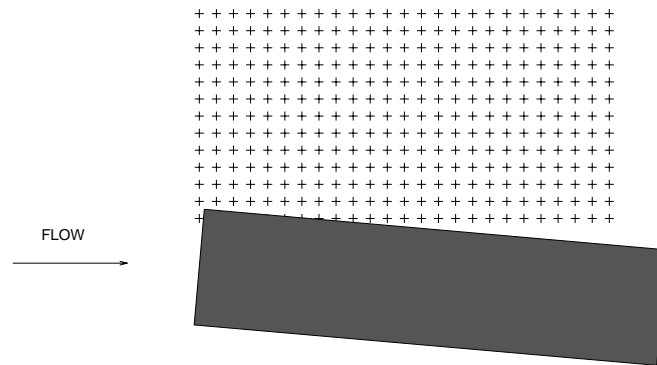
Figure 4: Observation window on the upper surface of the static cylinder at 5°

The POD technique is applied to the velocity fields obtained from the PIV measurements and the two numerical tools. We concentrate here on the comparison of the spatial patterns (POD modes) and their energy content. Figure 5 shows the six first modes obtained by decomposing the experimental and numerical results. It is based on 500 time instances and the sample length corresponds to 50 shedding periods.
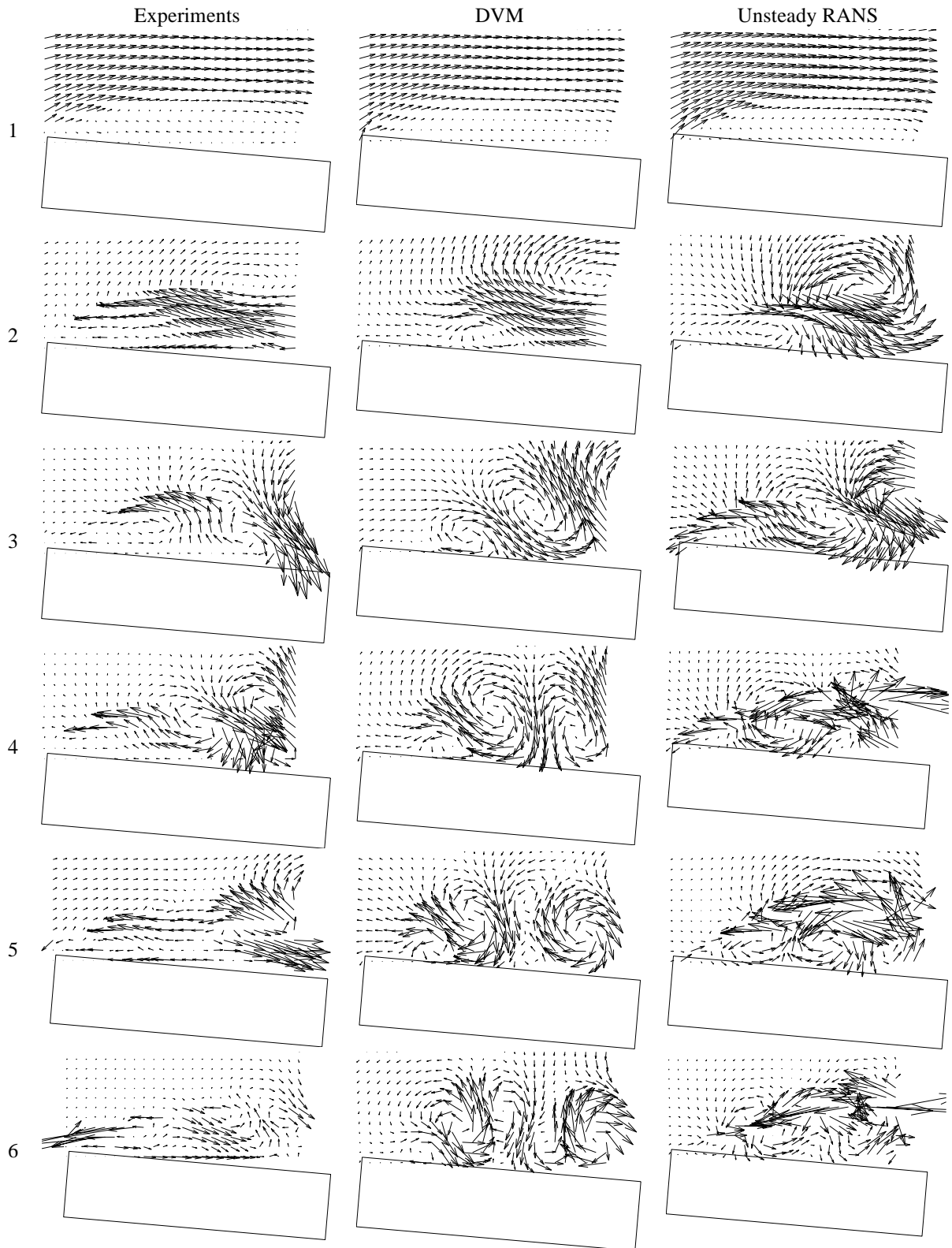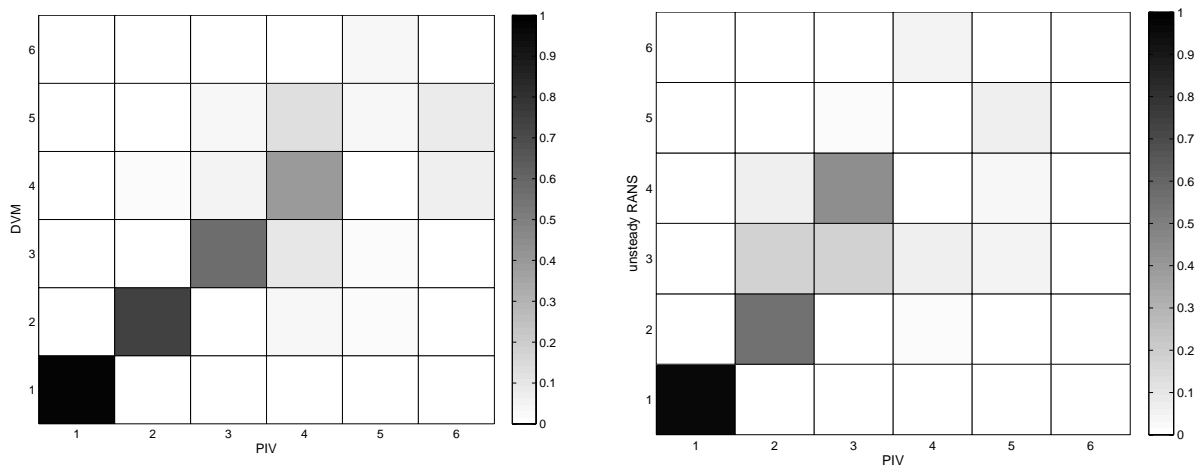
Experiments   DVM   Unsteady RANS

Figure 5: First six POD modes: Experiments (left), DVM (center), Unsteady RANS (right)

One can observe that the first POD mode is correctly capture by both numerical models. This mode corresponds to the mean flow, because the mean value of the fields u(x,y,t) and v(x,y,t) are not subtracted when applying the POD technique (see [5] for details about the consideration of the mean flow in the POD analysis). Nevertheless, the phenomena of interest are typically related to the unsteadiness of the flow-field. Hence, it is necessary to analyze the other POD modes. The second POD mode is relatively well captured by the DVM simulation. On the other hand, fewer similarities can be observed observed with the unsteady RANS. It is also very interesting to note that the third mode given by the unsteady RANS is very similar to the fourth experimental mode.

Generally speaking, it is difficult to have a global view of the resemblance of the numerical POD modes, with the experimental ones. Hence, it is proposed to use the MAC to obtain a more quantitative comparison between the three different sets of results. A 6 by 6 MAC matrix is calculated for each numerical results (DVM and Unsteady RANS), taking into account the first six modes presented in Figure 5. These two matrices are shown graphically in Figure 6.

Figure 6: Static rectangle at 5° - MAC matrices
DVM vs Experiments (left), Unsteady RANS vs Experiments (right)

It is observed that the first four POD modes from the DVM simulations are well reproduced (MAC values higher than 0.4). On the other hand, only the first and second POD modes seem to be correctly captured by the unsteady RANS. As qualitatively observed from Figure 5, the MAC analysis confirms that the third POD mode from the unsteady RANS simulation corresponds to the fourth experimental mode (with a MAC value of 0.45 off the diagonal). Hence, three POD modes are relatively well identified using unsteady RANS simulations.

It is interesting to analyze the eigenvalues corresponding to each of the first six POD modes. These quantities are proportional to the kinetic energy of the POD modes [5]. They are plotted in Figure 7, where it is clear that the first POD mode ('mean flow' mode) contains most of the energy of the flow. For the experimental, the DVM and the unsteady RANS results, the energy content of this mode is equal to 97.6%, 95.9% and 99.4%, respectively.

An enlarged view on the eigenvalues 2 to 6 is shown in Figure 7. Despite their low absolute values, the energy content is distributed over these POD modes in the case of experiments and DVM results. In order to emphasis this observation, Figure 8 presents the residual energy percentage for modes 2 to 6. The residual energy is defined by the ratio of the eigenvalue of a mode divided by the sum of the eigenvalues for modes 2 to 6. From Figure 8, it is clear that each POD mode between 2 and 4 contains between 10% and 30% of the residual energy in the case of the experiments and the DVM simulations. On the other hand, the POD modes 2 and 3 from the unsteady RANS simulations contain most of the energy of the flow-field, the contribution of modes 4, 5 and 6 being negligible.

This discussion about the energy distribution is in agreement with the observations made about the MAC matrices in Figure 6. If a POD mode does not appear in a simulated set of data, its energy content is very low

and the corresponding element of the MAC matrix is also close to zero. Note that the information about the energy level of a POD mode can be used in the case of Reduce Order Modelling, where it can orient the choice of the retained modes for reconstructing the signal.
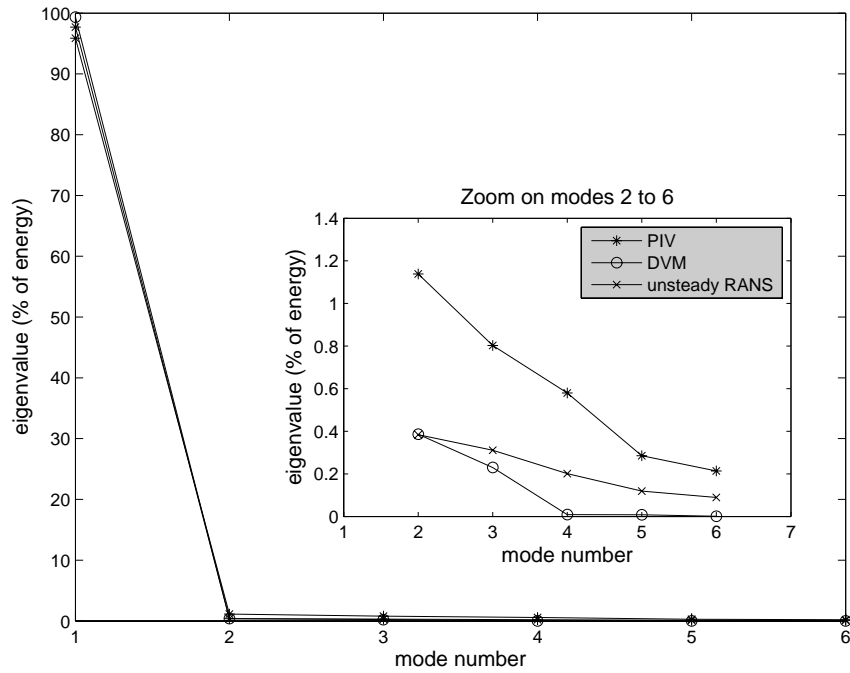

Figure 7: Static rectangle at 5° - Eigenvalues of the POD modes: percentage of the total flow energy
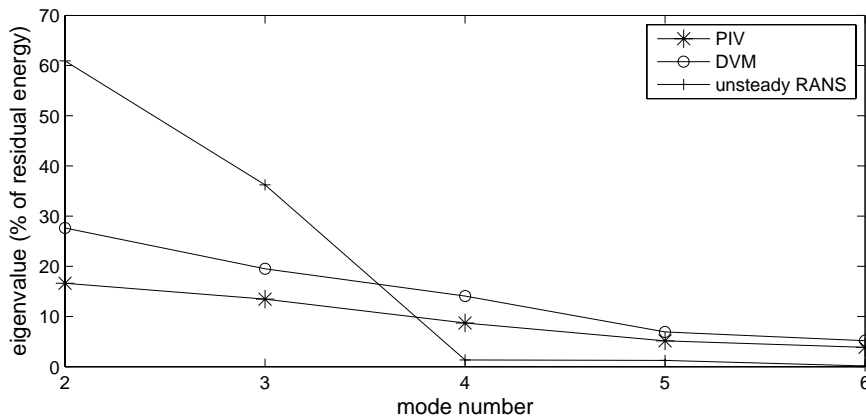

Figure 8: Static rectangle at 5° - Eigenvalues of POD modes 2 to 6: percentage of the residual flow energy

Unsteady flow around an oscillating body

The second application of this paper concerns the analysis of the flow-field around the oscillating rectangle. A pitching motion is applied to the rectangle according to $\alpha(t)=10°\sin(2\pi 8.1t)$, where t is the dimensional time, expressed in seconds. The Reynolds number is identical to the one of the static case above.

This application involves only DVM simulations and its comparison with the Tr-PIV measurements is performed on the upper surface of the rectangle. The observation window is slightly bigger than for the static case, as shown in Figure 9. In this figure, the dashed rectangle represents the center of oscillation at 0°. The two plain rectangles correspond to the maximum and minimum values of the pitch angle (+/- 10°). Note that the position of the observation window enable to cover the entire upper surface of the rectangle when it reaches its maximum and minimum pitching positions.
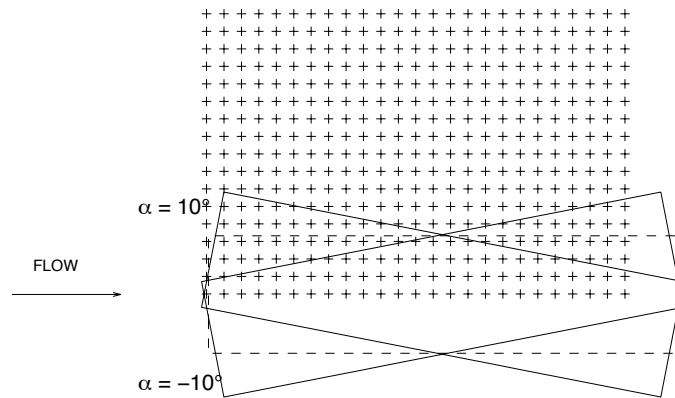
Figure 9: Observation window on the upper surface of the cylinder for the oscillating cylinder

The numerical parameters of the static application are retained in this section, hence no description of the DVM simulations is presented here.

Experimental measurements are performed during three periods of oscillation of the rectangle. A preliminary computation is carried out using the DVM tool in order to get rid of the starting effects. This fast initial step lasts 10 pitching oscillations. Then flow is computed in the observation window during three pitching oscillations and is saved for further post-processing.

POD analysis

Similarly to the static rectangle case, the POD technique is applied on the computed unsteady velocity fields $u(x,y,t)$ and $v(x,y,t)$. Nevertheless, because of the oscillation of the rectangle in the observation window, some grid points will periodically be inside the solid domain, where the components of the velocity vanish. It is decided here to keep these zero values, i.e. $u(x_i,y_i,t_i) = v(x_i,y_i,t_i) = 0$, where (x_i,y_i,t_i) denotes the coordinates of the grid points inside the rectangle.

The MAC matrix built from the numerical (DVM) and experimental (PIV) POD modes is shown in Figure 10. The first three modes are well reproduced (MAC > 0.75) and the fourth one is also reasonably well predicted (MAC = 0.47).

Figure 11 presents the energy distribution of the six POD eigenvalues. The distribution of the simulated results follows the experimental distribution. Note that the energy of the first mode from DVM results is higher than the experimental one: 87% and 78%, respectively.

The distribution of the residual energy between modes 2 to 6 is similar for the experimental results and the DVM simulations (see Figure 12). This figure also confirms the statements made in the case of the static rectangle concerning the energy level of the modes: the POD modes that are correctly identified (1 to 4) are associated with a non-negligible energy level.
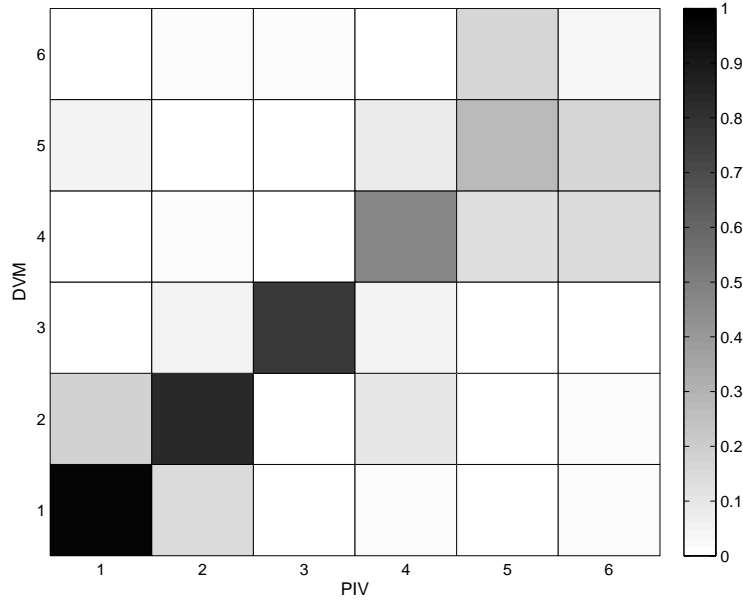

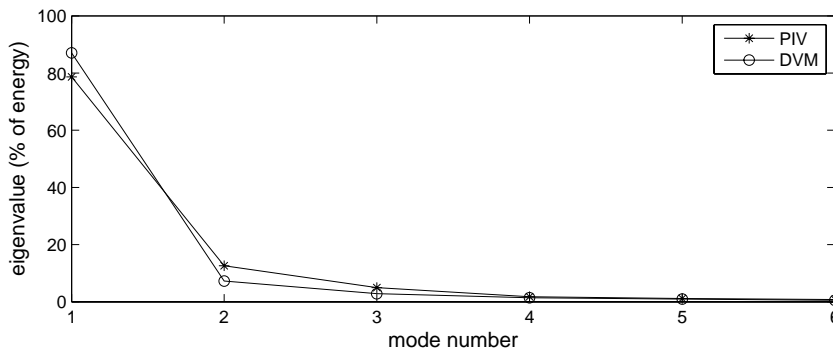**Figure 10: Oscillating rectangle - MAC matrix of DVM vs Experiments**

Figure 11: Oscillating rectangle: Eigenvalues of the POD modes: percentage of the total flow energy
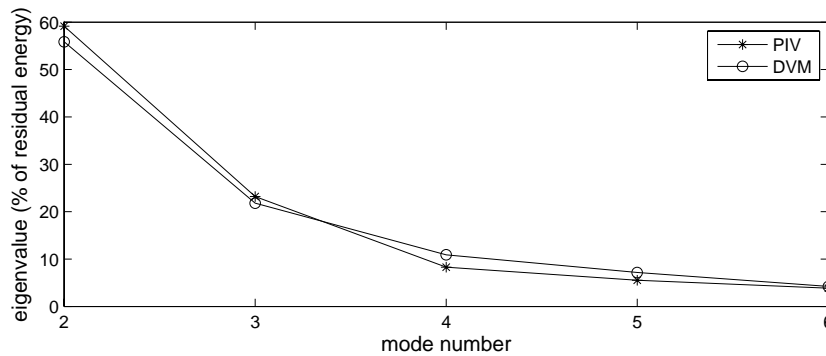
Figure 12: Oscillating rectangle: Eigenvalues of POD modes 2 to 6: percentage of the residual flow energy

Discussion

Through the two applications presented in this paper, it is shown that the extraction of the first POD modes enables an effective comparison between experimental measurements and numerical results. In particular, the case of the oscillating rectangle highlights the fact that energetic simulated POD modes compare better to the experimental ones than in the static rectangular case.

The advantage of this approach is that the complete PIV measurements are used for comparing with the numerical simulations. In the case of hot wire measurements, the signal measured is better in terms of time resolution but limited in its spatial resolution. Hence, the frequency contents of the experimental and numerical data can be compared but no spatial comparison is possible. Furthermore, the use of the POD technique allows taking into account the measurements where flow separation and reattachment occur, i.e. where the flow velocities are very small and thus, very sensitive to the measurement noise. It is then an efficient method for evaluating if a numerical tool is capable of modelling flow separation and reattachment, which are of prime importance when dealing with bluff bodies.

Additionally, the MAC-matrix represents a quantitative and direct tool for comparing POD modes from experimental measurements and numerical simulations. It can be used to guide the choice of the different numerical parameters (turbulence models in the case of CFD simulations, time step or number of panels for DVM simulations, etc.). Note that the MAC and POD-based comparison method can also be used for comparing two sets of experimental data or two sets of numerical data.

Finally, a numerical tool validated in a critical region of the flow (i.e. upper surface here) by comparison of the most energetic experimental and numerical POD modes, is complementary to experimental measurements. Additional information that cannot be easily extracted from experimental fluid dynamics are then available: other quantities (pressure, vorticity,...) in other regions, with an higher resolution and in more controlled conditions. This situation is depicted in Figure 13, where the unsteady velocity field is computed over a larger domain.

In these terms, we would like to emphasize that the present POD-based validation methodology is essentially a manner of integrating CFD and experimental studies. In this way, the advantages of both approaches are combined.
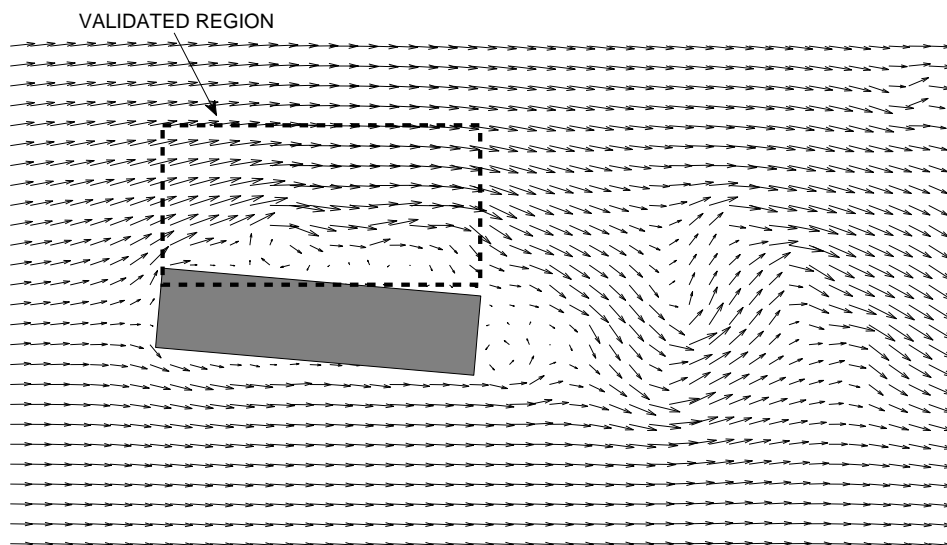

Figure 13: Large fluid domain

Conclusion

This paper proposes the use of the POD technique as a preliminary step for comparing experimental measurements to numerical results. The methodology is demonstrated in the case of the flow around a bluff body, where flow separation and reattachment occur, leading to very small velocities near the surface of the body. Once extracted from the experimental measurements and the corresponding numerical simulations, the energetic patterns of the flow-field are compared.

The extraction of the most energetic characteristics of the flow-field is valuable because it simplifies the comparison between two sets of complex spatio-temporal data. The proposed method is enhanced by the use of the MAC, which results in a limited number of quantitative values.

References

[1] P. Sagaut: *Large Eddy Simulation for Incompressible Flows*. Springer, third edition, 2006.

[2] M. Raffel, C. Willert, S. Wereley, and J. Kompenhaus: *Particle Image Velocimetry - A practical guide.* Springer, second edition, 2007.

[3] R. Mills, J. Sheridan, J. and K. Hourigan: *Particle image velocimetry and visualization of natural and forced flow around rectangular cylinders*. Journal of Fluid Mechanics, 478: 299-323, 2003.

[4] K. Mulleners and M. Raffel: *A Time-Resolved Dynamic Stall Investigation Based on Coherent Structure Analysis*. 15th International Symposium of Laser Techniques to Fluid Mechanics, Portugal, 2010.

[5] T. Andrianne, N. Abdul Razak and G. Dimitriadis: *Flow Visualization and Proper Orthogonal Decomposition of Aeroelastic Phenomena*, in Wind Tunnels, edited by Satory Okamato, ISBN 978-953-307-295-1, InTech, 2011

[6] R. Allemang and D. Brown: *A correlation coefficient for modal vector analysis*, Proccedings of the 1st International Modal Analysis Conference, p 110-116, Orlando, 1982.

[7] R. Allemang: *Vibrations: Experimental Modal Analysis*, UC-SDRL-CN-20-263-663/664, 1990.

[8] A. Léonard: *Vortex methods for flow simulation*, Journal of Computational Physics, vol. 37, pp.289-335, 1980.

[9] G. Morgenthal: *Aerodynamic analysis of structures using high-resolution vortex particle methods*, PhD Thesis, Cambridge, 2002.

[10] T. Andrianne: *Experimental and numerical investigations of the aeroelastic stability of bluff structures,* PhD Thesis, University of Liège, 2012.

[11] J.H. Ferziger and M. Peric: *Computational Method for Fluid Dynamics*. Springer, third edition, 2002.

[12] F., Menter: *Two-Equation Eddy-Viscosity Turbulence Models for Engineering Applications*, AIAA Journal, 32 (8), pp. 1598-1605, 1994.

[13] M. Casey and T. Wintergerste: *ERCOFTAC Special Interest Group on "Quality and Trust in Industrial CFD": Best Practice Guidelines*. 2000.

[14] Y. Nakamura and T. Mizota: *Torsional flutter of rectangular prisms*, Journal of the engineering mechanics division, ASCE, vol. 101, n° EM2, pp. 125-142, 1975.

Experience in the application of numerical methods to TsAGI's wind-tunnel testing techniques

S.L. Chernyshev
V.Ya. Neyland
S.M. Bosnyakov
S.A. Glazkov
A.R. Gorbushin
I.A. Kursakov
V.V. Vlasenko

1, Zhukovsky street,
Central Aerohydrodynamic Institute (TsAGI),
Zhukovsky, Moscow region, 140180,
Russian Federation
gorbushin@tsagi.ru

Abstract

This paper briefly presents the history of numerical methods' implementation into TsAGI's experimental technologies since the launch of the Buran-Energiya space system program in the 1980s. New features of the method developed at TsAGI within the framework of Electronic Wind Tunnel software package for numerically solving the Navier-Stokes equations are described. Application examples of the programs for solving problems associated with the test methodology adapted for the TsAGI T-128 and T-104 wind tunnels are provided.

Keywords: aerodynamics, numerical methods, wind tunnel.

Introduction

The application of numerical methods within TsAGI's wind tunnel testing technology is under way since the 1980s in connection with the need for improving the aerodynamic characteristics accuracy for the Buran-Energiya aerospace system models. For example, the numerical methods were used for the first time to account for the effect of the test section perforated walls on results of transonic tests in the T-128 wind tunnel. The T-128 transonic wind tunnel [1] has a unique feature among industrial test facilities: its test section wall perforation-openness ratio can be selectively regulated. The walls are divided into 128 panels, whose openness ratio can be varied from 0 to 18%. The arrangement of the panels and the position of the model being tested within the test section, as shown in Figure 1, were selected in accordance with Ref. [2]. The combination of the numerical evaluations and the wall permeability regulation have allowed the researchers to develop an effective

Figure 1. Arrangement of the T-128 perforated panels and the location of the model in the test section No 1
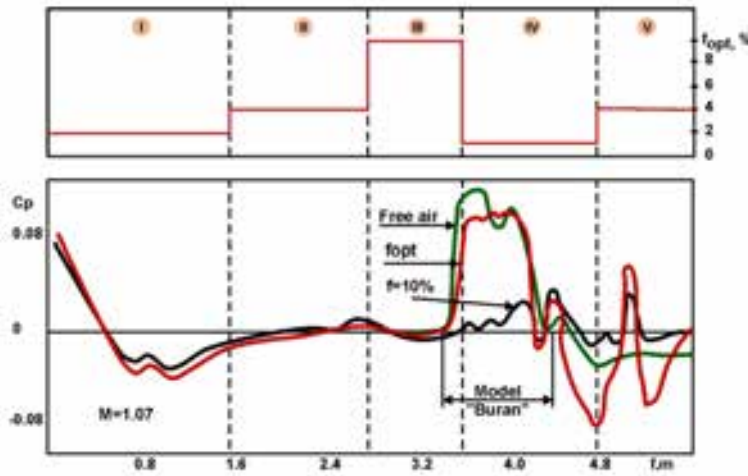
Figure 2. Optimal openness ratio distribution along the test section No 1 and pressure coefficient distribution over the wall

adaptation technology of the perforated panels of test section No 1 in the T-128 wind tunnel [2-5] and to use it since 1986. The gist of the adaptation is following. The distributions of the flow parameters near the perforated panels (far field) were calculated for the free conditions by numerically integrating the Euler equations. Based on the transonic area rule, the calculations were performed for the equivalent body of rotation for low incidence angles. This significantly reduced the calculation time. During testing, pressure distributions were measured on the test section walls and were compared with computed data. Further, the openness ratio of the panels was changed until the difference between the calculated and measured pressures reaches a minimum. Figure 2 shows the distribution of the openness ratio along the test section as well as the computed and measured pressure distributions on the walls [5]. It can be seen that the optimal distribution of the openness ratio provides an acceptable level of the pressure coefficient in the far field. The adaptation methodology at transonic flow speeds allowed one to evaluate with sufficient accuracy the maximum load acting on the attachment fitting between the Buran orbiter and the Energiya booster.

The numerical methods were also used together with the theoretical and experimental studies in the cases, when it was impossible to simulate in wind-tunnel tests all flight parameters of the Buran orbiter [6, 7]. In particular, hypersonic wind tunnels failed to simulate the air dissociation effect, which distorted the pitching moment [8]. The combination of numerical and experimental methods has provided reliable estimations of the aerodynamic characteristics at high altitudes in passing from free molecular flow to continuum as well as for heat flux with the natural laminar-turbulent transition of the boundary layer [9]. Thus, application of the numerical methods in experimental studies has allowed one to enhance the trustworthiness of the aerodynamic characteristics of the Buran orbiter for its entire flight trajectory, which was supported by a flight experiment and, as a result, ensured Buran's successful flight in the automatic mode in 1988.

The adaptation methodology was later used for testing half-models of passenger aircraft in T-128 test section No 2 [3-5].

To take into account the effect of slotted walls of test section No 3 on the airfoil profile characteristics for subsonic aircraft, a special methodology was developed [10-12] on the basis of Euler equations' potential approximation. The calculation of the turbulent boundary layer on the airfoil was based on the extension of Green's lag-entrainment method. As the boundary condition on the perforated walls, the pressure distribution measured experimentally was adopted. The computations were performed both for the free flow and in the case with perforated walls. The problem of free flow around airfoil was solved for corrected incidence angle and Mach number, so the functional representing the integral of the absolute value of the difference between computed and experimental pressure distributions over the profile surface reaches a minimum. As a result, integral corrections to the incidence angle and incoming flow Mach number were determined for free flow case with flow around airfoil being the most close to that obtainable in wind-tunnel tests.

Since 1996, to account for the effect of flow boundaries at transonic speeds, the numerical solutions of the Euler equations are being employed. The EWT (Electronic Wind Tunnel) computer code package [13-16] was developed at TsAGI. The boundary conditions at the perforated walls were presented in the form of the Darsy law (the linear relation between the normal and longitudinal components of perturbed velocity) and were determined experimentally [17, 18].

Using the EWT computer code package, the range of the fast linear method applicability [19] was determined as a function of Mach number. It turned out that for a moderate blockage of test section the linear methods can be applied up to M=0.9.

Later on, a module for numerically solving the Reynolds-averaged Navier-Stokes equations (RANS) was added to the EWT package. Presently, the code allows numerical solving stationary (RANS) and non-stationary (URANS) equations and large eddy simulation (LES). Special initial and boundary conditions are provided, such as the wind tunnel start, permeable walls (perforated and slotted), moving runway, plenum chamber, cryogenic effects, etc. As a special feature, a grid templates for different wind tunnels were created and a special block for investigated model was included. Another special block represents model support systems. An algorithm was developed for restructuring the calculation grids in accordance with variations of incidence and slip angles.

The EWT code package allows researchers to solve the three main groups of problems:
- minimization of the effect of flow boundaries (perforated walls) within the transonic speed range using the adaptive perforation technology;
- taking into account the systematic experimental errors due to flow boundary effects, support systems for complete and half-models, inherent wind-tunnel flow turbulence;
- designing the optimal contours of model support systems and panels of perforated walls to minimize flow disturbances in the test section.

Description of the EWT code computational method novel features

An in-depth description of the EWT computational method is given in [20]. The method has passed a complete evaluation and turned out to be stable in operation and providing accurate results. During the parametric computations, its algorithm was subjected to significant improvements. The flow in the wind tunnel has rather a complicated structure. It is defined by essentially viscous phenomena combined with well-developed turbulent boundary layers. Separated flow zones appear around different elements including highly deflected slats. In the case of moderate incidence angles, time-averaged approach of [20] is acceptable because the flow is stable and can be simulated numerically with the use of RANS. But there are some problems with correct prediction of drag and lift coefficients in the case of high incidence angles. Non-stationary processes connected with strong interaction between developed separation zones and non-stationary vortex sheet past the wing become essential and force to use URANS in TsAGI's computational technology [20].

Because of flow non-stationary features, one should choose explicit schemes for simulation. These schemes allow one to describe non-stationary processes with high quality. But an essential obstacle to realize such an approach is multi-scale feature of task. Characteristic times and sizes of different physical processes can differ by some orders of magnitude. Therefore, implementation of explicit schemes leads to extremely large calculation time. Contrary to that, implicit schemes are good for multi-scale problems but they show poor quality of non-stationary processes description.

A possible way to resolve this contradiction is to use zonal method. In this method, flow zones with very small scales of physical processes (mainly, inner zones of boundary layers) are calculated using an implicit scheme, while the other part of flow is calculated using explicit one. As a result, non-stationary processes in inviscid core of flow are simulated with a high quality. In the inner part of boundary layers, an implicit scheme is used and one may hope for good results, because the information has to be transmitted across the boundary layer and non-stationary processes in the inner zone of the boundary layer have mainly to be determined by the laws persistent to the inviscid core of flow. This consideration reduces scheme requirements from the viewpoint of non-stationary process description quality and permits using the implicit scheme in such concrete zones.

Let's consider an explicit scheme of the second order in time that is used for numerically solving the Euler and Reynolds equations. In this scheme, the time step is performed using a two-step predictor-corrector procedure:

$$\begin{cases} \dfrac{\tilde{u}_i^{n+1} - u_i^n}{\tau_n} + \dfrac{F_{i+1/2}(u^n) - F_{i-1/2}(u^n)}{h_i} = 0, \\[3mm] u_i^* = \dfrac{u_i^n + \tilde{u}_i^{n+1}}{2}, \\[3mm] \dfrac{u_i^{n+1} - u_i^n}{\tau_n} + \dfrac{F_{i+1/2}(u^*) - F_{i-1/2}(u^*)}{h_i} = 0. \end{cases}$$

Here, i is a number of calculation cell in space. Half-integer indices correspond to sides of calculation cell, n is time step number, h_i is grid step in space (cell size), τ_n is a time step value. The used scheme belongs to Godunov-type class. Therefore, to calculate parameters on sides of cells, a Riemann problem solution about decay of an arbitrary discontinuity is used:

$$F_{i+1/2}(u) = F(U_{i+1/2}) , \quad U_{i+1/2} = \mathrm{Decay}(u_L, u_R) .$$

To achieve the second approximation order in space, a linear reconstruction of space distribution of parameters over cell is used:

$$u_L = u_i + \left(\frac{\partial u}{\partial x} \right)_i \frac{h_i}{2} , \quad u_R = u_{i+1} - \left(\frac{\partial u}{\partial x} \right)_{i+1} \frac{h_{i+1}}{2} .$$

To calculate gradients of parameters in the cells, TsAGI-developed minimal derivative principle (MUSCL) is used. Details can be found in [1].

Such explicit scheme is stable, when time step τ satisfies the known Courant-Friedrichs-Levi condition:

$$\mathrm{CFL} \equiv |a(u_i)| \frac{\tau_n}{h_i} \leq 1 \quad \Leftrightarrow \quad \tau_n \leq \tau_i^{stab} \equiv \frac{h_i}{|a(u_i)|} \quad a(u) \equiv \frac{dF}{du} .$$

Advantages of the scheme above are clear due to physical sense and small errors. They make this scheme optimal for high-quality description of non-stationary processes. However, attempt to use this scheme for description of flow with turbulent boundary layers was unsuccessful.

Because the velocity $\dfrac{dx}{dt} = a(u)$ is known, the information propagates per one time step as $\mathrm{CFL}_i \cdot h_i$, where $\mathrm{CFL}_i = a_i \dfrac{\tau_n}{h_i}$ is local Courant number. A standard approach for time stepping (global time stepping) is the following. The most rigid condition for time stepping ($\tau_{\min} = \min\limits_i \tau_i^{stab}$) is used for global calculations (Figure 3a). It is typical for strongly non-uniform grids that $\tau_{\min} \ll \tau_{\max} = \max\limits_i \tau_i^{stab}$. It means that Courant number
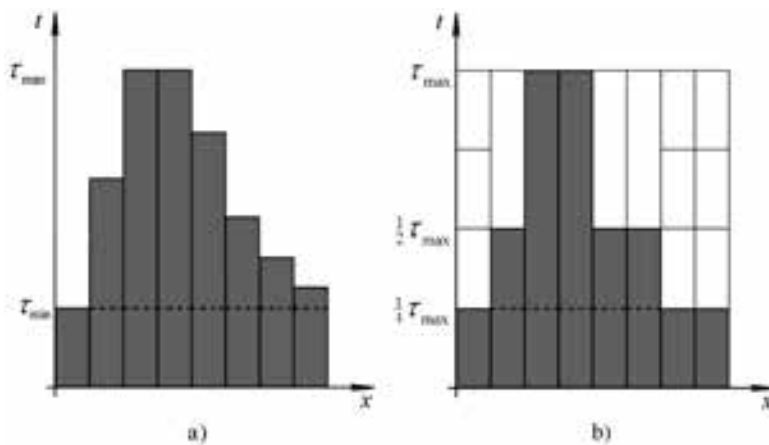
$$\mathrm{CFL}_i = a_i \frac{\tau_{\min}}{h_i} = \frac{\tau_{\min}}{\tau_i^{stab}} \ll 1 \qquad \text{in}$$

most cells. Therefore, the information propagates very slowly over the computational domain and a lot of time steps are necessary to describe the characteristic interval of global flow changing. This is the well-known problem of small time steps.

On the other hand, an implicit scheme permits one to perform the calculation with arbitrarily large values of time steps and to achieve the result immeasurably

Figure 3. Global, local and fractional time stepping

faster. This factor makes implicit schemes so popular. But, as it is shown in [20], the payment for the velocity of result obtaining is loss of non-stationary process description quality. There are some methods to accelerate the calculation in the case of explicit approach to approximation of equations. When a stationary flow is calculated using time-marching method, we aren't interested in a quality of intermediate non-stationary process description. Only its convergence to a correct stationary state is important. In this case, different methods of convergence acceleration may be used. One of them is a method of local time stepping. It is a known approach (see, for example, [21]). In this case, the calculation in each cell is performed with time step that is defined by local restrictions in this cell (Figure3a). As a result, the time step value changes from one cell to another. But when all the parameters u_i^{n+1} are given, they are formally prescribed to the same time layer. Later on, this procedure is repeated up to the moment, when a stationary solution is achieved. In the framework of this procedure, convergence to stationary solution accelerates essentially. The flow faster adapts to the stationary boundary conditions. It is easy to understand that the number of time steps should be $O(\tau_{max}/\tau_{min})$ times less in comparison with global stepping. If non-stationary flow is calculated and it is important to describe each moment of this flow development correctly, then neither local time stepping nor multigrid method are acceptable. In the current work, a method of fractional time stepping is proposed. The idea of fractional time stepping is that the calculation in each cell is performed with the greatest time step (i.e. with maximal possible Courant number). But the numbers of local time steps are different in different cells and they are chosen so as all the cells achieve the same layer of physical time at some moments (Figure 3b). When the same time layer is achieved, let's name it as a completion of global time step. For example, if a local time step in the cell A is equal to τ_{max}, in B - $\tau_{max}/2$ and in C - $\tau_{max}/8$, then, during one global time step, one should perform one local time step in the cell A, two local time steps in the cell B and eight local time steps in the cell C. Therefore, the global time step in each cell is divided (fragmented) into smaller local time steps so as the local time steps satisfy the local restriction on time step in the given cell. That's why the procedure is named fractional time stepping.

It should be noted that the first description of such method is known from [22]. Let's consider fractional time stepping organization in details. Before beginning of the calculation, the maximal possible value of time step (τ_i^{stab}) is determined in each cell of computational domain. Then, the maximal time step in the whole computational domain ($\tau_{max} = \max_i \tau_i^{stab}$) is determined. Then, the value of local time step is determined in each cell. The time step value in the cell with the number i is taken equal to $\tau_i = \dfrac{\tau_{max}}{2^l}$. The integer-valued parameter l is chosen so as local stability condition ($\dfrac{\tau_i^{stab}}{2} < \tau_i \le \tau_i^{stab}$) is satisfied in the given cell. As a result of this procedure, the whole collection of computational domain cells is divided into some subsets that will be named as levels. In all the cells of m-level, the value of local time step is equal to $\tau_i = \dfrac{\tau_{max}}{2^{M-m}}$, where M is the number of levels. In the cells of the first level, the local time step is minimal; it is equal to $\tau_i = \tau_{max}$ in the cells of M-level. Let's emphasize that, because the time step in each cell is defined by local time-dependent conditions of flow, the procedure of dividing the cells into the levels is performed before each global time step. During one global time step, 2^{M-m} local time steps are performed in the cell of m-level. The number of local time steps is different in different cells. But towards the end of the global time step, time in all the cells increases by the same value - τ_{max}. As a result, non-stationary development of flow is correct. This procedure diminishes total calculation time in rational programming (because few time steps is performed in large cells) and guaranties that the local value of stability coefficient ($C_{stab} \in [0.5;1]$) is used in each cell.

Now we dwell on practical aspects of implementation of implicit schemes. Let's consider such scheme in the near-wall zone of boundary layers. The scheme must be "time-accurate" and approximate the space operator similar to explicit one. This can be written as

$$\left(1 + \frac{\tau_n}{\tau_{n-1}+\tau_n}\right)\frac{u_i^{n+1}-u_i^n}{\tau_n} - \frac{\tau_n}{\tau_{n-1}+\tau_n}\frac{u_i^n-u_i^{n-1}}{\tau_{n-1}} + \frac{F_{i+1/2}(u^{n+1})-F_{i-1/2}(u^{n+1})}{h_i} = 0.$$

In the linear case, it can be proved that proposed scheme is absolutely stable. Formally, the time step τ_n may be arbitrarily large ($CFL \gg 1$). It permits one to accelerate essentially the calculation in near-wall zones.

Different approaches to solution of such non-linear equation systems are possible. For example, it's well-known Newton's method. The system of equations may be presented as: $\vec{R}(\vec{u}^{n+1}) = 0$, where

$$\vec{u}^{n+1} = \left[u_1^{n+1}, u_2^{n+1}, ..., u_N^{n+1} \right]^T, \ \vec{R} = \left[R_1, R_2, ..., R_N \right]^T, \ \text{where}$$

$$R_i = \left(1 + \frac{\tau_n}{\tau_{n-1} + \tau_n} \right) \frac{u_i^{n+1} - u_i^n}{\tau_n} - \frac{\tau_n}{\tau_{n-1} + \tau_n} \frac{u_i^n - u_i^{n-1}}{\tau_{n-1}} + \frac{F_{i+1/2}(u^{n+1}) - F_{i-1/2}(u^{n+1})}{h_i}.$$

As result, Newton's algorithm may be realized as following iterative procedure:

$$\begin{cases} \vec{u}^{(0)} = \vec{u}^n, \\ \vec{u}^{(k)} = \vec{u}^{(k-1)} - \left[\frac{\partial \vec{R}}{\partial \vec{u}}(\vec{u}^{(k-1)}) \right]^{-1} \cdot \vec{R}(\vec{u}^{(k-1)}), \\ \qquad k = 1, ..., M, \\ \vec{u}^{n+1} = \vec{u}^{(M)}. \end{cases}$$

It is easy to see that procedure needs vast resources of RAM (it is necessary to store in RAM the matrix $\frac{\partial \vec{R}}{\partial \vec{u}}$) and it is quite time expensive (costs per iteration are very large, the matrix above is calculated at each iteration).

That's why the dual-time stepping method is more popular in technical applications. In the case of dual approach, a fictitious non-stationary term is added to the main equation (let's name it as pseudo one):

$$\frac{\partial u}{\partial \xi} + \left(1 + \frac{\tau_n}{\tau_{n-1} + \tau_n} \right) \frac{u - u_i^n}{\tau_n} - \frac{\tau_n}{\tau_{n-1} + \tau_n} \frac{u_i^n - u_i^{n-1}}{\tau_{n-1}} + \frac{F_{i+1/2}(u) - F_{i-1/2}(u)}{h_i} = 0.$$

Here, ξ is pseudo-time. The idea of method is quite clear: the iterative solution of the pseudo system coincides with the solution of the main system in the stationary state, $u = u^{n+1}$. So, the solution of the main equation can be obtained as a set of the pseudo solutions stabilized at different times. One of the first realizations of the dual-time method was proposed by E. Jameson [21]. It is written as:

$$\begin{cases} u_i^{(0)} = u_i^n, \\ \dfrac{u_i^{(k+1)} - u_i^{(k)}}{\Delta\xi} + \dfrac{3}{2}\dfrac{u_i^{(k)} - u_i^n}{\tau} - \dfrac{1}{2}\dfrac{u_i^n - u_i^{n-1}}{\tau} + \dfrac{F_{i+1/2}(u^{(k)}) - F_{i-1/2}(u^{(k)})}{h} = 0, \ k = 1, ..., M, \\ u_i^{n+1} = u_i^{(M)}, \end{cases}$$

$$F_{i+1/2}(u^{(k)}) = F(U_{i+1/2}), \ U_{i+1/2} = \text{Decay}(u_L, u_R), u_L = u_i^{(k)} + \left(\frac{\partial u}{\partial x} \right)_i^{(k)} \frac{h}{2}, \ u_R = u_{i+1}^{(k)} - \left(\frac{\partial u}{\partial x} \right)_{i+1}^{(k)} \frac{h}{2}.$$

To accelerate the convergence to the stationary state, it's possible to use a local time stepping. It's a quite expensive procedure. The TsAGI approach uses a highly-efficient implicit scheme with a significantly simplified implicit operator. Such a hyper-fast operator is presented below:

$$\begin{cases} u_i^{(0)} = u_i^n, \\ \dfrac{u_i^{(k+1)} - u_i^{(k)}}{\Delta\xi} + \dfrac{3}{2}\dfrac{u_i^{(k+1)} - u_i^n}{\tau} - \dfrac{1}{2}\dfrac{u_i^n - u_i^{n-1}}{\tau} + \\ \qquad + \dfrac{A_{i+1/2} \cdot \left[\tilde{U}_{i+1/2}^{(k+1)} - \tilde{U}_{i+1/2}^{(k)} \right] - A_{i-1/2} \cdot \left[\tilde{U}_{i-1/2}^{(k+1)} - \tilde{U}_{i-1/2}^{(k)} \right]}{h} + \\ \qquad + \dfrac{F_{i+1/2}(u^{(k)}) - F_{i-1/2}(u^{(k)})}{h} = 0, \quad k = 1, ..., M, \\ u_i^{n+1} = u_i^{(M)}. \end{cases}$$

It is easy to see that the proposed scheme has the first order of approximation in pseudo-time. The implicit part of space operator is obtained using linearization. Jacobeans $A_{i+1/2} = A(u_i^n, u_{i+1}^n)$ are calculated only once for each physical step. This approach results in a system of linear algebraic equations for all the cells in computational domain. This system has banded matrix (its non-zero elements are aggregated near the main diagonal of the matrix). But, in the case of a 3D problem, this "band" is a quite wide. The elements of non-zero diagonals are blocked in matrix with size 7x7. This scheme doesn't require essential RAM, because it uses modified Gauss-Seidel method [22] with iterative architecture.

In this modified technology [20], the computational domain is subdivided into two zones. The first one is located near walls deeply inside of boundary layer. The calculations in this zone are performed using implicit scheme with dual-time stepping. The second one contains the other part of computational area. The calculations here are performed using explicit scheme with fractional time stepping. This method allows one to pose and solve non-stationary problems associated with wind-tunnel testing.

Application of the EWT program package to T-128 transonic wind-tunnel testing

Initially, the EWT program package was adapted to the T-128 operating conditions. The application of half-models (Figure 4) in this wind tunnel allows one to reach higher Reynolds numbers (about $20 \cdot 10^6$) corresponding to flight conditions for regional aircraft. A major methodological problem in testing half-models is the effect of the boundary layer developing on the test section wall and encountering the model's fuselage. The influence of the boundary layer on the flow around models can be partially eliminated by employing a peniche. It is intermediate support element between the wall and the model to move it farther from the wall.

Using the EWT code package, massive computation were performed to determine the effect of the skirt-like peniche on the aerodynamic characteristics of tested half-models as well as to evaluate optimal dimensions of this support element. A numerical investigation was devoted to find out the peniche height's impact on the aerodynamic loads acting on the model. The flow past the model was computed twice. The first series was performed using different peniche heights: 17 mm, 35 mm and 70 mm. The second series was performed using the isolated model. Comparison gave estimation for the best peniche, which almost didn't influence on the model. The boundary layer parameters were chosen so that at a certain section the computed flow velocity profile closely agreed with the experimental one (Figure 5). This section is located within the nozzle on

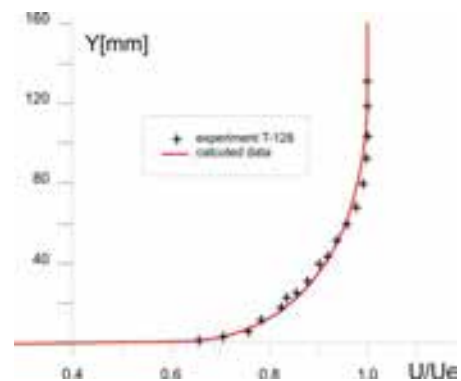**Figure 4. A half-model of a passenger aircraft in T-128 test section No 2**

Figure 5. Flow velocity profile in the boundary layer in the nozzle

the upper wall of the T-128 wind tunnel, where the velocity profile in the boundary layer was measured.

The computation grid for the half-model on the peniche of 37 mm height consisted of 411 blocks and 6.4 million nodes. The entire computational domain was divided into three parts. The first part is the far field with a coarse computation grid. The second part is the region, where the development of the boundary layer is being modeled on the test section wall. The third part is the surface of the semi-span model on the peniche. The greatest number of the nodes are located near the model (Figure 6).
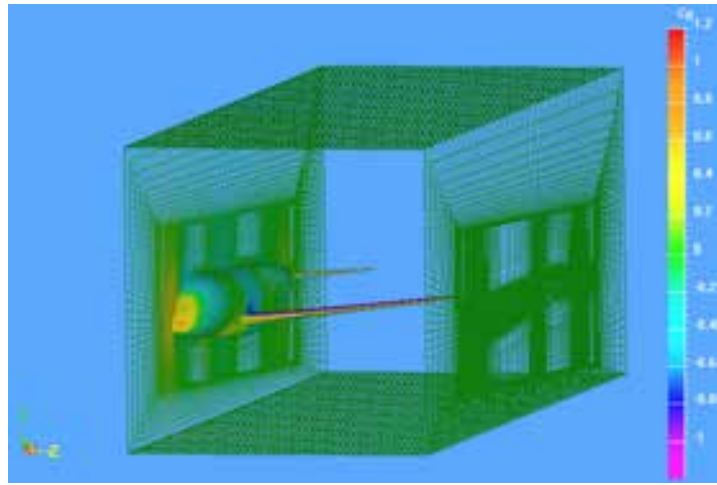
Figure 6. Computation grid on the model and the test section walls

The computations were performed for M=0.78, two values of the incidence angle and two values of stagnation pressure, P_t =0.5 and 2.5 atm. Figure 7 demonstrates the computation results in terms of pressure coefficient
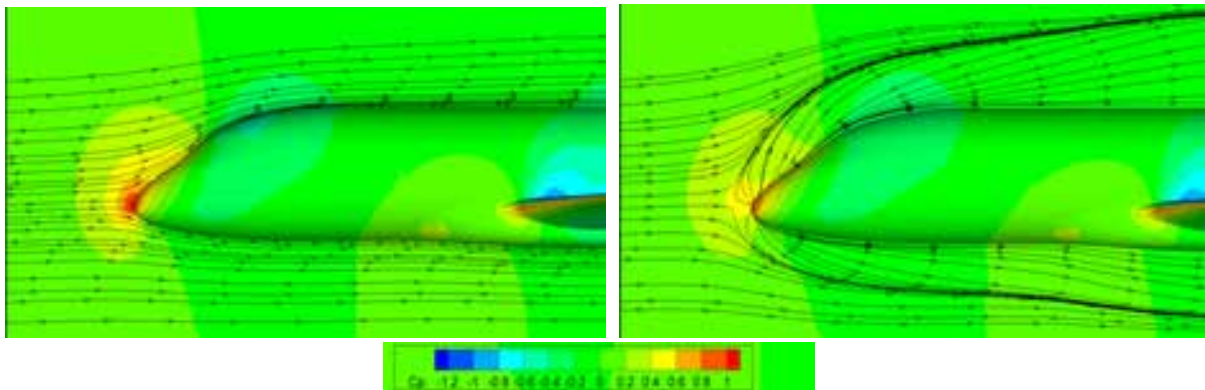
Figure 7. Flow about the complete model and the half-model with a peniche

distribution over the model surface and over the test section wall and streamlines on the wall without the boundary layer (the case of the complete model) and in the presence of the wall (the case of the half-model). These computations revealed the presence of a stagnation point on the wall upstream of the fuselage and dividing streamlines outgoing from the point. Figure 8 compares the limiting streamlines on a solid wall near the model and on the peniche, which were obtained computationally and through surface oil flow visualization. The oil flow patterns confirmed the peculiarities of flow around the model fuselage revealed computationally.
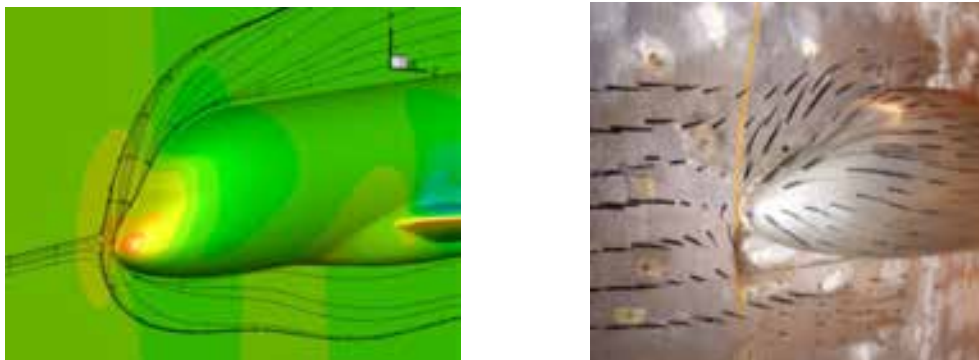
Figure 8. Limiting streamlines on the solid wall near the fuselage at M=0.78 and α =2.4° . Computation versus visualized experiment

Figure 9 demonstrates the effect of the peniche height on pressure coefficient in terms of the difference between the drag coefficients for the complete model and the half-model with peniche. The computational results show that the optimal height for the T-128 environment is about 35 mm, which correspond to twice the boundary layer displacement thickness, $2\delta^*$, on the test section wall at the location of the model. Similar optimal height of peniche was obtained in Refs. [23, 24]. The computer analysis has allowed one not only to determine the corrections for the effect of the test section wall carrying the model and its peniche, but also to evaluate the optimal height of the peniche. To obtain the optimal

Figure 9. The effect of the peniche height on the drag coefficient of the fuselage-wing-horizontal tail model

height experimentally would be extremely laboring and time consuming compared to computations.

Another important area of application of numerical methods in behalf of T-128 experiments is the studies into the effect of the model support devices and permeable flow boundaries. In wind tunnel testing, aircraft models employ support systems of different types; because of this, the test conditions differ from real flight conditions. The support devices disturb flow near the model and distort the measurements of its aerodynamic characteristics. In addition, depending on the type of support devices, the shape of models also varies in one way or another, which is must be taken into consideration. There are two important aspects in the problem on the support devices' effect:

- Direct measurement of the influence of support devices on the tested models and correction of experiment results.
- Design of support devices' aerodynamic contours to minimize their effects on the aerodynamic characteristics of models under testing.

The T-128 wind tunnel is fitted with a set of support systems of different types including straight and fin stings. In assessing the effect of support devices, integral corrections to incidence angle and Mach number of incoming flow must first be determined. Since the model wing is the element most sensitive to these parameters, the integral corrections are determined for the 25% MAC. Next, numerical computations are performed for two configurations of the model: with the support system and without it. For the isolated model, the required parameters of the free-stream flow are specified, whereas for the model with the support device the incidence angle and Mach number are given with the aid of preliminary computations and corrections. The differences between the aerodynamic coefficients obtained numerically for the two configurations constitute the corrections for the effect of the support system. Pressure coefficient distributions at two wing sections are compared in Figure 10.
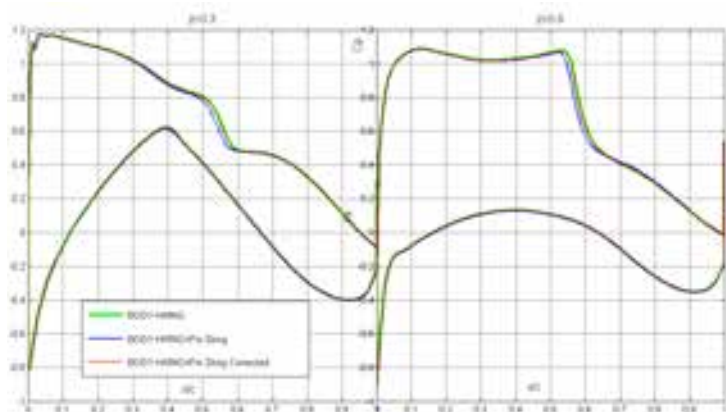

Figure 10. Comparison of pressure distributions at two wing sections for a model with and without a fin sting. Corrected pressure data are given for the model with the fin sting

Computations are made for the model with a fin sting and without it. The data with the fin sting taken into consideration are given with corrections to incidence angle and Mach number and with no corrections. The effect of the fin sting is seen as an upstream displacement of the pressure shock. Using the obtained integral correction, it was possible to ensure the flow around the wing corresponding to the isolated model.

The numerical results furnish insights into the nature of the flow in the area of the fuselage-straight sting joint. Figure 11 demonstrates streamlines in the internal cavity of the fuselage and the pressure distribution over the sting surface and the internal surface of the fuselage. The gas in the internal cavity is practically stagnant. It confirms the hypothesis put forward in the 1940s on the pressure constancy within the cavity. Based on this hypothesis, the correction is defined for the base drag in wind tunnel testing. In the area of the sting-fuselage joint, a complicated vortical flow is observed.

The possibility of numerically determining the corrections for the effect of support devices also allows one to use these corrections for aerodynamic design. This problem is similar to the aerodynamic design of aircraft and their components. With this in mind, for testing the passenger aircraft configurations in the T-128, an optimal fin sting was designed (the middle one in Figure 12). The initial version was an available Base fin sting (the lower one in Figure 12). Parametric computations were performed for different positions and configurations of the sting elements. Figure 13 shows the distribution on the fuselage side of the difference between the pressure coefficients for the configurations with and without sting. Besides, the Figure 13 also demonstrates the effect of the fin (there are data for the model with and without fin). The optimal fin sting provides the pressure distribution close to that produced by the model fin. Based on the analysis, a version was selected with the lowest effect
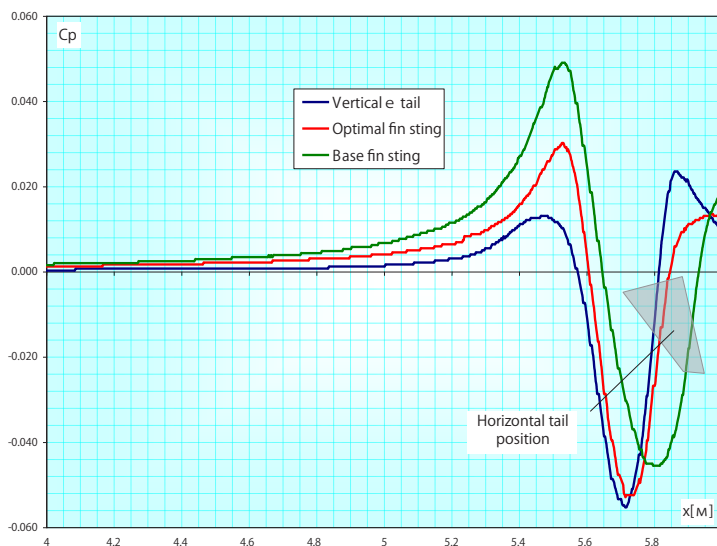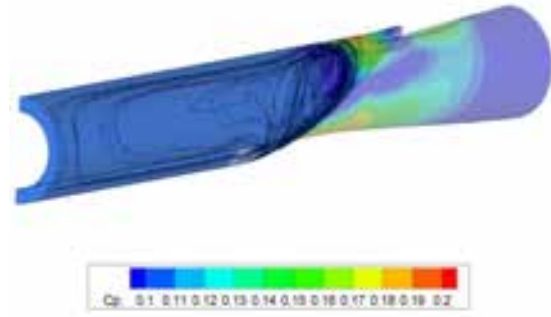

Figure 11. Flow structure in the internal cavity of the fuselage. Fuselage-straight sting configuration, M_∞=0.80; $\alpha = -1.25°$
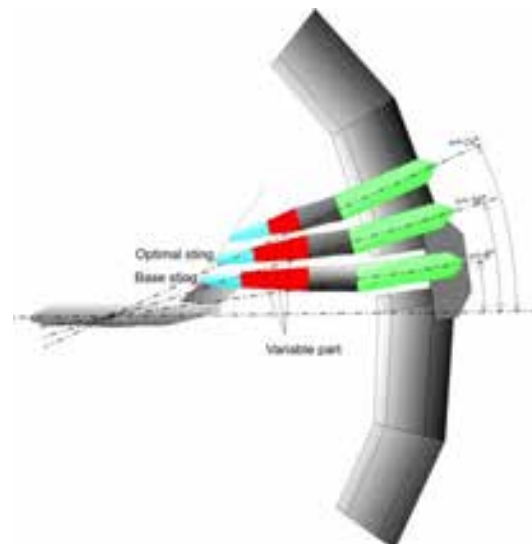

Figure 12. Variants of fin sting for a passenger aircraft model

on the aerodynamic characteristics of the passenger aircraft model under study and meeting strength requirements.

For assessing the effect of the porous boundaries on models' characteristics in the T-128 wind tunnel, in parallel with using the linear aerodynamics methods [19], the Euler equations and Reynolds-averaged Navier-Stokes equations were numerically solved. Most often the numerical methods were used to support large-scale half-models' testing (Figure 4). Presently, a Darcy-type boundary condition is specified at the external edge of the boundary layer on the perforated walls of the test section. This is dictated by insufficient speed and RAM of the modern computers.
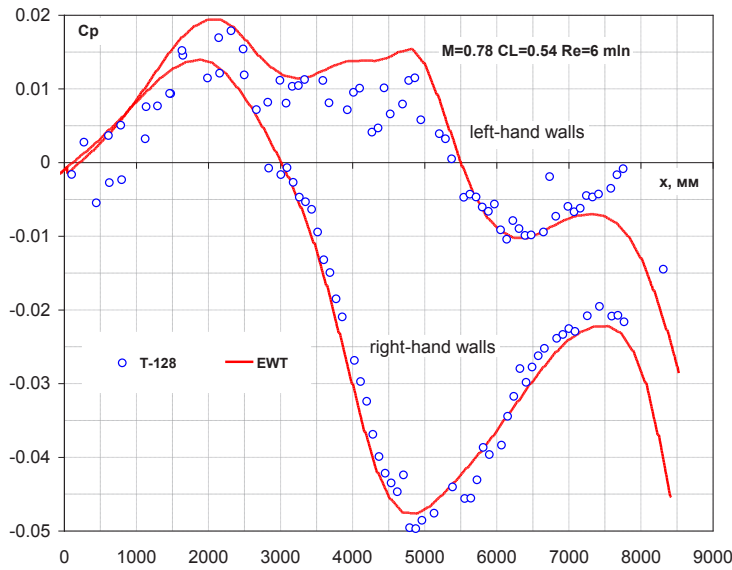

Figure 13. The effect of fin stings on the flow around the model

Figure 14. Pressure distribution over the wall beneath (upper curve) and above (lower curve) the half-model's wing in test section No 2

The methodology of determining the corrections for the effect of flow boundaries is similar to that used for handling support systems. Verification of numerical results is performed by comparison pressure distributions on the test section walls obtained experimentally and numerically. This is a necessary condition for providing accurate calculations. Figures 14 shows computed and experimental pressure coefficient distributions along the axes of the right- and left-hand walls of the test section No 2. The good agreement of the results indicates the correct problem statement and accurate assessment of the flow boundaries' effect.

EWT application to support testing in the T-104 wind tunnel

In 2008, a special version of the EWT code package with simulation of a moving ground board ("moving runway") was developed for the TsAGI T-104 subsonic wind tunnel. The T-104 is intended for testing full-scale power plants, propellers and large-scale flutter models. More recently, the facility was fitted with a stationary ground board to simulate takeoff, landing and ground run modes. Mathematical model of the T-104 wind-tunnel test section is presented in Figure 15. The aircraft model is positioned above the ground board representing a runway. All elements of the open test section are included into the mathematical model. In each computational block, an adapted computational grid is constructed. It is denser in the zones, where large gradients of flow parameters are expected.
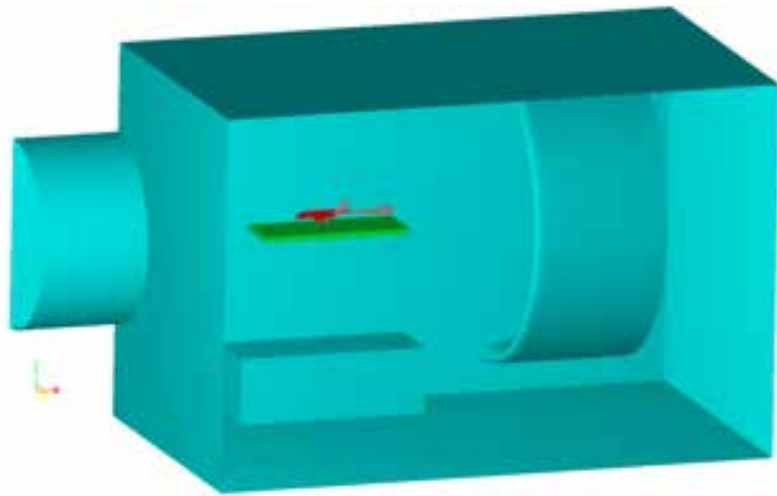

Figure 15. Mathematical model of the T-104 wind-tunnel test section

For example, it is compressed around the leading and trailing edges of the wing. On the outer boundaries of the computational domain, the boundary conditions are specified. Some of them are written in a standard way, for example, the no-slip boundary condition on the solid surface. Other conditions have special formulations, peculiar only to a problem under consideration.

For example, the "moving runway" condition is formulated similarly to flow slip condition for a specified velocity. Particular attention is given to prescribing levels and scales of flow turbulence at the entry into the test section. There is reason to hope, that with proper representation of flow gradients in the wind tunnel, the levels and scales of turbulence in the zone of the model location will correspond to the full-scale conditions, at least in terms of the order of magnitude. To simulate the aircraft retardation during ground run, the model is fitted with a reverser (Figure 16). The air is supplied to the engine through a special pylon installed under the nacelle; the operating mode of engine (thrust setting) is controlled by an ejector connected via a pipe with the exit of the

nozzle (Figure 16). It can be seen that the aforementioned elements are sufficiently large to influence the experimental results. To assess the magnitude of this influence, the mathematical model of the wind tunnel was used. Computations were performed for two configurations - with and without pylon. A critical mode of exhaust reingestion (reinjection), when, at a specific tunnel flow Mach number, the hot exhaust jet began to enter the engine inlet, was considered. In testing, this condition was determined by means of temperature-sensitive elements installed at the entry of the inlet. In computing, this was performed by painting streamlines (Figure 17) and stagnation temperature fields.

The computed data have shown that the pylon supplying air for the engine simulator increases the pressure in front of the inlet. Because of this, reingestion takes place at higher Mach numbers of the tunnel flow. The computations allowed one to estimate the correction to the Mach number. It was impossible in the experiment, because the pylon is an integral part of the experimental setup. Another reason for the implementation of numerical methods in this study is the fact that moving ground simulation was impossible in the T-104 wind tunnel.

Computations with a special boundary condition on the ground board supplemented the experimental results. To demonstrate such a capability, two new computations were performed (without pylon for air supply): (1) with moving ground board (runway simulation) and (2) with the fixed ground board, a component of the facility.

Figure 18 demonstrates flow fields constructed in a plane at some distance from the ground board. These flow patterns are analogous to those obtained by oil techniques that are widely used in physical testing. The analysis has shown that, in the fixed ground case, reingestion begins earlier. This is clearly seen in Figure 18a representing a 3D
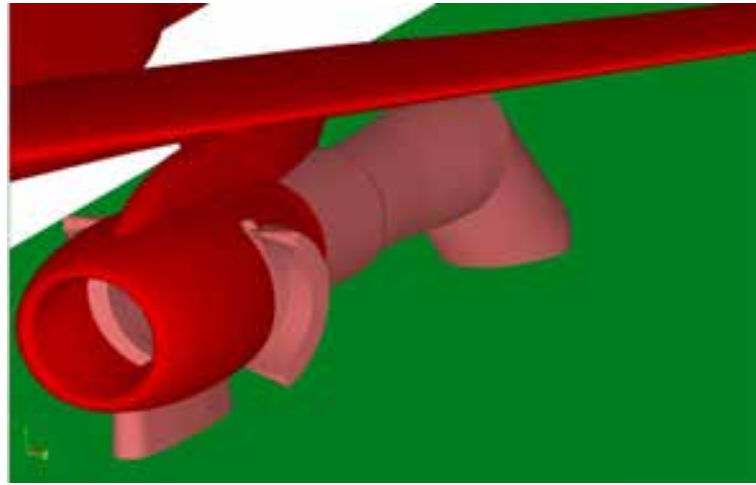

Figure 16. Engine model with the feeding pylon and ejector

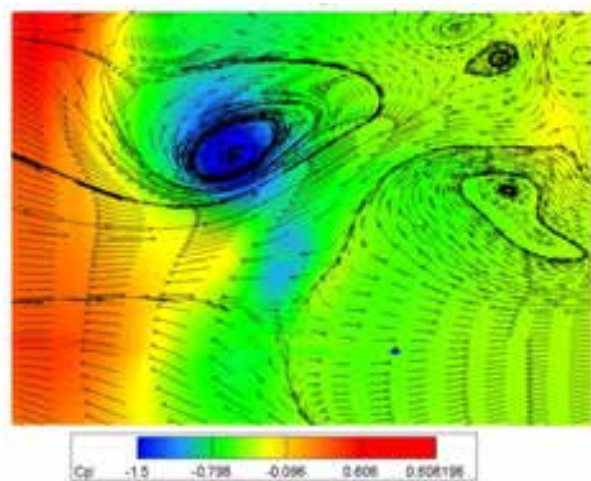**Figure 17. 3D flow reconstruction of reingestion**

Figure 18a. Flow field over the fixed ground board

reconstruction of the flow field with a vortex providing reingestion. The same vortex can be seen in Figure 18a. The moving board results in shift of the vortex downstream and the exhaust jets do not enter the inlet (Figure 18b). Thus, very interesting phenomena were revealed: the effects of the pylon and moving board which cannot be reproduced in experiment provide opposite contributions to the resulting flow pattern and practically compensate each other.

Concluding remarks

Predicting aircraft aerodynamic characteristics is provided both by wind-tunnel experiments and computations. Experimental studies feature systematic errors inherent in various elements of any wind tunnel: compressor, nozzle, diffuser, flow boundaries, support systems, etc. Their effects distort averaged speed components in the test

Figure 18b. Flow field over the moving ground board

section and result in pulsations of speed, temperature and density of the working gas. Besides, researchers are not always able to provide in wind-tunnel testing all required similarity parameters, Reynolds number in particular. In spite of the accuracy of measurement equipment greatly increased in resent years, experimenters have failed to eliminate random errors, mainly attributed to insufficient representation of non-stationary and averaged flow parameters in the test section. It makes difficult to determine the effects of small disturbances on the global aerodynamic characteristics of the models experimentally. Specifically, such problems include measuring the small increments of loads during optimization of aircraft layout and its local aerodynamics and determining the effects of flow boundaries and support systems.
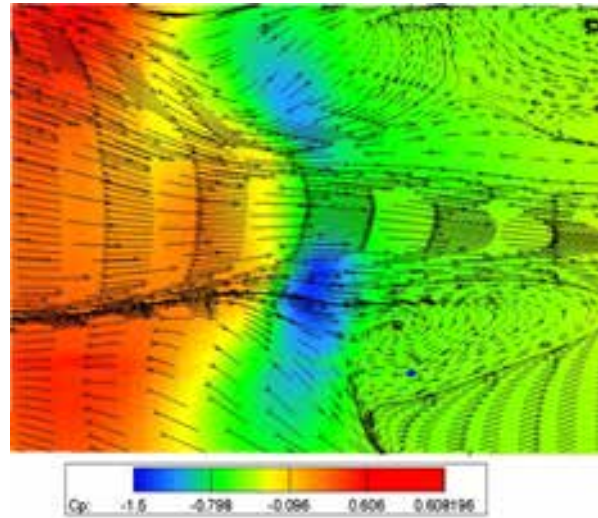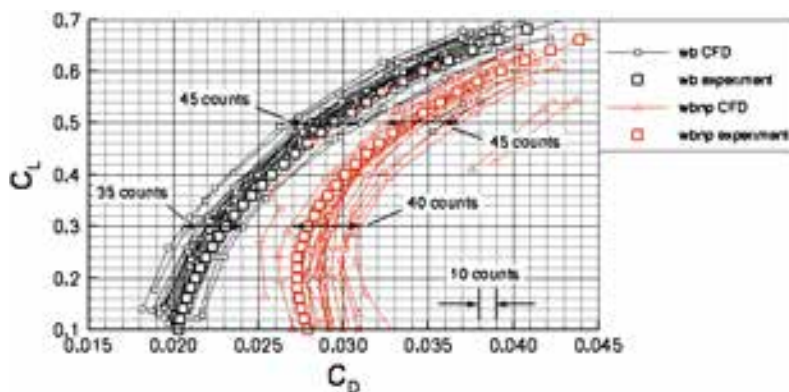

Figure 19. Comparison of experiment vs computation data ([25])

Contrary to experiments, computational methods feature no random errors. Besides, computations furnish insights into the nature of the interference between the models and the elements of the wind tunnels. The main systematic errors of numerical methods are associated with imperfections of turbulence models and laminar-turbulent transition. Figure 19 compares experimental results and numerical solutions of the Navier-Stokes equations obtained by different authors using different computer codes [25] for two configurations of a passenger aircraft. The half-span of the computed data is 18-20 drag counts ($\Delta C_D = 0.0018 - 0.0020$) for attached flow regimes. Taking into account that the modern requirements for the accuracy of passenger aircraft drag coefficients is 18-20 times more stringent ($\Delta C_D = 0.0001$), it may be concluded that the level of computational methods' systematical errors is still rather high.

As for now, it appears that the numerical methods are efficient being applied to wind-tunnel experiments: determination of the flow boundaries and minimization of the effects of the boundaries and support systems on the aircraft aerodynamic characteristics, the design of aerodynamic contours of wind-tunnel components and support systems.

A 30-year experience of computational activities at TsAGI has shown that only a combination of numerical and experimental methods can give significant impetus to development of computational aerodynamics and wind-

tunnel testing alike, which will eventually lead to substantially more reliable results of numerical and experimental studies.

References

[1] Neiland V.Ya.: Review of TsAGI Wind Tunnels. *Wind Tunnels and Wind Tunnel Test Techniques*, Proceedings, The Royal Aeronautical Society, Southampton, UK, 1992.

[2] Neyland V.M., Semenov A.V., Semenova O.K., Glazkov S.A., Ivanov A.I., Khozyaenko N.N.: Testing Technique Features of the Experiments in the Wind Tunnel with Adaptive Perforated Walls. *Preprint TsAGI*, No 47, 1991.

[3] Neyland V.M., Ivanov A.I., Semenov A.V., Semenova O.K., Amirjanz G.A.: Adaptive-Wall Perforated Test Section for Transonic Wind Tunnels. *AGARD-CP-585*, 1997.

[4] V.M. Neiland.: Adaptive Wall Wind Tunnels with Adjustable Permeability – Experience of Exploitation and Possibilities of Development. *Proceedings of International Conference on Adaptive Wall Wind Research and Wall Interference Correction*, Xian, China, 1991.

[5] Neyland V.M.: Recent Experience of Oversized Models Testing in T-128 of TsAGI Using Wall Adaptation Technique. *PICAST'1*, pp. 1153-1158, 1993.

[6] V.Ya. Neiland.: The convergence of the Orbiter "Buran" Flight Test and Preflight Study Results and the Choice of a Strategy to Develop a Second Generation Orbiter. *AIAA Paper 89-5019*.

[7] V.Ya. Neiland.: Experimental, Computational and Theoretical Techniques of the Simulation of Hypersonic Flows in TsAGI Wind Tunnels. *Proceedings of the 2nd International Conference on Experimental Fluid Mechanics*. Torino, Italy, pp. 64-89, 1994.

[8] V.Ya. Neiland.: The Effect of the Air Dissociation on the Orbiter Aerodynamic Characteristics. *Journal of Aircraft*, Vol. 30, No 4, 1993.

[9] V.Ya. Neiland.: Aerothermodynamic Configuration of the First Generation Orbiters (Buran-Type) and the Results of the First Flight. *The first European Symposium on the Orbiter Aerothermodynamics*, the Netherlands, 1991.

[10] Velichko S.A., Lifshits Yu.B., Neyland V.M., Solntsev I.A., Sorokin A.M.: Numerical Modeling of Transonic Flow Past an Airfoil in a Wind Tunnel. *Computational Mathematics and Mathematical Physics*, Vol. 35, No 10, pp. 1221-1235, 1995.

[11] Velichko S.A., Vladimirova N.A., Lifshits Yu.B., Solntsev I.A., Sorokin A.M.: Permeable Wall Interference on Transonic Flow over an Airfoil. *Computational Mathematics and Mathematical Physics*, Vol. 36, No 10, pp. 166-179, 1996.

[12] Velichko S.A., Lifshits Yu.B., Neyland V.M., Solntsev I.A.: Correction of the Influence of Transonic Wind Tunnel Walls. *Computational Mathematics and Mathematical Physics*, Vol. 36, No 12, pp. 80-90, 1996.

[13] Bosniakov S.M.: Approach to Real Aircraft 3D Calculation Based on Time-Dependent Euler Equation System with boundary Layer Taking into Account. Warsaw University of Technology, Research Bulletin No 6, 1997.

[14] S. Bosniakov, S. Glazkov, S. Matyash, S. Mikhailov, V. Neyland, N. Remeev, N. Yatskevich.: Numerical Modeling of Flow-Field Around Model in the Big Transonic Wind Tunnel Using Monotone 2-nd Order Godunov-Type Scheme. *Wind Tunnels and Wind Tunnel Test Techniques*, Proceedings, The Royal Aeronautical Society, Cambridge, UK, 1997.

[15] Bosniakov, S.: Experience in integrating CFD to the technology of testing models in wind tunnels. *Progress in Aerospace Sciences*, No 34, 1998, pp. 391-422.

[16] Neyland V., Bosniakov S., Glazkov S., Ivanov A., Matyash S., Mikhailov S., Vlasenko V.: Conception of electronic wind tunnel and first results of its implementation. *Progress in Aerospace Sciences*, Vol. 37, No 2, 2001, pp. 121-145.

[17] Ivanov A.I.: An experimental Study of Gas Flow Near the Perforated Walls of a Transonic Wind Tunnel. *Fluid Mechanics – Soviet Research*, Vol. 17, No 4, 1988.

[18] S.A. Glazkov, A.R. Gorbushin, N.N. Khozyenko.: Determination of air flow rate performance of perforated walls *"The TsAGI Journal"*, Vol. XXII, No 2, 1991.

[19] S.A. Glazkov, A.R. Gorbushin, A.I. Ivanov, A.V. Semenov.: Recent experience in improving the accuracy of wall interference corrections in TsAGI T-128 wind tunnel. *Progress in Aerospace Sciences*, Pergamon Press, Vol. 37, No 3, 2001.

[20] S. Bosnyakov, I. Kursakov, A. Lysenkov, S. Matyash, S. Mikhailov, V. Vlasenko, J. Quest.: Computational tools for supporting the testing of civil aircraft configurations in wind tunnels. *Progress in Aerospace Sciences*, Vol. 44, pp.67–120, 2008.

[21] A. Jameson.: A perspective on computational algorithms for aerodynamic analysis and design. *Progress in Aerospace Sciences*, Vol. 37, No 2, p.197, 2001.

[22] M.J. Ortega.: Introduction to parallel and vector solution of linear systems. *Plenum Press*, New York, 1988.

[23] William, E., Milholen II, Chokani, N., McGhee, Robert, J.: Development of Semi-Span Model Test Techniques. *AIAA Paper* 96-02412, 1996.

[24] Y. Yokokawa, M. Murayama, H. Uchida, K. Tanaka, T. Ito and K. Yamamoto.: Aerodynamic Influence of a Half-Span Model Installation for High-Lift Configuration Experiment. *AIAA Paper* 2010-684, 2010.

[25] K. Laflin.: Data Summary and Comparison. *2nd AIAA CFD Drag Prediction Workshop*, Orlando, FL, June 21-22, 2003.

A Methodology to Derive Wind Tunnel Wall Corrections from RANS Simulations

Jean-Luc Hantrais-Gervois
Jean-François Piat

Onera – The French Aerospace Lab
F-92190, Meudon
France
Jean-Luc.Hantrais-Gervois@onera.fr

Abstract

This paper presents a methodology to estimate the wind tunnel wall interference with RANS simulations. The method involves a pairing process between confined and aerodynamically equivalent free air simulations that is carried out through automatic optimisation.
Wall corrections are derived for a major industrial wind tunnel (ONERA S2MA wind tunnel located in Modane). The tunnel is a transonic pressurised tunnel with perforated walls that can be sealed to achieve a guided test section. In order to model the porous walls in the RANS simulations, the characteristics of the walls were measured with a specific experiment.
On the whole, in the linear aerodynamic domain, the RANS corrections are similar to the current correction strategy but require a higher CPU cost. The benefit appears in non-linear regimes (high lift or high Mach number).

Key words: aerodynamics, wind tunnel wall corrections, wall porosity, RANS simulations, optimisation.

Background of wall interference

First and second order corrections

Each aircraft undergoes intensive wind tunnel test campaigns before the maiden flights. Because of the experimental test set up, the in tunnel flow deviates from free air aerodynamics. Typically, the wind tunnel test section where the model is located usually features walls (solid, porous or slotted) that impede the flow from expanding in the same manner as it would do in free flight (see Figure 1). Thus, the pressure field around the model is affected and an equivalent free air condition needs estimating for each wind tunnel measurement. The supporting system (sting line) is also a significant source of difference with the free stream.

For each model tested in a wind tunnel, the wind tunnel operator transposes the rough aerodynamic measurements to equivalent free air aerodynamic data. The transposition is achieved through different correction procedures involving experimental, semi-empirical and simple numerical methods. The purpose of the wind tunnel wall corrections consists in:

- Defining the closest fictive free air physical state corresponding to the aerodynamic state measured in the confined environment. This is the purpose of the **first order corrections** (ΔM, $\Delta \alpha$, $\Delta \beta$) to the main aerodynamic parameters (Mach number, attitude toward the flow). These corrections are an average global correction establishing a link between a confined and a free air states. These twin states are not identical, but they present similar features (average pressure level and shock position, see Figure 1). When large interferences are experienced, no equivalent free air flow can be defined and the confined test cannot

represent any free air aerodynamic feature. In this case, the flow cannot be corrected. This can occur when the model is too large for the wind tunnel (the ratio of the model maximum cross section to the tunnel cross section – the obstruction – should not exceed 1% for transonic tests) or when too high Mach numbers are tested (the tunnel can even be shocked).

- Accounting for the residual deviations to the average equivalent free air flow. These corrections correspond to local deviations of the aerodynamic field (for example see Figure 2). The integration of these local effects consists in the **second order corrections** to the forces and moments ($\Delta \vec{F}, \Delta \vec{M}$).
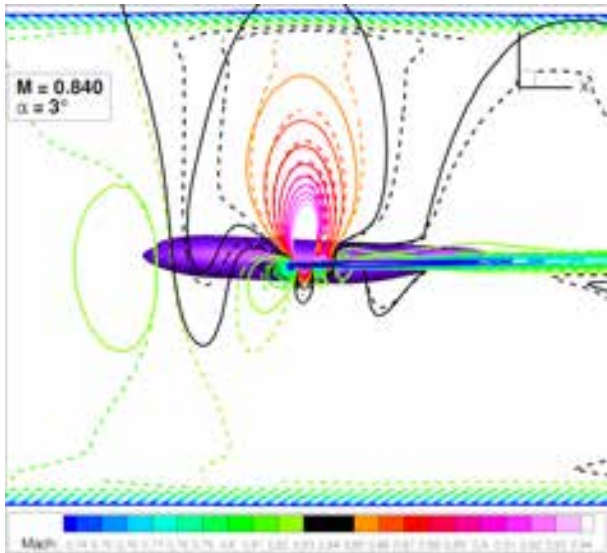
Figure 1: Comparison of iso-Mach number lines in free-air (solid lines) and confined environments (dashed lines).
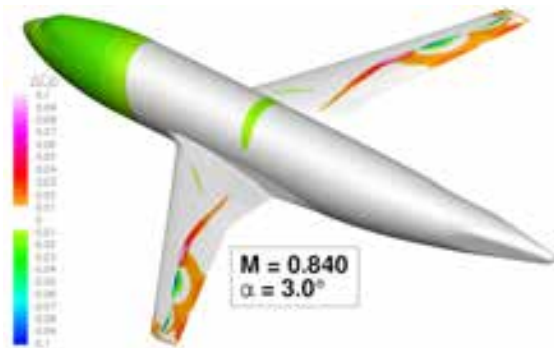
Figure 2: Cp deviations between free-air and confined environments.

Computational Fluid Dynamics (CFD) for the evaluation of wall interference

State of the art

The state of the art of the wall interference estimation is well presented in an exhaustive AGARD publication [1]. Depending on the wind tunnel, the estimation methods can be empirical (based on comparisons with reference wind tunnels either large or with a guided test section), analytical (formulations based upon the potential flow model resorting for instance to wall pressure signatures and Green functions), computational (up to Euler simulations as in the AEDC [2]). Few RANS simulations have been attempted to model wind tunnel flow fields (see [3], [4]).

At ONERA, in the large industrial facilities in Modane, the wall interference are estimated with the linear potential flow code DXV [5] (with some experimental contributions). This method is very efficient and proved accurate among the numerous wind tunnel tests carried out in Modane. Nevertheless, the linear potential flow assumption is not adequate for high transonic Mach numbers, large model obstructions or high angles of attack near the maximum lift.

Scope of this communication

This paper presents a correction methodology based on RANS simulations that encompasses in a single method both the corrections to the reference state and the corrections to forces and moments. The principle is to match confined simulations of the model in the wind tunnel with free air simulations of the model. Based on these paired simulations, first order and second order corrections can be derived. The corrections being derived by differences between paired simulations, the RANS CFD is required to predict increments. Thus, in this work, the absolute aerodynamic values on a specific model are not of interest.

The methodology is applied to a major industrial facility (S2MA wind tunnel located in Modane). The tunnel is a transonic pressurised tunnel with perforated walls that can be sealed to achieve a guided test section.

The aims of this study are twofold:
- studying the feasibility of RANS wall corrections;
- assessing the RANS wall corrections against the current ONERA wall correction procedure.

In a first part, this paper will introduce the RANS methodology used to derive wall corrections. In this part, the wind tunnel correction procedure will be detailed (empty tunnel corrections and wall interference). An automatic pairing process between a confined and an equivalent free air simulation will be introduced.

The S2MA wind tunnel will be described in the second part with a detailed focus of an experimental characterisation of the porous walls over the range of functioning of the wind tunnel (Mach number, plenum pressure, stagnation pressure).

A third chapter will present the numerical modelisations (wind tunnel and model configurations, meshes and RANS software and porous walls model).

A validation of the confined simulations will then be presented prior discussing the values of corrections obtained by the RANS simulations in comparison with the correction process in use in the ONERA wind tunnels.

RANS methodology to compute wall interference

Wall correction process in use at ONERA

To produce the results of the tests, the raw measurements of the balance weighting the model are converted into aerodynamic coefficients through several modifications:
1. measurement of balance signals (electric signals);
2. conversion of these signals into Newton and Newton times meters (through a calibration of the response of the balance);
3. derivation of the aerodynamic conditions in the wind tunnel (through a calibration of the wind tunnel);
4. reduction of forces and moments by the kinetic pressure and the model reference area and length in order to get aerodynamic coefficients;
5. estimation of the aerodynamic interferences (walls, sting);
6. interpolation of all the results to produce polars at round values of Mach numbers, if necessary (thanks to the Mach number stability in the tunnel considered in this paper, this step is not applied).

Looking into the details of the 3rd and 5th points, the correction process is decomposed into several contributions that are detailed in Table 1. This table evidences the complexity of the wall interference correction process. Some of the steps of this process are estimated through experimental calibrations and the others through basic aerodynamic simulations. Each contains its own inaccuracy and it is the responsibility of the wind tunnel to achieve a certain degree of accuracy for the results.
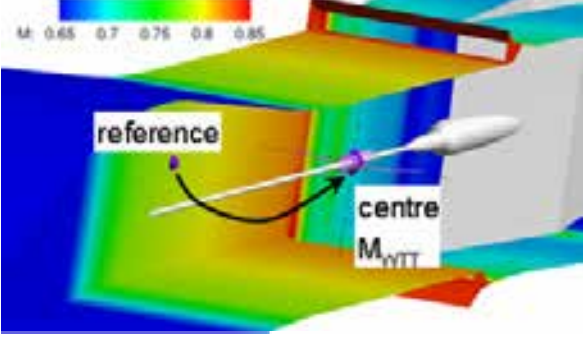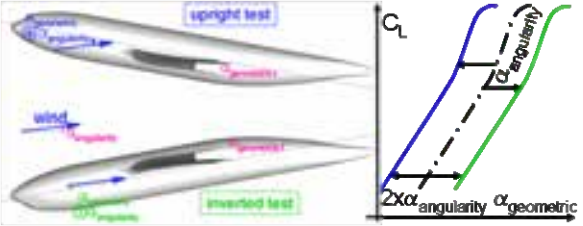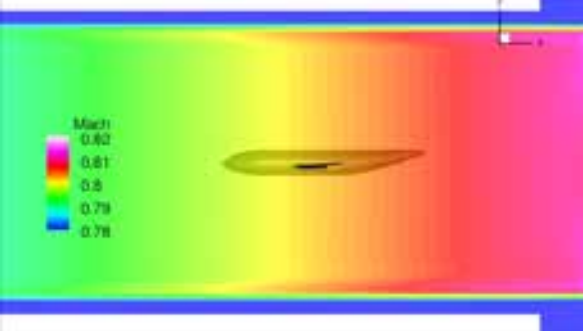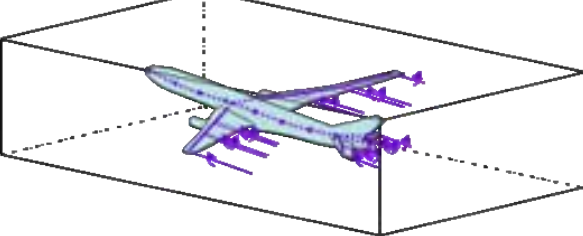
For a wind tunnel operator, the wall interference term refers only to the estimation of the confined flow interference for the model (last step that establishes 1st and 2nd order corrections through linear potential simulations in the process depicted in Table 1). The other steps are considered as wind tunnel calibrations. Nevertheless, all the steps have a connection with the wall interference topic as treated in this communication.

For the ONERA wind tunnels, the wall corrections are assessed using an analytic method called DXV based on the linearised potential equation [5]. The main interest of this method is that the mathematical formulation relies on the addition of the perturbations. Thus, the wall influence is directly known from a unique simulation of the flow field in the wind tunnel with the installed model. The model is simulated by singularities (sources, sinks and doublets for the fuselage, horseshoe vortices for the wings). For guided test sections, a slipping boundary condition is modelled and the wall effect is simply the effect of the infinite series of model "images" through the four walls. For porous test sections the walls are modelled with a velocity through the perforated wall proportional to the pressure drop through the wall (between plenum and test section). An adequate choice of the location of the correction to the angle of attack (at 75% of the aerodynamic mean chord, see [6]) enables to derive corrections at iso-lift.

Typically, under the best conditions (adequate balance, model and aerodynamic conditions), a good performance wind tunnel test aims at reaching an accuracy of $\pm 1 \ 10^{-3}$ in Mach number, $\pm 0.01°$ in angle of

attack, $\pm 1\ 10^{-4}$ in drag, $\pm 1\ 10^{-3}$ in lift and $\pm 1\ 10^{-3}$ in pitching moment. We see that the levels of corrections are well above these accuracies. Nevertheless, the level of the corrections does not reflect the quality of the test because the corrections are well handled.

Table 1: Wall correction procedure in use in the ONERA wind tunnels.

Type of correction	Explanation	Typical values Guided test section (porous test section)
Determination of the uncorrected Mach number M_{WTT}. The tunnel reference tap is located upstream of the model and it provides an indication of a tunnel Mach number at the tunnel centre (unperturbed by the model). This Mach number is only a convention that does not reflect a real aerodynamic state for the model. The link between the reference tap and the tunnel centre is made thanks to empty tunnel calibrations carried out over the Mach number range.	 *Empty tunnel calibration with a centreline probe (the model is represented to show its position in the test section).*	$M_{WTT} =$ $M_{reference} + \Delta M_{calibration}$ $\Delta M_{calibration}$ dependent on the reference tap position.
Determination of the uncorrected angle of attack α_{WTT}. The geometric inclination of the model is measured through a goniometer. But each wind tunnel features a flow angularity that is inherited from the history of the air circuit and the tunnel design. This angularity is obtained by comparing lift polars obtained in upright and inverted model position	 *Principle of the upright and inverted tests to determine the flow angularity.*	$\Delta\alpha_{angularity} \approx 0.1°$ $(0.1°)$, mostly independent on the test conditions.
Determination of a buoyancy correction on drag $\Delta C_{D\ buoyancy}$. Each wind tunnel presents an evolution of the Mach number from the nose to the tail of the models. The Mach number evolution is measured during the empty wind tunnel calibration and the gradient (buoyancy) is applied to the surfaces of each model. The correction accounts for the boundary layer growth and the wall divergence (evolution of the tunnel area).	 *Empty tunnel Mach number gradient (solid walls). The model is represented to show its position within this gradient.*	Highly dependent on the tunnel, the Mach number and the model. For solid wall tunnels without wall divergence compensating the boundary layer growth, about 15 dc can be achieved. A small correction can be achieved in porous tunnels or guided tunnels with wall divergence (about ± 2 dc).
Determination of the 1st and 2nd order corrections (ΔM, $\Delta\alpha$) and ($\Delta\vec{F}$, $\Delta\vec{M}$). This step accounts for the interaction between the model and the walls. At ONERA these corrections related to the walls are achieved through CFD (linear potential). The walls are modelled parallel and without boundary layer.	 *Principle of the linear potential simulations to estimate the wall interference.*	$\Delta M \approx$ from 0 to $10\ 10^{-3}$ (less than $2\ 10^{-3}$), highly dependent on M. $\Delta\alpha \approx$ from $0.0°$ to $0.3°$ (less than $0.1°$) and highly dependent on lift. $\Delta C_D \approx 5\ 10^{-4}$ ($5\ 10^{-4}$). $\Delta C_m \approx 2\ 10^{-3}$ ($2\ 10^{-3}$).

RANS wind tunnel correction methodology

RANS correction procedure

Contrary to the potential flow approach, a single RANS simulation does not provide directly the additive effects of the walls on a model. Using RANS simulations that are non-linear and thus non-additive in nature, implies to come back to the definition of the corrections. The corrections aiming at relating a confined flow field to an equivalent free stream flow field, pairs of RANS simulations need to be computed: one free air simulation of the model paired with one in-tunnel simulation. These effects might be determined in the presence of the sting line or without.

The interest of this method relies on its exhaustiveness. If the confined simulation reflects correctly the confined flow physics, the comparison of the flow fields of the pair of computations provides directly the first and second order corrections:

- First order (ΔM, $\Delta\alpha$): the free stream Mach number corresponding to the confined flow field is known without resorting to a fictive uncorrected confined Mach number. Both the empty tunnel effects and wall interference are accounted for. The angle of attack correction contains the flow angularity and the wall interference. In this communication, sideslip will not be considered as both S2MA and the models are symmetric.
- Second order ($\Delta\vec{F}$, $\Delta\vec{M}$): the corrections to the forces and moments are self-sufficient, and especially, the buoyancy does not need to be accounted by additional methods as it is embedded in the pair of simulations.

This method supposes to be able to match pairs of simulations and to exploit the pairs to derive the corrections. So as to correct a wind tunnel test, a matrix of aerodynamic conditions (M, α) needs to be assessed to cover the aerodynamic domain.

This simple approach is appealing, but it has two major drawbacks: i) it can't be connected with actual correction procedure and ii) it supposes a perfect modelling of the flow physics of the wind tunnel. Thus, in order to be able to validate separately the tunnel calibration and the corrections, the experimental process must be mimicked numerically. Thus, empty tunnel simulations have to be computed. These simulations can be carried out once and for all for one wind tunnel as it has no connection with any model to be tested in the test section.

Finally, 3 different simulations must be obtained for a set of correction at (M_∞, α_∞) that can be embedded in the current wind tunnel correction procedure:

1. empty wind tunnel simulation to be able to define the fictive confined Mach number, the flow angularity and the buoyancy correction;
2. free air simulation at (M_∞, α_∞);
3. in-tunnel simulation with adapted (M_{WTT}, α_{WTT}) to match the aerodynamic of the free air simulation.

Pairing process

The free-air and the confined simulations are said to be paired when the flow fields around the wing are similar. In this study, the criterion of similarity is based on the pressure field at the skin. The pressure is converted into the isentropic Mach number in order to work with figures without dimensions that can easily be compared for different Mach numbers and especially different stagnation pressures. As the in-tunnel pressure field is distorted on the wing, an exact match cannot exist. Thus the isentropic Mach number on each cell is compared between the free-air and the confined simulations. We then sum the deltas (squared) for each cell (with a weighting by the cell area) and divide by the number of cells. Taking the square root of this figure corresponds to the root mean square error of the Mach number fields and it is used in this study as the similarity factor (see Figure 3). Two paired fields achieve a minimal similarity factor.

In this study, the similarity factor is computed on the suction side where the relevant transonic flow features arise. The pressure side might be added for low lift coefficients.
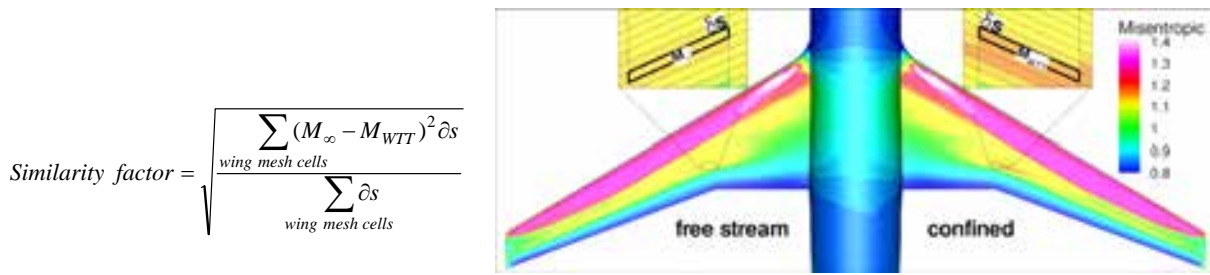
$$Similarity\ factor = \sqrt{\dfrac{\displaystyle\sum_{wing\ mesh\ cells}(M_\infty - M_{WTT})^2\,\partial s}{\displaystyle\sum_{wing\ mesh\ cells}\partial s}}$$

Figure 3: Definition of the similarity factor between the free air and the confined simulations.

In practice, for a given aerodynamic condition in the wind tunnel (M_{WTT}, α_{WTT}), the equivalent aerodynamic condition in free air must be searched by adjusting the (M_∞, α_∞) couple until the similarity factor is deemed satisfying. The process can also be inversed when a precise (M_∞, α_∞) is the main interest. In that case, the confined conditions are adjusted. An example of optimisation process is sketched in Figure 4 where the gradient based optimization strategy developed by Vanderplaats [7] is used within the optimization software DAKOTA [8]. A loop in python language [9] enables to feed the optimizer with evaluations of (M_{WTT}, α_{WTT}) couples.
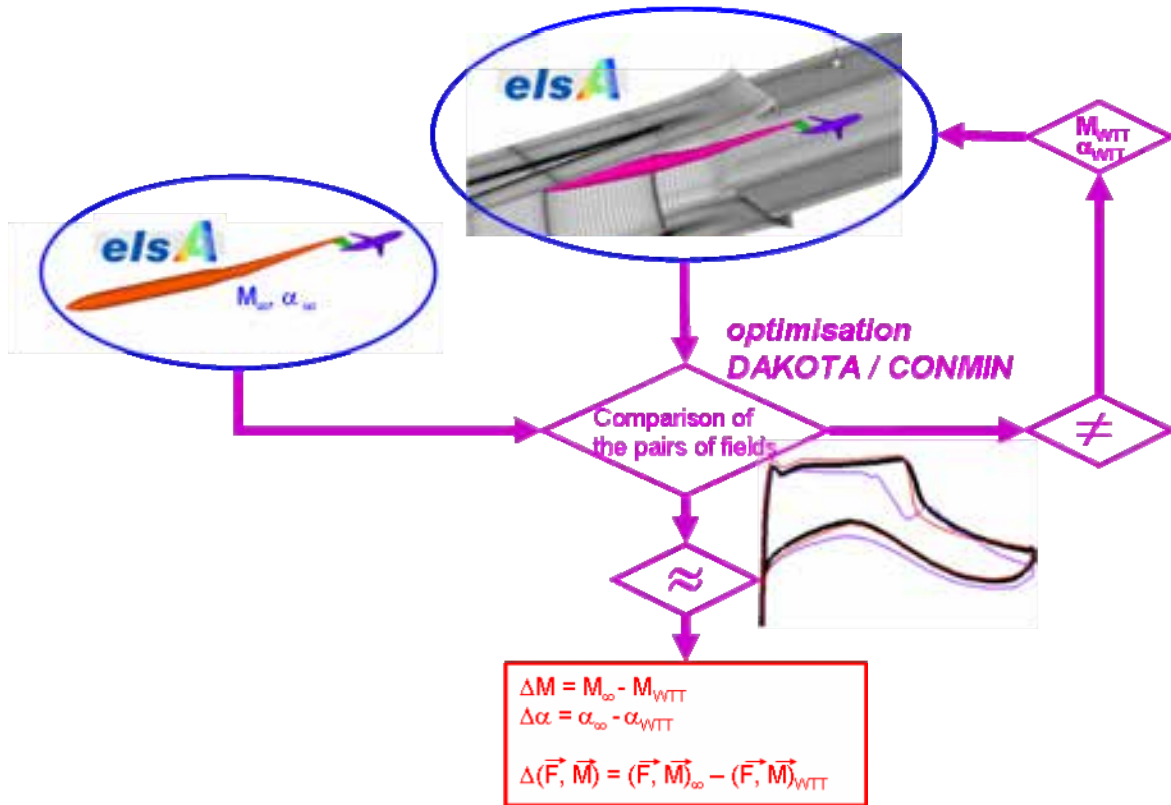
Figure 4: Pairing procedure by optimisation.

Empty tunnel simulations

The RANS simulations of the wind tunnel take into account many features of the wind tunnel (see Figure 5):

- wind tunnel geometry from the settling chamber enabling to simulate the major Mach number evolutions and flow orientation;
- development of the boundary layers on the wind tunnel walls enabling to simulate the subtle Mach number evolutions in the test section.

To separate the empty tunnel effects from the pure wall interference, empty tunnel simulations can be carried out. The comparison with the experimental ones provides information on the quality of the confined flow simulations.

These simulations deliver numerical equivalents for quantities used in actual correction process:

- Simulating a range of Mach numbers and stagnation pressures (once and for all) allows establishing the numerical calibration between the reference sensor on the wall and the centre of the tunnel. Thus, $M_{WTT\ CFD}$ can be determined in the same fashion as in the experiments.
- On top of the link between the reference pressure tap and the tunnel centre, the pressure gradient in the region of the models is also obtained. Thus, through an integration of the gradient over the model, the numerical buoyancy drag can be determined ($\Delta C_{D\ buoyancy\ CFD}$). This gradient can be removed from the Cp discrepancy between the free stream and the confined simulations. It enables to separate visually the pressure effects from buoyancy and the interference effects (see Figure 6). It will also enable to compare the computed interference with the linear potential flow simulations in the last part of this paper.
- In these simulations, the flow angularity can also be determined ($\alpha_{angularity\ CFD}$). Nevertheless, this quantity can't be directly compared to the experimental one because the flow simulation does not account for the flow history in the wind tunnel air circuit. In the simulations, the flow in the settling chamber is strictly horizontal which can differ slightly from the experiment.
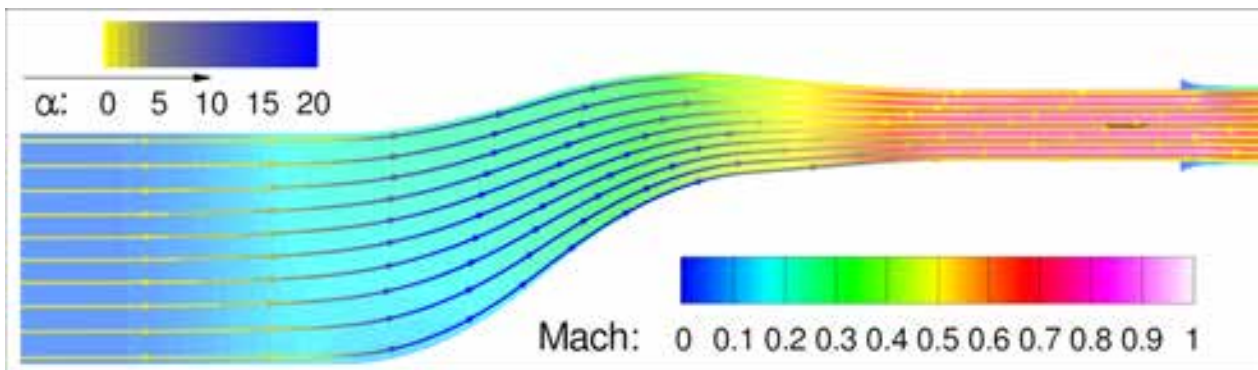

Figure 5: Empty tunnel flow simulations taking into account the flow accelerations and orientation (the model is represented in the test section, but it is not included in the computations).
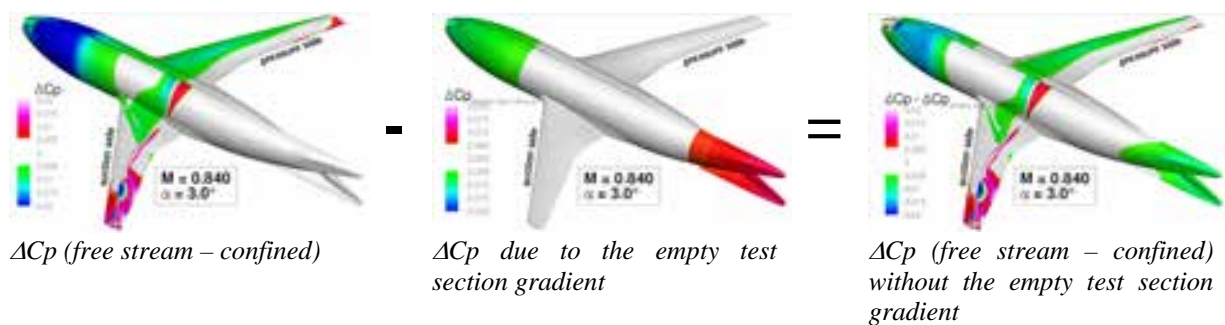

ΔCp (free stream – confined)

ΔCp due to the empty test section gradient

ΔCp (free stream – confined) without the empty test section gradient

Figure 6: Distinction between the buoyancy and the other wall effects at the model's skin (guided test section).

<u>Deriving the RANS wall corrections</u>

When pairs of simulations are obtained, it is possible to compare the aerodynamic conditions (M, α) and the aerodynamic coefficients to derive the first and second order corrections.

For the first order corrections, a direct comparison of the conventional Mach number of the confined simulation to the Mach number of the free stream simulation gives **ΔM**. For the correction in angle of attack, the numerical empty test section angularity is combined with the geometric angle of attack of the model in the wind tunnel to define the uncorrected angle of attack. A direct comparison with the free stream angle of attack provides **Δα**.

Once the free stream Mach number is established, the corresponding free stream dynamic pressure is used to remove the dimension from the aerodynamic coefficients for both the free stream and the confined forces and moments. In this communication, the forces and moments are expressed in the body axis to avoid any conflict between the coefficients and the angle of attack. Thus, we will look at the normal force (CN), the axial force (CA) and the pitching moment (Cm). The corrections to forces and moments are deduced from the differences between the integrated forces over the model in free-stream and confined environments.
These corrections originate from local deviations of the flow field between the confined and the free air environments (see Figure 6). In this RANS approach, the corrections include both the effect of empty tunnel buoyancy and the other interference effects. So as to separate the effects for comparison with the experimental procedure, the buoyancy can be estimated using the empty tunnel gradients.

The current correction procedure with potential flow simulations is such that the confined states correspond to the free air states at the same lift (here, ΔCN = 0). With the RANS simulations, two paired simulations exhibit a different lift coefficient (see Figure 7). Thus, for a direct comparison with the linear potential flow corrections, the RANS corrections presented in this paper have been interpolated to be derived at fixed normal coefficient. This choice is neutral to correct polars, but it removes the link between the pressure on the model and the associated lift.
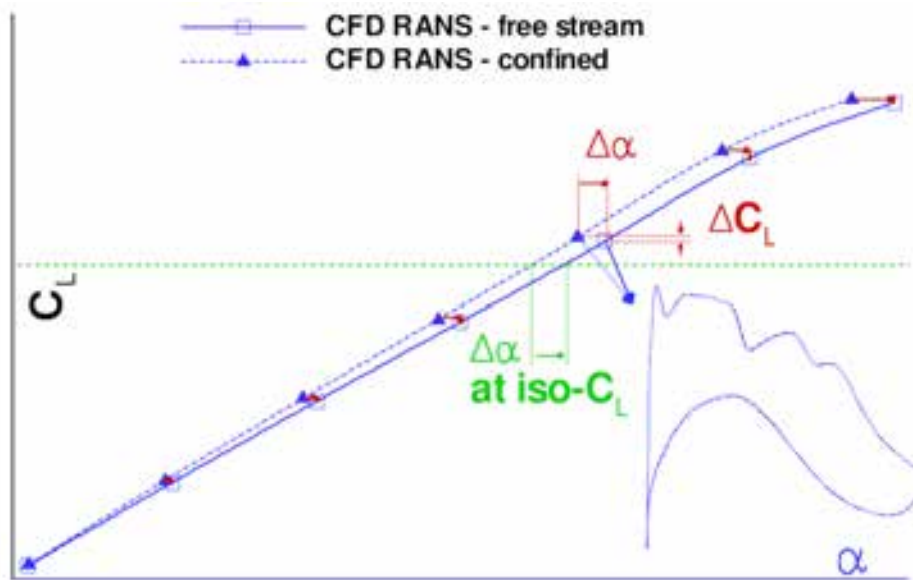

Figure 7: RANS corrections at iso-lift.

S2MA wind tunnel and porous walls

Generic features

Among the ONERA facilities in Modane-Avrieux, the S2MA wind tunnel has been chosen for this numerical application because of its intensive use for industrial purposes (see Figure 8). The facility can be operated for transonic and supersonic regimes with a possibility to vary the stagnation pressure from 0.2 up to 2.5 bars. It presents a rectangular test section by 1.75 m width and 1.77 m high (test section area 3.1 m^2).
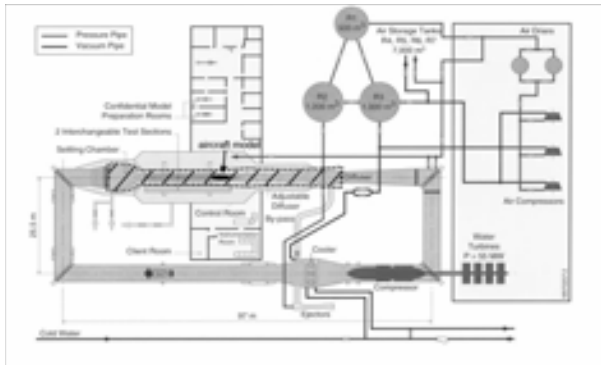

Figure 8: S2MA air circuit (the hatched zones represent the portions modelled in this study).
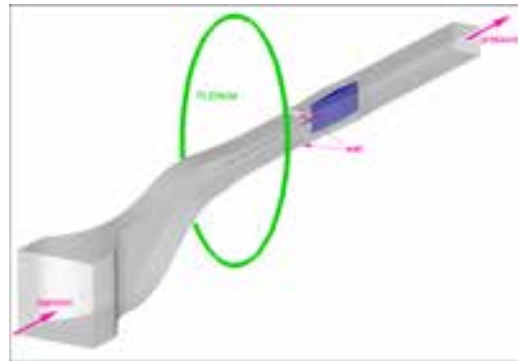
Figure 9: Numerical model of the S2MA wind tunnel.

Description of the porous walls

Wall porosity is used in transonic wind tunnels to limit the wall interference and to avoid blockage conditions. In S2MA, the porosity consists in holes drilled in the upper and bottom walls with an inclination (see Figure 10 and Figure 11). The inclination tends to favour the movement of air from the test section to the plenum. On the plenum side of the porous plates, a grid was used to adapt the effective porosity. Nowadays, this grid is fixed and the porosity is 5.2% for each top and bottom wall (or 2.6% for the entire test section).

Porosity evolves longitudinally along the test section (see Figure 12 to Figure 15). The first third of the test section (upstream) consists in a progressive establishment of the porosity. The last two thirds are porous but the beams sustaining mechanically the porous walls impede a full periodicity of the holes (some holes are more closed than others).

The setting of the walls is set at null inclination. Nevertheless, the Mach number gradient is about zero since the flow outside of the test section compensates the growth of the boundary layer. When a guided test section behaviour is needed, the holes are sealed, and a Mach number gradient is present.

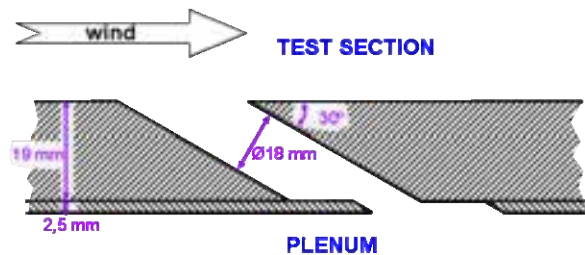**Figure 10: Porous wall of the S2MA test section.**
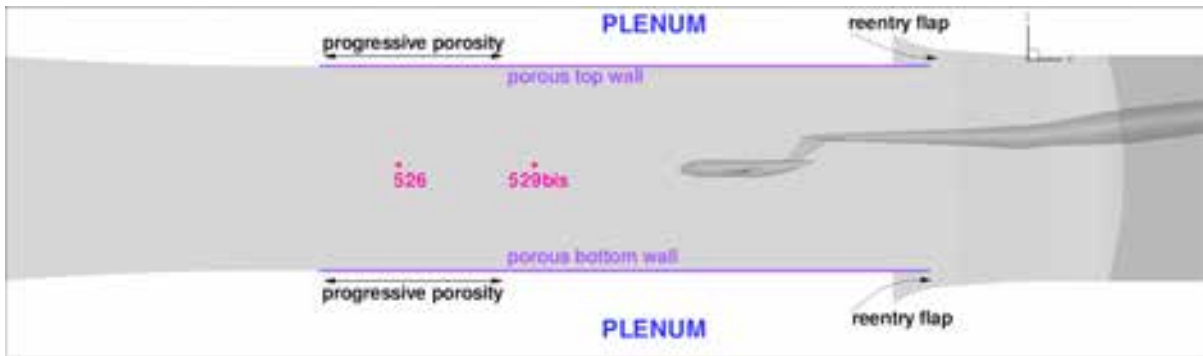

Figure 11: Hole layout in S2MA.

Figure 12: General arrangement of the S2MA test section and the porous walls.

Figure 13: Progressive porosity.

Figure 14: Top wall (with a pressure rail).

Figure 15: Re-entry flaps.

Measurements of the S2MA wall porosity

Experimental set up

The test set up is presented schematically in Figure 16. A can was installed in the plenum on the top porous wall, upright the test section centre (Figure 17). Its height was 0.4 m and it covered an area **S** equal to 0.112 m^2, including about thirty holes. The can was connected through a flexible tube to a high pressure supply or to a vacuum supply, located outside the wind tunnel. The high pressure came from a big sphere with an adjustable pressure, up to 64 bars. The low pressure was obtained with the help of an ejector supplied by the high pressure from the sphere.

The air mass flow **m** going through the can and the porous wall could be adjusted by means of control valves, from 0.03 kg.s^{-1} to 1 kg.s^{-1}, and was measured by a sonic flowmeter (pressure) or by a venturi (vacuum). At the beginning of the test, the can had been isolated and the sonic flowmeter and the venturi had been connected on the same circuit. A very good agreement was observed between the two mass flow measurements.

The pressure inside the can was measured by 4 transducers and the mean value **Pc** was calculated.

The objective of the tests is to measure the cross flow characteristic of the portion of the porous wall. It consists in measuring the relation between the flow velocity through the porous wall $w = m/\rho_0 S$ and the pressure coefficient in the plenum $C_P = (P_c - P_0)/Q_0$. We then seek the function $w/V_0 = f(C_P)$. Where ρ_0, P_0, Q_0, V_0 are the density, static pressure, kinetic pressure and velocity of the wind tunnel flow.

In addition, in order to examine the local flow disturbances on the test section side of the porous wall, a boundary layer rake and a static pressure rail were installed on the top wall (Figure 16 and Figure 14).
- the rake was located at about 0.2 m downstream from the tested wall portion;
- the rail had a length equal to 0.7 m and was located at about 0.15 m on the side of the tested wall portion.

The experiments were performed in the empty test section (no model) at:
- Mach number M = 0.70, 0.80, 0.85 and 0.90;
- stagnation pressure Pi = 1.0, 1.5 and 2 bars;

- about twenty mass flow values for each (M, Pi) condition, including inflow (from the plenum to the test section) and outflow (from the test section to the plenum).
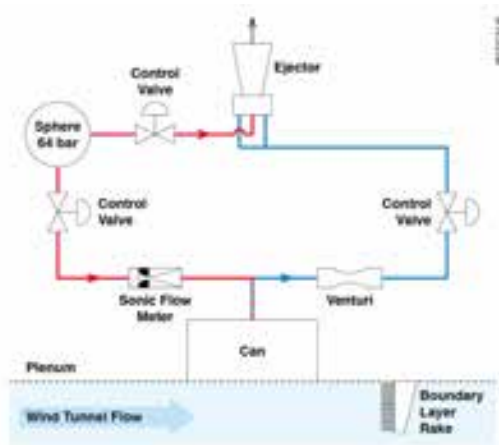

Figure 16: General set up.

Figure 17: Set up of the can in the plenum.

Experimental results and discussion

The cross flow correlation $w/V_0 = f(C_P)$, measured at M = 0.80 and Pi = 1 bar, is shown in Figure 18. The following comments can be given:

- repeatability of measurements between two runs, performed at the beginning and at the end of the test, is very good;
- as expected, the vertical velocity is much higher for the outflow than for the inflow since the holes are inclined in the wind direction;
- the mass flow m = 0 is obtained for Cp = 0.065. Since during tests in S2MA the pressure coefficient of the plenum is about equal to 0.040 and change in Cp at the bottom and top walls induced by the model are typically limited to ± 0.020, the difference in Cp through the porous walls range from 0.020 and 0.060, being wholly in outflow. As a conclusion the S2MA test section runs nearly always in outflow;
- over the range of Cp of usual tests (0.02 to 0.06), the graph in Figure 18 looks relatively well linear. The use of a constant porosity coefficient, whatever the Cp level, in the flow simulations when modelling the porous walls, is so justified;
- it is to be noted that the porosity coefficient derived from Figure 18 is equal to only about 2/3 of the coefficient used in the linear potential flow code and which was determined empirically. In fact the relevant vertical velocity w for this latter code is the one measured at the outer boundary of the wall boundary layer [15]. The longitudinal change in the boundary layer displacement thickness $d\partial 1 / dx$ amplifies the vertical velocity at the wall. Recent boundary layer measurements in the S2MA test section showed that this amplification explained roughly the 1/3 lacking.

The change in cross flow correlation in terms of Pi, measured at M = 0.80, is shown in Figure 19. Deviations are low, significant only at Pi = 2 bars in outflow and in the beginning of inflow.
The change in cross flow correlation in terms of Mach number, measured at Pi = 1 bar, is shown in Figure 20. Deviations are about zero in inflow but notable in outflow; so between M = 0.70 and 0.90, over the usual test Cp range, the porosity (slope) is reduced by 1/3.
The velocity distribution into the boundary layer measured by the rake for a large range of mass flow is presented in Figure 21. As expected the boundary layer gets thinner in outflow and grows in inflow. The displacement thickness $\partial 1$, which is equal to 11 mm for the mass flow m = 0, reaches 6 mm and 23 mm for the extreme mass flow.
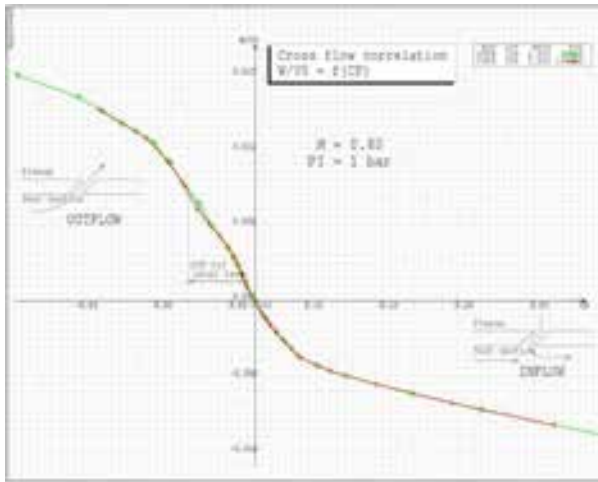
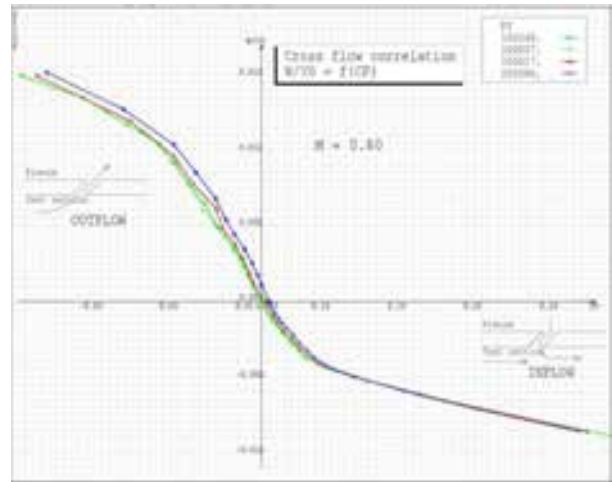**Figure 18: Repeatability of the cross flow correlation.**

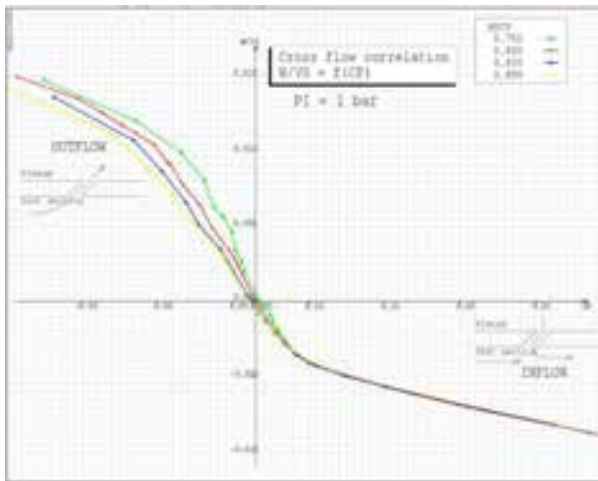**Figure 19: Stagnation pressure effect.**
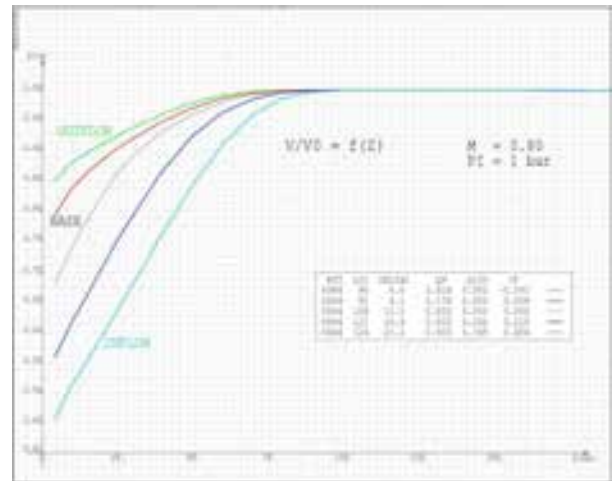

Figure 20: Mach number effect.

Figure 21: Velocity distribution into the boundary layer.

Numerical models for the CFD simulations

S2MA wind tunnel

As for the purpose of the wall interference, we need to represent several important factors such as the growth of the boundary layers in the test section (progressive contraction of the apparent tunnel section). Thus, the wind tunnel has been modelled from the settling chambers to the divergent (see Figure 9).

From a numerical point of view, apart from walls, the boundary conditions consist in the inlet (settling chamber) and the outlet (part of the diffuser). Only half of the CAD could be meshed with 3.1 million nodes, thanks to the left-right symmetry. For the wind tunnel walls, the y+ varies between 0.7 and 2.0 depending on the stagnation pressure in the wind tunnel.

This study builds upon a former study dedicated to the validation of the numerical tools to model the confined flows in wind tunnels (see [10], [11]).

Model and sting line

The S2MA wind tunnel was computed with its reference model (A310 research wing body model on a fin sting, see the experimental set-up in Figure 22). This model cruises at Mach number 0.80 and the blockage ratio in the S2MA test section is 0.8%.

The mesh of the model features 3.5 million nodes and the sting line features 0.9 million nodes (see Figure 23). An additional cartesian bloc (1.4 million nodes) around the model ensures correct interpolations between the small cells around the A310 research model and the S2MA relatively large cells. The complete configuration installed in the S2MA test section features about 9 million nodes.

Due to the geometric complexity of the elements present in any wind tunnel (sector, sting, blade, model) the Chimera [12], [13] technique has been used. The technique consists in overlapping grids. The meshing process is eased because more simple elements are meshed. The assembly of the grids is ensured through high order interpolations.

Figure 22: A310 model installed in the S2MA wind tunnel.

Figure 23: Mesh of the A310 research model in the S2MA test section.

Numerical software

The computations resort to RANS modeling computed with the elsA software [14]. The software solves the equations in a finite volume formulation (cell-centered). For this study, a LU implicit scheme has been used together with a second order central difference for the spatial discretisation of the mean flow (Jameson scheme with second and fourth order dissipation terms). As for the turbulent quantities, a first order central discretisation is used. The time scheme is the first order backward-Euler. The local time stepping and multigrid techniques are applied to speed up the convergence process. The turbulence model is the one equation Spalart-Allmaras.

Boundary condition formulation in the RANS software

The experimental porous boundary condition has been implemented in the elsA aerodynamic software. The formulation consists in a modification to the wall boundary condition. The non slip boundary condition formulation is modified to allow an added momentum perpendicular to the wall. In each wall cell, the momentum depends on the local pressure.

The test section aerodynamic conditions are now determined from three different places of exchange with the fluid outside of the computation domain (each involving a specific pressure parameter):
- settling chamber (stagnation pressure);
- diffuser (static pressure);
- plenum (stagnation pressure).

For solid walls, the communication with the plenum was simply blocked and setting the static pressure at the diffuser directly sets the Mach number in the test section. With porous walls, both the plenum pressure and the diffuser pressure act on the Mach number in the test section. Several attempts have been tried to determine an adequate plenum pressure automatically adjusted from the diffuser pressure, but the results were not stable.

Thus, the experimental pressures have been directly used for both the diffuser and the plenum pressure. Another formulation should be attempted to free the simulations from the dependence on the experimental values.

Another aspect must be taken care of. As the porous walls see mainly outflow, a balance must be achieved between the plenum and the test section. This balance is established through the re-entry flaps at the end of the test section, upstream of the sector (see Figure 12). In order to model this balance, an iterative process is carried out:

- porous simulation with an average inflow at the re-entry flaps;
- integration of the outflow over the porous walls at the end of the simulation;
- new porous simulation with an inflow at the re-entry flaps corresponding to previous porous wall outflow.

Rapidly, the mass fluxes reach stable values (two coupling steps are sufficient).

Validation of the porous formulation

A validation has been carried out for the empty tunnel at various Mach numbers. For this paper, as corrections will be derived only for Pi = 1.5 bar and M = 0.80, only the porous characteristics at these conditions are used.

A preliminary validation consists in verifying that the boundary condition is used in the range of the measurements. In Figure 24, the velocity at the porous wall is represented, together with the velocity in the re-entry flaps.

In the empty test section (see Figure 24 a), the velocity evolves rapidly from the most upstream part of the porous wall to reach about 0.5 m.s^{-1} over most of the porous wall. Then, locally, the velocity rises at the re-entry flaps to reach about 1 or 2 m.s^{-1}. In the computations with the model at cruise (see Figure 24 b) the velocities are more contrasted. The velocities can reach locally 1 m.s^{-1} and some inflow through the porous walls can occur in the vicinity of the model (at low velocity).

These velocities are well in the range of the linear region found in the porosity measurements. The inflow through the re-entry flaps corresponds to about 10 to 15 m.s^{-1}.
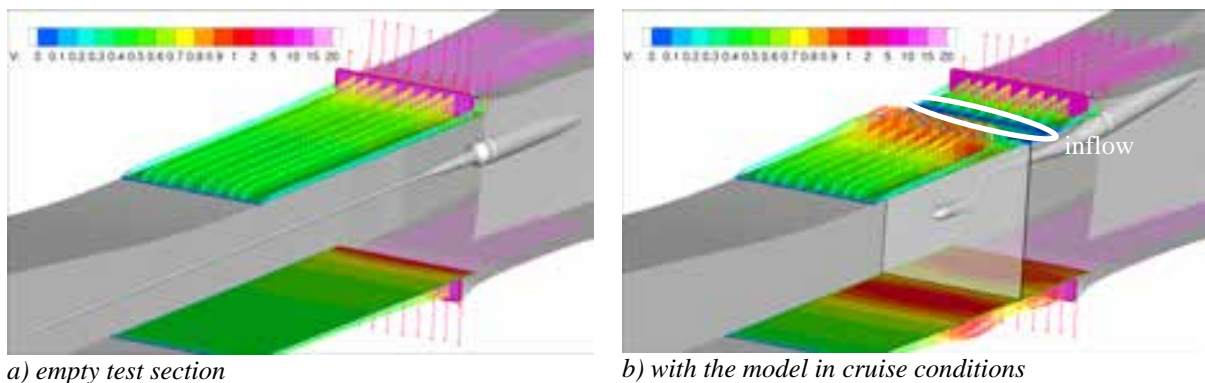

a) empty test section   b) with the model in cruise conditions

Figure 24: Examples of velocities through the porous walls at M = 0.800.

Assessment of the confined flow simulations

Wall signatures in the empty tunnel

The wall signatures obtained with CFD are compared to the experimental ones in Figure 25. A good match is achieved all along the wind tunnel, from the convergent to the diffuser, for both the guided and the porous test sections. The various Mach numbers tested exhibit satisfying results. In the vicinity of the model where all the wall interference resides, the diminution of the Mach number gradient from guided to porous is well simulated by RANS CFD.

When the simulations are carried out for several test conditions, it is possible to determine the numerical calibration of the empty wind tunnel. In Figure 26, several relations are presented for the RANS simulations and for the experiments (both guided and porous walls):

- The relation between the tunnel reference pressure tap and the centre of the tunnel is in green. This relation will enable to define the uncorrected Mach number for the confined simulations with the model.
- The relation between the Mach number in the centre of the tunnel and the pressure at the diffuser is in black. This relation shows the link between the locus where the boundary condition is applied (diffuser) in the simulation and the achieved Mach number at the tunnel centre.

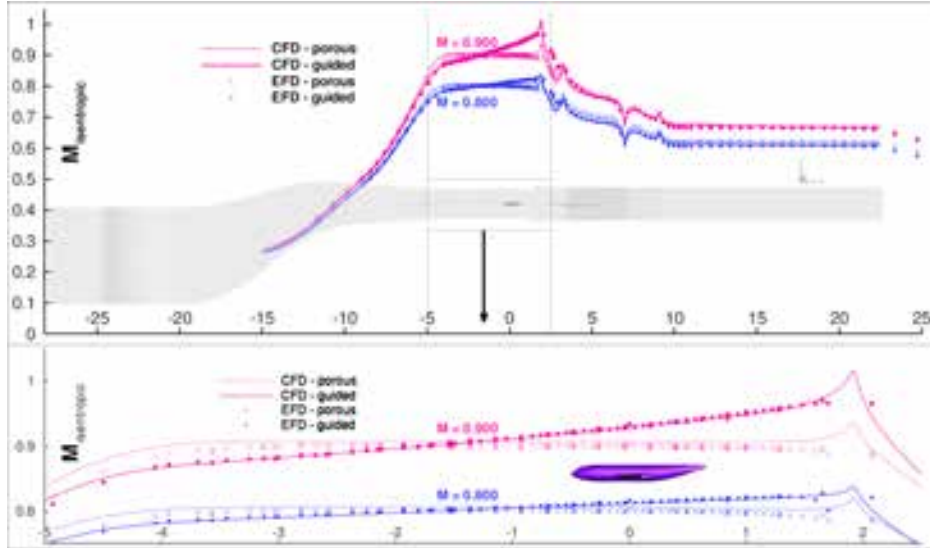Both relations compare well with the experiments, for both the guided and the porous test sections.

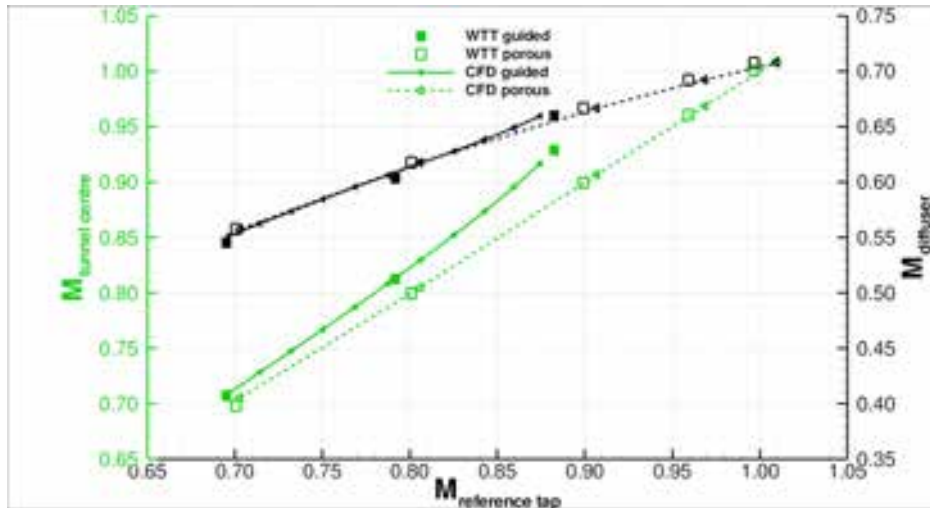**Figure 25: Empty tunnel wall signatures for the guided and the porous test sections.**

Figure 26: Numerical and experimental empty tunnel calibrations (guided and porous walls).

Wall signatures with the model in S2MA

Based on the good validations achieved for the empty tunnel simulations the validation is now carried out on the tunnel with the model and its sting line. The validation resorts to the comparison of wall signatures on several rows of pressure taps between CFD and EFD (Experimental Fluid Dynamics).

The comparison is carried out by subtracting the pressure without model (empty wind tunnel) from the pressure with model (see Figure 27). This enables comparing with the potential flow code that does not account for empty tunnel gradients. As the empty tunnel pressures are removed, the empty test section Mach number gradient disappears for the guided test section (this gradient is minor for the porous test section). Thanks to this operation, the Mach number is constant upstream of the model. Near the model, the top and bottom signatures

separate because of the effects of lift and we can see a larger effect in the guided test section than in the porous one. Across the model (nose to tail), a gradient is noticeable and it continues downstream of the model.

The general trends are correctly predicted by both the RANS simulations and the linear potential code. Especially on the guided test section, a very good agreement between all the methods is achieved.

For the porous test section, a too large Mach number gradient across the model is present in the RANS simulations, whereas the potential flow simulations predict very well the pressure signatures in both conditions.

Globally, the RANS results are in a good agreement with the experiments and we can thus proceed to the analysis of the corrections.
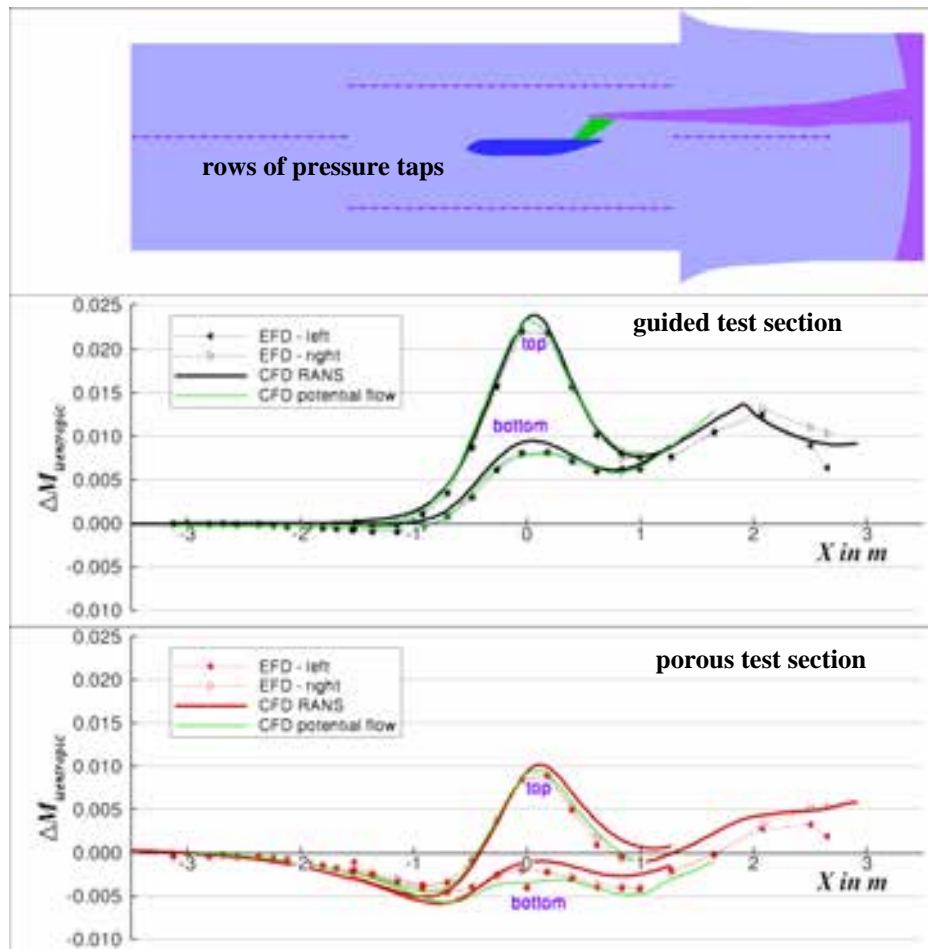

Figure 27: Wall signatures in S2MA at cruise (M = 0.80, CL = 0.50).

Discussion on the wall corrections

Two sets of computations are presented in this paper.

The first set of computations aims at validating the RANS correction process against the linear potential flow method. In order to do so, we have represented the guided test section (well defined wall boundary treatment) and the model without the sting line (to remove the junction between the model and the sting that is difficult to model with singularities). Mach number regimes from linear to non-linear have been explored (from 0.700 to 0.840).

The second set of computations includes the sting line and the porous walls and aims at testing the RANS correction procedure on a concrete applied case (at M = 0.800 only).

First order corrections (ΔM, $\Delta \alpha$)

The first order corrections are presented in Figure 28. For the Mach number correction (red lines), a good general agreement is found between the potential flow simulations and the RANS simulations. In the guided test section, the corrections range from 0.004 to 0.012 from low Mach number to high transonic Mach number. A gradient in Mach number correction is shown in the RANS simulations between the zero lift to the high lift for the transonic cases (evolution in Mach number correction by about 0.002). The discrepancy between the methods lies within ±0.001 in Mach number correction. For the porous test section, the average correction in Mach number is nearly null, but the RANS simulations exhibit a ±0.002 variability. The correction at low lift exhibits a reverse trend but it is deemed unreliable because of the low quality of the pairing for this point.

For the angle of attack correction, a good agreement is achieved for both the porous and the guided test sections. The reduction of the slope of the correction with lift in the porous case is well predicted, and the minor impact of the Mach number effect in the guided test section is confirmed. Nevertheless, the RANS corrections exhibit a tendency to move from a linear behaviour at high lift. This trend increases with the Mach number.
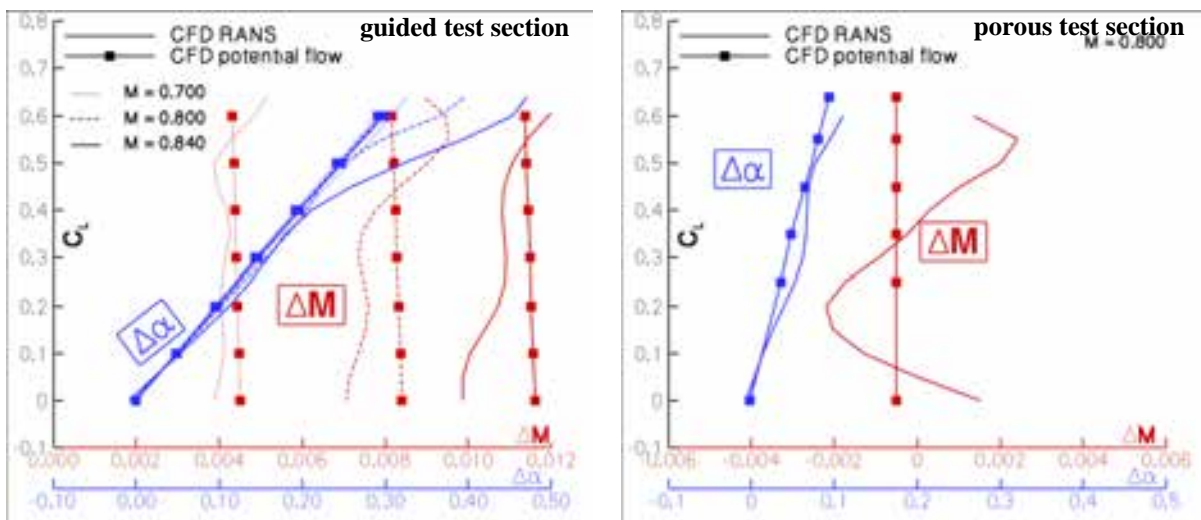

Figure 28: First order corrections in S2MA.

Second order corrections ($\Delta \vec{F}$, $\Delta \vec{M}$)

The pitching moment correction is shown in Figure 29 (top). Linear corrections are found for the potential flow model and quadratic shapes are found for the RANS model for the guided test section. As a consequence, a good agreement between both methods is obtained at low lift (discrepancy in correction lower than $1 \ 10^{-3}$) but for higher lift coefficients discrepancies increase rapidly. In the porous test section (where the sting is present), the corrections are similar in trend but with a deviation by about $2 \ 10^{-3}$. The origin of this discrepancy is not obvious, but it is likely to stem from the large influence of the fin sting on the pitching moment in the RANS simulations.

The corrections in axial coefficient are presented in Figure 29 (bottom) and a good match between the approaches is evidenced. The EFD corrections contain both the linear potential corrections and the experimental empty tunnel gradient (buoyancy) that compares directly to the RANS corrections.

In the guided test section, an excellent match is achieved at M = 0.700 (discrepancies lower than ±1 dc). When Mach number increases, the RANS corrections exhibit local deviations from the average CA correction along the lift polar. For these transonic Mach numbers, the typical discrepancy between the methods is ±2 dc for an average correction by about 20 dc.

As for the porous test section, the corrections are of lower amplitude, because the buoyancy is quite small (buoyancy even cancels part of the wall corrections). A large discrepancy between the RANS simulations and the EFD corrections can be noted (about 8 dc). Most of this discrepancy is located on the rear fuselage, where the fin sting goes through the model (large impact on the pitching moment) and where the fuselage contracts (impact on the axial coefficient). In these areas, the RANS CFD provides a detailed flow pattern whereas the linear potential method has difficulties in modelling the geometry.
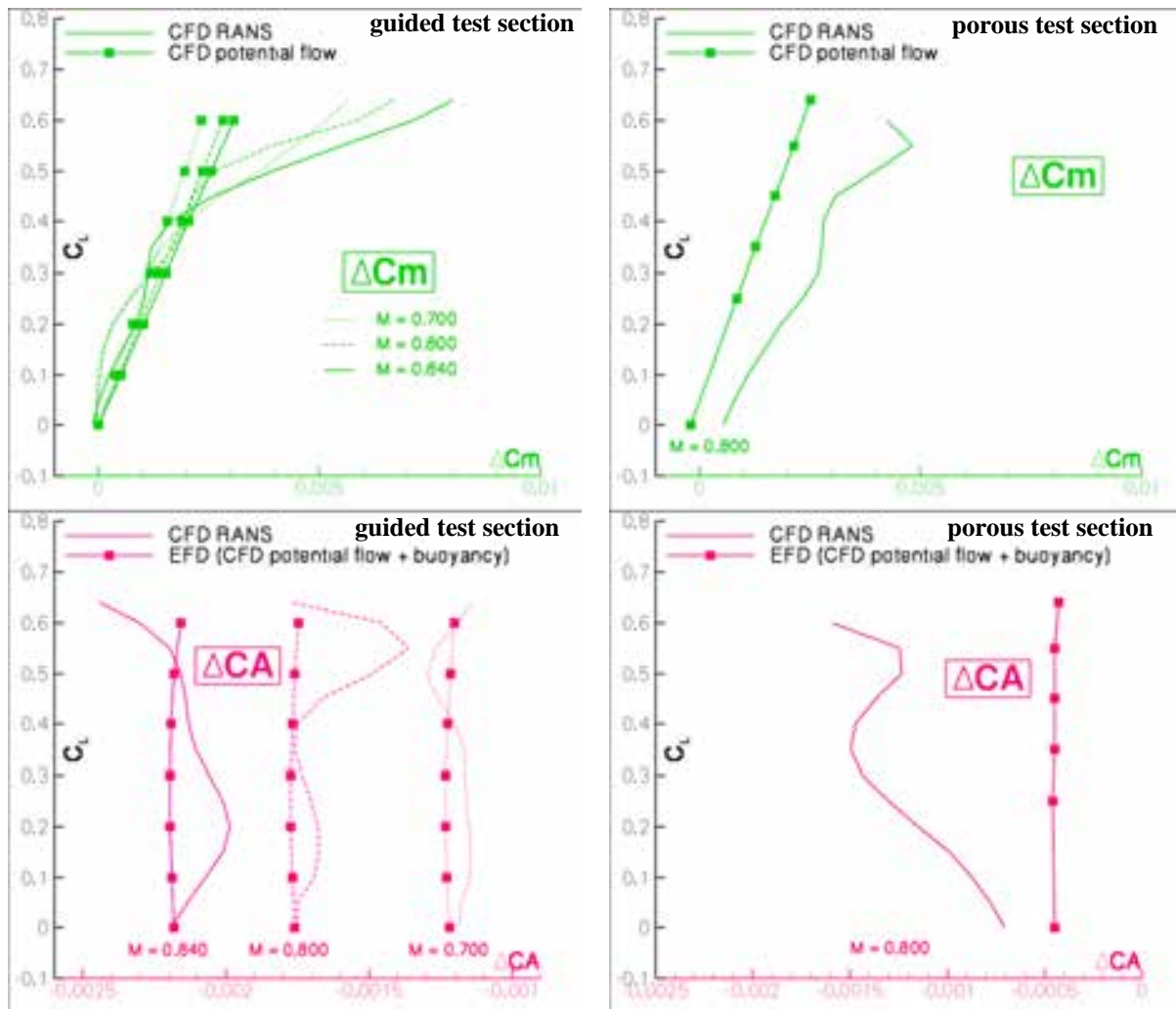
Figure 29: Second order corrections (pitching moment on top and axial coefficient in the bottom).

So as to go further in the analysis of the RANS correction procedure in comparison with the linear potential approach used currently at ONERA, it is also possible to compare the interference in axial force without the buoyancy (see Figure 30 a). This is directly what the linear potential code predicts. At this scale, we can see that only about 2 dc correction remains. But for this correction, a difference by about 2 dc can be experienced between the RANS and the linear potential code.

To investigate this difference, this correction is split between its components for the fuselage and for the wing (see Figure 30 b and c). Even if the pressure discrepancies between the confined flow and free air were especially visible on the wing, they are very local and thus, the corrections on the wing are marginal (less than ±1 dc). The correction on the fuselage is the most important one. The same progression with Mach number is present in the RANS simulation and in the linear potential flow corrections. Nevertheless the RANS corrections exhibit an influence of the lift that increases with Mach number when the linear potential flow corrections are constant in lift. We can see a close match at the low Mach number where the flow is indeed linear and a discrepancy by about ±1 dc at high Mach number when non-linearities arise.

If we compare the CA correction in Figure 30 (without buoyancy) to the correction in the porous test section in Figure 29 (that contains only few buoyancy), we may have the false impression that the correction is larger in the porous test section. If the magnitude of the correction is larger, this is because of the presence of the sting in that case. When looking at comparable settings (wall interference in the presence of the sting for example), the porous and the guided test sections produce about the same interference (this is not shown in this paper).
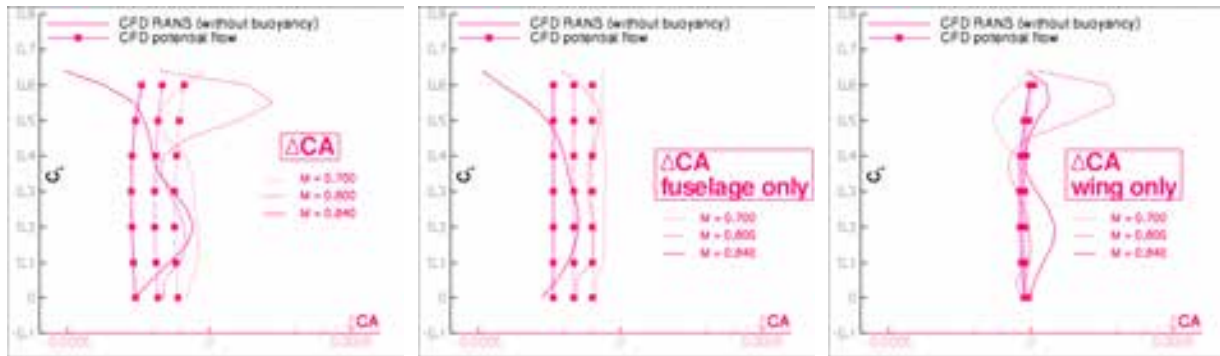
a) Correction for the whole model   b) Correction for the fuselage   c) Correction for the wing

Figure 30: Breakdown of the axial coefficient correction without the buoyancy (guided test section).

Conclusions and perspectives

This paper describes in details a methodology to estimate the wind tunnel wall interference with RANS simulations. We have taken care of the experimental aspects to define a concrete process that can be embedded in current test data process. The current ONERA method relying on fast linear potential flow simulations, we have focused on the benefit that could be gained from the modelling of non-linearities with high fidelity RANS simulations (requiring more CPU time). The paper presents both methodological developments and applied simulations on a transonic ONERA wind tunnel in Modane (pressurised S2MA tunnel with both guided and porous walls).

The RANS simulations need to model the physics of the confined flows including boundary layer development over the tunnel walls, accelerated and decelerated flows in the convergent and the diffuser, corner flows at the tunnel wall junctions and aerodynamic interference between the model and the confined environment. A specific attention has been devoted to the modelling of the S2MA porous walls thanks to a measurement campaign focusing on the average porosity characteristics of this wind tunnel. Good validations with wall signatures have been achieved on the empty tunnel and on the tunnel with the model. Some complementary modelling activities on the porous test section should be carried out.

Thanks to the use of automatic optimisation to obtain equivalent simulations in free air and in the wind tunnel, RANS wall corrections could be established for many test conditions (Mach number and angle of attack) and test set up (porous or guided, with or without model support). The comparison of the RANS corrections with the current correction procedure has enabled to draw several conclusions. In terms of CPU cost, the potential flow simulation requires only seconds whereas the RANS procedure requires several days and can't be operated in real time during a test. As for accuracy, both correction procedures predict similar correction levels for the aerodynamic conditions (first order corrections) as well as for the aerodynamic coefficients (second order corrections). The differences arise at high lift or high Mach number when the non-linearities increase. In these regimes, the RANS corrections show a non-linear behaviour whereas the potential flow corrections remain intrinsically linear.

The procedure developed to compute the corrections being principally an automated means of finding pairs of similar flows, it can handle any interference effect such as mounting effects, for instance. Finally, we should focus on only the two meaningful configurations of interest: model with its sting line in the wind tunnel and model in free stream. Thus, the intermediate steps with the model on its sting in free stream allowing computing wall interference in the presence of the sting and sting interference without walls can be avoided to tackle directly the global and coupled wall and support interference.

Acknowledgements

References

[1] Ashill P.R., Binion T., Cooper K.R., Crites R., Everhart J.L., Ewald B.F., Hackett J., Holst H., Krynytzky A.J., Malmuth N.D., Mokry M., Newman P.A., Sickles W.L., Steilne F.W.J., Taylor C.R., Taylor N.J., Voss R., Wedemeyer E.H.: Wind Tunnel Wall Corrections, *AGARD Advisory Group for Aerospace Research and Development*, AGARD-AG-336, 1998.

[2] Kraft E.M., Ritter A., Laster M.L.: Advances at EADC in Treating Transonic Wind Tunnel Wall Interference. *15th Congress of the International Council of the Aeronautical Sciences*, Vol. 2, pp. 748-769, 1986.

[3] Bosnyakov S., Kursakov I., Lysenkov A., Matyash S., Mikhailov S., Vlasenko V., Quest J.: Computational Tools for Supporting the Testing of Civil Aircraft Configurations in Wind Tunnels. *Progress in Aerospace Sciences*, No. 44, pp 67-120, 2008.

[4] Kohzai M., Sudani N., Yamamoto K., Ueno M., Hashimoto A.: Experimental and Numerical Studies of Support Interference in the JAXA 2m x 2m Transonic Wind Tunnel. *27th AIAA Aerodynamic Measurement Technology and Ground Testing Conference*, 2010.

[5] Vaucheret X.: Recent Calculation Progress on Wall Interferences in Industrial Wind Tunnels. *La Recherche Aérospatiale*, No. 3, pp 45-47, 1988.

[6] Pistolesi, E.: Considerations respecting the mutual influence of system of airfoils. *Collected lectures of the principal meeting of the Lilienthal society*, Berlin, 1937.

[7] Vanderplaats G.N.: CONMIN – A FORTRAN Program for Constrained Function Minimization. User's Manual. NASA TMX 62282, 1973.

[8] The DAKOTA Project, Large-Scale Engineering Optimization and Uncertainty Analysis, http://www.cs.sandia.gov/DAKOTA

[9] Python Programming Language, http://www.python.org

[10] Hantrais-Gervois J.-L., Cartiéri A., Mouton S., Piat J.-F.: Empty Wind Tunnel Flow Field Computations. *AAAF, 44th Applied Aerodynamics Symposium*, Nantes, 2009.

[11] Hantrais-Gervois J.-L., Cartiéri A., Mouton S., Piat J.-F.: Empty wind tunnel flow field computations. *Int. J. Engineering Systems Modelling and Simulation*, Vol. 2, No. 1/2, 2010.

[12] Benek J.A., Steger J.L., Dougherty F.C.: A Flexible Grid Embedding Technique with Application to the Euler Equations. *AIAA Aerospace Science Meeting & Exhibit*, 1983.

[13] Benoit C., Jeanfaivre G., Canonne E.: Synthesis of ONERA Chimera Method Developed in the Frame of CHANCE Program. *31st European Rotorcraft Forum*, Florence, 2005.

[14] Cambier L., Veuillot J.-P.: Status of the elsA Software for Flow Simulation and Multi-Disciplinary Applications. *46th AIAA Aerospace Sciences Meeting and Exhibit*, Reno, Nevada, 2008.

[15] Crites R. and Rueger M.: Modeling the ventilated wind tunnel wall. *30th AIAA Aerospace Sciences Meeting and Exhibit*, Reno, Nevada, 1992.

Wall Interference Analysis by Whole Wind Tunnel CFD

Atsushi Hashimoto
Masataka Kohzai

Aerospace Research and Development Directorate
Japan Aerospace Exploration Agency
Chofu, Tokyo, 182-8522
JAPAN
ahashi@chofu.jaxa.jp

Abstract

For wall interference correction, the potential-based methods such as Mokry's method are commonly used. In fact, the linear correction methods cannot be used for transonic and stall conditions. In this study, the Mokry's method is applied to wind tunnel CFD, and the corrected aerodynamic coefficients are compared with CFD without wall to investigate validity and limitation of the method. We have simulated the whole wind tunnel flow of JAXA 2m×2m Transonic Wind Tunnel (JTWT). The pressure distribution on the wind tunnel wall agrees well with the measurements. In addition, the computed C_L and C_D agree well with the measured values. The differences between standard and long stings are almost same as the experiment. It is found that the aerodynamic characteristics of ONERA-M5 and its wall/support interferences are well reproduced in this computation. In the case of M=0.7, long sting, and $\alpha=0^{\circ}$, the results corrected by the Mokry's method show good agreement with those without wall. However, the accuracy is degenerated by shock wave, separation, and support interference, since the Mokry's method is based on the linear potential theory. It is found that the effect of support interference is not so large, whereas the effect of separation is serious.

Key words: Wind tunnel, CFD, Wall interference.

Introduction

Highly accurate aerodynamic data is required for development of civil aircrafts. For example, the requirement of drag forces measured at wind tunnel testing in the high-speed regime is ideally less than 1 count (1 count is 0.0001 of C_D). To achieve this severe accuracy requirement for force and moment measurements, the following techniques are important: flow quality maintenance, balance calibration, wall correction, and support correction. For JAXA 2m×2m transonic wind tunnel (JTWT), a series of activities to improve the measurement accuracy have been recently conducted; measurement of the flow angularity[1], calibration of test section Mach number[2], correction of thermal zero-shift of balance[3] and wall and support corrections[4].

For the wall correction, the potential-based methods such as Mokry's method[5] are commonly used. These correction methods are based on the small perturbation potential equation. Taking advantage of the linearity, the effect of wall interference can be extracted from the flow field in the wind tunnel. In fact, the linear correction methods cannot be used for transonic and stall conditions. However, the methods are widely used since the computation is simple and fast, and the accuracy is believed to be appropriate even under these conditions, although the methods are not strictly verified.

Recently, CFD especially RANS simulation is used for investigation of wall interference. ETW with slotted walls is directly simulated in Ref. 6. The guided far field model is also proposed to model the effect of ETW wall[7]. However, the verification of current wall correction method is rarely done with CFD, though the wind tunnel CFD considering the slotted or porous walls is commonly carried out. An example is the wall interference analysis of S2MA at ONERA[8]. The linear potential code DXV used for wall correction is validated with CFD results.

In this study, flow inside the JTWT is simulated to investigate the wall interferences under the transonic and stall conditions. The support effect on the wall interference is also investigated. The Mokry's method is applied to wind tunnel CFD, and the corrected aerodynamic coefficients are compared with CFD without wall. CFD is a powerful tool since it can simulate both conditions with and without wall, which is impossible by experiment.

Configuration of JTWT

The JTWT is a closed-circuit and continuously operating facility (Fig. 1). The wind tunnel has a square test section of 2m×2m. The JTWT can maintain the Mach number from 0.1 to 1.4 at the total pressure from 50 to 140 kPa.

An aircraft model installed in JTWT is shown in Fig. 2. We consider the ONERA-M5 wing-body model[16] as an aircraft model. The wing span is 0.9819m and the span to wind tunnel width ratio is 49%. The walls at the test section are porous ones. The support devices are sting, pod, and strut behind the model. In addition, there is a plenum chamber surrounding the test section. Here, we assume that the air is static and uniform in the plenum chamber.

In the computation, we consider a part of JTWT inside the red box in Fig. 1; nozzle, test section, and diffuser. Figure 3 shows the whole computational domain. The upstream converging nozzle region is also included to compute the growing turbulent boundary layer on the wind tunnel wall precisely. The diffuser behind the test section is also included in the computation to reduce the effect of outflow boundary. The closed-up figure of the test section is shown in Fig. 4. The ONERA-M5 model and the support devices (sting, pod, and strut) are included in the computation. The light-blue transparent walls in Fig. 4 are the porous walls. The windows in the side porous wall are also modeled precisely.

We employ two lengths of sting; standard and long stings shown in Fig. 5. The long sting is produced to investigate the buoyancy effects due to the support devices. The ONERA-M5 is located from STA=7409 to 8467 for standard sting and from STA=6968 to 8026 for long sting. The porous walls exist from STA=5200 to 9500.

Computational Methods

As a flow solver, the TAS (Tohoku University Aerodynamic Simulation) code[9] is used in this study. It is a well-validated code and used in a variety of aerospace applications[10]. In TAS, full Navier-Stokes equations are solved on the unstructured grid by a cell-vertex finite volume method. The HLLEW (Harten-Lax-van Leer-Einfeldt-Wada) method is used for the numerical flux computations. The LU-SGS (Lower/Upper Symmetric Gauss-Seidel) method is used for time integration. The second-order spatial accuracy is realized by a linear reconstruction of the primitive variables with Venkatakrishnan's limiter and Unstructured MUSCL-scheme (U-MUSCL). The Spalart-Allmaras model is used as a turbulence model and turbulent transition is not taken into account. The equations for the turbulence model are also solved using the second-order scheme. The time integration is carried out by the local time stepping. Since the wall interference is small, exactly same schemes must be used for all cases. Otherwise, the difference of scheme causes difference of aerodynamic forces and moments.

A grid is generated with MEGG3D[11]. The generated grid is a mixed element grid that consists of mainly tetrahedra and prismatic layers. The total number of node is 7.2 million for standard sting and 8.6 million for long sting. In this study, we compare results with and without wind tunnel walls to understand the wall interferences. To avoid the grid dependency, the exactly same surface grids are used for ONERA-M5, sting, pod, and strut. The grid resolution around the ONERA-M5 is almost same between the grids to be compared. We checked that the employed grids are sufficient to investigate the wall effects[15].

As for a porous wall model, a simple model developed by Nambu et al.[12,13] is employed. The model is developed specifically for JTWT conditions, where the hole geometry and thickness of turbulent boundary layer are considered. The mass flow rate through the porous wall is determined with this model from the pressure difference between the wind tunnel and the plenum chamber.

When we determine the velocity across the wall, at first, the pressure of plenum chamber is determined so that the mass inflow and outflow through the porous wall can be conserved. Here, we assume the pressure of plenum chamber is uniform. The computed velocity is set as boundary conditions of porous walls.

To realize the desired Mach number flow at the test section, the total pressure and temperature are fixed at the inflow boundary and the static pressure is adjusted at the outflow boundary. Additionally, we use the initial

conditions calculated with the quasi one-dimensional nozzle theory. Otherwise, the computation becomes unstable and the local time stepping is not applicable. The detail of computational method is described in Ref.14.

Computational Conditions

Mach numbers at the test section are 0.70 and 0.84. Reynolds numbers based on the mean aerodynamic chord of 137mm are 1.56×10^6 and 1.67×10^6 for M=0.70 and 0.84, respectively. The total pressure is 100kPa and the total temperature is 322K. The angle of attack is 0° for all cases.

We conduct five computational cases in Table 1 to reveal the wall and sting effects. Table 1 shows which components are included in the computation. The pod and strut are included with the standard or long sting.

Validation of Whole Wind Tunnel Simulation

Figure 6 shows Cp contour on the model and tunnel wall surfaces, where the upper and side porous walls are removed to see the inside of wind tunnel. We compare the pressure distribution on the porous wall with measurements along the three lines illustrated in Fig. 7: upper, lower, and side walls. In Fig. 8, the computed Cp distributions are compared with the measurements for M=0.7, $\alpha=0°$, and long sting. The ONERA-M5 is located from STA=6968 to 8026 for long sting (Fig. 5(b)). The porous walls exist from STA=5200 to 9500. The results agree with the measurements for all walls. Especially, the location and variation of suction peak show good agreement with those of measurement on the upper wall. The pressure becomes low around the model on the upper and side walls due to the low pressure above the wing, whereas the pressure becomes high on the lower wall since the wall interferes with downwash flow coming from the model. Additionally, the pressure distribution on the side wall is affected by the window, since the wall around the window is not porous (Fig. 4). The other cases with different Mach numbers and sting lengths are compared with measurement and show good agreement with measurement as well[15]. The difference of Mach number and sting length is found to be well captured in these computations.

Tables 2 and 3 show aerodynamic data for M=0.7 and 0.84, respectively, where the C_L, C_D, and C_m are listed. The aerodynamic data are evaluated on the forward body excepting the base. The experimental data is corrected using the measured base and cavity pressures. The values of dC_L, dC_D, and dC_m in Tables 2 and 3 are the difference due to the sting length: "Long sting"-"Standard sting". Figures 9 and 10 are the comparison of C_L, C_D, and C_m between computation and experiment for the standard and long stings. Although the experiment data are obtained for attack angles from $-5°$ to $2°$, the computation is carried out only at $0°$ and $2°$ for the standard sting and $2°$ for the long sting.

As shown in Fig. 9 and 10, the computed C_L and C_D agree well with measurement, though Cm is a little higher. Moreover, the differences between standard and long stings are almost same as the experiment (Figs. 9-10 and Tables 2-3). The difference due to the sting length is large in the drag force CD.

Validation of wall correction method

We apply the Mokry's method to the wind tunnel CFD to investigate validity and limitation of the method. The following steps are carried out to validate the method.
1. Implement wind tunnel CFD under the original conditions (M, α). ("Standard sting + Wall" or "Long sting + Wall" in Table 1)
2. Probe the wall pressure distribution of CFD result.
3. Calculate the correction values (ΔM, $\Delta\alpha$) from the wall pressure using the Mokry's method.
4. Correct the aerodynamic coefficients using ΔM and $\Delta\alpha$.
5. Implement CFD without wall under the corrected conditions (M+ΔM, $\alpha+\Delta\alpha$). (e.g. "Standard sting" or "Long sting" in Table 1)

Here, we compare the results of step 4 and 5 for the cases in Table 4, where the original and corrected values are shown. If the aerodynamic coefficients of step 4 and 5 are same, the Mokry's method is found to be valid. Shock waves exist for M=0.84, whereas they do not exist for M=0.70. In addition, the flow is largely separated at the leading edge for $\alpha=2°$, whereas it is separated behind the shock wave for $\alpha=0°$.

Figures 11-13 show C_D, C_L, and C_m data for M=0.70 and 0.80 with the standard and long stings. These figures show uncorrected and corrected aerodynamic coefficients (e.g. "CFD Standard Support" and "CFD

Standard Support Corrected" in Fig. 11). The uncorrected data are obtained by the wind tunnel CFD. These coefficients are corrected with the Mokry's method using the wall pressure distribution of wind tunnel CFD. Moreover, the coefficients are computed again without wall under the corrected conditions (e.g. "CFD Standard Support w/o wall" in Fig. 11). If the results without wall agree with the corrected values, the Mokry's method is validated. Experimental data are also shown as a reference. The experimental data are adjusted to match the uncorrected CFD data at $\alpha=0^\circ$ in Figs 11 and 13, at $\alpha=2^\circ$ in Fig 12 to see the relative displacement.

As a whole, the corrected values of CFD are almost same as those of experiment, since the wall pressure is almost same between experiment and CFD as shown in Fig. 8. The case of M=0.7, long sting, and $\alpha=0^\circ$ shows the best agreement among them (Fig. 13) since this condition is adequate for potential-based methods. There is no shock wave, separation, and the support interference is small in this case. We mention these effects on the Mokry's method as follows, comparing this case with another case.

The difference between M=0.7 and 0.84 in Fig.13 is caused by the shock wave. Drag and pitching moment are not corrected accurately. In addition, Figs. 14-15 show the surface Cp and difference between uncorrected wind tunnel CFD and corrected CFD without wall for M=0.7 and 0.84, respectively. The difference is so small for M=0.7 (Fig. 14), whereas the pressure is different around the shock wave for M=0.84 (Fig. 15). It is found that the shock location is not corrected accurately with this method.

The difference between the standard and long stings (Figs.11 and 13) is caused by support interference. The differences are not large especially for M=0.7. The pitching moment becomes better for M=0.84 with standard support interference than that of long support. In fact, the pressure distribution on the wind tunnel wall is affected by the support interference. Although the empty pressure gradient (the buoyancy effect) is removed when the wall pressure is used for Mokry's method, these results indicate that the nonlinear interference between ONERA-M5 and support is not removed perfectly. Figure 16 show the Cp contour in the case of the standard sting, M=0.7. The difference is as small as that of the long sting (Fig. 11).

The difference between the attack angles of 0° and 2° (Figs.11 and 12) is caused by the separated flow around the wing tip. This difference is rather large, compared with the effects of shock wave and support interference. All coefficients of C_D, C_L, and C_m are not corrected accurately. The Cp contour for attack angle of 2°, M=0.7 are shown in Fig. 17. The difference is large at the separation region around the wing tip.

Finally, the summary of results is shown in Table 5. The accuracy is degenerated by shock wave, separation, and support interference. It is found that the effect of support interference is not so large, whereas the effect of separation is serious.

Conclusions

We have simulated the whole wind tunnel flow of JAXA 2m×2m Transonic Wind Tunnel (JTWT) to investigate wall interference and its correction method. The Mokry's method is applied to wind tunnel CFD, and the corrected aerodynamic coefficients are compared with CFD without wall.

The pressure distribution on the wind tunnel agrees well with the measurements. Therefore, the corrected aerodynamic coefficients of CFD are almost same as those of experiment. In addition, the computed C_L and C_D agree well with the measured values, though Cm is a little higher. The differences between standard and long stings are almost same as the experiment. It is found that the aerodynamic characteristics of ONERA-M5 and its wall/support interferences are simulated accurately.

In the case of M=0.7, long sting, and $\alpha=0^\circ$, the results corrected by the Mokry's method show good agreement with those without wall. However, the accuracy is degenerated by shock wave, separation, and support interference, since the Mokry's method is based on the linear potential theory. The effect of support interference is not so large, whereas the effect of separation is serious. The limitation of the method becomes clear in this study.

Acknowledgement

References

[1] Ueno, M., Sudani, N., "Flow Angularity Measurement of 2m×2m Transonic Wind Tunnel," AIAA paper 2008-849, 2008.

[2] Kohzai, M., Ueno, M., Shiohara, T., Sudani, N., "Calibration of the test section Mach number in the JAXA 2m×2m Transonic Wind Tunnel," AIAA 2008-848, 2008.

[3] Kohzai, M., Shiohara, T., Ueno, M., Komatsu, Y., Karasawa, T., Koike, A., Sudani, N., Gahana, Y., Ikeda, M., Watanabe, A., Haraguchi, T., Nakagawa, M., Udagawa, D., "Thermal Zero Shift Correction of Strain-Gage Balance Output in the JAXA 2m×2m Transonic Wind Tunnel," JAXA Research and Development Report, JAXA-RR-07-034E, 2008.

[4] Kohzai, M., Sudani, N., Yamamoto, K., Ueno, M., Hashimoto, A., "Experimental and Numerical Studies of Support Interference in the JAXA 2m×2m Transonic Wind Tunnel," AIAA paper 2010-4200, 2010.

[5] Mokry, M., "Subsonic Wall Interference Corrections for Finite-Length Test Sections Using Boundary Pressure Measurements," Proceedings of the Fluid Dynamics Panel Specialists' Meeting, 1982, pp.10.1-10.5, AGARD CP-335.

[6] Bosnyakova, S., Kursakova, I., Lysenkova, A., Matyasha, S., Mikhailova, S., Vlasenkoa, V., Quest, J., "Computational Tools for Supporting The Testing of Civil Aircraft Configurations in Wind Tunnels," Progress in Aerospace Sciences, 44, 2008, pp. 67–120.

[7] Heidebrecht, A., "Simulation and model support correction for slotted wall transonic wind tunnels," 47th International Symposium of Applied Aerodynamics, 2012.

[8] Hantrais-Gervois, J.-L., Mouton, S. and Piat, J.-F., "RANS simulations to compute wind tunnel wall corrections," 47th International Symposium of Applied Aerodynamics, 2012.

[9] Nakahashi, K., Ito, Y., Togashi, F., "Some challenges of realistic flow simulations by unstructured grid CFD," *International Journal for Numerical Methods in Fluids*, Vol.43, pp.769-783, 2003.

[10] Murayama, M. and Yamamoto, K., "Comparison Study of Drag Prediction by Structured and Unstructured Mesh Method," *Journal of Aircraft*, Vol.45, No.3, 2008, pp. 799-822.

[11] Ito, Y., Shih, A., Soni, B. K., "Unstructured Mesh Generation Using MEGG3D - Mixed-Element Grid Generator in Three Dimensions," Proceedings of the International Conference on Numerical Geometry, Grid Generation and Scientific Computing (NUMGRID2008), Moscow, Russia, June 2008, pp. 5-11.

[12] Nambu, T., Hashimoto, A., Aoyama, T., Sato, T., "Analysis and Modeling of Flow through wind tunnel porous wall", AIAA paper 2010-4858, 2010.

[13] Nambu, T., Hashimoto, A., Murakami, K., Sato, T., "Numerical Analysis of Wind Tunnel Wall Interference on Two-dimensional Airfoil by New Porous Wall Model," AIAA paper 2012-3229, 2012.

[14] Hashimoto, A., Aoyama, T., Kohzai, M., Yamamoto, K., "Transonic Wind Tunnel Simulation with Porous Wall and Support Devices," AIAA paper 2010-4201, 2010.

[15] Hashimoto, A., Kohzai, M., Takashi, A., and Murayama, M., "Wall Interference Analysis of Transonic Wind Tunnel with Porous Wall Model," AIAA paper 2011-3017, 2011.

[16] Second Aerodynamics Division, National Aerospace Laboratory (NAL), "Results of the Test on ONERA Calibration Model M5 in NAL 2m×2m Transonic Wind Tunnel," NAL-TR-774T, 1983, Japan.
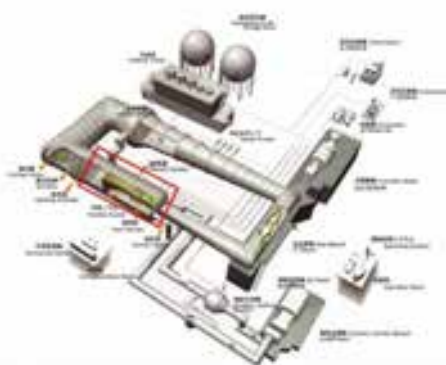
Figure 1   JAXA 2m×2m Transonic Wind Tunnel

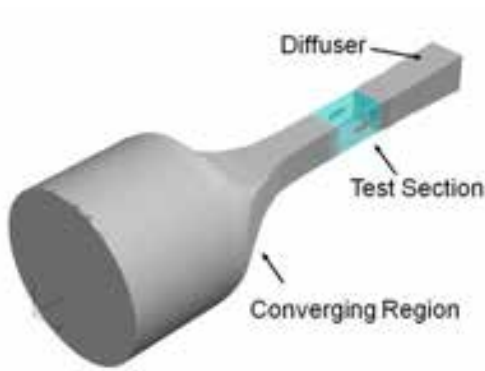**Figure 2   ONERA-M5 model installed in JTWT**

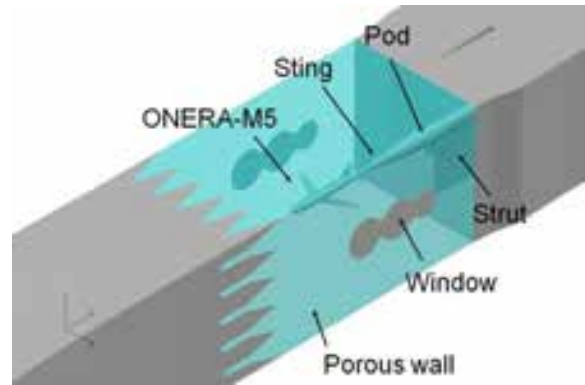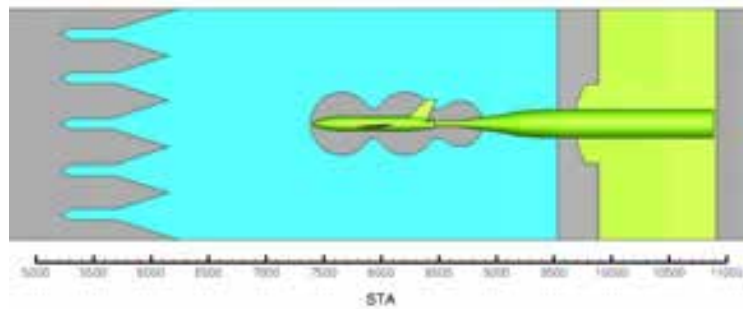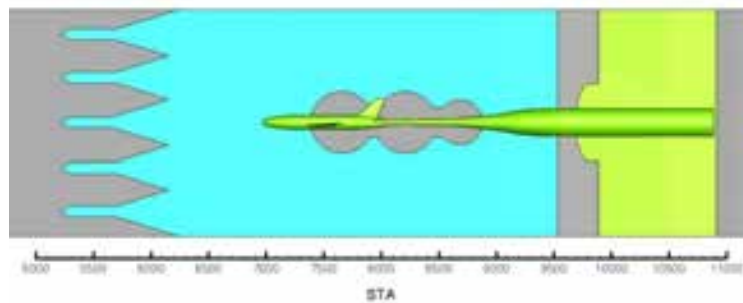Figure 3   Whole computational domain

Figure 4   Closed-up view of test section

(a)   Standard sting

(b) Long sting

Figure 5   two types of sting

Table 1   Computational cases

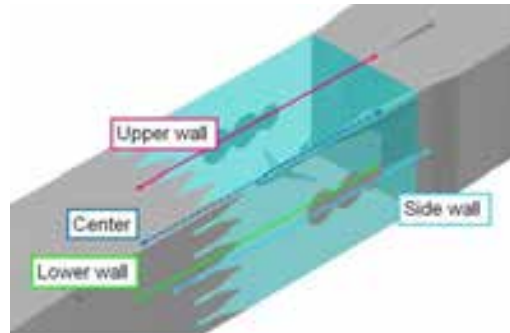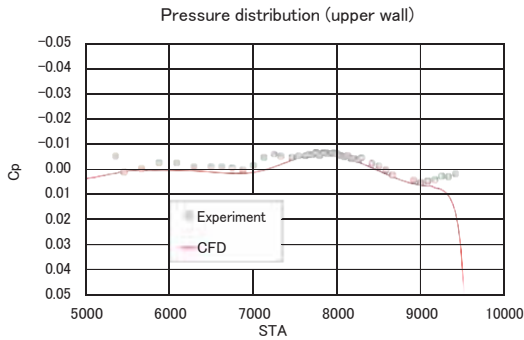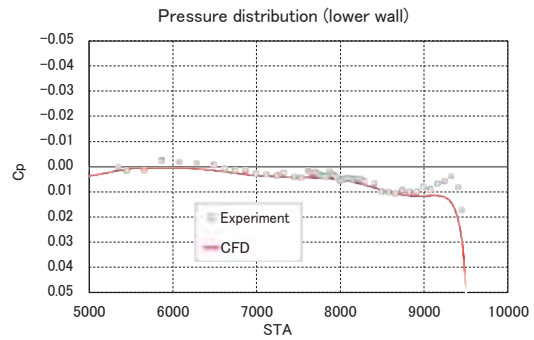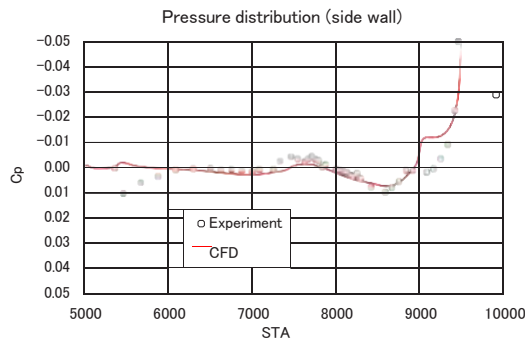| Name	M5	Standard sting	Long sting	Pod	Strut	Wall
M5 Only	✓					
Standard sting + Wall	✓	✓		✓	✓	✓
Standard sting	✓	✓		✓	✓	
Long sting + Wall	✓		✓	✓	✓	✓
Long sting	✓		✓	✓	✓	
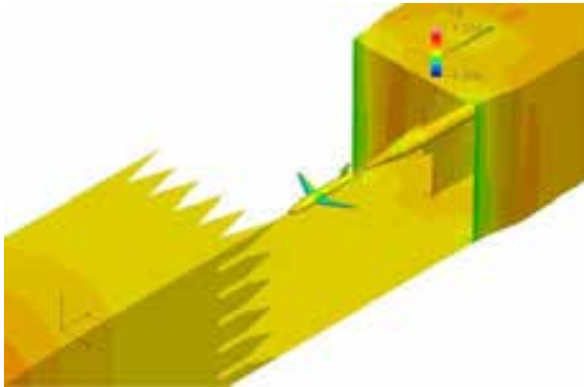
Figure 6   Cp contour

Figure 7   Line locations

(a) Pressure distribution on the upper wall

(b) Pressure distribution on the lower wall

(c) Pressure distribution on the lower wall

Figure 8   Comparison of pressure on the porous wall (M=0.70, Long sting case)

Table 2   Aerodynamic data for M=0.7, α=0°, standard and long stings

	CL	CD	Cm	dCL	dCD	dCm	
Long Sting + Wall	0.307	0.0302	0.083	0.000	0.0010	0.003	″Long Sting + Wall″−″Standard Sting + Wall″
Standard Sting + Wall	0.307	0.0292	0.080				
Long Sting	0.311	0.0301	0.083	0.001	0.0012	0.003	″Long Sting″−″Standard Sting″
Standard Sting	0.309	0.0290	0.080				
M5 Only	0.309	0.0327	0.082				
Long Sting + Wall (EXP)	0.306	0.0304	0.078	−0.002	0.0010	0.004	″Long Sting + Wall(EXP)″−″Standard Sting + Wall(EXP)″
Standard Sting + Wall (EXP)	0.309	0.0293	0.075				

Table 3   Aerodynamic data for M=0.84, α=0°, standard and long stings

	CL	CD	Cm	dCL	dCD	dCm	
Long Sting + Wall	0.368	0.0437	0.092	−0.001	0.0018	0.005	″Long Sting + Wall″−″Standard Sting + Wall″
Standard Sting + Wall	0.369	0.0419	0.088				
Long Sting	0.376	0.0437	0.091	0.001	0.0018	0.003	″Long Sting″−″Standard Sting″
Standard Sting	0.375	0.0419	0.088				
M5 Only	0.377	0.0460	0.091				
Long Sting + Wall (EXP)	0.359	0.0424	0.083	−0.004	0.0014	0.004	″Long Sting + Wall(EXP)″−″Standard Sting + Wall(EXP)″
Standard Sting + Wall (EXP)	0.363	0.0410	0.079				

(a) C_L-α (b) C_D-α (c) C_m-α
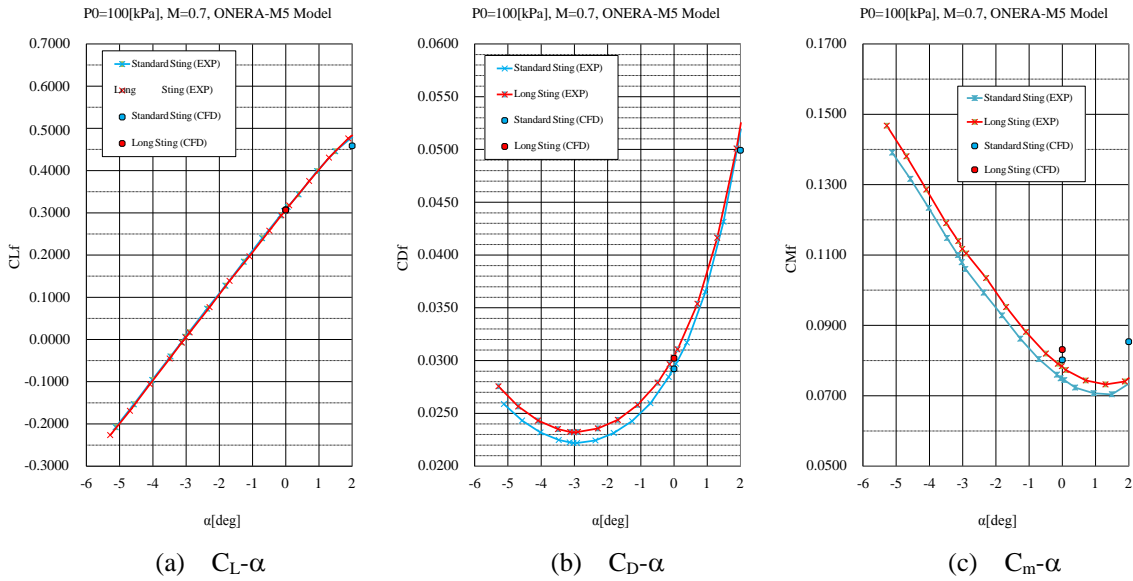
Figure 9   Comparison of forces with experiment data (M=0.7, standard and long sting)

(a) C_L-α (b) C_D-α (c) C_m-α
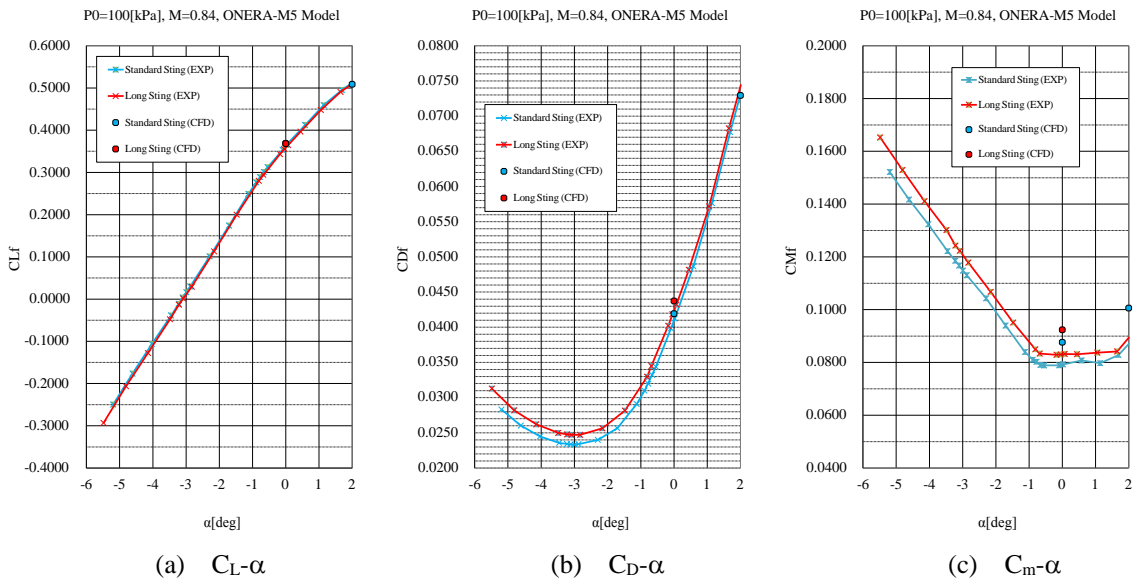
Figure 10   Comparison of forces with experiment data (M=0.84, standard and long stings)

Table 4 Conditions corrected by Mokry's method

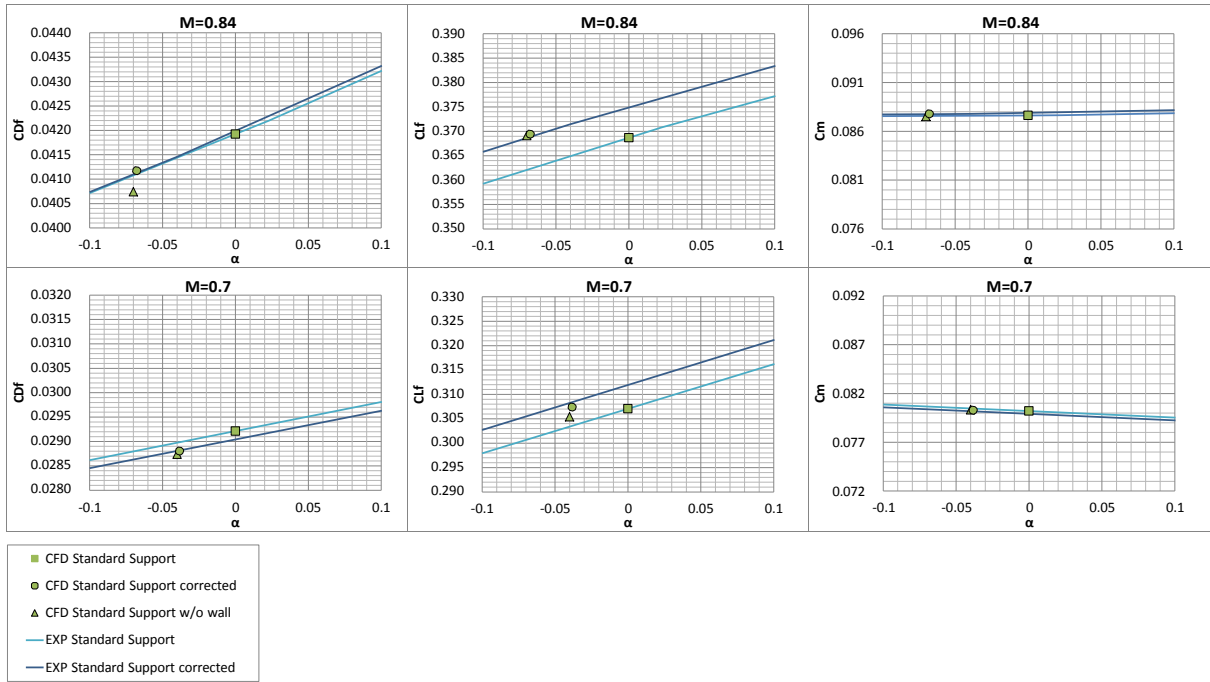|	Original		Corrected	
	M	Alpha (deg)	M	Alpha (deg)
Standard sting	0.70	0	0.699	-0.04
	0.70	2	0.699	1.95
	0.84	0	0.839	-0.07
	0.84	2	0.838	1.91
Long sting	0.70	0	0.700	-0.04
	0.84	0	0.839	-0.07

Figure 11   Corrected force and moment (Standard sting, α=0°)
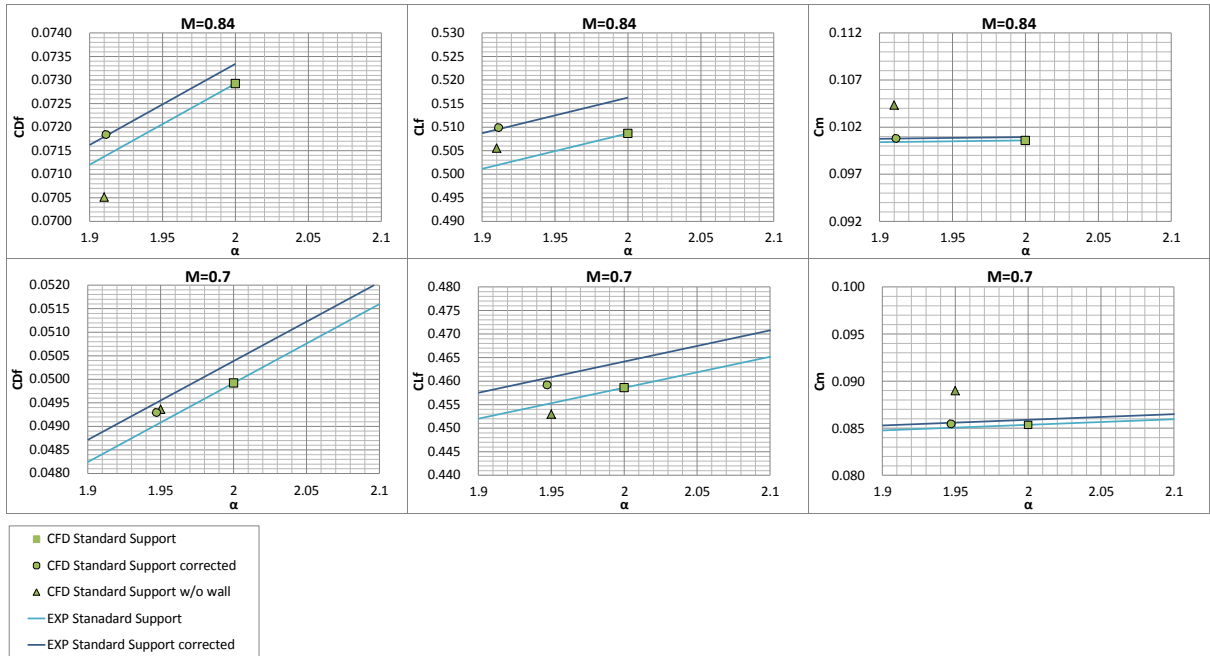
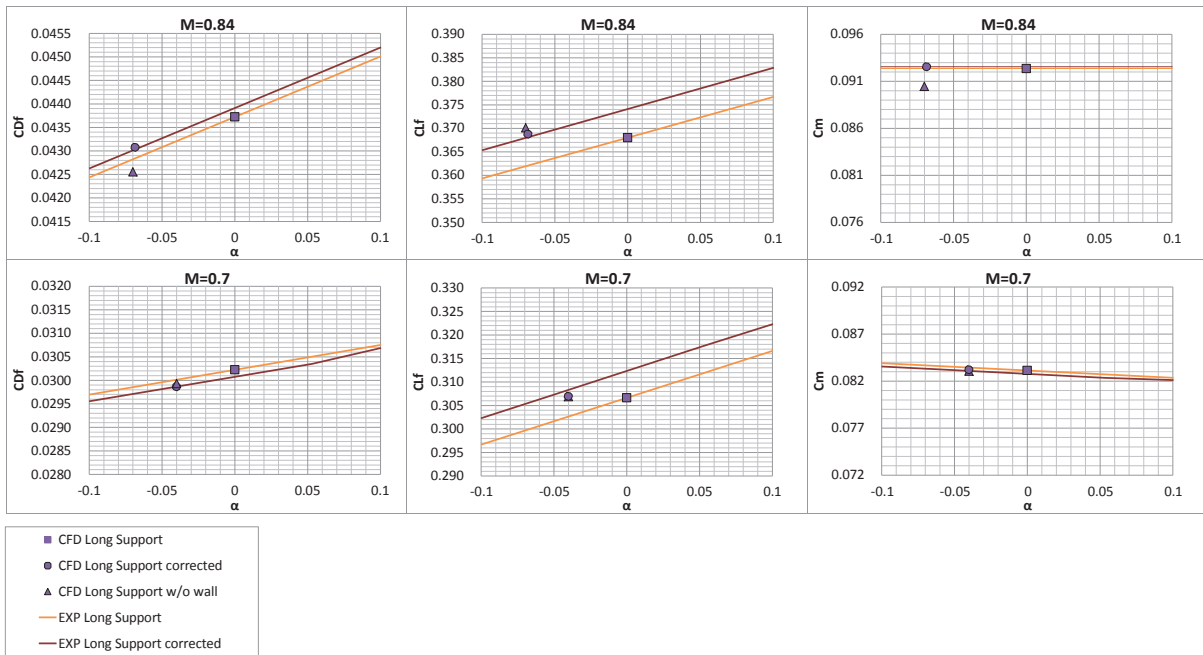**Figure 12   Corrected force and moment (Standard sting, α=2°)**

Figure 13   Corrected force and moment (Long sting, α=0°)

(a) With wall (original condition)   (b) Without wall (corrected condition)   (c) difference
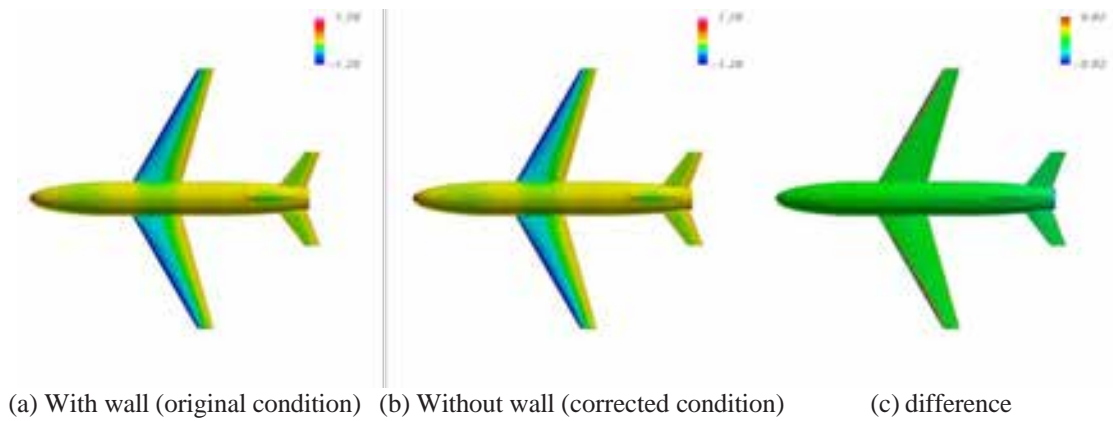
Figure 14   Surface Cp contour (M=0.7, Long sting, α=0°)

(a) With wall (original condition)   (b) Without wall (corrected condition)   (c) difference
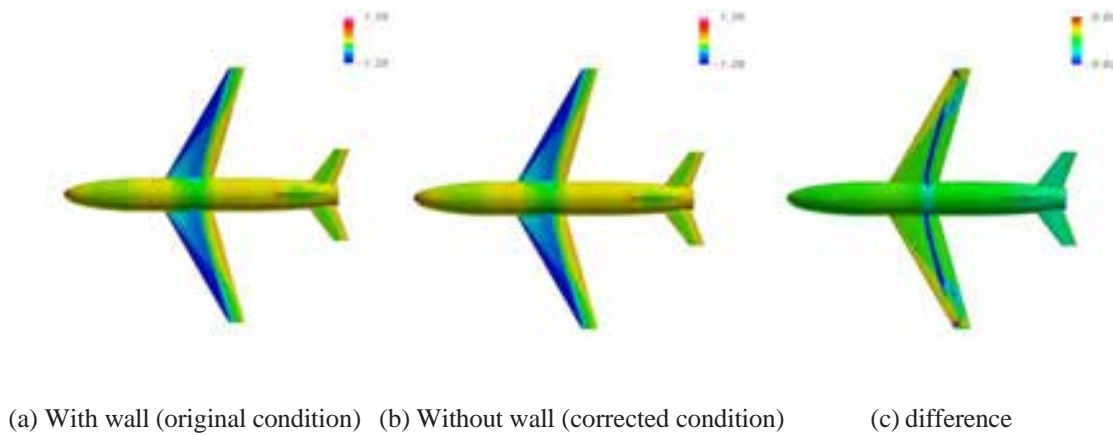
Figure 15   Surface Cp contour (M=0.84, Long sting, α=0°)

(a) With wall (original condition)　(b) Without wall (corrected condition)　　　(c) difference
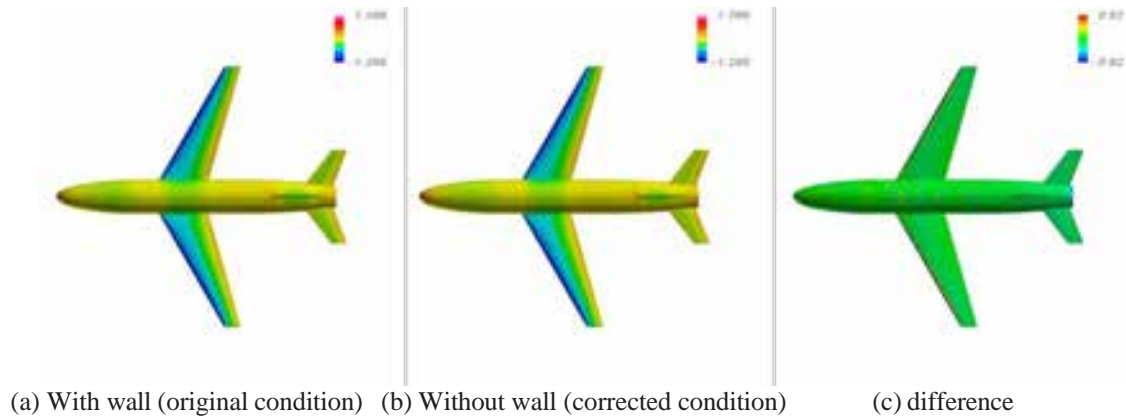
Figure 16　Surface Cp contour (M=0.7, Standard sting, α=0°)

(a) With wall (original condition)　(b) Without wall (corrected condition)　　　(c) difference

Figure 17　Surface Cp contour (M=0.7, Standard sting, α=2°)

Table 5　Validation summary of Mokry's wall correction method

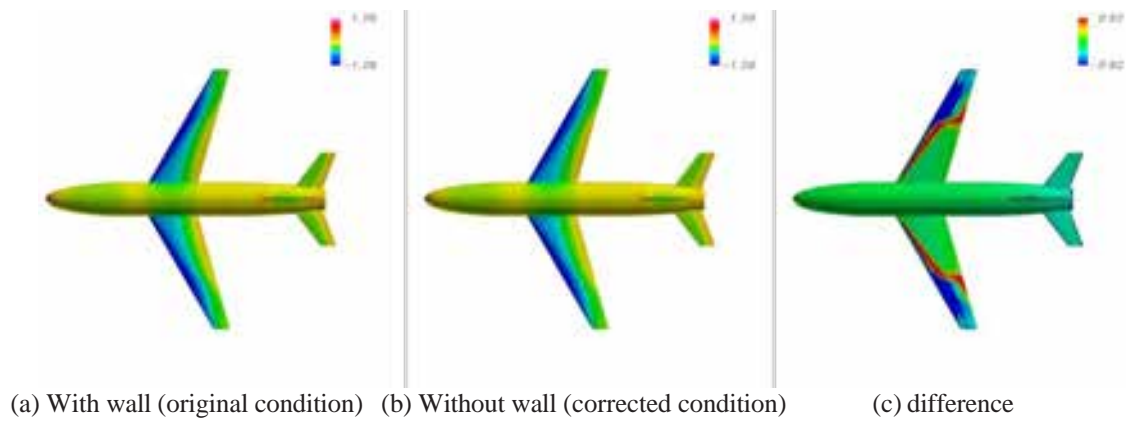| Sting	Mach	Attack angle	Shock wave	Separation	Support Interference	Mokry's method
Standard	0.7	0			✓	Good
Standard	0.84	0	✓	✓ (Small)	✓	Good
Standard	0.7	2		✓ (Large)	✓	Bad
Standard	0.84	2	✓	✓ (Large)	✓	Bad
Long	0.7	0				Excellent
Long	0.84	0	✓	✓ (Small)		Poor

Prediction of the Aerodynamic Effect of Model Deformation during Transonic Wind Tunnel Tests

Sylvain Mouton
Marianne Lyonnet
Yves Le Sant

ONERA – the French Aerospace Lab
F-59045 Lille
sylvain.mouton@onera.fr

Abstract

During wind tunnel tests, any aircraft model deforms as a result of aerodynamic loads. This behaviour is generally regarded as a spurious effect of the testing technique that needs to be accounted for and corrected. This paper presents available optical technique to measure wing deformation in ONERA wind tunnels, and introduces a simulation method to predict the effect of the deformation on the model aerodynamic characteristics.

Key words: aerodynamics, fluid dynamics, wind tunnel test, wing deformation, MDM

Introduction

Because the internal structure of a wind tunnel model radically differs from that of the real aircraft, the observed deformation in wind tunnel has no similarity property with the deformation of the aircraft in flight. Consequently, the deformation of the wind tunnel model is generally seen as a spurious effect of the testing technique that needs to be accounted for and corrected. As a matter of fact, the observed aerodynamic effect was long expected to be caused by Reynolds effect, while the real cause, wing deformation, had been ignored for a long time. The likely reason is that the deformation level was unknown and barely measurable because of the lack of an appropriate method. Indeed, model deformation was considered a major source of error only recently [1].

This paper focuses on the deformation of the wing of an airplane model, although the method itself could apply to other type of models. The wing of the model is by far the piece that deforms the most because it generates most of the aerodynamic loads and also because of its slender shape. Unfortunately, the wing aerodynamic characteristics are also greatly sensitive to its shape, especially in transonic flow. This problem is even more acute in pressurized wind tunnels.

The complete modelling of the phenomenon would imply to solve a coupled aero-elastic problem, assuming the structural characteristics of the model are well identified. The solution of this problem would yield both the deformed wing shape and the flow-field. This is not the approach presented in this paper. Indeed, the state of deformation of the wing is now systematically measured during most wind tunnel tests, using optical techniques that will be briefly presented. Therefore, we are not interested in determining the deformed wing shape, which is readily available from measurements, but we investigate the effect of this deformation on the aerodynamic characteristics of the wing.

Model Deformation Measurement technique

There are several methods but the only one that provides real time results is based on marker detection and stereovision which is well known by the Computer Vision (CV) community. Markers are stuck on the model

surface which is imaged with two cameras. The Figure 1 shows two typical images as well as a marker. The angle between the two cameras is close to 45°. These cameras (usually more than 2000x2000 pixels) must have been calibrated previously. The challenge for applications in large facilities is the size of the calibration body. It has to be stiff but must not be too heavy and then cannot be expected without defect. This is why the calibration method includes a tool (known as *bundle adjustment* by CV), which enables to compensate for shape defects.

The basic tool for stereovision is marker detection. The final uncertainty depends on it; this is why a fast and accurate marker detector has been developed. Its uncertainty is of 0.06 pixel which provides a measurement uncertainty lower than 0.1 mm for a full scale of 1 m. The twist uncertainty is lower than 0.05°, even at the wing tip.

Figure 1: The two images obtained by the two cameras and a marker.

The 3D location of the marker is obtained by using the stereovision principle which is simple: a marker in an image defines a viewing line and the real point is located at the intersection of the two lines deduced from the two cameras. However, they never intersect exactly and there is a small error which is called the epipolar error. The average epipolar error is a good indicator for camera calibration quality. It can be lower than 0.1 pixel and it is considered that it is acceptable for values lower than 0.5 pixel. Greater values mean that the cameras start to be decalibrated, because of their displacement relative to each other.

The ONERA MDM system is routinely available in the largest wind tunnels such as S1MA and F1. It is monitored by the wind tunnel control system as any other usual measurement tool [4]. It can work at a frequency of 1 Hz mostly limited by the frame rate.

Up to this point, this system could be compared to industrial vision systems and is more an engineering application than a scientific one. However recent developments are scientific matters. The first development is related to the effect of thick windows (several centimetres) or medium change (air/pressurized air) that makes the standard pinhole model not fully reliable. A second one is to track small parts of the wing and to move the cameras to track them when the model moves. The cameras would become decalibrated (only the external parameters) and may be recalibrated minimizing the epipolar error [4]. The effect of air density gradients in the flow around the model (especially through shock waves) was experimentally assessed and found negligible.

The MDM method can be used for other applications than wind tunnel testing. It can be used for conventional shape measurement, for flight testing or for scientific applications that require knowing the object shape with a non contact method. This would be the case for PIV or LDV measurements close to the model surface.

First order Formulation

During wind tunnel tests, data is acquired about the local aerodynamic field (e.g. pressure, temperature, velocity measurements at given points on the model surface or within the flow) and about integral quantities (e.g. forces, mass flow). The local measurements are related to the aerodynamic flow field, represented by a vector of conservative variables w. The integral measurements are the result of an integral of w field over some subspace of flow domain (e.g. the skin of the model for forces).

Both the flow field w and the integral J formally depend firstly upon the aerodynamic upstream flow conditions (angle of attack (AoA), Mach number, Reynolds number) and secondly upon the state of deformation of the model wing. We formally regroup the parameters defining upstream conditions under the vector variable α, and similarly the deformation state of the wing is supposed to be represented by a vector of n scalar parameters θ:

$$J = J(\alpha, \theta)$$
$$w = w(x, \alpha, \theta)$$

The effect of the model deformation θ at constant α can be expanded as a Taylor series in θ, yielding:

$$\Delta J(\alpha, \theta) = J(\alpha, \theta) - J(\alpha, 0) = \frac{\partial J}{\partial \theta}^T \theta + O\left(\|\theta\|^2\right)$$

The first order effect of the deformation appears as the scalar product of the deformation vector θ with the sensitivity vector $\dfrac{\partial J}{\partial \theta}$, i.e. the gradient of J with respect to θ.

To illustrate the application of this, let us consider the three following deformation

- θ_0 is a reference deformed shape called the design shape, which generally corresponds to the shape observed under loads corresponding to cruise conditions;
- θ_s is the shape observed in wind tunnel at given flow conditions
- θ_v is the shape that would be obtained in flight for the same set of upstream flow conditions

It turns out that:

$$J(\alpha,\theta_0) = J(\alpha,\theta_s) - \left(\frac{\partial J}{\partial \theta}(\alpha,\theta_0) \right)^T (\theta_s - \theta_0) + O\left(\|\theta_s - \theta_0\|^2 \right)$$

When the gradient of the performance J is evaluated for the shape θ_0, the performance of the shape θ_0 can be obtained from the performance $J(\alpha,\theta_s)$ measured in wind tunnel, with first order accuracy with respect to the distance between design shape and wind tunnel shape.

Assuming that the flight shape is known, the performance J can be extrapolated to flight thanks to:

$$J(\alpha,\theta_v) = J(\alpha,\theta_s) + \left(\frac{\partial J}{\partial \theta}(\alpha,\theta_s) \right)^T (\theta_v - \theta_s) + O\left(\|\theta_v - \theta_s\|^2 \right)$$

But the sensitivity at θ_s can itself be expanded as:

$$\frac{\partial J}{\partial \theta}(\alpha,\theta_s) = \frac{\partial J}{\partial \theta}(\alpha,\theta_0) + \left(\frac{\partial^2 J}{\partial \theta^2}(\alpha,\theta_0) \right)(\theta_s - \theta_0) + O\left(\|\theta_s - \theta_0\|^2 \right)$$

which finally yields:

$$J(\alpha,\theta_v) = J(\alpha,\theta_s) + \left(\frac{\partial J}{\partial \theta}(\alpha,\theta_0) \right)^T (\theta_v - \theta_s) + O\left(\|\theta_v - \theta_0\|^2 \right) + O\left(\|\theta_s - \theta_0\|^2 \right) + O\left(\|\theta_v - \theta_s\|^2 \right)$$

This means that it is possible to extrapolate the wind tunnel performance to the flight performance using the same sensitivity as before, within first order accuracy. The truncation error is made smaller when the chosen reference shape is close from the flight shape and from the wind tunnel shape. Similar formulae can be obtained for the local flow field w.

Within the limits of first order accuracy, determining the effect of deformation on the aerodynamic flow field and performance reduces to the determination of their sensitivity with respect to the vector of deformation parameters. Interestingly, once the sensitivity is determined, the calculation of any deformation effect is immediate, meaning they could be accounted for on line during wind tunnel tests.

In this work, RANS equations are solved for the flow around the model to determine performances and the adjoint and linearised methods are used to compute this sensitivity.

Parameterisation

The above development imposes to represent the displacement of the wing surface under deformation as a finite vector of n scalar parameters.

The slender shape of the wing advocates for the use of beam parameters: vertical displacement (or bending) and twist at different spanwise sections. Hence, we use in this work the local bending δz, defined as the displacement in the vertical direction of the point lying at 50% of local wing chord; and the local aerodynamic twist $\delta \alpha$ defined as the rotation of the wing section with respect to the span axis. With this definition, it must be mentioned that most of the aerodynamic torsion comes from the bending, since the rotation associated to bending has a projection onto the span axis because of the sweep angle of the wing.

A wing section which displacement and torsion are components of θ is called a controlled section. Of course, the controlled sections will correspond to the sections were deformation measurement are available from the wind tunnel test. With this parameterization, the twist of one given section has a local effect, mostly limited to the area between current section and its two neighbouring ones.

In the present work, the deformation of both the surface and the volume mesh relied on the free form deformation technique, using direct manipulation [7], but other morphing methods, even analytical ones, would have been efficient as well, provided there are differentiated, as explained in next section.

Adjoint and linearised methods

The present work made intensive use of the adjoint and linearised methods to compute sensitivities of solutions of partial differential equation with respect to input parameters. The principles of the methods are not recalled here. A good introduction can be found in reference [6], which gives an overview of its history and present developments. These methods present significant advantages over classical finite difference approach.

It is recalled that the sensitivity of the flow field with respect to each shape parameter is obtained by inverting the linearised equation. For each shape parameter, this implies solving a system of linear equations of very large size, but mostly empty. Once this is done, the sensitivity of any function J is immediately obtained by combination of flow field sensitivities, which permits to evaluate a large number of functions.

In case one is not interested in the sensitivity of the flow field itself, but only in the sensitivity of a small number of functions J, the use of adjoint equation method is attractive for cost reason. The adjoint method leads to the inversion of one large size linear system per functions of interest J. But the evaluation cost of the sensitivity does no longer depend on the dimension of θ. In the present case, there are few objective functions (typically lift, drag and pitching moment), but a larger number of design parameters (two per controlled wing section).

Both linearised and adjoint equations require complete linearization of the calculation chain to evaluate J, from the parameterization to the post-processing, in order to compute the partial derivatives at each stage. In the present work, the parameterization and mesh deformation rely on free form deformation, which is naturally differentiable. Concerning post-processing, the near-field and far-field analyses [3] were also differentiated, using for the far-field an approximation of frozen area of drag production.

Validation case

Configuration

The validation case chosen for this study is a civil transport aircraft configuration called HiReTT [2]. It is composed of a generic fuselage and a wing representative of the design of modern transonic aircraft. The wind tunnel model has been designed so that the wing adopts its design shape (corresponding to aircraft cruise shape) under a lift coefficient of 0.5 and with a dynamic pressure of 88 kPa.

Unless one sets up a wind tunnel campaign using several models with different wing deformations or a model deformable on demand, which was never attempted to the author's knowledge, the only way to study the effect of model deformation is to vary the dynamic pressure q of the tunnel. If one demands in the same time that the Reynolds number be constant, not only the pressure but also the temperature of the tunnel should be controlled.

The loads applied to the model are proportional to the dynamic pressure q, while the response of the model to the applied loads, i.e. the resulting deformation, is inversely proportional to the Young's modulus E. The shape solution of this aero-elastic problem then depends on the non dimensional ratio q/E. Due to the order of magnitude of q and E, this ratio is of the order 10^{-6}. In the following, the 10^{-6} is sometimes omitted, and figures are presented in millionth.

Experimental database

This configuration was tested several times in the European Transonic Wind Tunnel ETW [8], both in 1/50 scale full model and in 1/30 scale half model. Test results presented in this paper where obtained in the framework of European projects HiReTT (full model), M-DAW (half-model) and FLIRET (half model) between 2001 and 2007.

ETW is a cryogenic pressurized wind tunnel, enabling the investigation of pure deformation effects by simultaneously varying pressure and temperature. Among the available database, tests at Mach 0.85 and 32.5 millions Reynolds number are presented here. They were carried out for 4 levels of stagnation pressure: 1.6 bar, 2.6 bars, 3.4 bars and 4.4 bars, corresponding respectively to the following q/E ratios: 0.265, 0.437, 0.565 and 0.768 millionth.

To avoid introducing bias related to the differences existing between half and full model campaigns, performance comparison is always carried out between data from the same test campaign. One well identified bias is that the "plinth" used to raise the half model out of the boundary layer of the tunnel was included in force measurements, and drag of the half model tests is consequently higher.

Wing deformation measurements

The deformation of the wing was either directly measured or evaluated during the above mentioned campaigns. During HiReTT campaign, the deformation was evaluated thanks to a finite element model calibrated against the real model and on which the loads measured during the test were applied. Various crosschecks not detailed here and carried out by partners of the project lead to a good confidence in the deduced deformation. During subsequent campaigns at ETW, an optical technique similar to the MDM previously presented was available and used. Comparison between the different results reveals a very good agreement in torsion, but a difference in bending that might be attributed to the difference in stiffness of the wing-fuselage junction between full model and half model configurations.

Flow simulations

Direct flow simulations

Flow simulations were carried out with *elsA* software that solves RANS equations with a finite volume discretization on multiblock structured meshes [5]. The mesh used comprises 3,796,864 cells and 56 blocks (Figure 2).

Figure 2: Surface mesh of the model

The simulations presented in this paper used the one-equation Spalart-Allmaras turbulence model for which exhaustive validation is available on similar configurations. Following numerical parameters were used:
- Roe scheme with Harten entropic correction, extended to second order with MUSCL method, using a Van Albada limiter
- Time marching using a backward Euler method and using implicit formulation solved by a scalar LU-SSOR method
- Convergence acceleration using a 3-level multigrid cycle.

Convergence is obtained after about 800 iterations, but the computation is continued until 1,500 iterations to bring residuals close to machine zero. This indeed contributes to ease the convergence and accuracy of subsequent adjoint computations.

Once the solution flow-field is obtained, it is post-processed using FFD41 software, which computes the seven force coefficients we are interested in: lift, pitching moment, pressure and friction drag, viscous, wave and induced drag, as well as their derivatives with respect to the flow field and the mesh. For a complete definition of drag breakdown, please refer to reference [3].

Adjoint and linearised computations

The wing deformation is parameterized thanks to 7 controlled wing sections, i.e. 14 scalar parameters. The evaluation of the sensitivities of each function *J* then leads to 7 adjoint computations or 14 linearised computations.

The adjoint as well as the linearised equations constitute systems of linear equations of very large size, mostly empty and made up of multidiagonal blocks. The resolution method used relies on the same iterative method as the one used in the implicit formulation for time marching during the resolution of the RANS equations, i.e. a LU-SSOR method with four relaxation cycles. At the time of this work, the turbulence model was not differentiated and the adjoint and linearised computations made use of the frozen eddy viscosity hypothesis.

Validation of computed gradients

In order to validate the sensitivities of aerodynamic coefficients computed by adjoint method and linearised method, it is necessary to establish reference values by means of finite difference (FD) method.

Computing an undisputable reference value with FD method is not necessarily an easy task, because the gradient depends on the FD step chosen for each parameter. If the step is too large, second order terms are not negligible, and if it is too small, the difference between computations becomes so tiny that the numerical noise (insufficient convergence, round-off errors) predominates. Therefore, the choice of the FD step needs careful validation.

In this study, the determination of the FD step was carried out on the wing section n°4 ($y/b = 0.611$). The local twist and bending were varied and resulting variations of the aerodynamic coefficients obtained at Mach 0.85, at a lift coefficient of 0.5 and around the wing shape for q/E = 0.437 are observed. The gradient of the aerodynamic coefficients is computed using first order and second order FD for different steps of twist $\delta_{DF}\alpha$ and bending $\delta_{DF}z$ (in figures rendered non-dimensional using wing local chord c). Results are presented in Figure 3.
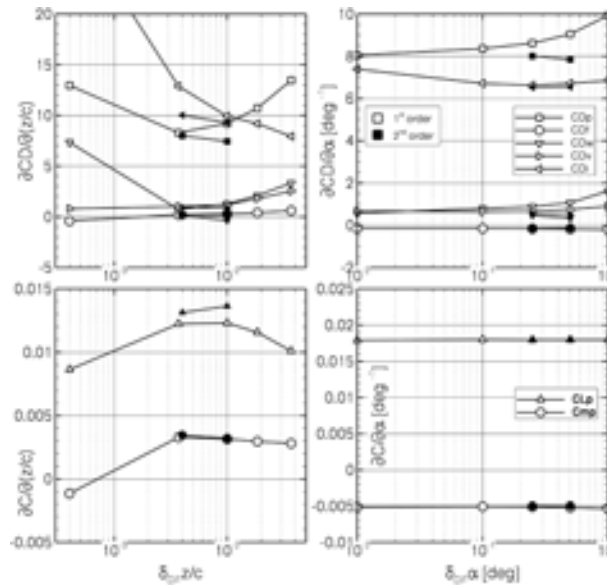

Figure 3: Gradient of different objective functions computed by finite difference on wing section n°4

From this figure, it appears that the sensitivity of some coefficients such as lift is weakly dependent on the FD step. On the contrary, FD estimates of the sensitivity of viscous and wave drag, which behaviour close to the design point is highly non-linear as will appear later on, are sensitive to the choice of FD step. This is especially true for sensitivity with respect to bending. As expected, second order FD is less subject to this problem.

From these results, for all subsequent FD computations carried out on all wing sections, a step of 1% of local chord for bending and of 0.01° for twist were selected, guided by best estimates originating from second order FD.

The gradients obtained by adjoint computations are compared to FD results in Figure 4. The agreement is generally very good, with the exception of pressure drag sensitivity with respect to bending variables. Although the contribution of bending is small compared to the one of twist, this error could not be explained and drag results were evaluated using far-field coefficients. Another minor defect of the gradient computed by adjoint method lies in the breakdown of the far field drag sensitivity between wave and induced drag. The later is slightly overestimated in disfavour of the former. The results of the linearised method (not shown) were also generally in good agreement with finite difference.
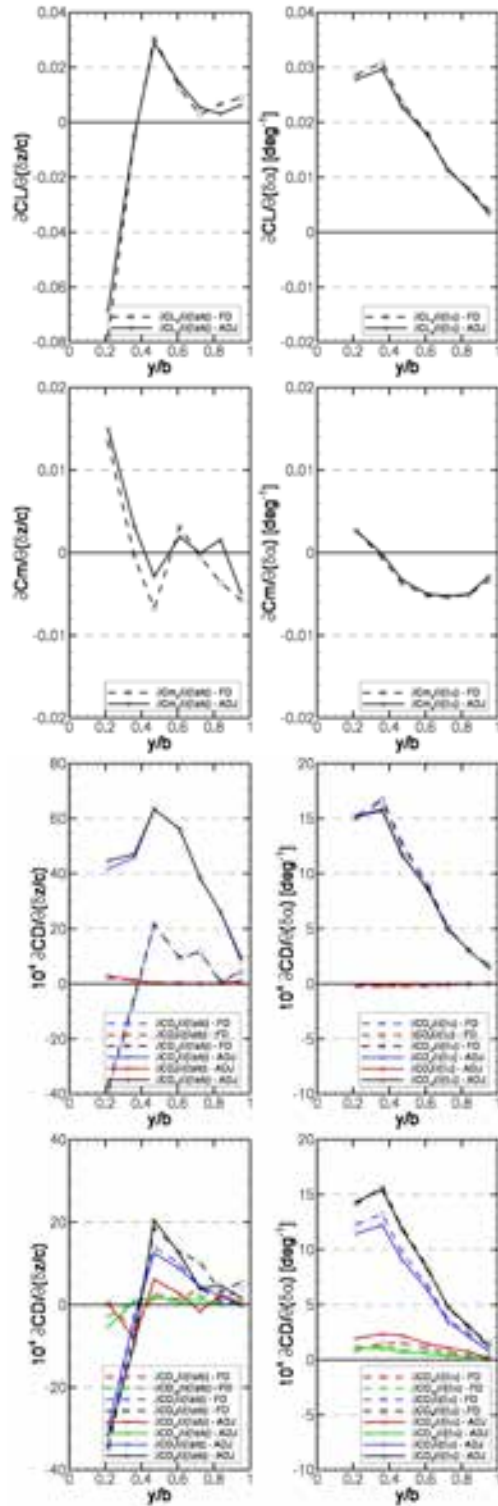
Figure 4: Gradient of lift, pitching moment, near-field and far-field drag coefficients (from top to bottom) with respect to bending (left) and twist (right) as a function of position on span of controlled wing section

It is worth mentioning that the contribution of bending to the deformation effect is small in comparison to the twist contribution. On this validation case, it is less than 10% of the total effect.

Effect of deformation on aerodynamic coefficients

Effect at cruise point

The effect of wing deformation at cruise point, corresponding to Mach 0.85 and CL 0.5 was first investigated. Experimental data for wing deformation is available for four dynamic pressures and shown in Figure 5. The deformations presented in this figure are taken with respect to the "wind off" shape. In this work, we used as a reference shape the one obtained at $q/E = 0.437$, and deformation are computed with respect to this reference.
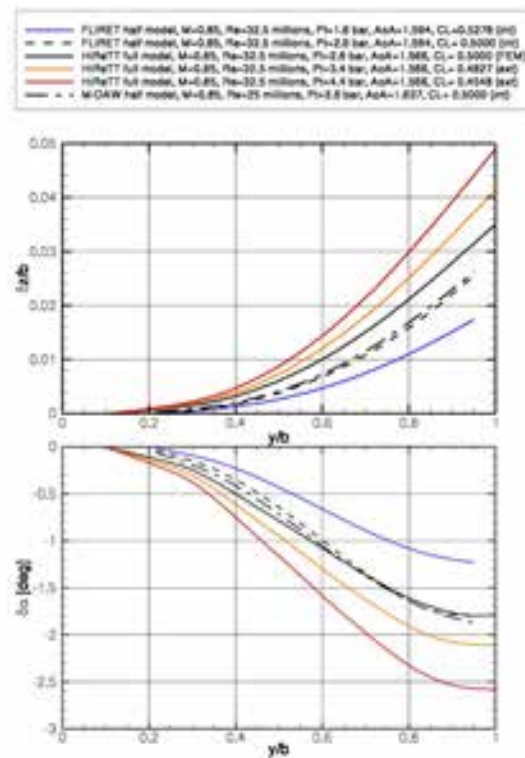
Figure 5: Wing deformation at Mach 0.85 and fixed AoA for several test campaigns

The corresponding flow-field exhibits very weak shock waves. This is a result of careful wing optimization in order to minimize wave drag in cruise.

The effect of deformation on force coefficients was computed by three different methods:

- with several direct computations, i.e. solving RANS equations on deformed meshes;
- with one direct and several adjoint computations on the mesh corresponding to reference shape;
- with one direct and several linearised computations on the mesh corresponding to reference shape.

The first method yields the exact effect of wing deformation, under the usual restrictions associated with numerical simulations, whereas the last two methods only yield the first order effect of the deformation (see formulae in first section).

Comparison between the different results should be made in two steps:

- comparison between adjoint or linearised computations on the one side and direct computations on deformed meshes on the other side to investigate the magnitude of truncated higher orders in the Taylor development of the deformation effect;
- comparison between direct computations and experiments to characterize the fidelity of the flow simulation.

Such comparisons are carried out in Figure 6. When dynamic pressure is increased keeping all other parameters constant, the load on the model increases. As a consequence of greater lift, the wing bending increases. Mostly because of the sweep of the wing, this bending translates into aerodynamic twist that causes outer wing section to pitch nose down. Therefore, the local lift coefficient of these sections diminishes. Consequently, the lift coefficient of the model also decreases. Because of this change in lift distribution along the span of the swept wing, the nose down pitching moment of the wing is alleviated, i.e. the pitching moment coefficient increases.

Finally, the decrease in lift coefficient is associated with a reduction in induced drag, and a variation of wave drag and viscous drag.
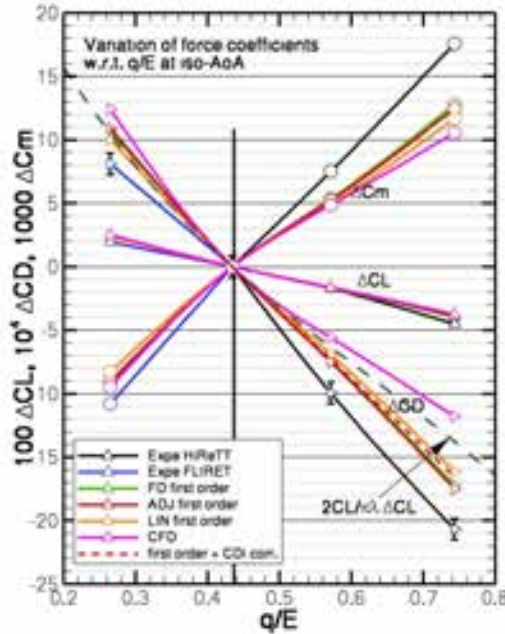

Figure 6: Force increment due to deformation around reference shape at Mach 0.85 and CL = 0.5

First order increments of force coefficient with respect to q/E are tangent to the complete deviation as expected from the Taylor development. The difference between those two curves represents the higher orders of the development, which magnitude grows when getting farther from the reference shape. Concerning lift and pitching moment coefficient, the higher order terms are negligible over the whole range of deformation under study (which is quite large, covering a twist range of 1.35° degree at wing tip). On the contrary, higher order terms for drag coefficients represent 40% of the total deviation (6 drag counts) for the larger deformation available. The origin of this behaviour is investigated thanks to the plot of Figure 7.
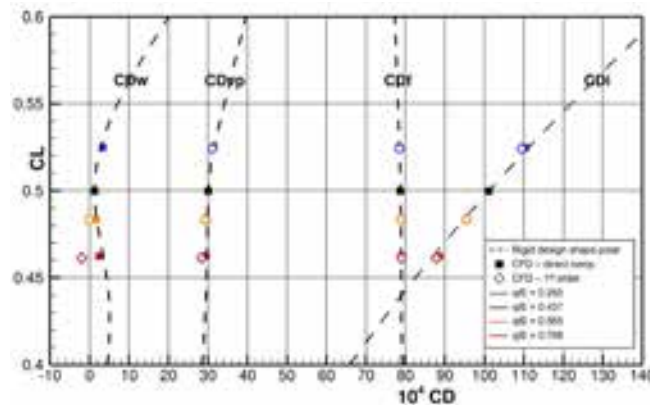

Figure 7: Drag breakdown for different wing shapes at Mach 0.85

This plot presents a drag breakdown of the different computations carried out at Mach 0.85 and a fixed AoA on the shapes corresponding to the four investigated dynamic pressures. It can be seen that the major part of the discrepancy between direct and first order calculations originates from the wave drag. Wave drag behaviour is highly non-linear (with respect to deformation and also to AoA) as a result of wing optimization for cruise. It even presents a local minimum close to the point under study. As a consequence, knowledge of the gradient of

wave drag close to this point is of poor interest since higher order terms quickly dominates the results. Consequently, 1st order predictions around the reference shape fall increasingly far from the direct computations when the deformation grows. The same is true to a lesser extent for viscous pressure drag. Finally, induced drag also exhibits slightly non-linear behaviour with respect to deformation, as a response to the lift variations. For the latter, although the first order term already gives a very good approximation of the effect of deformation on induced drag, a second order term can be modelled from lifting line results. If one models the induced drag by the classical Prandtl formula:

$$CD_i = \frac{CL^2}{\pi\lambda}$$

Then, variation of induced drag under a deformation writes as:

$$\Delta CD = \frac{2}{\pi\lambda} CL \frac{\partial CL}{\partial \theta} \delta\theta + \frac{1}{\pi\lambda} \left(\frac{\partial CL}{\partial \theta} \delta\theta \right)^2$$

$$= \frac{2}{\pi\lambda} CL \Delta CL + \frac{1}{\pi\lambda} \Delta CL^2$$

The second order term (in $\delta\theta^2$ or ΔCL^2) identified thanks to this development can be added to the first order term computed by adjoint / linearised computation. This minor correction brings the results a little closer to direct computations as shown in Figure 6 (curve with label 'CDi corr'). In the same figure, the first order term deduced from this model is plotted for comparison (dashed grey line).

In a second step, the fidelity of the direct calculations with respect to experimental data can be examined in Figure 6. At first sight, this comparison is rather disappointing since curves fall far from each other. However, one can notice that the two wind tunnel campaigns (HiReTT full model and FLIRET half model) yield a very different slope for drag behaviour, with calculations falling somewhere in between. Careful investigations reveal that the shock pattern is different between the two campaigns, with probable consequences on the wave drag behaviour close to the local minimum identified in Figure 7.

Beyond the examination of the force coefficients, the linearised computations also give insight into the effect of the deformation onto the flow field itself, and especially on wing pressure distribution for which exhaustive experimental data is available. The field of pressure sensitivity is displayed in Figure 8. One may note that any deformation in the inner part of the wing has a highly non-local effect that propagates outward to the tip of the wing, even though the deformation itself is local to one wing section. This explains why the effect of those sections on lift is more than proportional to their size.

By taking the scalar product of this sensitivity flow field with the vector of deformation parameters, one obtains the first order effect of the deformation onto pressure distribution. Like for forces, this effect can be compared to direct computations carried out for each deformed shape in order to investigate the magnitude of higher order terms. Then, the direct computations can themselves be compared to experimental data to validate the fidelity of the solution of RANS equations to the experiments.
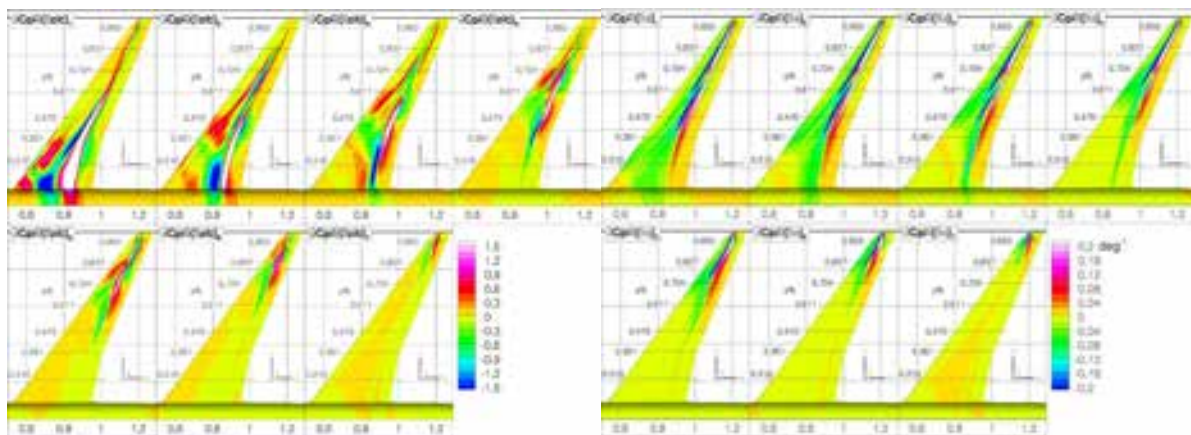

Figure 8: Sensitivity of upper side pressure coefficient with respect to bending parameters (left) and twist parameters (right)
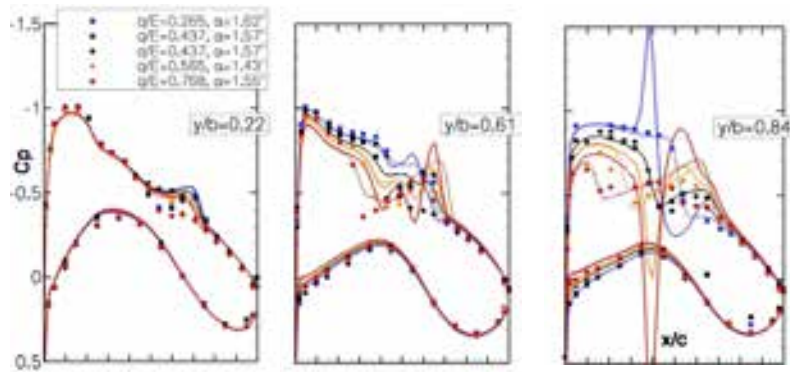
Figure 9: Wing pressure distribution for different wing shapes
symbols: ETW experiments ; lines: direct calculations (dashed), linearised calculation (continuous)

Those comparisons, presented in Figure 9, show that direct computations predicts very well the effect of the deformation for most wing sections, meaning the RANS solutions are accurate. This is less true concerning the shock behaviour close to mid-span where some discrepancies arise between experiments and calculations, but also between experiments themselves, a phenomenon to be linked to previous remark concerning wave drag.

Concerning linearised computations, apart from the vicinity of shock wave, the prediction is in excellent agreement with direct computations. On the contrary, near the shock waves the discrepancy is considerably large and grows with the magnitude of the deformation. This illustrates again the non-linear behaviour of the flow field around this flight point and the dominance of higher order terms over the first order ones.

Effect at low lift coefficient

The flight point under study in this section corresponds to a Mach number of 0.85 and a lift coefficient of 0.41. Two dynamic pressure levels are available from experimental data, along with measured deformations. Once again the wing shape obtained at $q/E = 0.437$ is chosen as the reference shape, the flow field around this shape is computed and then adjoint and linearised computations are carried out. A direct computation is also carried out around the deformed shape for comparison.

Results are presented in Figure 10 in a way similar to Figure 6. Comparing first order to direct computations, it appears that the first order approach gives prediction that are much closer to direct computations than before, i.e. that higher order terms are much more negligible for this flight point (curves are superimposed on the figure).
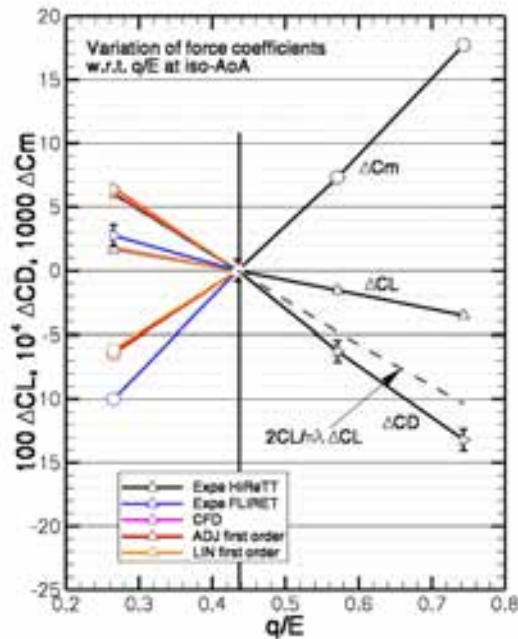
**Figure 10: Force increment due to deformation around reference shape
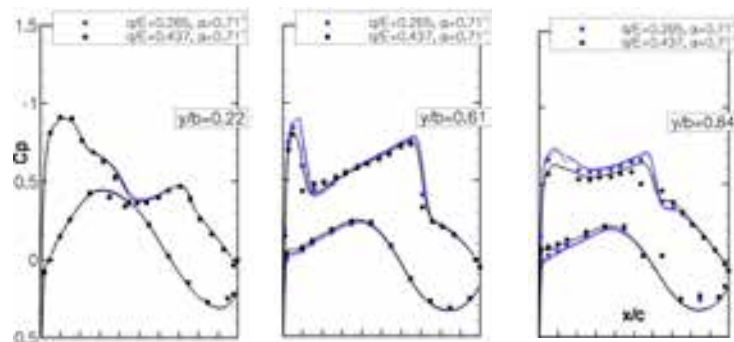at Mach 0.85 and CL = 0.41**

**Figure 11: Wing pressure distribution for different wing shapes
symbols: ETW experiments
lines: direct calculations (dashed), linearised calculation (continuous)**

Comparison to experimental data shows fair agreement, including on drag coefficient that exhibit large discrepancies in previous section. The only remaining discrepancy in drag is between FLIRET half model test and calculations. If one refers solely to data from HiReTT campaign, the slope of the curve is in very good agreement with computations. For reasons not detailed here, the full model data from HiReTT campaign are considered more reliable. The largest observed discrepancy comes from the pitching moment coefficient for which the effect of the deformation is underestimated by about 35%.

The effect of deformation on the pressure field can now be observed in Figure 11. This agreement between all computations and experimental data is excellent.

Effect at high lift coefficient

The case at Mach 0.85 and CL 0.64 is now examined. This corresponds to a flight point well beyond drag divergence. The shock wave has become so strong that the boundary layer separates at the root of the shock wave over 60% of span. Consequently, the wave and viscous drag are considerably increased compared to cruise point. On that point, the linearised computations exhibited unsatisfactory convergence. Although they are presented thereafter, they should be interpreted with caution.

Once again, the effect of deformation on forces and pressure distribution is presented in Figure 12 and Figure 13. Here again, the agreement between computations and experiment is good to excellent, the only exception concerning the effect on pitching moment, still slightly underestimated. This good agreement appears quite surprising considering the larger viscous effect due to the behaviour of the separated region in response of variations of shock intensity. Indeed the flow separation on the shape at higher dynamic pressure has small chord extension (1-2%), whereas at low dynamic pressure with increased shock intensity, the separation extends over 10 to 30% of chord. One would expect that such variations be sensitive to a precise modelling of turbulence behaviour and that the frozen eddy viscosity hypothesis would fail in predicting the correct flow sensitivity. Such failure was not observed in the present case.
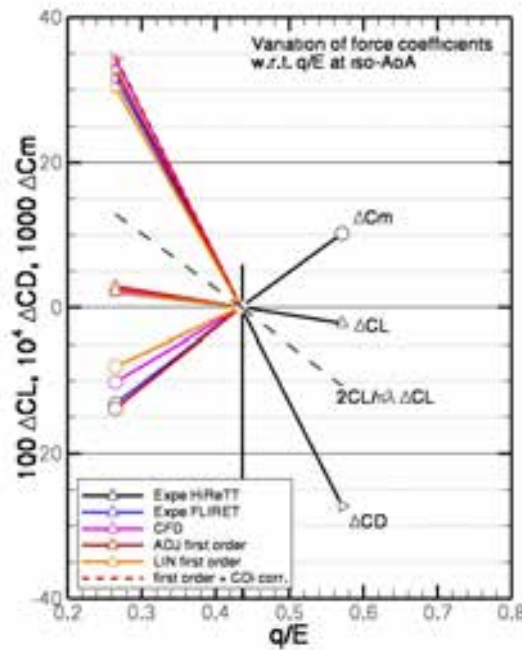

**Figure 12: Force increment due to deformation around reference shape
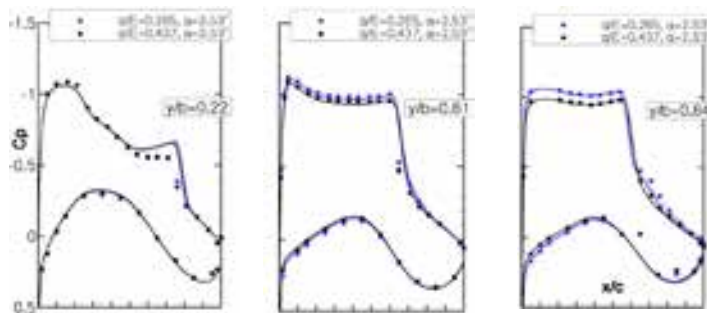at Mach 0.85 and CL = 0.64**

**Figure 13: Wing pressure distribution for different wing shape
symbols: ETW experiments
lines: direct calculations (dashed), linearised calculation (continuous)**

Evolution of gradient with incidence

As illustrated from the above sections, the gradient of the flow field with respect to wing deformation is a quantity that evolves with angle of attack. This dependency of the gradient with respect to angle of attack is investigated in this section.

Of course, it is not possible to validate against experimental data the evolution of the gradient component by component. Instead, the sensitivity of force coefficients with respect to dynamic pressure is evaluated. For a given coefficient C_X, this sensitivity writes as:

$$\frac{\partial C_X}{\partial q/E} = \frac{\partial C_X}{\partial \theta_i} \frac{\partial \theta_i}{\partial q/E}$$

where derivatives are taken at constant flow conditions (AoA, Mach, Reynolds) as before.
Geometrically, this quantity is the slope of the curves showing force increments with respect to q/E in Figure 6, Figure 10 and Figure 12. Experimentally, this sensitivity is evaluated by finite difference between polars at different dynamic pressures. Numerically, the gradient $\dfrac{\partial C_X}{\partial \theta_i}$ is the one computed by adjoint/linearised method

and the shape sensitivity $\dfrac{\partial \theta_i}{\partial q/E}$ is evaluated by finite difference from experimental data.

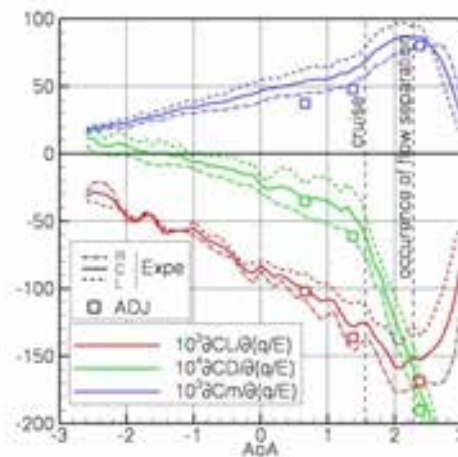The results are plotted in Figure 14 using first and second order finite difference.

Figure 14 : Evolution with AoA of force sensitivities to wind deformation caused by a change in dynamic pressure at iso-AoA and around q/E = 0.437
Symbols: simulations by adjoint method
Lines: ETW experiments (continous: centered 2nd order FD, dashed: right (R) or left (L) first-order FD)

In this figure, experimental data obtained using right-side finite difference are probably the most reliable since other data (left side and centered) relies on measurement from the half model campaign which, as previously mentioned, exhibits certain incoherencies. It can be said that the discrepancies between numerical and experimental data are close to the experimental uncertainty. The evolution of the shape sensitivity with the AoA is well predicted by numerical simulations, including beyond the drag divergence where its behaviour radically changes.

Conclusion

Adjoint and linearised computations on a civil transport aircraft allowed the prediction of the sensitivity of force coefficients with respect to the wing shape. The calculations were validated against direct simulations of the deformed shape and against available experimental data from cryogenic wind tunnel, exhibiting reasonable agreement. Thanks to MDM measurements technique also presented, the deformed wing shape is known during wind tunnel tests. Such computations may then be used to extrapolate wind tunnel test results to the design shape (infinitely rigid aircraft) or even to any other known shape (like flight shape for example). The extrapolation is accurate to the first order, which was shown to be sufficient for most of the polar, but presented some shortage close to the design point where the flow field behaviour, especially the shock wave, is far from linear.

References

[1] Liu, T., Radeztsky, R., Garg, S., Cattafesta, L. A Videogrammetric Model Deformation System and its Integration with Pressure Paint. *37th AIAA Aerospace Sciences Meeting and Exhibit*, AIAA 99-0568, Reno, January 11-14, 1999.

[2] Rolston S., Elsholz E. Initial Achievements of the European High Reynolds Number Aerodynamic Research Project HiReTT. *40th AIAA Aerospace Science Meeting and Exhibit*, AIAA 2002-0424, Reno, January 14-17, 2002.

[3] Destarac, D. Far-Field / Near-Field Drag Balance Applications of Drag Extraction in CFD. *VKI Lecture Series 2003*.

[4] Le Sant, Y., Mignosi, A., Touron, G., Deléglise, B., Bourguignon, G. Model Deformation Measurement (MDM) at ONERA. *25th AIAA Applied Aerodynamics Conference*, AIAA 2007-3817, Miami, June 25-28, 2007.

[5] Cambier, L., Veuillot J.-P. Status of the elsA CFD Software for Flow Simulation and Multidisciplinary Applications, 26th *AIAA Applied Aerodynamics Conference*, AIAA 2008-664, Reno, January 7-10, 2008.

[6] Peter, J., Dwight, R. Numerical Sensitivity Analysis for Aerodynamic Optimization: a Survey of Approaches, *Computers and Fluids*, Vol. 39, Issue 3, pp 373-391, 2010.

[7] Yamazaki, W., Mouton, S., Carrier, G. Geometry Parameterization and Computational Mesh Deformation by Physics-Based Direct Manipulation Approaches. *AIAA Journal*, Vol. 48, No. 8, 2010.

[8] Green, J., Quest J. A short history of the European Transonic Wind Tunnel ETW, *Progress in Aerospace Sciences*, Vol. 47, Issue 5, pp 319-368, 2011.

InfoSymbiotic Systems:

The Power of Dynamic Data Driven Applications Systems (DDDAS)

Integration 2012

JAXA – Tokyo, Japan

October 2012

Dr. Frederica Darema

Air Force Office of Scientific Research

(AFOSR)

Integrity ★ Service ★ Excellence

DISTRIBUTION STATEMENT A – Unclassified, Unlimited Distribution

1

OUTLINE

InfoSymbiotic Systems

- **The essence of Dynamic Data Driven Applications Systems (DDDAS)**
- **Examples of new capabilities through DDDAS (aerospace & other)**

Why now timely more than ever

Research and Technology Development Modalities:

- **Multidisciplinary R&D**
  - **Fostering Transformative Innovations**
  - **Expanding Fundamental Knowledge and Capabilities**
  - **Transformative Partnerships across Academe-Industry &International**

Technology Advances/Trends:

- **Multicores - Exascale – Unified High-End with RT/DA&Control**
- **Ubiquitous Sensing - New Wave in Data Intensive**
- **Increased emphasis in multiscale modeling and UQ**

Summary

2

Dynamic Data Driven Applications Systems (DDDAS)

OLD *(serialized and static)*

Theory (First Principles)

Simulations (Math.Modeling Phenomenology)

Measurements Experiments Field–Data User

Theory (First Principles)

Simulations (Math.Modeling Phenomenology DesignModeling)

Measurements Experiment Field-Data (on-line/archival) User

Dynamic *Feedback & Control* Loop

InfoSymbiotic Systems

DDDAS: *ability to dynamically incorporate additional data into an executing application, and in reverse, ability of an application to dynamically steer the measurement process*

a "revolutionary" concept enabling to design, build, manage, understand complex systems

Dynamic Integration of Computation & Measurements/Data
Unification of
Computing Platforms & Sensors/Instruments
(from the High-End to the Real-Time, to the PDA)
DDDAS – architecting & adaptive mngmnt of sensor systems

Challenges:
Application Simulations Methods
Algorithmic Stability
Measurement/Instrumentation Methods
Computing Systems Software Support

Synergistic, Multidisciplinary Research

Dynamic Data Driven Applications Systems (DDDAS)

OLD *(serialized and static)*

Theory (First Principles)

Simulations (Math.Modeling Phenomenology)

Measurements Experiments

Computational Science – the 3rd paradigm

Data – the 4th paradigm

corporate
uting application, and in
application to dynamically
rement process

revolutionary" concept enabling to
sign, build, manage, un...and complex systems

Dynamic ...tion of
Computation ...ement...

...ents

Simulations (Math.Modeling Phenomenology DesignModeling)

Measurements Experiment Field (on-line/arch... User

DDDAS /InfoSymbiotics

is the _unifying_ paradigm

LEAD: Users INTERACTING with Weather
Infrastructure:
NSF Engineering Research Center for Collaborative Adaptive Sensing of the Atmosphere (CASA)

- **Current (NEXRAD) Doppler weather radars are high-power and long range – Earth's curvature prevents them from sensing a key region of the atmosphere: ground to 3 km**
- **CASA Concept: Inexpensive, dual-polarization phased array Doppler radars on cellular towers and buildings**
  - **Easily view the lowest 3 km (most poorly observed region) of the atmosphere**
  - **Radars collaborate with their neighbors and dynamically adapt the the changing weather, sensing multiple phenomena to simultaneously and optimally meet multiple end user needs**
  - **End users (emergency managers, Weather Service, scientists) drive the system via policy mechanisms built into the optimal control functionality**

5
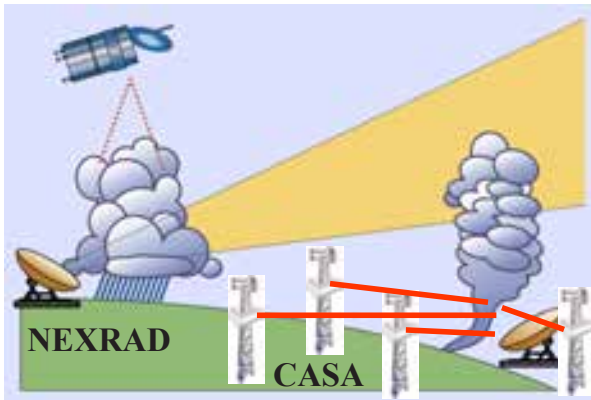
LEAD: Users INTERACTING with Weather
"The LEAD Goal Restated - to incorporate DDDAS " - Droegemeier

Interaction Level II: Tools and People Driving Observing Systems – Dynamic Adaptation

NWS National Static Observations & Grids

Mesoscale Weather

Experimental Dynamic Observations

Local Observations

Virtual/Digital Resources and Services

Remote Physical (Grid) Resources

Local Physical Resources

Users

Tools

"Sensor Networks & Computer Networks"

6

March 2000 Fort Worth Tornadic Storm
Local TV Station Radar
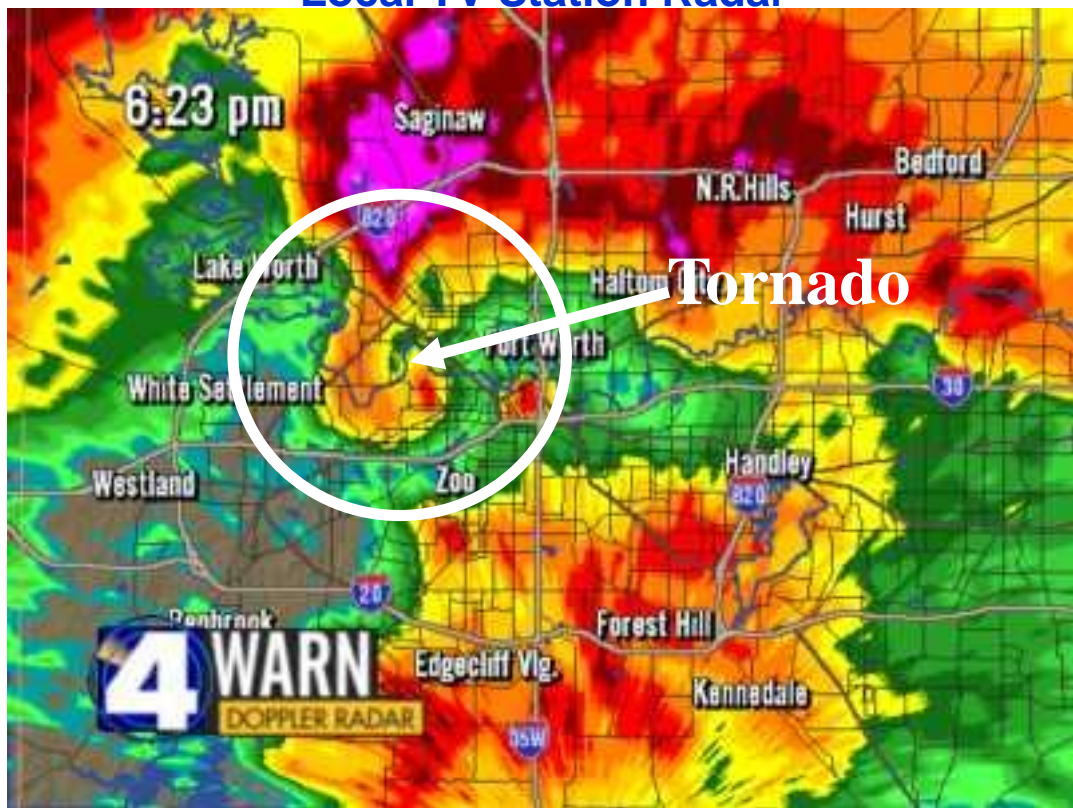
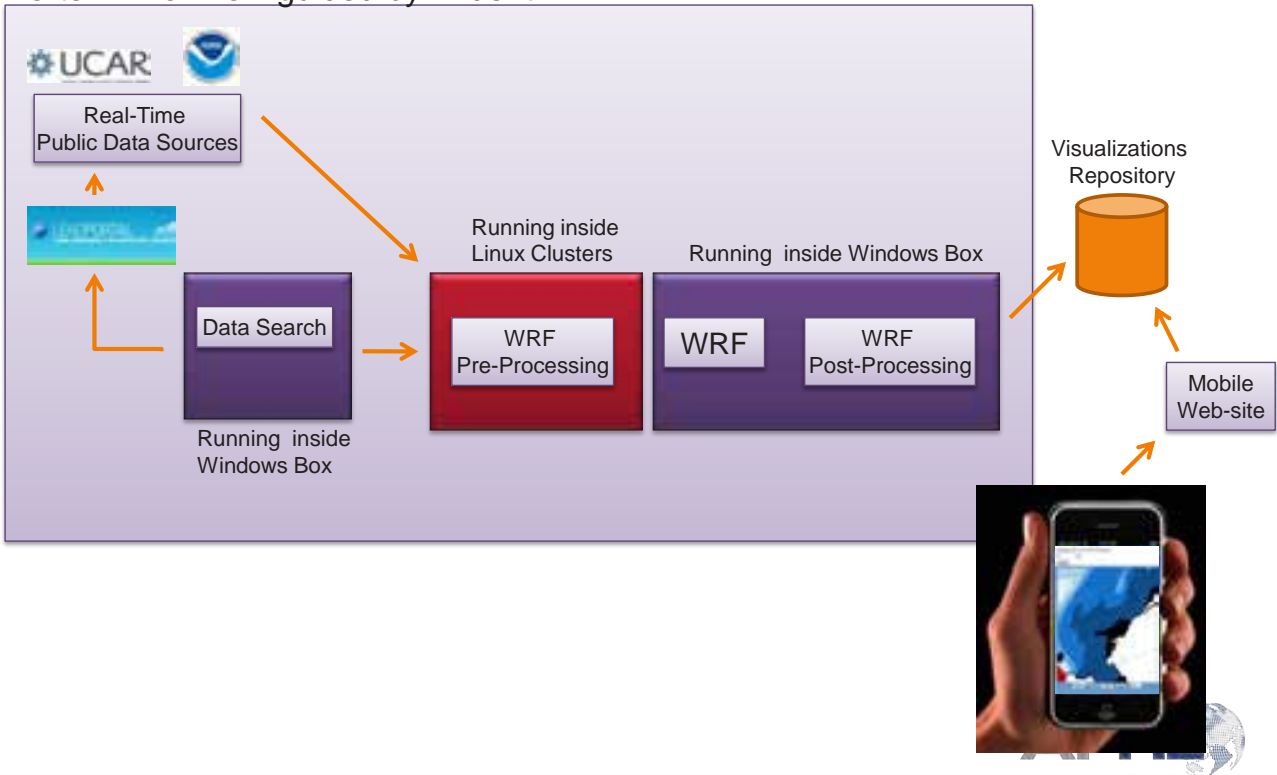# Corrected Forecast with LEAD(DDDAS)
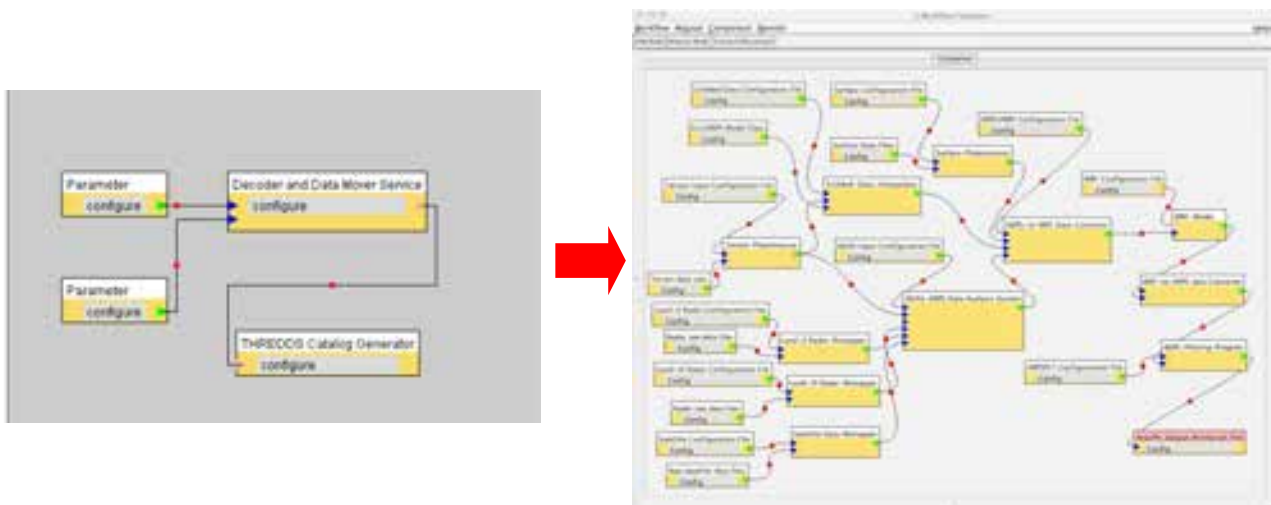### (Slide – Courtessy K. K. Droegemeier)
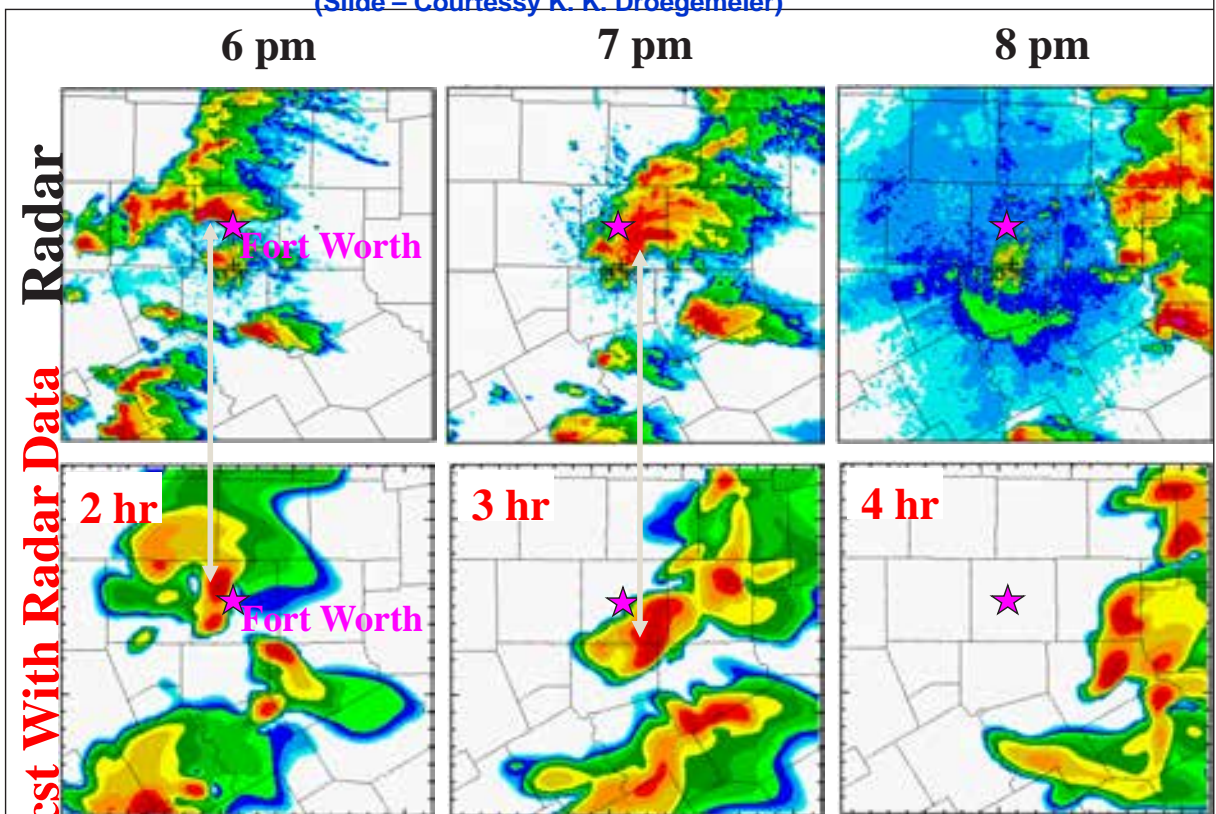
Xue et al. (2003)

Vortex2 Experiment with Trident

Vortex2 Workflow guided by Trident
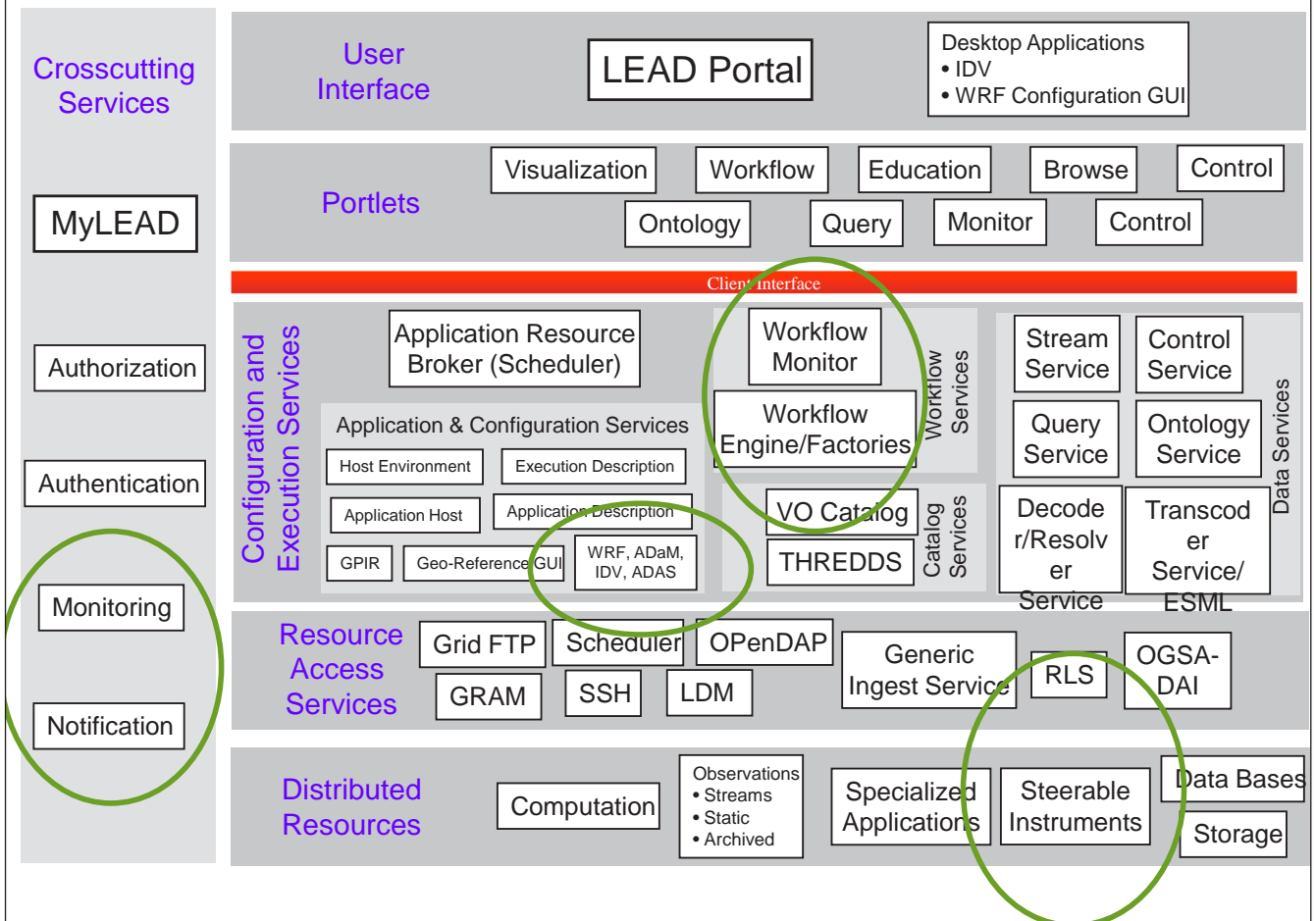

9

Dynamic Workflow: THE Challenge

Automatically, non-deterministically, and getting the resources needed

10

LEAD Architecture: adaptivity service interaction

Crosscutting Services

User Interface

LEAD Portal

Desktop Applications
• IDV
• WRF Configuration GUI

MyLEAD

Portlets

Visualization | Workflow | Education | Browse | Control

Ontology | Query | Monitor | Control

Client Interface

Authorization

Configuration and Execution Services

Application Resource Broker (Scheduler)

Workflow Monitor

Workflow Engine/Factories

Workflow Services

Stream Service | Control Service

Authentication

Application & Configuration Services

Host Environment | Execution Description

Application Host | Application Description

GPIR | Geo-Reference GUI | WRF, ADaM, IDV, ADAS

VO Catalog

THREDDS

Catalog Services

Query Service | Ontology Service

Decoder/Resolver Service

Transcoder Service/ ESML

Data Services

Monitoring

Notification

Resource Access Services

Grid FTP | Scheduler | OPenDAP

GRAM | SSH | LDM

Generic Ingest Service

RLS

OGSA-DAI

Distributed Resources

Computation

Observations
• Streams
• Static
• Archived

Specialized Applications

Steerable Instruments

Data Bases

Storage

Examples of Areas of DDDAS Impact

- **Physical, Chemical, Biological, Engineering Systems**

  Materials, system health monitoring, molecular bionetworks, protein folding.. chemical pollution transport (atmosphere, aquatic, subsurface), ecological systems, …

- **Medical and Health Systems**

  MRI imaging, cancer treatment, seizure control

- **Environmental (prevention, mitigation, and response)**

  Earthquakes, hurricanes, tornados, wildfires, floods, landslides, tsunamis, …

- **Critical Infrastructure systems**

  Electric-powergrid systems, water supply systems, transportation networks and vehicles (air, ground, underwater, space), …

  condition monitoring, prevention, mitigation of adverse effects, …

- **Homeland Security, Communications, Manufacturing**

  Terrorist attacks, emergency response; Mfg planning and control

- *Dynamic Adaptive Systems-Software*

  Robust and Dependable Large-Scale systems

  Large-Scale Computational Environments

  **List of Projects/Papers/Workshops in www.dddas.org
  e.g: August2010 MultiAgency InfoSymbtiotics/DDDAS Workshop
  ICCS/DDDAS Workshop Series (2003 –to date)**

AFRL

12

Examples of Areas of DDDAS Impact

- **Physical, Chemical, Biological, Engineering Systems**

  Materials, system health monitoring, molecular bionetworks, protein folding.. chemical pollution transport (atmosphere, aquatic, subsurface), ecological systems, …

- **Medical and Health Systems**

  MRI imaging, cancer treatment, seizure control

- **Environmental (prevention, mitigation, and response)**

  Earthquakes, hurricanes, tornados, wildfires, floods, landslides, tsunamis, …

- **Critical Infrastructure systems**

  Electric-powergrid systems, water supply systems, transport networks and vehicles (air, ground, and space), …

revolutionary" concept enabling to design, build, manage and understand complex systems
NSF/ENG Blue Ribbon Panel (Report 2006 – Tinsley Oden)
"DDDAS … key concept in many of the objectives set in Technology Horizons"
Dr. Werner Dahm, (former/recent) AF Chief Scientist

Large-Scale Computing Environments

List of Projects/Papers, Workshops in www.dddas.org
e.g: August2010 MultiAgency InfoSymbtiotics/DDDAS Workshop
ICCS/DDDAS Workshop Series (2003 –to date)

AFRL   13

The AirForce 10yr + 10 Yr Outlook:
Technology Horizons Report
Top Key Technology Areas

DDDAS … key concept in many of the objectives set in Technology Horizons

- ☐ **Autonomous systems**
- ☐ **Autonomous reasoning and learning**
- ☐ **Resilient autonomy**
- ☐ **Complex adaptive systems**
- ☐ **V&V for complex adaptive systems**
- ☐ **Collaborative/cooperative control**
- ☐ **Autonomous mission planning**
- ☐ **Cold-atom INS**
- ☐ **Chip-scale atomic clocks**
- ☐ **Ad hoc networks**
- ☐ **Polymorphic networks**
- ☐ **Agile networks**
- ☐ **Laser communications**
- ☐ **Frequency-agile RF systems**

- ☐ **Spectral mutability**
- ☐ **Dynamic spectrum access**
- ☐ **Quantum key distribution**
- ☐ **Multi-scale simulation technologies**
- ☐ **Coupled multi-physics simulations**
- ☐ **Embedded diagnostics**
- ☐ **Decision support tools**
- ☐ **Automated software generation**
- ☐ **Sensor-based processing**
- ☐ **Behavior prediction and anticipation**
- ☐ **Cognitive modeling**
- ☐ **Cognitive performance augmentation**
- ☐ **Human-machine interfaces**

http://www.af.mil/shared/media/document/AFD-100727-053.pdf

AFRL   14

Advances in Capabilities through DDDAS

- **DDDAS: integration of application simulation/models with the application instrumentation components in a dynamic feed-back control loop**
  - ➤ **speedup of the simulation, by replacing computation with data in specific parts of the phase-space of the application**
    and/or
  - ➤ **augment model with actual data to improve accuracy of the model, improve analysis/prediction capabilities of application models**
  - ➤ **dynamically manage/schedule/architect heterogeneous resources, such as:**
  - ▪ **networks of heterogeneous sensors, or networks of heterogeneous controllers**
  - ➤ **enable ~decision-support capabilities w simulation-modeling accuracy**
- **unification from the high-end to the real-time data acquisition and control**

AFRL 15

What makes DDDAS(*InfoSymbiotics*) TIMELY NOW MORE THAN EVER?

- **Emerging scientific and technological trends/advances**
  - ➤ *ever more complex applications – systems-of-systems*
  - ➤ **increased emphasis in complex applications modeling**

  - ➤ **increased computational capabilities (multicores)**
  - ➤ **increased bandwidths for streaming data**

  - ➤ **Sensors– Sensors EVERYWHERE…   *(data intensive Wave #2)***
    - ▪ *Swimming in sensors and drowning in data* - **LtGen Deptula (2010)**
    - **Analogous experience from the past:**
    - ▪ *"The attack of the killer micros(microprocs)"* - **Dr. Eugene Brooks, LLNL (early 90's)**
      about microprocessor-based high-end parallel systems
      then seen as a problem – have now become an opportunity - advanced capabilities
    - **Back to the present and looking to the future:**
    - ▪ *"Ubiquitous Sensing – the attack of the killer micros(sensors) – wave # 2"*
                                Dr. Frederica Darema, AFOSR (2011, LNCC)
  - *challenge: how to deal with heterogeneity, dynamicity, large numbers of such resources*
  - *opportunity: "smarter systems" – InfoSymbiotics DDDAS - the way for such capabilities*

- **Need capabilities for adaptive management of such resources**
  - ➤ **advances made thus far, can be furthered in an accelerating way**

AFRL 16

Fundamental Science and Technology Challenges for Enabling DDDAS Capabilities

- **Application modeling (in the context of dynamic data inputs)**
  - **interfacing applications with measurement systems**
  - **dynamically invoke/select appropriate application components**
    - **multi-modal, multi-scale – dynamically invoke multiple scales/modalities**
  - **switching to different algorithms/components depending on streamed data**
    - **dynamic hierarchical decomposition (computat'nal platform - sensor) and partitioning**
- **Algorithms**
  - **tolerant to perturbations of dynamic input data**
  - **handling data uncertainties, uncertainty propagation, quantification**
- **Measurements**
  - **multiple modalities, space/time-distributed, heterogeneous data management**
- **Systems supporting such dynamic environments**
  - **dynamic execution support on heterogeneous environments**
    - **new fundamental advances in compilers (runtime-compiler)**
    - **integrated architectural frameworks/cyberifrastructures encompassing apps-sw-hw layers**
  - **extended spectrum of platforms (*beyond traditional computational grids*)**
    - **grids of: sensor networks and computational platforms**
  - **architect and manage heterogeneous/distributed sensor networks**

DDDAS environments entail new capabilities but also new requirements and environments
  … beyond GRID Computing -> SuperGrids
  and… beyond the (traditional) Clouds

AFRL   17

Examples of Projects aerospace related (from DDDAS/AFOSR funded research)

range from the "nano"-scale to the "terra"-scale

AFRL   18

Development of a Stochastic Dynamic Data-Driven System for Prediction of Material Damage

J.T. Oden (PI), P. Bauman, E. Prudencio, S. Prudhomme, K. Ravi-Chandar - UTAustin

- **Goal**: Dynamic Detection and Control of Damage in Complex Composite Structures
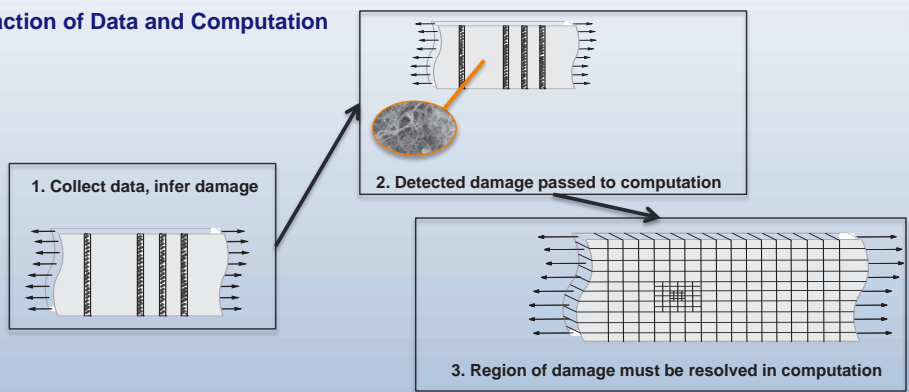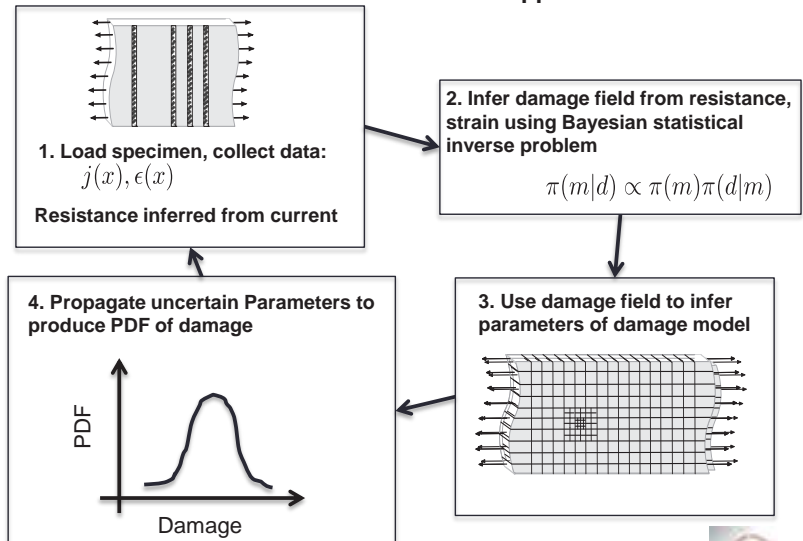
- **Approach and Objectives:**
  - Coupled simulation and sensoring&control
  - Advanced methods of detecting potential or onset of damage
  - Damage evolution dynamically controlled by "limited load amplitude"
- **Methodology:**
  - Simulations based on a family of continuum damage models
  - Cyclic loading of composite plates with a distributed system of carbon nano-particle sensors
  - Dynamic calibration and model selection based on Bayesian methods driven by sensor data
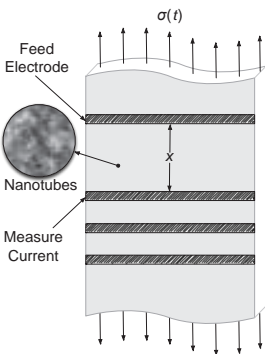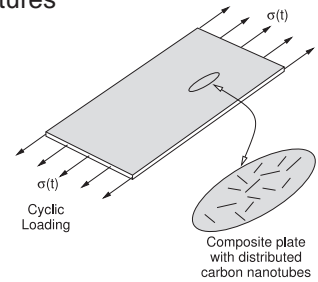
Interaction of Data and Computation

1. Collect data, infer damage

2. Detected damage passed to computation

3. Region of damage must be resolved in computation

Feed Electrode

Nanotubes

Measure Current

Development of a Stochastic Dynamic Data-Driven System for Prediction of Material Damage

J.T. Oden (PI), P. Bauman, E. Prudencio, S. Prudhomme, K. Ravi-Chandar - UTAustin

- **Features of Approach**
  - Models based on continuum damage mechanics theories (e.g. Lemaitre and Chaboche)
  - Experiments done on fiber-reinforced composite plates enriched with distributed carbon nano-tubes acting as sensors of material stiffness loss
  - Experimentally observed data and parameters will be used in Bayesian-based model selection algorithms
  - Actual tests up to fatigue failure will determine the effectiveness of variants of approach

- **Experimental Testbed:**
  Damage Generation and Detection
  - Specimen: fiber composite with embedded carbon nanotubes (by Designed Nanotubes, Austin, TX)
  - Mechanical load profile:
    - Quasi-static, but time dependent (ramp, load cycling, creep)
    - Cyclic loading of composite plates with a distributed system of carbon nano-particle sensors
  - Mechanical measurement: Digital image correlation to find spatial variation of strain
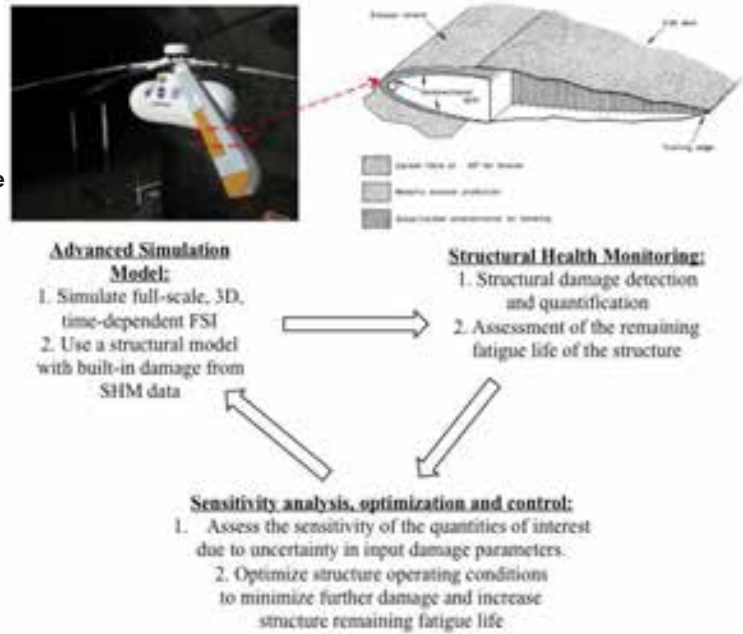 - Electrical measurement: Current measured at different locations, load levels, and times

1. Load specimen, collect data:
$$j(x), \epsilon(x)$$
Resistance inferred from current

2. Infer damage field from resistance, strain using Bayesian statistical inverse problem
$$\pi(m|d) \propto \pi(m)\pi(d|m)$$

3. Use damage field to infer parameters of damage model

4. Propagate uncertain Parameters to produce PDF of damage

PDF

Damage

AFRL

20

Advanced Simulation, Optimization, and Health Monitoring of Large Scale Structural Systems

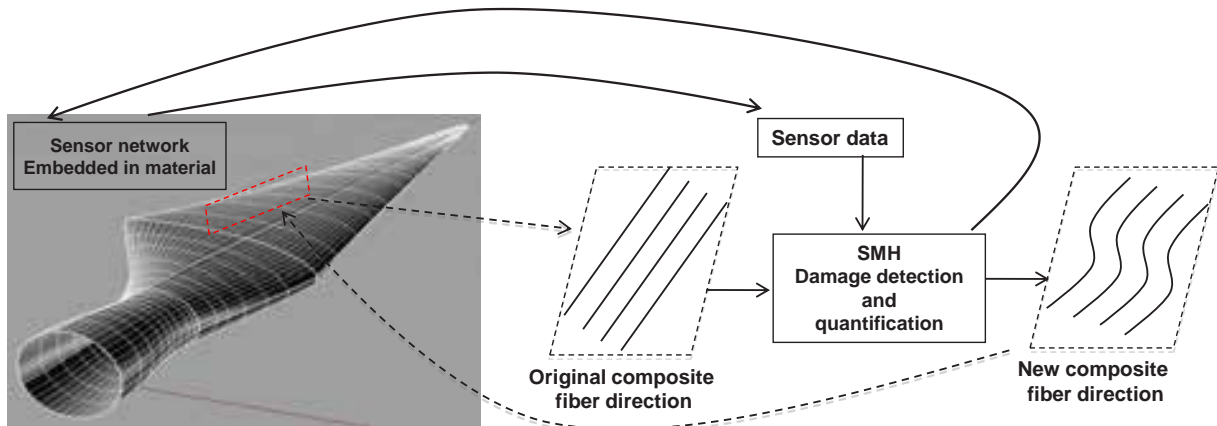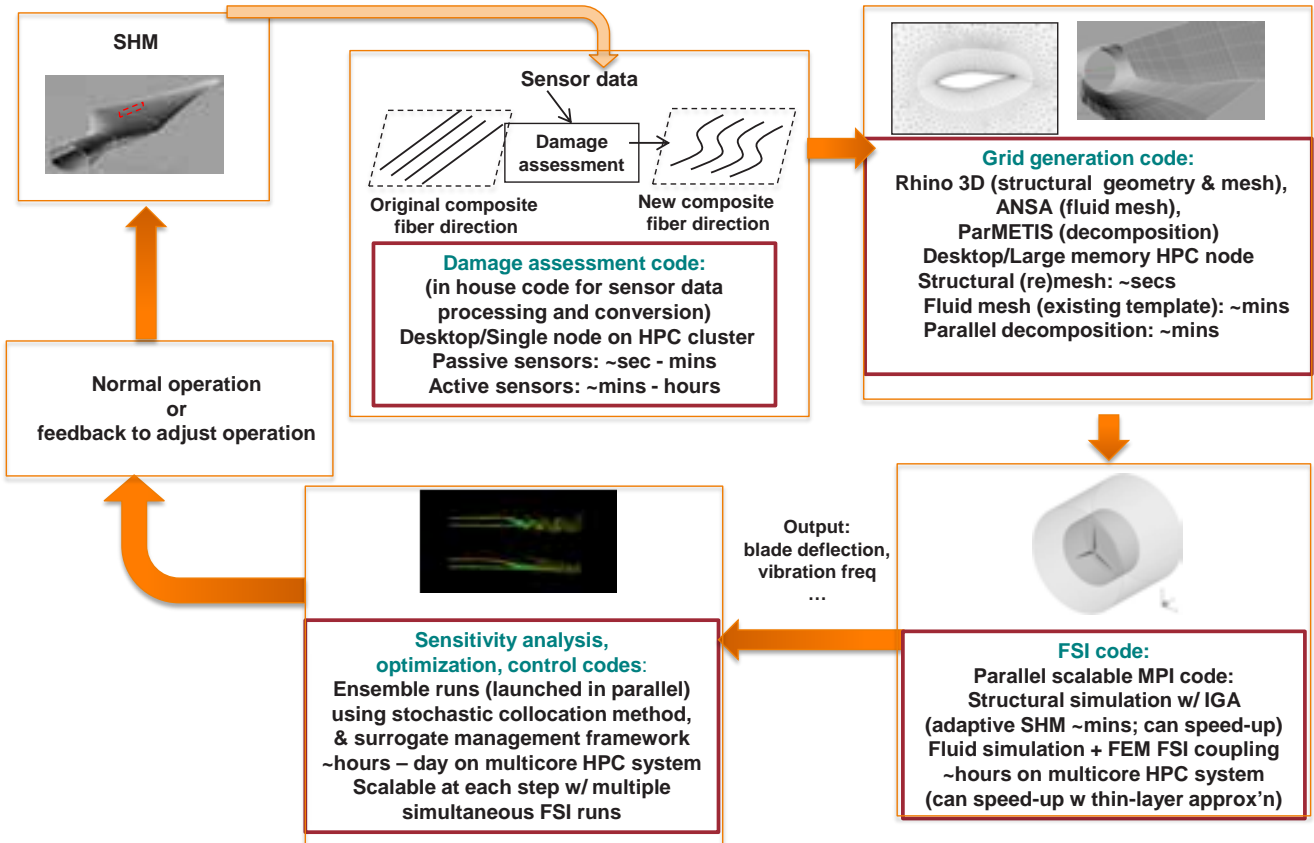*Y. Bazilevs, A.L. Marsden, F. Lanza di Scalea, A. Majumdar, and M. Tatineni (UCSD)*

- **Main Objective:**
  A Computational Steering Framework for Large-Scale Composite Structures & Environment-coupled, based on Continually and Dynamically Injected Sensor Data

- **Key Features:**
  - A structural health monitoring (SHM) system
  - Simulation model of a structural system with fluid-structure interaction (FSI)
  - Sensitivity analysis, optimization and control software module
  - Implementation framework in high-performance computing (HPC) environments
  - Integration of FSI, SHM, sensitivity analysis, optimization, control, and HPC into a unified DDDAS framework

Advanced Simulation Model:
1. Simulate full-scale, 3D, time-dependent FSI
2. Use a structural model with built-in damage from SHM data

Structural Health Monitoring:
1. Structural damage detection and quantification
2. Assessment of the remaining fatigue life of the structure

Sensitivity analysis, optimization and control:
1. Assess the sensitivity of the quantities of interest due to uncertainty in input damage parameters
2. Optimize structure operating conditions to minimize further damage and increase structure remaining fatigue life

21

Example Case 1: DDDAS Loop for Detected In-plane Waviness

Sensor network Embedded in material

Sensor data

SMH Damage detection and quantification

Original composite fiber direction

New composite fiber direction

Re-compute constitutive matrix and update structural model on the fly!

Example Case 2: DDDAS Loop for Shear-Web-to-Skin Adhesive Disbond

Sensor data

SHM
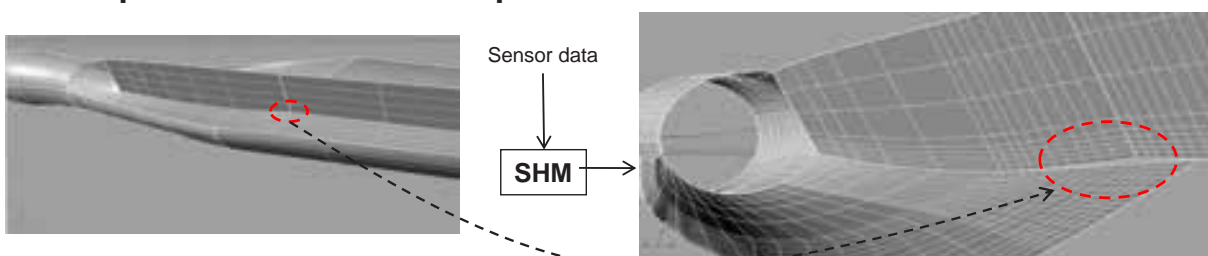
Introduce disbond by disconnecting structural patches

22

Advanced Simulation, Optimization, and Health Monitoring of Large Scale Structural Systems

Y. Bazilevs, A.L. Marsden, F. Lanza di Scalea, A. Majumdar, and M. Tatineni (UCSD)

- **Methodology:**
  - ➢ advanced simulation models encompassing time-dependent complex geometry, and non-linear material behavior producing high-fidelity outputs (stress distributions)
  - ➢ structural simulation will make use of isogeometric analysis; fluid simulation will make use of finite element methods, with appropriate FSI coupling
  - ➢ SHM system testbed comprised of ultrasonic sensor arrays and infrared thermographic imaging and a full-scale wind turbine blade with in-build structural defects
  - ➢ ability to dynamically update the simulation model with damage data and enable the prediction of the remaining fatigue life of the structure
  - ➢ (presently) GPU implementation for near-real-time performance

Sandia blade: Rhino 3D

23
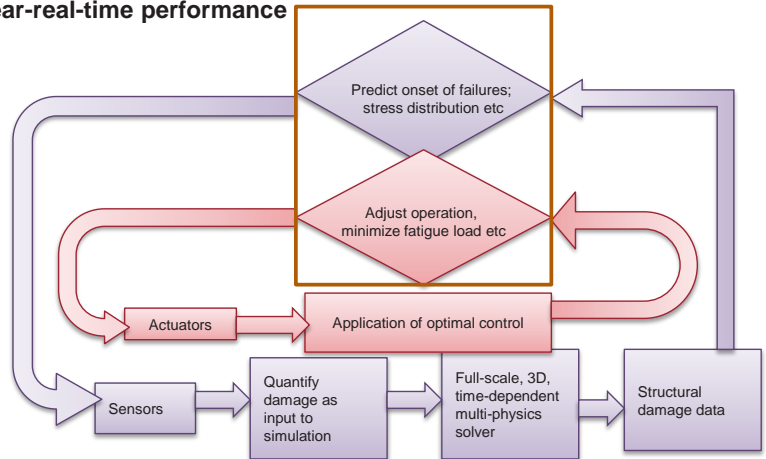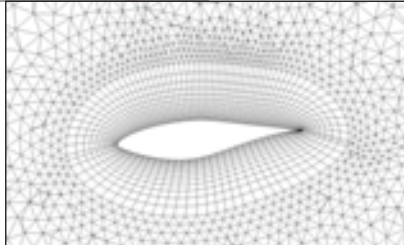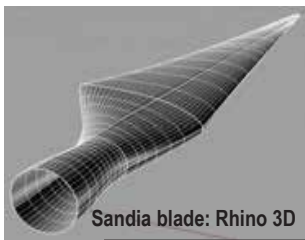
Computational Workflow Diagram

24

PROGNOSIS

STANFORD
MECHANICAL
ENGINEERING

Slides Courtesy C. Farhat

Real-Time On-Board Sensing and Processing

Pilot Display of Crisis

Real-Time On-Board Prognosis and Processing

On-Line Asset Management Report Sent to Commanders

crack locations

High-Performance Off-Line Prognosis by Modeling and Simulation

Detailed Prognosis Results

AFRL

25
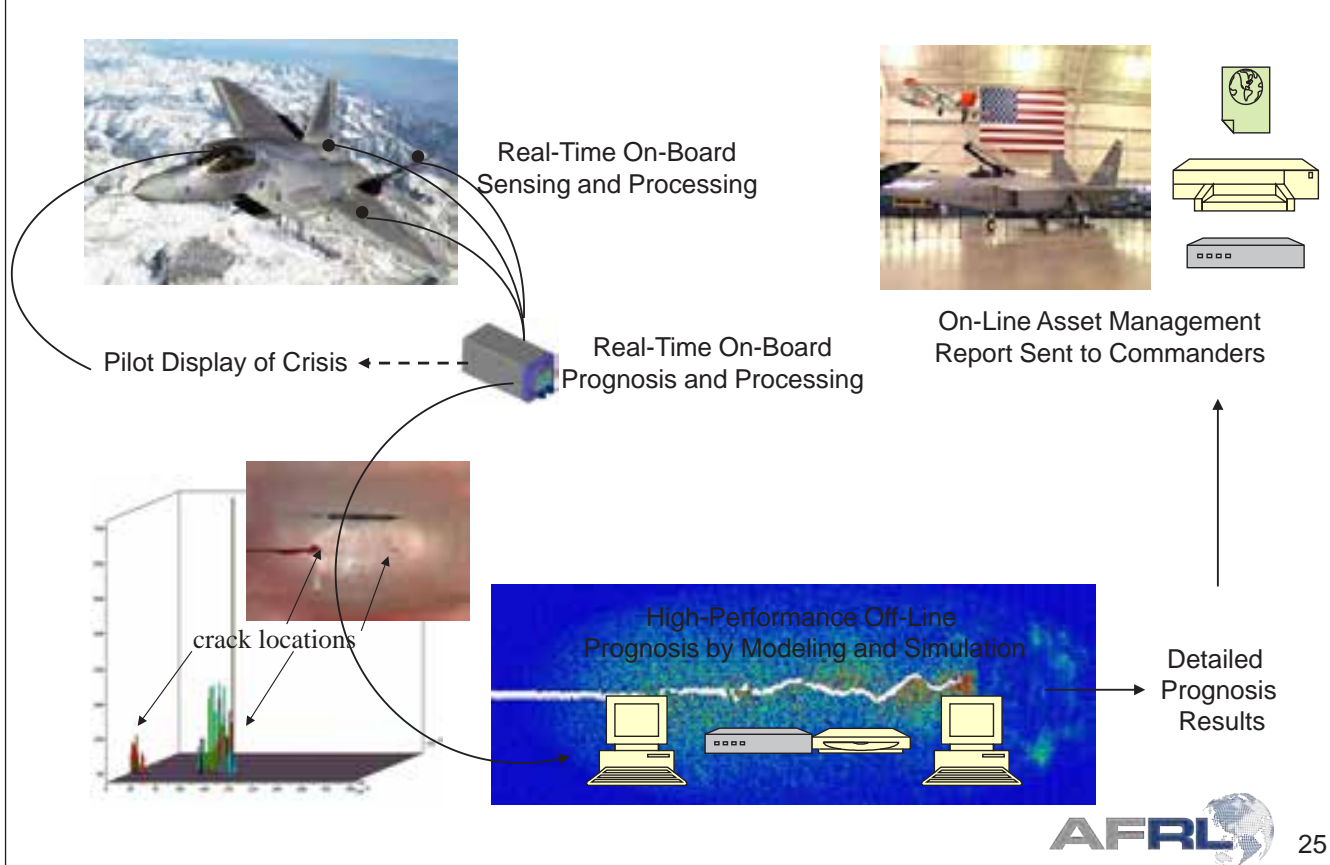
Real-Time Support for *supersonic/hypersonic multiphysics simulation*-based paltform management: Flutter, Temperature & Softening of Skin Material Degredation etc.

Slides Courtesy C. Farhat
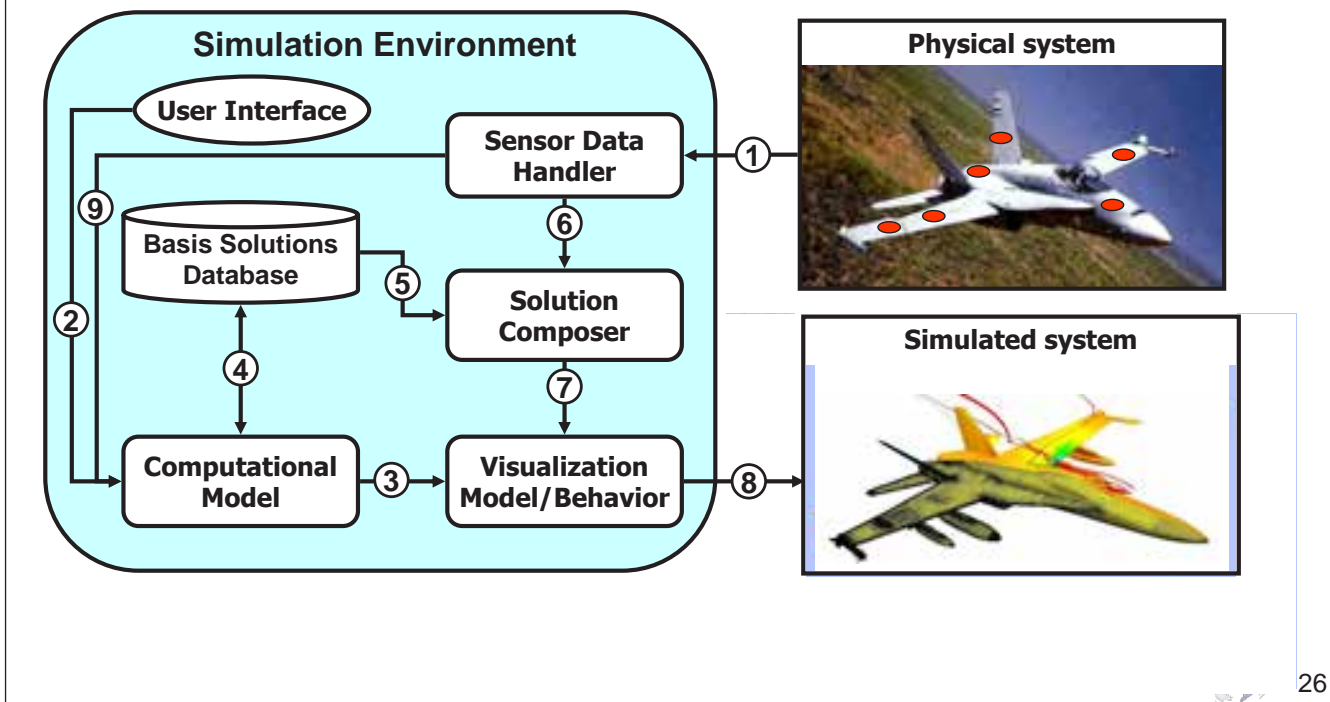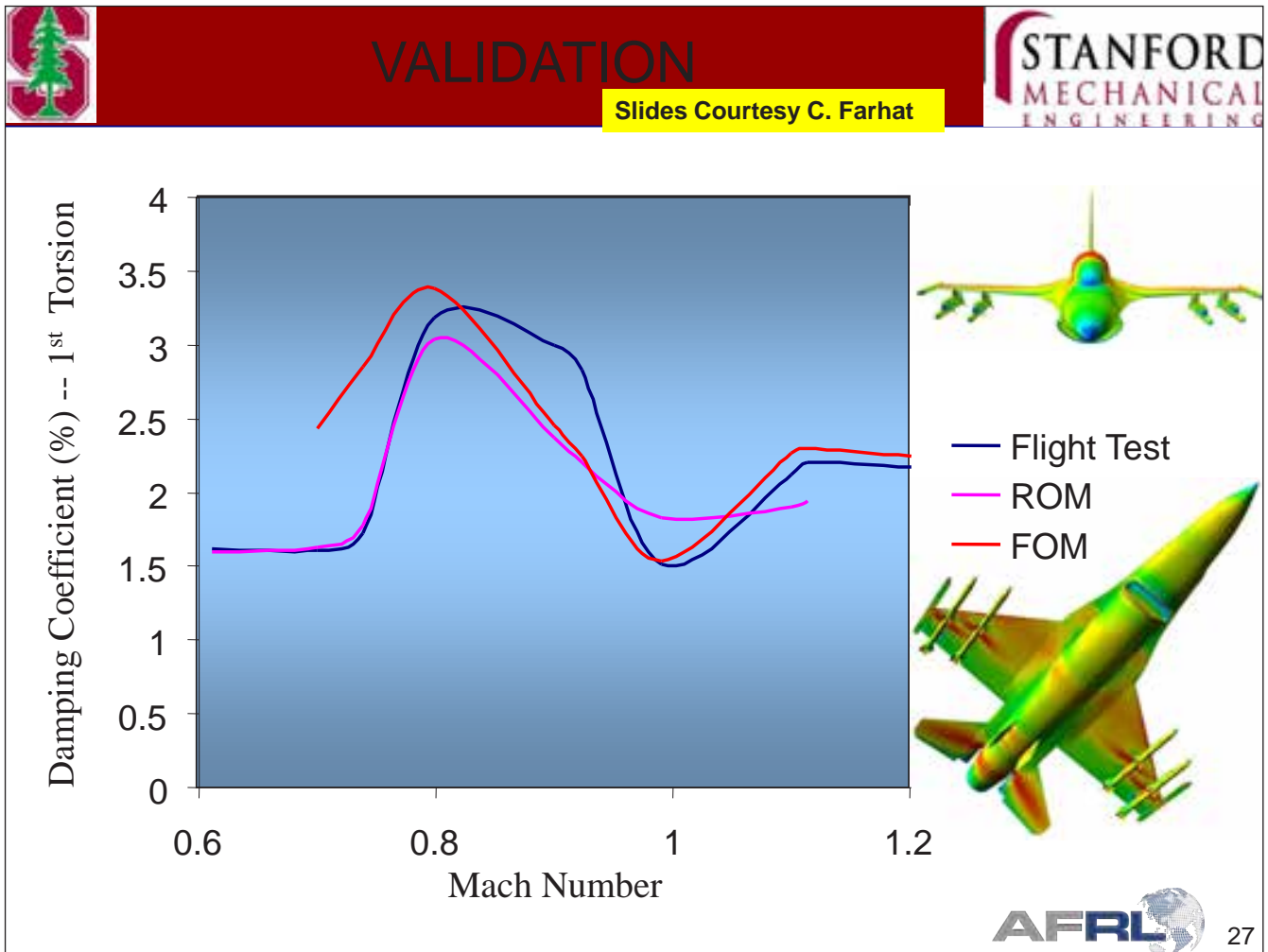
Simulation Environment

User Interface

Sensor Data Handler

Basis Solutions Database

Solution Composer

Computational Model

Visualization Model/Behavior

Physical system

Simulated system

26

VALIDATION

Slides Courtesy C. Farhat

27

Dynamic Data-Driven Methods for Self-Aware Aerospace Vehicles

D. Allaire, K. Willcox (MIT); G. Biros, O. Ghattas (UT Austin); J. Chambers, D. Kordonowy (Aurora)
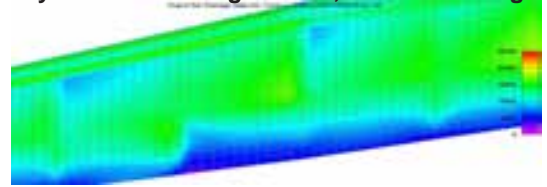
- Create capabilities for **self-aware aerospace vehicles**
 where each vehicle can dynamically adapt the way it performs missions
  by gathering information about itself and its surroundings,
  and responding intelligently

- **Approach and objectives**
  - **infer** vehicle health and state through dynamic integration of sensed data, prior information and simulation models
  - **predict** flight limits through updated estimates using adaptive simulation models
  - **re-plan** mission with updated flight limits and health-awareness based on sensed environmental data
- **Methodologies**
  - statistical inference for dynamic vehicle state estimation, using machine learning and reduced-order modeling
  - adaptive reduced-order models for vehicle flight limit prediction using dynamic data
  - on-line management of multi-fidelity models and sensor data, using variance-based sensitivity analysis
  - quantify the reliability, maneuverability and survivability benefits of a self-aware UAV

28

Dynamic Data-Driven Methods for Self-Aware Aerospace Vehicles

D. Allaire, K. Willcox (MIT); G. Biros, O. Ghattas (UT Austin); J. Chambers, D. Kordonowy (Aurora)

Data Incorporation Examples

Surrogate Models

QoI — **high fidelity model data**

QoI — **surrogate model**, **surrogate model uncertainty**

QoI — **fused (updated) model**, **sensor datum**, *fused model uncertainty*
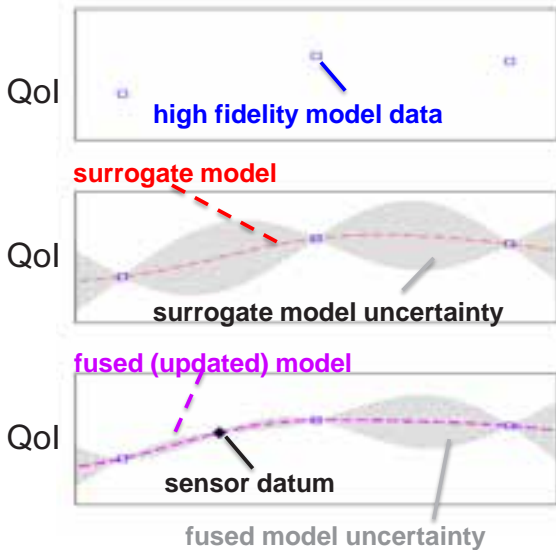
Structural Damage Models

Medium-fidelity model of a wing section, with no damage

Sensors indicate damage at two locations, elements removed/modified
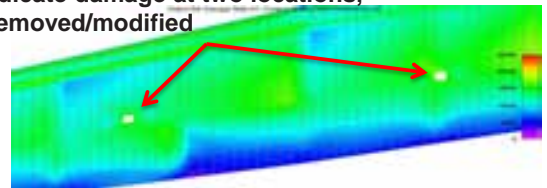
Damage extent determines additional elements Removed/modified

29

Dynamic Data-Driven Methods for Self-Aware Aerospace Vehicles

D Allaire, K Willcox (MIT); G Biros, O Ghattas (UT Austin); J Chambers, D Kordonowy (Aurora)

Dynamically evolving DDDAS process:
—Infer—Predict—Plan—Act—

Decision-making needs are informed by current quantity of interest estimates

Quantities of Interest
- Mission Plan
- Flight Limits
- Vehicle State

Models
- Adaptive Structural Response Models
- Information Fusion Models
- Planning Models

Models provide current estimates of the quantities of interest

Models drive adaptive sensing

Environmental data inform planning models

Sensors
- Sensors: structural health, stress/strain, pressure
- Sensors: IMS/GPS, temperature

Quantities of interest drive adaptive sensing

INFERENCE
- Confident estimation of vehicle state in offline phase, time-sensitive estimation of vehicle state in online phase
- Onboard damage model updated using sensed structural data/state
- Efficient algorithms scale well on GPU and manycore architectures

PREDICTION
- Update estimates of flight limits via adaptive reduced-order models
- Progressively fuse higher fidelity information with current information as more time and resources become available
- Sensitivity analysis for dynamic online management of multifidelity models & sensors for vehicle state & flight limit

PLANNING
- Dynamic environmental data inform online adaption of reduced-order models for mission planning
- Multifidelity planning approaches using reduced-order models
- Quantification of reliability, maneuverability, survivability

Application of DDDAS Principles to Command, Control and Mission Planning for UAV Swarms

*M.B. Blake, G. Madey, C. Poellabauer – U. Of Notre Dame*

Advancing ISR Capabilities

Intelligence, Surveillance, Reconnaissance
Situational Awareness
Wide Area Airborne Surveillance (WAAS)
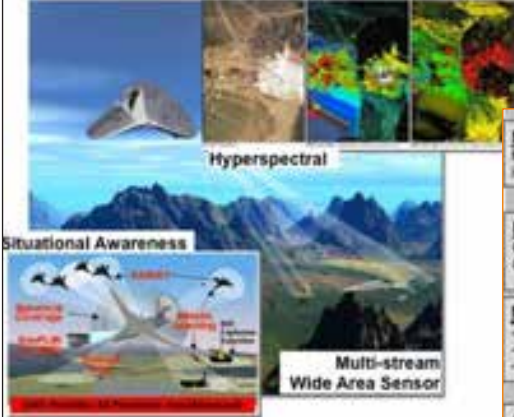
Heterogeneity: Micro and Nano-sized Vehicles, Medium "fighter sized" Vehicles, Large "tanker sized" Vehicles, and Special Vehicles with Unique Capabilities

Hyperspectral

Situational Awareness

Multi-stream Wide Area Sensor

Family of Systems
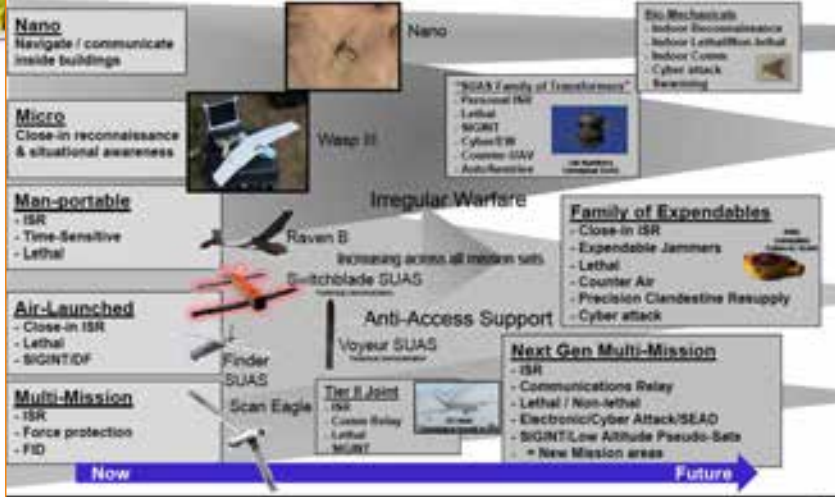
Lt. Gen. Deptula, 2010

Complex UAV Missions

- Cooperative Sensing
  - HUMINT
  - SIGINT
- Mixed Platforms / Capabilities
- Cooperation with Air and Ground Forces
- Dynamic Adaptive Workflows
- Adaptive Sensing, Computation, Communications

AFRL 31

Application of DDDAS Principles to Command, Control and Mission Planning for UAV Swarms

Increasing Operator Load – pilot and sensor operators may need to control "the swarm" not just one UAV

More Complex Missions – cooperate with other aircraft, ground resources, heterogeneous mix of UAVs

Dynamic Mission Re-Planning – surveillance, search & rescue, damage assessment

Resource Constraints – bandwidth, storage, processing, and energy

Maj. Gen. Hansen, 2009

DDDAS Simulation Test-bed

AFRL UAV Swarm Simulator – Dynamic Data Source

Agent-Based DDDAS Simulation – Dynamically Updated Application

Dynamic Adaptive Workflow – DDDAS System Software

Mission Performance – Global & Local Metrics Optimization

AFRL 32

Application of DDDAS Principles to Command, Control and Mission Planning for UAV Swarms

Ground Station

Operator Team
Mission Planning & Re-Planning
Command & Control
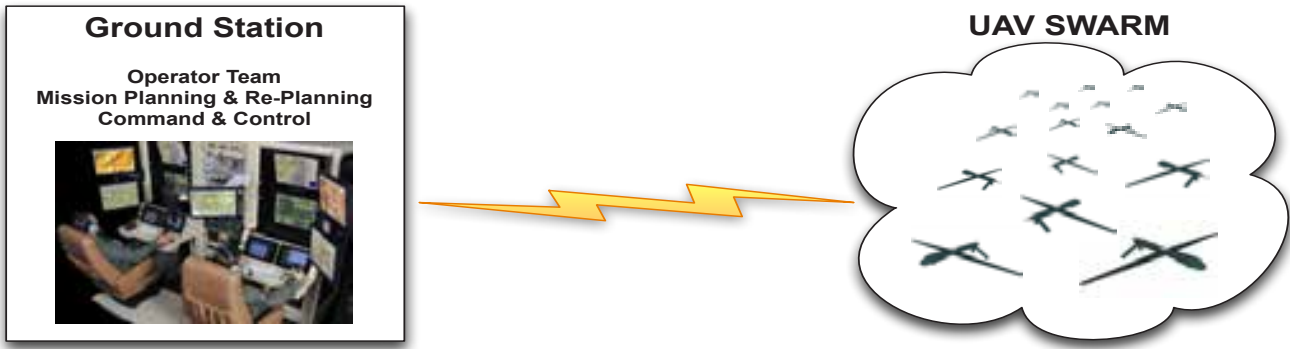
UAV SWARM

Application of DDDAS Principles to Command, Control and Mission Planning for UAV Swarms
Research Test-Bed

Agent-Based Simulator
Java/RePast/MASON

Abstract Simulation of Air Vehicles, Interaction with Environment and other Vehicles, and other Agents

Dynamically Updated Application

Control Parameters

System Software QoS Service Composition

Real-Time Sensor Feedback

UAV Swarm Simulator
MultiUAV2 - AFRL/RBCA

6DOF Simulation of Air Vehicles Tactical Maneuvering, Sensor, Target, Cooperation, Route, and Weapons

Sensor & Air Vehicle Performance

DDDAS Simulation of UAV Swarm   Synthetic UAV Swarm

How to ensure correctness and consistency in simulation that is dynamically updated?

Challenges / Possible Solutions

How to ensure correctness and completeness of dynamically updated workflows?

Atomic execution/rollbacks?   Deadlock detection?   Two phase commits?   Checkin/checkout?   Parallel execution paths?

DDDAS Approach To Volcanic Ash Transport & Dispersal Forecast

A. Patra, M. Bursik, E. B. Pitman, P. Singla, T. Singh, M. Jones – Univ at Buffalo; M. Pavolonis Univ. Wisconsin/NOAA;
B. P. Webley, J. Dehn – Univ Alaska Fairbanks; A. Sandu Virginia Tech

Problem: Currently used forecasts of ash transport in eruption of Eyjafjallajokull, Iceland caused total shutdown of large swathes of airspace, cancellation of more than 100,000 flights and total disruption! Significant discrepancy between no-fly zones, actual ash observation, and multiple model forecasts!
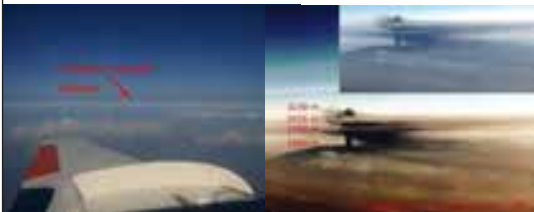
Solution: *Provide **probabilistic map** that can be updated dynamically with observations using a DDDAS approach*

Challenges: Uncertainty Analysis; High fidelity models representing the complex physics capable of needed near real time execution; Data and Workflow Management; Sensor error; measurement mismatch; imagery analysis
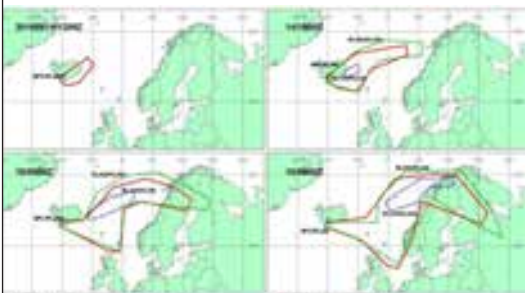
Opportunities: Platform for developing DDDAS; Support optimal flight planning; Timely and accurate hazard analysis preserves life and property

AFRL

34

DDDAS Approach To Volcanic Ash Transport & Dispersal Forecast

A. Patra, M. Bursik, E. B. Pitman, P. Singla, T. Singh, M. Jones – Univ at Buffalo; M. Pavolonis Univ. Wisconsin/NOAA;
B. P. Webley, J. Dehn – Univ Alaska Fairbanks; A. Sandu Virginia Tech

CALIPSO/SEVIRI

Satellite Image

Bayes

pdf Satellite Ash loading/footprint

pdf of Ash Plume

PCQ: Ensemble BENT-PUFF

Source Parameter pdf

AGMM

Uncertain Wind-Field (Data + NWP)

High Fidelity Simulator

Source Parameter ID

+
−

BENT: Eruption Plume Model
PUFF: Ash transport and Dispersal Model
PCQ: Polynomial Chaos Quadrature
AGMM: Adaptive Gaussian Mixtures
CALIPSO/SEVIRI: Satellite based sensors for ash detection

35

Other Examples DDDAS Projects funded by AFSOR (posted in www.DTIC.mil

- **Real-time Stream Mining: A New Dynamic Signal Processing Paradigm; PI: Suvra Bhattacharyya, UMD**
- **DDDAS: Computational Steering of Large-Scale Structural Systems Through Advanced Simulation, Optimization, and Structural Health Monitoring; PI: Yuri Bazievs, UCSD**
- **Transformative Advances in DDDAS with Application to Space Weather Monitoring; PI. Dennis Bernstein, U. of Michigan**
- **Dynamic Data-Driven Modeling of Uncertainties and 3D Effects of Porous Shape Memory Alloys; PI: Craig Douglas, U. of Wyoming**
- **Energy-Aware Aerial Systems for Persistent Sampling and Surveillance; PI: Eric Frew, U. of Colorado Boulder**
- **DDDAS-based Resilient Cyberspace (DRCS); PI: Salim Hariri, U of Arizona**
- **Bayesian Computational Sensor Networks for Aircraft Structural Health Monitoring; PI: Thomas Henderson, U. of Utah**
- **An Adaptive Property-Aware HW/SW Framework for DDDAS; PI: Phillip Jones, Iowa State U.**
- **Developing Dynamic Data-Driven Protocols to Study Complex Systems: The Case of Engineered Granular Crystals; PI: Yannis Kevrekidis, Princeton U.**
- **Dynamic Predictive Simulations of Agent Swarms; PI: Gregory Madey, U. of Notre Dame**
- **Development of a Stochastic Dynamic Data-Driven System for Prediction of Material Damage; PI: Tinsley Oden, UTAustin**
- **Application of DDDAS Ideas to the Computation of Volcanic Plume Transport; PI: Abani Patra, SUNY-Buffalo**
- **Dynamic Data Driven Machine Perception and Learning for Border Control; PI: Phoha et al, Penn State U.**
- **Fluid SLAM and the Robotic Reconstruction of Localized Atmospheric Phenomena; PI: Sai ravela, MIT**
- **A Framework for Quantifying and Reducing Uncertainty in InfoSymbiotic Systems Arising in Atmospheric Environments; PI: Adrian Sandu, VTech**
- **DDDAMS-based Urban Surveillance and Crowd Control via UAVs and UGVs; PI. Young-Jun Son, U. of Arizona**
- **PREDICT: Privacy and Security Enhancing Dynamic Information Monitoring with Feedback Guidance; PI: Vaidy Sunderam, Emory U.**
- **Active Data: Enabling Data-Driven Knowledge Discovery through Computational Reflection; PI: Carlos Varela, RPI**
- **DDDAS for Object Tracking in Complex and Dynamic Environments (DOTCODE); PI: Anthony Vodacek, RIT**
- **Dynamic Data Driven Methods for Self-aware Aerospace Vehicles; PI: Karen Wilcox, MIT**

36

Multicore-based Systems (InfoGrids)
(Multicores everywhere!)

Multicores in High-End Platforms
- Multiple levels of hierarchies of processing nodes, memories, interconnects, latencies

Multicores in "measurement/data" Systems
- Instruments, Sensors, Controllers, Networks, ...

Multiple levels of multicores

MPP   NOW   SP/instrumentation   PDA
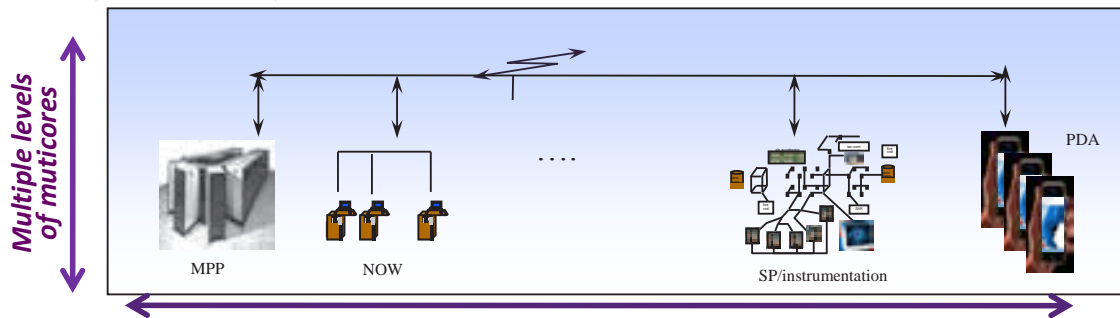
DDDAS - Integrated/Unified Application Platforms

Adaptable Computing and Data Systems Infrastructure
spanning the high-end to real-time data-acquisition & control systems
manifesting heterogeneous multilevel distributed parallelism
system architectures – software architectures

Fundamental Research Challenges in Applications- and Systems-Software
- Map the multilevel parallelism in applications to the platforms multilevel parallelism and for multi-level heterogeneity and dynamic resource availability
- Programming models and environments, new compiler/runtime technology for adaptive mapping
- Adaptively compositional software at all levels (applications/algorithms/ systems-software
- "performance-engineering" systems and their environments

SuperGrids: Dynamically Coupled Networks of Data and Computations

AFRL

37

Transformative Partnerships between Academe and Industry/Business

What will drive these U-I/B partnerships?
Address and Solve Hard Problems, that
Industry alone cannot do
Universities alone cannot do

Multidisciplinary R & D – Globalization

Methods and Tools to *enable* **Advanced Research in Academe**
Methods and Tools for ***New Capabilities for Industry***

Combine broad expertise in Academe

With Industry/Business know-how for building robust systems(prototypes)

Examples: **CyberInfrastructures for Complex Applications Systems**
(Need comprehensive systems frameworks – not just system components)

Models exist for long-term viability of such partnerships in self-sustaining ways (and where government funding contribution becomes minimized)

New Capabilities - New Directions through Advanced CyberInfrastructures (★)

"Innovation through CyberInfrastructure Excellence" (ICIE) (★)

(★) **Darema, Report on:** *CyberIfrastructures of Cyber-Applications-Systems & Cyber-Systems-Software*
(★) **Darema, Report on:** Industrial Partnerships in Cyberinfrastructure , *October 2009*

AFRL

38

- **DDDAS/InfoSymbiotics Multi-agency Workshop (August 2010)**
  - ➢ **AFSOR – NSF co-sponsored**
  - ➢ **Report posted at www.dddas.org (academic community website)**

Cross-Agencies Committee

DOD/AFOSR:
F. Darema
R. Bonneau
F. Fahroo
K. Reinhardt
D. Stargel
DOD/ONR: Ralph Wachter
DOD/ARL/CIS: Ananthram Swami
DOD/DTRA: Kiki Ikossi

NASA: Michael Seablom

NSF:
H. E. Seidel (MPS)
J. Cherniavsky (EHR)
T. Henderson (CISE)
L. Jameson (MPS)
G. Maracas (ENG)
G. Allen (OCI)

NIH:
Milt Corn (NLM),
Peter Lyster (NIGMS)

39

Summary

New discoveries and research and technology advances
at the interface and confluence of multiple science and engineering areas
through multidisciplinary approaches and multidisciplinary efforts

Computer Sciences and Information Technologies have become
key for advances in any other Scientific, Engineering, Societal fields

Transformative Innovations
through
University-Industry/Business partnerships catalyzed by Government

International component is important!

**AFOSR BAA www.afosr.af.mil
www.dddas.org**

40

The ascent towards exascale
… and the next wave of data

Data Intensive Systems

EF

PF

TF

GF

AFRL

43
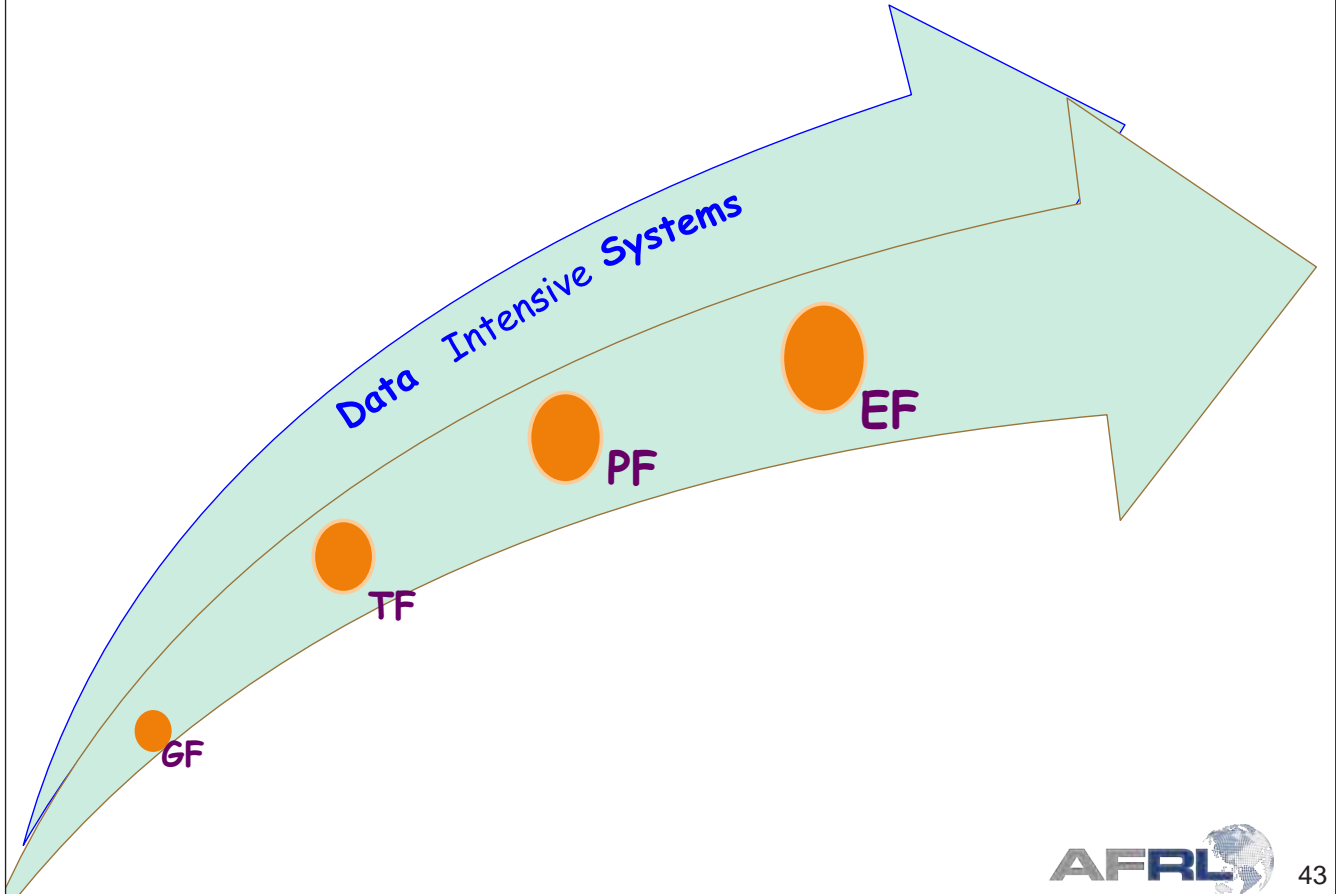
The ascent towards exascale
… and the next wave of data

Managing and exploiting the next generation of "data-intensive":
- **data from single large instruments; from complex "systems of systems" (including motoring data of the exascale platform itself)**
- **data from the large exascale simulations (to note also that in exascale, data movement becomes an over-riding factor – so "all?" exascale computations will be "data-intensive")**
- **the avalanche of data from the multitudes of heterogeneous networks of sensors (with adaptive resource management needs)**

Data Intensive Systems

EF

PF

TF

AFRL

44
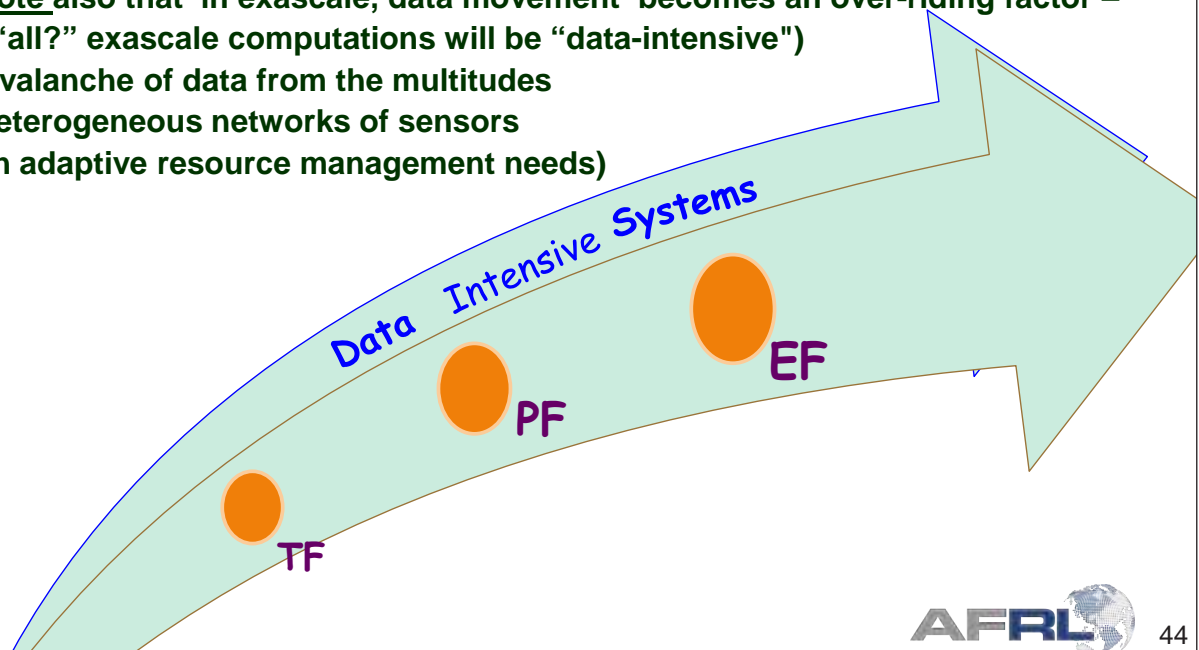
The ascent towards exascale

- **Achieving exascale poses significant challenges**
  (we saw some of that going from TF to PF)
- **Amounts to climbing several walls!**
  - **power constraints**
  - **multiple levels of hierarchy and heterogeneity**
  - **scalability challenge**
  - **accessing data challenge**
  - **fault/tolerance / resilience**

EF

PF

TF

GF
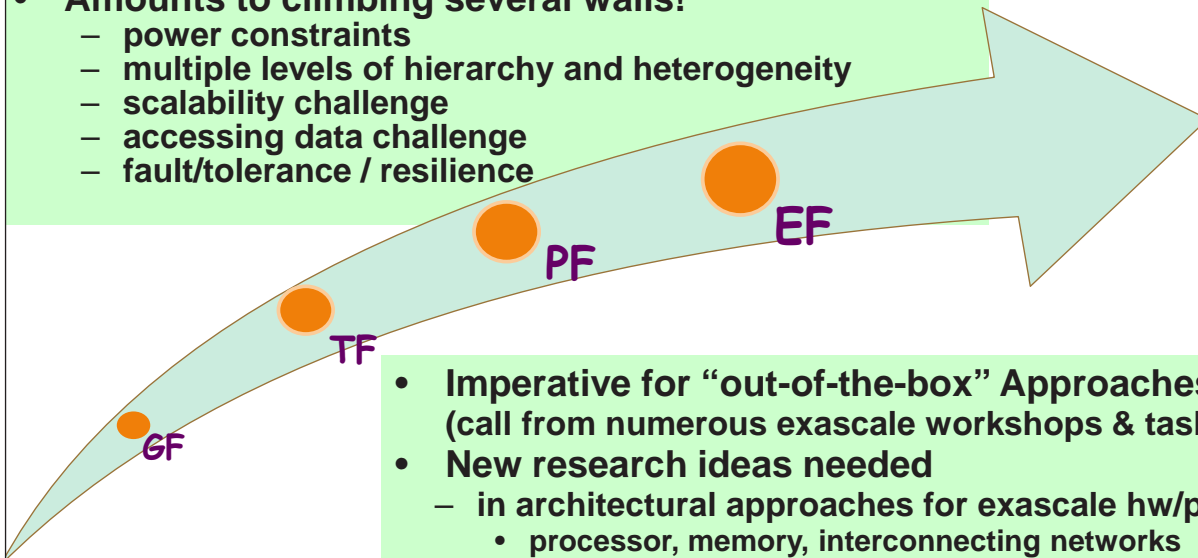
- **Imperative for "out-of-the-box" Approaches**
  (call from numerous exascale workshops & taskforces)
- **New research ideas needed**
  - **in architectural approaches for exascale hw/platforms**
    - **processor, memory, interconnecting networks**
  - **in applications, and application algorithms**
  - **in systems software**
    - **programming environments, compilers, OS, runtime, …**
- **Multidisciplinary Research&Technology**
  - **synergistic development:
    Applications – Systems Software – Hardware**

DDDAS for Object Tracking in Complex and Dynamic Environments (DOTCODE)

Anthony Vodacek , John Kerekes, Matthew Hoffman (RPI)

- Create capabilities to *enhance remote object tracking* in difficult imaging situations where single imaging modality is in general insufficient

- **Approach and objectives**
  - *Use the DDDAS concept of model feedback to the sensor which then adapts the sensing modality*
  - *Employ an adaptive multi-modal sensor in a simulation study*

- **Methodology**
  - Simulation study will leverage existing high spatial resolution Digital Imaging and Remote Sensing Image Generation (DIRSIG) scenes of a cluttered urban area and a desert industrial complex

DIRSIG: desert industrial complex

DIRSIG: obscurations and shadows

AFRL   46

DDDAS for Object Tracking in Complex and Dynamic Environments (DOTCODE)

Anthony Vodacek , John Kerekes, Matthew Hoffman (RPI)

- Research will leverage existing DIRSIG capability to model an adaptive multimodal sensor (HSI and polarization)
- DIRSIG animations of moving objects
- Object tracking will be done using particle filter approach
- Adaptive image processing routines to be developed
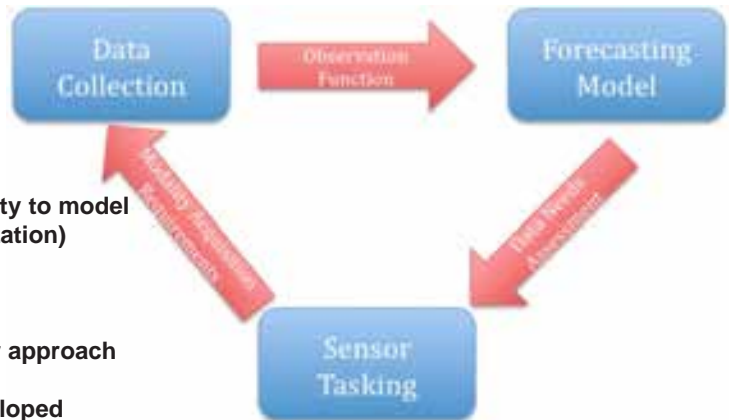
HSI/polarization sensor concept

The multi-modal sensor - hyperspectral imaging (HIS) and polarization is under development with AFOSR funding

Vertical Displacement

MEMS etalon
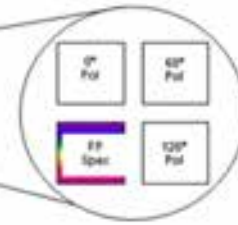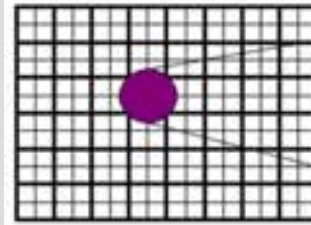
Super pixel concept with etalon and polarization

47

Where we are … & QUO VADIMUS

- **DDDAS/InfoSymbiotics**
  - high pay-off in terms of new capabilities
  - need fundamental and novel advances in several disciplines
  - research agenda comprehensively defined
- **Progress has been made – it's a "multiple S-curve"**

  Applications Modeling Math&Stat Algorithms Systems Software Instrumentation/Control Systems

  - experience/advances cumulate to accelerate progress in the future
  - we have started to climb the upwards slope of each of these   S-curves
  - reinforce need for sustained, concerted, synergistic support
- **Workshop and Report (August 30&31, 2010)**
  - DDDAS/InfoSymbiotics broad impact - Multi-agency interest
  - can capitalize on past/present progress through projects started
  - timely in the landscape of: ubiquitous sensing/instrumentation, big-data, multicore-based high-performance systems, multicore modeling, uncertainty quantification,
  - the present landscape enriches the research agenda and opp

In 2002 DDDAS provided the initial funding for the Generalized Polynomial Chaos work (Karniadakis and Xiu)

48

DDDAS Approach To Volcanic Ash Transport & Dispersal Forecast

A. Patra, M. Bursik, E. B. Pitman, P. Singla, T. Singh, M. Jones – Univ at Buffalo; M. Pavolonis Univ. Wisconsin/NOAA;
B. P. Webley, J. Dehn – Univ Alaska Fairbanks; A. Sandu Virginia Tech

Interim Progress:

- **Developed parallelized PCQ/Bent-Puff HPC based tool for probabilistic ash forecasting**

- **Physics based methodology for VATD "transport and dispersion" model inputs –**
  poorly characterized column height, mass eruption rate replaced by pdf of observable vent parameters and speed.

- **PCQ based probabilistic hazard analysis replaces predictions of existing tools.**

- **Results for Eyjafjallojokull are very promising –**
  all ash observed was inside a Probability>0.2 contour with most in Probability >0.7

- **Presently, this is the only risk-based (probabilistic) forecast for ash cloud with full transport modeling**

49
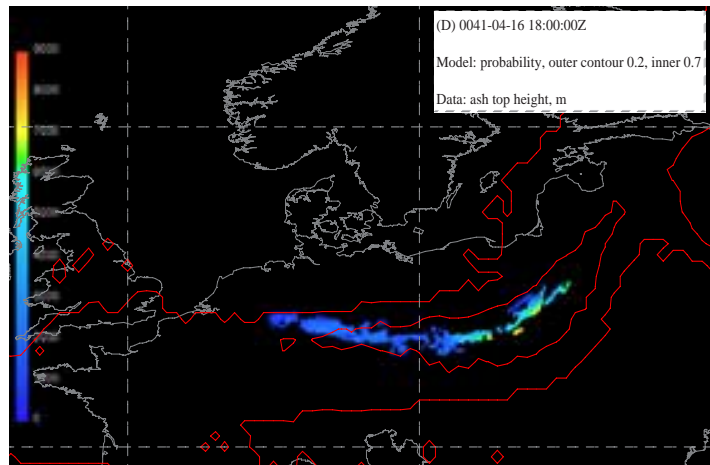
Numerical noise prediction of a generic flap configuration

Lilla Kapa-Koloszar
Patrick Rambaud
Philippe Planquart
Christophe Schram

von Karman Institute
B-1640 Rhode-Saint-Genèse,
Belgium
koloszar@vki.ac.be

Abstract

The present work deals with the turbulent flow simulation of an airfoil with a generic flap. The purpose of this simulation is to provide the time history of the pressure field on the wing and on the flap for noise prediction. The configuration and the flow conditions were defined in the FP7 VALIANT project. Within this framework measurements were performed in Ecole Central de Lyon, to which the present simulation is compared. In order to be able to reproduce the measurements with numerical simulation, the experimental velocity profiles on the middle of the wing were used as inlet boundary conditions. In this work three different inlets were used and the resulting flow fields were compared.

Key words: aerodynamics, large eddy simulation, incompressible flow, high-lift device.

Introduction

During aircraft approach and landing, a significant portion of noise is generated by the high-lift devices. Reducing the noise during landing is very important for the comfort of the residents living nearby an airport. The airframe noise during take-off maneuver is less important, since the slope of the take-off is much steeper, and the engines are in full trust, louder than any other component. Among the various noise sources during approach and landing, the landing gear, leading-edge slat and the side edges of the flap where identified as the main airframe noise sources [2].

In order to isolate the noise produced by an aircraft flap in landing configuration, a semi infinite wing was considered in front of the flap. The flap is placed under the wing with a bit of overlap. This configuration was installed in the anechoic wind tunnel of Ecole Central de Lyon and both flow and acoustic measurements were performed in the framework of VALIANT (VALidation and Improvement of Airframe Noise prediction Tools [3]) FP-7 European project [1]. The main characteristics defining the flow are the free-stream velocity $U_\infty = 51\,m/s$, which corresponds to approach condition with $Ma = 0.15$. The resulting Reynolds number, $Re = 1.36 \cdot 10^6$, is approximately $1/10^{th}$ of the Reynolds numbers corresponds to a real aircraft wing during approach. Roughness elements (sandpaper ISO P150) were placed on both sides of the wing in order to trigger an established incoming turbulent boundary layer. The experimental database obtained by ECL includes the following data: time-dependent microphone signals, time-dependent wall pressure signals, time-dependent series of the velocities acquired from hot wire measurements.

The current paper describes an incompressible Large-Eddy simulation of this geometry with different inlet boundary conditions. The first section describes the computational domain and the structured mesh used. The second part of the paper introduces the numerical method and the boundary conditions applied. The next section

discusses the effect of the inlet boundary condition on the resulted flow field, while the last part concludes the work.

Solution domain and grid

The computational domain and applied boundary conditions are graphically presented in Figure 1. As can be seen in the figure the flap is placed under the wing with a bit of overlap. In the experiments the wing is represented as a semi-infinite plate and it is starting inside the convergence section of the wind tunnel. In the computations half of the semi-infinite wing is considered where hot-wire measurements are available on both side of the wing.

The lateral boundaries are implemented as symmetry planes. The boundary follows the shape of streamlines predicted by the 2D RANS simulation. The downstream boundary is placed 5 flap-chords away from the objects.
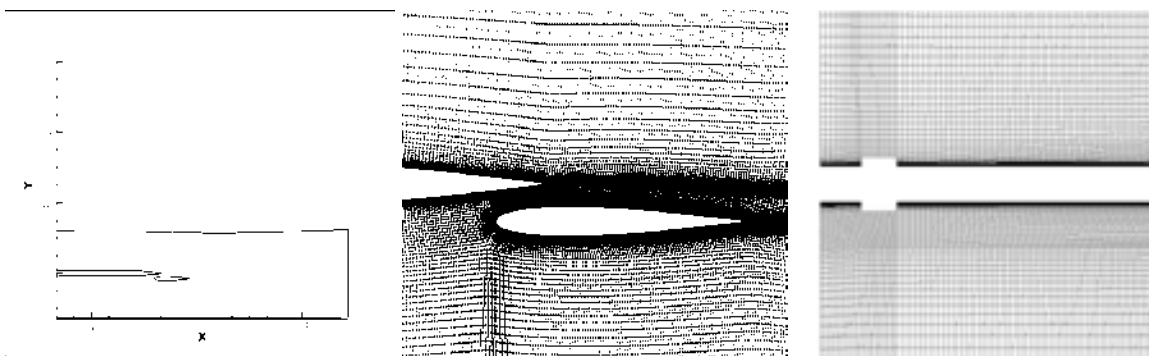
Figure 1: Computational domain, the mesh around the flap and the inlet bump

The grid requirement of high fidelity simulations, such as the presently applied Large Eddy Simulation, is scaling with the Reynolds number on the power of $9/4^{th}$. Therefore, it is still very challenging to perform numerical simulation of a wing with deployed high-lift system due to the high Reynolds number (Re $\sim 10^6$-10^7). This is even truer for acoustic simulations, where the smallest grid size is determined by the Kolmogorov length scale, while the largest grid size is restricted by the frequency resolution of interest.

A block mesh was generated to ensure a mesh with sufficient quality for Finite Volume Method. First, a 2D mesh was constructed and was extruded in the span-wise direction. The measurement setup had quasi-2D geometry as well. The span-wise extend was chosen to be 10% of the setup chord only (chord of the wing + chord of the flap - overlap). The final mesh has 6.08 million cells.

Flap noise is greatly affected by the flow around the main wing. Therefore, a correct representation of the boundary layer on the wing is important. In the present simulation the inflow conditions were provided by hot-wire measurements. In order to capture the dynamics of the incoming boundary layer a dense boundary fitted mesh was generated. The y^+ never exceed 3 in the whole domain.

Aeroacoustic noise at subsonic velocities is mostly generated when turbulent structures impact and pass-over solid boundaries. The overlapping region is highly refined in order to accurately resolve the incoming turbulence arriving from the wing and impacting on the leading edge of the flat. Due to this intensive turbulence-body interaction, the mush weaker noise generated by the finite trailing-edge is neglected. A sharp trailing edge was considered in case of the wing and in case of the flap as well.

Away from the region of interest, the grid was coarsened in order to keep to the minimum the cost of the computation. Previous studied showed that the grid can induce spurious reflections if the cell-to-cell ratio is higher than 1.1, so the grid coarsening was performed according.

Model and simulation details

The setup described in the previous section is initialized by a steady-state RANS simulation. Then the incompressible Large-Eddy simulation solver of the open-source simulation environment OpenFOAM version 1.7.1 [4] was used in order to resolve the pressure fluctuations in time on the solid surfaces. The dynamic Smagorinsky model was used to model the unresolved scales.

In the first part of the unsteady simulation a first order upwind scheme was used (half flow through) and once the flow was established it was changed to second order upwind combined with backward Euler time discretization. The time-step was chosen to keep the Courant number under 0.75. Accumulation of data for averaging purposes only commences after flushing of the calculation domain for three and a half flow-through time. Ideally the averaging time should be large enough so that the mean data reaches steady state. Computations were carried out on the SGI Altix ICE 8200 dual plane cluster of VKI (64 blades equipped with 128 quad cores Xeon processors at 2.5 Ghz/12M/1333MHz, with 256 set of 4 GB DIMM (2x2GB 667 MHz) and Infiniband connection). 0.001s of simulation time took approximately 30 CPU hours of physical time on 64 nodes.

In the measurements, at the inlet of the wing, a turbulent strip was attached to in order to mimic the flow field induced by a deployed slat. Three different approaches have been used to impose the inlet boundary condition in the numerical simulation. In all the cases, the measured, time-averaged velocity profiles were used as base. In Case 1 no perturbations were imposed to this profile, in Case 2 random perturbations were superimposed, which were scaled with the measured turbulent intensity. This approach is rather rough, since turbulence is much more than a random perturbation around the mean flow. The coherence of the incoming boundary layer won't be captured that way, but it was hoped that the long wing section will be enough to build up the missing coherence.

Finally, in Case 3, again a constant profile was used, but the wing geometry was modified such that the turbulent strip was represented by a bump. As it can be seen in the right side of Figure 1, the mesh is not resolved around the bump, since the aim of the object is only enhance turbulence and not its correct physical description. The height of the bump was chosen to 5mm, which is approximately half of the boundary layer thickness on the wing. This height is somewhat arbitrary and needs further investigation to correlate it with the desired r.m.s. velocity.

The three different boundary conditions are summarized in Table 1.

Table 1: Simulation cases

Case specification	Applied inlet boundary condition
Case 1	Mean velocity profiles
Case 2	Mean velocity profiles with random perturbation
Case 3	Mean velocity profiles with bump

Above and below the wing, the free-field boundaries were set as symmetry planes. These boundaries were extracted along the streamlines of an initial 2D RANS simulation of the whole experimental setup, through which no flow is possible. On the spanwise boundaries periodic boundary condition is applied, since it was not possible to simulate the whole experimental domain with the endplates due to the high computational cost. Measurements later confirmed that the shielding of the endplates successfully reduced the noise generated by the flow around them, so considering just this small slice of wing with periodic BCs can be sufficient [3].

Flow features and dynamics

Case 1 and Case 2 gave approximately the same velocity filed, so in the following Case 1 and Case 3 will be compared. The first set of results show the flow around the wing and flap in a pure qualitative sense. The different inlet approaches results in different flow fields. The suction side of the main wing is undisturbed. In Case 1 and 2 a recirculation zone is formed near the trailing edge upstream. At the pressure side the recirculation bubble is still present, but its size is smaller than on the suction side, due to the accelerated flow between the wing and flap (Figure 2). Three separation bubbles are predicted by Case 1 (and 2) simulation.

There is one large in the upper part of the wing around the trailing edge and one smaller in the lower part. The third separation bubble can be found at the lower part of the flap trailing edge.
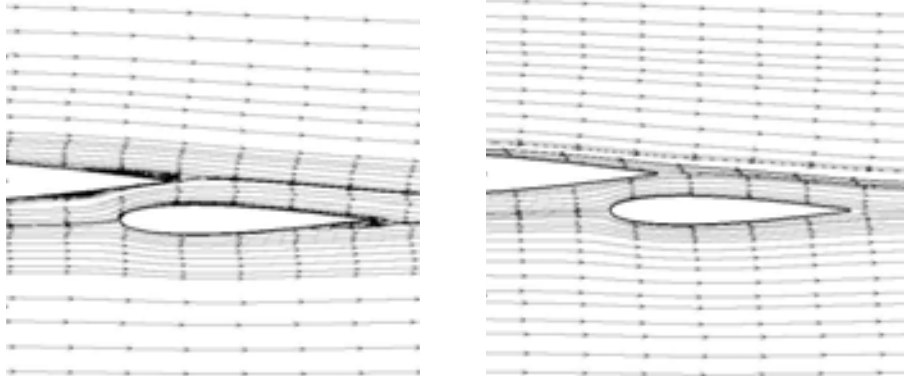.

Figure 2: Mid-span plane velocity: mean streaklines: Case 1 (left) and Case 3 (right)

In the simulation with the bump no separation bubble is present. This is due to the higher energy contents of the turbulent boundary layer triggered by the bump. The flow is indeed turbulent over the wing as visualized by the Q structures in Figure 3. In case of the random perturbations no coherent structures can be observed over and below the wing, transition to turbulence starts at the wing trailing edge. In order to trigger the turbulence along the wing, the magnitude of the random perturbation was increased, but this attempt leaded the simulation to diverge.
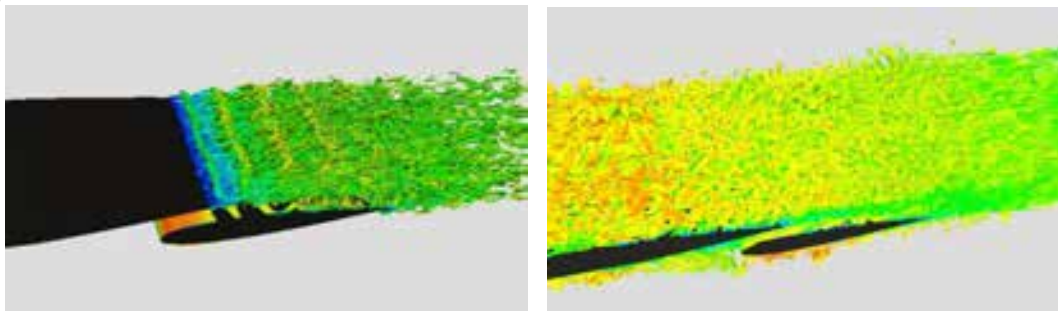
Figure 3: Iso-Q surfaces colored by the velocity magnitude (Q=106). Left – Case 1, right – Case 3

It can be seen (Figure 4) that in Case 1 periodic vortices are shedding from the main wing trailing edge. These vortices partially impact on the flap suction side. The presence of the strong vortex shedding is the indication that the boundary layer on the wing stays laminar. These structures travel along the flap and are feeding energy into its boundary layer, such that it stays attached. The strong periodic vortices are not present in the Case 3 simulation. Much weaker, but more distributed velocity fluctuations can be observed in the right side of Figure 4, corresponding to this simulation.
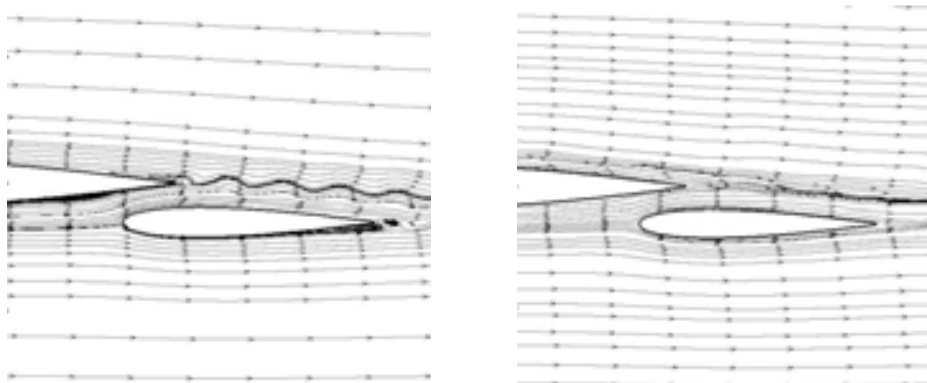
Figure 4: Mid-span plane velocity: instantaneous streaklines: Case 1 (left) and Case 3 (right)

Indeed, in Figure 5 we can see that the vorticity is homogenous along the wing in Case 1, while shows a turbulent structure for Case 3. On the left figure, strong large vortices can be identified, while on the right figure several, small fluctuations are visible.
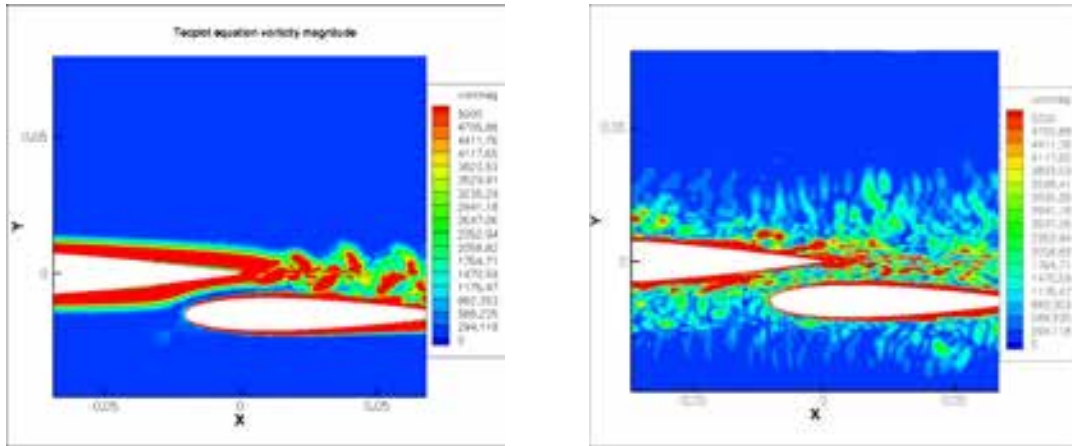
Figure 5: Mid-span instantaneous vorticity at the mid-plane: Case 1 (left) and Case 3 (right)

Figure 6 and Figure 7 compares mean- and r.m.s. velocity profiles at two streamwise locations. The first velocity profile is extracted *5mm* upstream to the wing trailing edge. It means that it contains the boundary layer of the wing suction side, the gap between the wing and the flap and the boundary layer on the flap pressure side. As we can see on the mean velocity profiles, the application of the bump indeed improves the boundary layer on the wing, however we got a faster flow along the flap and inside the gap, than in case of the laminar inflow. Moving downstream on the flap, the situation improves a bit on the suction side of the flap, however, the CFD simulation still over predicts the experimental values.
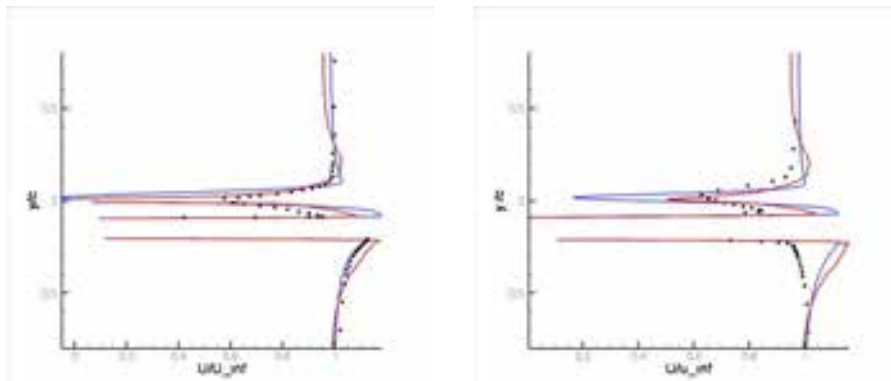
Figure 6: Mean streamwise velocity profiles 5mm before the wing trailing edge and before the flap trailing edge (x= -0.005, 0.079). Black
dots – measurement, blue line – Case 1, red line – Case 3.
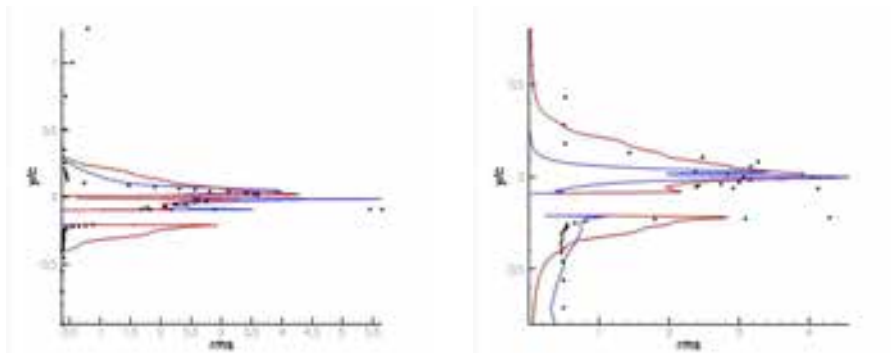
Figure 7: R.m.s. streamwise velocity profiles at 5mm before the wing trailing edge and before the flap trailing edge (x= -0.005, 0.079).
Black dots – measurement, blue line – Case 1, red line – Case 3.

The wall pressure sensors in the experiments are indicated in Figure 8.
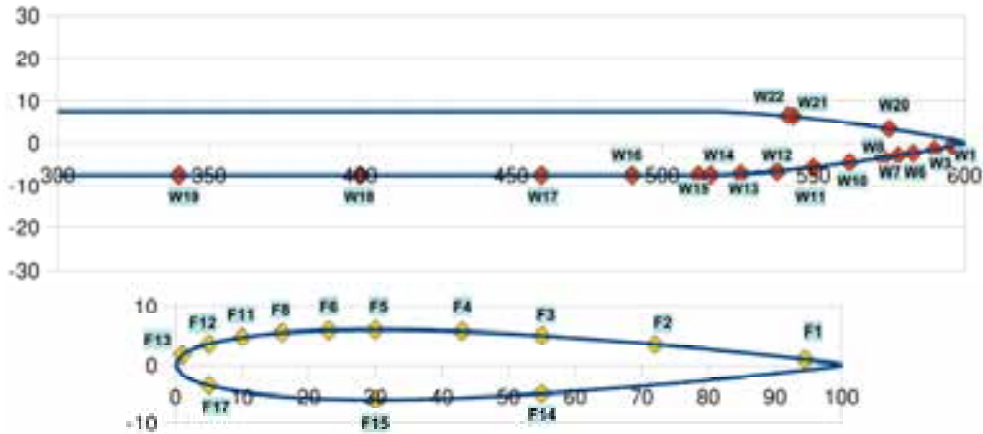
Figure 8: Wall pressure sensors along the wing and the flap

After post-processing the wall-pressure signals at different locations another artefact of the random turbulent inlet were discovered. Despite the laminar, but still meaningful velocity field, the pressure signal was completely uncorrelated due to the white noise inlet perturbation (Figure 9).
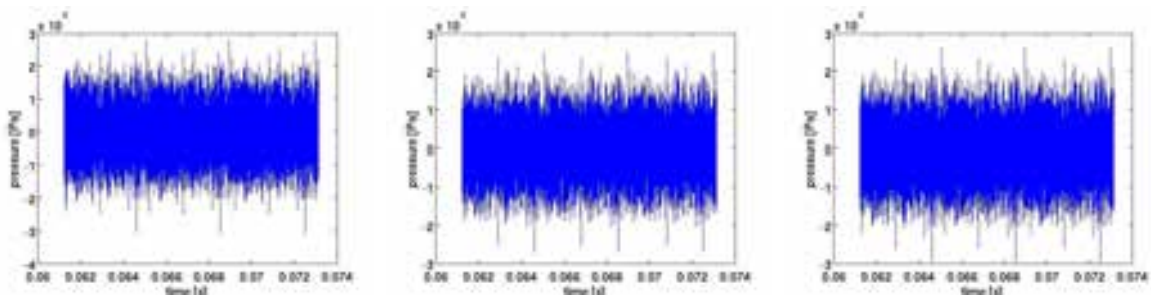
Figure 9: Case 2 pressure time-history at various x locations (W12, W15, W20)

To cure this problem, the random perturbation at the inlet has been switched off. Within few time-steps, the pressure signal seemed to be recovered (Figure 10).
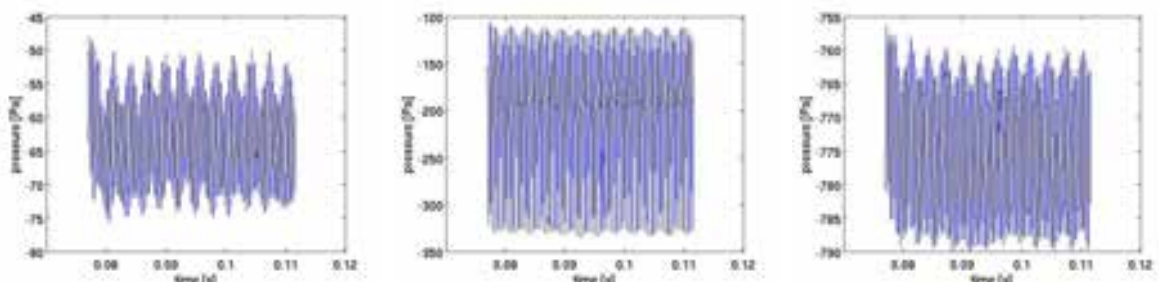
Figure 10: Case 1 pressure time-history at various x locations (W12, W15, W20)

Turning off the random velocity perturbation gave a correlated velocity-pressure signal, but is resulted a laminar dominated flow-field. To be able to reproduce the physics in the experiments a physical bump was introduced in the solution domain mimicking the effect of the turbulent strip. As we could see previously, the flow structure around the wing and flap has changed considerably. The mean and r.m.s. velocities got closer to the measured ones. The corresponding pressure signals are less periodic than the ones correspond to the laminar Case 1 simulation (Figure 11). The simulation time corresponding to Case 3 is approximately half of the other two, which means that we should expect less accurate pressure spectra in the low frequency range corresponding to this case.
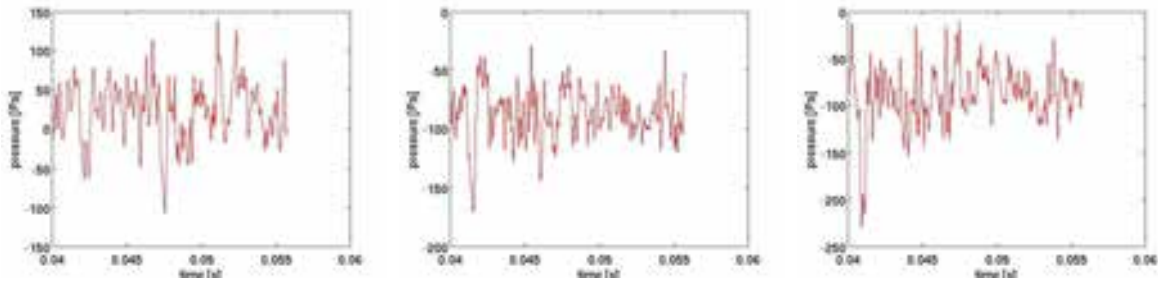
Figure 11: Case 3 pressure time-history at various x locations (W12, W15, W20)

In the following, the wall pressure spectra of Case 1 and Case 3 will be compared with the measurement data provided by ECL in various locations. Figure 12 shows three pressure spectra on the wing. The first probe depicted is located on the pressure side furthest upstream from the wing trailing edge. The measurement shows a completely broadband spectrum, indicating an energetic, stable turbulent boundary layer. At the high frequency region ($f \approx 9-10 kHz$) there is a tonal peak which can be found in the next spectra corresponding a bit further downstream, but on the suction side. They are both very close to the geometrical change due to the trailing edge, which might induce some high frequency instabilities. This effect cannot be observed any more very close to the trailing edge, Figure 12 last picture, where the spectrum is decaying in the high frequency region. This high frequency bump is not reproduced by any of the simulations due to the insufficient grid resolution.

The laminar-like vortex shedding is pronounced by a strong peak in the pressure spectra corresponding to Case 1. The vortex shedding frequency is 1100 Hz. This peak can be observed in all the spectra due to the non-compactness of the trailing edge noise. In the Case 1, all other frequencies are damped and the general broadband noise level is lower.

The turbulent boundary layer corresponding to Case 3 results in a completely broadband spectrum, all the frequencies represented equally. This simulation is capturing better the measurements. The discrepancies in the low frequencies are due to the short simulation time, as pointed out earlier.
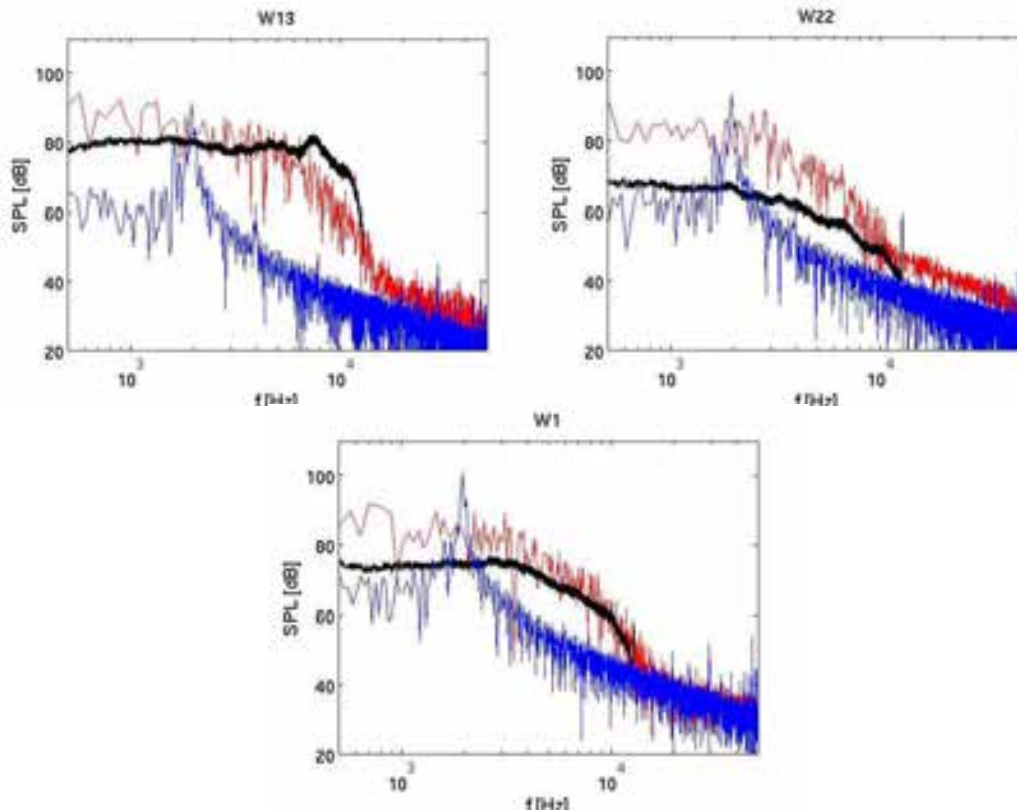
Figure 12: Pressure spectra on the wing. Black – measurements, blue – Case 1, red – Case 3.

Figure 13 shows pressure spectra on the flap starting from the flap trailing edge suction side to the leading edge till the flap pressure side trailing edge. Along the suction side in the laminar case, Case 1, not just the main vortex shedding frequency is present, but its harmonics, too, indicating vortex pairing along the passage over the flap. In pressure spectra corresponding to the pressure side only the vortex shedding peak is present. Again, the Case 3 simulation compares better with the measurements. However, it over predicts the measured noise levels close to the leading edge of the flap, which means that the incoming boundary layer is more energetic in the simulation than in the experiments. This is confirmed by the higher r.m.s. velocity levels shown in Figure 7.
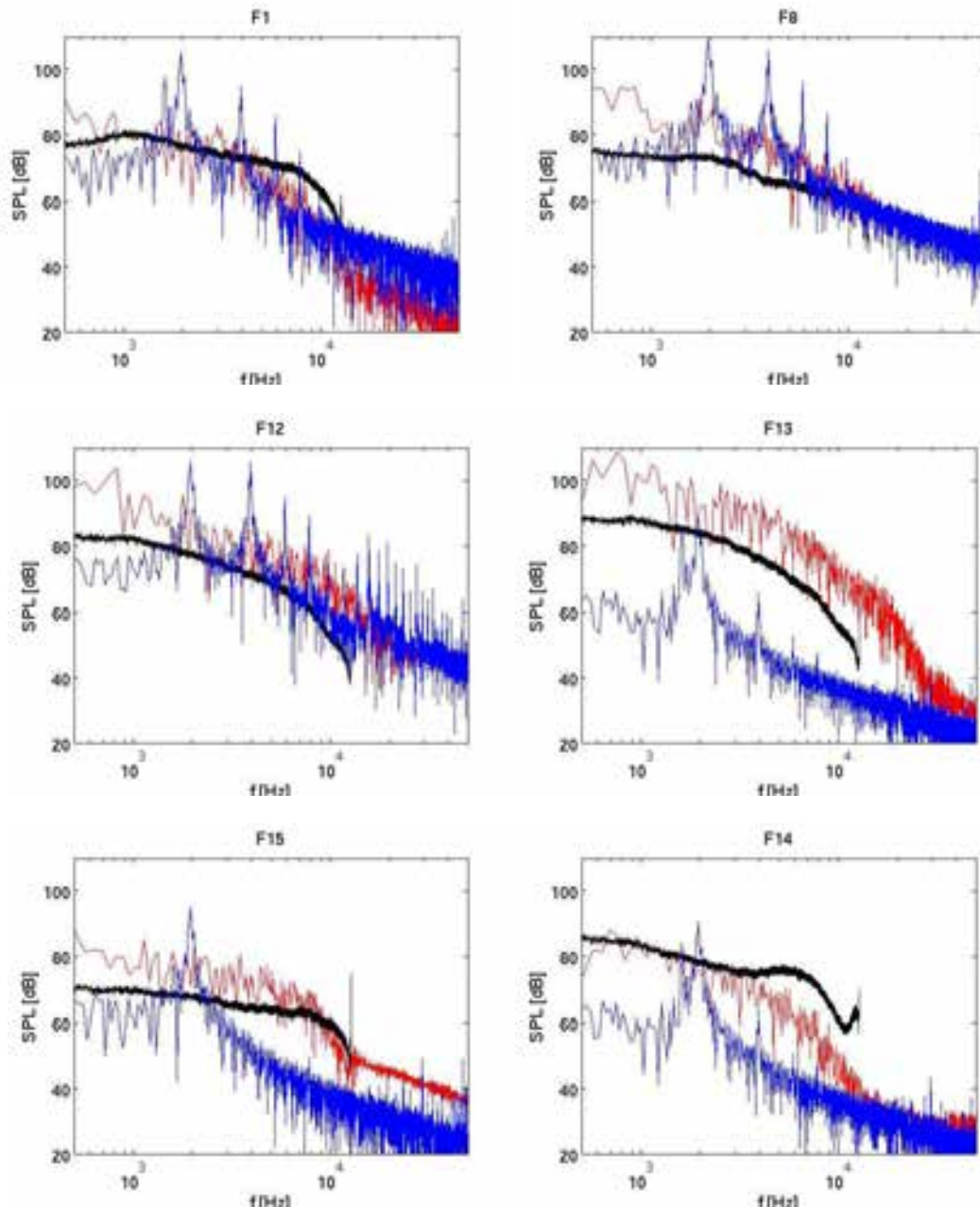
Figure 13: Pressure spectra on the flap. Black – measurements, blue – Case 1, red – Case 3.

The spectrum at the trailing edge of the flap is very similar to the ones on the wing. The shape is different, however, in the flap nose region. The turbulence arriving from the wing impinges to the flap inducing higher noise levels in the low frequency regions, while lower levels in the high frequency region. This is most probably due to the fact that in the leading edge region the turbulent boundary layer is not developed yet. A relatively homogeneous turbulence is impinging on the flap, which gives the decaying spectrum. At the suction side, the

decay is less fast. Due to the gap, the structures got elongated which feeds energy to the mid-frequency region. These elongated structures then interact with the shear layer developed after the wing trailing edge and are advected downward along the flap suction side.

Conclusions and further work

An incompressible Large-Eddy Simulation was carried out to study the aerodynamics of simplified flap and wing configuration, with a particular emphasis on the pressure field on the solid surfaces. Three different inlet boundary conditions were used in order to reproduce the measurements performed at Ecole Central de Lyon. This comparison showed that the inlet boundary condition strongly determines the physics involved in the numerical simulation. Imposing a steady measured profile at the inlet of the computational domain resulted in a laminar vortex shedding from the wing trailing edge. This deterministic behavior is not present in the measurements. Therefore, a better representation of the flow field in the experiments thought to be achieved by triggering the incoming flow.

Two simple approaches were used to establish a turbulent boundary layer over the wing. First a random perturbation was superimposed to the mean measured velocity profile. Since it resulted in an uncorrelated pressure field a different solution had to be found. A physical bump was added to the computational domain to mimic the strip installed on the wing in the experimental mock-up. The effect of the bump was not strongly pronounced in the mean and r.m.s. velocity profiles, but are well visible in the vorticity field. The flow turned to turbulent over the wing, as desired. It has improved significantly the pressure spectra indicating that the energy contents of the flow have changed due to the presence of the bump in the right direction.

None of the simulations were able to reproduce the high frequency peak in the pressure spectra close to the wing or the flap trailing edge due to the insufficient grid resolution. Besides this, the Case 3 simulation fairly well captures the spectra along the wing. The spectrum at the trailing edge region of the flap is very similar to the ones on the wing and the pressure levels are well captured by this simulation, too. In the flap leading edge region the spectra is considerably different. It resembles more to the spectrum corresponding to homogeneous turbulence. Indeed, the upper part of the wing boundary layer is impinging to the flap nose, where the boundary layer is not developed yet. In terms of pressure levels, this is the region where most deviation is observed, indicating that the turbulence level of the wing boundary layer is higher than the one present in the measurements.

The current simulation successfully reproduces the basic physics that occurs in the generic wing with flap configuration, however some improvements are still recommended. The mesh should be refined in the wing and flap trailing edge region in order to capture the high frequency peak in the spectra. The height of the bump added to the computational domain should be optimized to retrieve the correct dynamics of the boundary layer along the wing.

Acknowledgement

References

[1] B. Lemoine, M. Roger & I. Legriffon: Aeroacoustics of a Model Non-Lifting Wing-Flap System in a Parallel Flow, 17th AIAA/CEAS Aeroacoustics Conference, 6-8 June, Portland OR, AIAA paper 2011-2735, 2011.

[2] W. Dobrzynski, K. Nagakura, B. Gehlar and A. Buschbaum: Airframe noise studies on wings with deployed high-lift devices, AIAA - 98-2337, 1998

[3] http://www.cimne.com/websasp/valiant/

[4] http://www.openfoam.com

Computational Efforts in Designing Experiment for High-lift Aeroacoustics

Mitsuhiro Murayama
Yuzuru Yokokawa
Kazuomi Yamamoto
Yasushi Ito

Aviation Program Group, Japan Aerospace Exploration Agency
7-44-1 Jindaiji-Higashi, Chofu, Tokyo 182-8522
Japan
murayama.mitsuhiro@jaxa.jp, yokokawa.yuzuru@jaxa.jp, yamamoto.kazuomi@jaxa.jp, ito.yasushi@jaxa.jp

Kazuhisa Amemiya

Advanced Science & Intelligence Research Institute
1-18-14 Uchikanda, Chiyoda-ku, Tokyo 101-0047
Japan
amemy@chofu.jaxa.jp

Kentaro Tanaka
Tohru Hirai

Ryoyu Systems Co., Ltd.
2-19-13 Takanawa, Minato-ku, Tokyo 108-0074
Japan
kentaro@chofu.jaxa.jp, thirai@chofu.jaxa.jp

Abstract

In this paper, computational efforts in designing experiment for a series of wind tunnel tests of high-lift airframe noise measurement and the importance are shown. This paper describes computational evaluations of the design of wind tunnel testing model, the model sizing and mounting in wind tunnel, and influences of shear layer and mounted plate on the sound propagation in open-cart test section. It is shown that preliminary CFD investigation of the wind tunnel tests can decrease unknowns and improve the accuracy of the wind tunnel test.

Key words: high-lift, aeroacoustics, computational fluid dynamics, wind tunnel test

Introduction

With recent interest in the environmental problems, regulations for aircraft noise around airports have tightened. Due to successive efforts for noise reduction from aircraft engines, airframe noise is getting prominent for the overall noise level, especially during approach where engines are throttled down. Therefore, noise reduction technologies for the airframe noise are getting important for developments of future commercial aircraft. The

noise from high-lift devices deployed during landing and take-off such as leading-edge slat and trailing-edge flap is known as one of major noise sources of the airframe noise besides the noise from landing gears [1-3].

Recent progresses of CFD technologies solving Reynolds-Averaged Navier-Stokes (RANS) equations and computer resources have improved the accuracy to predict the steady-state aerodynamics phenomena and performance to a useful level applicable in the design process, even for full-aircraft configurations deployed high-lift devices [4-6]. In recent years, efforts to validate and improve CFD/CAA (Computational AeroAcoustics) for airframe noise computations have been promoted internationally through several workshops such as BANC (Workshop on Benchmark problems for Airframe Noise Computations) [7-8]. However, the daily use of CFD/CAA to simulate the noise from high-lift devices especially for full aircraft configurations still requires to solve several difficulties in the grid generation, prediction accuracy and computational resources. The airframe noise research still relies largely on wind tunnel testing, collaborating with numerical simulations. JAXA has conducted research work using a series of wind tunnel tests and numerical simulations on the noise generation mechanism and reduction technologies around the high-lift devices and landing gears [9-15]. To investigate the airframe noise from high-lift devices, several research models such as a simple rectangular single wing model and a realistic wing-fuselage model deployed high-lift devices have been used for the wind tunnel tests and numerical simulations [6, 16-17]. The research using the most complicated wing-fuselage model deployed high-lift devices with an engine nacelle, which is the wind tunnel testing model basically for aerodynamic test purpose, had tried to identify the noise sources and characteristics generated from the realistic aircraft configurations such as slat side-edges. On the other hand, dimensions of slat and flap are small in the half-span wind tunnel testing model of complete aircraft configuration with 2.3m half-span length. The flowfields are complicated with interferences of engine-nacelle. They made it difficult to investigate the detail flowfields around identified noise sources and basic noise characteristics from each component. The research using a simplified three-dimensional high-lift wing model, "OTOMO", shown in Fig. 1 had clarified the details of noise characteristics and generation mechanisms from high-lift devices [9-15]. The studies using the models had improved techniques of the wind tunnel tests such as noise source identification using phased-array microphones and flow visualization using PIV and numerical simulation methods such as LES and LES/RANS hybrid method. In addition, the devices and concepts to reduce the noise have been also proposed and validated using the models.
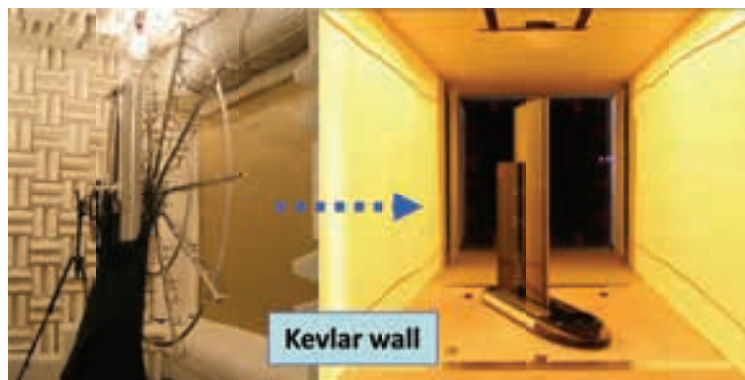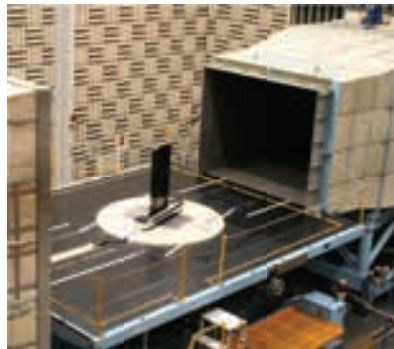

(i) Solid-wall cart   (ii) Anechoic Kevlar-wall cart
(a) 2m × 2m JAXA-LWT2

(b) 3m × 2.5m Large-Scale Anechoic Wind Tunnel in Railway Technical Research Institute

Fig. 1 JAXA high-lift device noise research model, "OTOMO" mounted in the wind tunnel facilities [9-15]
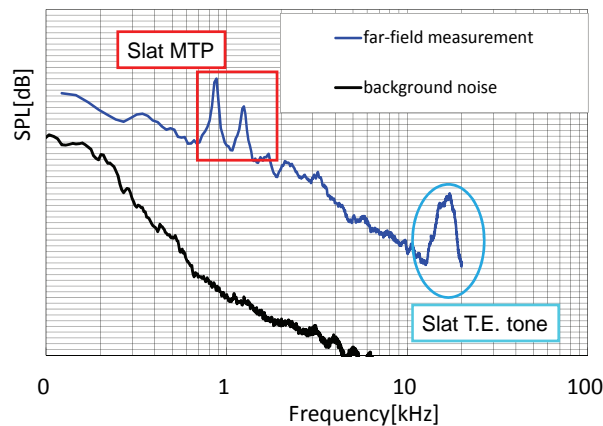
Fig. 2 Example of narrow-band spectra of far-field SPL of OTOMO model [11]

The research model shown in Fig. 1 employed a rectangular wing planform and omitted the sweep angle, taper, and dihedral angle. Toward further improvements to predict and reduce the airframe noise from actual aircrafts, the influences of the omitted parameters on the noise generation mechanisms and the effectiveness of devices and concepts to reduce noise should be investigated well. For example, in several wind tunnel test results such as two-dimensional wind tunnel test results and test results using JAXA's rectangular high-lift wing model [11], Multiple Tonal Peaks (MTPs) generated from slat are observed as shown in Fig. 2. On the other hand, it has been said that MTPs are not necessarily observed in flight test results. In addition, noise sources are often identified around detail parts such as slat tracks and cavities in flight test results of actual aircrafts, which are specific in the actual aircrafts and not modeled or simplified in the wind tunnel testing model. The influences of such detail parts in actual aircrafts should be also clarified for further improvements to predict and reduce the airframe noise from actual aircrafts.

To investigate the influences, a half-span three-element high-lift wing model with taper and sweep angle were designed and fabricated for the purpose of high-lift device noise research. A series of wind tunnel tests have been conducted since 2011. In this paper, the computational efforts in designing experiment for the wind tunnel tests and its importance are shown. For successful wind tunnel tests of high-lift device noise research, preliminary CFD investigation of the wind tunnel tests can decrease unknowns and improve the accuracy of the wind tunnel test. The preliminary CFD results help to appropriately and efficiently locate steady/unsteady pressure sensors to be measured. The model has to be appropriately designed to simulate expected flowfields and conditions in the wind tunnels. The model sizing and mounting method should be carefully selected to avoid strong wind tunnel interference at high-lift conditions. In the case of open-cart test to evaluate far-field noise, careful consideration is required. If the model generates unexpected extra noise, it is difficult to distinguish the influence from the measured spectra. In addition, in the case of open-cart test, generated shear-layers largely deflect due to high-lift. The deflected flow has to be in the collector without generating extra noise at the required conditions. For the purpose of high-lift device noise research, not only the wind tunnel data correction for aerodynamic forces, but also the influence on the sound propagation through the deflected shear-layers and sound reflection on the mounted plate should be evaluated.

Designed Wind Tunnel Testing Model for High-lift Device Noise Research, OTOMO2

The model is designed to have a leading-edge slat and a trailing-edge single-slotted flap assuming an outer wing with sweep angle of a 100-passenger-class civil jet aircraft. The designed model configuration, OTOMO2, is shown in Fig. 3.

Noise sources around slat are mainly derived from unsteadiness of the shear layers from the cusp and the slat trailing edge. Three noise components have been observed up to now [11]. The first component is the low frequency broadband component. The second component is the multiple tonal peaks (MTP) superimposed on

the low frequency broadband component. The third component, high frequency tone noise, is governed by the Karman vortex shedding from the trailing edge of the slat. Several other possibilities are the slat tracks, the cavities around the slat track, and anti-icing vent. In addition, to seal gaps between slat and the leading-edge of the main wing when the slats are stowed at the cruise conditions, blade seal and bulb seal are often attached as shown in Fig. 4. They change the shear layers from the cusp and the flow pattern in the cove. Besides the basic characteristics of noise from slat, the influences of such detail parts in actual aircrafts should be also clarified for further improvements to predict and reduce the airframe noise from actual aircrafts. This model is designed to allow the additional evaluation of the influences. Figure 5 shows the examples of additional parts of simulated slat tracks and cavities.

As for noise from flap, flap side-edge is recognized to be a major noise source. The noise sources at the flap-edge were clarified as three main sources; noise at low-frequency around the aft of flap trailing edge by vortex instability, broadband noise at mid-frequency around the side-edge of flap by shear-layer instability, and broadband noise at high-frequency around the gap between main wing and flap by shear-layer instability [18-19]. In this model, flap-tip region is designed to be exchangeable. As for the flap track, a flap track fairing can be evaluated as shown in Fig. 6.

Two CFD codes had been used to design the model. One is a flow solver on multi-block structured grids, UPACS, which is a standard CFD code for multi-block structured grids in JAXA [20-23]. The other one is a flow solver on unstructured grids, TAS code [20, 24], which is one of major CFD codes for unstructured grids used in APG/JAXA. The mixed element unstructured grids composed of tetrahedrons, prisms, and pyramids for viscous flows with high Reynolds number were generated using unstructured surface/volume mesh generators, TAS-Mesh and MEGG3D [25-29].
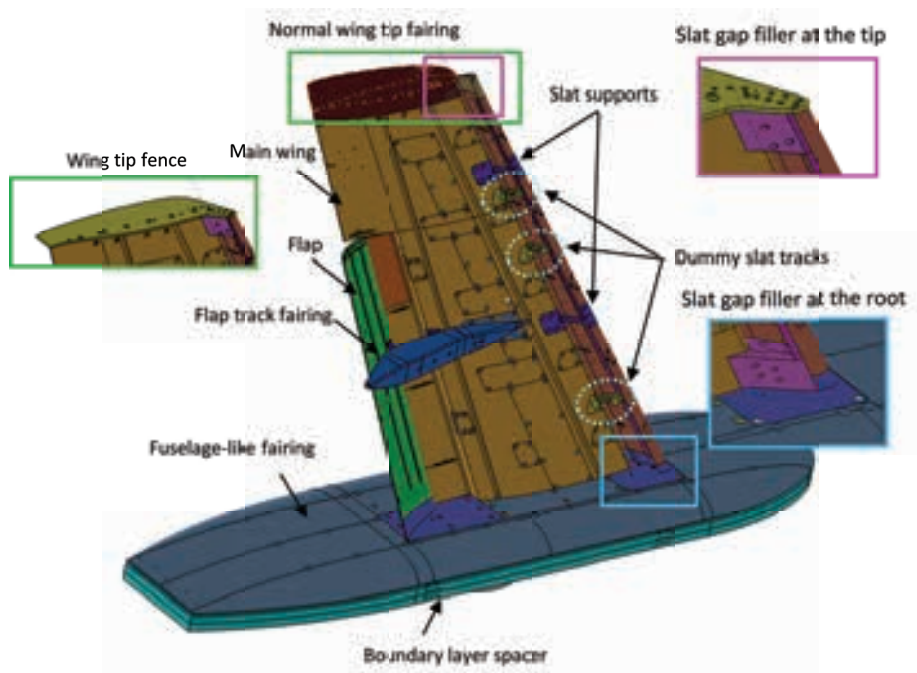

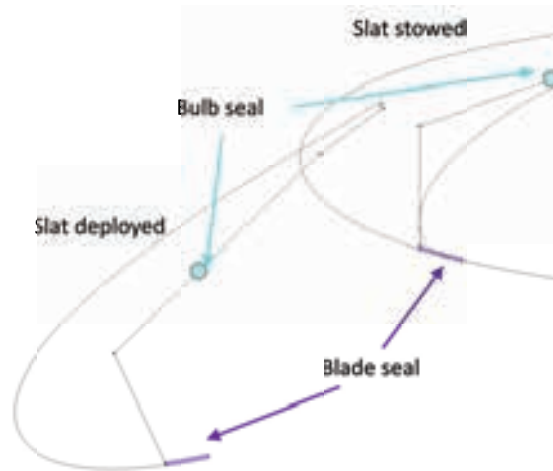Fig. 3 Designed JAXA high-lift device noise research model with taper and sweep angle, "OTOMO2"

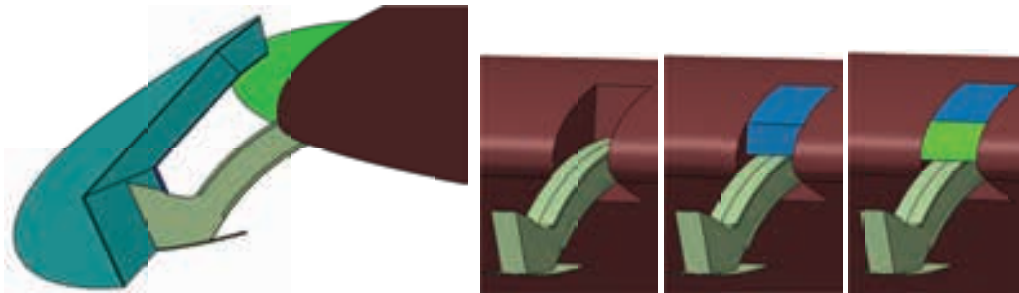**Fig. 4 Schematic of blade seal and bulb seal**

Fig. 5 Examples of additional parts of simulated slat tracks and cavities in the wind tunnel test model
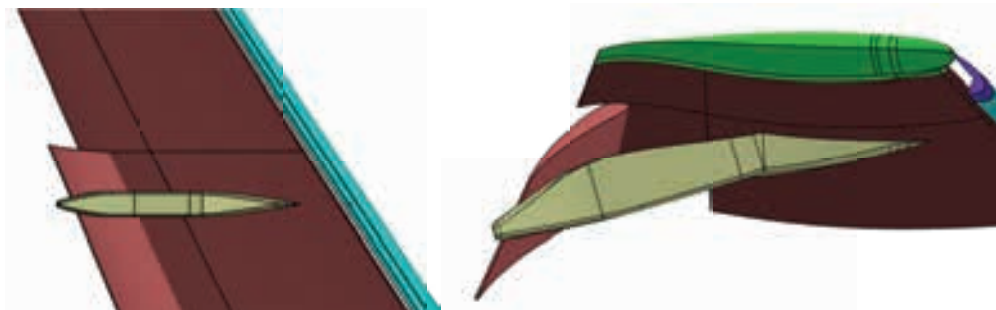

Fig. 6 Simulated flap track fairing in the wind tunnel test model

Design of Wing Geometry

In this research, use of two different wind tunnel facilities is assumed. One is the JAXA-LWT2 Lowspeed Wind Tunnel shown in Fig. 1(a). The facility is used for measurements of noise source identification by microphone phased-array, aerodynamic force and moment, static/unsteady pressure, and flowfield by oil-flow and PIV. It is an atmospheric pressure closed-circuit tunnel with a solid wall square test section or a Kevlar wall square test section. The size of the test section is 2m in height, 2m in width, and 4m in length. The other one is the Large-Scale Anechoic Wind Tunnel in Railway Technical Research Institute (RTRI) [30] shown in Fig. 1(b). The tunnel has an open-jet nozzle with a rectangular cross-section. The size of the test section is 3m in width, 2.5m in height, and 8m in length. The facility is used for measurements of far-field noise spectra including directivity characteristics, aerodynamic force and moment, and static/unsteady pressure. In order to investigate details of noise sources, the model size is designed to be maximized in the wind tunnels.

To be consistent with a series of JAXA's high-lift noise researches, the wing geometry is designed based on two models, a realistic aircraft wing-fuselage model deployed high-lift devices, JSM (JAXA Standard Model) [6, 16-

17], shown in Fig. 7 and a simplified high-lift model, OTOMO, shown in Fig. 1. The wing planform is based on the outer wing of JSM. The half-span length should be less than 1.5m in the JAXA-LWT2 for high-lift configuration. The half-span length of JSM is 2.3m. To be full-span slat and 70% span flap, the wing planform of from 54% to 88% span is used for the baseline planform. The stowed section airfoil and the setting parameter of slat and flap are identical with those of OTOMO. The slat and flap are deployed in three-dimensional direction based on the wing planform to evaluate under realistic aircraft situations. The differences of flowfields by the deployment methods are preliminary evaluated by CFD as shown in Fig. 8.
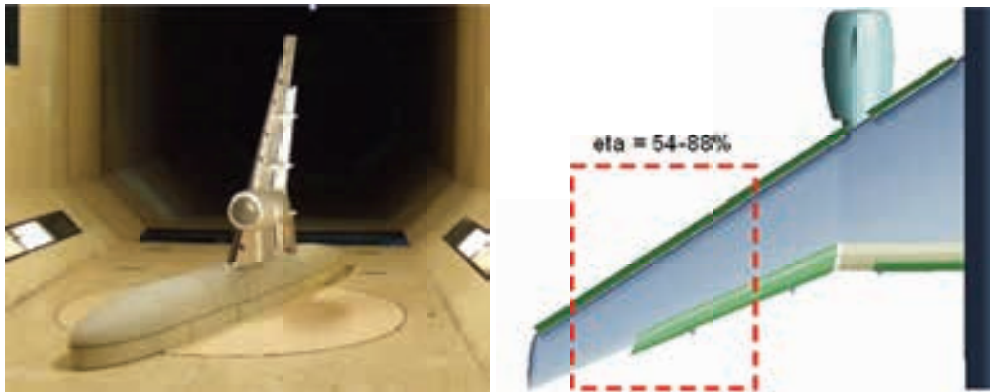
Fig. 7 JAXA high-lift device research model, "JSM"

(a) Deployed in two-dimensional direction

(b) Deployed in three-dimensional direction
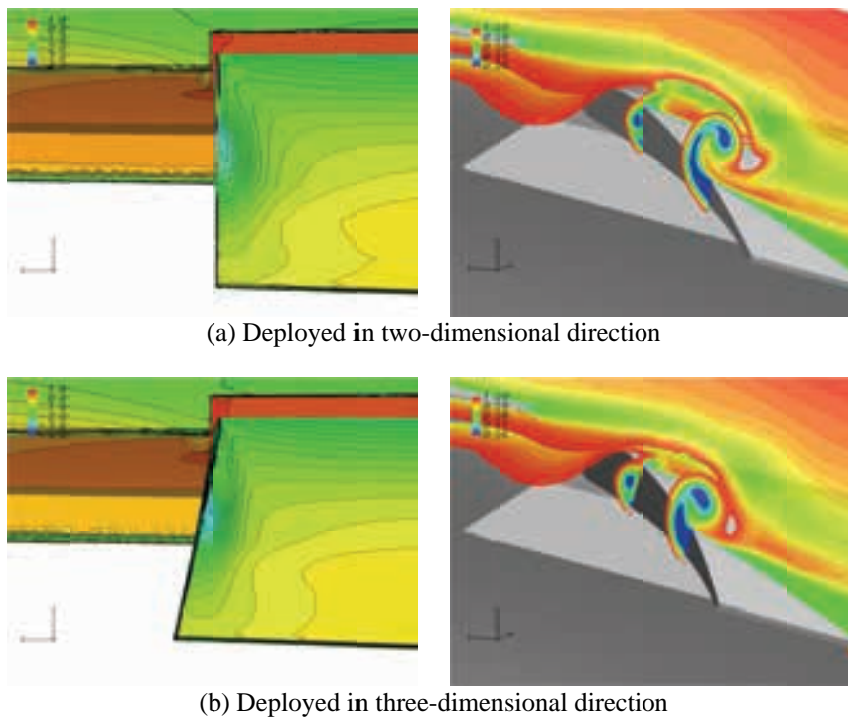
Fig. 8 The difference of flowfields by the deployment methods of slat and flap preliminary evaluated by CFD (left: surface pressure distribution, right: total pressure loss)

If the load distribution of the JSM is reproduced on the model, it is expected that the model can reproduce the noise. Figure 9 shows the aerodynamic forces and moment of JSM measured in the wind tunnel test. Figure XXX indicates two results with different flap settings; (A) inboard single/outboard double flaps with 35deg deflection and (B) inboard/outboard single flaps with 30deg deflection. The lift coefficient at landing $C_{L(LD)}$ is estimated using C_{Lmax}.

$$V_{s1g} = \sqrt{2W/\rho S C_{Lmax}} \tag{1}$$

$$V_{L/D} = 1.23 V_{s1g} = \sqrt{2W/\rho S C_{L(L/D)}} \tag{2}$$

$$C_{L(L/D)} = C_{Lmax}/1.23^2 \tag{3}$$

$C_{L(LD)}$ is estimated to be 1.89 and 1.84 and the corresponding angles of attack α are around 3°~4° and 5°~6° degrees for each flap setting.

Figure 10 compares the load distribution of JSM with inboard single/outboard double flaps with 35deg deflection at $\alpha=4°$ and the preliminary configuration of OTOMO2 obtained using CFD. In the preliminary configuration, the twist and dihedral angle are set to be zero. The load distribution of JSM from 54% to 88% span is re-scaled to be from 0% to 100%. Compared with the load distribution of JSM, it is confirmed that the load distribution of the preliminary configuration around 70% where the flap-edge is located shows good agreement at $\alpha=12°$ although the load distribution from 0% to 50% span is relatively lower. The load distribution will be adjustable to match better by considering twist distribution, while it complicates the model. Therefore, the twist distribution is not considered in the model.
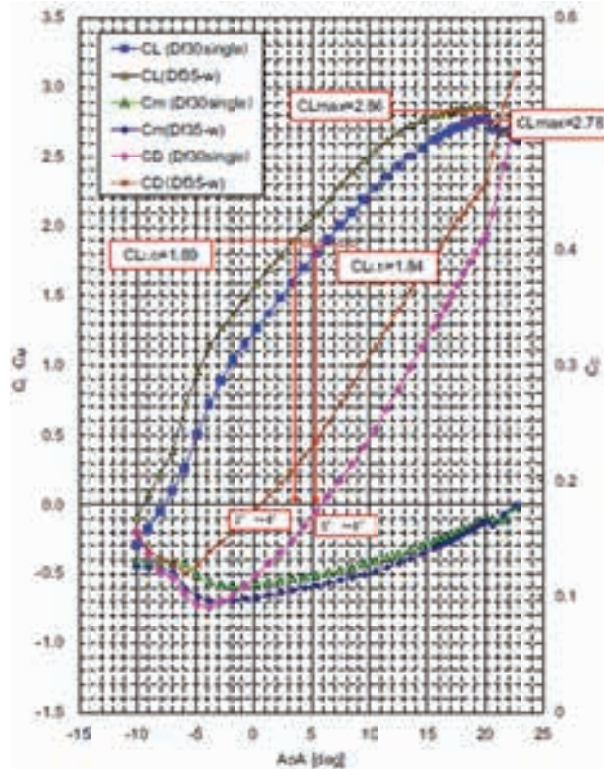
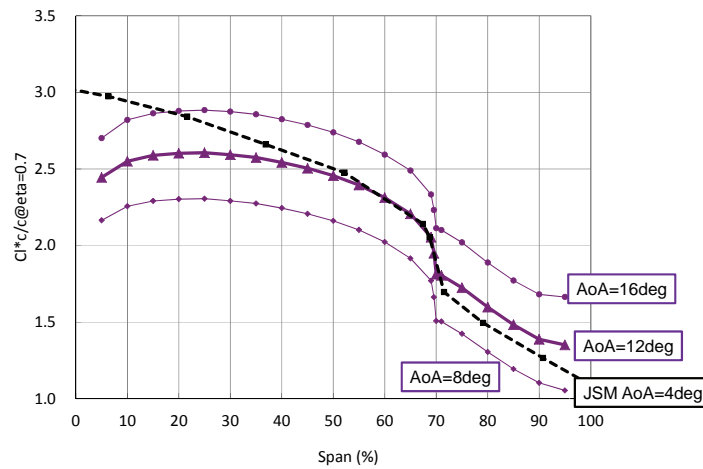**Fig. 9 Aerodynamic forces and moment of JSM measured in the wind tunnel test**

**Fig. 10 Load distributions of JSM with inboard single/outboard double flaps with 35 deg deflection at α =4°
from 54% to 88% span which is re-scaled to be from 0% to 100% and the preliminary configuration of
OTOMO2 obtained using CFD**

Model Sizing and Mounting in Wind Tunnel

As for the model sizing, the chord and span lengths of OTOMO are used for the baseline dimensions. The chord length and half wing span length are 0.6m and 1.35m. The stowed chord length at 70% span where the flap-tip locates is set to 0.6m. The appropriate scale is investigated based on the estimated amount of blockage and classical wind tunnel wall correction in JAXA-LWT2, the measurement frequency range, and the capacity to mount measurement sensors and tubes in the model. CFD simulation including wind tunnel of JAXA-LWT2 shown in Fig. 11 was used to validate the wind tunnel wall correction and to check the change of flowfields such as flow separation and vortices. To reduce the model scale to 80% from the baseline makes it difficult to mount all measurement sensors and tubes in the model. To increase the scale over 90% will increase the wind tunnel wall interferences compared with the results of OTOMO. Therefore, the model scale was decided to 85% scale of the baseline sizing. The angle of attack to be corrected is around 2° for the scale.
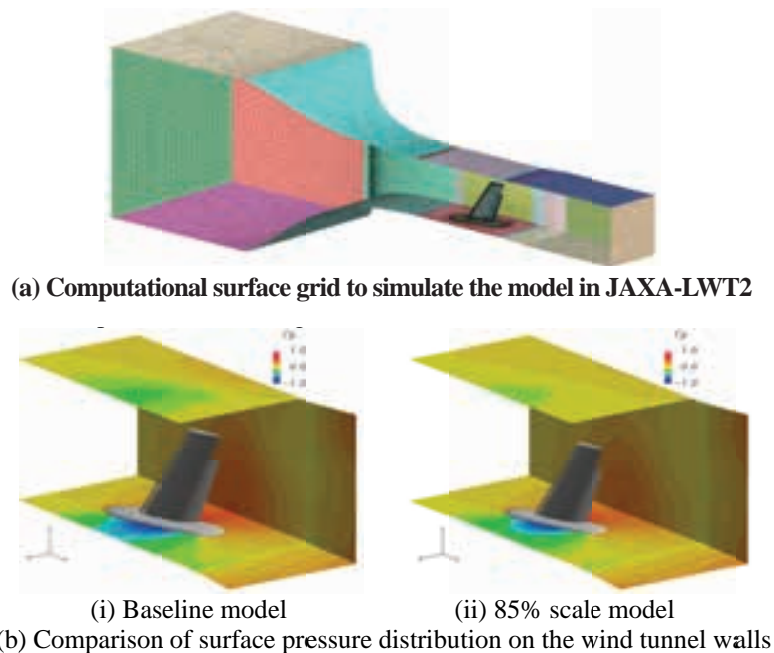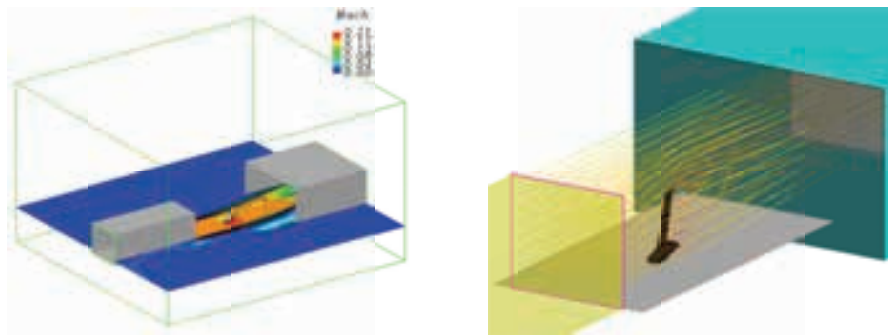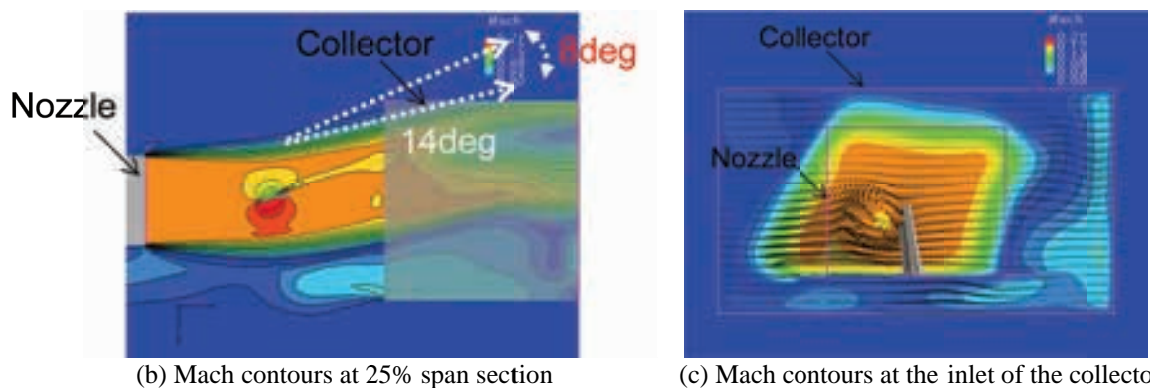

(a) Computational surface grid to simulate the model in JAXA-LWT2

(i) Baseline model   (ii) 85% scale model
(b) Comparison of surface pressure distribution on the wind tunnel walls

Fig. 11 Computations of the model in JAXA-LWT2 to investigate the wind tunnel wall interferences

(a) Overview of computational domain and close-up view near the model

(b) Mach contours at 25% span section

(c) Mach contours at the inlet of the collector

Fig. 12 Computation of the model in RTRI open-cart test section

In the case of open-cart test to measure the far-field noise, flow with shear-layer deflected due to high-lift has to be in the collector without generating extra noise at the required conditions. It was also evaluated by CFD. Figure 12 shows the computational results of the model in RTRI open-cart test section at $\alpha=16°$. From the computational results, the flow is appropriately in the collector. The results also indicate the allowance to increase the angle of attack. These preliminary evaluations help to plan the wind tunnel test conditions and understand the test results.

In the half-span model testing mounted vertically on the wind tunnel, a spacer to avoid interferences between the model and the boundary layer of the bottom wind tunnel wall is often used. With less height of the boundary layer spacer, the inboard wing is influenced by the boundary layer interaction. The excessive height of the spacer increases lift and decrease drag. The careful selection of the height is important for half-span model tests. The appropriate height was evaluated by CFD. At a representative test condition in JAXA-LWT2, 99% height δ and displacement thickness δ^* of the floor boundary layer is 80mm and 7.5mm. Figures 13(a) and 13(b) shows the distribution of total pressure loss and surface pressure coefficients Cp. Figure 13(c) shows the influence on the spanwise load distribution. In Fig. 13(c), BL80 indicates the results with the floor boundary layer of $\delta=80$mm. H20, H40 and H60 indicate that the height of the boundary layer spacer, H, are 20mm, 40mm and 60mm. In the computations, the floor boundary layer is modeled, but the wind tunnel itself is not simulated. As shown in Fig. 13(a), the floor boundary layer passes over the fuselage-like fairing and affects the inboard wing. In the case with H=20mm, the load reduces at a spanwise range from 5% to 30%. In the case with H=60mm, the load shows good agreement at 10% span, while increases at a spanwise range from 10% to 60%. From these observations, the height of the spacer was decided to be 40mm in JAXA-LWT2. Our previous computational and experimental studies using a realistic high-lift model, JSM, for high-lift aerodynamics research [31-32] had shown that a height of the spacer with the displacement thickness of the floor boundary layer δ^* or twice of δ^* is appropriate. For the present model, use of much thinner fuselage-like fairing requires much higher boundary layer spacer than the guideline.

The aft-part of the fuselage-like fairing was also modified by CFD considering the boundary layer spacer. Figure 14 shows the computational results with different aft-part of the fuselage-like fairing. The flow separation around the aft-part is reduced in the modifications. Space with height of 10*mm* is opened between the spacer and fuselage to exclude the measurement of the forces on the spacer. Then, a labyrinth seal is inserted in the space between the spacer and fuselage. The flow rate and flow speed passing through the labyrinth seal by the size of gaps were evaluated as shown in Fig. 15. Based on the observations, the labyrinth seal shown in Fig. 15(c) was selected.

(i) δ=0mm, H=0mm   (ii) δ=80mm, H=20mm   (iii) δ=80mm, H=40mm   (iv) δ=80mm, H=60mm

(a) Total pressure loss

(i) δ=0mm, H=0mm   (ii) δ=80mm, H=20mm   (iii) δ=80mm, H=40mm   (iv) δ=80mm, H=60mm

(b) Surface pressure distribution

(c) Load distribution
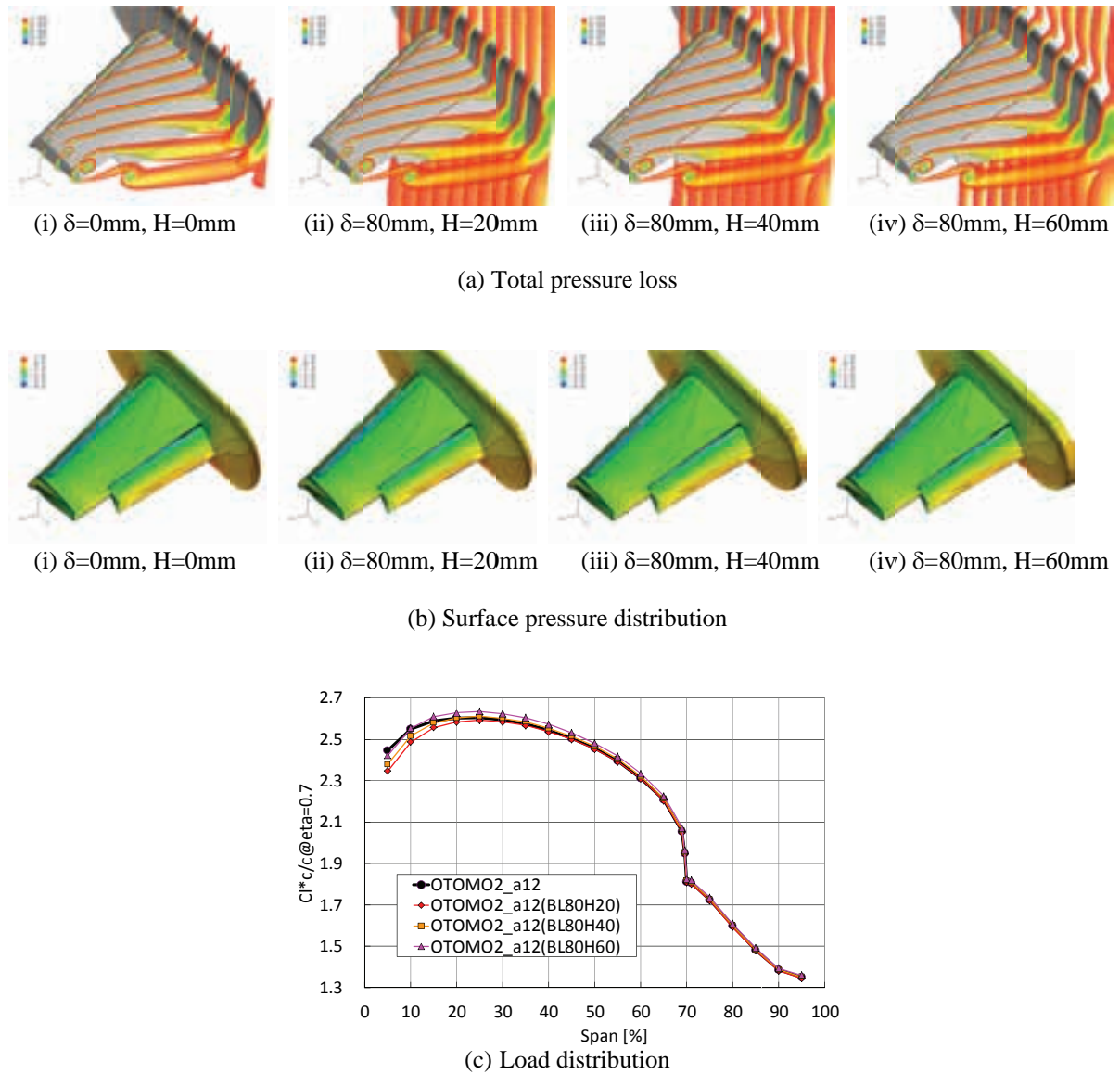
Fig. 13 Evaluation of influence of the floor boundary layer with different height of the spacer at $\alpha = 12°$
(δ : 99% thickness of boundary layer, H: height of boundary layer spacer)

(a) Baseline fuselage-like fairing

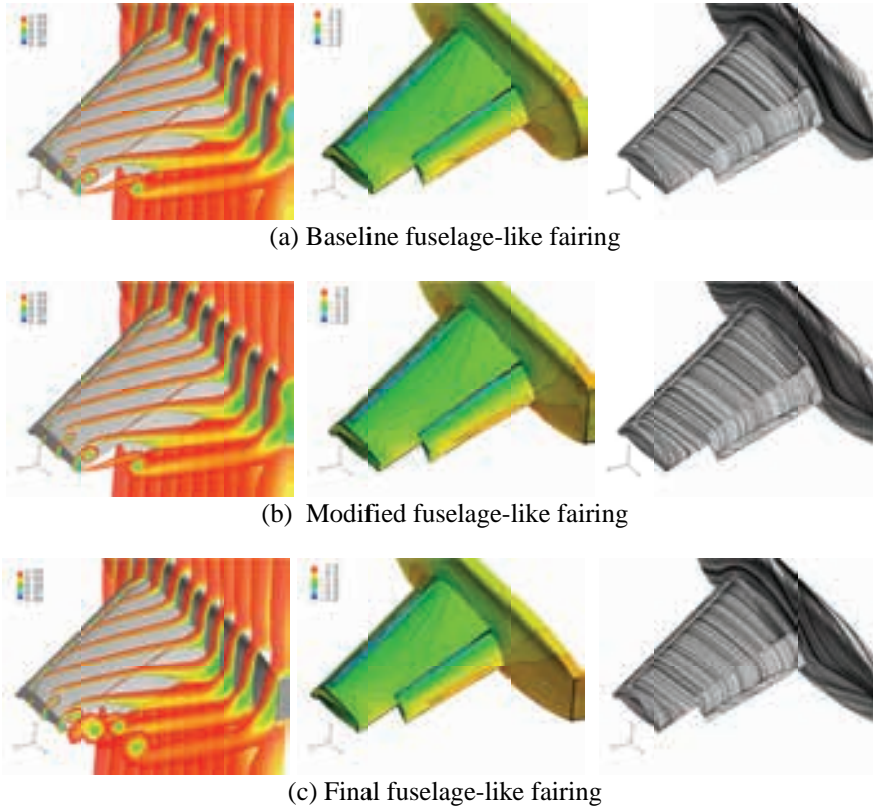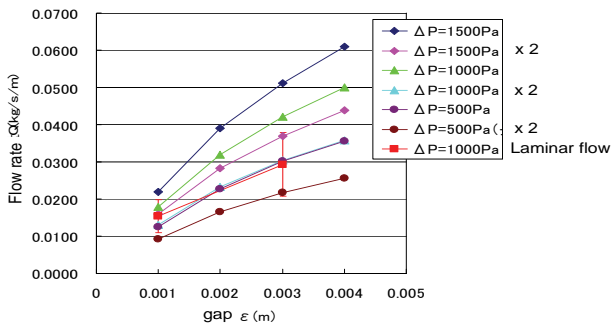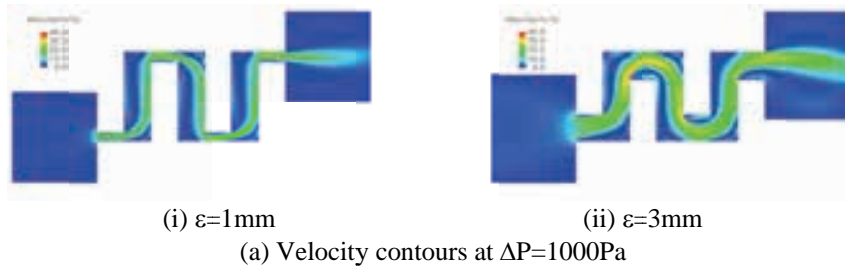(b) Modified fuselage-like fairing

(c) Final fuselage-like fairing

Fig. 14 Evaluation of aft-part of fuselage-like fairing with boundary layer spacer at $\alpha = 12°$ (left: total pressure loss, center: surface pressure, right: surface restricted streamlines)

(i) ε=1mm   (ii) ε=3mm

(a) Velocity contours at ΔP=1000Pa

(b) Flow rate through the labyrinth seal

(c) Selected labyrinth seal
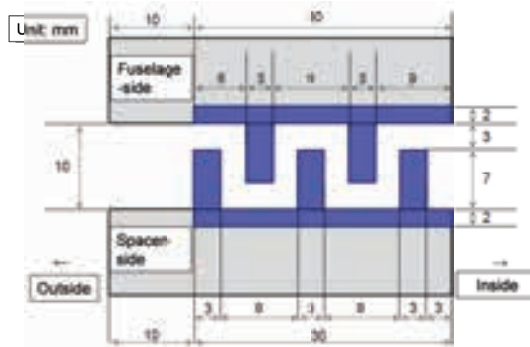
Fig.15 Design of labyrinth seal

Influences of Shear Layer and Mounted Plate on the Sound Propagation in Open-cart Test Section

In the case of open-cart test section, generated shear-layers largely deflect due to high-lift. For the purpose of high-lift device noise research, not only the wind tunnel data correction for aerodynamic forces, but also the influence on the sound propagation through the deflected shear-layers and sound reflection on the mounted plate should be evaluated. The influences were roughly evaluated using Linearized Euler Equations (LEE). Figure 16 shows a computational set-up to evaluate the sound reflection on the floor and structure to support the floor in the open-cart test section. A monopole sound source is set to a location. The location is changed from root to tip. Figures 17 and 18 show the influence of SPL by reflection on the floor and structure to support the floor for 500Hz and 1kHz sound sources, respectively. The results with the sound sources near the tip show more clear stripe pattern at X=0 section. By the location and frequency, the interferences are quite different.
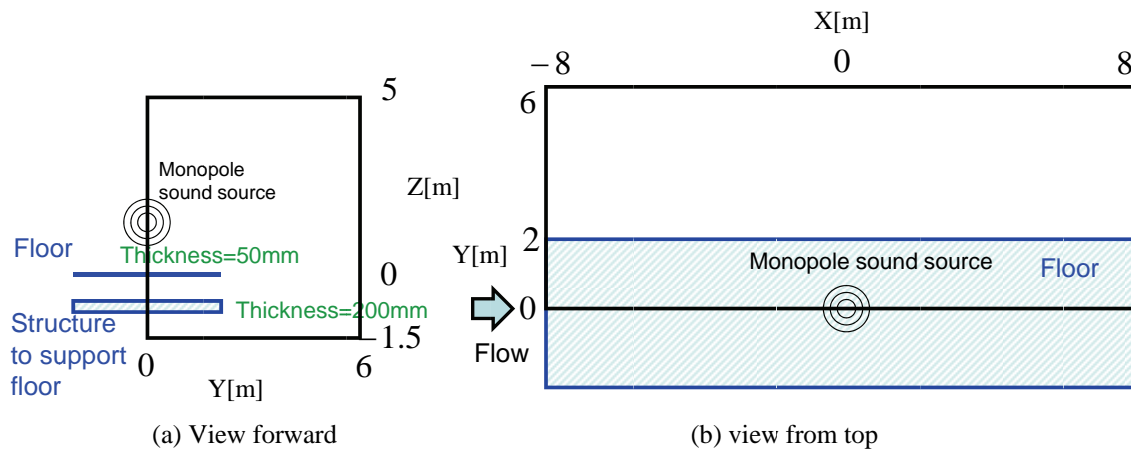

(a) View forward

(b) view from top

Fig. 16 Computational set-up to evaluate the sound reflection on the floor and structure to support the floor

(i) X=0   (ii) Z=0

(a) Sound source at Z=145mm (root)

(i) X=0   (ii) Z=0

(b) Sound source at Z=1275mm (tip)
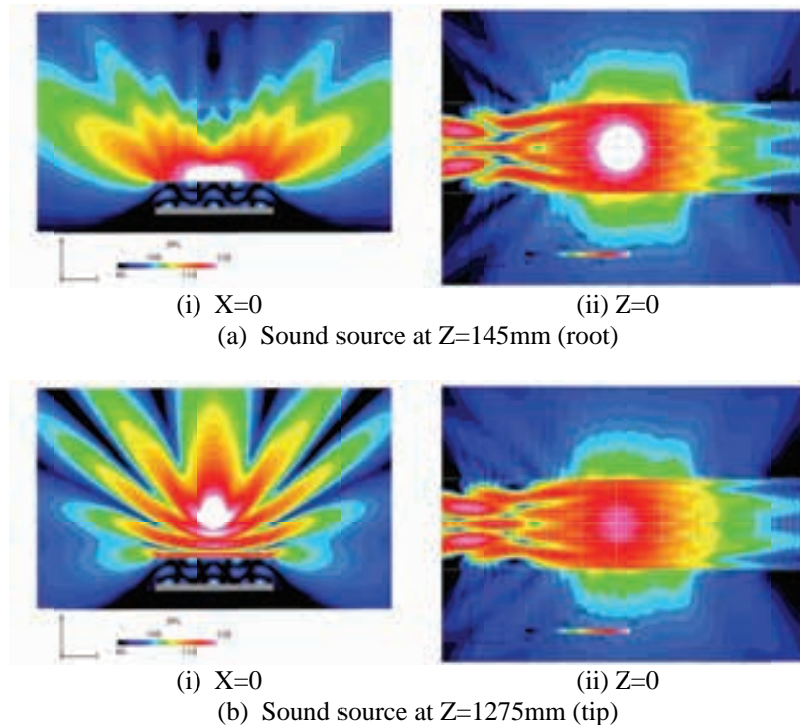
Fig. 17 Influence of SPL by reflection on the floor and structure to support the floor (monopole, 500Hz)

(i) X=0   (ii) Z=0
(a) Sound source at Z=145mm (root)

(i) X=0   (ii) Z=0
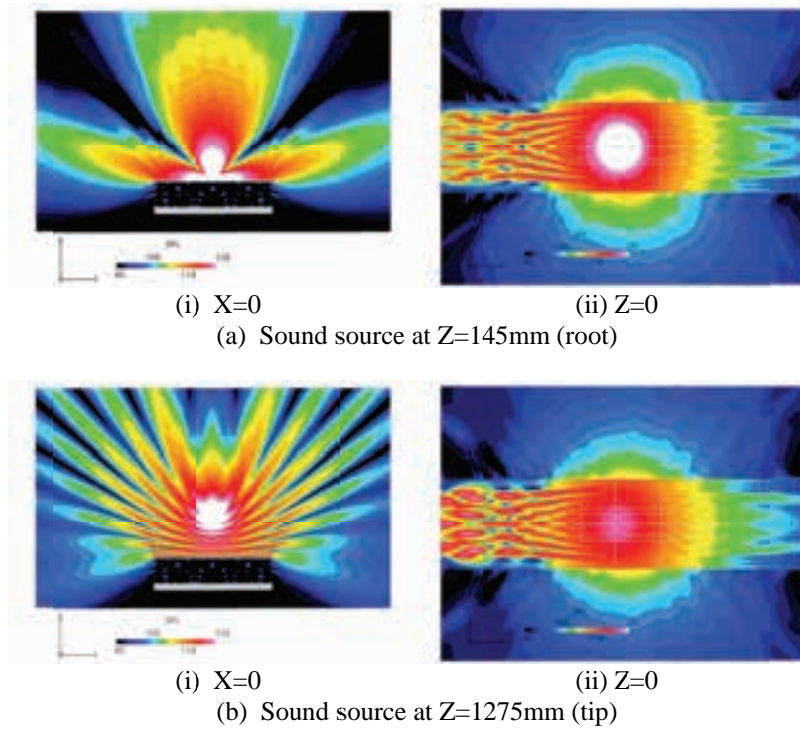(b) Sound source at Z=1275mm (tip)

Fig. 18 Influence of SPL by reflection on the floor and structure to support the floor (monopole, 1000Hz)

Figure 19 shows computational set-up to evaluate influence on the sound propagation through the deflected shear-layers. CFD results shown in Fig. 12 are used as the background data for LEE. Figure 20 shows the influence of SPL by the wind tunnel flow. Figure 21 shows comparison of directivity change of SPL by the deflected shear-layers. Major influence is found in the downstream region. The influence is larger when the sound source locates near the tip. The difference is around 4dB at maximum. These data were compared with classical pressure correction methods. By the comparison, it turned that some parts of the influcences can be corrected by the classical method, while the downstream region can not be corrected. It is important to understand these characteristics for discussion of the real directivity of the noise removing wind tunnel interferences. The result is expected to contribute to sophisticate the classical correction method.
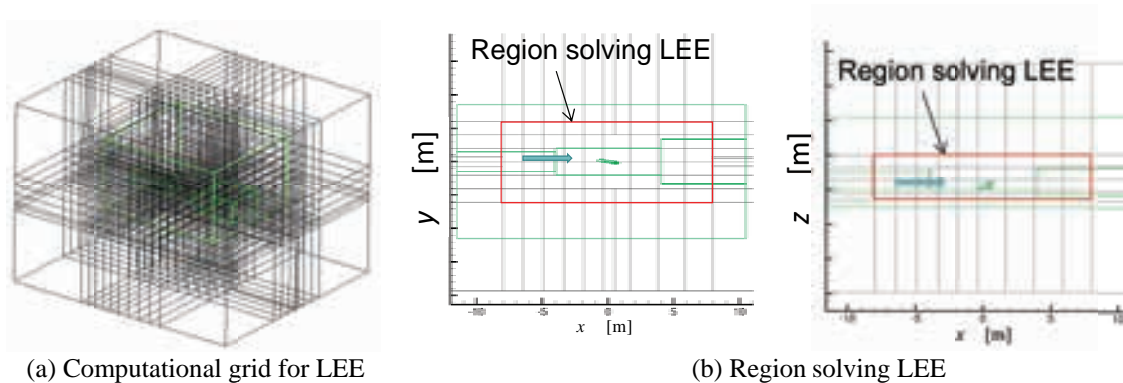

(a) Computational grid for LEE   (b) Region solving LEE

Fig. 19 Computational set-up to evaluate influence on the sound propagation through the deflected shear-layers

(i) Wind tunnel flow w/o model   (ii) Wind tunnel flow w/ model
(a) Cross-section at Z=145mm (sound source at Z=145mm (root))

(i) Wind tunnel flow w/o model   (ii) Wind tunnel flow w/ model
(b) Cross-section at Z=1275mm (sound source at Z=1275mm (tip))

Fig. 20 Influence on the sound propagation through the deflected shear- layers

(a) Sound source at Z=145mm (root)   (b) Sound source at Z=1275mm (tip)
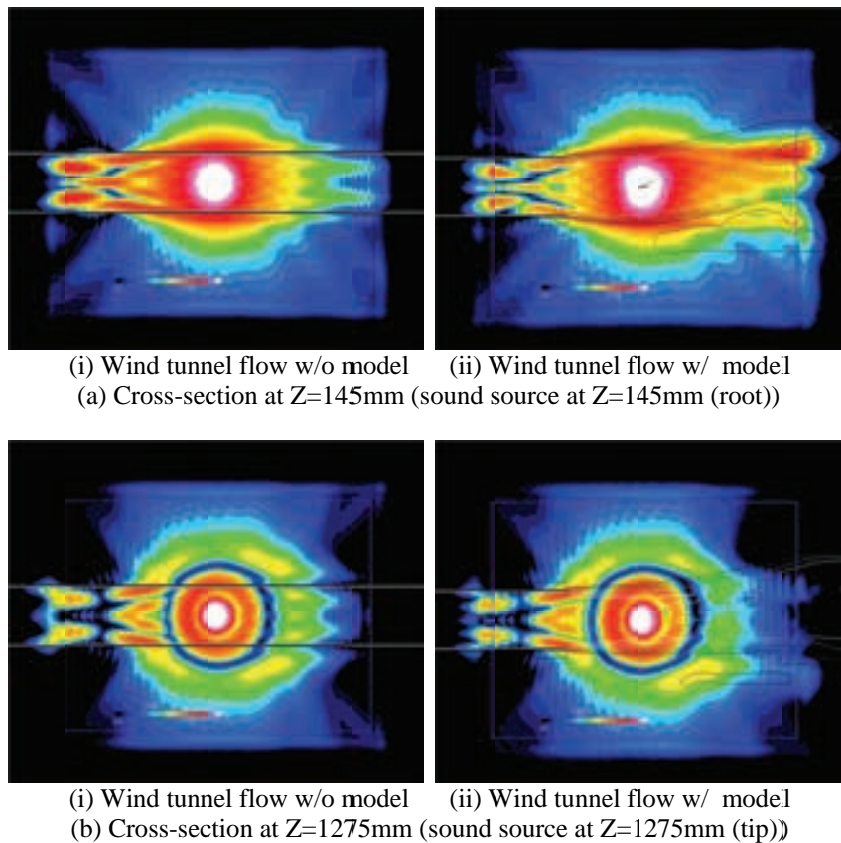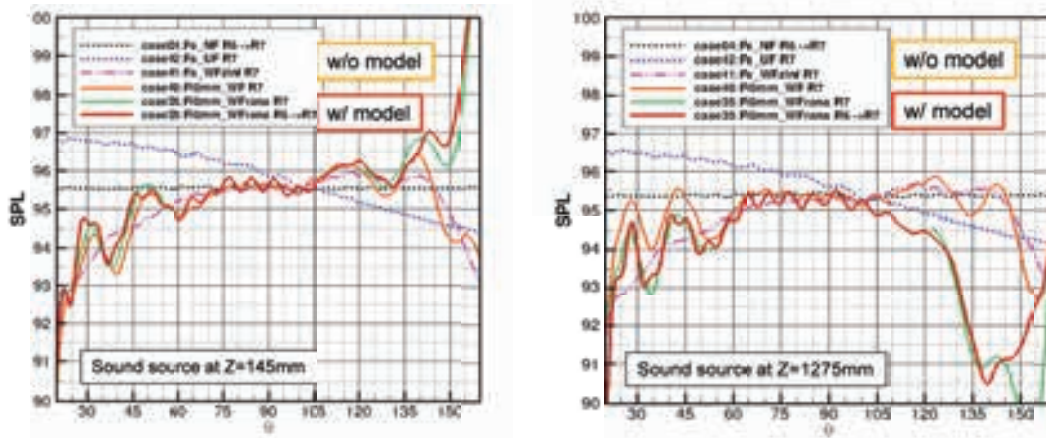
Fig. 21 Comparison of directivity change of SPL by the deflected shear -layers

Concluding Remarks

Computational efforts in designing experiment for a series of wind tunnel tests of high-lift airframe noise measurement have been shown. The daily use of CFD/CAA towards airframe noise predictions especially for full aircraft configurations is still difficult and the airframe noise research relies largely on wind tunnel testing. For the airframe noise research, requirements of the accuracy of wind tunnel testing are severe. It has been

shown that preliminary CFD investigation of the wind tunnel tests can decrease unknowns and risks and improve the accuracy of the wind tunnel test. In the investigation, computations of a lot of configurations at many flow conditions had conducted with a limited schedule to design and fabricate the model, while improvement of the turnaround time of CFD would contribute to improve the wind tunnel test further. The continuing improvement and combination of CFD and EFD will be important for high-lift device noise research.

References

[1] Astley, J., "Predicting and Treating Fan and Turbomachinery Noise Current Technology, Research & Facilities," UK-Japan Bilateral Workshop (Aircraft Emissions and Noise), Tokyo, 2006.

[2] Hardin, J. C., "Airframe self-noise: Four years of research; aircraft noise reduction for commercial aircraft," NASA-TM-X-73908, 1976.

[3] Dobrzynski, W., "Almost 40 Years of Airframe Noise Research: What Did We Achieve?," *Journal of Aircraft*, Vol. 47, No. 2, 2010.

[4] Rudnik, R., and Geyr, H., "The European High Lift Project EUROLIFT II – Objectives, Approach, and Structure," AIAA Paper 2007-4296, Jun. 2007.

[5] Rumsey, C.L., Long, M., Stuever, R. A., and Wayman, T. R., "Summary of the First AIAA CFD High Lift Prediction Workshop," AIAA Paper 2011-0939, 2011.

[6] Murayama, M., Yokokawa, Y., Yamamoto, K., and Ueda, Y., "CFD Validation Study for a High-Lift Configuration of a Civil Aircraft Model," AIAA Paper 2007-3924, June 2007.

[7] https://info.aiaa.org/tac/ASG/FDTC/DG/BECAN_files_/Workshop_June_2010_Final_problem_Statements Contact_Information.pdf

[8] https://info.aiaa.org/tac/ASG/FDTC/DG/BECAN_files_/BANCII_Workshop_Announcement_051011.pdf

[9] Imamura, T., Ura, H., Yokokawa, Y., Enomoto S., Yamamoto K., Hirai, T., "Designing of Slat Cove Filler as a Noise Reduction Device for Leading-edge Slat," AIAA Paper 2007-3473, 2007.

[10] Imamura, T., Ura, H., Yokokawa, Y., Hirai, T., Yamamoto K., "Numerical and Experimental Research of Low-Noise Slat Using Simplified High-lift Model," AIAA Paper 2008-2918, 2008.

[11] Imamura, T., Yokokawa, Y., Ura, H., and Yamamoto, K., "A Far-field Noise and Near- field Unsteadiness of a Simplified High- lift- configuration Model (Slat)," AIAA Paper 2009-1239, 2009.

[12] Yokokawa, Y., Imamura, T., Ura, H., Ito T., Uchida, H., and Yamamoto, K., "Studies on Airframe Noise Generation at High-lift Devices in Relation to Aerodynamic Performances," AIAA Paper 2008-2960, 2008.

[13] Yokokawa, Y., Imamura, T., Ura, H., and Yamamoto, K., "A Far-field Noise and Near- field Unsteadiness of a Simplified High- lift- configuration Model (Flap-edge)," AIAA Paper 2009-283, 2009.

[14] Yamamoto, K., Imamura, T., Yokokawa, Y., "Progress on Experimental and Numerical Research for Slat Noise in JAXA," *International Journal of Aeroacoustics*, accepted.

[15] Murayama, M., Yokokawa, Y., Yamamoto, K., Imamura, T., and Ura, H., "Computational and Experimental Study on Noise Generation from Flap Side-Edge of a Simplified High-Lift Wing Model," Inter- Noise 2012, 2012.

[16] Yokokawa, Y., Murayama, M., Ito T., and Yamamoto, K., "Experiment and CFD of a High-Lift Configuration Civil Transport Aircraft Model," AIAA 2006-3452, 2006.

[17] Ura, H., Yokokawa, Y., Ito, T., and Yamamoto, K., "A Study of Airframe Noise from HLD by using Beamforming Techniques," Proceedings of 49th Aircraft Symposium, JSASS-2011-5103, 2011 (in Japanese).

[18] Streett, C. L., Lockard, D. P., Singer, B. A., Khorrami, M. R., and Choudhari, M. M., "In Search of the Physics: the Interplay of Experiment and Computation in Airframe Noise Research; Flap-Edge Noise," AIAA Paper 2003-977, 2003.

[19] Choudhari, M. M., Lockard, D. P., Macaraeg, M. G., Singer, B. A., Streett, C. L., Neubert, G. R., Stoker, R. W., Underbrink, J. R., Berkman, M. E., Khorrami, M. R., Sadowski, S. S., "Aeroacoustic Experiments in the NASA Langley Low-Turbulence Pressure Tunnel," NASA TM-2002-211432, 2002.

[20] Murayama, M. and Yamamoto, K., "Comparison Study of Drag Prediction by Structured and Unstructured Mesh Method," *Journal of Aircraft*, Vol.45, No.3, 2008, pp. 799-822.

[21] Yamamoto, K., Tanaka, K., Murayama, M., "Comparison Study of Drag Prediction for the 4th CFD Drag Prediction Workshop using Structured and Unstructured Mesh Methods," AIAA Paper 2010-4222, Jun. 2010.

[22] Takaki, R., Yamamoto, K., Yamane, T., Enomoto, S. and Mukai, J., "The Development of the UPACS CFD Environment," *High Performance Computing, Proceedings of the 5th International Symposium of ISHPC 2003*, edited by Vie-denbaum et al., Springer-Verlag, 2003, pp. 307-319.

[23] Imamura, T., Enomoto, S., Yokokawa, Y., and Yamamoto, K., "Simulation of the Broadband Noise from a Slat Using Zonal LES/RANS Hybrid Method," AIAA Paper 2007-0226, Jan. 2007.

[24] Nakahashi, K., Ito, Y., and Togashi, F, "Some challenges of realistic flow simulations by unstructured grid CFD", *International Journal for Numerical Methods in Fluids*, Vol.43, 2003, pp.769-783.

[25] Ito, Y. and Nakahashi, K. "Direct Surface Triangulation Using Stereolithography Data," AIAA Journal, Vol. 40, No. 3, pp. 490-496, 2002.

[26] Ito, Y. and Nakahashi, K., "Surface Triangulation for Polygonal Models Based on CAD Data," International Journal for Numerical Methods in Fluids, Vol. 39, Issue 1, pp. 75-96, 2002.

[27] Sharov, D. and Nakahashi, K., "A Boundary Recovery Algorithm for Delaunay Tetrahedral Meshing," Proceedings of 5th International Conference on Numerical Grid Generation in Computational Field Simulations, 1996, pp. 229-238.

[28] Ito, Y. and Nakahashi, K., "Improvements in the Reliability and Quality of Unstructured Hybrid Mesh Generation," International Journal for Numerical Methods in Fluids, Vol. 45, Issue 1, May 2004, pp. 79-108.

[29] Ito, Y., Shih, A., Soni, B., and Nakahashi, K., "An Approach to Generate High Quality Unstructured Hybrid Meshes," AIAA Paper 2006-0530, Jan. 2006.

[30] Maeda, T., and Kondo, Y., "RTRI's Large-scale Low-noise Wind Tunnel and Wind Tunnel Tests", Quarterly Report of RTRI, 2001, vol.42, no.2, pp.65-70.

[31] Murayama, M., Yokokawa, Y., Tanaka, K., Yamamoto, K., and Ito, T., "Numerical Simulation of Half-span Aircraft Model with High-Lift Devices in Wind Tunnel," AIAA Paper 2008-0333, Jan. 2008.

[32] Yokokawa, Y., Murayama, M., Uchida, H., Tanaka, K., Ito, T., and Yamamoto, K., "Aerodynamic Influence of a Half-Span Model Installation for High-Lift Configuration Experiment," AIAA Paper 2010-0684, Jan. 2010.

Integrating CFD, CAA, and Experiments towards Benchmark Datasets for Airframe Noise Problems

Meelan Choudhari

NASA Langley Research Center
Hampton, VA 23693
USA
Meelan.M.Choudhari@nasa.gov

Kazuomi Yamamoto

Japan Aerospace Exploration Agency
Chofu, Tokyo 182-8522, Japan
yamamoto.kazuomi@jaxa.jp

Abstract

Airframe noise corresponds to the acoustic radiation due to turbulent flow in the vicinity of airframe components such as high-lift devices and landing gears. The combination of geometric complexity, high Reynolds number turbulence, multiple regions of separation, and a strong coupling with adjacent physical components makes the problem of airframe noise highly challenging. Since 2010, the American Institute of Aeronautics and Astronautics has organized an ongoing series of workshops devoted to Benchmark Problems for Airframe Noise Computations (BANC). The BANC workshops are aimed at enabling a systematic progress in the understanding and high-fidelity predictions of airframe noise via collaborative investigations that integrate state of the art computational fluid dynamics, computational aeroacoustics, and in depth, holistic, and multi-facility measurements targeting a selected set of canonical yet realistic configurations. This paper provides a brief summary of the BANC effort, including its technical objectives, strategy, and selective outcomes thus far.

Key words: aeroacoustics, airframe noise, computational fluid dynamics, computational aeroacoustics

Introduction

With the advent of quieter, ultra-high-bypass-ratio engines, flow unsteadiness in the vicinity of various airframe components has emerged as an important contributor to the noise signature of subsonic commercial transports during their approach for landing. The major sources of airframe noise include high-lift devices (i.e., leading-edge slat and trailing-edge flaps) and the aircraft undercarriage. The combination of geometric complexity, high Reynolds number turbulent flow with multiple regions of separation and a strong coupling between adjacent physical components makes the problem of airframe noise prediction highly challenging. Therefore, it is critical to integrate experiments with computational fluid dynamics (CFD) related to the nearfield unsteadiness (i.e., noise sources) and computational aeroacoustics (CAA) for the propagation of nearfield information to predict the acoustic signature at the location(s) of interest. A similar integration is also essential on the purely experimental front to enable combined (and preferably simultaneous) measurements of the unsteady flow and the acoustic signature. Furthermore, such interplay across multiple levels has to begin from the outset of any fundamental investigation of the airframe noise sources.

As a consequence of the increased maturity of CAA, the field has outgrown the range of simple problems with closed form solutions, forcing the community to rely upon measured data as a means of validation/accuracy

assessment for the progressively complex configurations of interest. This, too, has made an increased coupling between unsteady CFD, CAA, and experiments very important in the context of airframe noise problems.

The BANC Workshops

The paradigm shift from exact analytical solutions towards imperfect measured "solutions" as a yardstick for benchmarking aeroacoustic simulations imposes additional requirements on the quality and details of the benchmark dataset. The extra requirements pertain to both the accuracy/uncertainty and spatio-temporal resolution of the measurements involved and the need to quantify the multiple links within the causal chain from flow unsteadiness to far-field noise. Due to practical constraints, such stringent requirements cannot be easily met by a single investigator or even a single organization, especially in the context of airframe noise because of the combined complexity of flow geometry and the delicate unsteady flow physics.

Even though fundamental investigations of airframe noise have become increasingly common in recent years, the efforts have typically been fragmented across the community, which has impeded both the pace and the impact of these efforts. Due to the continued need for noise reduction on flight configurations, the fundamental efforts have sometimes assumed a secondary role to the applied research focused on the development of low fidelity prediction tools for real world airframe systems and/or the typically empirical development of noise reduction devices. To accelerate the understanding of airframe noise sources and to help develop validated high-fidelity computational models, a grass-roots effort was initiated in 2007 by the Discussion Group on Benchmark Experiments and Computations for Airframe Noise (BECAN DG) of the American Institute of Aeronautics and Astronautics [1]. The BECAN DG is jointly sponsored by the Fluid Dynamics and Aeroacoustics Technical Committees of AIAA. This effort has led to a series of international workshops on Benchmark Problems for Airframe Noise Computations (BANC). Several organizations within the airframe noise community have participated in the collective development of a hierarchy of benchmark configurations by contributing experimental data and/or computational solutions to help advance the state of the art at the fundamental level. As described later, the benchmark configurations have ranged from trailing edge noise from a single airfoil to a variety of canonical configurations relevant to nose and main landing gears and the leading edge slat under approach conditions.

In part, the BANC series of workshops has followed the modus operandi of the highly successful Drag Prediction Workshops [2] and Unsteady CFD Validation Workshop [3] in the purely aerodynamics arena but has been more ambitious in targeting additional elements related to the delicate physics of the unsteady flow and/or its coupling with the radiated acoustic field from the outset. The objectives of the BANC workshops are to:
1. Provide a forum for a thorough assessment of simulation-based noise-prediction tools in the context of airframe configurations including both near-field unsteady flow and the acoustic radiation generated via the interaction of this flow with solid surfaces.
2. Identify current gaps in physical understanding, experimental databases, and prediction capability for the major sources of airframe noise.
3. Help determine best practices, and accelerate the development of benchmark quality datasets.
4. Promote future coordinated studies of common configurations for maximum impact on the current state of the art in the understanding and prediction of airframe noise.

The following four problem categories were included in the BANC-I workshop, which was held in Stockholm in June 2010:
1. Airfoil trailing edge noise
2. Unsteady wake interference between a pair of inline tandem cylinders
3. Minimal 4-wheel landing gear
4. Partially-dressed, cavity-closed nose landing gear

The above categories were identified by the BECAN DG and subsequently vetted with the technical community during special sessions at the 2008 and 2009 AIAA Aeroacoustics Conferences in Vancouver and Miami, respectively. The workshop configurations reflected a compromise based on several criteria [1], including:
i.   Non-proprietary geometry and of wide interest
ii.   More realistic than previous CAA benchmarks, providing a balance between geometric complexity, relevant physics, computational requirements, and experimental constraints
iii.   Experiments conducted in more than one facility, with measurements addressing the full causal chain from unsteady flow structures to far-field acoustics

It was recognized that the requirements of a benchmark dataset will not be achieved in all cases and, hence, the title of this workshop series reflects the quest for the benchmark datasets and the collective journey towards that goal.

The BANC-I workshop was attended by over eighty-five researchers from fourteen countries. Eight government organizations from Asia, Europe and the United States, five major industry organizations, five software vendors, and a number of academic institutions participated in the workshop. A broad set of computational techniques were applied to a common set of problems, spanning structured, unstructured, overset and Cartesian grid solvers, low- and high-order algorithms, finite volume, finite difference, and lattice Boltzmann schemes, and Large Eddy Simulation (LES) or hybrid Reynolds Averaged Navier-Stokes (RANS)/LES methods [4]. Most evident was the community spirit in coming together to support the BECAN DG's goals and, in particular, the paradigm shift in benchmark activities for computational aeroacoustics, from closed form analytical solutions and single facility, single organization experiments, to collaboratively planned, multi-facility, multi-group experiments.

The follow on BANC-II workshop was held in Colorado Springs, Colorado, in June 2012. To broaden the portfolio of the BANC datasets and, in particular, to address additional noise sources related to high-lift devices, the BANC-II workshop included new problem categories in addition to categories 1 through 4 from the BANC-I workshop, which continue to be used by the research community since their introduction at the BANC-I Workshop:
    5. The LAGOON Simplified Landing Gear configuration tested by Airbus and ONERA,
    6. Slat Noise (DLR/ONERA Configuration)
    7. Slat Noise (NASA led effort on a modified 30P30N High Lift Configuration)
   8. Acoustic Propagation Phase of Airframe Noise Prediction

Technical details of the integration between CFD, CAA, and both fluid dynamic and aeroacoustic measurements in the context of each technical category are beyond the scope of this brief overview and the reader is referred to the problem statement definitions at the BECAN DG website [5] as well as summary documents for individual categories. See, for instance, Refs. [6], [7] for summaries pertaining to categories 2 and 3.

Category 2, i.e., unsteady wake interference between a pair of circular cylinders in tandem (Figs. 1 and 2) was developed as a canonical example of component interactions within the complex assembly of a typical aircraft undercarriage. This deceptively simple configuration was computationally demanding because of a number of factors such as (i) an often bistable flow behavior within computational solutions [6], which alternated between a co-shedding state observed in the experiments at the cylinder spacing of interest and an altogether different state resembling the measured flow behavior at smaller, subcritical spacings such that only the rear cylinder shed a Karman vortex street, (ii) the intricate effects of boundary layer tripping on the rear cylinder in spite of being buffeted by the strong unsteady wake from the front cylinder [8], and (iii) the effects of model installation within a wind tunnel facility and other facility details involving extraneous noise sources (e.g., mixing layers bounding the open jet tunnel stream) and secondary scattering agents (e.g., nozzle lips, side plates, collector plate) that exerted a significant influence on the measured acoustic field [9, 10, 11].

Multiple factors contributed to the successful bridging of the gap between computations and farfield acoustic measurements for the tandem cylinder configuration. The combination of factors included: careful design and planning of experiments, close coordination between experimental team and computational stakeholders throughout the experimental campaign [12, 13, 8], near-field computations performed by different groups using a variety of methodologies [14-23] and their comparison with the holistic set of multi-facility measurements as well as with each other, coupled aeroacoustic predictions, and finally, dedicated investigations to isolate the effects of secondary scattering [9, 11, 22], tunnel installation effects [11, 22], and extraneous noise sources associated with the facility [22]. An interesting finding was that, in spite of the relatively long span of the cylinder models (a span of 16 times the cylinder diameter), the decay in spanwise correlations was impacted by the presence of the side walls wherein the cylinders were mounted and, furthermore, that including the signature of unsteady flow events over the side plate surfaces accounted for a measurable correction to the far field acoustics [22]. Accounting for the model installation effects enabled a close match with the measured acoustics, including both the tonal peaks associated with vortex shedding and the broadband portion and, hence, also provided a meaningful basis to assess the computations without any installation effects, i.e., with spanwise periodic boundary conditions.
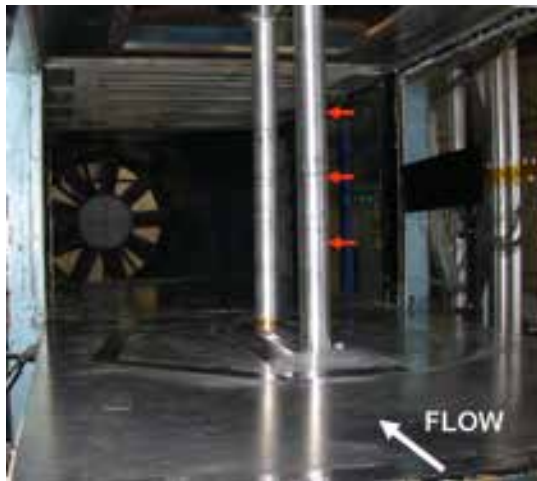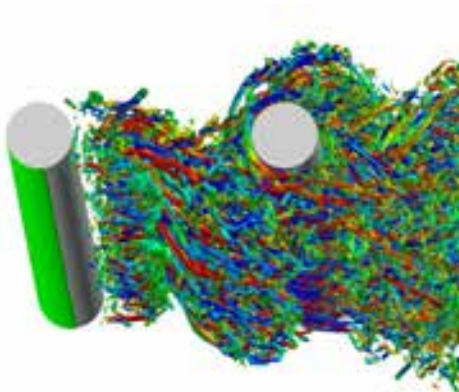
(a) Installation in a closed wall wind tunnel: Basic Aerodynamics Research Tunnel (red arrows indicate azimuthal arrays of static pressure ports) [13]
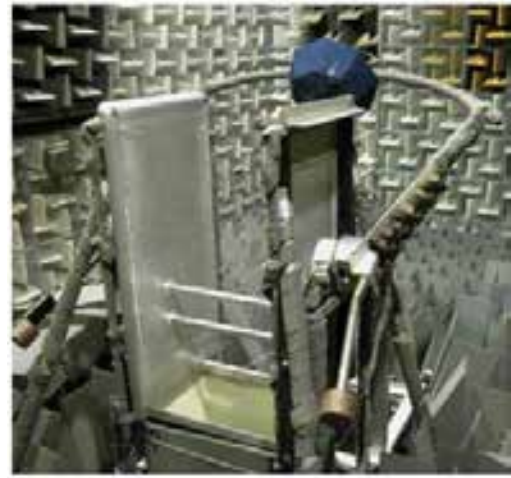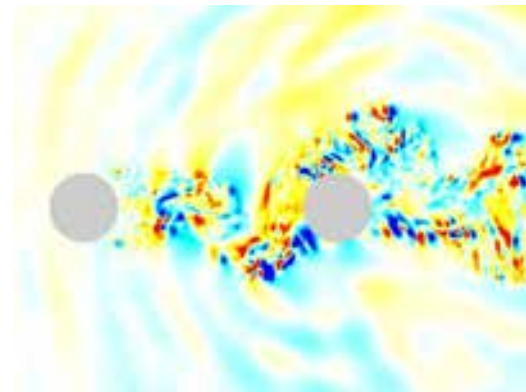
(b) Installation in an open jet facility: Quiet Flow Facility (QFF) at NASA Langley Research Center [16]

Fig. 1 Category 2 of BANC-I and BANC-II Workshops: Unsteady wake interference between a pair of inline tandem cylinders

(a) Vorticity structures within turbulent wake behind tandem cylinders

(b) Instantaneous pressure fluctuation around tandem cylinders showing noise generation and propagation

Fig. 2 A hybrid RANS/LES computation around the inline tandem cylinders [19]

Developed as an anchor for the initial BECAN-DG activities, the integration between computational and experimental activities for the tandem cylinder configuration was primarily sequential in nature. Because of the relative simplicity of the configuration and a reasonable body of prior results from the literature (albeit at low Reynolds number and purely aerodynamic in nature), with due planning, it was possible to acquire a thorough set of measurements without a great deal of *a priori* assistance from numerical computations. Of course, as discussed above, computations were essential to understand the limitations of the measurements as well as to raise the quality of the benchmark dataset.

The modus operandi for most other BANC configurations has been different from category 2, with a tighter and necessarily parallel coupling between CFD and experiments. Hence, a concomitant set of multi-phase investigations has been a necessity for these configurations as exemplified by the slat noise categories (categories 6 and 7) from the BANC-II workshop [5]. The flow configuration for category 7 (Fig. 3(a)), in particular, has already undergone multiple rounds of experimental and computational investigations (see, for instance, Refs. [24-30]) and further measurements led by NASA as well as JAXA are currently under way or

planned for the near future. The detailed flow measurements using established techniques, along with the scrutiny afforded through multiple computational investigations, is also providing the opportunity to mature promising techniques such as unsteady pressure sensitive paint [31] that could provide measurement detail that has not been possible in the context of airframe noise experiments thus far. The interplay between computations and measurements has also established the need to pay careful attention to the spatial resolution of global measurement techniques like particle image velocimetry, especially in high gradient regions such as the initial region of shear layer development behind the slat cusp [27]. Measurements at multiple resolutions are necessary to adequately characterize the scale disparity across noise relevant unsteady flow structures (Figs. 3(b) and 4(a)).

(a) 30P30N airfoil installed in the Basic Aerodynamics Research Tunnel [25]
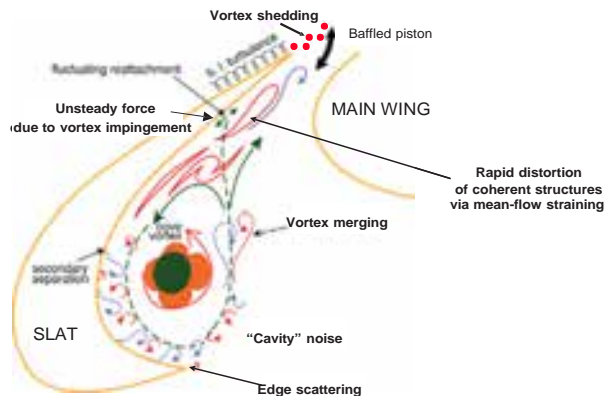
(b) Potential sources and physical mechanisms behind noise generation near a leading edge slat [27]

Fig. 3. Category 7 of BANC-II Workshop: 30P30N 3-Element, Simplified High-Lift Configuration
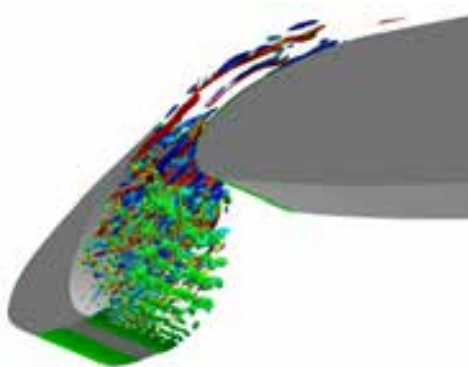
(a) Vortex structure of turbulent shear-layer inside of 30P30N slat
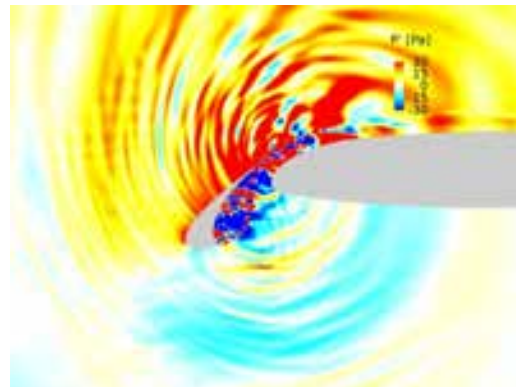
(b) Instantaneous pressure fluctuation around 30P30N slat showing noise generation and propagation

Fig. 4. A hybrid RANS/LES computation of 30P30N 3-Element, Simplified High-Lift Configuration [32]

The difficulties encountered in the context of the tandem cylinder configuration are amplified in category 7 (Fig. 3(a)). The factors contributing to the extra difficulties include: (i) the increased complexity of noise generation (Fig. 3(b) and 4(b)) including multiple narrow-band peaks superimposed on the primarily broadband spectrum of slat cove noise, (ii) large time averaged lift on the model which leads to large deflections of the tunnel stream in an open jet facility and, hence, leads to unacceptable variations in the aerodynamic characteristics of the model, (iii) aerodynamic and aeroacoustic effects of brackets connecting the slat and flap elements to the main wing, (iv) extraneous noise sources within the model such as main element cove, main and flap trailing edges, and possible separation over the flap, (v) more complex sidewall interference effects on the high-lift configuration, and (vi) Reynolds number effects that may not be fully amenable to holistic measurements. Yet,

the computational results presented at the BANC-II workshop [5] suggest a good prognosis provided the installation effects can be addressed satisfactorily.

Summary

The BANC effort has been rather unique in pursuing a simultaneous development of experimental and computational methodologies to achieve the targeted goal of benchmark quality datasets, rather than merely using the best set of previously available measurements as a source of validating the computations. Thus, both the experimental dataset and the CFD/CAA solutions have continued to grow, feeding off of each other and allowing the benchmarks to evolve at a rapid pace. The datasets developed as part of the BANC workshops should continue to be of value to the technical community, not only for the validation of noise prediction approaches including high fidelity simulations and reduced order models, but also in the computation of unsteady flows using large-eddy-simulation and other hybrid RANS/LES techniques.

Integration between simulations and experiments has been a critical ingredient in facilitating the BANC goal of enabling substantial collaborative advances in physics based predictions of airframe noise. In each case, the integration began from the outset with a stronger than usual role by computational researchers in the design of the experimental campaign, continuing through the execution and analysis of the data. The holistic focus on measurements has been another core aspect of the BANC effort, mandating in-depth characterization of each significant link between flow turbulence and the final metric of interest in the form of farfield acoustics. The multi-faceted understanding of the aeroacoustic phenomena in terms of both mean-flow features and near-field unsteadiness, surface and off-body flow features relevant to the noise source of interest, and simultaneous acoustic measurements based on individual microphones and, wherever possible, phased microphone arrays have enabled a thorough comparison between computations and experiments. Such comparison has provided increased confidence into the reliability of the simulation process as well as a better understanding of the physics of noise generation. This, in turn, opens the doors to the application of the knowledge base towards the development of reduced-order prediction models for design cycle applications as well as robust yet efficient noise reduction techniques. Furthermore, the successful integration in the context of simpler benchmarks has provided valuable lessons regarding the measurement and simulation of more complex airframe noise configurations. Yet, several opportunities still remain to improve the computational and experimental methodologies and those would be addressed during the future BANC workshops.

Acknowledgment

References

[1] "Discussion Group on Benchmark Experiments and Computations for Airframe Noise," URL:https://info.aiaa.org/tac/ASG/FDTC/DG/BECAN.aspx [cited September 2012].

[2] Vassberg, J., "Introduction: Drag Prediction Workshop," *J. Aircraft*, Vol. 45, No. 3, pp. 737-737, 2008.

[3] Rumsey, C.L., Gatski, T.F., Sellers, W.L., III, Vatsa, V.N., and Viken, S.A., "Summary of the 2004 CFD Validation Workshop on Synthetic Jets and Turbulent Separation Control," *AIAA J.*, Vol. 44, No. 2, pp. 194-207, 2006.

[4] Choudhari, M. and Visbal, M., eds., Proceedings of the 1st AIAA Workshop on Benchmark Problems for Airframe Noise Computations (BANC-I), Stockholm, Sweden, June 10-11, 2010.

[5] "Second Workshop on Benchmark Problems for Airframe Noise Computations," URL:https://info.aiaa.org/tac/ASG/FDTC/DG/BECAN_files_/BANCII.htm [cited September 2012].

[6] Lockard, D. P., "Summary of the Tandem Cylinder Solutions from the Benchmark Problems for Airframe Noise Computations-I Workshop," AIAA Paper 2011-353, 2011.

[7] Spalart, P. R. and Mejia, K. M., "Analysis of Experimental and Numerical Studies of the Rudimentary Landing Gear," AIAA Paper 2011-355, 2011.

[8] Neuhart, D., Jenkins, L., Choudhari, M., and Khorrami, M., "Measurements of the Flowfield Interaction Between Tandem Cylinders," AIAA Paper 2009-3275, 2009.

[9] Tinetti, A. F. and Dunn, M. H. , "Acoustic Simulations of an Installed Tandem Cylinder Configuration," AIAA Paper 2009-3158, 2009.

[10] Br`es, G., Freed, D., Wessels, M., Noelting, S., and Perot, F., "Flow and Noise Predictions for Tandem Cylinders in a Realistic Wind-Tunnel Configuration," AIAA Paper 2011-2824, 2011.

[11] Redonnet, S., Lockard, D.P., Khorrami, M.R., and Choudhari, M., "CFD-CAA Coupled Calculations of a Tandem Cylinder Configuration to Assess Facility Installation Effects," AIAA Paper 2011-2841, 2011.

[12] Jenkins, L. N., Khorrami, M. R., Choudhari, M. M., and McGinley, C. B., "Characterization of Unsteady Flow Structures around Tandem Cylinders for Component Interaction Studies in Airframe Noise," AIAA Paper 2005-2812, 2005.

[13] Jenkins, L. N., Neuhart, D. H., McGinley, C. B., Choudhari, M. M., and Khorrami, M. R., "Measurements of Unsteady Wake Interference between Tandem Cylinders," AIAA Paper 2006-3202, 2006.

[14] Khorrami, M. R., Lockard, D. P., Choudhari, M. M., Jenkins, L. N., Neuhart, D. H., and McGinley, C. B., "Simulations Of Bluff Body Flow Interaction For Noise Source Modeling", AIAA Paper 2006-3203, 2006.

[15] Khorrami, M. R., Choudhari, M. M., Lockard, D. P., Jenkins, L. N., and McGinley, C. B., "Unsteady Flowfield around Tandem Cylinders as Prototype Component Interaction in Airframe Noise," *AIAA J.,* Vol. 45, No. 8, pp. 1930-1941 (2007).

[16] Lockard, D. P., Khorrami, M. R., Choudhari, M. M., Hutcheson, F. V., Brooks, T. F., and Stead, D. J., "Tandem Cylinder Noise Predictions," AIAA Paper 2007-3450, 2007.

[17] Weinmann, M., Sandberg, R. D. , and Doolan, C. J. , "Flow and Noise Predictions for a Tandem Cylinder Configuration Using Novel Hybrid RANS/LES Approaches," AIAA Paper 2010-3787, 2010.

[18] Br`es, G. A., Wessels, M., and Noelting, S. "Tandem Cylinder Noise Predictions using Lattice Boltzmann and Ffowcs Williams–Hawkings Methods," AIAA Paper 2010-3791, 2010.

[19] Imamura, T., Hirai, T., Enomoto, S., and K. Yamamoto, "Tandem Cylinder Flow Simulations Using Sixth Order Compact Scheme," AIAA Paper 2011-2943, 2011.

[20] Seo, J.H. and Mittal, R., "Computation of Aerodynamic Sound around Complex Stationary and Moving Bodies," AIAA Paper 2011-1087, 2011.

[21] Greschner, B., Eschricht, D., Mockett, C., and Thiele, F., "Turbulence Modelling Effects on Tandem Cylinder Interaction Flow and Analysis of Installation Effects on Broadband Noise Using Chimera Technique," AIAA Paper 2012-3033, 2012.

[22] Bres, G., Freed, D., Wessels, M., Noelting, S., and Perot, F., "Flow and Noise Predictions for the Tandem Cylinder Aeroacoustic Benchmark," *Phys. Fluids*, Vol. 24, 036101, 2012; doi: 10.1063/1.3685102.

[23] Fu, S., Xiao, Z., Liu, J., and Huang, J., "Numerical Dissipation Effects on Massive Separation Around Tandem Cylinders," *AIAA J.*, Vol. 50, No. 5, pp. 1119-1136, 2012.

[24] Choudhari, M., Khorrami, M. R., and Lockard, D. P., "Slat Cove Noise: 30P30N 3-Element, Simplified High-Lift Configuration (Modified Slat)," URL:https://info.aiaa.org/tac/ASG/FDTC/DG/BECAN_files_/BANCII_category7/Summary_Category_7_Slat_Noise_30P30N.pdf [cited September 2012].

[25] Jenkins, L. N., Khorrami, M. R., and Choudhari, M. M., "Characterization of Unsteady Flow Structures

Near Leading-Edge Slat: Part I. PIV Measurements," AIAA Paper 2004-2801, 2004.

[26] Khorrami, M. R., Choudhari, M. M., and Jenkins, L. N., "Characterization of Unsteady Flow Structures Near Leading-Edge Slat: Part II. 2-D Computations," AIAA Paper 2004-2802, 2004.

[27] Choudhari, M. and Khorrami, M. R., "Effect of Three-Dimensional Shear-Layer Structures on Slat Cove Unsteadiness," *AIAA J.*, Vol. 45, No. 9, pp. 2174–2186, 2007.

[28] Lockard, D. P. and Choudhari, M., "Noise Radiation from a Leading-Edge Slat," AIAA Paper 2009-3101, 2009.

[29] Lockard, D. P. and Choudhari, M., "The Effect of Cross Flow on Slat Noise," AIAA Paper 2010-3835, 2010.

[30] Lockard, D. P. and Choudhari, M., "Variation of Slat Noise with Mach and Reynolds Numbers," AIAA Paper 2011-2910, 2011.

[31] Nakakita, K., "Scanning Unsteady PSP Technique for High-Frequency and Small-Pressure Fluctuation in Low-Speed," AIAA Paper 2010-4920, 2010.

[32] Imamura, T., Murayama, M., Hirai, T. and Yamamoto, K., "Aeroacoustic Simulations of 30P30N Configuration (JAXA's result)," Proceedings of Second AIAA Workshop on Benchmark Problems for Airframe Noise Computations, Colorado Springs, CO, June 7-8, 2012.

Integration of CFD and EFD for Analysis of Complex Real Flows

Toshiyuki Hayase

Institute of Fluid Science
Tohoku University
Sendai, 980-8577
Japan
Hayase@ifs.tohoku.ac.jp

Abstract

In this article formulation of MI simulation and equations of linearized error dynamics and eigenvalue analysis of MI simulation were first explained. Example of MI simulation was presented for a fully developed turbulent flow in a square duct. Numerical experiment was performed for MI simulation with a feedback signal from the predetermined standard turbulent flow solution. Convergence of MI simulation to the standard solution was investigated as a function of feedback gain and spatial and temporal density of feedback signal. Eigenvalue analysis was performed to examine the validity of the linearized error dynamics approach in the design of feedback signal.

Key words: measurement-integrated simulation, turbulent flow, eigenvalue analysis, convergence.

Introduction

Recent advances in computational fluid dynamics enable calculation of complex flows including turbulent flows appearing in many practical applications with reasonable accuracy. However, an *accurate solution* usually does not mean a solution that reproduces the exact instantaneous structure of the real flow, but rather one having the same statistical characteristics as those of the relevant flow. It is quite difficult to obtain the exact turbulent flow solution because (1) it is difficult to specify the initial and/or boundary conditions of real turbulent flows correctly, and (2) even if these data are available, a very small error in the initial condition will increase exponentially in structurally unstable dynamical systems such as turbulent flows [1] (see Fig. 1).

In spite of the inherent difficulty, reproducing the exact structure of real turbulent flows is a critically important issue in many fields, such as weather forecasting or feedback flow control. Extensive studies have been carried out to obtain information on real flows, including turbulent flows. Assimilation is a method commonly used in numerical weather prediction [2]. In a numerical simulation to calculate future weather states, the initial condition is updated at every time interval using the latest computational result and the measurement data around the computational grid points. 4 Dimensional variation (4DVAR) is widely used in numerical weather forecasting [3-5], but it requires huge computational power to repeatedly solve flow dynamics and its adjoint, and, therefore, is not suitable to apply to problems of real-time flow reproduction such as feedback flow control.
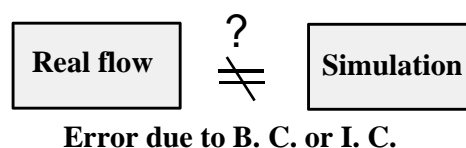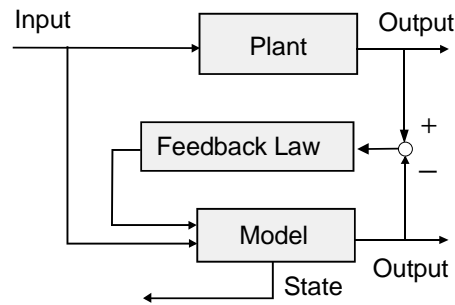

Fig.1 Real flow and simulation.

Fig.2 Block diagram of observer.

A similar concept, namely, interactive computational-experimental methodology (ICEME), was proposed by Humphrey [6] for application to engineering problems, in which the measurement data is supplied to a thermal-flow simulation to enhance the efficiency of computation. Possible advantages of ICEME as well as further necessary studies were discussed in relation to a complex flow related optimization problem seeking the arrangement of electrical heat sources to minimize the temperature in a ventilated box under some constraints. At that time, however, little was known as to how computational and experimental methods should be integrated in general to obtain useful information on the flow. Zeldin and Meade applied Tikhonov regularization method, which is common in inverse problems, to obtain an optimum solution to estimate the real flow from the numerical and measurement results of the relevant flow [7]. Particle imaging velocimetry has become a mature method to obtain velocity vectors in a flow domain. Studies have been made on the application of CFD schemes to modify PIV measurement so as to satisfy physical constraints such as the continuity equation [8]. State estimator or observer, which is fundamental methodology in modern control theory to estimate the state variables from the state equation with the aid of partial measurement data, has been used in flow problems. Uchiyama and Hakomori [9] reproduced the unsteady flow field in a pipe using a Kalman filter, which is a special observer [10]. Recently, Högberg *et al.* constructed a Kalman filter to estimate the flow state from the information on the wall in a numerical experiment for the optimum control of the subcritical instability of a channel flow based on a linearized equation [11]. Kalman filter and observer seek the asymptotic convergence to the optimum state requiring only one forward integration from arbitrary initial condition. They are potential candidates to solve the problem to reproduce real flows due to much less computational load than the variational methods. By comparing Kalman filter and observer, the latter has a simpler structure retaining essential part of the state estimation. One of the present authors proposed a measurement-integrated simulation (hereafter abbreviated as "MI simulation"), which is a kind of observer using a CFD scheme as the mathematical model of a relevant system, and successfully applied it to a turbulent flow in a square duct [12], a Karman vortex street behind a square cylinder [13, 14], and blood flow in an aneurismal aorta [15].

Among these studies intending to reproduce real flows, none has been successful in exactly reproducing instantaneous structures of a turbulent flow. From both theoretical and practical points of view, it is interesting to examine if any of these methods is capable of exactly reproducing turbulent flows using partial measurement data. As mentioned above, 4DVAR may be a sophisticated way to solve the problem but is practically inappropriate due to its large computational load. The present paper deals with this problem for MI simulation considering a low computational load and an accurate physical model.

Table 1 Comparison among observer-based methods.

	Model	Feedback design
Observer	Linear ordinary differential equation	Pole placement
Kalman filter	Linear ordinary differential equation	Optimum design
MI simulation	CFD model	Trial and error

As mentioned above, MI simulation is a kind of observer. In the following we give a general explanation of observers and show the differences between the MI simulation and other existing observers, including the Kalman filter. An observer is a common tool in control theory to estimate the real state from a mathematical model and partial measurement [13]. As shown in the block diagram in Fig. 2, the real system ("Plant" in the figure) is modeled as a differential equation ("Model"). Real time computation is performed parallel to the measurement, and the difference between the outputs of the computation and measurement, or the estimation error, is fed back to the model through the feedback law. This feedback signal modifies the dynamical structure of the model system and the properly designed feedback law results in an asymptotic reduction of the estimation error. In observable linear systems, convergence of the output signal guarantees coincidence of all state variables [16]. In design of the observer, determination of the mathematical model and that of the feedback law are the key (see Table 1). For finite dimensional linear dynamical systems satisfying observability condition, the observer of an arbitrary exponential convergence property can be designed by the standard pole placement technique [16]. A Kalman filter is also a kind of observer in which the feedback gain is determined to minimize the cost function in consideration of the statistical behavior of the measurement in stochastic dynamical systems [10]. Extension of the observer for application to nonlinear systems has been studied extensively for finite dimensional cases [17]. For infinite dimensional linear systems, the state observer is designed in the same manner as in finite dimensional cases and implemented after finite-dimensional approximation [18]. However, a general theory of the observer applicable to infinite dimensional and nonlinear dynamical systems such as flows has not yet been established [19]. As a methodology to reproduce real flows, the authors have proposed an MI simulation. The main feature of the MI simulation, which distinguishes it from other existing observers, is usage of CFD scheme as a mathematical model of the physical flow. A large dimensional nonlinear CFD model makes it difficult to design the feedback law in a theoretical manner; therefore, it has been determined by a trial and error method based on physical considerations. However, it makes it possible to accurately reproduce real flows once the feedback law is properly designed.

In this article formulation of MI simulation and equations of linearized error dynamics and eigenvalue analysis of MI simulation are explained [20]. Example of MI simulation is presented for a fully developed turbulent flow in a square duct. Numerical experiment is performed for MI simulation with a feedback signal from the predetermined standard turbulent flow solution [21]. Convergence of MI simulation to the standard solution is investigated as a function of feedback gain and spatial and temporal density of feedback signal. Eigenvalue analysis is performed to examine the validity of the linearized error dynamics approach in the design of feedback signal [20].

Measurement Integrated Simulation

In this section formulation of MI simulation and equations of linearized error dynamics and eigenvalue analysis of MI simulation are explained [20].

Formulation

This paper deals with incompressible and viscous fluid flow. The dynamic behavior of the flow field is governed by the Navier-Stokes equation:

$$\frac{\partial \mathbf{u}}{\partial t} = -(\mathbf{u} \cdot \nabla)\mathbf{u} + \nu \cdot \Delta \mathbf{u} - \nabla p + \mathbf{f}$$

(1)

and the equation of mass continuity:

$$\nabla \mathbf{u} = 0$$

(2)

as well as by the initial and the boundary conditions. In the Navier-Stokes equation (1), $\mathbf{f}$ denotes the external force term as the feedback signal in the MI simulation, $\rho\mathbf{f}$ denotes the body force, and p denotes pressure divided by density. The pressure equation is derived from Eqs. (1) and (2) as

$$\Delta p = -\text{div}\left\{(\mathbf{u} \cdot \nabla)\mathbf{u}\right\} + \nabla \mathbf{f}$$

(3)

We use Eqs. (1) and (3) as the fundamental equations. In the following, Eqs. (1) and (3) are simplified as Eqs. (4).

$$\begin{cases} \dfrac{\partial \mathbf{u}}{\partial t} = \mathbf{g}(\mathbf{u}) - \nabla p + \mathbf{f} \\ \Delta p = q(\mathbf{u}) + \nabla \mathbf{f} \end{cases} \tag{4}$$

where

$$\begin{cases} \mathbf{g}(\mathbf{u}) = -(\mathbf{u}\cdot\nabla)\mathbf{u} + \nu\cdot\Delta\mathbf{u} \\ q(\mathbf{u}) = -\operatorname{div}\{(\mathbf{u}\cdot\nabla)\mathbf{u}\} \end{cases} \tag{5}$$

The basic equation of the numerical simulation is represented as a spatially discretized form of governing equations (4):

$$\begin{cases} \dfrac{d\mathbf{u}_N}{dt} = \mathbf{g}_N(\mathbf{u}_N) - \nabla_N \mathbf{p}_N + \mathbf{f}_N \\ \Delta_N \mathbf{p}_N = \mathbf{q}_N(\mathbf{u}_N) + \nabla_N{}^T \mathbf{f}_N \end{cases} \tag{6}$$

where $\mathbf{u}_N$ and $\mathbf{p}_N$ are computational results for the $3N$-dimensional velocity vector and the N-dimensional pressure vector, respectively, N denotes the number of grid points, and ∇_N and Δ_N are matrices which express the discrete form of operators ∇ and Δ. It is noted that effects of the boundary conditions are included in the functions $\mathbf{g}_N$ and $\mathbf{q}_N$.

We define the operator $\mathbf{D}_N(\bullet)$ to generate the N-dimensional vector consisting of the values of a scalar field sampled at N grid points. Definition of $\mathbf{D}_N$ is naturally extended to the case when the variable is a velocity vector field as $\mathbf{D}_N(\mathbf{u}) = \begin{bmatrix} \mathbf{D}_N(u_1)^T & \mathbf{D}_N(u_2)^T & \mathbf{D}_N(u_3)^T \end{bmatrix}^T$. Applying the operator to the Navier Stokes equation and the pressure equation, we obtain the sampling of these equations at N grid points as,

$$\begin{cases} \dfrac{d}{dt}\mathbf{D}_N(\mathbf{u}) = \mathbf{D}_N(g(\mathbf{u})) - \mathbf{D}_N(\nabla p) \\ \mathbf{D}_N(\Delta p) = \mathbf{D}_N(q(\mathbf{u})) \end{cases} \tag{7}$$

We assume that there is no external force ($\mathbf{D}_N(\mathbf{f}) = 0$) in the real flow. On the other hand, we apply external force denoted by a function of real flow and numerical simulation in MI simulation. In this study, we consider the case in which external force $\mathbf{f}_N$ is denoted by a linear function of the difference of velocity and pressure between real flow and numerical simulation:

$$\mathbf{f}_N = -\mathbf{K}_u\left\{\mathbf{C}_u\mathbf{u}_N - \mathbf{C}_u(\mathbf{D}_N(\mathbf{u}) + \varepsilon_u)\right\} - \mathbf{K}_p\left\{\mathbf{C}_p\mathbf{p}_N - \mathbf{C}_p(\mathbf{D}_N(p) + \varepsilon_p)\right\} \tag{8}$$

where $\mathbf{K}_u$ denotes the $3N$-by-$3N$ feedback gain matrix of velocity, $\mathbf{K}_p$ denotes the $3N$-by-N feedback gain matrix of pressure, $\mathbf{C}_u$ and $\mathbf{C}_p$ denote the $3N$-by-$3N$ and N-by-N diagonal matrices consisting of diagonal elements of 1 for measurable points or 0 for immeasurable points, and $3N$-dimensional vector ε_u and N-dimensional vector ε_p mean measurement error. By introducing Eq. (8) into Eq. (6), we derive the general formulation of MI simulation:

$$\begin{cases} \dfrac{d\mathbf{u}_N}{dt} = \mathbf{g}_N(\mathbf{u}_N) - \nabla_N \mathbf{p}_N - \mathbf{K}_u\mathbf{C}_u\left\{\mathbf{u}_N - (\mathbf{D}_N(\mathbf{u}) + \varepsilon_u)\right\} - \mathbf{K}_p\mathbf{C}_p\left\{\mathbf{p}_N - (\mathbf{D}_N(p) + \varepsilon_p)\right\} \\ \Delta_N \mathbf{p}_N = \mathbf{q}_N(\mathbf{u}_N) - \nabla_N{}^T\mathbf{K}_u\mathbf{C}_u\left\{\mathbf{u}_N - (\mathbf{D}_N(\mathbf{u}) + \varepsilon_u)\right\} - \nabla_N{}^T\mathbf{K}_p\mathbf{C}_p\left\{\mathbf{p}_N - (\mathbf{D}_N(p) + \varepsilon_p)\right\} \end{cases} \tag{9}$$

Linearized error dynamics

We derive the linearized error dynamics of MI simulation. Disregarding the second order and higher order terms in Taylor expansion for the difference between real flow as Eq. (7) and the basic equation of MI simulation as Eq. (9) with respect to $\mathbf{u}_N$-$\mathbf{D}_N(\mathbf{u})$ and $\mathbf{p}_N$-$\mathbf{D}_N(p)$, we can derive the linearized error dynamics:

$$\frac{d}{dt}\left(\mathbf{u}_N-\mathbf{D}_N(\mathbf{u})\right)=\left(\left.\frac{d\mathbf{g}_N}{d\mathbf{u}_N}\right|_{\mathbf{u}_N}-\mathbf{K}_{\mathbf{u}}\mathbf{C}_{\mathbf{u}}\right)\left(\mathbf{u}_N-\mathbf{D}_N(\mathbf{u})\right)+\left(-\nabla_N-\mathbf{K}_p\mathbf{C}_p\right)\left(\mathbf{p}_N-\mathbf{D}_N(p)\right)$$

$$+\underline{\left\{\mathbf{g}_N\left(\mathbf{D}_N(\mathbf{u})\right)-\mathbf{D}_N\left(\mathbf{g}(\mathbf{u})\right)\right\}+\left(-\nabla_N\mathbf{D}_N(p)+\mathbf{D}_N(\nabla p)\right)}+\underline{\underline{\mathbf{K}_{\mathbf{u}}\mathbf{C}_{\mathbf{u}}\varepsilon_{\mathbf{u}}}} \tag{10}$$

and complementary static equation for pressure error:

$$\left(\mathbf{p}_N-\mathbf{D}_N(p)\right)=\left(\Delta_N+\nabla_N^T\mathbf{K}_p\mathbf{C}_p\right)^{-1}\left(\left.\frac{d\mathbf{q}_N}{d\mathbf{u}_N}\right|_{\mathbf{u}_N}-\nabla_N^T\mathbf{K}_{\mathbf{u}}\mathbf{C}_{\mathbf{u}}\right)\left(\mathbf{u}_N-\mathbf{D}_N(\mathbf{u})\right)$$

$$+\underline{\left(\Delta_N+\nabla_N^T\mathbf{K}_p\mathbf{C}_p\right)^{-1}\left\{\mathbf{g}_N\left(\mathbf{D}_N(\mathbf{u})\right)-\Delta_N\mathbf{D}_N(p)\right\}}+\underline{\underline{\left(\Delta_N+\nabla_N^T\mathbf{K}_p\mathbf{C}_p\right)^{-1}\nabla_N^T\left(\mathbf{K}_{\mathbf{u}}\mathbf{C}_{\mathbf{u}}\varepsilon_{\mathbf{u}}+\mathbf{K}_p\mathbf{C}_p\varepsilon_p\right)}} \tag{11}$$

where the underlined terms are caused by the model error including that in the boundary conditions and the double-underlined terms are caused by measurement error.

Here, we derive the basic equation of eigenvalue analysis for the linearized error dynamics which are formulated as Eqs. (10) and (11) in previous section. In this paper, we consider the case of no model error including that in the boundary conditions, no measurement error, and feedback with only velocity components ($\mathbf{K}_p$=0). In this case, Eq. (10) is written as

$$\frac{d\mathbf{e}_{\mathbf{u}}}{dt}=\mathbf{A}\mathbf{e}_{\mathbf{u}}-\nabla_N\mathbf{e}_p \tag{12}$$

where $\mathbf{e}_{\mathbf{u}}$, $\mathbf{e}_p$ and A are the difference in velocity and pressure between the MI simulation and the real flow and the 3N-by-3N matrix defined as

$$\mathbf{e}_{\mathbf{u}}=\mathbf{u}_N-\mathbf{D}_N(\mathbf{u}),\quad \mathbf{e}_p=\mathbf{p}_N-\mathbf{D}_N(p),\quad \mathbf{A}=\left.\frac{d\mathbf{g}_N}{d\mathbf{u}_N}\right|_{\mathbf{u}_N}-\mathbf{K}_{\mathbf{u}}\mathbf{C}_{\mathbf{u}} \tag{13}$$

Next we reduce the dimension of the velocity error vector $\mathbf{e}_{\mathbf{u}}$ based on the Weyl decomposition. In Weyl decomposition, any vector field $\mathbf{w}$ can be uniquely decomposed into the orthogonal vector fields $\mathbf{v}$ and grad ϕ as,

$$\mathbf{w}=\mathbf{v}+\mathrm{grad}\,\phi$$

$$\mathrm{div}\,\mathbf{v}=0 \quad \mathrm{and} \quad \mathbf{v}\cdot\mathbf{n}=0, \mathbf{x}\in\partial V \tag{14}$$

where $\mathbf{n}$ denotes the unit vector normal to the boundary. In the present analysis, the velocity error $\mathbf{e}_{\mathbf{u}}$ consists only of $\mathbf{v}$ component in Weyl decomposition since it satisfies the divergence-free condition and it vanishes on the boundary due to the above mentioned assumption of no model error. This enables us to reduce the dimension of $\mathbf{e}_{\mathbf{u}}$ corresponding to that of the component of grad ϕ.

Referring to Fig. 3, we define B as the range of ∇_N in Eq. (12),

$$\mathbf{B}=\mathrm{Range}\left(\nabla_N\right) \tag{15}$$

and 3N-by-2N matrix $\tilde{\mathbf{B}}$ consisting of $\tilde{\mathbf{b}}_1,\tilde{\mathbf{b}}_2,\cdots,\tilde{\mathbf{b}}_{2N}$ the orthonomal basis of $\mathrm{B}^\perp$, the orthogonal complementary space of B.

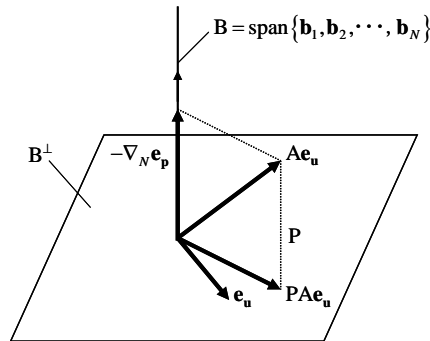**Fig. 3 Schematic Diagram for projection of vector field.**

$$\tilde{\mathbf{B}} = \begin{bmatrix} \tilde{\mathbf{b}}_1 & \tilde{\mathbf{b}}_2 & \cdots & \tilde{\mathbf{b}}_{2N} \end{bmatrix} \tag{16}$$

The projection of Eq. (12) onto $\mathbf{B}^{\perp}$ results in the following relation.

$$\frac{d}{dt}\mathbf{e}_u' = \mathbf{A}'\mathbf{e}_u' \tag{17}$$

where the $2N$ dimensional vector $\mathbf{e}_u'$ and A' are given as

$$\mathbf{e}_u = \tilde{\mathbf{B}}\mathbf{e}_u', \quad \mathbf{A}' = \tilde{\mathbf{B}}^T\mathbf{A}\tilde{\mathbf{B}} \tag{18}$$

We can analyze the linearized error dynamics from the eigenvalues of the $2N$-by-$2N$ system matrix $\mathbf{A}'$.

Numerical Experiment for Turbulent Flow in Square Duct

In this section example of MI simulation are presented for a fully developed turbulent flow in a square duct. Numerical experiment is performed for MI simulation with a feedback signal from the predetermined standard turbulent flow solution [21]. Convergence of MI simulation to the standard solution is investigated as a function of feedback gain and spatial and temporal density of feedback signal. Next, eigenvalue analysis is performed to examine the validity of the linearized error dynamics approach in the design of feedback signal [20].

Reproduction of turbulent flow

A numerical experiment was performed to examine whether a turbulent flow structure is exactly reproduced by an MI simulation using partial information on the real flow. We consider a fully developed turbulent flow in a pipe with a square cross section, which is a typical flow case [22, 23]. In our former attempt of MI simulation for this flow, a real turbulent flow was modeled by a pre-calculated standard solution, and an ad-hoc feedback law using a limited number of data of the standard solution was derived based on a physical consideration; a pressure difference proportional to the difference in the axial flow velocity component on a specified cross section normal to the pipe axis was added to the pressure boundary condition [12]. By choosing a feedback gain, the estimation error was reduced by a factor of 0.6, but it was far from an exact reproduction of the standard solution. In the present paper, we intend to reproduce the standard solution exactly with a more general feedback law using as much information on the standard solution as available and then investigate the possibility of reducing the number of data.

In the followings, a numerical experiment is performed for a relevant flow. After validation of the numerical solution procedure, a standard turbulent flow solution is obtained as a model of a physical flow. The MI simulation is performed for the cases in which (1) all velocity components of the standard solution are available at all grid points, (2) partial velocity components are available at all grid points, and (3) all velocity components are available at partial grid points. We investigate the convergence of the MI simulation to the standard solution for these cases.

The computational scheme used in this study is the same as that of our previous study [23]. A brief explanation of the numerical scheme is presented here. The discretized representations of the Navier-Stokes equation (1) and the pressure equation (3) are obtained by the finite volume method on a three-dimensional orthogonal
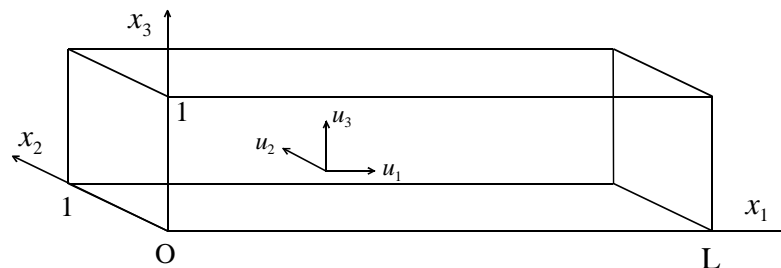

Fig. 4 Domain and coordinate system.

equidistant staggered grid system. Convection terms are discretized by the reformulated QUICK scheme, which assures the continuity of the momentum flux on the control volume boundaries in the iteration process [25]. A two-time level implicit scheme is used for time dependent terms [26]. The resultant set of finite difference equations is solved using the iterative procedure based on the SIMPLER method of Patankar [27].

The geometry and the coordinate system treated in this study are shown in Fig. 4. As to the boundary condition, the periodical velocity condition and the constant pressure difference, δ_p is assumed between the upstream and downstream boundaries, and a non-slip condition is assumed on the walls. In this paper all the values are expressed in dimensionless form using the side length of the square cross section $\tilde{b}$, the density of fluid $\tilde{\rho}$ and the mean axial velocity $\tilde{u}_{m0}$ given by

$$\tilde{u}_{m0} = \sqrt{2\tilde{\delta}_p \tilde{b}/(\lambda \tilde{L} \tilde{\rho})}, \tag{19}$$

where the coefficient of resistance λ is given by the Blasius' formula [24]

$$\lambda = 0.316 R_{e0}^{-1/4}, \tag{20}$$

A constant pressure difference $\delta_p = \tilde{\delta}_p/(\tilde{\rho}\tilde{u}_{m0}^2)$ corresponding to a specified Reynolds number $R_{e0} = \tilde{u}_{m0}\tilde{b}/\tilde{\nu}$ is assumed between the upstream and downstream boundaries for the duct of the periodical length L.

The calculations were carried out on the SGI ORIGIN 2000 and Altix 3700 Bx2 at the Institute of Fluid Science, Tohoku University. An ordinary numerical simulation was first carried out to obtain two solutions: the one solution was used as the model of a real flow (hereafter we call it "standard solution"), and the other solution was obtained from the initial condition different from that of the standard solution (hereafter we call the solution as "ordinary simulation"). Then MI simulation was performed from the same initial condition as that of the ordinary simulation but with the feedback signal in which the standard solution was used as the velocity of the real flow. Convergence of the MI simulation to the standard solution was evaluated by the error norm in the convergent state and the time constant in the transient state. Conditions investigated are shown in table 2. A feedback signal was applied at all grid points using all three velocity components (Case 1), or at all grid points but using partial components (Case 2), or at limited grid points using all velocity components (Case 3). The effect of the initial condition was also investigated in Case 1.

Table 2 Conditions of MI simulation

	Case 1	Case 2	Case 3
Feedback points	All	All	Partial
Feedback velocity components	All	Partial	All
Initial condition	Independent solution and null velocity	Independent solution	Independent solution

Table 3 Computational conditions

Periodical length L	4
Pressure difference δ_p	0.0649
Standard Reynolds number R_{e0} ($R_{e\tau}$)	9000 (573)
Grid points $N_1 \times N_2 \times N_3$	$80 \times 40 \times 40$
Grid spacing $h_1 \times h_2 \times h_3$	$0.05 \times 0.025 \times 0.025$
Time step h_T	0.025
Total residual at convergence	0.015
CPU time [s] for one time step	10.4

Standard solution and ordinary simulation without feedback

This section explains the standard solution and the ordinary simulation. The present computer code, ROTFLO2, was validated in detail in former studies [23, 25]. For a fully developed turbulent flow with the same geometry, the authors have previously examined the convergence of the solution with grid refinement [23]. Under the computational conditions summarized in Table 3, we obtained a proper turbulent flow solution in good agreement with the DNS solution by Huser & Biringen [22] in the mean u_1-velocity profile, the Reynolds stress distribution, and the energy spectrum of u_1-velocity perturbation [23] (see Fig. 5).

A standard solution was first obtained as a model of a real turbulent flow. The final velocity field of the statistically steady solution for a fully developed turbulent flow in the former study [23] was used as the initial condition of the standard solution.

The present study focused on the convergence of the solution of the MI simulation to the standard solution. The initial condition of the MI simulation was defined as the state of the standard solution at t = 20 (we confirmed that the autocorrelation function of the velocity fluctuation at the center of a cross section sufficiently reduces at t = 10). The two solutions are very different although their statistical properties are the same. This initial condition is used in most of the following MI simulations except for the special case of the null velocity condition.

MI simulation with feedback of full velocity components

A numerical experiment for MI simulation was performed using the above-mentioned standard solution as the model of real turbulent flow. The feedback signal in the MI simulation in this section was applied at all grid points as the artificial force vector in the discretized Navier-Stokes equation proportional to the difference in velocity vector between the standard solution and the simulation, and as the source term in the pressure equation (Case 1 in Table 2). MI simulation for the feedback signal determined with partial information of velocity components (Case 2) or partial grid points (Case 3) are considered in the following sections.

MI simulation was performed for various values of the feedback gain K_u, which represents diagonal components of the diagonal matrix $\mathbf{K_u}$. In order to evaluate the error of the MI simulation from the standard solution, we define the error norm $E_\mathbf{u}$ and E_p as follows:
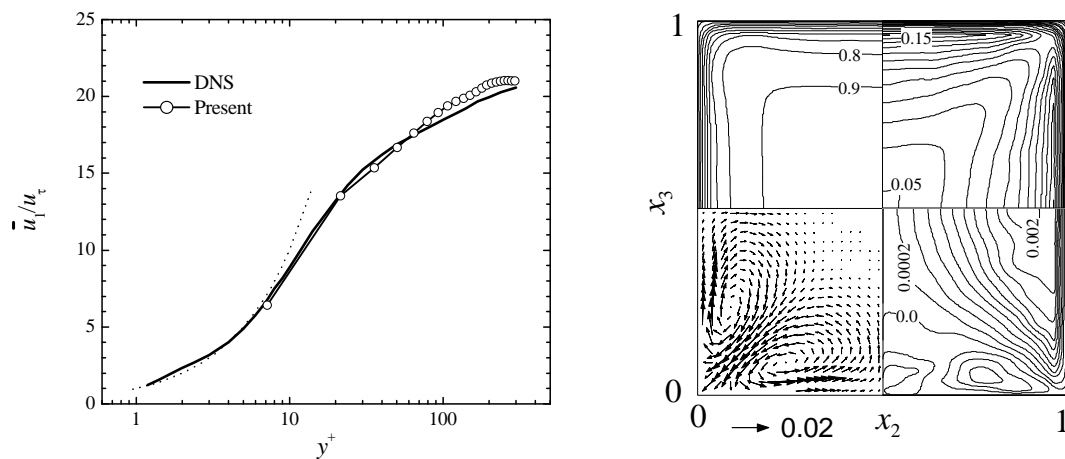
Fig. 5 (a) Comparison of mean axial velocity profile with DNS solution (Huser & Biringen 1993), and (b) Flow structure on a cross section for the present numerical solution for a fully developed turbulent flow through a square duct (Hayase 1999). Upper left: mean u_1-velocity contours normalized by the mean center velocity u_c; lower left: mean transverse velocity vectors normalized by the mean center velocity u_c; upper right: contours of RMS value of u_1-velocity fluctuation, $\overline{(u_1'^2)}^{1/2}/u_c$; lower left: contours of the Reynolds stress, $\overline{u_1'u_2'}/u_c^2$

$$
\begin{cases}
E_{\mathbf{u}} = \left[\dfrac{1}{3N} \sum_{n=1}^{3N} \left(u_n - u_n^* \right)^2 \right]^{1/2} \\[3mm]
E_p = \left[\dfrac{1}{N} \sum_{n=1}^{N} \left(p_n - p_n^* \right)^2 \right]^{1/2}
\end{cases}
, \tag{21}
$$

where u_n denotes a component of $\mathbf{u}_N$, or u_1, u_2, u_3 at any grid point.

Variations of the error norms $E_{\mathbf{u}}$ and E_p for MI simulations with different values of the feedback gain K_u are plotted in Fig. 6. For the error norm of the velocity vector field in Fig.6 (a), the result for $K_u = 0$, corresponding to the ordinary simulation, remains almost constant ($E_0 = 0.13\pm0.02$) showing that the standard solution and the solution of the ordinary simulation maintain the same distance in the state space. In a range of the feedback gain, the error norm is reduced almost exponentially and afterwards deviates irregularly within some range. The exponential reduction rate in the transient stage increases with the feedback gain for $K_u \leq 32$, but becomes negative (meaning that the error increases) for $K_u = 64$, showing instability characteristics which are typical in feedback systems. The range of deviation of the error norm in the steady stage is almost constant with time for each gain. By carefully examining the variation of the error norm in that range, the error norm is seen to switch between two typical states near the bottom and top of the range: a quasi-stationary state near the bottom and a steady oscillation state near the top. The level of the bottom state, which takes the minimum value around 1×10^{-6} for $K_u = 2$, increases with increasing gain. The level of the top state, which gives the accuracy of the MI simulation, first decreases with increasing gain and remains almost constant for $K_u = 2$ and 8, but increases rapidly with further increases of the gain, and for $K_u = 64$ it becomes ten times larger than the error norm of the ordinary simulation. It is noted that the time of the bottom state or the top state seems to be correlated among the results of different feedback gains. This can probably be ascribed to the stability of the feedback system dependent on the standard solution, but further examination should be made in a future study.

The results for the error norm of the pressure field shown in Fig.6 (b) are qualitatively the same as those of the velocity vector field mentioned above. This is a natural consequence of convergence of MI simulation in the velocity field resulting in convergence in the pressure field. Therefore, we mainly focus on the velocity field in the followings.

(a)   **(b)**
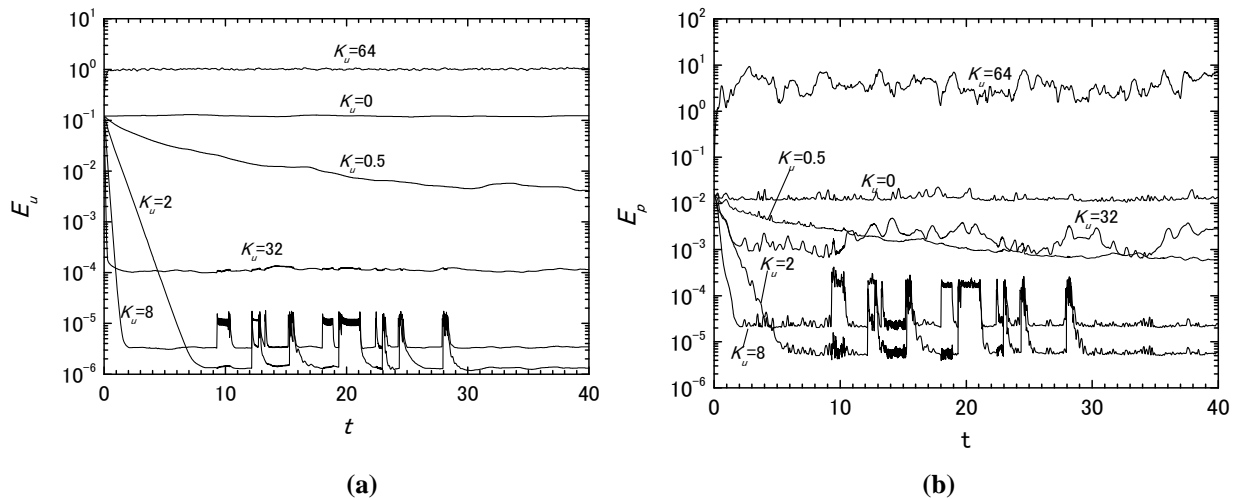
Fig. 6 Variation of error norm of MI simulations with different feedback gains for (a) velocity, and (b) pressure.
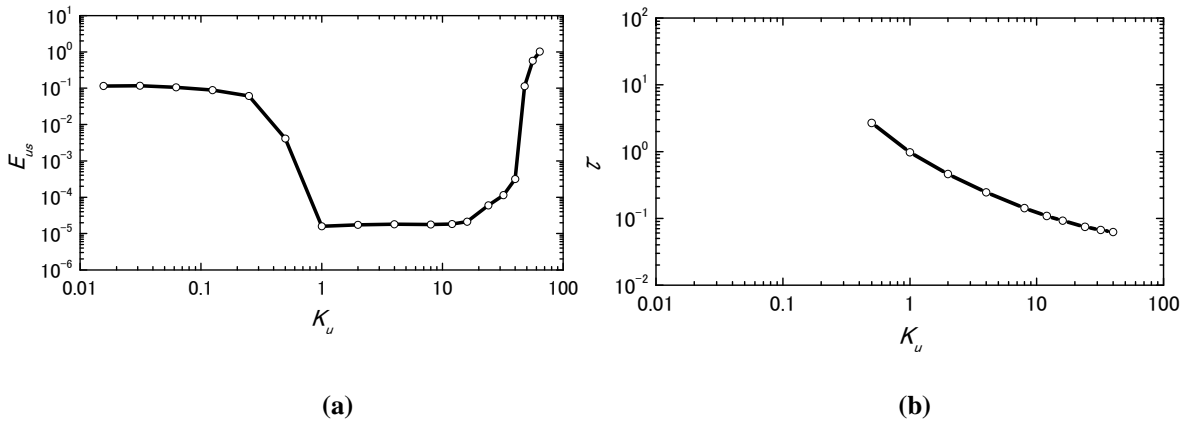
Fig. 7 Variation of (a) steady error norm, and (b) time constant of MI simulation with the feedback gain.

The steady state error and time constant of the MI simulation obtained from the above results are plotted with the feedback gain in Fig. 7 (a) and (b), respectively. Steady state error in Fig.7(a) is determined as the maximum value of the error norm in the steady stage for $t \leq 40$ if the steady stage exists or the error norm at $t = 40$ otherwise. It is noted that the steady state error defined here gives the error bound of the MI simulation. Fig.7 (a) shows that a significant reduction of the error norm by a factor on the order of 10^{-4} is achieved in a range of the feedback gain of $1 \leq K_u \leq 16$. For larger feedback gains, the error norm gradually increases up to $K_u = 40$ and then suddenly increases and exceeds the error norm of the ordinary simulation. Stability analysis of the present feedback system remains as a future work. It is noted that the results for feedback gains smaller than 1 do not show the error norm in the steady stage as mentioned above. However, this is not important since little advantage is expected by using feedback gains which are too small. The time constant in Fig.7 (b) is determined as the time in which the excess of the error norm from its steady value decreases to 37 %, or e^{-1}, of its initial value [16]. The time constant decreases almost inversely proportional to the feedback gain in a range of $0.5 \leq K_u \leq 40$.

In order to evaluate the influence of different initial conditions in the whole domain, variation of error norms for the above results are plotted in Fig. 8. The figure also includes the result for when the feedback was terminated
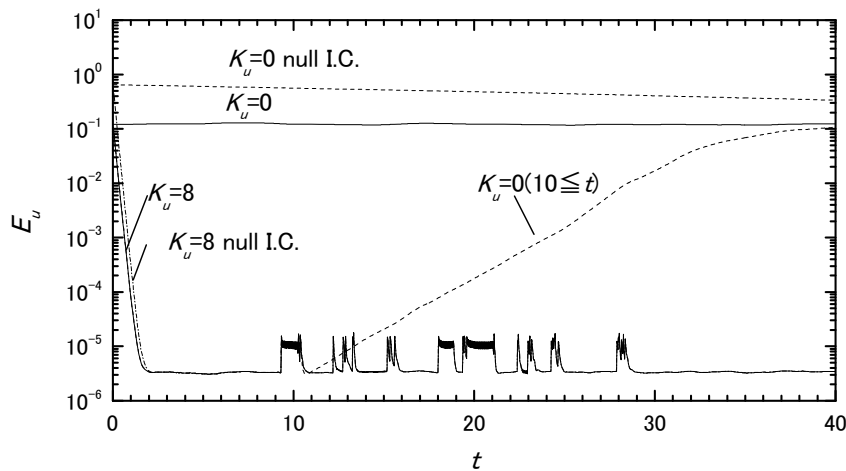
Fig. 8 Variation of the error norm for MI simulations with different initial conditions and when case feedback was terminated at t = 10.

in the middle of the calculation at $t = 10$. In the figure, the error norms for the ordinary simulations from the two relevant initial conditions are also plotted for purposes of comparison. It is noted that the ordinary simulation from the null initial velocity corresponds to the MI simulation with a feedback gain $K_u = 0$. Its error norm decreases to the level of the other ordinary simulation as it converges to the fully developed turbulent flow solution in a large amount of time as expected in the figure. By comparing two MI simulations having different initial conditions, the error norms are seen to decrease at the same exponential rate, and interestingly, come to have the same steady values with irregular perturbation ranging between 7×10^{-6} and 1.5×10^{-5}.

The MI simulation after termination of the feedback at $t = 10$ is identical to the ordinary simulation starting from the initial condition very close to the standard solution. Its error norm stays in a range of the MI simulation for a short time but then increases exponentially. This exponential rate is considered to be a structural instability characteristic of the relevant turbulent flow by which a small difference in initial condition diverges exponentially. This is the reason why ordinary simulation is incapable of reproducing the instantaneous structure of the relevant turbulent flow over a long period of time. In the MI simulation, on the other hand, the feedback loop modifies the dynamical structure of the system. The computational results from different initial conditions converge exponentially to the standard turbulent flow solution and stay close to it within a distance in the state space.

MI simulation with feedback of partial velocity components

In the former section, it was revealed that the MI simulation converged to the standard solution when the feedback signal proportional to the error in velocity vector was applied to the governing equations at the all grid points. In this section we consider the case in which the feedback signal includes partial velocity components: two velocity components u_1 and u_3 (by omitting one transverse velocity component), or u_2 and u_3 (omitting the primary velocity component), or one velocity component u_1 or u_2 (Case 2 in Table 2). It is noted that the other cases using two components u_1 and u_2, and one component u_3 are omitted considering the symmetry of the problem.

The steady state error and time constant of the MI simulation for each case are plotted with feedback gain in Fig. 9 (a) and (b), respectively. The former results using all three velocity components are also included in the figures for reference. Steady state error in Fig. 9 (a) is determined in the same way in Fig.7 (a). The result using u_1 and u_2 velocity components by omitting one transverse velocity component u_3 is somewhat degraded in comparison with that of the former case using all three velocity components, but still achieves sufficient reduction of the error by a factor of 10^{-4}. The other results using two velocity components, u_2 and u_3, and one component, u_1 or u_2, are all substantially degraded in comparison with the former two cases, although the unstable behavior for $K_u > 40$ is similar in all cases. Comparison of the time constants in Fig. 9 (b) shows a similar result as mentioned above. The result using u_1 and u_2 velocity components is almost comparable to that of the case using all three velocity components, but the time constants for the other cases are more than ten times larger implying slow convergence.
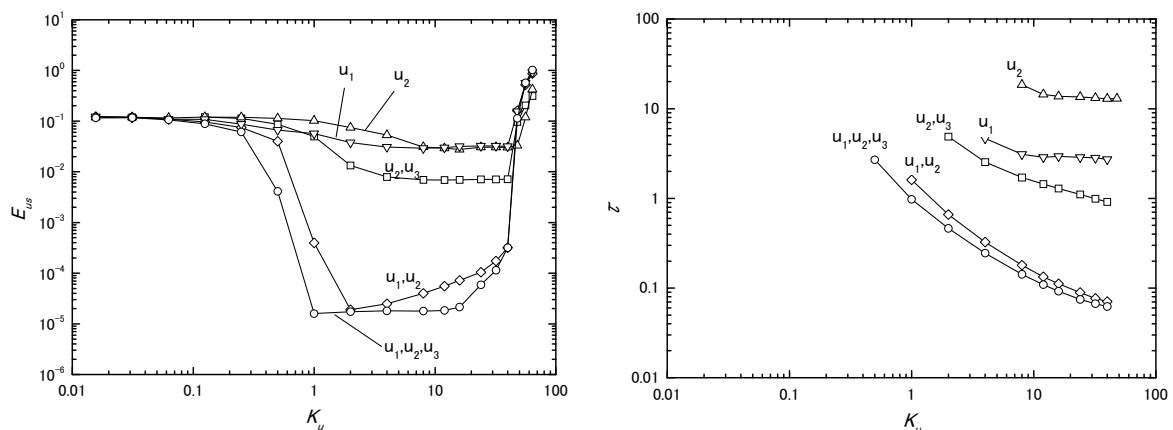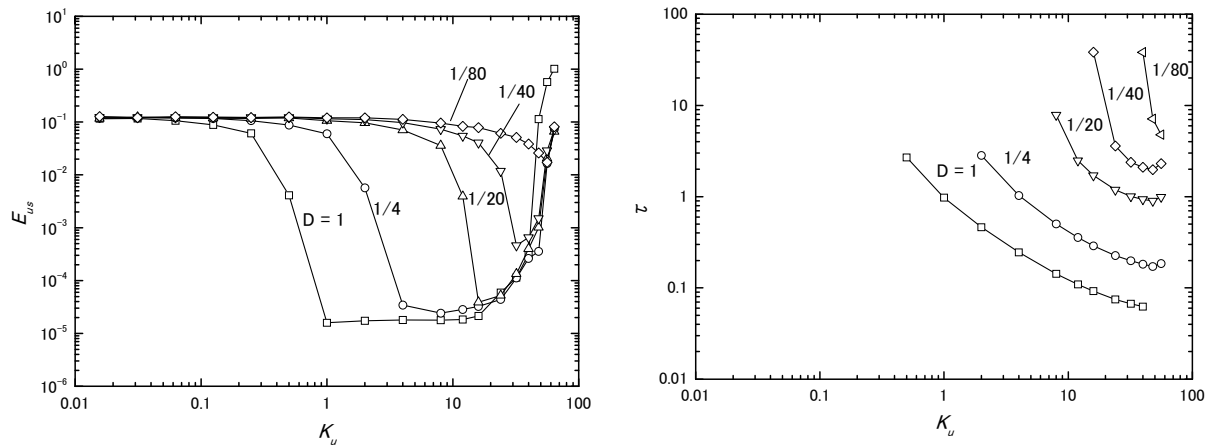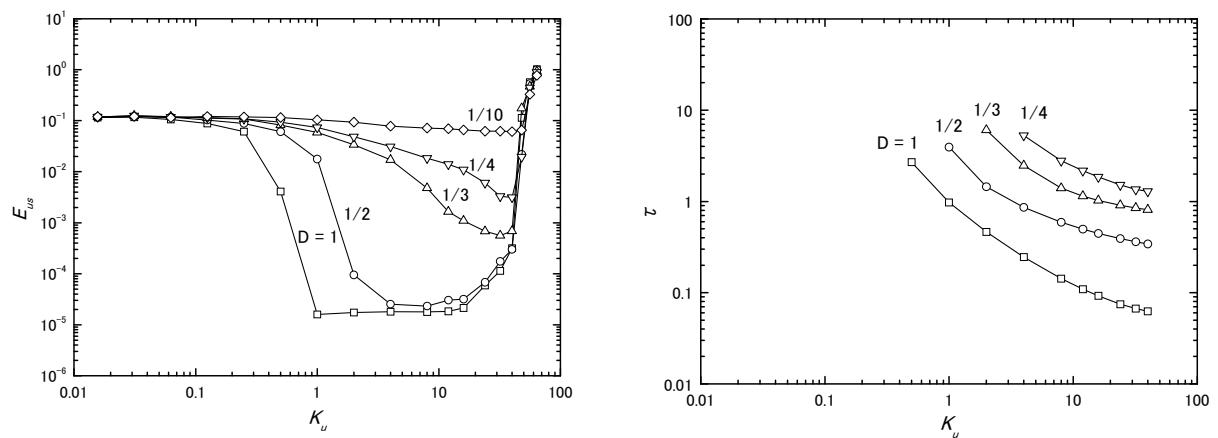

Fig. 9 Variation with gain for (a) steady error norm, and (b) time constant of MI simulations with the feedback of partial velocity components.

MI simulation with feedback at partial points

In the former section, it was revealed that MI simulation with the feedback at all grid points but using two velocity components by omitting one transverse velocity component showed a good result, while the other cases using other combinations of partial velocity components did not. In this section we consider the case in which the feedback signal is determined from all three velocity components but applied at limited grid points in the domain (Case 3 in Table 2). We perform MI simulations applying the feedback at the grid points on the planes skipped in the x_1 direction or those skipped in the x_2 direction.

Figure 10 and Figure 11 show the steady state error and the time constant of the MI simulation in which the feedback signal determined with all three velocity components was applied on selected planes in the x_1 direction or x_2 direction. As expected from the former results, reduction of the feedback points in the x_1 direction did not seriously influence the steady state error, as shown in Fig.10 (a). For example, feedback on the planes with a density of 1/20 of the whole domain still reduced the error by a factor on the order of 10^{-4} from the ordinary simulation if the gain is optimized for that condition. In Fig. 10 (b), however, the time constant increased monotonically with decreasing density of the planes. The results of MI simulation were seriously degraded

Fig. 10 Variation with gain for (a) steady error norm, and (b) time constant of MI simulations with the feedback at the grid points on the planes skipped in the x_1 direction.

Fig. 11. Variation with gain for (a) steady error norm, and (b) time constant of MI simulations with the feedback at the grid points on the planes skipped in the x_1 direction.

when the feedback points were reduced in the x_2 direction as shown in Fig. 11 (a). For example, the density of planes necessary to maintain the reduction of the error by the order of 10^{-4} is 1/2, which is ten times larger than that of the former case of skipping in the x_1 direction. The time constant increased monotonically with decreasing density of the planes.

Eigenvalue analysis

In the followings a numerical experiment is performed to examine the validity of the eigenvalue analysis presented in the previous section. Eigenvalue analysis and MI simulation are performed for the case of simple model turbulent flow through a square duct with feedback using all three velocity components (Case (A)), or using the mainstream and one transverse velocity component (Case (B)) (see Table 4).

In the numerical experiment, we deal with a numerical solution for a fully developed turbulent flow in a square pipe as a model of real flow, or a standard solution. The computational conditions are shown in Table 5. Although the grid resolution is not fine enough to correctly simulate the detailed structure of the turbulent flow, the numerical solution has the fundamental characteristics of the relevant turbulent flow [23]. This simplification is justified because the purpose of this numerical experiment is not to investigate the turbulent flow but to examine whether the eigenvalue analysis can be used to design the MI simulation.

In the following, all the values are expressed in dimensionless form using the side length of the square cross section $\tilde{b}$, the density of fluid $\tilde{\rho}$, and the mean axial velocity $\tilde{u}_{m0}$ given by $\tilde{u}_{m0} = \sqrt{2\Delta\tilde{p}/\lambda L}$ where the coefficient of resistance λ is evaluated by means of Blasius' formula [24] $\lambda = 2\Delta p/L = 0.316 R_{e0}^{-1/4}$. Time scale is given by $\tilde{b}/\tilde{u}_{m0}$. As to the boundary condition, periodical velocity condition and the constant pressure difference δ_p corresponding to a specified Reynolds number $R_{e0} = \tilde{u}_{m0}\tilde{b}/\tilde{\nu}$ is assumed between the upstream and downstream boundaries for a duct with a periodical length of 4. A non-slip condition is assumed on the walls [6]. Computational scheme used in this study is the same as that in former section. The discretized representations of the governing equations are obtained through the finite volume method on an orthogonal equidistant staggered grid system. Convection terms are discretized by a reformulated QUICK scheme. A two-time level implicit scheme is used for time dependent terms. The resultant set of finite difference equations is solved using the iterative procedure based on the SIMPLER method.

The standard solution or the model of the real flow was obtained using the final result of the statistically steady flow solution for a fully developed turbulent flow as the initial condition. As to the MI simulation considered here, we use a computational scheme identical to that for the standard solution. The feedback gain matrix $\mathbf{K_u}$ in Eq. (9) is assumed to be a diagonal matrix whose diagonal components are all of identical value k_u:

Table 4 Conditions of MI simulation

	Case A	Case B	Case C
Simulation	Ordinary	MI	MI
Feedback points	None	All	All
Feedback velocity components	None	All (u_1, u_2, u_3)	Partial (u_1, u_2)

Table 5 Computational conditions

Periodical length L	4
Pressure difference	0.0649
Standard Reynolds number	9000
Grid points	$20 \times 10 \times 10$
Time increment	0.025
Total residual at convergence	0.01

$$\mathbf{K_u} = k_u \mathbf{I}$$

(22)

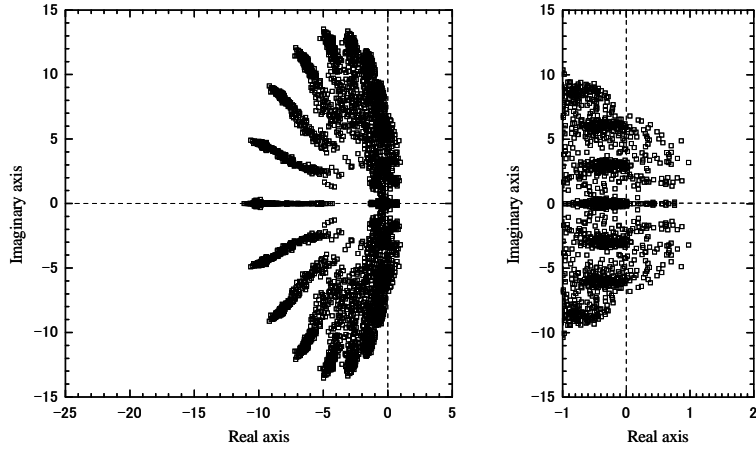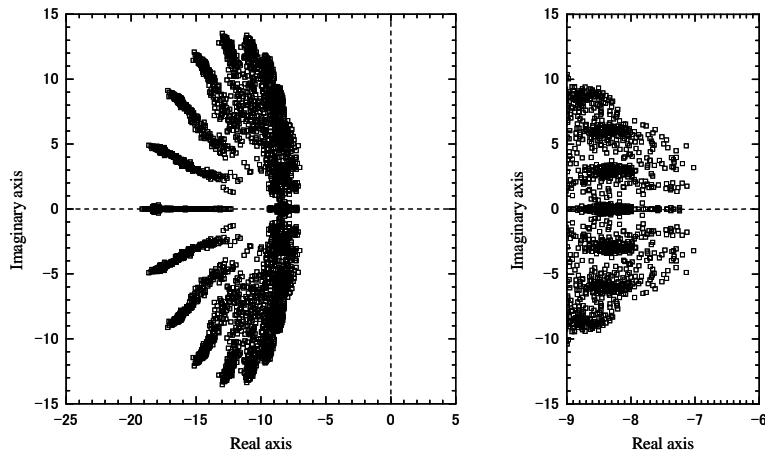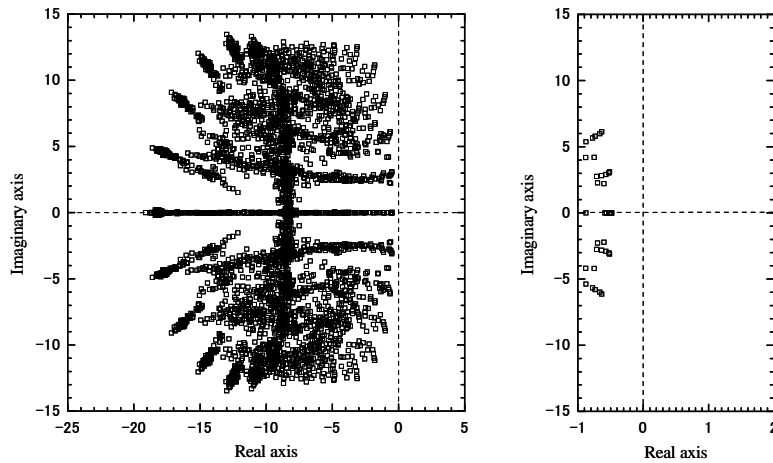Hereafter, the orthogonal component k_u is called the feedback gain. The resultant feedback signal accelerates or

Fig.12 Eigenvalue distribution of ordinary simulation (case A)

(a) Case B

(b) Case C

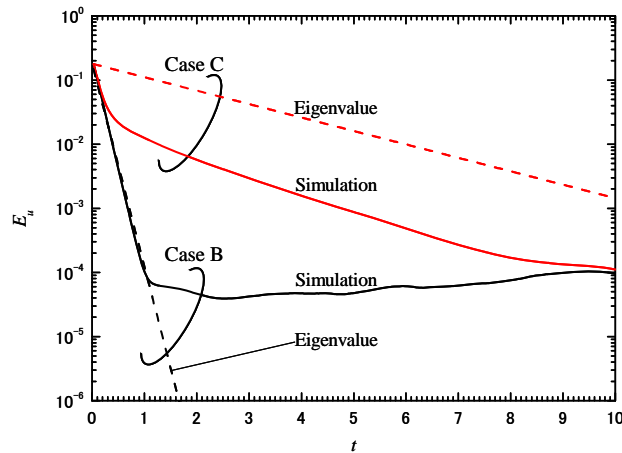**Fig. 13 Eigenvalue distribution of MI simulations (ku=8)**

Fig. 14 Comparison of variation of error norm between eigenvalue analysis and numerical simulation

decelerates the fluid in a control volume to reduce the error in velocity. As for $\mathbf{C_u}$ in Eq. (9), we consider two cases: all three velocity components, or the mainstream and one transverse velocity component are available at all the grid points.

As to the eigenvalue analysis, we assume no measurement error. Terms due to model errors are also ignored since we use the same computational scheme for both the standard solution and MI simulation canceling out the model error terms in Eqs. (10) and (11). For calculation of system matrix $\mathbf{A'}$ in Eq. (18), $\tilde{B}$ in Eq. (16) is numerically obtained from singular value decomposition by using MATLAB R2006b (ver7.3, The MathWorks). The expression of matrix A is similar to the expression of the basic equation of the SIMPLER method (omitted due to space limitation). The eigenvalues of matrix $\mathbf{A'}$ are calculated by the QR method by using SCSL library. Computation using MATLAB was performed with SX-9 in Cyberscience Center, Tohoku University, and other computation was performed with Altix 3700 Bx2 using one CPU in the Advanced Fluid Information Research Center, Institute of Fluid Science, Tohoku University.

In the following we consider three cases: case (A), ordinary simulation; case (B), MI simulation with feedback using all three velocity components; and case (C), MI simulation with feedback using the mainstream and one transverse velocity component (see Table 4).

Eigenvalues, λ_i ($i=1,2,\cdots,2N,N=2000$) of the system matrix A' of the error dynamics for the ordinary simulation are shown in Fig. 12. The right figure of Fig.12 is a figure whose real axis is enlarged to show the most unstable eigenvalues. For ordinary simulation, a number of eigenvalues are unstable, the most unstable eigenvalues being $\lambda_m=0.98\pm3.2j$. This means that the numerical simulation starting from an initial condition near the standard solution deviates from it exponentially, representing a sensitive dependence on the initial condition, which is typical for turbulent flows.

Figures 13 (a) and (b) show the eigenvalues for MI simulation of cases (B) and (C) with feedback gain $k_u = 8$. In each case, all eigenvalues have a negative real part, implying that the error dynamics is stable due to the effect of feedback, and the error of the MI simulation decreases exponentially. The result for case (B) in Fig. 13 (a) is a translation of the result of Fig. 12 in the negative real direction with an amount of the feedback gain k_u. This is obvious from the definition of A in Eq. (13). The least stable eigenvalues are $\lambda_m=-7.02\pm3.2j$ (see right figure of Fig. 13 (a)). In the result for case (C) in Fig. 13 (b), the eigenvalues also shift to the left, but the amount of the shift is less than in case (B) for some eigenvalues. The least stable eigenvalues are $\lambda_m=-0.48\pm0.029j$ (see right figure of Fig. 13 (b)) .

In the following, the results of the eigenvalue analysis and MI simulation are shown and compared. Here, the norm of velocity error is defined as

$$E_u \equiv \left[\frac{1}{3N}\mathbf{e_u}^T\mathbf{e_u}\right]^{1/2}$$
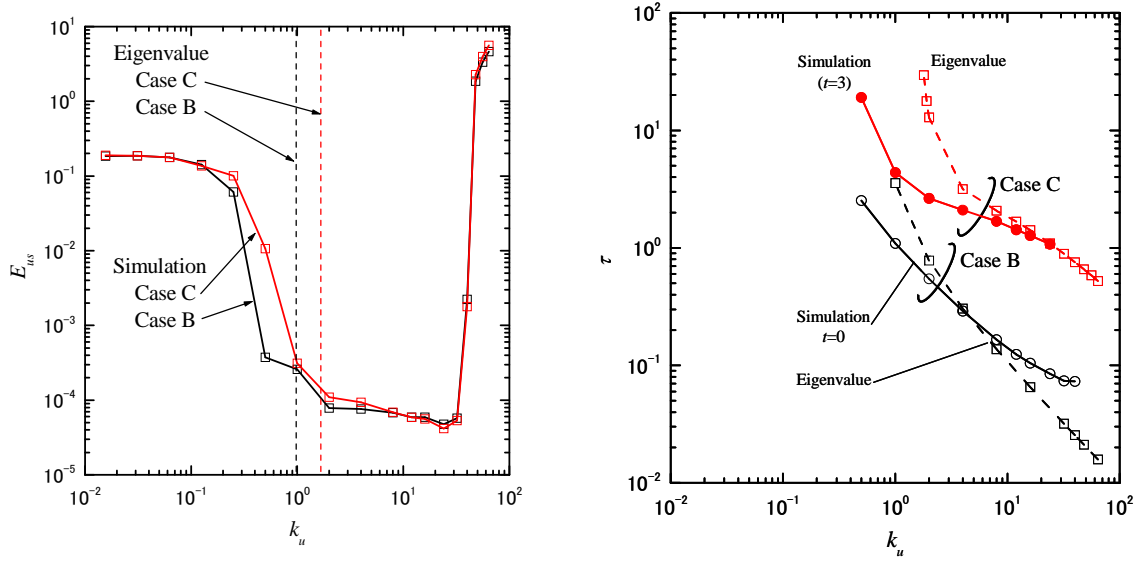
(23)

Fig.15 Steady error norm and time constant with feedback gain

Time-variation of the error norm E_u for the MI simulation with the feedback gain $k_u = 8$ in the cases of (B) and (C) are indicated in Fig. 14 by the solid lines. In case (B), the error norm first decreases exponentially and then remains in a certain range. On the other hand, in case (C), the error norm first decreases exponentially in the same way as in case (B), but the reducing rate changes around $t = 0.6$ and the error decreases more slowly afterwards. Broken lines in the figure represent the variation of the error norm for the least stable mode obtained from the eigenvalue analysis for cases (B) and (C). These are calculated using the real part of the eigenvalue and the initial magnitude identical to that of the MI simulation.

In MI simulation, the error norm reaches some steady value as time passes. Fig. 15 (a) shows steady error with the feedback gain. As shown in this figure, the steady error norm E_{us} decreases to order of 10^{-4} in the range of $0.5 < k_u < 24$ for case (B) or $1 < k_u < 24$ for case (C), respectively. The broken lines correspond to the critical feedback gain, or the lower limit of the feedback gain, below which there exist unstable eigenvalues. The error norm increases with excessive feedback gain above 30 in the MI simulation. This result is possibly explained by the discrete-time system analysis, and is beyond the scope of present paper.

Next, we consider the time constant τ as the time in which the error norm decreases by a factor of $1/e$. In MI simulation, as shown in Fig. 14, the rate of the error norm reduction is almost constant for case (B), while it changes around $t = 0.6$ for case (C). We evaluated the time constant at $t = 0$ for case (B), or the value at $t = 3$ for case (C). For eigenvalue analysis, the time constant τ of E_u is estimated as

$$\tau = -\frac{1}{\lambda_k},$$

(25)

where λ_k is the real part of the eigenvalue for the least stable mode. Generally, as time passes, the least stable mode becomes the dominant mode.

The variation of the time constant with the feedback gain is compared between the MI simulation and the eigenvalue analysis for cases (B) and (C) in Fig. 15 (b). The results of eigenvalue analysis agree well with those of the MI simulation except for case (C) with small feedback gain below 4.

The time required for calculation of the 2000 dimensional eigenvalues was about 30 minutes while the corresponding computation of MI simulation was about 7 minutes. Large computational time to obtain eigenvalues of large dimensional system is an inherent problem of the proposed method, and will be treated in a future work.

Summary

In this article formulation of MI simulation and equations of linearized error dynamics and eigenvalue analysis of MI simulation were explained. Example of MI simulation was presented for a fully developed turbulent flow in a square duct. Numerical experiment was performed for MI simulation with a feedback signal from the predetermined standard turbulent flow solution. Convergence of MI simulation to the standard solution was investigated as a function of feedback gain and spatial and temporal density of feedback signal. Eigenvalue analysis was performed to examine the validity of the linearized error dynamics approach in the design of feedback signal.

References

[1]   Thompson JMT, Stewart HB. Nonlinear Dynamics and Chaos. John Wiley and Sons; 1986.

[2]   Benjamin SG, Dévényi D, Weygandt SS, Brundage KJ, Brown JM, Grell GA, Kim D, Schwartz BE, Smirnova TG, Smith TL, Manikin GS. An Hourly Assimilation-Forecast Cycle. The RUC Mon Wea Rev 2004; 132:495-518.

[3]   Talagrand O. A study of the Dynamics of Four Dimensional Data Assimilation. Tellus 1981; 33: 43-60.

[4]   Zupanski M. Regional 4-Dimensional Variational Data Assimilation in a Quasi-Operational Forecasting Environment. Mon Wea Rev 1993; 121: 2396-2408.

[5]   Bouttier F, Rabier F. The Operational Implementation of 4D-VAR. ECMWF Newsletter 1997; 78: 2-5

[6]   Humphrey JAC, Devarakonda R, Queipo N. Interactive Computational-Experimental Methodologies (ICEME) for Thermofluids Research: Application to the Optimized Packaging of Heated Electronic Components. Computers and Computing in Heat Transfer Science and Engineering, (ed. Yang, K. T. and Nakayama, W.). CRC Press and Begell House. New York. 1993; 293-317.

[7]   Zeldin BA, Meade AJ. Integrating experimental data and mathematical models in simulation of physical systems. AIAA J 1997; 35:1787-1790.

[8]   Ido T, Murai Y, Yamamoto F. Postprocessing Algorithm for Particle-Tracking Velocimetry Based on Ellipsoidal Equations. Exp in Fluids 2002; 32:326-336.

[9]   9. Uchiyama M, Hakomori K. Measurement of Instantaneous Flow Rate Through Estimation of Velocity Profiles. IEEE Trans Automat Contr 1983; AC-28; 380-388.

[10] Sorenson H, ed. Kalman filtering: theory and application. IEEE press; 1985.

[11] Högberg M, Bewley TR, Henningson DS. Linear feedback control and estimation of transition in plane channel flow. J Fluid Mech 2003;481:149-175.

[12] Hayase T, Hayashi S. State Estimator of Flow as an Integrated Computational Method with the Feedback of Online Experimental Measurement. Trans ASME J Fluids Eng 1997; 119(4):814-822.

[13] Nisugi K, Hayase T, Shirai A. Fundamental Study of Hybrid Wind Tunnel Integrating Numerical Simulation and Experiment in Analysis of Flow Field. JSME Int J Ser B 2004; 47(3):593-604.

[14] Hayase T, Nisugi K, Shirai A. Numerical Realization for Analysis of Real Flows by Integrating Computation and Measurement. Int J Num Meth Fluids 2005; 47: 543-559.

[15] Funamoto K, Hayase T, Shirai A, Saijo Y, Yambe T. Fundamental study of Ultrasonic-Measurement-Integrated simulation of real blood flow in the aorta. Ann Biomed Eng 2005; 33: 413-426.

[16] Skelton RE. Dynamic Systems Control. John Wiley & sons; 1988.

[17] Misawa EA, Hedrick JK. Nonlinear Observers: A State-of-the-art Survey. J Dynamic Sys Meas Control Trans ASME 1989; 111: 344-352.

[18] Curtain RF, Zwart HJ. An Introduction to Infinite-Dimensional Linear Systems Theory. Springer- Verlag, New York; 1995: 246.

[19] Li X, Yong J. Optimal Control Theory for Infinite Dimensional Systems, Birkhäuser; 1995.

[20] Imagawa K, Hayase T, Eigenvalue analysis of linearized error dynamics of measurement integrated flow simulation, Computers & Fluids 2010; 39, 1796-1803.

[21] Imagawa K, Hayase T, Numerical experiment of measurement-integrated simulation to reproduce turbulent flows with feedback loop to dynamically compensate the solution using real flow information, Computers & Fluids 2010; 39, 1439-1450.

[22] Huser A, Biringen S. Direct Numerical Simulation of Turbulent Flow in a Square Duct. J Fluid Mech 1993; 257: 65-95.

[23] Hayase T. Monotonic Convergence Property of Turbulent Flow Solution With Central Difference and Quick Schemes. Trans ASME J Fluids Eng 1999; 121(2):351-358.

[24] Schlichting H. Boundary-Layer Theory 7th edition. McGraw-Hill. New York. 1979.

[25] Hayase T, Humphrey JAC, Greif R. A Consistently Formulated QUICK Scheme for Fast and Stable Convergence Using Finite-Volume Iterative Calculation Procedures. J Compt Phys 1992; 98:108-118.

[26] Fletcher CAJ. Computational Techniques for Fluid Dynamics. Springer-Verlag 1988:302.

[27] Patankar SV. Numerical Heat Transfer and Fluid Flow. Hemisphere. Washington DC/New York. 1980.

Sensitivity Analysis of Unsteady Flow Fields and Numerical Experiments for Optimal Measurement

Takashi Misaka
Shigeru Obayashi

Institute of Fluid Science, Tohoku University
Sendai, 980-8577
Japan
misaka@edge.ifs.tohoku.ac.jp

Abstract

Difficulty of data assimilation arises from a large difference between the sizes of a state vector to be determined, i.e., the number of spatiotemporal grid points of a discretized numerical model, and a measurement vector, i.e., amount of measurement data. Flow variables on a large number of grid points are hardly defined by spatiotemporally limited amount of measurement data that poses an underdetermined problem. In this study we conduct sensitivity analysis of a vortex flow field by the use of an adjoint method. The idea of optimal/targeted observation in meteorology which aim to effectively determine a flow state by limited observations is interpreted in fluid dynamic problems where unsteady flows of much smaller scales are of interest.

Key words: sensitivity analysis, 4D-Var, large-eddy simulation.

Introduction

The use of observation data to improve a numerical prediction is known as data assimilation method in meteorological and oceanography communities [1]. The data assimilation is based on the optimal control theory. As a consequence there are two major approaches: sequential and variational methods, where the former includes a Kalman filter. The application of these methods to large scale problems in meteorology made the development of data assimilation methods slightly independent from optimal control studies, that is, the effort is put into the reduction of numerical costs of those methods. One example is the invention of ensemble Kalman filter, which approximately represents the system error covariance by an ensemble of model runs. By this the cost of matrix operations in Kalman filter can be drastically reduced. The numerical cost of variational methods such as the four-dimensional variational method (4D-Var) is usually smaller than the ensemble Kalman filter, therefore, the introduction of the 4D-Var into the operational weather forecast was earlier than that of ensemble Kalman filter. However, the cost for maintaining the adjoint code in the 4D-Var and the need for parallel computation accelerate the use of ensemble Kalman filters in meteorological community. Because of its rational approach to estimate a true state based on both measurement and simulation, the application of data assimilation methods is not limited to the area of meteorological and oceanographic studies.

We have been studying the applicability of data assimilation methods in aeronautical researches. Numerical simulations of atmospheric turbulences such as clear air turbulence and aircraft wake turbulence were performed with the 4D-Var method based on an aeronautical computational fluid dynamics (CFD) code [2,3]. Recent attempt is the mitigation of uncertainty of Reynolds-averaged Navier-Stokes (RANS) turbulence modeling by the use of ensemble Kalman filter, where parameters of the Spalart-Allmaras turbulence model are optimized based on pressure measurement around an airfoil [4]. On the other hand, a classical nudging technique is used to initialize aircraft wake in a computational domain to simulate realistic wake turbulence, where a high-fidelity RANS flow field is nudged instead of measurement data [5]. Nevertheless, the numerical approach used there is

very similar to that of data assimilation. Based on experiences gained from those applications our interest is to have a more general guidance to apply data assimilation methods successfully to problems with given conditions for measurement and simulation.

As a small step to that direction, the present study is an attempt to investigate the impact of measurement in a data assimilation system by a sensitivity analysis method and to use the information for optimal/targeted measurements. Here again we refer the preceding work of sensitivity analysis in meteorology [6]. We consider here an idealized situation in numerical experiments, i.e., a two vortex system where self-induced advection velocity realizes a transient flow field. The impact of the number of measurement points is firstly investigated, and the possibility of optimal measurement is exploited in the numerical experiments where locations of the measurement points are optimized to use the limited number of measurement points efficiently.

Approach

In this study we employ the 4D-Var method. The objective of data assimilation based on the 4D-Var method is to obtain an initial flow condition which reproduces corresponding measurements during a certain time period (assimilation window) [1]. Figure 1 shows a schematic of the 4D-Var method. Vertical and horizontal axes show flow state and time, respectively. A solid line shows a trajectory of a real flow state. Broken lines show trajectories of the simulated flow state starting from different initial conditions. The 4D-Var method is the method to obtain the initial condition of the real flow state by evaluating the difference of these trajectories within a assimilation window.
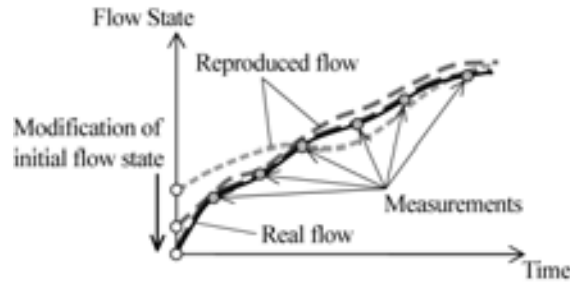
Figure 1. Schematic of data assimilation based on 4D-Var method.

The differences of measurements (usually measurements have less information compared to the numerical simulation) and corresponding numerical results evaluated by conducting the numerical simulation over a period of time are represented as an objective function with respect to an initial flow variable $\boldsymbol{Q}_0$,

$$J(\boldsymbol{Q}_0) = \frac{1}{2}\sum_{i=1}^{N}[H_i(\boldsymbol{Q}_i) - \boldsymbol{y}_i]^T \boldsymbol{R}_i^{-1}[H_i(\boldsymbol{Q}_i) - \boldsymbol{y}_i]. \tag{1}$$

Here, H_i is an observation operator which converts the dimension of computational flow variables into that of measurement data to evaluate these differences. Subscript i shows a time step of the flow computation and N is the total time number of the time steps. Equation (1) is a function of $\boldsymbol{Q}_0$, that is, the data assimilation process is formulated as a minimization problem of $J(\boldsymbol{Q}_0)$ with control variables of $\boldsymbol{Q}_0$. The 4D-Var method has a capability to treat measurement error through a measurement error covariance matrix R_i, where its elements are the covariance between each measurement points. In this study R_i is set to unit matrix. Basically the covariance matrix defines relative importance of measurements; therefore, we do not consider the effect in the present numerical experiments.

To obtain the gradient of $J(\boldsymbol{Q}_0)$ used for the minimization of $J(\boldsymbol{Q}_0)$, a Lagrange function is introduced using a Lagrange multiplier vector $\boldsymbol{\lambda}_i$. The procedure to obtain the gradient is finally written as follows [2]:

$$\boldsymbol{\lambda}_{N+1} = 0, \tag{2}$$

$$\boldsymbol{\lambda}_i = \boldsymbol{M}_i^T \boldsymbol{\lambda}_{i+1} + \boldsymbol{H}_i^T[H_i(\boldsymbol{Q}_i) - \boldsymbol{y}_i], \quad (i = N \frown 0), \tag{3}$$

$$\nabla J(\boldsymbol{Q}_0) = \boldsymbol{\lambda}_0. \tag{4}$$

Equations (2)-(4) show that the gradient of $J(\boldsymbol{Q}_0)$ is obtained by the inverse time integration of $\boldsymbol{\lambda}_i$ using the adjoint operator $\boldsymbol{M}_i^T$ with a force term: $\boldsymbol{H}_i^T[H_i(\boldsymbol{Q}_i) - \boldsymbol{y}_i]$. After obtaining the gradient, the minimization of $J(\boldsymbol{Q}_0)$ is conducted by the quasi-Newton method through modifying the initial flow variable $\boldsymbol{Q}_0$. The Hessian matrix is approximated using the limited-memory Broyden-Fletcher-Goldfarb-Shanno (BFGS) method. In this method, memory requirements are reduced because the approximated Hessian matrix is not stored explicitly.

Here we investigate the impact of measurement data on a retrieved flow field within a framework of the data assimilation system based on the 4D-Var method. The sensitivity of the cost function with respect to the observation vector $\boldsymbol{y}_i$ is represented as follows [6]:

$$\nabla_{\boldsymbol{y}_i} J(\boldsymbol{Q}_0) = \boldsymbol{H}_i \boldsymbol{M}_{0,i} \big[\nabla^2_{\boldsymbol{Q}_0 \boldsymbol{Q}_0} J(\boldsymbol{Q}_0)\big]^{-1} \nabla J(\boldsymbol{Q}_0), \tag{5}$$

where $\nabla^2_{\boldsymbol{Q}_0 \boldsymbol{Q}_0} J(\boldsymbol{Q}_0)$ represents a Hessian matrix, and we can use the approximated Hessian matrix obtained from the limited-memory BFGS. A mapping of the sensitivity on measurement points onto the grid points of numerical simulation is performed as follows:

$$\boldsymbol{H}_i^T \nabla_{\boldsymbol{y}_i} J(\boldsymbol{Q}_0) = \boldsymbol{M}_{0,i} \big[\nabla^2_{\boldsymbol{Q}_0 \boldsymbol{Q}_0} J(\boldsymbol{Q}_0)\big]^{-1} \nabla J(\boldsymbol{Q}_0). \tag{6}$$

For flow simulations we employ incompressible Navier-Stokes equations. The equations are discretized by the fully-conservative fourth-order central difference scheme [7]. Time integration is performed by third-order low storage Runge-Kutta scheme [8]. The Lagrangian dynamic model is used as a subgrid scale model for large-eddy simulation [9], which has superiority in vortical flows [10]. The adjoint codes are derived first by linearizing the above equations, then by rewriting it from backward by replacing inputs and outputs of each code line. The latter operation corresponds to a transpose of the matrix composed of coefficients of the linearized Navier-Stokes equations. The both Navier-Stokes and the adjoint codes are parallelized by using message passing interface (MPI) for large scale computations.

The development of linear and adjoint codes can be done step by step processes in the following way. First the derived linear code is checked by $|M(\boldsymbol{Q} + \alpha\delta\boldsymbol{Q}) - M(\boldsymbol{Q})|/|\alpha M \delta\boldsymbol{Q}| - 1 = O(\alpha)$ where the left-hand-side decreases with the order of α. It is also possible to check the angle: $[M(\boldsymbol{Q} + \alpha\delta\boldsymbol{Q}) - M(\boldsymbol{Q})]^T [M\delta\boldsymbol{Q}]/ (|M(\boldsymbol{Q} + \alpha\delta\boldsymbol{Q}) - M(\boldsymbol{Q})||M\delta\boldsymbol{Q}|) - 1 = O(\alpha^2)$, which decreases with α^2. The adjoint code is a transpose of the linearized code and is derived line by line without composing an explicit matrix. In the adjoint code, the following relation $[MQ]^T MQ - Q^T[M^T[MQ]] = O(\epsilon)$ is true on the order of 10^{-14} in the Fortran double precision real. The above processes can be conducted in small program modules such as convective and diffusion terms of Navier-Stokes equations as well as a whole code including all terms and a time integration part. Finally, the computed gradient is confirmed by $|J(\boldsymbol{Q} + \alpha\delta\boldsymbol{Q}) - J(\boldsymbol{Q})|/[\alpha\delta\boldsymbol{Q}^T(\nabla J(\boldsymbol{Q}))] - 1 = O(\alpha)$, where again the left-hand-side decreases with α. Table 1 shows the computed gradient, while Table 2 shows the strong scaling of the gradient computation in parallel where the number of total grid points is fixed with increasing processor numbers.

**Table 1. Confirmation of gradient computation.**

α	$\nabla J(\boldsymbol{Q}_0)$
1.E+1	1.394683E+1
1.E+0	1.614762E+0
1.E-1	1.626424E-1
1.E-2	1.626592E-2
1.E-3	1.626596E-3
1.E-4	1.626548E-4
1.E-5	1.623851E-5
1.E-6	1.414659E-6
1.E-7	-2.144048E-6

Table 2. Strong scaling of the gradient computation.

Number of processors	Wall-clock time [sec]
8	1476.56
16	638.72
32	277.10
64	184.39
128	93.93
256	109.62
512	42.15

The computational setting is as follows (see also Fig. 2). We consider a flow field defined by a pair of Lamb-Oseen vortices which are characterized by vortex circulation $\Gamma_0 = 300 \text{ m}^2/\text{s}$, vortex core radius of $r_c = 4$ m and vortex separation $b_0 = 40$ m. The vortex flow field is initialized two-dimensionally along x-axis within a domain bounded by $L_x = 64$ m, $L_y = 128$ m, $L_z = 128$ m sides. A constant mesh spacing of 2 m is used for all three spatial directions. Time integration is conducted until one tenth of vortex reference time t_0, i.e., 3.3 s in the present condition, where the vortex pair moves a distance of one tenth of vortex separation b_0 during this period. Parallel computation is performed by a domain decomposition approach, where typically $n_x = 2$, $n_y = 4$, $n_z = 4$ processors are used in the present study.

Numerical experiment is conducted first by generating reference flow fields starting from the above conditions. In this process we acquire pseudo measurement data based on the following strategies, i.e., velocity components of the all grid points are considered as measurements (Case 1), velocity components from every second grid points in both y- and z-directions are used (Case 2), and the data on every fourth grid points are used as measurements (Case 3). Compared to Case 1, the number of measurements is one fourth in Case 2 and one sixteenth in Case 3. Then the 4D-Var cycle (forward time integration for the evaluation of a cost function, backward time integration of the adjoint code, Hessian matrix computation with limited-memory BFGS and linear search) is started with an arbitrary flow field, where we consider a weaker vortex pair compared to the reference flow field ($\Gamma_0 = 200 \text{ m}^2/\text{s}$, $r_c = 6$ m and $b_0 = 60$ m). Adaptive measurement processes starts after a few iterations of the 4D-Var cycle. Having an approximated Hessian matrix and the gradient from the adjoint code, the observation sensitivity can be computed by using Eq. (5). In this paper we only consider the observation sensitivity at the beginning of time integration. Using the observation sensitivity mapped onto the numerical grid, measurement points are redistributed based on the magnitude of the observation sensitivity, where the total number of the measurement points is kept constant.
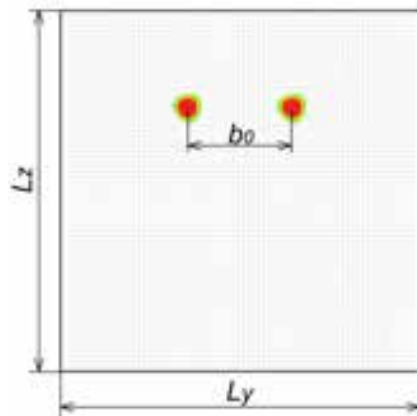
Figure 2. Computational domain with grid lines and initial vortex positions.

Results

Figure 3 shows histories of cost function defined by Eq. (1) for three measurement strategies, while the global error is evaluated by using the whole mesh points. This indicates that the decrease of the cost function in the 4D-Var is not always connected with the convergence of the retrieved flow field to the reference flow field. In Case 1 the value of the cost function and the global error are identical because three velocity components on all grid

points in the domain are used as measurements. The value of the cost function is proportional to the number of measurement points and time steps, therefore, the values reduce from Case 1 to Case 3. On the other hand, the decrease of the global error becomes slow as the number of measurements is reduced. This confirms that there is a limitation for defining a flow field by using a limit number of measurements, i.e., a number smaller than a degree of freedom in the numerical model. Please note that the behaviors of the cost function and the global error might vary depending on the data assimilation methods used and parameters included in the optimization algorithms, however, the tendency shown here may be true also for other methods.

Figure 4 shows a similar plot as Fig. 3 but with optimal measurement strategies described above. Here the redistribution of measurement points is done in the every 5th iteration of the 4D-Var assimilation cycle. Until 5th iteration the values of cost function and the global error are the same as those of Fig. 3. At the 6th iteration the value of cost function rapidly increases because the measurement points are redistributed to the regions where the global error is relatively large. The cost function again decreases after a few iterations. During the reduction of cost function, the global error values are also decreased in Case 2 and Case 3, and the values become smaller than those in Fig. 3. This implies that the global error can be effectively reduced by locating measurement points on places where the relative error is large. And it becomes possible by checking the observation sensitivity in the data assimilation cycle. Even with the adaptive measurement strategy the global error is larger than the Case 1 where measurements of all grid points are given.
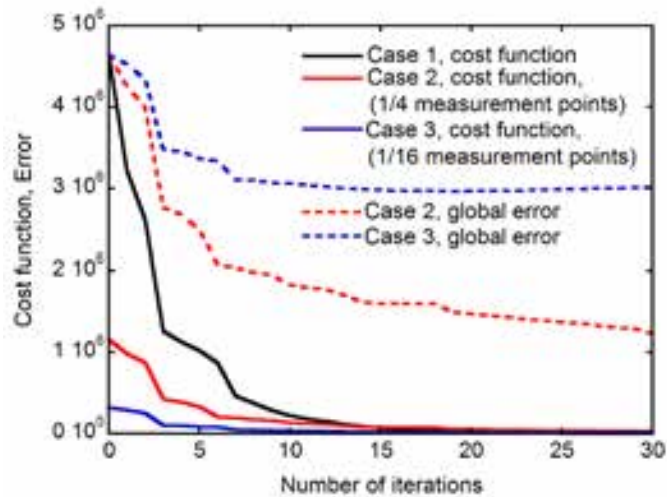
Figure 3. Histories of cost function and global error with different measurement points
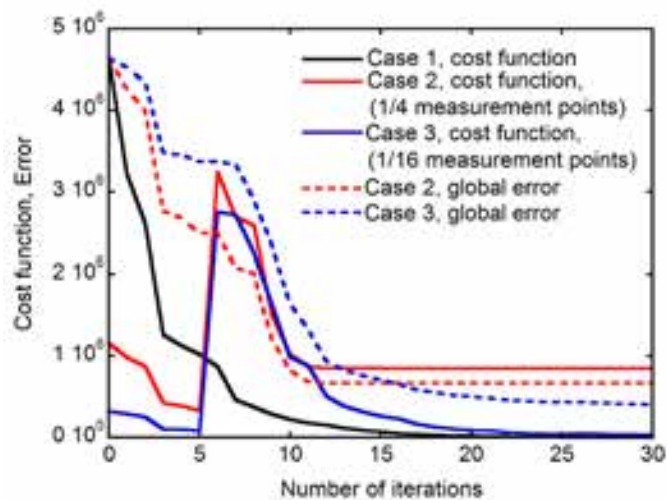
Figure 4. Histories of cost function and global error with adaptive measurement

Figure 5 shows the distribution of measurement points in Case 2, where every second grid points in both *y*- and *z*-directions have measurements. The total number of measurement points is one fourth of that in Case 1. Figure 5(a) shows the initial distribution, and Fig. 5(b) shows the distribution after the first rearrangement of measurement points. These measurement points are colored by the magnitude of observation sensitivity at those locations. Since the measurement points are redistributed using the grid points of the numerical simulation, the measurement points do not come closer than the grid spacing. The resolution of measurements finer than that of numerical simulation may not improve the retrieved flow field in the context of data assimilation. Figure 5(c) shows the distribution of measurement points at 16th iteration, where the distribution is similar to that of Fig. 5(b) where the points are clustered near vortices. In the same way Fig. 6 show the Case 3 where every fourth grid points in both *y*- and *z*-directions has measurements. The total number of measurements is one sixteenth of that in Case 1. As in the Case 2 the measurement points are clustered near vortices at the first adaptation.
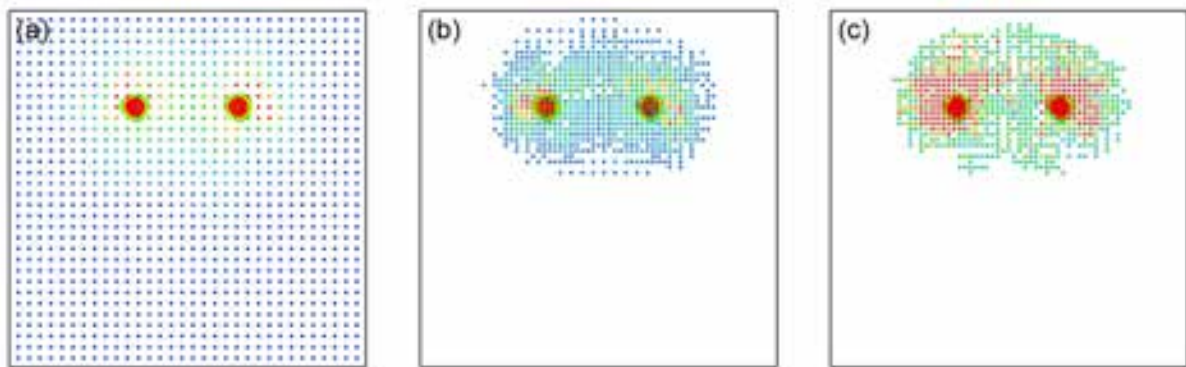
Figure 5. Distribution of measurement points with optimal measurement (Case 2), where the color of the points shows the magnitude of observation sensitivity at those locations.
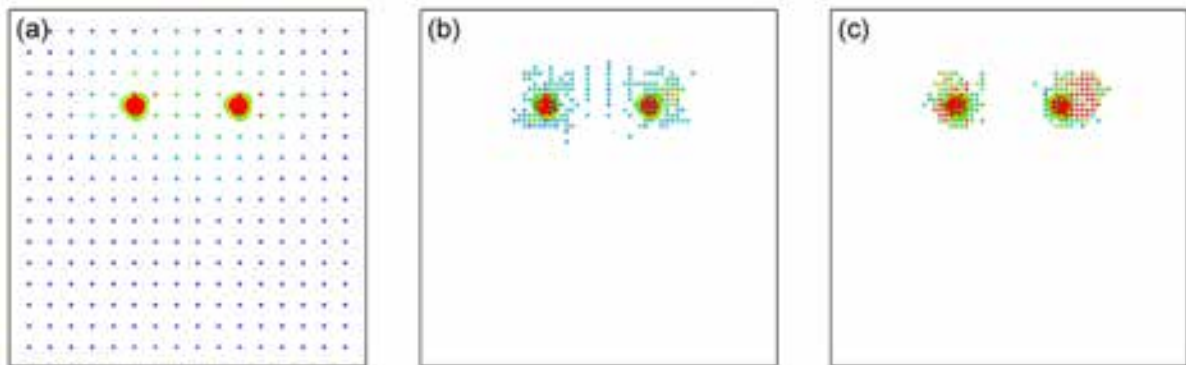
Figure 6. Distribution of measurement points with optimal measurement (Case 3) , where the color of the points shows the magnitude of observation sensitivity at those locations.

Conclusions

In this study we conduct sensitivity analysis of a vortical flow field by the use of an adjoint method. The idea of optimal/targeted observation in meteorology which aim to effectively determine a flow state by limited observations are interpreted in fluid dynamic problems where unsteady flows of much smaller scales are of interest. The present approach enables to investigate the impact of measurements in an actual data assimilation system of the 4D-Var. We investigated a simple case with a pair of vortices which move due to self-induced advection velocity. The amount of measurement points affects the convergence of the cost function as well as the global error against the reference flow field. The optimal measurement strategy based on the observation sensitivity effectively redistributes measurement points near vortices. This results in the further reduction of the global error. As for future work the impact of the number of measurements in time as well as of assimilation window size should be investigated. A series of investigations might show the applicability limit of the 4D-Var for given experimental and numerical conditions.

Acknowledgements

References

[1] E. Kalnay, *Atmospheric Modeling, Data Assimilation and Predictability*, Cambridge University Press, 2003.

[2] T. Misaka, S. Obayashi, and E. Endo, "Measurement-Integrated Simulation of Clear Air Turbulence Using Four-Dimensional Variational Method," *Journal of Aircraft*, Vol. 45, pp. 1217-1229, 2008.

[3] T. Misaka, S. Obayashi, I. Yamada, and Y. Okuno, "Assimilation Experiment of Lidar Measurements for Wake Turbulence," *JSME Journal of Fluid Science and Technology*, Vol. 3, pp. 512-518, 2008.

[4] H. Kato, S. Obayashi, "Statistical Approach for Determining Parameters of a Turbulence Model," *IEEE 15th International Conference on Information Fusion (FUSION)*, pp. 2452-2457, July 2012.

[5] T. Misaka, F. Holzäpfel, T. Gerz, "Wake Evolution of Wing-Body Configuration form Roll-Up to Vortex Decay," *50th AIAA Aerospace Science Meeting*, AIAA Paper 2012-0428, January 2012.

[6] D. N. Daescu, "On the Sensitivity Equations of Four-Dimensional Variational (4D-Var) Data Assimilation," *Monthly Weather Review*, Vol. 136, pp. 3050-3065, 2008.

[7] Y. Morinishi, T. S. Lund, O. V. Vasilyev, and P. Moin, "Fully Conservative Higher Order Finite Difference Schemes for Incompressible Flow," *Journal of Computational Physics*, Vol. 143, pp. 90-124, 1998.

[8] J. H. Williamson, "Low-Storage Runge-Kutta Schemes," *Journal of Computational Physics*, Vol. 35, pp. 48-56, 1980.

[9] C. Meneveau, T. S. Lund, and W. H. Cabot, "A Lagrangian Dynamic Subgrid-Scale Model of Turbulence," *Journal of Fluid Mechanics*, Vol. 319, pp. 353-385, 1996.

[10] T. Misaka, F. Holzäpfel, I. Hennemann, T. Gerz, M. Manhart, and F. Schwertfirm, "Vortex Bursting and Tracer Transport of a Counter-Rotating Vortex Pair," *Physics of Fluids*, Vol. 24, pp. (025104-1)-(025104-21), 2012.

Application of the Measurement Integrated Simulation Method to Compressible Fluid Problems

Kentaro Imagawa
Kanako Yasue
Shigeru Kuchi-Ishi

Japan Aerospace Exploration Agency
7-44-1, Jindaiji-Higashi, Chofu, Tokyo 182-8522, JAPAN
Email: imagawa@chofu.jaxa.jp

Abstract

Measurement Integrated Simulation (MIS) is a data assimilation method using the idea of a flow observer. MIS is already used in the analysis of incompressible fluids in biomedical and pipe flows. In this study, a coupled system of a CFD solver and an MIS algorithm was constructed, and an identical twin experiment for the flow field around a 2-dimensional airfoil subject to different boundary conditions was performed. It was found that the MIS reproduced the aerodynamic coefficients of target data even if different boundary conditions are set. The accuracy of MIS was demonstrated, not only for the physical properties used for the assimilation but also for unassimilated properties. In addition, for sample data with random or bias error, the difference between the simulated and sample data achieved by the computation with MIS was much smaller than the difference achieved without MIS.

Key words: Experimental Fluid Dynamics (EFD), Computational Fluid Dynamics (CFD), Data Assimilation, Measurement Integrated Simulation (MIS).

1. Introduction

At the Japan Aerospace Exploration Agency (JAXA), the complementary use of Experimental Fluid Dynamics (EFD) and Computational Fluid Dynamics (CFD) is currently being studied[1]. In flow analysis, EFD and CFD are commonly used. EFD is a direct method to obtain the state of real flow phenomena, and its reliability is ensured by calibration techniques. However, there are differences from real flight condition, such as Reynolds number, the walls and support of the wind tunnel, and model deformation. Moreover, it is impossible to obtain complete information about the flow state both spatially and temporally. On the other hand, CFD provides the full state of

flow phenomena on grid points of the computational domain. However its reliability is always a concern, especially for complicated phenomena such as turbulence, transition, separation, and reacting flow; so validation by experiment is required. These advantages and disadvantages of the two approaches are summarized in Table 1.

A primary aim of EFD/CFD integration is to improve the accuracy and reliability of data by the complementary use of EFD and CFD. Such data assimilation techniques have been employed in many fields. In aerodynamics, 4-dimensional variational assimilation (4D-Var) [2], the extended Kalman filter (EKF) [3], [4], the ensemble Kalman filter (EnKF) [5] and the particle filter (PF) [6] are used. These methods use the error covariance matrices of EFD and CFD to optimize the assimilation parameter. However it is sometimes difficult to estimate precisely the error components in determining the matrix. When 4D-Var or the EKF is used, the reliability of the estimated matrices is a concern. When the EnKF or PF is used, the matrices are estimated by ensemble computation and the computational cost is high.

In maritime engineering, the nudging method is also used to overcome the disadvantages of these methods [7]. The nudging method is a simple method and its computational cost is low because, in contrast to other methods in which the assimilation parameter is optimized from the covariance matrices, this parameter is specified a priori.

Measurement integrated simulation method is a data assimilation method that uses the idea of a flow observer [8]. It is used in the analysis of incompressible fluids in biomedical [9], [10] and pipe [11], [12] flows. The observer algorithm [13] is similar to the Kalman filter [14] in the sense that it is a maximum likelihood estimation method using the error covariance matrices of CFD and EFD. However, it is a method of reproducing EFD data itself and it is also a nudging method since the assimilation parameter is chosen a priori.

In this study, a coupled system of a CFD solver and an MIS algorithm was constructed, and an identical twin experiment, studying the flow field around a 2-dimensional airfoil, was performed to investigate the accuracy and versatility of the method.

Table 1: Advantages and disadvantages of EFD and CFD

	Advantage	Disadvantage
EFD	· A direct way to obtain real flow phenomena · Reliability is ensured by calibration techniques	· Differences from real flight conditions · Difficulty in obtaining complete information
CFD	· Provides the full state of flow phenomena	· Reliability is always a concern · Validation by experiment is required

2. Measurement Integrated Simulation method (MIS)

MIS is a method of integrating measurement and simulation data by applying the idea of a flow observer (Figure 1). This is similar to the EKF, but is a method of reproducing EFD data itself. It is useful for the problem of interpolating missing or immeasurable measurement data. The main feature of MIS, which distinguishes it from other existing observers, is the use of the CFD scheme as a mathematical model of the physical flow.

The governing equations of the CFD model are generally written as

$$\frac{d\mathbf{Q}_N}{dt} = f(\mathbf{Q}_N) \tag{1}$$

where $\mathbf{Q}_N$ is a 5N-dimensional conservative vector

$$\mathbf{Q}_N = \begin{pmatrix} \mathbf{Q}_1^T & \mathbf{Q}_2^T & \cdots & \mathbf{Q}_i^T & \cdots & \mathbf{Q}_N^T \end{pmatrix}^T \tag{2}$$

$$\mathbf{Q}_i = \begin{pmatrix} \rho_i & (\rho u)_i & (\rho v)_i & (\rho w)_i & e_i \end{pmatrix}^T \tag{3}$$

and N and $\mathbf{Q}_i$ are the number of grid points and the conservative vector at grid i, respectively. When the vector constructed from measurement data is denoted by $\mathbf{y}$, the basic equation of MIS is

$$\frac{d\mathbf{Q}_N}{dt} = f\left(\mathbf{Q}_N\right) + \mathrm{K}\left(\mathbf{y} - h\left(\mathbf{Q}_N\right)\right) \tag{4}$$

where the second term is the additional term of MIS derived from the difference between EFD and CFD. Function *h* is called the "observation function" and is the relation between the measurement vector **y** of EFD and the conservative vector $\mathbf{Q}_N$ of CFD. K is called the "feedback gain matrix". This matrix is constructed from the assimilation parameter. In MIS, the assimilation parameter is not optimized from the error covariance matrices, as it is in the EKF or EnKF. In previous studies of MIS, the matrix was designed by trial and error based on physical considerations, because the theory of the observer cannot be directly applied [15], [16].

In this study, the feedback matrix is designed using the Jacobi matrix H of the nonlinear observation function *h*. The details are given in Section 3.3.
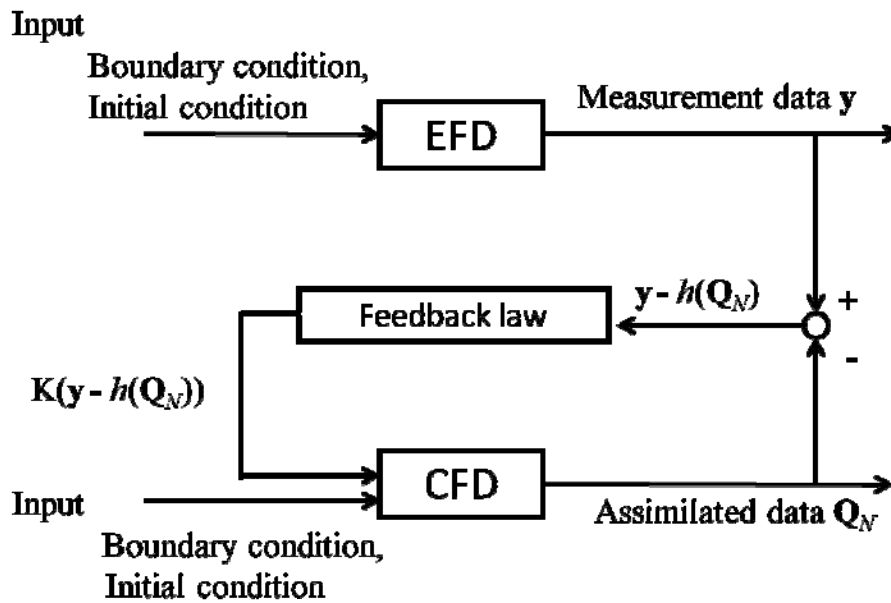
Figure 1: Block diagram of MIS

3. Numerical Experiment

In this section, a coupled system of a high-speed CFD solver (FaSTAR)[17], and MIS is described, and an identical twin experiment investigated flow field around a 2-dimensional airfoil with different boundary conditions is discussed. First, the twin experiment used in this study is explained briefly. Then, the computational conditions are given and the corresponding feedback matrix is derived.

3.1. Twin experiment

Twin experiments are a method of numerical experiment commonly used for benchmark tests of data assimilation techniques. This method uses pseudo-measurement data derived from simulation instead of measurements.

Figure 2 shows a schematic diagram of the twin experiment. The target data is original CFD data, and the sample data is created by adding an error component to the target data. Generally, the benchmark test of the integrated

analysis system is comparing comparison with the target data. The benchmark in this study is, however, a comparison with the sample data since MIS is a method of reproducing sample data.

The procedure of the twin experiment is as follows.

(1) Produce target data according to specified boundary conditions.

(2) Produce sample data by adding artificial error components to the target data.

(3) Perform integrated analysis with varying boundary conditions by regarding the sample data as measurement data.

(4) Compare the integrated analysis data with the sample data.

3.2. Numerical conditions

The twin experiment deals with flow field around a 2-dimensional airfoil as shown in Fig. (3). The Mach number of the uniform flow is 0.8. The flow field in this study is assumed to be steady, hence the integrated data are obtained as an asymptotic solution of Eq. (4). The flow chart of the algorithm is shown in Fig. (4).

In the twin experiment, the angle of attack in the target data is 3 degrees, and integrated computation is made using intentionally different angles of attack. The sample cases in the present experiment are shown in Table 2. The sample data is the velocity field over the whole computational domain. In this study, three types of sample data are employed: (1) data without measurement error (exactly same as the target data); (2) data with random errors of 1%, 2%, 5%, or 10%; and (3) data with bias error of 1%, 2%, 5%, or 10%. All computations were done using the JAXA Super computer System (JSS).
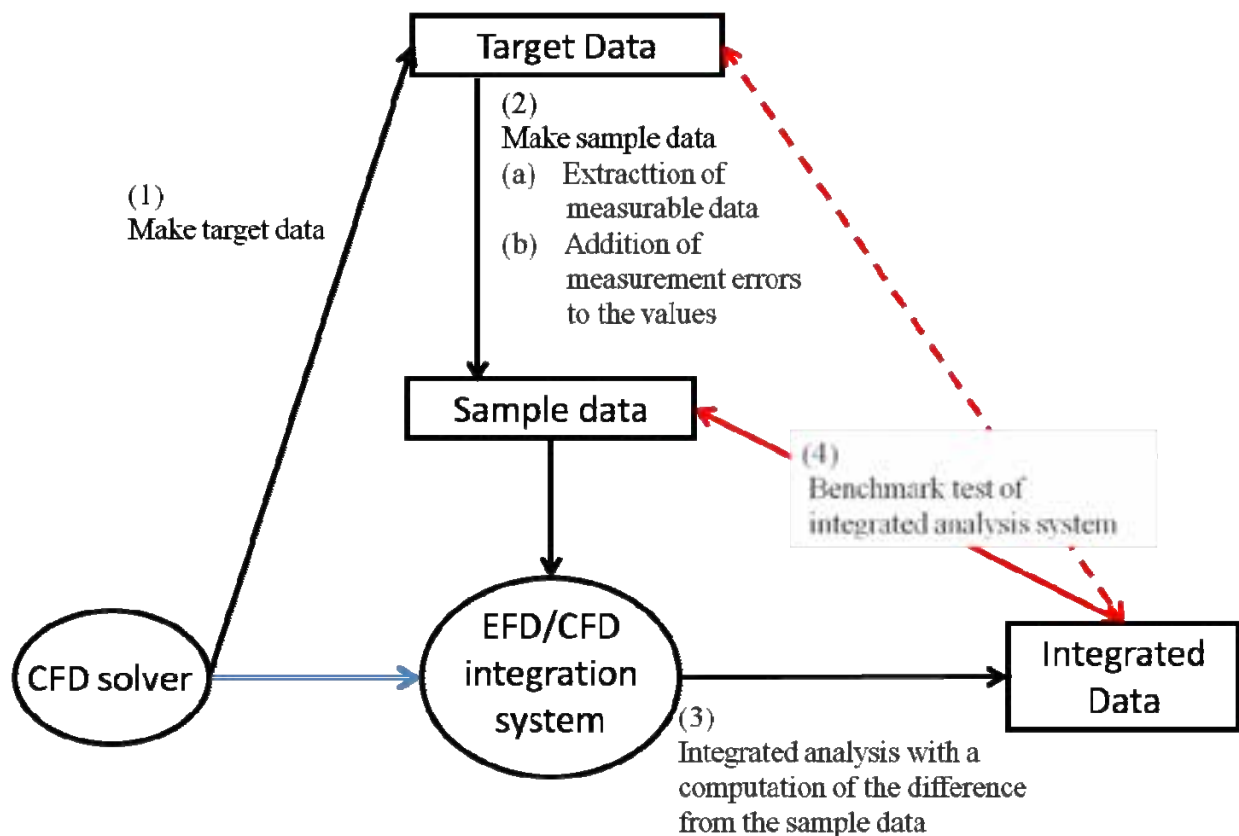
Figure 2: Schematic diagram of twin experiment
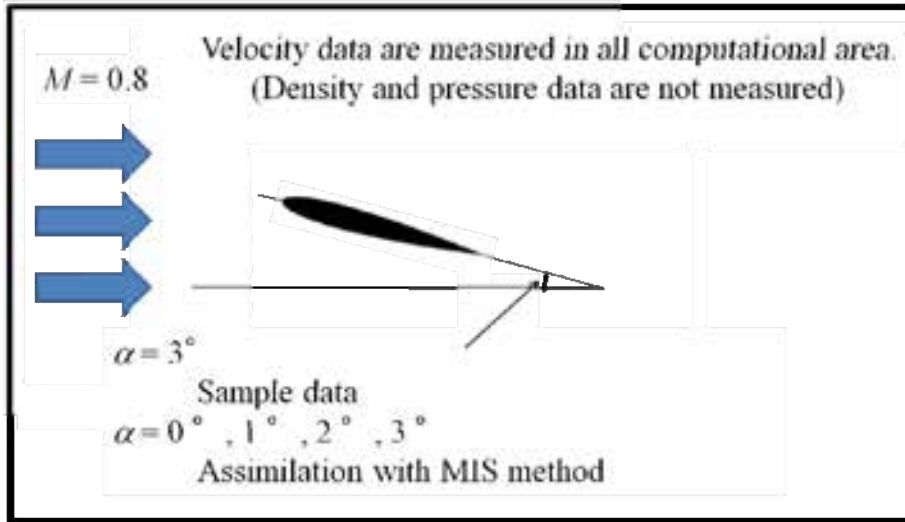
Figure 3: Setup of this twin experiment
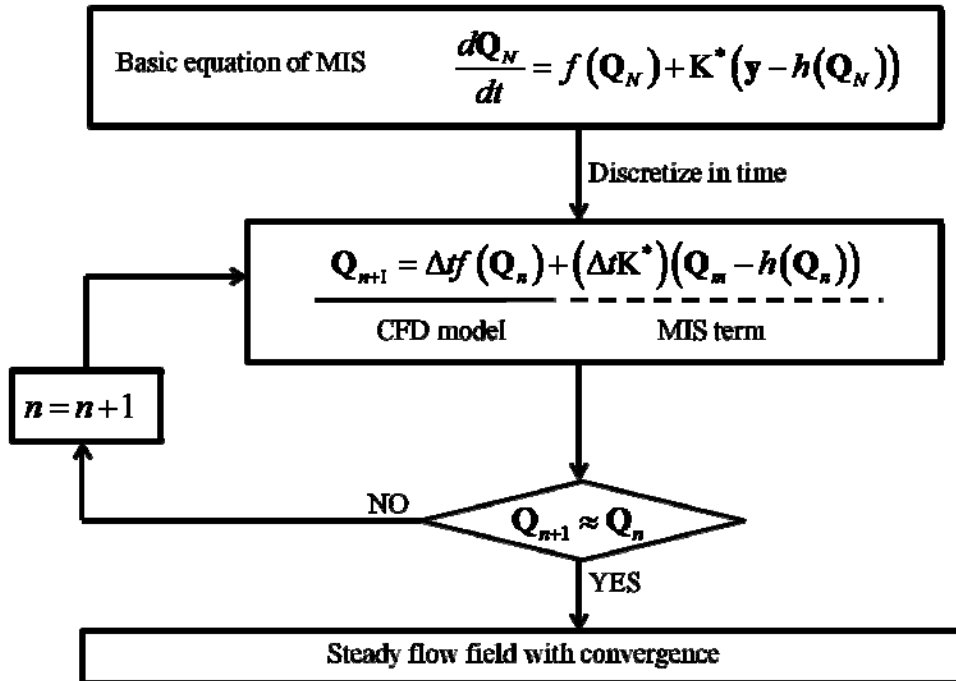
Figure 4: Flow chart of EFD/CFD integrated computation of MIS

Table 2: Sample cases of twin experiment

	Angle of attack (AoA)
Case (1)	0°
Case (2)	1°
Case (3)	2°
Case (4)	3° (Same AoA as the target data)

3.3. Feedback gain matrix design

In this study, the feedback gain matrix K in Eq. (4) is derived as a pseudo-inverse matrix of the Jacobi matrix of the observation function.

If the velocity components are employed as measurement data, $\mathbf{y}$ in Eq. (4) is

$$\mathbf{y} = \begin{pmatrix} \mathbf{y}_1^T & \mathbf{y}_1^T & \cdots & \mathbf{y}_i^T & \cdots & \mathbf{y}_N^T \end{pmatrix}^T, \tag{5}$$

$$\mathbf{y}_i = \begin{pmatrix} u_i & v_i \end{pmatrix}^T, \tag{6}$$

and the Jacobi matrix H of the observation function h is

$$H = \frac{\partial \mathbf{y}}{\partial \mathbf{Q}_N} = diag\begin{pmatrix} H_1 & H_2 & \cdots & H_i & \cdots & H_N \end{pmatrix} \tag{7}$$

$$H_i = \frac{\partial \mathbf{y}_i}{\partial \mathbf{Q}_i} = \frac{\partial (u_i \quad v_i)^T}{\partial \left(\rho_i \quad (\rho u)_i \quad (\rho v)_i \quad (\rho w)_i \quad e_i \right)^T}$$

$$= \frac{\partial (u_i \quad v_i)^T}{\partial \left(\rho_i \quad u_i \quad v_i \quad w_i \quad p_i \right)^T} \frac{\partial \left(\rho_i \quad u_i \quad v_i \quad w_i \quad p_i \right)^T}{\partial \left(\rho_i \quad (\rho u)_i \quad (\rho v)_i \quad (\rho w)_i \quad e_i \right)^T} = M_i L_i \tag{8}$$

where

$$L_i = \frac{\partial \left(\rho_i \quad u_i \quad v_i \quad w_i \quad p_i \right)^T}{\partial \left(\rho_i \quad (\rho u)_i \quad (\rho v)_i \quad (\rho w)_i \quad e_i \right)^T}$$

$$= \begin{pmatrix} 1 & 0 & 0 & 0 & 0 \\ -\dfrac{u_i}{\rho_i} & \dfrac{1}{\rho_i} & 0 & 0 & 0 \\ -\dfrac{v_i}{\rho_i} & 0 & \dfrac{1}{\rho_i} & 0 & 0 \\ -\dfrac{w_i}{\rho_i} & 0 & 0 & \dfrac{1}{\rho_i} & 0 \\ \dfrac{1}{2}(\gamma-1)(u_i^2 + v_i^2 + w_i^2) & -(\gamma-1)u_i & -(\gamma-1)v_i & -(\gamma-1)w_i & \gamma-1 \end{pmatrix}, \tag{9}$$

and

$$M_i = \frac{\partial (u_i \quad v_i)^T}{\partial \left(\rho_i \quad u_i \quad v_i \quad w_i \quad p_i \right)^T} = \begin{pmatrix} 0 & 1 & 0 & 0 & 0 \\ 0 & 0 & 1 & 0 & 0 \end{pmatrix}. \tag{10}$$

Further, L_i is the transformation matrix from conservative vector to primitive vector. L_i^{-1}, the inverse matrix of L_i, is the transformation matrix from primitive vector to conservative state vector which is given by

$$L_i^{-1} = \frac{\partial \left(\rho_i \ (\rho u)_i \ (\rho v)_i \ (\rho w)_i \ e_i \right)^T}{\partial \left(\rho_i \ u_i \ v_i \ w_i \ p_i \right)^T} = \begin{pmatrix} 1 & 0 & 0 & 0 & 0 \\ u_i & \rho_i & 0 & 0 & 0 \\ v_i & 0 & \rho_i & 0 & 0 \\ w_i & 0 & 0 & \rho_i & 0 \\ \frac{1}{2}\left(u_i^2 + v_i^2 + w_i^2\right) & \rho_i u_i & \rho_i v_i & \rho_i w_i & \frac{1}{\gamma-1} \end{pmatrix},$$

$$(11)$$

and M_i^{-1}, the pseudo-inverse matrix of M_i, is

$$M_i^{-1} = \begin{pmatrix} 0 & 1 & 0 & 0 & 0 \\ 0 & 0 & 1 & 0 & 0 \end{pmatrix}^T \tag{12}$$

Then, H^*, the pseudo-inverse matrix of H, is

$$H^* = diag\left(H_1^* \quad H_2^* \quad \dots \quad H_i^* \quad \dots \quad H_N^* \right) \tag{13}$$

$$H_i^* = L_i^{-1} M_i^* = \begin{pmatrix} 0 & \rho_i & 0 & 0 & \rho_i u_i \\ 0 & 0 & \rho_i & 0 & \rho_i v_i \end{pmatrix}^T \tag{14}$$

In this experiment, the feedback gain matrix K^* is designed using H^* and is given by

$$K^* = kH^* \tag{15}$$

where k is a stability parameter. In previous studies, this parameter was determined by trial and error. These studies indicated that this parameter depends on the time increment Δt of the time-marching scheme from the viewpoint of scaling. When the first order implicit scheme is used as the time-marching algorithm, the stabilization condition becomes[18]

$$k \leq \frac{1}{\Delta t} \tag{16}$$

Hence, in the present study, the parameter k is set to

$$k = \frac{1}{\Delta t} \tag{17}$$

Finally we obtain the feedback gain matrix K^* as

$$K^* = diag\left(K_1^* \quad K_2^* \quad \dots \quad K_i^* \quad \dots \quad K_N^* \right) \tag{18}$$

$$K_i^* = \frac{1}{\Delta t} H_i^* = \frac{1}{\Delta t} \begin{pmatrix} 0 & \rho_i & 0 & 0 & \rho_i u_i \\ 0 & 0 & \rho_i & 0 & \rho_i v_i \end{pmatrix}^T \tag{19}$$

4. Results and Discussion

First, we discuss the results for the case using the sample data without error. The comparisons of the drag coefficients C_D and lift coefficients C_L with and without MIS are shown in Table 3. The computation without MIS is equivalent to a simple CFD computation, and its difference from the target data becomes large as the angle of attack recedes from the target value. On the other hand, the computations with MIS successfully reproduce the sample data.

The accuracy of the MIS method can be evaluated by using the norms of the difference between two sets of data

$$l_\rho^{S-M} = \sqrt{\frac{1}{N}\sum_{i=1}^{N}\left(\rho_i^{sample} - \rho_i^{MIS}\right)^2} \tag{20}$$

$$l_u^{S-M} = \sqrt{\frac{1}{2N}\sum_{i=1}^{N}\left\{\left(u_i^{sample} - u_i^{MIS}\right)^2 + \left(v_i^{sample} - v_i^{MIS}\right)^2\right\}} \tag{21}$$

$$l_p^{S-M} = \sqrt{\frac{1}{N}\sum_{i=1}^{N}\left(p_i^{sample} - p_i^{MIS}\right)^2} \tag{22}$$

$$l_\rho^{S-C} = \sqrt{\frac{1}{N}\sum_{i=1}^{N}\left(\rho_i^{sample} - \rho_i^{CFD}\right)^2} \tag{23}$$

$$l_u^{S-C} = \sqrt{\frac{1}{2N}\sum_{i=1}^{N}\left\{\left(u_i^{sample} - u_i^{CFD}\right)^2 + \left(v_i^{sample} - v_i^{CFD}\right)^2\right\}} \tag{24}$$

$$l_p^{S-C} = \sqrt{\frac{1}{N}\sum_{i=1}^{N}\left(p_i^{sample} - p_i^{CFD}\right)^2} \tag{25}$$

where the upper subscript *sample* denotes the sample data, *CFD* the result without MIS, and *MIS* the computation with MIS. The subscript i is the grid index and N is the number of grid points.

Table 4 shows a comparison of the norms derived from Eqs. (20)-(25). Since the velocity data are employed as the target data, in all cases, the value of velocity norm obtained with MIS is much smaller than that obtained without MIS. On the other hand, for the norms for density and pressure obtained with MIS are also much smaller than those obtained without MIS. This means that the present method can even reproduce physical properties that are not assimilated directly. Figure 5 shows pressure contours in Case (1). Figure 5 (b) shows the computation without MIS and of course the distribution is different from that of the target data. On the contrary, as can be seen in Fig. 5 (c), an almost identical result is obtained from the computation with MIS.

Next we consider the results obtained when random and bias errors are introduced. This is to confirm the validity of the MIS method even if the sample data includes a typical amount of uncertainty. The sample data including random or bias errors are derived from the target data as

Table 3: Comparison of aerodynamic coefficients with and without MIS

	C_D		C_L	
	Without MIS	With MIS	Without MIS	With MIS
Case (1)	0.022518	0.030731	-0.000230	0.260082
Case (2)	0.023963	0.030776	0.142230	0.260634
Case (3)	0.027097	0.030815	0.221770	0.261135
Target data	0.030849		0.261591	

Table 4: Differences between the results of calculations with and without MIS for the sample data without errors

	Without MIS			With MIS		
	l_ρ^{S-C}	l_u^{S-C}	l_p^{S-C}	l_ρ^{S-M}	l_u^{S-M}	l_p^{S-M}
Case (1)	0.05255	0.1492	0.04382	0.006436	0.003614	0.004457
Case (2)	0.03925	0.1132	0.03355	0.004305	0.002409	0.002969
Case (3)	0.02305	0.06211	0.01903	0.002181	0.001204	0.001485

$$\mathbf{y}_i^{random} = \left(1 + r_i\right)\mathbf{y}_i^{target} \tag{26}$$

$$\mathbf{y}_i^{bias} = (1 + b)\mathbf{y}_i^{target} \tag{27}$$

where r_i is a random number chosen so that the level of uncertainty attains a specified value. Similarly, b is a constant which represents the bias error component. A total of 4 cases, with levels of uncertainty of 1%, 2%, 5%, and 10%, are considered both for random error and bias error. The results of including random or bias error are shown in Tables 5 and 6, respectively. In both cases, the difference norms for the computation with MIS are much smaller than those obtained without MIS.

By solving Eq. (4), MIS reproduces the flow field so that it minimizes the difference from the sample data. Hence, when the sample data exactly satisfies the flow equations, the sample data itself is reproduced. However, if the sample data does not satisfy the flow equations due to the presence of random or bias error, the difference between the sample data and the MIS computation remains. The degree of difference between the MIS and sample data is comparable to that between the target and sample data. The difference becomes large as the error included in the sample data becomes large, as shown in Tables 5 and 6.
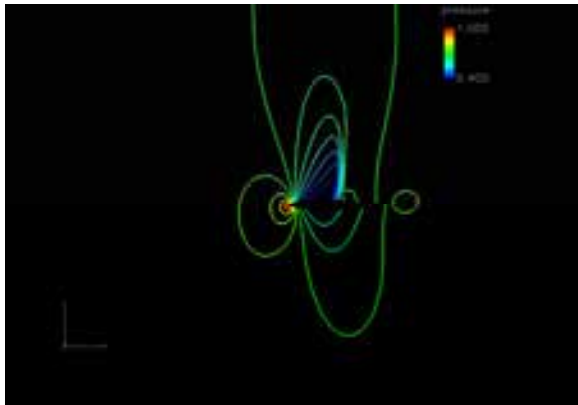
(a)　Target data
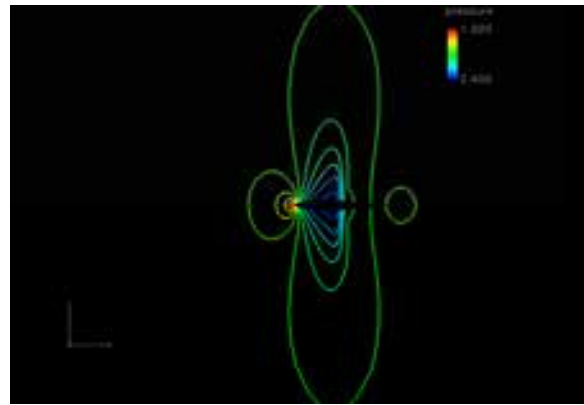
(b)　Without MIS
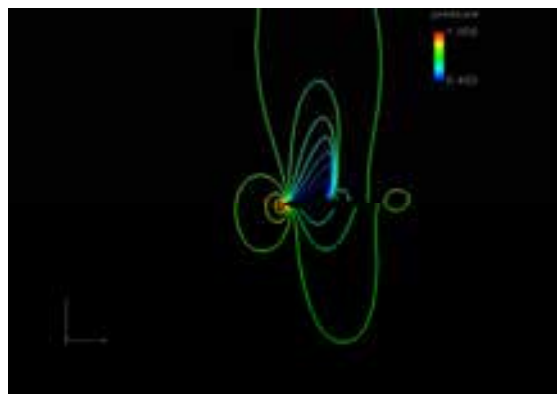
(c)　With MIS

Figure 5: Comparison of pressure contours

Finally, we consider the effects of random or bias error on the MIS results for Case (4) in which results that are identical to those of the sample data are expected to be obtained if there is no error in the sample data. Table 7 shows the comparison of the difference norms obtained with random or bias error

$$l_u^{S-T} = \sqrt{\frac{1}{2N}\sum_{i=1}^{N}\left\{\left(u_i^{sample}-u_i^{target}\right)^2+\left(v_i^{sample}-v_i^{target}\right)^2\right\}} \qquad (28)$$

and those obtained by the MIS computation. In both cases, the norm from the MIS computation is comparable to that from the computation with random or bias error. This means that, even if the assimilated data has a series of uncertainties, MIS does not amplify the uncertainty level, and hence, we can say that MIS is a numerically stable approach.

Table 5: Differences between the results of calculations with and without MIS for the sample data including random errors

(a) 1%

	Without MIS l_u^{S-C}	With MIS l_u^{S-M}
Case (1)	0.1497	0.0055
Case (2)	0.1136	0.0040
Case (3)	0.0625	0.0027
Case (4)	0.0041	0.0022

(b) 10%

	Without MIS l_u^{S-C}	With MIS l_u^{S-M}
Case (1)	0.1587	0.0212
Case (2)	0.1236	0.0208
Case (3)	0.0765	0.0206
Case (4)	0.0413	0.0206

Table 6: Differences between the results of calculations with and without MIS for the sample data including bias errors

(a) 1%

	Without MIS l_u^{S-C}	With MIS l_u^{S-M}
Case (1)	0.1502	0.0058
Case (2)	0.1141	0.0041
Case (3)	0.0630	0.0028
Case (4)	0.0072	0.0023

(b) 10%

	Without MIS l_u^{S-C}	With MIS l_u^{S-M}
Case (1)	0.1730	0.0176
Case (2)	0.1396	0.0172
Case (3)	0.0980	0.0169
Case (4)	0.0718	0.0168

Table 7: Effect of size of random or bias error in calculations with and without MIS

(a) Random error

Level of uncertainty	Without MIS l_u^{S-T}	With MIS l_u^{S-M}
1%	0.0030	0.0022
2%	0.0059	0.0042
5%	0.0147	0.0104
10%	0.0295	0.0206

(b) Bias error

Level of uncertainty	Without MIS l_u^{S-T}	With MIS l_u^{S-M}
1%	0.0051	0.0023
2%	0.0102	0.0042
5%	0.0256	0.0100
10%	0.0512	0.0168

5. Conclusions

Measurement Integrated Simulation (MIS) is a data assimilation method that uses the idea of a flow observer and has already been applied to the analysis of incompressible fluids in biomedical and pipe flows. In this study, a coupled system of a CFD solver and MIS was constructed, and an identical twin experiment studying the flow field around a 2-dimensional airfoil with different boundary conditions was performed. The velocity data for all parts of the computational domain were used as the target data. The target data were used as "sample data without error" and further sample data was created by adding random and bias error components. In cases using the sample data without error, it was found that the MIS reproduced the aerodynamic coefficients of target data even if we set different boundary conditions. Based on the evaluation of the L2 norms for the differences between the target data and the simulated data, the accuracy of the MIS method was demonstrated, not only for the physical properties used for the assimilation but also for unassimilated properties. Also, for the cases involving sample data with random or bias error, the difference between the simulated and target data achieved by the computation with MIS was much smaller than the difference achieved without MIS.

MIS is a nudging method and has a computational cost comparable with single CFD. Therefore, in future research, we will apply this method to 3-dimensional problems using actual measurement data, for example, collected by particle image velocimetry.

Acknowledgments

References

[1] Watanabe S., Kuchi-Ishi S., Aoyama T.; A Prototype System towards EFD/CFD Integration: Digital/Analog Hybrid Wind Tunnel, *27th Congress of International Council of the Aeronautical Science*, 2010, http://www.icas.org/ICAS_ARCHIVE_CD1998-2010/ICAS2010/ABSTRACTS/244.HTM

[2] Misaka T., Ogasawara T., Obayashi S., Yamada I., Okuno Y.; Assimilation Experiment of Lidar Measurements for Wake Turbulence, *Journal of Fluid Science and Technology*, 3(4), pp.512-518, 2008.

[3] Chowdhary G., Jategaonkar R.; Aerodynamic Parameter Estimation from Flight Data Applying Extended and Unscented Kalman filter, *Aerospace Science and Technology*, 14 (2), pp.106-117, 2010.

[4] Suzuki T., Ji H., Yamamoto F.; Reduced-order Kalman-Filtered Hybrid Simulation Combining PTV and DNS,*9th International Symposium on Particle Image Velocimetry*, p. 118, 2011.

[5] Kato H., Obayashi S., Integration of CFD and Wind Tunnel by Data Assimilation, *Journal of Fluid Science and Technology*, 6 (5), pp.717-728,2011.

[6] Imagawa K., Yasue K., Kuchi-Ishi S.; Identification of flow condition around a 2-dimensional airfoil using data assimilation, *43th Fluid Dynamics Conference/ Aerospace Numerical Simulation Symposium 2011*, 2A12 (in Japanese).

[7] Hoke, J., Anthes, R. A.; The initialization of numerical models by a dynamic initialization technique, *Monthly Weather Review*, 104, 1551- 1556, 1976.

[8] Hirose N., Kawamura H., Lee H. J., Yoon J. H., Sequential Forecasting of the Surface and Subsurface Conditions in the Japan Sea, *Journal of Oceanography*, Vol. 63, pp. 467 to 481, 2007

[9] Hayase T, Hayashi S.; State estimator of flow as an integrated computational method with the feedback of online experimental measurement. *Trans. ASME J. Fluids Eng.* 119(4), pp.814–22, 1997.

[10] Funamoto K, Hayase T, Saijo Y, Yambe T.; Numerical study on variation of feedback methods in ultrasonic-measurement- integrated simulation of blood flow in the aneurysmal aorta, *JSME Int. J. Ser C*, 49(1), pp.144–55, 2006.

[11] Funamoto K, Hayase T, Saijo Y, Yambe T.; Numerical Analysis of Effects of Measurement Errors on Ultrasonic-Measurement-Integrated Simulation, *IEEE Trans. Biomedical Engineering*, 58(3), pp.653-663, 2011.

[12] Imagawa K., Hayase T.; Numerical experiment of measurement- integrated simulation to reproduce turbulent flows with feedback loop to dynamically compensate the solution using real flow information, *Computers and Fluids*, 39 (11), pp.1439-1450, 2010.

[13] Nakao M., Kawashima K., Kagawa T.: Application of MI Simulation Using a Turbulent Model for Unsteady Orifice Flow, Journal of Fluids Engineering, 131(11), pp.111401-111409, 2009.

[14] Luenberger D. G.: Observing the State of a Linear System, *IEEE Trans. Military Electronics*, 8(2), pp.74-80, 1964.

[15] Kalman R. E.: A New Approach to Linear Filtering and Prediction Problems, *Trans. ASME*, 82(D), pp.35-45, 1960.

[16] Imagawa K., Hayase T.: Eigenvalue analysis of linearized error dynamics of measurement integrated flow simulation, *Computers and Fluids*, 39(10), pp.1796-1803, 2010.

[17] Hashimoto A., Murakami K., and Aoyama, T, JAXA Digital/Analog Hybrid Wind Tunnel: Development of Digital Wind Tunnel, *JAXA-SP-09-003*, 2010.

[18] Hayase T., Imagawa K., Funamoto K., Shirai A.: Stabilization of Measurement- Integrated Simulation by Elucidation of Destabilizing Mechanism, *Journal of Fluid Science and Technology*, 5(3), pp.632-647, 2010.

Toward the Development of Measurement Integrated Simulation

Hiroshi Kato
Shigeru Obayashi

Institute of Fluid Science
Tohoku University
Sendai, 980-8577
Japan
kato@edge.ifs.tohoku.ac.jp

Abstract

In this research, the ensemble Kalman filter, a data assimilation method, is employed to estimate the turbulent viscosity for the flow field around the RAE2822 airfoil. The turbulent viscosity is estimated directly from the experimental pressure distribution on the airfoil, without a turbulence model. The turbulent viscosity estimated by the ensemble Kalman filter shows lower magnitude around the airfoil than that estimated with the Spalart–Allmaras turbulence model and is almost zero in the wake region. Computation with the estimated turbulent viscosity can predict the separated flow region at the shock-boundary layer interaction. Due to this separation, the computed pressure coefficient agrees better with the experiment. These results suggest that this data assimilation method can be used to estimate the turbulent viscosity without a turbulence model.

Key words: EFD/CFD, measurement integrated simulation, data assimilation, turbulence model

Introduction

Wind tunnel experiments (EFD: Experimental Fluid Dynamics) and numerical simulation (CFD: Computational Fluid Dynamics) have been used to predict the aerodynamic characteristics of aircraft and spacecraft. With the remarkable development of CFD techniques, methods for the integration of EFD and CFD (EFD/CFD, which our group calls EFD/CFD "measurement integrated simulation") have been discussed for prediction of aerodynamic characteristics with higher accuracy, efficiency, and reliability than either EFD or CFD alone [1].

To achieve EFD/CFD, the meaning of the word "integration" should first be defined. The definition of the word "integration" differs between groups, which results in the various realization of EFD/CFD. Various methods to integrate EFD and CFD are available.

Currently, the authors are focusing on turbulent viscosity—a method to represent the Reynolds stress term in the Reynolds-averaged Navier–Stokes (RANS) equations—to integrate EFD and CFD. Turbulent viscosity is computed by a turbulence model, such as the Spalart–Allmaras model [2] or the Menter SST model [3]. The computation is strongly affected by turbulent viscosity; however, most turbulence models still cannot be used for precise analysis of complex flows. Obviously, the large eddy simulation (LES) and direct numerical simulation (DNS) can be used to accurately compute fluid phenomena, because the equations employed in LES and DNS have fewer approximations than that of RANS. However, LES and DNS are not yet practical tools to predict aerodynamic characteristics efficiently, as they require massive computational resources and time. In the engineering field, CFD is expected to be an efficient tool for prediction of aerodynamic characteristics. Therefore, RANS simulation is essential as a design tool, and a method to compute the turbulent viscosity with a high accuracy will be required in future.

In the field of engineering, turbulence models are techniques to represent the turbulent viscosity. Turbulence models include artificial parameters unlike the Navier–Stokes equations, and actually different turbulence models yield different results for complex flows.

In the past, our group adjusted the parameter values in the Spalart–Allmaras turbulence model using experimentally obtained values for more precise computation than that with CFD alone [4, 5, 6]. Our previous studies showed the following:
1. Different turbulence models can predict the same flow field by adjusting the parameter values in a turbulence model.
2. The parameter values calibrated by the model proposer, Spalart and Allmaras, are determined by the ensemble Kalman filter.
3. Computation with the adjusted parameter values agrees with the experimental values better than that with the original parameter values.

These results suggest that computation integrating a turbulence model with experimental results can predict fluid phenomena better than CFD alone. On the other hand, the method to adjust the parameter values in the turbulence model was able to not compute the turbulent viscosity beyond the solution space of the turbulence model; that is, even computation integrating a turbulence model with experiment cannot predict fluid phenomena with the turbulent viscosity that current turbulence models cannot express.

This study was performed to investigate computation of the turbulent viscosity directly from experimental values without a turbulence model. For the investigation, the flow field around the RAE2822 airfoil [7] was computed. The method can compute the turbulent viscosity beyond the solution space of the turbulence model; that is, the computation with experimental values can predict fluid phenomena with the turbulent viscosity that current turbulence models cannot express. The ensemble Kalman filter [8], a data assimilation method [9], can be applied to compute the turbulent viscosity from experimental values.

The rest of the paper is organized as follows. The methods are described in Section 2. Section 3 describes the procedure of the ensemble Kalman filter. Section 4 describes the results. Finally, the conclusion is presented in Section 5.

Methods

I. Ensemble Kalman filter

The ensemble Kalman filter (EnKF) is a data assimilation method. Data assimilation was developed as a method combining observation (experiment) and numerical simulation in the field of meteorological and oceanic research. Data assimilation methods can estimate the optimal state variables for nonlinear and large-scale systems, such as flow simulation.

The nonlinear system can be expressed as in Eq. (1).

$$x_t = f_t(x_{t-1}), \tag{1}$$

where x_t represents the state variables. In the Reynolds-averaged Navier–Stokes (RANS) simulation with turbulent viscosity μ_t, x_t consists of the state variables as shown in Eq. (2).

$$x_t = (\rho, u, v, w, p, \mu_t)^T, \tag{2}$$

where ρ represents the density, u, v, w represent the velocity components, and p represents the pressure. Generally, the density, the velocity components, and the pressure are calculated from the RANS equations, and the turbulent viscosity is calculated from an additional model that is called the "turbulence model."

The ensemble Kalman filter estimates the optimal state variables thorough the following procedure:
1. Determine the initial ensemble members $\left\{x_0^{(i)}\right\}_{i=1}^N$ and $t \leftarrow 1$.
2. At time t
   (Prediction step)

A) Generate system noise $\left\{\boldsymbol{v}_t^{(i)}\right\}_{i=1}^{N}$. (System noise was not considered in this study)

B) Calculate $\boldsymbol{x}_t^{(i)} = f_t\left(\boldsymbol{x}_{t-1}^{(i)}, \boldsymbol{v}_t^{(i)}\right)$ for each ensemble member.

(Filtering step)

A) Generate observation noise $\left\{\boldsymbol{w}_t^{(i)}\right\}_{i=1}^{N}$.

B) Calculate variance-covariance matrix $\widehat{\boldsymbol{V}}_t$, $\widehat{\boldsymbol{R}}_t$, and Kalman gain $\widehat{\boldsymbol{K}}_t$.

C) Calculate $\boldsymbol{x}_t^{(i)} = \boldsymbol{x}_t^{(i)} + \widehat{\boldsymbol{K}}_t\left(\boldsymbol{y}_t - \boldsymbol{H}_t\boldsymbol{x}_t^{(i)} + \boldsymbol{w}_t^{(i)}\right)$ for each ensemble member.

3. Set $t \leftarrow t + 1$ and repeat step 2.

In the above procedure, $\left\{\boldsymbol{x}_t^{(i)}\right\}_{i=1}^{N}$ is the ensemble of $\boldsymbol{x}_t^{(i)}$, $\boldsymbol{y}_t$ represents the experimental values, and N is the number of realizations, which is called the "ensemble number."

The detailed procedure of the ensemble Kalman filter is presented in the next section. (For the detailed mathematical description of the ensemble Kalman filter, please refer to [10, 11, 12], etc.)

II. Computational schemes

In this study, the fast aerodynamic routine (FaSTAR) [13] developed by the Japan Aerospace Exploration Agency (JAXA) was used for flow simulation. FaSTAR has several computational schemes, and we used those shown in Table 1.

Table 1. Computational schemes used in this study

	Schemes
Inviscid flux	HLLEW
Gradient	Least-square
Limiter	Van Leer original limiter
Viscous flux	Cell gradient
Time integration	LU-SGS

III. Calculation conditions

The calculation conditions were: Mach number, 0.729; Reynolds number, 6.5×10^6; and angle of attack, 2.31. RANS computation was performed with CFL number of about 1200, and 5 inner iterations.

IV. Computational grid

The computational grid with a minimum grid spacing of 3.9×10^{-6}, where the chord length of the RAE 2822 airfoil was set to 1 as the reference length, was prepared. Figure 1 shows the computational grid. Reference [6] showed that the grid resolution was sufficient for the computation.
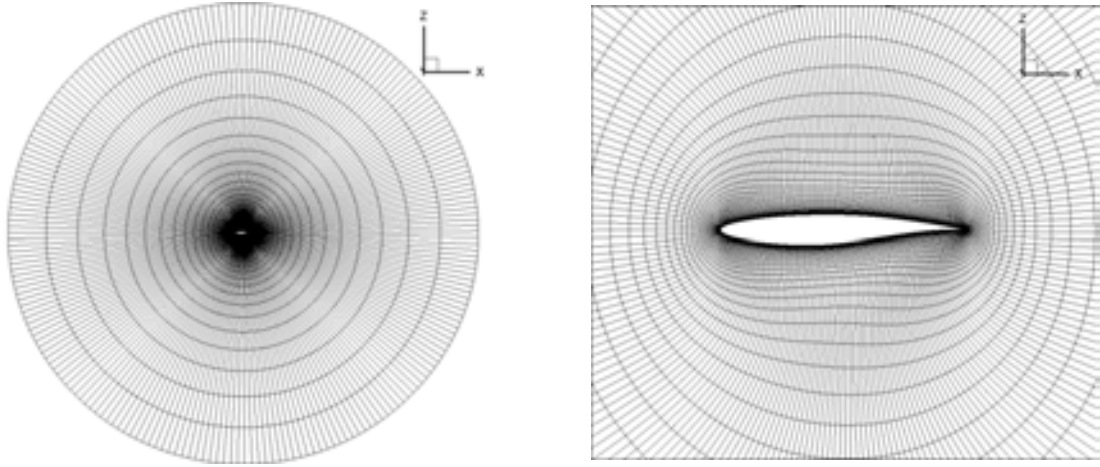
Figure 1. Computational grid

V.   Experimental values

The ensemble Kalman filter requires experimental values to estimate the optimal state variables. The pressure coefficient data from a wind tunnel experiment corresponding to the calculation conditions have been released on the NASA website in the file cp.exp.gen [14]. The non-dimensional pressure data were calculated from the pressure coefficient data using Eq. (3), a non-dimensional formula for the pressure coefficient. The data were utilized as experimental values y_t for the EnKF.

$$C_p = \frac{\left(p - \frac{1}{\gamma}\right)}{\frac{1}{2}M^2}, \tag{3}$$

where C_p is the pressure coefficient, γ is the specific heat ratio of 1.4, and M is the Mach number of 0.729.

Procedure

I.   Prediction step

The ensemble Kalman filter requires different state variables in each ensemble member at the beginning of the filtering step. For this requirement, various methods are available, such as assigning different boundary conditions or different initial conditions to each ensemble member. In this study, the state variables of each ensemble member were first computed with the Spalart–Allmaras turbulence model using the different parameter values for each ensemble member. As the parameter values were different for each ensemble member, each computed state variable was different. Then, the different state variables were assigned to each ensemble member. The Spalart–Allmaras turbulence model was used only for the assignment.

The values of each parameter of the Spalart–Allmaras turbulence model were selected equally from the ranges as in Eqs. (4) – (8) using Latin hypercube sampling [15]. Each range was defined by half of the original value of each parameter. Superscript (l) in Eqs. (4) – (8) indicates the number of the ensemble member.

$$5.325 < {C_{v1}}^{(l)} < 8.875 \tag{4}$$

$$0.101625 < {C_{b1}}^{(l)} < 0.169375 \tag{5}$$

$$0.4665 < {C_{b2}}^{(l)} < 0.7775 \tag{6}$$

$$0.225 < C_{\omega 2}{}^{(l)} < 0.375 \tag{7}$$

$$1.5 < C_{\omega 3}{}^{(l)} < 2.5 \tag{8}$$

II. Filtering step

The prediction step was repeated in each ensemble member to 50000 time steps to converge the computation in each ensemble member. Then, the filtering step was performed every 2000 prediction steps until 80000 time steps. The filtering step was performed through the following 6 steps. The number 100 in the equations below indicates the number of ensemble members in this study.

1) Calculate ensemble mean $\overline{x_t^*}$

$$\overline{x_t^*} = \frac{1}{100} \sum_{l=1}^{100} x_t^{*(l)} \tag{9}$$

2) Calculate variance-covariance matrix $\overline{V}_t$

$$\overline{V}_t = \frac{1}{100-1} \sum_{l=1}^{100} \left(x_t^{*(l)} - \overline{x_t^*}\right)\left(x_t^{*(l)} - \overline{x_t^*}\right)^T \tag{10}$$

3) Generate experimental noise w_t

$$w_t^{(l)} = N(\mathbf{0}, 1.0 \times 10^{-6} I) \tag{11}$$

I in (11) represents the unit matrix.

4) Calculate variance-covariance matrix of experimental noise $\overline{R}_t$

$$\overline{R}_t = \frac{1}{100-1} \sum_{l=1}^{100} w_t^{(l)} w_t^{(l)T} \tag{12}$$

5) Calculate Kalman gain $\overline{K}_t$

$$\overline{K}_t = \overline{V}_t H_t \left(\overline{R}_t + H_t \overline{V}_t H_t{}^T\right)^{-1} \tag{13}$$

Superscript -1 in Eq. (13) shows the inverse matrix. H_t represents the observation matrix used to extract experimental values from state variables.

6) Kalman filtering

$$x_t^{*(l)} = x_t^{*(l)} + \overline{K}_t \left(y_t - H_t x_t^{*(l)} + w_t^{(l)}\right) \tag{14}$$

In the Kalman filtering step, when the filtered turbulent viscosity was less than 0, the turbulent viscosity was set to 0. This process was required to avoid divergence of the computation.

III. Re-computation

The ensemble Kalman filter estimated the optimal state variables—density, velocity components, pressure, and turbulent viscosity—based on the experimental values. Then, the density, the velocity components, and the pressure were re-computed using the computational schemes alone so that the state variables other than the turbulent viscosity satisfied the computational schemes. This re-computation is not strictly necessary for data assimilation, but researchers of numerical simulation have questioned whether the state variables estimated by

the ensemble Kalman filter satisfy the computational schemes. Therefore, the state variables other than the turbulent viscosity were re-computed using the computational schemes alone to avoid such questions. The density, velocity components, and pressure estimated by the ensemble Kalman filter were used for the initial conditions of re-computation, and the estimated turbulent viscosity was fixed during re-computation.

Results

This section discusses a comparison of computation with the SA-R model using the original parameter values (SA-R model), that with the SA-R model using the adjusted parameter values in reference [6] (Parameter value estimation), and that with the turbulent viscosity estimated by the ensemble Kalman filter (Turbulent viscosity estimation).

First, the re-computation histories for the density residual, the drag coefficient (C_D), the lift coefficient (C_L), and the moment coefficient (C_m) at 25% of the chord length are shown in Fig. 2. These figures show that the computation gradually converged to 20000 time steps.

(a) Density residual
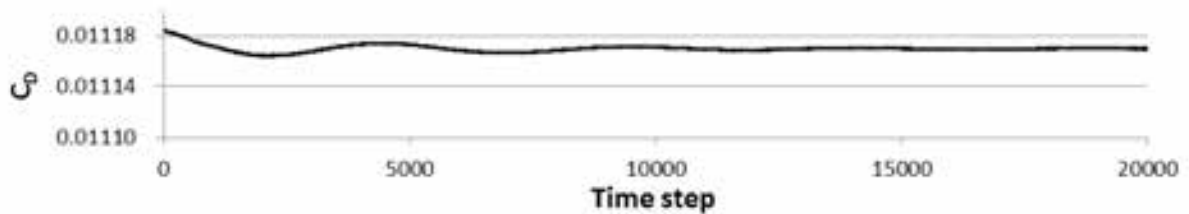
(b) Drag coefficient (C_D)
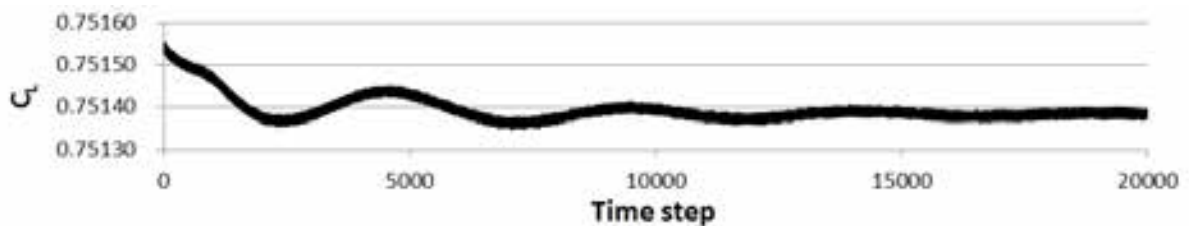
(c) Lift coefficient (C_L)
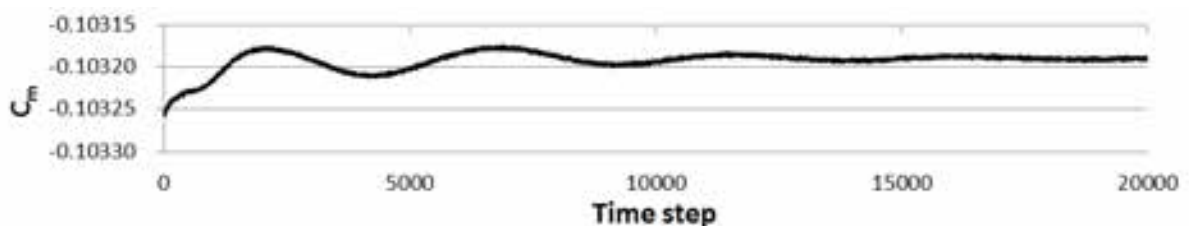
(d) Moment coefficient (Cm)

Figure 2. Re-computation history

Next, the computed pressure coefficients on the airfoil of each are compared with the experimental values in Fig. 3 and Fig. 4. In Fig. 3 and Fig. 4, the blue point shows the experimental pressure coefficient, the black dotted line shows the computed pressure coefficient with the turbulent viscosity of the SA-R model using the original parameter values (SA-R model), the green line shows that with the turbulent viscosity of the SA-R model using the adjusted parameter values (Parameter value estimation), and the red line shows that with the turbulent viscosity of the ensemble Kalman filter (Turbulent viscosity estimation).

The comparison shows that:
1. On the upper surface, the computed pressure coefficient of "Parameter value estimation" and "Turbulent viscosity estimation" agrees with the experimental pressure coefficient better than that of "SA-R model."
2. At the shock-boundary layer interaction, the computed pressure coefficient of "Turbulent viscosity estimation" agrees with the experimental pressure coefficient better than those of "SA-R model" and "Parameter value estimation."
3. At the trailing edge, the computed pressure coefficient of "Parameter value estimation" and "Turbulent viscosity estimation" agrees with the experimental pressure coefficient better than that of "SA-R model."

These observations indicate that computation with "Turbulent viscosity estimation" can predict the proper fluid phenomena. Actually, at the shock-boundary layer interaction, the computed pressure coefficient with "Turbulent viscosity estimation" agreed well with the experimental pressure coefficients. This result suggests that the ensemble Kalman filter can be used to estimate the proper turbulent viscosity based on the experimental values.
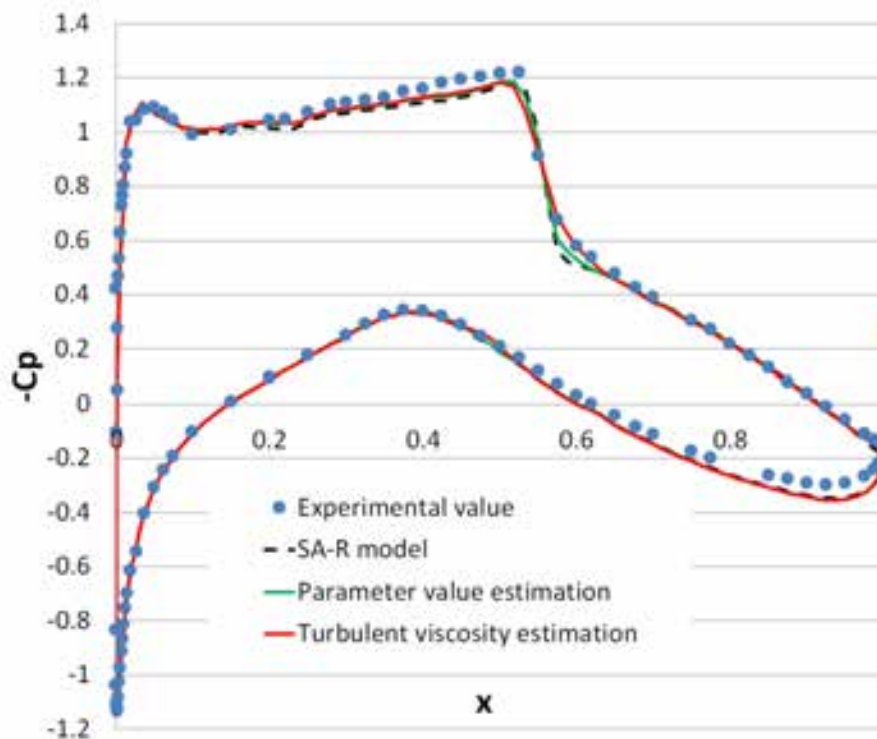
Figure 3. Computed pressure coefficients and experimental values
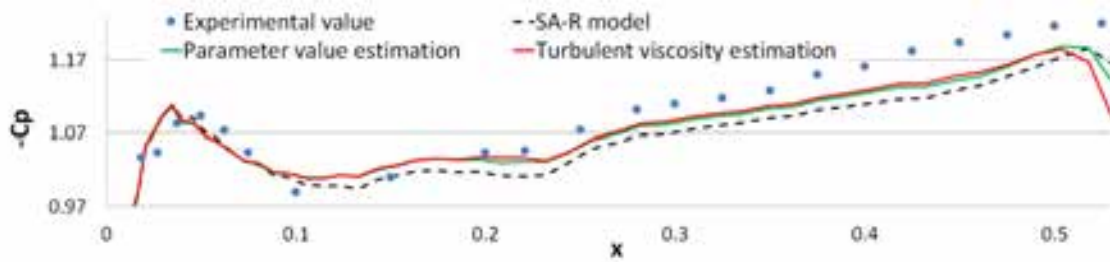
(a) on upper surface before shock location
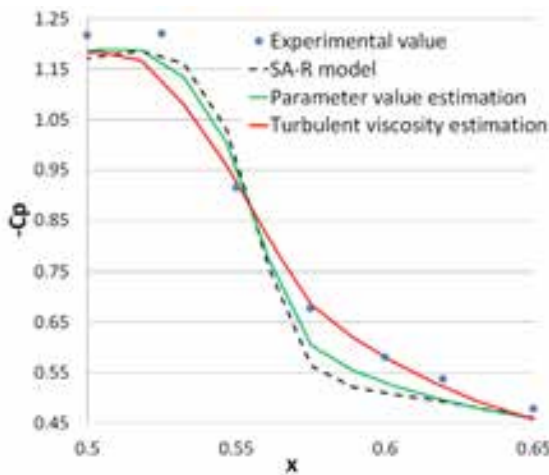
(b) at shock-boundary layer interaction
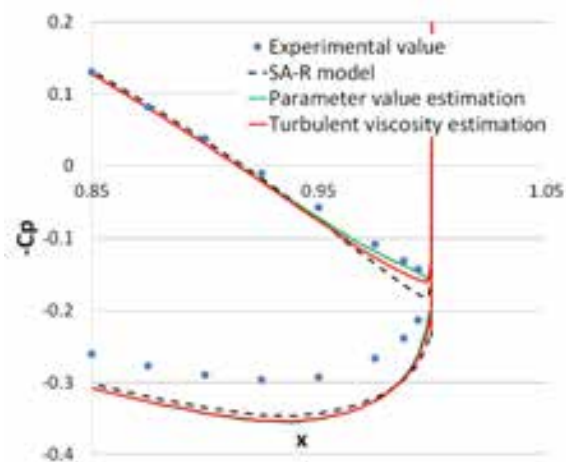
(c) at trailing edge

Figure 4. Computed pressure coefficients and experimental values (Enlarged view)

Next, the computed flow of each are compared. The experimental pressure coefficient at the shock-boundary layer interaction suggests that the separated flow occurs. To investigate the computed flow of each in detail, firstly, the computed turbulent viscosity of each are compared.

Figure 5 shows the turbulent viscosity computed with the SA-R model using the original parameter values, that computed with the SA-R model using the adjusted parameter values, and that computed with the ensemble Kalman filter. The computed turbulent viscosity with the ensemble Kalman filter shows:
1.   Lower turbulent viscosity on the airfoil than that with the SA-R model using the original parameter values.
2.   Lowest turbulent viscosity at the wake region of three
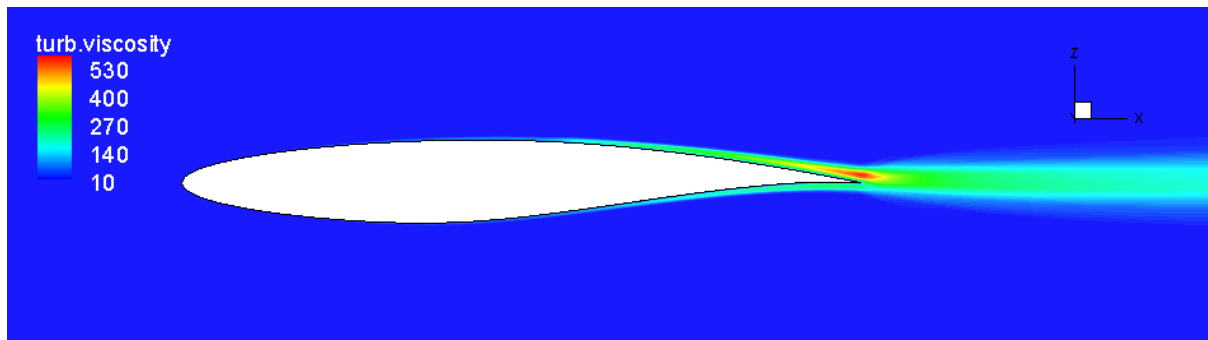
(a) SA-R model using original parameter values
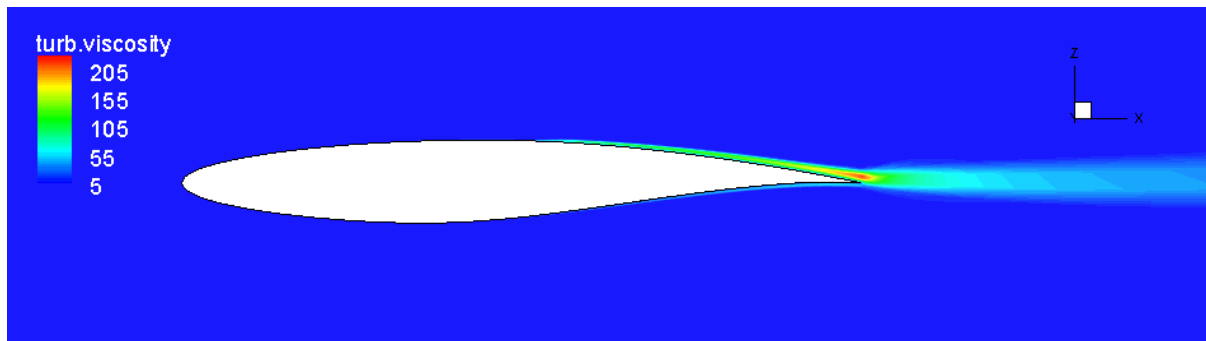
(b) SA-R model using adjusted parameter values
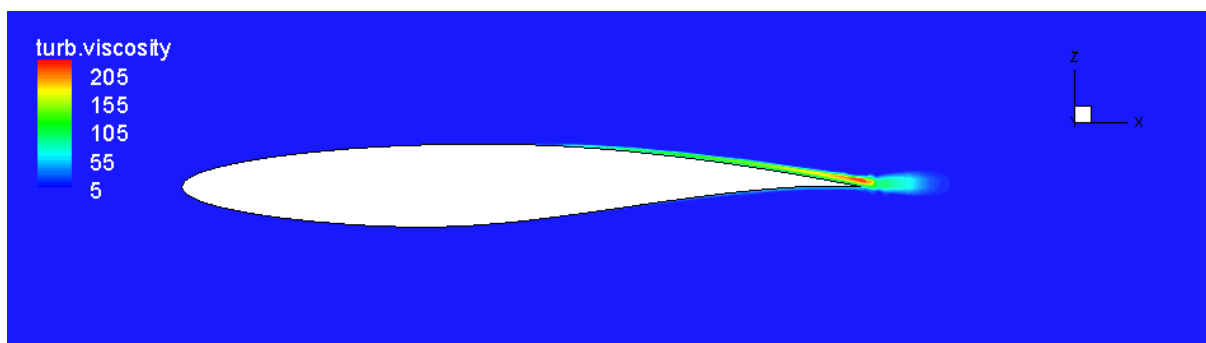
(c) Ensemble Kalman filter

Figure 5. Computed turbulent viscosity

In Fig. 6, the computed turbulent viscosities around the shock location of each are compared. In Fig. 6, the line shows the computed pressure coefficient of each. Each figure shows the following:

1. The SA-R model using the original parameter values predicts an increase in turbulent viscosity from before the shock location, and the turbulent viscosity before the shock location increases more at the shock location.
2. The SA-R model using the adjusted parameter values predicts an increase in the turbulent viscosity from near the front of the shock location.
3. The ensemble Kalman filter estimates an increase in the turbulent viscosity at the front of the shock location and from the inside of the shock location.
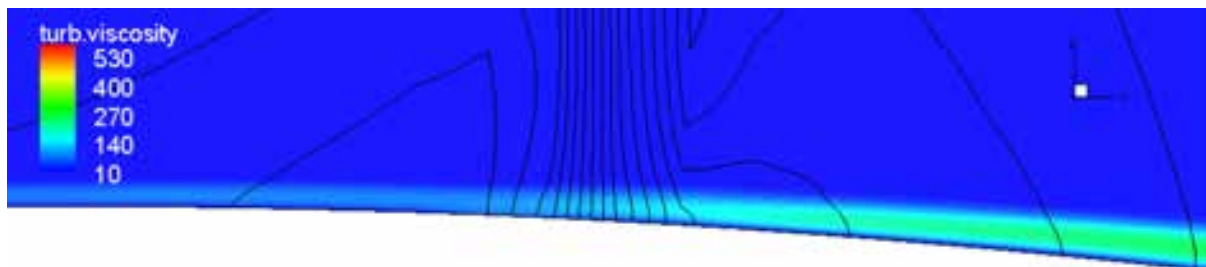
(a) SA-R model using original parameter values
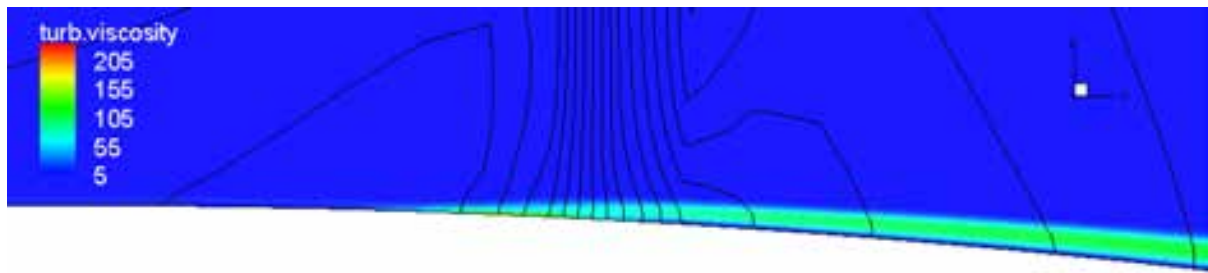
(b) SA-R model using adjusted parameter values
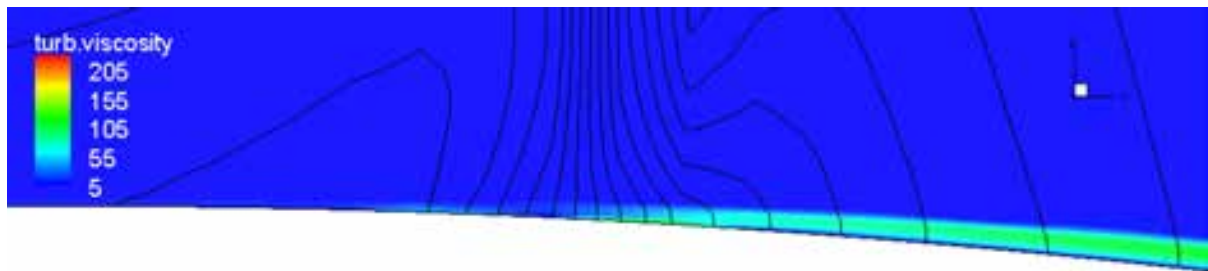
(c) Ensemble Kalman filter

Figure 6. Computed turbulent viscosity around the shock location

Next, the horizontal velocity components of each are compared in Fig. 8. The comparisons are conducted at (a) x = 0.54, (b) x = 0.56, (c) x = 0.58, (e) x = 0.60, and (e) x = 0.62 on the upper surface as shown in Fig. 7. The experimental pressure distribution indicates that separated flow occurs around the region.

In Fig. 8, the vertical axis shows the vertical distance above the airfoil and the horizontal axis shows the horizontal velocity component. In Fig. 8, the black dotted line shows the computed horizontal velocity component with the turbulent viscosity of the SA-R model using the original parameter values (SA-R model), the green line shows that with the turbulent viscosity of the SA-R model using the adjusted parameter values (Parameter value estimation), and the red line shows that with the turbulent viscosity of the ensemble Kalman filter (Turbulent viscosity estimation).

Each figure shows the following:
1. The computed horizontal velocity component with the turbulent viscosity of the SA-R model using the original parameter values differs from the distribution of separated flow at each location.
2. The computed horizontal velocity component with the turbulent viscosity of the SA-R model using the adjusted parameter values is close to the distribution of separated flow at (c) x = 0.58, (d) x = 0.60, and (e) x = 0.62; however, these are not the distribution of separated flow.
3. The computed horizontal velocity component with the turbulent viscosity of the ensemble Kalman filter is the distribution of separated flow at (b) x = 0.56, (c) x = 0.58, (d) x = 0.60, and (e) x = 0.62.

As the experimental pressure coefficient at the shock-boundary layer interaction suggests, the separate flow occurs in the flow computed with "Turbulent viscosity estimation." This result indicates that the turbulent viscosity estimated by the ensemble Kalman filter was appropriate for computation at the shock-boundary interaction.
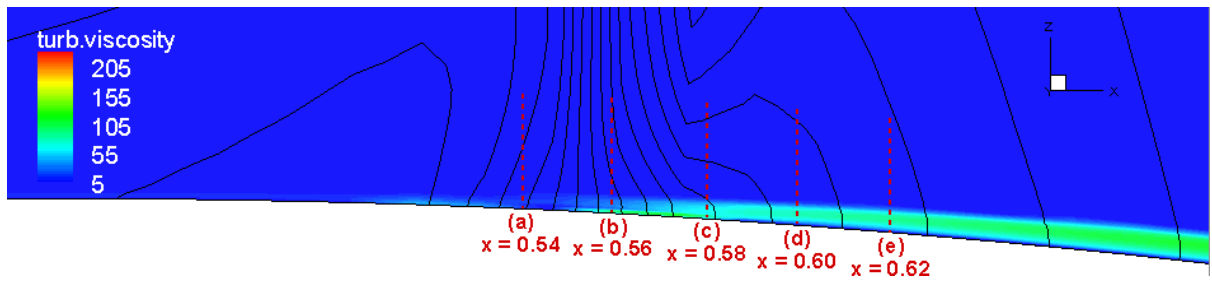
Figure 7. Locations for comparison of horizontal velocity components

(a) x = 0.54

(b) x = 0.56

(c) x = 0.58

(d) x = 0.60

(e) x = 0.62
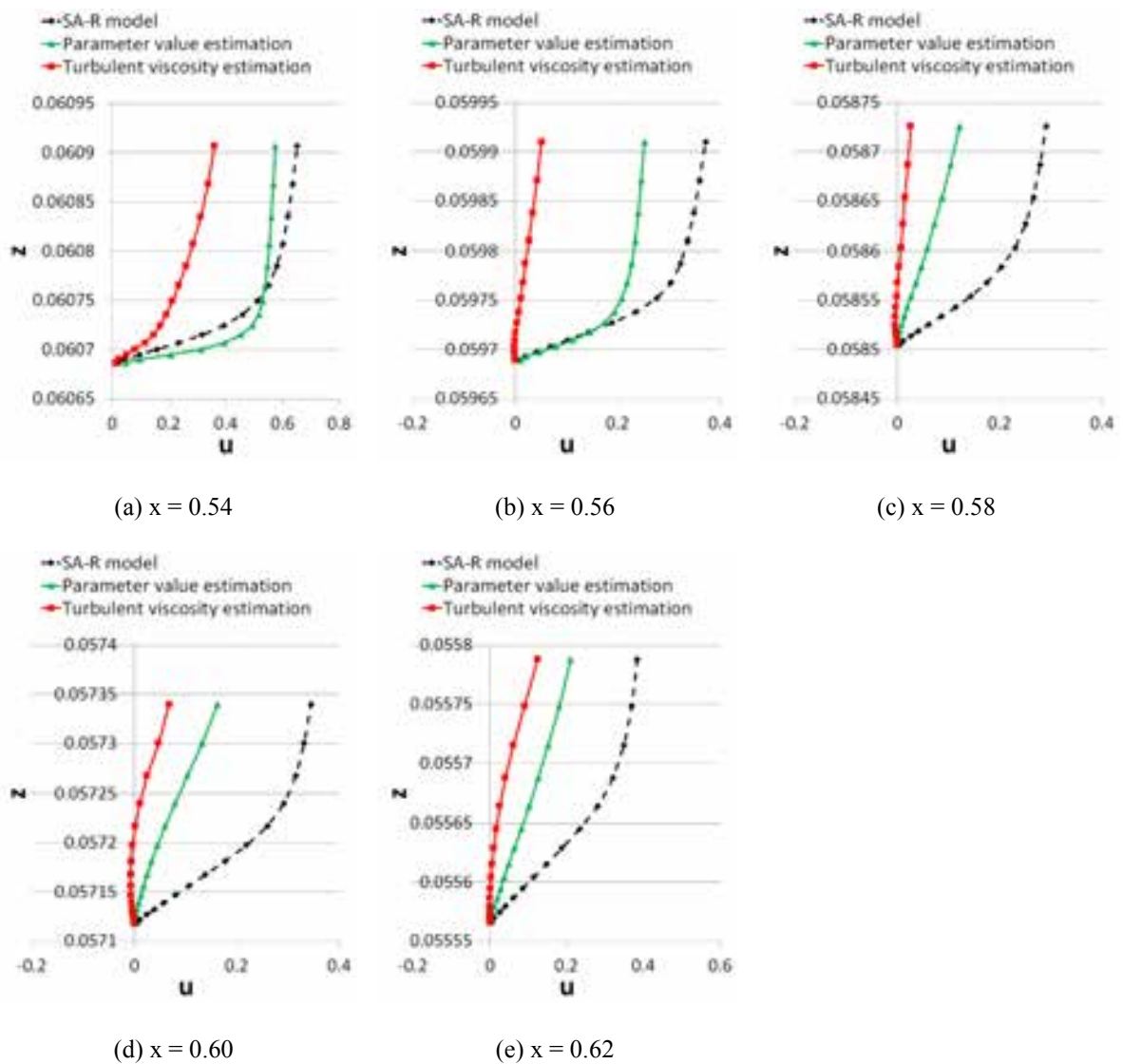
Figure 8. Distributions of horizontal velocity component

Conclusion

In this study, the turbulent viscosity in the flow field around the RAE2822 airfoil was estimated based on the experimental pressure values on the airfoil without a turbulence model. The ensemble Kalman filter, a data assimilation method, was employed to estimate the turbulent viscosity. The initial distribution of each ensemble member that is required in the process of the ensemble Kalman filter, was determined by computation with the Spalart–Allmaras turbulence model (SA-R). In the computation for the initial distribution of each ensemble member, the different parameter values of the SA-R model were assigned to each ensemble member. The turbulence model was used only to determine the initial distribution of each ensemble member. After estimation of the state variables by the ensemble Kalman filter, the estimated state variables other than turbulent viscosity—i.e., density, velocity components, and pressure—were re-computed by the computational schemes alone so that the state variables satisfied the computational schemes.

The estimated turbulent viscosity increased at the front of the shock location and from the inside of the shock location. Compared to the computed turbulent viscosity with the SA-R turbulence model using the original parameter values and the adjusted parameter values, the turbulent viscosity estimated by the ensemble Kalman filter showed (1) lower turbulent viscosity on the upper surface than that with the SA-R model using the original parameter values, and (2) the lowest turbulent viscosity at the wake region of three.

Computation with the estimated turbulent viscosity was able to predict (1) the pressure coefficients that agrees with the experimental pressure coefficients at the shock-boundary interaction, and (2) the separated flow at the shock-boundary interaction. These observations indicated that the estimated turbulent viscosity was appropriate for computation at the shock-boundary interaction and the ensemble Kalman filter was able to be used for estimation based on the experimental pressure distribution on the airfoil without a turbulence model.

These observations suggest that the computation can predict the proper flow field when the proper turbulent viscosity is given.

On the other hand, the present results still show the disagreement with the experiment on the upper surface of the airfoil and at the trailing edge. Although the disagreement might be caused by not the turbulent viscosity but other factors such as two dimensional calculation, this is an issue. Further studies are required to investigate and resolve this issue.

When this issue is resolved and some kind of physical quantity over the entire flow region become available, it will be possible to perform computation without a turbulence model, and the computation can predict the flow field more precisely than either EFD or CFD alone. This will be one form of EFD/CFD.

Appendix

Table 2 shows the computed aerodynamic coefficients with the turbulent viscosity of the SA-R model using the original parameter values (SA-R model), those with the turbulent viscosity of the SA-R model using the adjusted parameter values (Parameter value estimation), and those with the turbulent viscosity of the ensemble Kalman filter (Turbulent viscosity estimation). We do not know which of the computed aerodynamic coefficients are reliable because we do not have the experimental aerodynamic coefficients.

Table 2. Comparison of computed aerodynamic coefficients

Aerodynamic coefficient	SA-R model	Parameter value estimation	Turbulent viscosity estimation
C_D	0.01338	0.01126	0.01117
C_L	0.74098	0.74840	0.75139
C_m (0.25c)	−0.10139	−0.10294	−0.10319

References

[1] S. Watanabe, S. Kuchi-ishi, T. Aoyama.: A Prototype System Towards EFD/CFD Integration: Digital/Analog-Hybrid Wind Tunnel. 27th International Congress of the Aeronautical Sciences, 2010.

[2] P. R. Spalart and S. R. Allmaras.: A One-Equation Turbulence Model for Aerodynamic Flows. *Recherche Aerospatiale*, No. 1, pp. 5-21, 1994.

[3] F. R. Menter.: Two-Equation Eddy-Viscosity Turbulence Models for Engineering Applications. *AIAA Journal*, Vol. 32, No. 8, pp. 1598-1605, 1994.

[4] H. Kato, et al.: Adaptive Simulation of Turbulence Flow by using Data Assimilation. *Journal of Japan Society of Fluid Mechanics*, Vol. 31, No. 2, pp. 165-173, 2012. (in Japanese)

[5] H. Kato and S. Obayashi.: Approach for Uncertainty of Turbulence Modeling Based on Data Assimilation Technique. *Computers & Fluids Special Issue: Future of CFD.* (submitted for publication)

[6] H. Kato and S. Obayashi.: Optimization of a Turbulence Model by using Data Assimilation. European Congress on Computational Methods in Applied Sciences and Engineering (ECCOMAS 2012), 2012.

[7] NPARC Alliance Validation Archive: http://www.grc.nasa.gov/WWW/wind/valid/raetaf/raetaf05/raetaf05.html.

[8] G. Evensen.: Sequential data assimilation with a nonlinear quasi-geostrophic model using Monte Carlo methods to forecast error statistics. *Journal of Geophysical Research*, Vol. 99(C5), pp. 10 143- 10 162, 1994.

[9] C. Wunsch.: The Ocean Circulation Inverse Problem. Cambridge University Press, 1996.

[10] G. Evensen.: The ensemble Kalman filter: Theoretical formulation and practical implementation. *Ocean Dynamics*, Vol. 53, pp. 343-367, 2003.

[11] G. Evensen.: Data Assimilation. *The Ensembel Kalman Filter (2nd ed.)*, Springer-Verlag, 2009.

[12] G. Evensen.: The ensemble Kalman filter for combined state and parameter estimation. *IEEE Control Systems Magazine*, Vol. 29, No. 3, pp. 83-104, 2009.

[13] A. Hashimoto, K. Murakami, T. Aoyama, K. Ishiko.: Toward the Fastest Unstructured CFD Code 'FaSTAR'. 50th AIAA Aerospace Sciences Meeting including the New Horizons Forum and Aerospace Exposition, 2012.

[14] NPARC Alliance CFD Validation Archive: http://www.grc.nasa.gov/WWW/wind/valid/raetaf/raetaf05/cp.exp.gen.

[15] M. D. McKay, R. J. Beckman, W. J. Conover.: A Comparison of Three Methods for Selecting Values of Input Variables in the Analysis of Output from a Computer Code. *Technometrics*, Vol. 21, No. 2, pp. 239-245, 1979.

A Variable Fidelity Response Surface Approach towards Integration of CFD and EFD

Wataru YAMAZAKI
Nagaoka University of Technology
Nagaoka, 940-2188, Japan
yamazaki@mech.nagaokaut.ac.jp

Shigeru KUCHI-ISHI
Japan Aerospace Exploration Agency
Tokyo, 182-8522, Japan
shigeruk@chofu.jaxa.jp

Abstract

In this paper, a variable fidelity Kriging model approach, which is also referred to as cokriging, is proposed for efficient aerodynamic data modeling. In this approach, an accurate response surface is constructed by utilizing variable fidelity information. The variable fidelity information can be defined by different physical models, different accuracies of flow simulation as well as combination of experimental data and numerical data. The effectiveness of the developed variable fidelity Kriging model approach is discussed by using EFD/CFD aerodynamic data of a DLR-F6 configuration. The developed approach is promising for accurate aerodynamic data modeling by efficiently integrating EFD and CFD data.

Key words: Variable fidelity Kriging model, Aerodynamic data modeling, Response surface

Introduction

Recently, significances of experimental fluid dynamics (EFD) and computational fluid dynamics (CFD) are comparable in aerodynamic designs. Currently, CFD is not only a supplementary tool of EFD, but has intrinsic roles in aerodynamic design projects. In EFD approach, there are some restrictions in its measurement. For example, the difference of Reynolds number between wind tunnel testing and real flight testing, and the influence of wind tunnel wall/model support system are still essential problems to be taken into account in EFD approaches. Furthermore, the increase in lead time (mainly due to experimental model design/manufacture) is one of the major bottlenecks of EFD approach. In CFD approach, on the other hand, these issues can be eluded thanks to the availability of improved numerical algorithms and the growth of computer speed and memory. The CFD aerodynamic data is, however, considered to have less reliability than EFD data especially with fluid phenomena of large turbulence, transition and separation. The effect of numerical dissipation related to computational grid resolution is also significant for the accuracy of predicted aerodynamic performances. Since it may be difficult to resolve these problems individually in EFD and CFD fields, the integration of EFD and CFD data is promising to provide reliable aerodynamic data efficiently by utilizing the advantages of EFD/CFD approaches. In Japan Aerospace Exploration Agency (JAXA), a digital (CFD) / analog (EFD) hybrid wind tunnel system is being developed [1]. One of the major objectives of the development of this system is to comprehensively solve the issues mentioned above by effectively utilizing both EFD and CFD capabilities, resulting in the reduction of design time, cost, risk and the improvement of design data accuracy and reliability in the aircraft and aerospace vehicle development.

Response surface approaches have attracted increased attention recently in aerospace engineering since they offer substantial benefits for design optimization, aerodynamic database construction, and uncertainty

quantification. The idea of a response surface approach is to replace expensive functional evaluations (i.e. costly EFD measurements or high-fidelity CFD simulations) with an analytical model which is constructed through selective sampling of the high-fidelity data. When a response surface model is constructed with given exact functional data, a designer can efficiently explore the approximated (high-dimensional) design space at very low computational cost. To realize an accurate/efficient exploration on the response surface, the construction of an accurate response surface is essential. The Kriging model [2-8], which was originally developed in the field of geological statistics, has often been found to perform well in other engineering fields and has thus gained popularity in aerospace engineering and design. This response surface model predicts the functional value by using stochastic processes, and has the flexibility to represent multimodal/nonlinear functions. One of the major approaches to enhance the accuracy of response surface models efficiently is to utilize the derivative information of the function [4,5,7]. Utilizing low-fidelity functional values as secondary information represents an alternative approach to improve the accuracy of response surface models [6-10]. This approach is referred to as cokriging method or variable fidelity (VF) approach [11]. These concepts of the response surface approaches are summarized in Fig.1. In the VF response surface approach, the trends of low-fidelity functional values as well as high-fidelity functional absolute values are simultaneously utilized to construct an accurate response surface. This approach is promising for efficient aerodynamic data modeling by integrating EFD and CFD data.

In this research, a variable fidelity Kriging model approach is utilized to produce accurate aerodynamic data by integrating EFD and CFD data. The EFD/CFD aerodynamic data of a DLR-F6 configuration, that are mutually managed in the digital/analog hybrid wind tunnel system of JAXA, are utilized in this study.
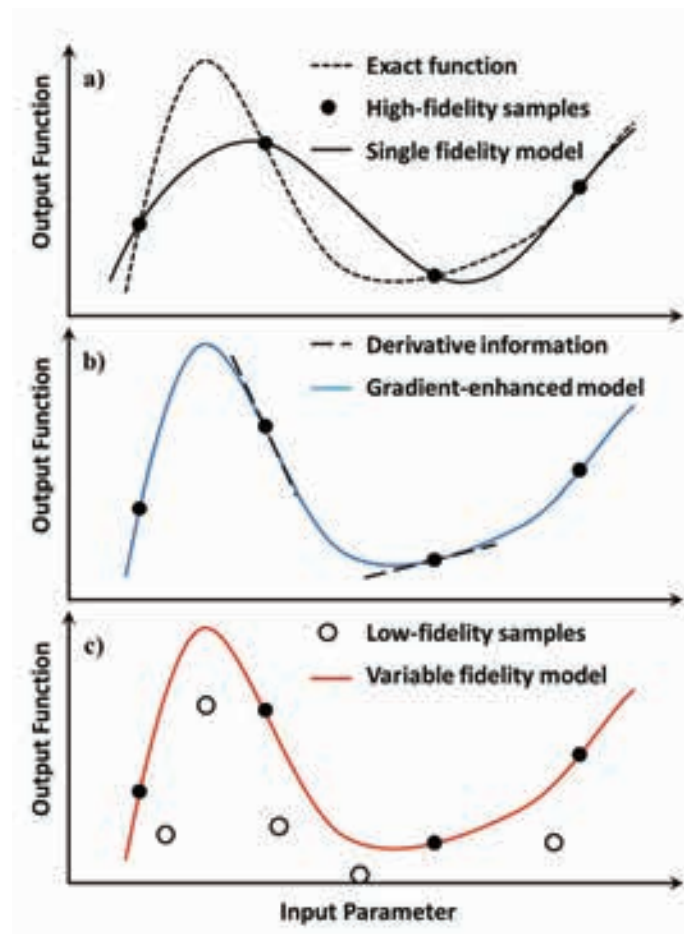
Fig.1 Concepts of Response Surface Approaches
a) Conventional Response Surface
b) Derivative-enhanced Response Surface
c) Variable Fidelity Response Surface

Variable Fidelity Kriging Model

In this section, our variable fidelity Kriging approach [7-8] is briefly introduced. In this approach, the high and low-fidelity functions are replaced by the following random functions:

$$\widetilde{y}_{l(\mathbf{x})} = \beta_l + Z_{l(\mathbf{x})} \tag{1}$$

where l means the index of fidelity level. The first term β_l is a constant model and the second term Z_l represents a random process model with zero mean, variance σ_l^2 and the covariance of two locations $\mathbf{x}_1$ and $\mathbf{x}_2$ is given as follows:

$$\mathrm{cov}\!\left[Z_{l_1(\mathbf{x}_1)}, Z_{l_2(\mathbf{x}_2)}\right] = \sigma_{l_1}\sigma_{l_2}R_{l_1 l_2(\mathbf{x}_1,\mathbf{x}_2)} \tag{2}$$

where $R_{l_1 l_2}$ is a correlation function which is usually defined as a radial basis function based on a distance between the two locations. Then a linear combination of the high and low-fidelity information at given sample points is considered for the high-fidelity functional prediction as follows:

$$\hat{y}_{(\mathbf{x})} = \sum_{i=1}^{n_1} w_{1i}y_{1i} + \sum_{i=1}^{n_2} w_{2i}y_{2i} = \mathbf{w}_1^T\mathbf{y}_1 + \mathbf{w}_2^T\mathbf{y}_2 \tag{3}$$

where $\mathbf{y}_l$ and $\mathbf{w}_l$ are respectively the known function values on given sample points and their unknown weight coefficients, and n_l is the number of sample points at l-th fidelity level. The first fidelity level ($l = 1$) is considered as high-fidelity data in this study. The Kriging approach finds the best linear unbiased predictor which minimizes the mean square error (MSE):

$$MSE = E\!\left[\left(\hat{y}_{(\mathbf{x})} - \widetilde{y}_{1(\mathbf{x})}\right)^2\right] \tag{4}$$

subject to the unbiasedness constraint of

$$E\!\left[\hat{y}_{(\mathbf{x})}\right] = E\!\left[\widetilde{y}_{1(\mathbf{x})}\right] \tag{5}$$

The weight coefficients can be found by solving this constrained minimization problem with the Lagrange multiplier approach. Finally, the high-fidelity functional prediction is achieved by the following formula:

$$\hat{y}_{(\mathbf{x})} = \mathbf{L}^T\widetilde{\beta} + \mathbf{r}_{(\mathbf{x})}^T\mathbf{R}^{-1}\!\left(\mathbf{Y} - \mathbf{F}\widetilde{\beta}\right) \tag{6}$$

where

$$\begin{aligned}
\widetilde{\beta} &= \left(\mathbf{F}^T\mathbf{R}^{-1}\mathbf{F}\right)^{-1}\mathbf{F}^T\mathbf{R}^{-1}\mathbf{Y} \in \Re^{2\times1} \\
\mathbf{Y} &= \left[\mathbf{y}_1^T, \mathbf{y}_2^T\,\sigma_1/\sigma_2\right]^T \in \Re^{(n_1+n_2)\times1} \\
\mathbf{F} &= \begin{bmatrix} 1 & 0 \\ 0 & 1 \end{bmatrix} \in \Re^{(n_1+n_2)\times2} \\
\mathbf{L} &= \begin{bmatrix} 1 & 0 \end{bmatrix}^T \in \Re^{2\times1}
\end{aligned} \tag{7}$$

The correlation matrix $\mathbf{R} \in \Re^{(n_1+n_2)\times(n_1+n_2)}$ expresses the correlations between all given sample points while the correlation vector $\mathbf{r} \in \Re^{(n_1+n_2)\times1}$ expresses the correlations between all given sample points and a location $\mathbf{x}$. The matrix form of Eq.(6) as well as the definition of all matrices/vectors are very similar with that of the original Kriging formulation. The factor of σ_1/σ_2 is a special parameter required in this variable fidelity Kriging formulation. This factor has the role to take into account the influence of low-fidelity information. The MSE of Eq.(4) can be expressed as follows:

$$MSE = \sigma_1^2\!\left[1 - \mathbf{r}^T\mathbf{R}^{-1}\mathbf{r} + \varphi^T\!\left(\mathbf{F}^T\mathbf{R}^{-1}\mathbf{F}\right)^{-1}\varphi\right] \qquad \left(\varphi = \mathbf{F}^T\mathbf{R}^{-1}\mathbf{r} - \mathbf{L}\right) \tag{8}$$

As the conventional Kriging approach, hyper-parameters (which appear in the correlation function) as well as the factor of σ_1^2 are estimated by a likelihood maximization approach [2]. In this research, the additional factor of σ_1/σ_2 is also estimated by the likelihood maximization approach. The computational cost to construct a variable fidelity response surface model is primary dependent on the total number of sample points $n_1 + n_2$, since a huge number of calculations of $\mathbf{R}^{-1}$ and $|\mathbf{R}|$ are required with different sets of the hyper-parameters. Nevertheless, the computational cost is much smaller than that of a high-fidelity CFD computation with general numbers of sample points (< 500).

Validation using Analytic Function

In this section, the validity of the variable fidelity Kriging response surface approach is shown in an analytic functional problem. In this study, the following analytic function, which is similar to the Rastrigin function, is considered as the high-fidelity (exact) function:

$$F_{(x)} = 20 + \sum_{i=1}^{2} \left[x_i^2 - 10\cos(\pi x_i / 2) \right] \tag{9}$$

The shape of the exact function is shown in Fig.2. As its low-fidelity functions, the following functions are defined in this study:

$$f_{1(x)} = F_{(x)} - 20$$

$$f_{2(x)} = \sum_{i=1}^{2} \left[x_i^2 \right] \tag{10}$$

$$f_{3(x)} = \sum_{i=1}^{2} \left[-10\cos(\pi x_i / 2) \right]$$

By using 10 high-fidelity samples as well as 90 low-fidelity samples, single fidelity (SF) / VF response surface models were constructed. These sample points were generated by a Latin Hypercube Sampling (LHS) approach. The shapes of the approximated functions are shown in Fig.3. The accuracy of the approximated function was increased with the low-fidelity sample points of f_1 and f_3. By using the low-fidelity function of f_2 which is the quadratic part of the exact function, the approximated model only had the quadratic functional tendency. The accuracy of a response surface model is evaluated by the following Root Mean Square Error (RMSE):

$$RMSE = \frac{1}{M} \sqrt{\sum_{j=1}^{M} \left(\hat{y}_{(x_j)} - F_{(x_j)} \right)^2} \tag{11}$$

where the coordinates x_j define an equally spaced Cartesian mesh which covers the entire design space. In Fig.4, the RMSE values are compared between the SF and VF Kriging model approaches. In the VF approaches, the number of low-fidelity sample points is increased while the number of high-fidelity sample points is fixed to 10. With the low-fidelity functions of f_1 and f_3, the accuracies of the response surface models are improved with the increase in the number of low-fidelity sample points. Thus, the accuracy of VF response surface models can be increased with appropriate low-fidelity sample points. As understood from these results, the important aspect of the low-fidelity sample points is not the absolute values of the function, but the trends of the function. When the appropriate low-fidelity sample points can be obtained inexpensively, an accurate response surface can also be constructed efficiently.
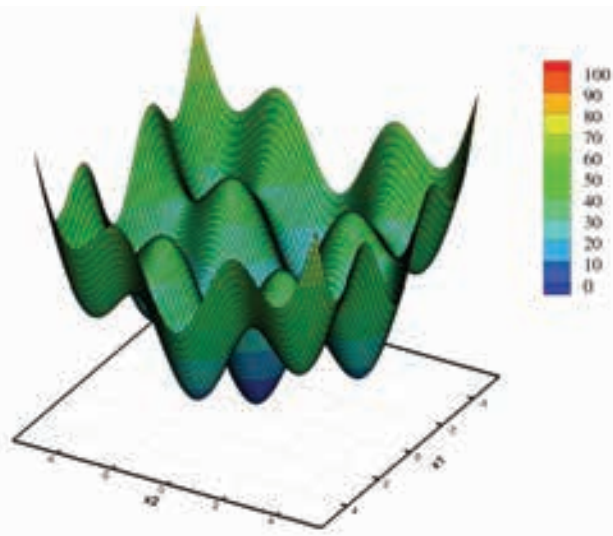
Fig.2 Exact Analytic Function
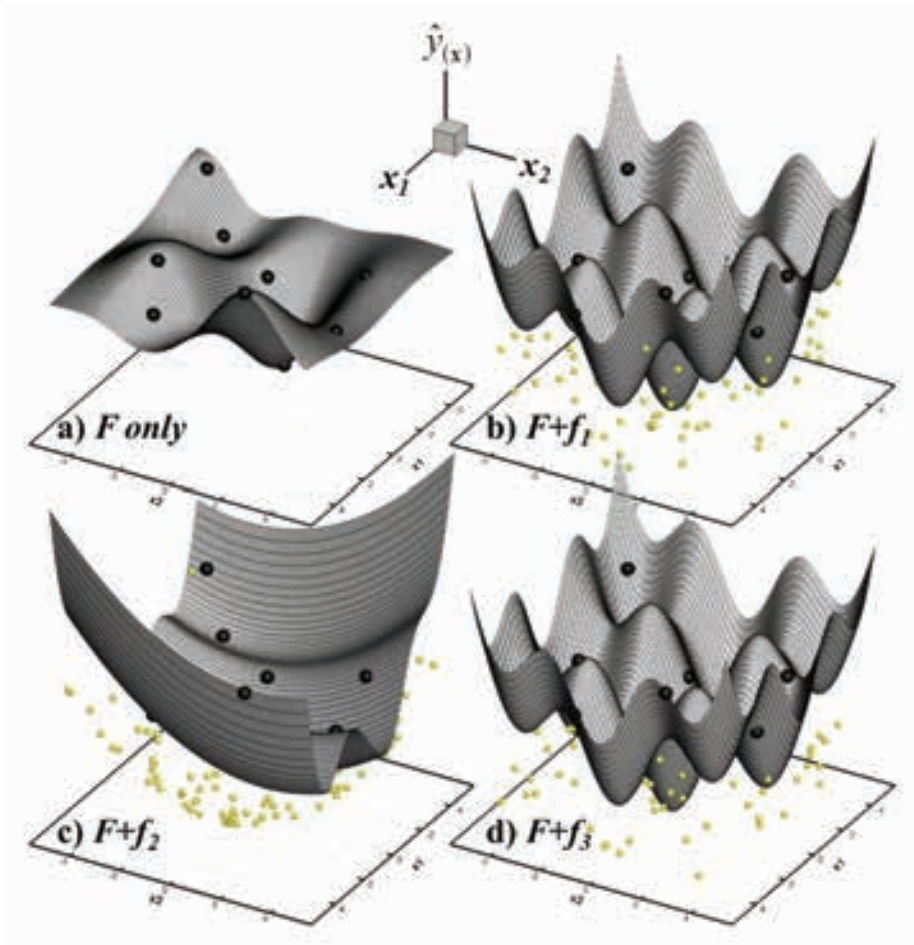
Fig.3 Estimated Functions by Response Surface Approaches,
Black Points: 10 High-Fidelity Samples
Yellow Points: 90 Low-Fidelity Samples
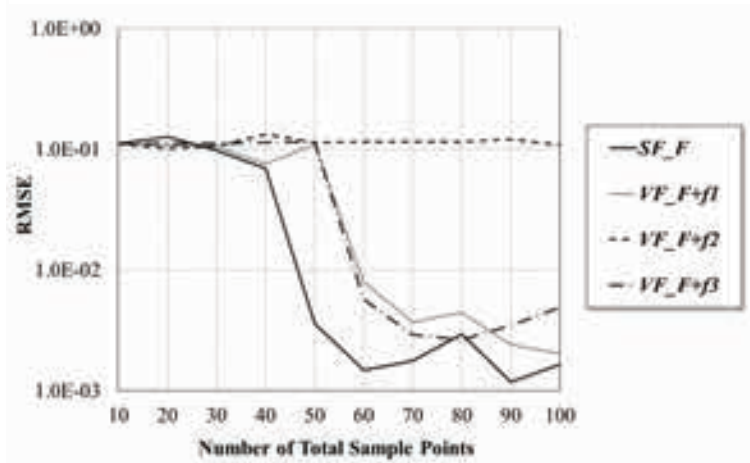
Fig.4 Comparison of Accuracies of Response Surfaces by RMSE Evaluations

Aerodynamic Data Modeling of DLR-F6 Configuration

The developed response surface approach is applied to the EFD/CFD aerodynamic data of a civil transport of DLR-F6 configuration [12]. The wind tunnel testing has been performed at JAXA 2m × 2m Transonic Wind Tunnel (JTWT) as shown in Fig.5. The CFD evaluation has been performed by a JAXA's in-house CFD solver of FaSTAR (FaST Aerodynamic Routine) [13] on JAXA Supercomputer System (JSS) as Fig.5. In this analysis, the Reynolds-Averaged Navier-Stokes (RANS) equations are solved with the Spalart-Allmaras turbulence model on a hexahedral grid [14]. The drag polar curves obtained by EFD/CFD analyses at Mach number (M_∞) of 0.75 and Reynolds number (Re) of 1.5×10^6 are compared in Fig.6. It can be confirmed that there is a certain level of difference between EFD and CFD data while the trends of drag polar curves are comparable between them except higher angles of attack (α). The EFD/CFD aerodynamic data were evaluated in the range of $0.6 \le M_\infty \le 0.85$, $0.8 \times 10^6 \le \text{Re} \le 2.0 \times 10^6$ and $-5 \le \alpha \le 5$ degrees. In these evaluations, 58 EFD data as well as 44 CFD data have been obtained.

In Fig.7, conventional SF response surfaces of C_L and C_D that are constructed only by the EFD or CFD data are visualized. Spheres indicate (high-fidelity) sample points that are utilized to construct the response surfaces. It can be confirmed that the SF response surfaces constructed by EFD/CFD data have comparable tendencies. In this study, the accuracy of a response surface is evaluated by the following mean error (ME):

$$ME = \frac{1}{58} \sum_{j=1}^{58} \left| \hat{y}(\mathbf{x}_j) - y(\mathbf{x}_j)^{EFD} \right| \tag{12}$$

where j indicates the index of the EFD data. In Fig.8, the ME values of C_D are compared between the SF and VF Kriging model approaches. In the VF approaches, the number of high-fidelity (EFD) sample points is increased while the number of low-fidelity (CFD) sample points is fixed to 9. Various sets of the high/low-fidelity sample points are chosen by a LHS approach. The improvement in accuracy is observed by the VF approach with smaller numbers of the high-fidelity (EFD) sample points (<15). Although the accuracy of the VF model is not improved with larger numbers of the high-fidelity (EFD) sample points, this is due to the difference of functional tendencies between EFD/CFD data. The functional tendencies obtained from the 9 CFD sample points are no longer effective with larger numbers of EFD sample points. In Fig.9, the SF/VF response surfaces of C_L and C_D that are constructed by 9 EFD and/or 9 CFD data are visualized. In Fig.10, estimated drag polar curves from the response surfaces of Fig.9 are indicated. It can be seen that the accuracies of the response surface models are increased by utilizing the VF Kriging approach. Despite only one EFD and two CFD sample points were set on (M_∞, Re) = (0.75, 1.5×10^6), the estimated drag polar curve by the VF approach showed a certain level of agreement with the EFD data.
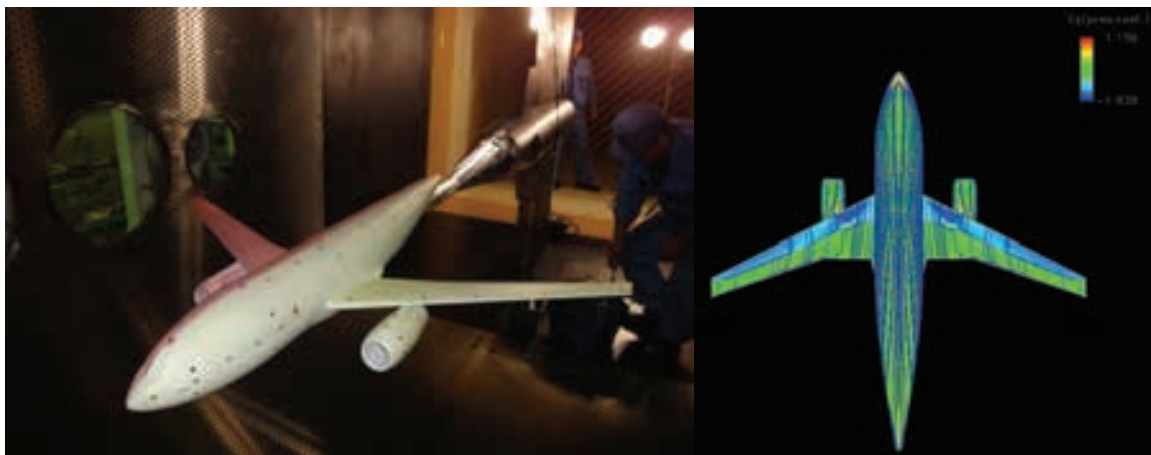
Fig.5 Aerodynamic Evaluations by EFD/CFD Approaches
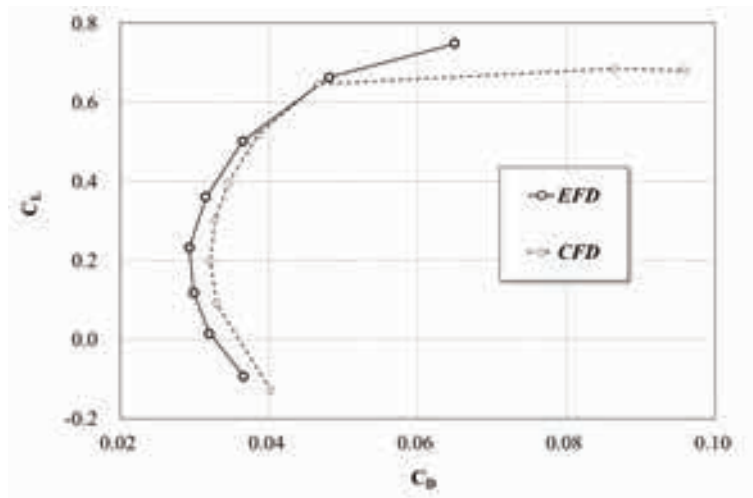
Fig.6 Comparison of Drag Polar Curves at M$_\infty$ of 0.75 and Re of 1.5 $\times$ 10^6
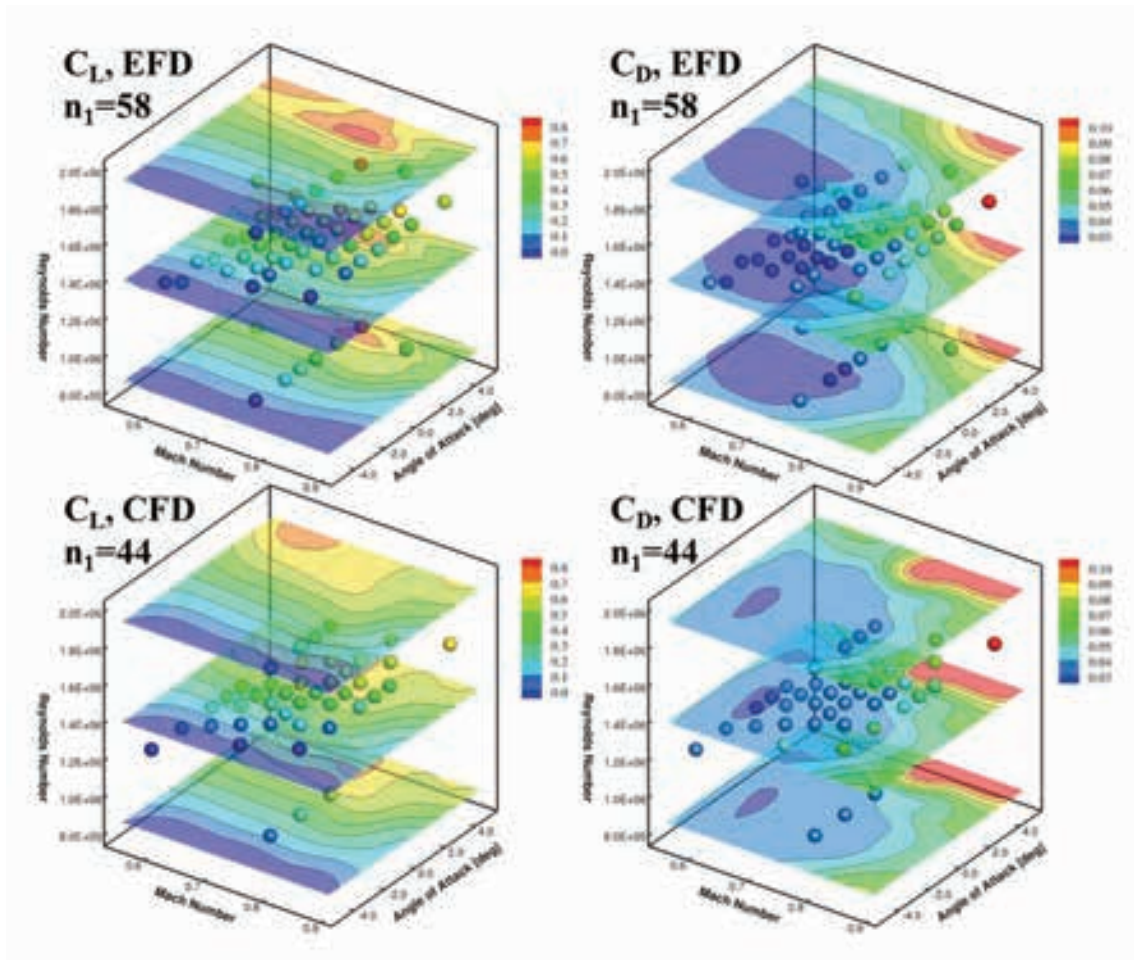
Fig.7 Single Fidelity Response Surfaces of C$_L$ and C$_D$
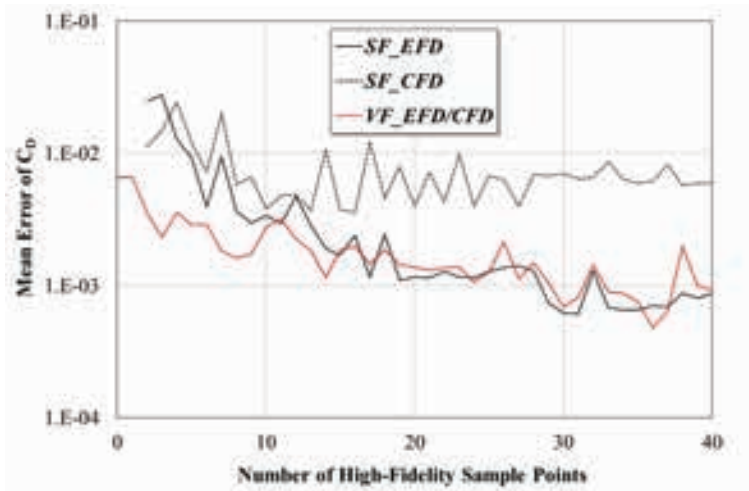
Fig.8 Comparison of Accuracies of Response Surfaces by ME Evaluations
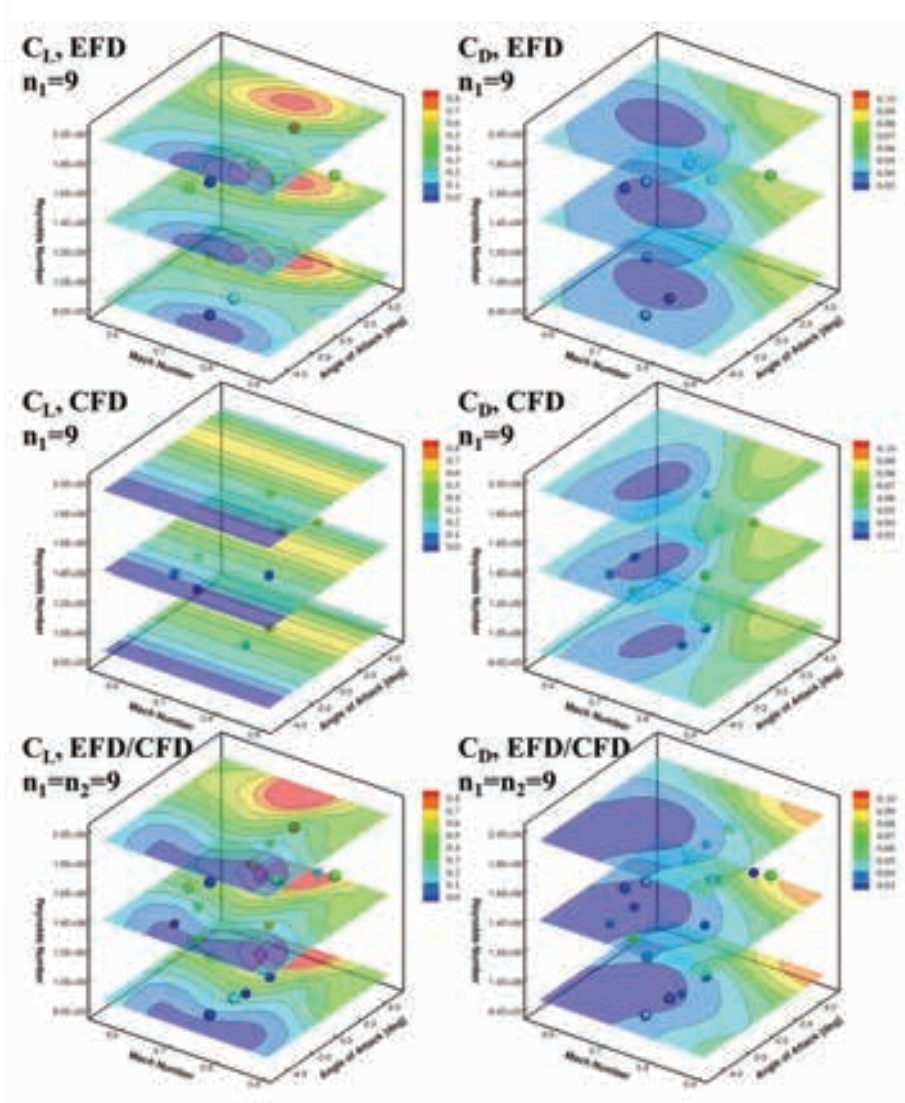

Fig.9 Single Fidelity / Variable Fidelity Response Surfaces of C_L and C_D
Upper: EFD-based SF, Middle: CFD-based SF, Lower: EFD/CFD-based VF Model
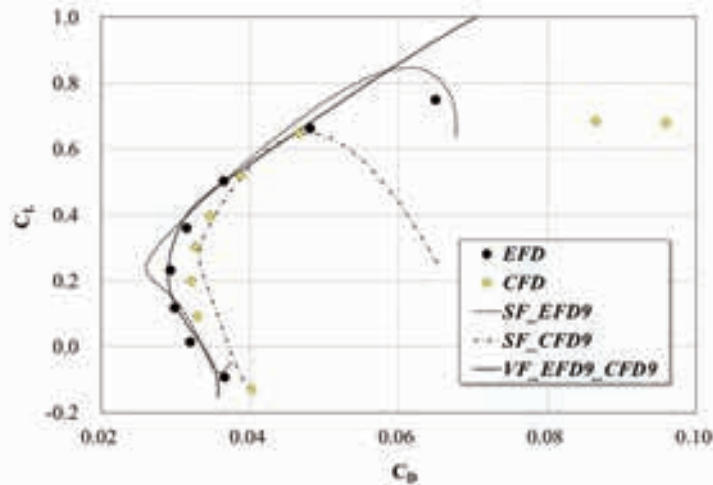**Spheres: EFD Samples, Cubes: CFD Samples**

Fig.10 Estimated Drag Polar Curves at M_∞ of 0.75 and Re of 1.5 $\times$ 10^6

Summary & Future Directions

In this research, a variable fidelity Kriging response surface approach has been utilized for aerodynamic data modeling by integrating EFD/CFD data. In this approach, a response surface model can be constructed by the absolute functional values of high-fidelity (EFD) sample points as well as the functional trends of low-fidelity (CFD) sample points. The EFD/CFD aerodynamic data of a DLR-F6 configuration, that are managed in the digital/analog hybrid wind tunnel system of JAXA, are utilized in this study. The variable fidelity approach provided better aerodynamic data modeling than the single fidelity conventional response surface approach with smaller numbers of EFD sample points. This result indicates the validity of the variable fidelity Kriging model approach for the fusion of EFD/CFD data.

Once an experimental model has been manufactured, it is not difficult to make massive aerodynamic database with respect to flow conditions (M_∞, Re, α etc) as long as wind tunnel facilities are available. In this context, the fusion of EFD/CFD data within the M_∞ - Re - α parameter space, which was examined in this paper, may not be interested by aerodynamic designers. One of the promising directions for the practical application of the variable fidelity Kriging approach is the fusion of EFD/CFD data between various model configurations. Although the manufacturing of various experimental models is difficult in terms of cost effectiveness, it is relatively easy in CFD by applying computational grid deformation techniques. By integrating EFD/CFD data between various configurations, efficient/reliable aerodynamic design (optimization) can be achieved with the variable fidelity Kriging response surface approach.

Acknowledgements

References

[1] Watanabe, S., Kuchi-ishi, S., Murakami, K., Hashimoto, A., Kato, H., Yamashita, T., Yasue, K., Imagawa, K., and Nakakita, K., "Development Status of a Prototype System for EFD/CFD Integration," Proceedings of 47th International Symposium of Applied Aerodynamics, FP54-2012, Paris, 2012.

[2] Jones, D. R., Schonlau, M., and Welch, W. J., "Efficient Global Optimization of Expensive Black-Box Functions," *Journal of Global Optimization*, Vol.13, pp.455–492, 1998.

[3] Jeong, S., Murayama, M., and Yamamoto, K., "Efficient Optimization Design Method Using Kriging

Model," *Journal of Aircraft*, Vol.42, No.2, pp.413-420, 2005.

[4] Chung, H. S., and Alonso, J. J., "Using Gradients to Construct Cokriging Approximation Models for High-Dimensional Design Optimization Problems," AIAA Paper 2002–0317, 2002.

[5] Laurenceau, J., and Sagaut, P., "Building Efficient Response Surfaces of Aerodynamic Functions with Kriging and Cokriging," *AIAA Journal*, Vol.46, No.2, pp.498-507, 2008.

[6] Han, Z. H., Zimmermann, R., and Görtz, S., "A New Cokriging Method for Variable-Fidelity Surrogate Modeling of Aerodynamic Data," AIAA Paper 2010-1225, 2010.

[7] Yamazaki, W., and Mavriplis, D. J., "Derivative- Enhanced Variable Fidelity Surrogate Modeling for Aerodynamic Functions," AIAA Paper 2011-1172, 2011.

[8] Yamazaki, W., "Uncertainty Quantification via Variable Fidelity Kriging Model," *Journal of the Japan Society for Aeronautical and Space Sciences*, Vol.60, No.2, pp.80-88, 2012. (in Japanese)

[9] Kennedy, M. C., and O'Hagan, A., "Predicting the Output from a Complex Computer Code when Fast Approximations are Available," *Biometrika*, Vol.87, No.1, pp.1-13, 2000.

[10] Reisenthel, P. H., Love, J. F., Lesieutre, D. J., and Dillenius, M. F. E., "Innovative Fusion of Experiment and Analysis for Missile Design and Flight Simulation," Proceedings of Innovative Missile Systems, Neuilly-sur-Seine, pp.23/1-18, 2006.

[11] Alexandrov, N. M., Lewis, R. M., Gumbert, C. R. Green, L. L., and Newman, P. A., "Approximation and Model Management in Aerodynamic Optimization with Variable-Fidelity Models," *Journal of Aircraft*, Vol.38, No.6, pp.1093-1101, 2001.

[12] Laflin, K. R., Vassberg, J. C., Wahls, R. A., Morrison, J. H., Brodersen, O., Rakowitz, M., Tinoco, E. N., and Godard, J., "Summary of Data from the Second AIAA CFD Drag Prediction Workshop," AIAA Paper 2004-0555, 2004.

[13] Hashimoto, A., Murakami, K., Aoyama, T., Ishiko, K., "Toward the Fastest Unstructured CFD Code 'FaSTAR'," AIAA Paper 2012-1075, 2012.

[14] Hashimoto, A., "Validation of Fully Automatic Grid Generation Method on Aircraft Drag Prediction," AIAA Paper 2010-4669, 2010.

A Study on the Performance of the Fluidic Thrust Vector Control Utilizing Supersonic Coanda Effects

MyungJun Song[1], SangHun Yoon[1], HongBeen Chang[1, 2], YongHo Cho[3], Yeol Lee[4]

1. Graduate School, Department of Aerospace & Mechanical Engineering, Korea Aerospace University
   Goyang-Si, 412-791
   Korea
   mjsong@kau.ac.kr, shyoon@kau.ac.kr
2. Agency for Defense Development
   Taejon, 305-600
   Korea
   humanchb@korea.com
3. Microfriend Inc.
   Seoul, 139-240
   Korea
   yhcho@microfriend.co.kr
4. School of Aerospace & Mechanical Engineering, Korea Aerospace University
   Goyang-Si, 412-791
   Korea
   ylee@kau.ac.kr, Corresponding author

Abstract

Co-flow fluidic thrust vector control is one of the efficient thrust-vectoring methods. The present technique controls the direction of a supersonic primary jet by utilizing coanda effects of the secondary jet exhausted at the nozzle exit. A multi-component force measurement system is developed to quantitatively evaluate the performance of the fluidic thrust control technique. Detailed calibration and data analysis have been performed to reduce measurement errors. It is found that the interaction error between load cells possibly introduced by misalignment of the test device is estimated to be less than 5%, and that the unwanted pressure errors associated with air supply tubes are negligible. Some preliminary thrust-vectoring test results and comparison with the results of flow visualization/numerical calculation are also provided. It is observed that the deflection angle the primary jet varies almost linearly with variation of the momentum ratio of the primary jet to the secondary coanda jet.

Key words: supersonic, thrust vector control, coanda effects, calibration

1. Introduction

There has been a strong demand to improve the capability of thrust vector control in supersonic rectangular nozzles in Unmanned Aerial Vehicles. A previous study showed that Fluidic Thrust Vector Control (FTVC) methods can improve the thrust capacity per engine weight by 7-12% and the operating costs by 37-53%[1], with additional advantages in nozzle cooling performances and fast response time in control[2, 3], as compared to other conventional (mechanical) control methods. Of the various FTVC methods[4-6] that have been studied to date, the method to utilize the coanda effect of the secondary flow injected at the nozzle exit becomes a

subject of interests. Some previous studies[6-8] demonstrated that the thrust vectoring technique utilizing the coanda effect works fine to deflect the primary jet's direction to some extents.

Those results, however, has been limited to control only yaw[7] in relatively low-speed subsonic regions[6]. Recent experimental[8] and numerical[9] studies also have limitations in assessing the quantitative performance-characteristics of the control technique. Therefore there is a strong need for a quantitative and accurate measurement of the performance of the co-flowing fluidic thrust vectoring control. Previous research[10-13] have shown that thrust-vectoring measurements could be substantially affected by the interaction between load cells in the test device and by the high pressure air supply lines, which requires detailed calibration and data analysis process to increase the accuracy and repeatability of the test device.

In the present work, a multi-component force measurement system using four load cells is developed to quantitatively evaluate the performance-characteristics of the thrust control technique in supersonic regime (Mach 2.0). Detailed calibration and data analysis have been performed to reduce measurement errors. An independent calibration load was used to evaluate the errors associated with to the unwanted interaction between load cells, and the additional errors caused by high-pressure air supply tubes is quantitatively evaluated for various combinations of the chamber pressures. Comparisons of the axial thrust calculated by 1-D theory with the thrust measured by the present device are also carried out to confirm the accuracy of the test device. Finally, some preliminary thrust-vectoring test results obtained by the present device are also carried out. Detailed comparisons with previous results obtained by the flow visualization and the numerical method are provided.

2. Experimental Method

2.1 Rectangular nozzle for thrust vector control

This section describes the FTVC nozzle rig developed in the present study. The schematic of the test facility layout is shown in Fig. 1. The primary and secondary high-pressure airs are supplied from an air storage tank (25atm, 3m^3). The primary chamber pressure is controlled by an electronic pressure controller (TESCOM, ER 3000SI-1), capable to maintain the constant pressure within 3% of the target values during tests.

Figure 2 shows the detailed configuration of the nozzle. The design Mach number of the two-dimensional primary nozzle flow is 2.0, and the exit Mach number of the converging secondary nozzle is 1.0. The nozzle width is 40mm, and the aspect ratio of the exit plane of the primary nozzle is 4:1. The nozzle block is designed to vary the height of the secondary nozzle (s) by movement of the flap assembly. The radius of curvature (R) of the coanda flap is also changeable to cover wide range of test cases of s/R that is possibly one of critical parameters of the present thrust-vectoring performances.
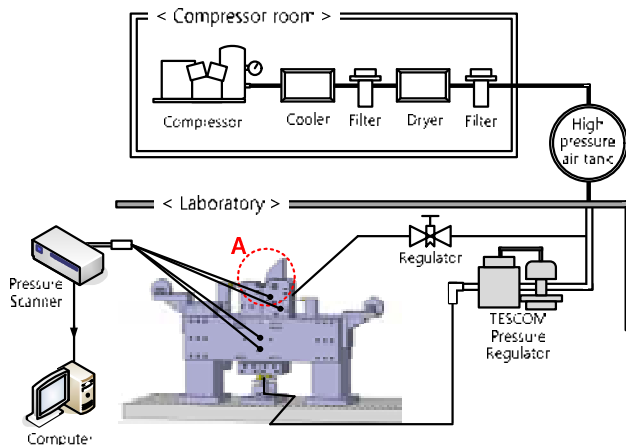
Figure 1. Layout of the present experimental set up
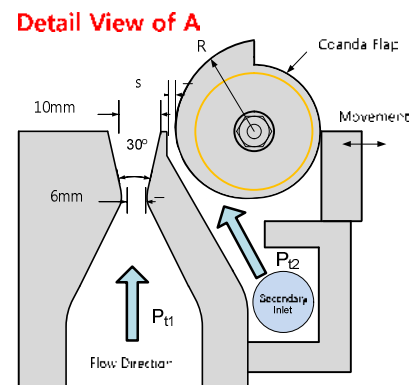
Figure 2. Schematic of the nozzle part

2.2 Design of multi-component force measurement device

The present test device is designed as vertical type that allows high accuracy measurement of normal force, and the schematic diagram of the test device is shown in Fig. 3. The test device consists of four load cells. Beam type load cell①, ②(CAS, BCA) at the side of the nozzle block measures the side force of thrust (pitch), and those are installed vertically to secure space for calibration. S type load cell③, ④(CAS, SBA) are installed at the bottom in the symmetry of the XY plane (the center plane of the primary nozzle) (see Fig. 3). Load cell③, ④ are connected in electronically parallel to be considered as one load cell. Since the interactions between the load cells due to misalignment of the device parts are main source of error in the test results[13], a right-angle ruler(RSK, squareness ±0.07mm) and laser level(±1mm/10m) are used to confirm if the test device is assembled in perfect orthogonal pattern.

Figure 4 shows the detailed configuration of thrust and force components in the FTVC assembly, where the x-axis is defined as the center line of the primary nozzle. A position of the weight attached to the side of the nozzle block is adjusted to control the center of gravity of the assembly, and thus tare load transmitted to load cell①, ② is eliminated by it. By the adjustment of the weight, the relations between thrust and component force can be simply derived as;

$$T_x = F_3 + F_4 = F_5$$
$$T_z = F_1 - F_2$$
(1)

where F_i indicates the components of force applied to each load cell ①.
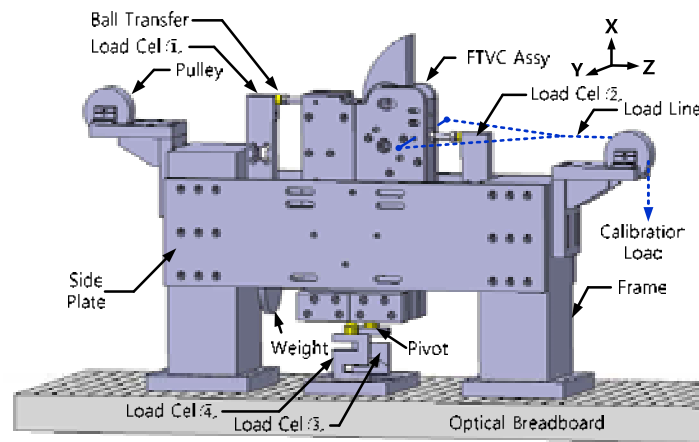
Figure 3. Layout of the force measurement device setup
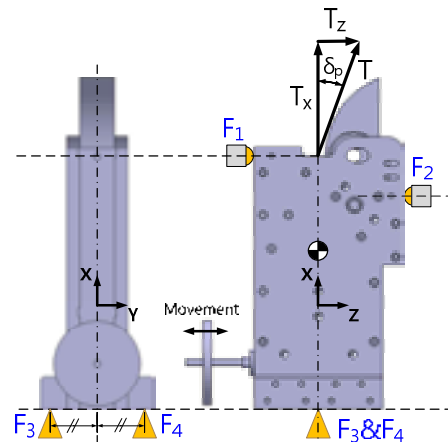
Figure 4. Configuration of thrust and force components

2.3 Data acquisition

Bridge-circuit module (NI 9237) is used to measure the signals of load cells. 10k of signal data from each load cells are acquired during 10 seconds and averaged for data analysis. The calibration weights are also weighed by a high precision electronic balance (CAS, MW-2N). Noises of the each load cell signals are also checked and it is shown that the intensity of noise-to-signal ratio is less than 1% when a load of 10kgf is applied. It is confirmed that the acquisition of each load cell signals is satisfactory and stable.

2.4 Calibration of the test device

2.4.1 Calibration of the interaction errors

Static calibrations were performed to obtain the coefficient matrix (refer the equation (2)), to account for the interaction between load cells. Independent separated calibration loads (L_1, L_2, L_5) are applied on the same axle of each load cells, as illustrated in Fig. 5. The calibration loads (L_1, L_2) are applied to calibrate load cell①, ② via an external pulley system (see Fig. 3). A physically separated calibration device is used to apply vertical calibration load (L_5) to load cell⑤.
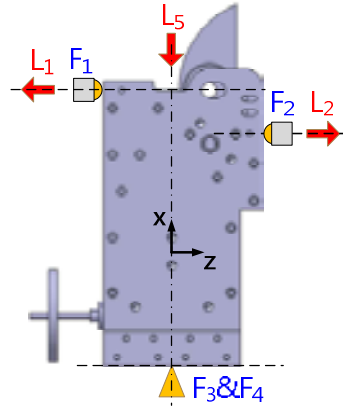
Figure 5. Schematic of the location of the calibration loads

The linear relation between the load cell signals and the actual forces is expressed as,

$$\begin{bmatrix} C_{1,1} & C_{1,2} & C_{1,5} \\ C_{2,1} & C_{2,2} & C_{2,5} \\ C_{5,1} & C_{5,2} & C_{5,5} \end{bmatrix} \begin{bmatrix} L_1 \\ L_2 \\ L_5 \end{bmatrix} = \begin{bmatrix} V_1 \\ V_2 \\ V_5 \end{bmatrix} \tag{2}$$

where matrix [C] is defined as the calibration coefficient matrix, calculated by the linear least square regression method. The subscript i in $C_{i,j}$ indicates locations of the load cell, and the subscript j indicates the locations of the calibration load. L_j is the applied calibration load and V_i is the load cell signals. Element of the calibration coefficient matrix [C] represents the weighting factor of calibration load(L_j) affecting the intensity of the load cell signal(V_i).

Evaluations of the interaction errors between load cells are performed 4 times after four re-assembles of the nozzle block. The range of calibration loads applied to each load cells has the maximum of 300N to cover the expected range of loads in actual test conditions. Four calibration data sets (Calib1~4) are obtained by getting the signals of all load cells for only one known calibration load (L_1, L_2, L_5, each) applied independently.

In the present study, the error of element of component force is defined as,

$$Error_{i,p} = \frac{L_{i,p} - L_{i,p}^*}{L_{i,p}} \times 100\% \tag{3}$$

where $L_{i,p}$ is the applied calibration load and $L_{i,p}^*$ is the calculated force using the load cell signal. The subscript i here indicates the location of the calibration load. The maximum errors of each component force(F_i) assessed by the equation (3) are shown in Table 1. It is shown that error of the load cell⑤ is less than approximately 0.3% for all conditions, proving that the accuracy of load cell⑤ is exceedingly good. The maximum error of the load cell①, ②, that is most critical in measurement of the pitch, is approximately 5% against the calibration load of 10N, showing that the good accuracy of the present test device for most loading conditions. Standard deviations and the repeatability of each elements of the coefficient matrix are also proved as small as less than 1%. For all calibration loading conditions, the interaction coefficients (off-diagonal term of the matrix [C]) were less than 1% of the direct coefficients (diagonal term of the matrix [C]). From the present detailed error analysis, it is conclude that the test device developed in the study is far better in measurement accuracy as compared to the test device presented in the previous research[12].

Table 1. Maximum error of the calibration loads

Error$_{max}$	F1	F2	F5
Calib 1	1.2%	5.3%	0.3%
Calib 2	0.9%	1.2%	0.3%
Calib 3	3.3%	2.1%	0.1%
Calib 4	1.9%	1.5%	0.1%

2.4.2 Calibration of errors of pressure loads

High-pressure air supply tubes are pressurized during the performance tests, and the unwanted forces transmitted to load cells can introduce substantial errors. In the present study, flexible tubes are used to minimize those pressure loads and the axis of the supply line is anchored to remain in right-angle to the direction of thrust[13]. The pressure load is also simulated by blocking air flow in the stagnation chamber as shown in Fig. 6. A spreader installed to stabilize the primary flow is replaced as a blocking plate as shown in Fig. 6-(a), and the secondary flow is blocked by a long cap, as illustrated in Fig. 6-(b).

(a) blocking the primary flow   (b) blocking the secondary flow
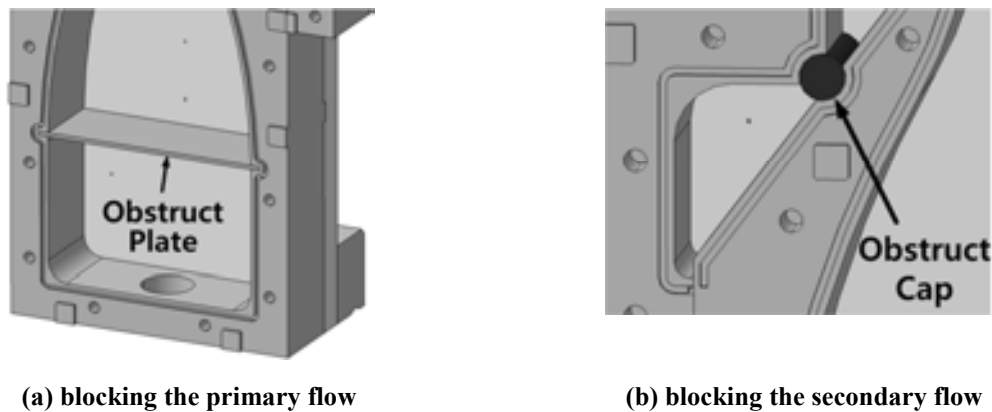
Figure 6. The method to block the primary/secondary flows

The range of applied pressures with the blocking plate installed covers up to 780kPa for the primary nozzle (about 780kPa) and up to 400kPa for the secondary nozzle. Each chamber is independently pressurized for various pressure conditions, and the measured component forces for each pressure loads are shown in Table 2. In the table, it is obvious that the component forces measured by the load cells are less than 1N, which is almost negligible. Since two chambers are pressurized at the same time in actual tests, the load cell signals are also observed for the cases that two chambers are all pressurized simultaneously in various pressure combinations. Similar results are observed such that the component forces measured by the load cells are less than 1N. Finally, it is proved that the magnitude of the error associated with the supplied air tubes is negligible, considering the range of expected axial/side thrusts in actual tests.

Table 2. Results of measured pressure loads introduced by air supply tubes

Primary nozzle blocked				Secondary nozzle blocked			
Pressure (kPa)	Load (N)			Pressure (kPa)	Load (N)		
P_{t1}	F1	F2	F5	P_{t2}	F1	F2	F5
400	-0.12	0.04	0.43	200	-0.08	0.05	0.17
600	0.35	0.04	0.58	300	-0.17	0.05	0.08
700	0.47	0.05	0.71	400	0.14	0.05	0.00
800	0.48	0.04	0.89				

3. Results and Discussion

3.1 Flow visualizations and numerical results

In Fig. 7 the results from flow visualization (shadowgraph) shows the characteristics of the supersonic primary jet associated with coanda effects of the secondary jet exhausted at the nozzle exit. The deflection angle (δ_p) measured by the present test device is also depicted in the figure. Figure 7 suggests that flow visualization results are qualitatively good to observe the deflection angle of the primary jet. It is also noticed that the deflection angle of the primary jet is influenced by s/R, however, further detailed study is required to evaluate the effects of the slot height of the secondary jet (s) and the radius of curvature of the coanda flap (R) independently.

(a) s/R=0.025	(b) s/R=0.02	(c) s/R=0.01
(s=1mm, R=40mm)	(s=2mm, R=100mm)	(s=2mm, R=200mm)
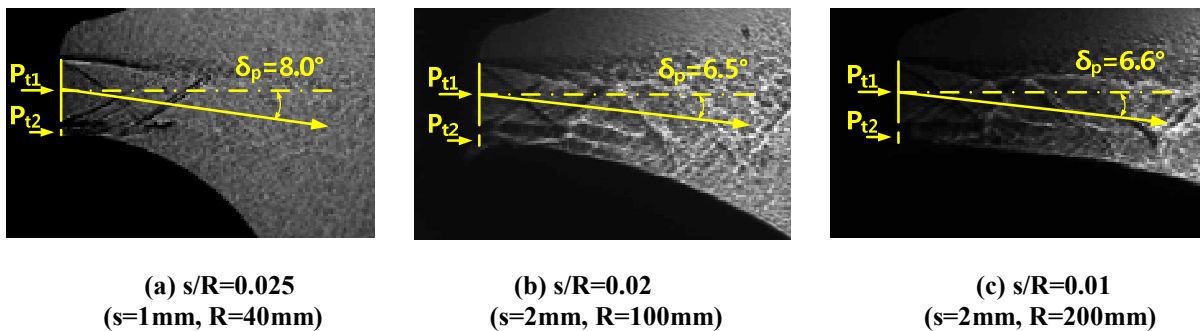
Figure 7. Flow visualization of supersonic coanda flows (shadowgraph, P_{t1}=500kPa, P_{t2}=300kPa)

Flow visualization and numerical results are also compared as shown in Fig. 8. The present numerical results showing the variation of density gradients in the flow fields reveals a good agreement with the flow visualization results.

(a) P_{t1}=300kPa, P_{t2}=200kPa

(b) P_{t1}=400kPa, P_{t2}=200kPa
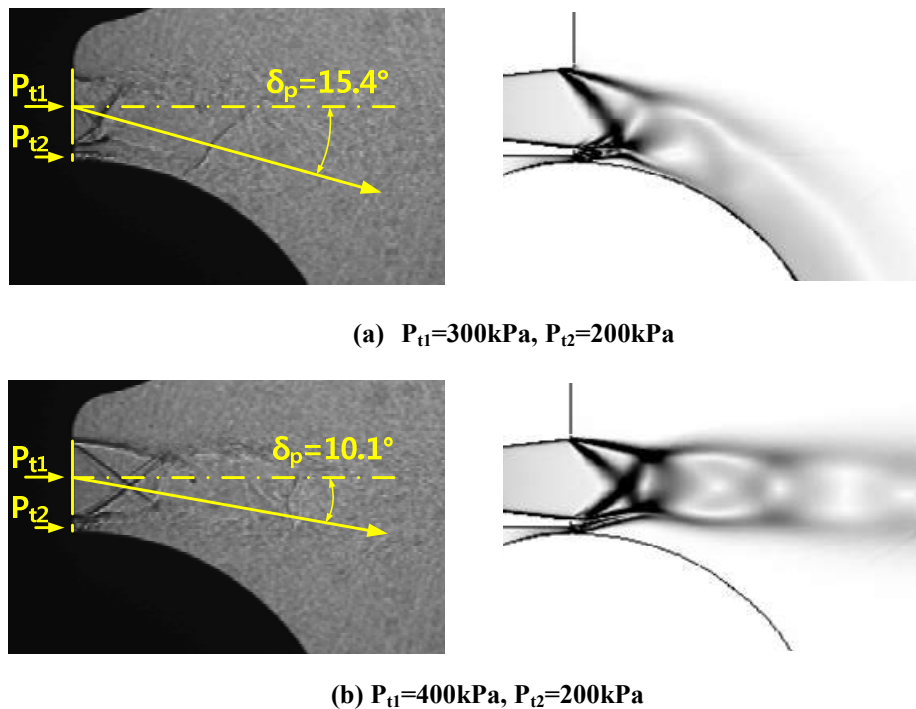
Figure 8. Thrust vectoring angles of FTVC nozzle(s/R=0.025)

3.2 Comparison with the 1-D theoretical thrust

The accuracy of the present test device is validated again by comparing the measured thrust of the primary nozzle with the calculated thrust using 1-D theory of the compressible flows. In the process, the nozzle divergence coefficient[14] is introduced to account for the effects of divergence of the nozzle. Comparison of the un-vectored (axial) thrust measured in over-expanded conditions with 1-D theoretical is shown in Table 3. In the tale, it is confirmed that the measured values agrees well within 5% with calculated theoretical values, demonstrating the present test device has good measurement accuracy.

Table 3. Comparison of the measured and the theoretical thrusts

Primary chamber pressure (kPa)	Load (N)		Error (%)
	1-D calculation	Present measured (F5)	
296	58.12	61.032	5.010896926
383	86.97	87.023	0.066265971
		87.564	0.688363955
		87.274	0.354038557
		88.750	2.052123788
497	124.76	126.709	1.558579023
		125.615	0.682492808
		124.427	-0.270267003
591	155.93	155.528	-0.260286729

3.3 Deflection angles for various momentum ratios

Thrust vectoring angles of the primary jet are presented in Fig. 9 for various momentum ratios of the primary to the secondary coanda jet. Here the momentum ratio is defined as,

$$\text{Momentum Ratio} \equiv \frac{mV_{e2}}{mV_{e1}} = \frac{\gamma P_{0,2} A_{e,2}\left(1+\frac{\gamma-1}{2}\right)^{\frac{\gamma}{1-\gamma}}}{\gamma P_{0,1} A_{e,1} M_e^2 \left(1+\frac{\gamma-1}{2}M_e^2\right)^{\frac{\gamma}{1-\gamma}}} \tag{4}$$

where γ is the specific heat ratio of air, M_e is the Mach number of primary flow at the exit plane(M_e=2.0 in the present study), and $A_{e,1}$, $A_{e,2}$ are the exit area of the primary nozzle and the secondary nozzle, respectively. In Fig. 9 it is shown that the thrust angle increases almost linearly as the momentum ratio increases for s/R=0.025 flap (see Fig. 9-(a)). Similar tests for different value of s/R=0.02 also shows the linear relation, as shown in Fig. 9-(b). For the same momentum ratio, the lower secondary pressures result in larger deflection angles, and thus it is presumed that the coanda effect in under-expanded secondary jet is not that strong.

(a) s/R=0.025 (s=1mm, R=40mm)   (b) s/R=0.02 (s=2mm, R=100mm)
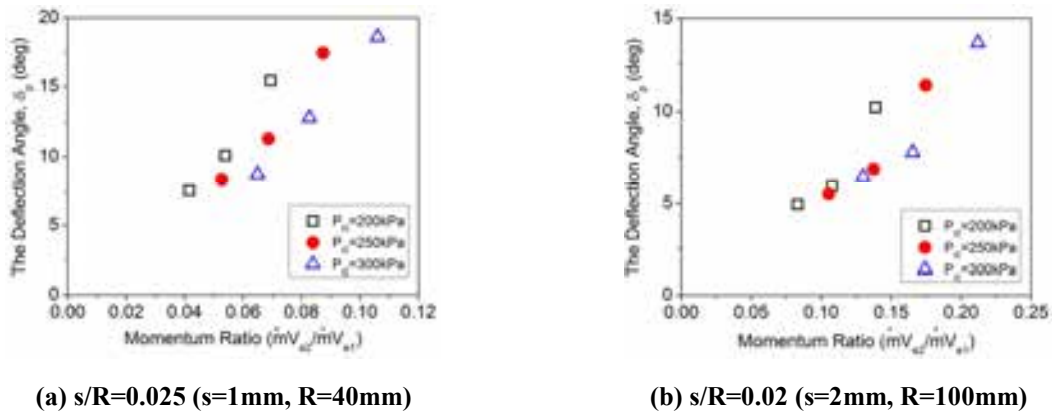
Figure 9. Thrust vectoring angles of FTVC nozzle

Detailed performances of the coanda nozzle are observed for various pressures and combinations of the secondary nozzle height (s) and the radius of curvature of coanda flap (R), and its results are summarized in Fig. 10. In the figure, it is observed that the deflection angle is decreased as the pressure ratio (P_{t2}/P_{t1}) increases and that the deflection angle for the maximum value of s/R (=0.025) is relatively larger as compared to the other cases. However, any specific consistent pattern in the variation of the deflection angle with s/R is not found.
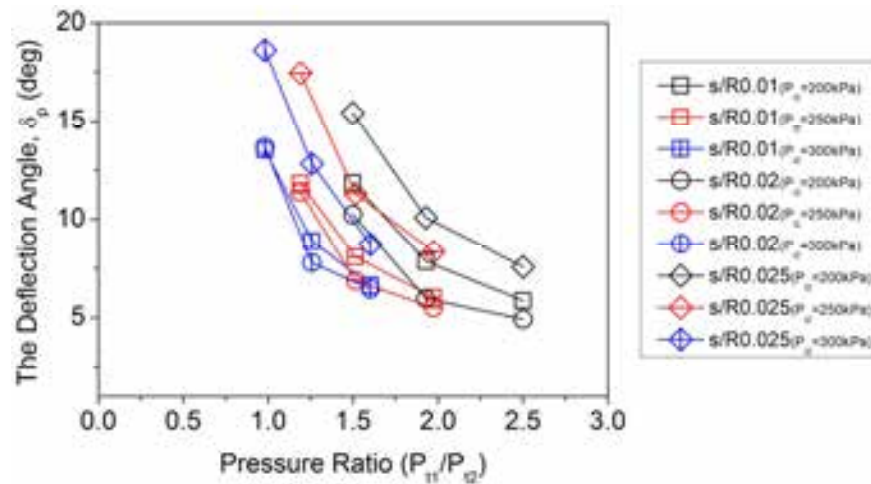
Figure 10. Thrust vectoring angles for various pressure ratios

It is obvious that the ratio of s/R is one of the influencing parameters in the performance of the coanda nozzle, but it is presumed that s/R is not only one sufficient parameter to reflect the performance of the fluidic thrust vector control. Even the decrease of s/R qualitatively weakens the performance of the primary jet's deflection, further detailed study is required to evaluate the effects of the slot height of the secondary jet and the radius of curvature of the coanda flap independently.

4. Conclusions

A multi component force test device is developed to measure the accurate and quantitative performance of the supersonic coanda nozzle. Detailed calibration and data analysis regarding the measurement accuracy of the test device reveals that the maximum measurement error of the device is less than about 5%, which shows the good accuracy and precision of the present measurement system. Unwanted pressure loads from pressurized air tubes are found to be less than 1N and thus the error associated with the air supply tubes are negligible. It is also noticed that the measured thrust values are close to the theoretical values within 5%.

Flow visualizations and numerical calculations are also carried out, and those results are compared to preliminary thrust-vectoring test results. It is shown that the flow visualization results are qualitatively good to observe the deflection angle of the primary jet, and that the results from numerical calculations are in fairly good consistency with the estimation by flow visualization.

Preliminary thrust-vectoring tests show that the variation of deflection angles of the primary jet increases almost linearly as the momentum ratio increases. It is also noticed that the decrease of s/R weakens the performance of the primary jet's deflection; however, further detailed study is required to evaluate the effects of the slot height of the secondary jet and the radius of curvature of the coanda flap independently.

Acknowledgments

References

[1] K. A. Deere: Summary of Fluidic Thrust Vectoring Research Conducted at NASA Langley Research Center. AIAA 2003-3800, 2003.

[2] C. Chiarelli, R. K. Johnsen, C. F. Shieh, D. J. Wing: Fluidic Scale Model Multi-plane Thrust Vector Control Test Results. AIAA 93-2433, 1993

[3] I. E. Diaz-Guardamino: Combining Suction Control and Transverse Jets for Fluidic Thrust Vector Control. *ProQuest*, 2008.

[4] D. J. Wing: Static Investigation of Two Fluidic Thrust-Vectoring Concepts on a Two-Dimensional Convergent Divergent Nozzle. *NASA Technical Memorandum 4574*, 1994.

[5] J. D. Flamm: Experimental Study of a Nozzle Using Fluidic Counterflow for Thrust Vectoring. AIAA 98-3255, 1998.

[6] M. S. Mason, W. J. Crowther: Fluidic Thrust Vectoring for Low Observable Air Vehicle. AIAA 2004-2210, 2004.

[7] F. Saghafi, A. Banazadeh: Coflow Fluidic Thrust Vectoring Requirements for Longitudinal and Lateral Trim Purpose. AIAA 2006-4980, 2006.

[8] S. H. Yoon, D. H. Jun, J. Y. Heo, H. G. Sung, Y. Lee: Experimental Study of Thrust Vectoring of Supersonic Jet Using Co-flowing Coanda Effects, *Journal of The Korean Society Aeronautical and Space Sciences*, Vol. 40, 2012 (to be published).

[9] S. H. Yoon, D. H. Jun, M.J. Song, Y. H. Cho, Y. Lee: Numerical Investigations on the Performance-Improvement of Fluidic Thrust Vector Controls, Proceeding of the KSME 2011 Spring Annual Meeting, 2011.

[10] A. J. Neely, F. N. Gesto, J. Young: Performance Studies of Shock Vector Control Fluidic Thrust Vectoring. AIAA 2007-5086, 2007.

[11] K. J. Lee, I. S. Park, Y. K. Choi: Design Method of the High Accuracy Thrust Stand. *Journal of the Korean Society of Propulsion Engineers*, Vol. 10, No. 1, pp.9~17, 2006.

[12] M. A. Ramaswamy, F. S. Alvi, A. Krothapalli: Special 6-Component Jet Rig Balance for Studying New Thrust Vectoring Concetps. Record International Congress on Instrumentation in Aerospace Simulation Facilities, pp.202~213, 1997.

[13] R. B. Runyan, J. P. Rynd, Jr., J. F. Seely: Thrust Stand Design. AIAA 92-3946, 1992.

[14] J. J. Berton: Divergence Thrust Loss Calculations for Convergent-Divergent Nozzles: Extensions to the Classical Case. *NASA Technical Memorandum 105176*, 1991.

[15] J. D. Flamm, K. A. Deere, M. L. Mason, B. L. Berrier, S. K. Johnson: Design Enhancements of the Two-Dimensional, Dual Throat Fluidic Thrust Vectoring Nozzle Concept. AIAA 2006-3701, 2006.

Measurements of Counter Flow Region in Averaged Wake-Velocity-Field of a Small Straight-Bladed Vertical Axis Wind Turbine

Yutaka Hara[1]
Takahiro Suzuki[1]
Hirofumi Kamon[2]

[1]Department of Mechanical and Aerospace Engineering, Graduate School of Engineering
 Tottori University
 Koyama-cho, Tottori 680-8552
 Japan
 hara@damp.tottori-u.ac.jp

[2]Department of Applied Mathematics and Physics, Faculty of Engineering
 Tottori University

Abstract

To determine the three-dimensional flow field around vertical axis wind turbines (VAWTs), an ultrasonic anemometer was used to measure the three components of flow velocity in the wake of a small VAWT (4-blade rotor; airfoil: NACA 0012; rotor diameter: 0.6 m; blade length: 0.47 m; chord length: 0.075 m). Counterflow in the direction of the mainstream was observed even in the averaged wake-flow field. For a more detailed investigation of the counterflow regions, the three-dimensional flow field was reconstructed through computation from the velocity data obtained at each measurement point and was analyzed by means of velocity vector maps, vorticity distributions, and path lines. A clear swirl pattern in two-dimensional path lines was observed near the counterflow region on the equatorial plane in the wake; however, the vorticity of the swirl pattern part was weak.

Key words: wind turbine, wake, VAWT, counterflow

Introduction

Research and development of various types of vertical axis wind turbines (VAWTs) has been conducted, focusing on the characteristic of being unaffected wind direction variations. Although calculations based on blade element momentum (BEM) theory [1-3] are generally useful for designing and evaluating the performance of wind turbines, in the case of small and micro wind turbines, the lack of high-precision aerodynamic data at low Reynolds number [4], the dynamic stall effect [1], and other factors have a large impact that makes it difficult to model experimental values with high precision. Gaining a three-dimensional understanding of the flow field around a wind turbine is considered important for improving the precision of BEM calculation of small VAWTs. An ultrasonic anemometer has previously been used to measure a particular cross section of VAWT wake, and these measurements have indicated the existence of a counterflow region in the averaged flow field [5-7].

In this research, velocity measurements were performed in many more cross sections, in addition to the particular cross section that was previously measured, in order to understand the details of the VAWT wake that produces the counterflow region. The three-dimensional averaged flow field was reconstructed by merging the obtained velocity data through computation. Details of the averaged flow field in the vicinity of the counterflow region observed in the VAWT wake were clarified by rendering information such as velocity vector maps, vorticity distribution, and flow paths of arbitrary cross sections of the obtained averaged flow field to analyze the flow from various perspectives.

Nomenclature

c: Blade chord length (m)
C_p: Power coefficient (Eq. (1))
C_q: Torque coefficient (Eq. (2))
D: Rotor diameter (m)
H: Rotor height (blade span length) (m)
N: Rotation speed (min^{-1})
P: Power (W)
Q: Torque (Nm)
R: Rotor radius (m)
Re_b: Blade Reynolds number ($V_{rel}\, c\, /\, \nu$)
U, V, W: Velocity components (m s^{-1})
U_0: Upstream uniform velocity (m s^{-1})
V_{rel}: Relative velocity (m s^{-1})
X, Y, Z: Position coordinates (m)
λ: Tip-speed ratio ($R\omega/U_0$)
ν: Coefficient of kinematic viscosity (m^2 s^{-1})
ρ: Air density (kg m^{-3})
ω: Angular velocity (rad s^{-1})

Experimental Apparatus and Methods

Figure 1 shows a schematic diagram of the experimental apparatus, and Fig. 2 shows a photograph of the experimental wind turbine as viewed from the downstream side. A straight-bladed vertical axis wind turbine employing the NACA 0012 airfoil (c = 0.075 m) was used in this research. The number of blades was 4, the rotor diameter was D = 0.6 m, and the rotor height was H = 0.47 m. The wind turbine rotation axis was located at a position 1.5 m downstream from the wind tunnel nozzle (1.5 × 1.5 m). The rotor was connected to an induction motor via a torque detector, and was made to rotate at a particular fixed rotation speed by an inverter. An ultrasonic anemometer was used for measurements. The coordinate system and range of measurements are shown in Fig. 3. Constant velocities of 5 and 10 m s^{-1} were generated in the wind tunnel, and the three velocity components (U, V, and W) were measured at 10 cross sections perpendicular to the main flow at positions in the range of 0.6 m $\leq X \leq$ 1.5 m downstream from the rotor center. The range of measurements in the direction perpendicular to the main flow was -0.6 m $\leq Y \leq$ 0.6 m and -0.5 m $\leq Z \leq$ 0.6 m, and the measurement points were spaced at intervals of 0.1 m along each of the Y axis and Z axis directions. The sampling frequency of the ultrasonic anemometer was 32 Hz, with approximately 1240 pieces of data (duration of approximately 40 s) acquired at each measurement point.
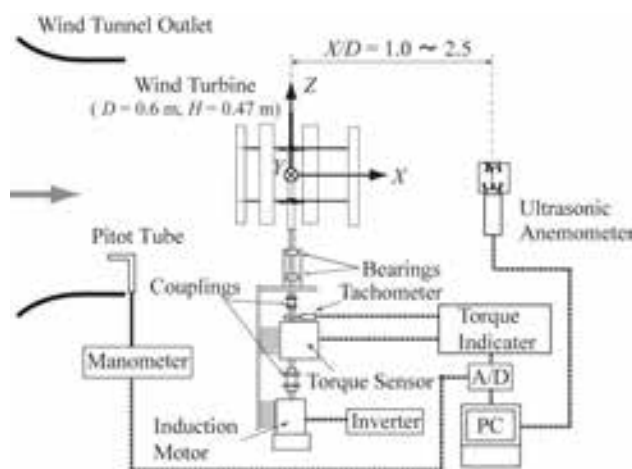
Fig. 1 Schematic of experimental system

Fig. 2 Photograph of experimental apparatus
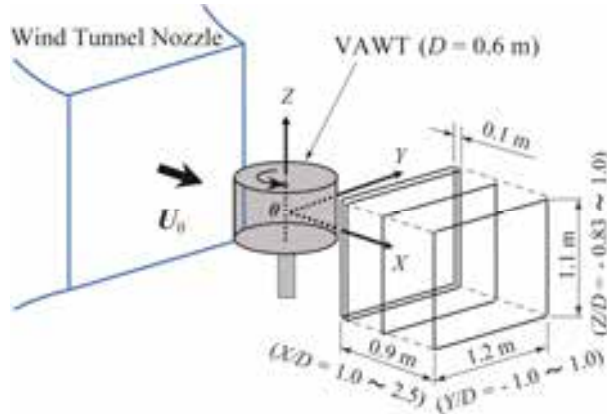
Fig. 3 Coordinate system and measurement domain
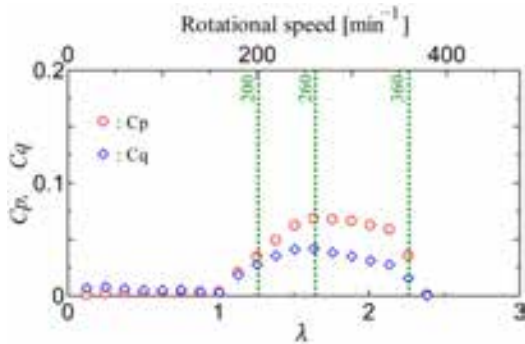
Fig. 4 Power and torque characteristics of experimental VAWT at $U_0 = 5$ m s^{-1}	Fig. 5 Power and torque characteristics of experimental VAWT at $U_0 = 10$ m s^{-1}
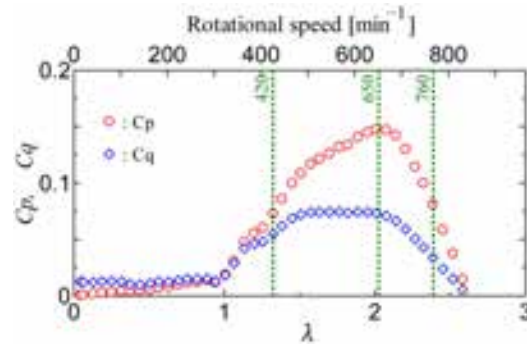
Figures 4 and 5 show the power coefficient (C_p) and torque coefficient (C_q) versus the tip-speed ratio (λ) at each of the wind velocities of 5 and 10 m s^{-1} at which the VAWT was evaluated in this research. The equations defining the power coefficient and torque coefficient are shown in Eqs. (1) and (2), where P is the wind turbine power, Q is the torque, and ρ is the air density.

$$C_p = \frac{P}{0.5\rho U_0^3 (DH)} \tag{1}$$

$$C_q = \frac{Q}{0.5\rho U_0^2 (DH)R} \tag{2}$$

Experiments were conducted under three conditions: the condition where the rotation speed equals the maximum efficiency point of the wind turbine; a low rotation speed condition where the power is 50% of the maximum efficiency point; and a high rotation speed condition. More specifically, for $U_o = 5$ m s^{-1}, the rotation speeds were 200, 260, and 360 min^{-1}, and for $U_o = 10$ m s^{-1}, the rotation speeds were 420, 650, and 760 min^{-1}. The Reynolds number of the blade based on the blade chord length Re_b at the maximum efficiency point is approximately 4×10^4 at $U_o = 5$ m s^{-1} and approximately 1×10^5 at $U_o = 10$ m s^{-1}.

Experimental Results and Discussion

Figure 6 shows the distribution of the U velocity component at the equatorial plane ($Z/D = 0$) for the case of wind velocity $U_o = 10$ m s^{-1} and rotation speed $N = 650$ min^{-1}. The area of filled circles is the counterflow area. Figure 7 shows a three-dimensional volume rendering of the counterflow region in this same state. The white solid line in Fig. 7 indicates the measurement range. The wind turbine rotates in the counterclockwise direction when viewed from above. From Figs. 6 and 7, the counterflow region exists centered at a position shifted slightly above and on the right side of the center as viewed from the downstream side.
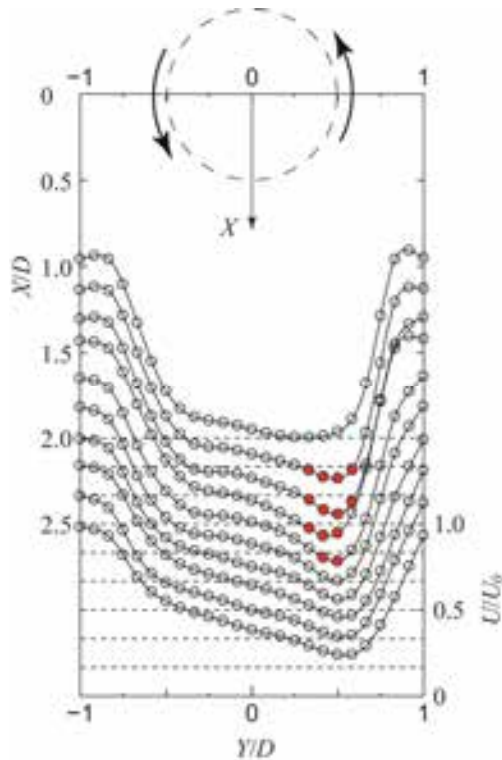
Fig. 6 Distributions of velocity component *U* on equatorial plane in wake ($U_0 = 10$ m s^{-1}, $N = 650$ min^{-1})
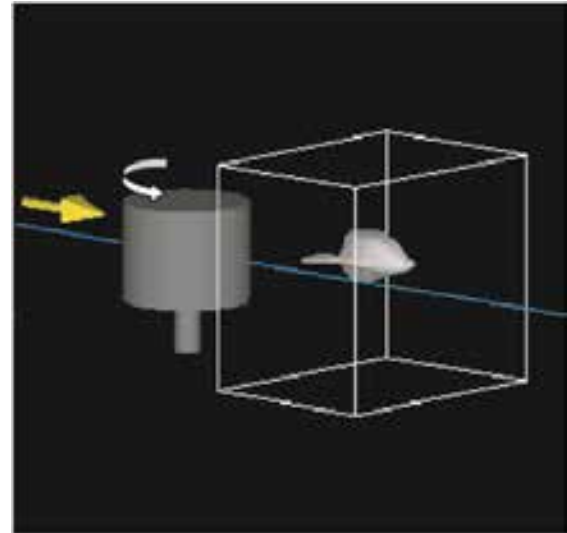
Fig. 7 Volume rendering of counterflow region ($U_0 = 10$ m s^{-1}, $N = 650$ min^{-1})

Figure 8 shows the distribution of the *U* velocity component versus rotor rotation speed in the *Y-Z* plane at the position $X/D = 1.5$ for the case of $U_0 = 10$ m s^{-1}. The dotted line in the figure shows the outline of the wind turbine and central support pillar. The blade near $Y/D = 0.5$ on the right side of the center in Fig. 8 is moving in the reverse direction to the main flow while the blade near $Y/D = -0.5$ on the left side of the center is moving in the same direction as the main flow. Although Fig. 8(c) shows that a counterflow region was observed in the wake region at the right edge of the rotor (near $Y/D = 0.5$), a counterflow region has also been observed in the wake region at the left edge of the rotor (near $Y/D = -0.4$) further upstream from $X/D = 1.17$ under the same rotation speed conditions [7]. Although Fig. 8 shows the case for the high wind velocity ($U_0 = 10$ m s^{-1}), since the wind velocity distribution patterns were the same at the low wind velocity ($U_0 = 5$ m s^{-1}), only the results for the high wind velocity are shown in this paper. Furthermore, we focus our discussion on the counterflow region in the maximum power state ($N = 650$ min^{-1}). The results presented subsequently are therefore all results for the averaged flow field in the $U_0 = 10$ m s^{-1} and $N = 650$ min^{-1} state.
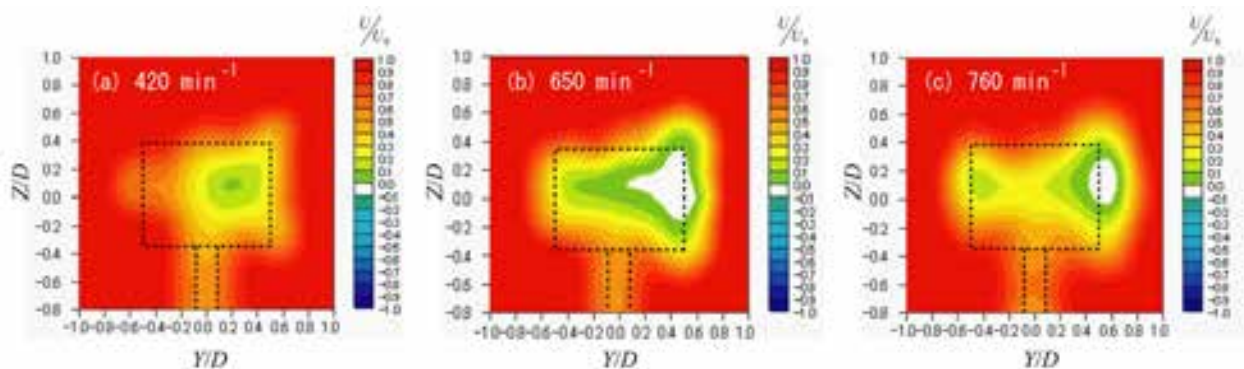
Fig. 8 Distributions of velocity component *U* on vertical plane of *X/D* = 1.5 ($U_0 = 10$ m s^{-1})
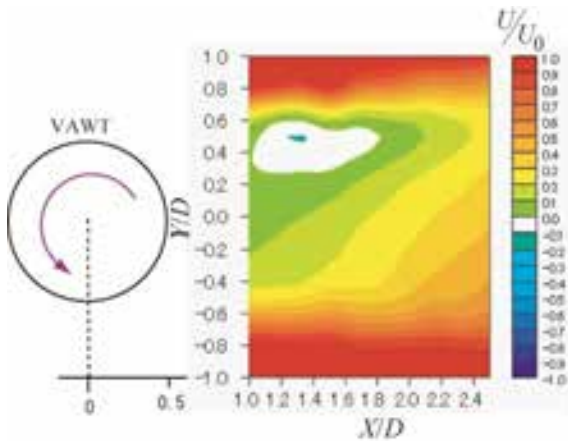
Fig. 9 Distribution of velocity component U on equatorial plane
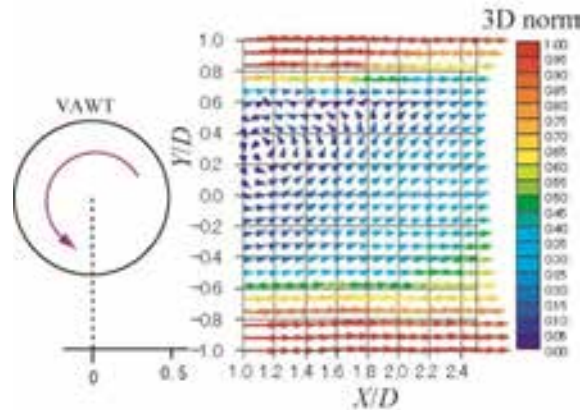
Fig. 10 Two-dimensional velocity vector map on equatorial plane
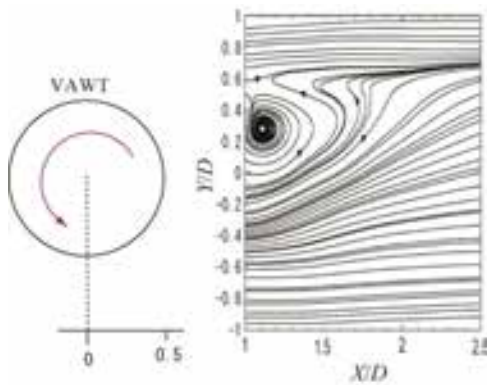
Fig. 11 Two-dimensional path lines on equatorial plane
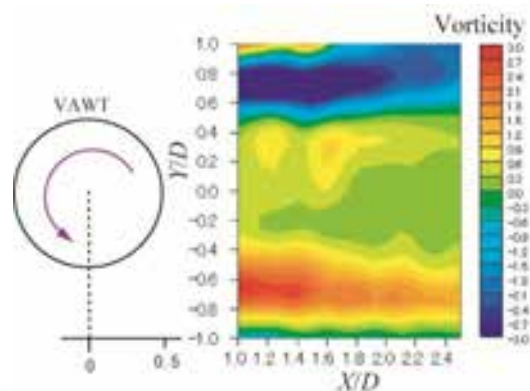
Fig. 12 Distribution of vorticity on equatorial plane

Figure 9 shows the distribution of the U velocity component at the equatorial plane ($Z/D = 0$) for the case of U_0 = 10 m s^{-1} using contour lines (i.e., a different representation of Fig. 6). The direction of the main flow is from left to right in the figure. According to Fig. 9, the region where counterflow exists in the equatorial plane gradually shrinks further downstream until it ceases to exist near $X/D = 1.8$.

Figures 10 to 12 show the two-dimensional velocity vector map (U, V), two-dimensional flow path lines, and vorticity distribution under the same conditions and at the same cross section as Fig. 9. Note that the color density of the vectors in Fig. 10 indicates the magnitude of the three-dimensional velocity vectors normalized by the main flow velocity in dimensionless units. A counterclockwise rotating vortex flow pattern (centered at X/D = 1.1, Y/D = 0.3) can be observed near the counterflow region in Figs. 10 to 12, and it is clear that the counterflow region in the U velocity component is generated by the drag into this vortex. However, as shown in the vorticity distribution in Fig. 12, the vorticity of the vortex pattern that is clearly observed in Fig. 11 does not exhibit a significantly higher value than the surroundings.

Figures 13 and 14 show the distribution of the U velocity component and the two-dimensional flow path lines in the X-Z vertical cross section at the position $Y/D = 0.5$. At this position, the counterflow region spreads out in the vertical direction (Z direction) and the flow path lines exhibit complex flow patterns. Although a pair of vertically aligned vortexes appears to exist by cursory inspection, the vorticity at the corresponding positions is not higher than in the surroundings (data not shown). From Fig. 14, the flow path lines coming from upstream in the counterflow region exhibit a flow pattern that diverts the counterflow region either upward or downward and that shrinks toward the equatorial plane direction from the periphery starting over halfway across the counterflow region.
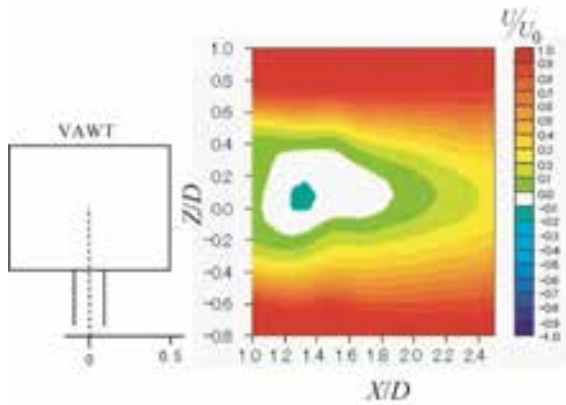
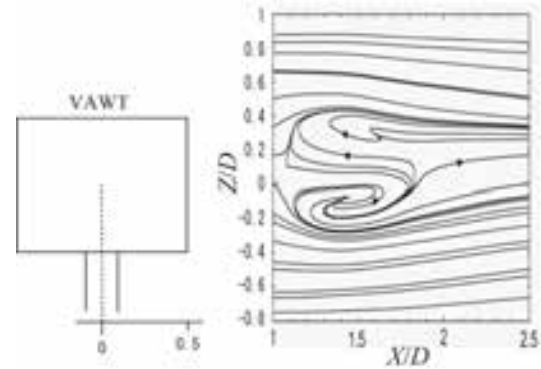**Fig. 13 Distribution of velocity component *U* on vertical plane of *Y/D* = 0.5**

Fig. 14 Two-dimensional path lines on vertical plane of *Y/D* = 0.5

Figure 15 shows the two-dimensional flow path lines in the *Y-Z* plane perpendicular to the main flow at position *X/D* = 1.33. From Fig. 15, relatively large secondary flows occur from the vertical direction toward the equatorial plane at the rotor center and on the left side as viewed from downstream, and a flow occurs from left to right near the equatorial plane. In the wake area of the rotor right edge (*Y/D* = 0.5), the flow path lines converge at two points above and below, showing that a complex flow field is formed.
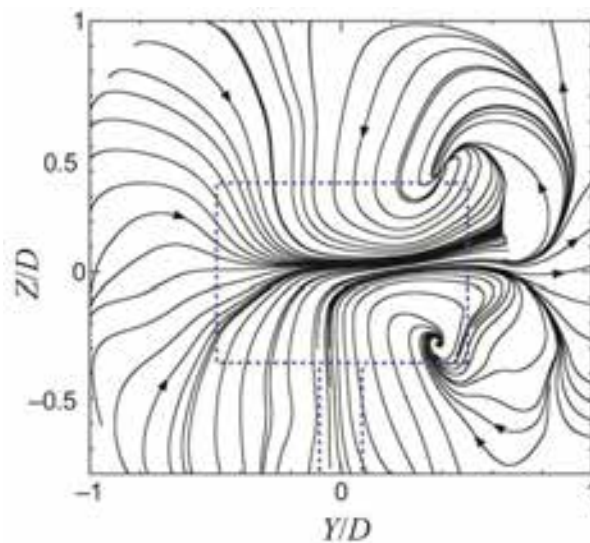
Fig. 15 Two-dimensional path lines on vertical plane of *X/D* = 1.33

As shown earlier, the averaged flow field exhibits an extremely complex flow state near the counterflow region, and the state of the flow field cannot be understood sufficiently well by examining only the flow patterns in two-dimensional cross sections in each direction. Calculations of the three-dimensional flow path lines of the average flow field were therefore performed taking several specific locations as the initial positions. An example of the results is shown in Fig. 16, which shows the trajectories of 6 test particles for which the initial positions were all on the equatorial plane (*Z/D* = 0) at *X/D* = 1 with *Y* coordinates *Y/D* = 0.4 for particle 1, *Y/D* = 0.25 for particle 2, *Y/D* = 0.1 for particle 3, *Y/D* = 0 for particle 4, *Y/D* = -0.25 for particle 5, and *Y/D* = -0.4 for particle 6. After starting, particle 1 first moved below the equatorial plane temporarily before returning to the vicinity of the equatorial plane again, and then returned to become only slightly upstream while moving in the +*Y* direction and then flowing downstream. Particles 2 and 3 had trajectories that traced out a single loop near the equatorial plane, and then after returning toward the upstream direction they flowed downward below the equatorial plane before flowing toward the outside while approaching the equatorial plane again. Particle 4 traced out a relatively large semicircular trajectory near the equatorial plane before returning upstream, and then

flowed downstream while shifting considerably in the $+Z$ direction, and then after reaching a height near the top edge of the rotor it flowed generally along the main flow direction. Particles 5 and 6 flowed from the $-Y$ side toward the $+Y$ side while shifting slightly toward the $+Z$ direction, and particle 6 in particular accelerated in the downstream direction.
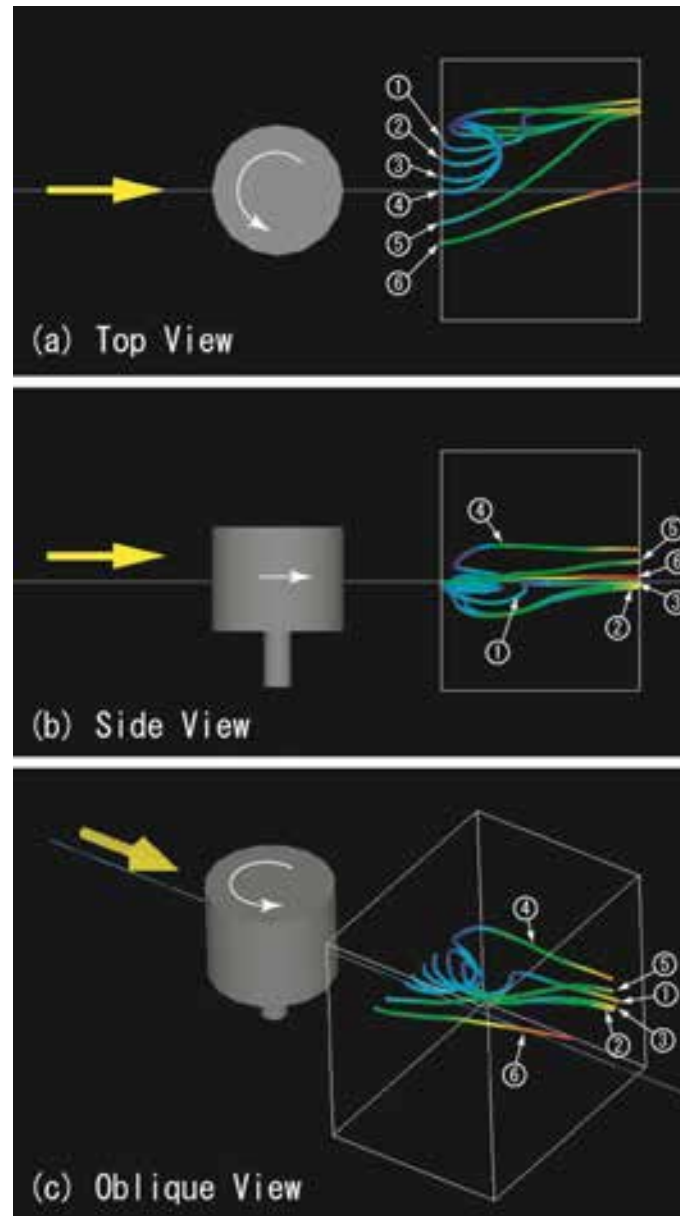

Fig. 16 Three-dimensional path lines in wake of VAWT

Conclusion

The counterflow region observed in the averaged flow field of VAWT wake was shown to have been formed by a vortex-shaped flow pattern. Furthermore, details of the complicated averaged flow field in the vicinity of the counterflow region were determined by calculation of three-dimensional flow path lines. Problems remaining for the future are finding the averaged dynamic flow field by other methods such as CFD in order to investigate whether the same averaged flow field can be obtained as in this research, and finding the three-dimensional velocity fields near the rotor and inside the rotor.

Acknowledgements

References

[1] I. Paraschivoiu. *Wind Turbine Design with Emphasis on Darrieus Concept.* Polytechnic International Press, pp. 147-264, 2002.

[2] M. O. L. Hansen. *Aerodynamics of Wind Turbines*. James & James, pp. 48-59, 2000.

[3] D. A. Spera (ed.). *Wind Turbine Technology*. ASME Press, pp. 215-282, 1994.

[4] V. Kumar, M. Paraschivoiu and I. Paraschivoiu. Low Reynolds Number Vertical Axis Wind Turbine for Mars. *Wind Engineering*, Vol. 34(4), pp. 461-476, 2010.

[5] Y. Hara, T. Suzuki, Y. Ochiai and T. Hayashi. Measurements of the Wake of a Small Straight-Bladed Vertical Axis Wind Turbine. *Proceedings of the JSME Fluids Engineering Conference 2010*, No.10-16, pp. 429-430, 2010, (in Japanese).

[6] Y. Hara, T. Suzuki, Y. Ochiai and T. Hayashi. Measurements of the Wake of Small Vertical Axis Wind Turbine by Using an Ultrasonic Anemometer. *Proceedings of the 49th General Assembly and Conference of the Chugoku-Shikoku Section of the JSME*, No. 115-1, pp. 383-384, 2011, (in Japanese).

[7] Y. Hara, T. Suzuki, Y. Ochiai and T. Hayashi. Velocity Field Measurements in Wake of a Straight-Bladed Vertical Axis Wind Turbine. *Proceedings of ASME-JSME-KSME Joint Fluids Engineering Conference 2011*, AJK2011-07002, 2011.

CFD for Aerodynamic Flight Performance Prediction:
From Irrational Exuberance to Sobering Reality (Invited)

Dr. Pradeep Raj

Professor, Aerospace and Ocean Engineering
Virginia Polytechnic Institute & State University
Blacksburg, VA 24061
USA
praj@vt.edu

Abstract

Accurate prediction of aerodynamic flight performance is critically important for all flight vehicle development projects. The primary motivation is to mitigate the risk of having to make design changes once the vehicle enters its flight-test phase. Experimental fluid dynamics (EFD) and computational fluid dynamics (CFD) are the two main tools for generating aerodynamic data needed to estimate flight performance. Both tools have some key differences. In the mid-1970s these differences created an irrational exuberance among some proponents of CFD who expected it to supplant wind tunnels. Since then, CFD capabilities have rapidly evolved but its limitations have also been widely recognized. Today's Reynolds-averaged Navier-Stokes (RANS) CFD codes are capable of simulating complex flows about full aircraft configurations in a relatively quick and inexpensive manner. However, a sobering reality has set in with the realization that producing credible data remains an overarching challenge. Deficiencies in numerical modeling and flow-physics modeling affect data credibility the most. Two approaches are proposed in this paper to address these deficiencies: (i) Tightly Coupled Test and Computations (TiCTaC) for the near term, and (ii) Direct Numerical Simulation for the long term.

Key words: aerodynamics, computational fluid dynamics, experimental fluid dynamics, flight performance

Introduction

The primary motivation for accurately predicting the aerodynamic flight performance during the design and development of all flight vehicles is to mitigate risk. If the actual flight performance substantially deviates from the predictions, developers risk (i) losing credibility by not delivering what was promised, (ii) schedule slips and cost escalation, and (iii) customer dissatisfaction. Three examples are included here to illustrate such risks.

C-141 Strategic Airlifter—This airplane, shown in Fig.1, was designed in early 1960s. The total drag predicted using wind-tunnel tests matched very well with flight data—within one count! However, the good match had little to do with the accuracy of predictions; it was a favourable outcome of compensating errors. The minimum drag was actually underpredicted and the compressibility drag was overpredicted. But the two added up to a nearly "correct" value. In the mid-1990s, US Air Force experts made an

Fig. 1. C-141 Starlifter

assessment of the impact of advancements in aerodynamic flow simulation capabilities in the preceding three decades on our ability to accurately predict cruise drag. Their conclusion: total drag would be underpredicted by 3.5% even with the more advanced capabilities of the 1990s [1]. This error translates into $688 million fuel cost increase (with 1996 fuel costs as the basis) over the service life of the fleet.

C-5 Galaxy Strategic Airlifter—Later on in the 1960s when C-5 (Fig.2) was designed, the total drag was overpredicted by about 2.5%. In the mid-90s, when US Air Force experts made an assessment of the impact of advancements in aerodynamic flow simulation capabilities on our ability to accurately predict cruise drag, they concluded that the total drag would be underpredicted by 1.5% [1]. This translates into $153 million fuel cost increase (using 1996 fuel costs as the basis) over the service life of the fleet.

Fig. 2. C-5 Galaxy

F-22 Air Superiority Fighter—Nearly 40,000 hours of wind-tunnel tests were conducted to support the development of F-22 (Fig. 3) which had its first flight in 1997. In Figure 4, differences between flight test-derived drag and the wind-tunnel predictions are shown for 1-g flight for a range of Mach numbers [2]. Clearly the subsonic and transonic drag rise were not predicted well by the wind-tunnel tests. This led to erroneous prediction of airplane performance in acceleration, deceleration, cruise and loiter flight conditions.

Fig. 3. F-22 air superiority fighter
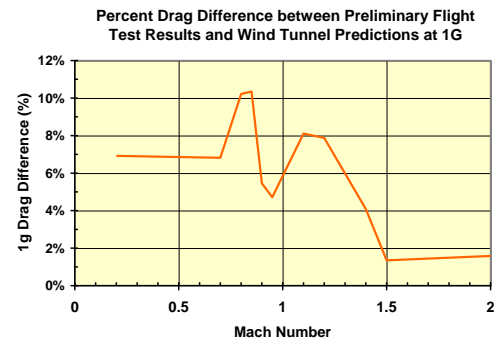
Fig. 4. Differences in F-22 flight-test and wind-tunnel test derived drag values

Aerodynamic Flight Performance Prediction Tools

The two primary tools for estimating flight performance are experimental fluid dynamics (EFD) and computational fluid dynamics (CFD). EFD provides the required aerodynamic data by testing scale models in wind tunnels, whereas CFD solves the governing fluid dynamic equations about a virtual model of the aircraft. Both have inherent strengths and weaknesses as summarized in Table 1.

Table 1. Summary of inherent strengths and weaknesses of EFD and CFD

Strengths	Weaknesses
EFD	**EFD**
• Perceived as "Real"	• High cost
• Management of Measurement Uncertainties	• Scale effects
• Large Excursions per entry	• Wall interference effects
	• Support interference effects
	• Aeroelastic distortion effects
	• Not conducive to MDO
CFD	• Not practical for some flight conditions
• Low cost	
• No scale effects	**CFD**
• No wall interference effects	• Perceived as "Virtual"
• No support interference effects	• Computational uncertainties
• Coupled CFD-CSM for aeroelastic distortions	o Numerical modeling
• Enables multidisciplinary design optimization	o Flow physics modeling
• Applicable to all flight conditions	

The potential advantages of CFD over wind tunnels were recognized in the early years of its evolution which led to an irrational exuberance in the minds of some of the leaders in the research community. In their celebrated article in 1975, Chapman et al [3] predicted that *"...within a decade computers should begin to supplant wind tunnels in the aerodynamic design and testing process..."* In addition they forecasted that *"To displace wind tunnels as the principal source of flow simulations for aircraft design....the required computer capability would be available in the mid-1980s."* However, it did not take long for rational sobriety to take hold. In spite of dramatic improvements in CFD and computer capabilities throughout the 1980s, computational methods did not become the principal source of flow simulation for aircraft design as envisioned in Reference 3. Based on CFD applications to F-22 design during the early 1990s, Bangert et al [4] surmised that their design team had to rely heavily on wind-tunnel data due to the limitations of CFD codes in modeling viscous effects, especially when applied to full aircraft geometries and the full speed, altitude, and manoeuver flight envelope. This is not too

surprising due to the then level of maturity of the RANS methods. The 1990s saw further advancement of RANS methods capable of modeling viscous effects. But in early 2000s, the development team of the Joint Strike Fighter (JSF) aircraft also relied on extensive wind-tunnel testing for generating aerodynamic performance data [5] to meet Key Performance Parameters and Performance Specifications related to its Mission Performance. Since 2002 more than 48,000 wind tunnel test hours on the JSF Lightening II have been completed at eighteen facilities around the world. Clearly, CFD has not supplanted or displaced wind tunnels.

It is important to note that there is one aspect of an aircraft design effort, namely, shape optimization, for which CFD is uniquely suited whereas EFD is totally inadequate. In designing a new airplane or modifying an existing one, it is clearly important to have good estimates of the configuration aerodynamic characteristics. However, it is significantly more valuable if an "optimum" shape can be determined for desired aerodynamic characteristics. The traditional cut-and-try approach—relying on the results of analyses and aerodynamic expertise to guide shape redesign—cannot provide an optimum shape. Combining CFD methods with a numerical optimizer is the most effective means of generating optimum shapes. The optimization approach requires computation of derivatives of an objective function with respect to the design variables. There are many different ways it can be done using computational techniques whereas it is totally impractical using wind tunnels. In addition, interdisciplinary considerations can be brought to bear on shape optimization through the specifications of constraints.

CFD Overarching Challenge

The ultimate value of CFD simulations depends entirely on the credibility of the predicted solutions for their intended use. As pointed out by Mehta [6], a solution lacks credibility unless its uncertainty is known, but the simulation uncertainty is ubiquitous. It is difficult to improve the credibility of simulations without knowing the model uncertainty. The intended use of a simulation identifies which errors should be tracked and quantified and also determines the acceptable level of accuracy. That is, a simulation may be credible for one use but not for another, even though the simulation accuracy is the same. For aerodynamic flight predictions, flow simulations of complete aircraft configurations using higher-level CFD methods are expected to provide credible predictions. *However, assessing the accuracy of computed viscous solutions remains an overarching challenge*. The two key factors determining solution accuracy are numerical modeling and flow-physics modeling as discussed next in this section.

Numerical Modeling

A solution may be considered numerically accurate if it shows little or no sensitivity to changes in grids as well as numerical parameters related to the algorithm. (It is assumed that the code in question has been verified as to the adequacy of its numerical formulation for solving the governing equations.) Figure 5, extracted from Reference 7, illustrates sensitivity of computed surface pressures to numerical parameters in the CFD code for the JSF Short Takeoff and Vertical Landing (STOVL) configuration. For this example, the numerical parameter is the flux-limiter
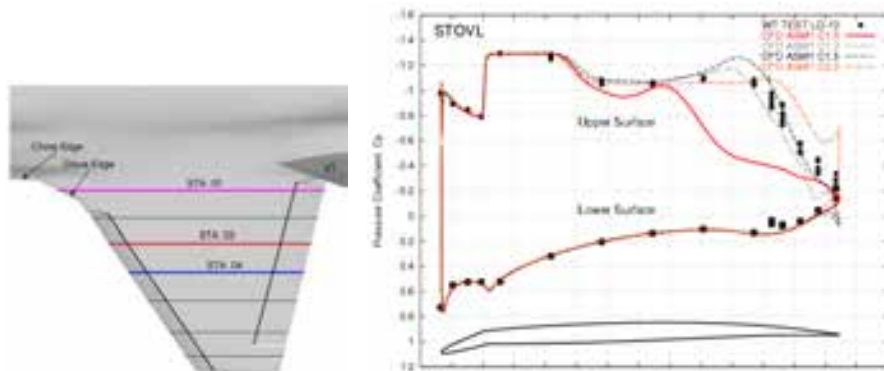

Fig. 5. Sensitivity of computed surface pressures on JSF STOVL variant to flux limiter compression factors in Falcon CFD code

compression factor for the upwind scheme incorporated in the Falcon CFD code used for this analysis. Note that the multiple symbols in this illustration denote run-to-run variations in the wind-tunnel test measurements—an important consideration in using experimental data to assess the credibility of computed solutions.

Cunningham et al [8] conducted low speed wind-tunnel tests and unsteady CFD analyses of the F-22 configuration to identify important characteristics of the buffeting loads on the fins and for evaluation of various aerodynamic modifications to alleviate these loads. Figure 6 shows surface pressure distribution along with regions of vortex flow computed using an unsteady unstructured-grid CFD code, USM3D. The grey envelopes depict the 3-D boundaries of the flow reversal surfaces associated with vortex breakdown. Inside of these surfaces, the velocity field is generally flowing forward relative to the airplane. The first set of CFD runs had a relatively coarse grid arrangement on the vertical fins for conservation of computational resources and faster turnaround times. However, the computed unsteady CFD pressure distributions

Fig. 6. F-22 flow-field features at high angle of attack computed using unsteady unstructured-grid CFD code

exhibited discrepancies with test data, and the computed root-mean-square (RMS) pressure levels were very low. When a finer grid was used for the vertical fin to more accurately represent a small rounded leading edge, computed RMS levels were very much in line with the measured wind tunnel data.

At present, systematic parametric studies are about the only means of estimating the effects of grid resolution and numerical parameters. Schedule and cost constraints of a typical design effort do not permit extensive investigations to determine "optimal" grids and numerical parameters. *What we need is built-in means of quantifying the level of accuracy*. Estimation of errors due to numerical modeling is admittedly a difficult problem but an effective solution is urgently needed.

Flow-Physics Modeling

Even if a code produces a numerically accurate solution, it is not trivial to determine how well the solution stacks up against reality because it depends on the accuracy of flow physics modeling. For a long time, the CFD community has advocated and conducted extensive validation exercises which generate computed vs. experimental data correlations to substantiate claimed levels of code accuracy. However, the exercises have contributed more to the proliferation of data than to increasing the credibility of CFD codes. Extensive correlations on geometries and flow conditions that differ substantially from those being considered by the design teams are of little value. This situation is particularly relevant to military aircraft projects since new designs are generally quite different from the previous ones (for which correlations might exist).

The traditional approach to code validation is fraught with many difficulties. How many test cases, what combination of flow conditions for each test case, and what turbulence models must we consider before a code can be declared "fully validated?" A matrix of runs using any reasonable set of test cases and flow conditions quickly grows into a monumental task. Even if we assume that adequate resources as well as high-quality measured data—with known error bounds—were available for carrying out such a task, we run against the tide of technology dynamics. The rapid pace of advances in hardware, numerical algorithms, and transition/turbulence modeling fosters an environment where codes are never quite "finished." Sometimes the changes are nominal, many times not. Any rational cost/benefit assessment of a plan that allocates huge amount of resources to validating a code that might be superseded the next day by a "new and improved" method does not support the traditional validation approach.

When RANS equations are solved to simulate aerodynamic problems in aircraft design where viscous effects dominate, the accuracy and reliability of the solutions continue to suffer from the inadequacies of turbulence models. One example is included here to illustrate the sensitivity of flow solution to turbulence models. In Figure 7, computed vorticity magnitudes on JSF STOVL configuration [7] are shown for a two-equation k-kl model [9] and two variations (ASM1 and ASM2) of an explicit algebraic stress model [9]. These solutions were generated using a patched multiblock structured-grid method using a 197-block grid with a total of 36 million grid points. Assessing the accuracy of these solutions is a truly monumental challenge because extensive flow field data were not acquired during wind-tunnel testing to support JSF development—a standard practice.
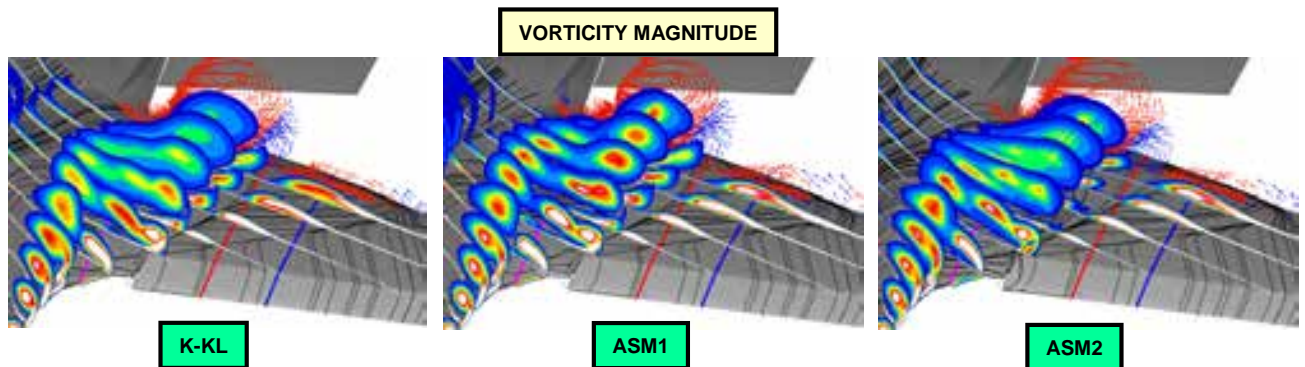
Fig. 7. Vortex Flow Sensitivity to Turbulence Models for JSF STOVL Configuration

Attempts at accurately simulating turbulent flows to date have had rather mixed outcomes. There have been many successes with relatively simple models and many failures with the more sophisticated ones. Attempts at refining existing models and developing new, improved ones continue unabated. Considerable effort has also been devoted to developing models for laminar to turbulent flow transition, an area of crucial importance for accurate viscous-flow simulation.

In this author's opinion, the prospect of a "universal" turbulence model that is equally effective for all types of flows is rather bleak because capturing the complex nature of turbulence into a model with a few free parameters is a long shot indeed. One option for CFD practitioners is to rationalize the use of RANS codes—in spite of their limitations—by accepting Bradshaw's observation [10]: *"...we cannot calculate all flows of engineering interest to engineering accuracy. However, the best modern methods allow almost all flows to be calculated to higher accuracy than the best informed guess, which means that the methods are genuinely useful even if they cannot replace experiments."* However, it does not obviate the desire to develop a highly effective, truly predictive CFD capability in order to capitalize on the tremendous advantages of CFD.

Whither CFD?

Continuing advances in large eddy simulation (LES) and direct numerical simulation (DNS) offer very attractive options for developing a CFD capability that can be *truly* predictive unlike the RANS methods which will continue to suffer from turbulence and transition model uncertainties. However, even rough order of magnitude estimates of the required computational resources for a full aircraft analysis at flight Reynolds number are staggering as shown in Figure 8. Due to the Re^3 computational work barrier, it appears that DNS will not be practical in a design environment for several decades. However, LES could become practical much sooner if computer memory and speed continue to increase at their current rate. Considering the ten-fold increase in speed and memory every 7 years since 1975, it is conceivable that the required computational resources will become available by 2020 or thereabouts. It is imperative that more effort be directed at several pacing items such as sub-grid scale modeling; numerical algorithms; boundary conditions; grid generation; and tools for analyzing, visualizing and managing extremely large amounts of data. Even more importantly, advances are required in wind tunnel measurement techniques to collect data required to assist the development of effective LES and DNS capability.
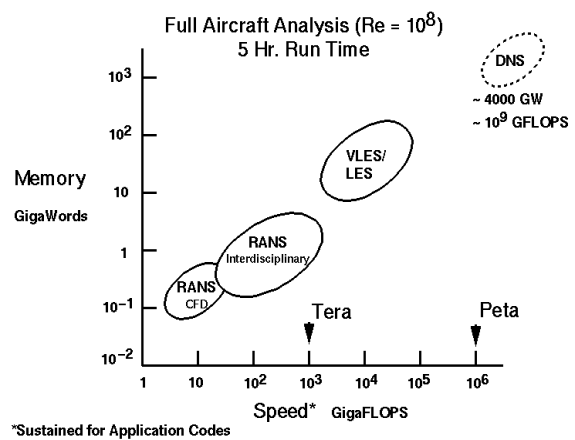

Fig. 8. Staggering amounts of computing resources required for full-aircraft analysis using Direct Numerical Simulation

In the near term, one can expect continuing evolution of both CFD and EFD with rapid yet incremental advances in capabilities which can be judiciously leveraged to improve our ability to predict credible data for aerodynamic flight performance estimation. As previously mentioned, CFD codes will not produce credible data for our particular application unless previously validated on the same or very similar geometry and flow configurations. However, a Tightly Coupled Test and Computations (TiCTaC) approach could pay handsome dividends if its promise could be effectively harvested in practice. This approach relies on developing and implementing a "Validation Plan" for a particular application targeted at maximizing prediction credibility. The three components of the proposed plan are:

1. Identify the principal source(s) of uncertainty related to modeling of relevant flow physics and numerics.

2. Perform dedicated tests for the sole purpose of "refining" modeling parameters.

3. Utilize updated models to maximize credibility of CFD simulations.

Concluding Remarks

In this paper, the author presents a perspective on the critical importance of accurately predicting aerodynamic flight performance for design and development of flight vehicles. Three examples of operational aircraft are used to illustrate the risk associated with errors in performance predictions. Inherent strengths and weaknesses of EFD and CFD—the two main tools for generating data for performance predictions—are compared which highlight their similarities and key differences. In the mid-1970s these differences created an irrational exuberance among some proponents of CFD who expected it to supplant wind tunnels. Although CFD capabilities have rapidly evolved since then, there is widespread recognition and better understanding of its limitations. A few RANS CFD solutions on full aircraft configurations are presented to convincingly demonstrate today's impressive flow simulation capabilities. However, with the realization that producing credible data remains an overarching challenge, a sobering reality has supplanted the irrational exuberance.

The challenge of producing credible data can be most effectively tackled by rectifying the deficiencies in numerical modeling and flow physics modeling in CFD methods. Two approaches are proposed to address these deficiencies: (i) Tightly Coupled Test and Computations (TiCTaC) for the near term, and (ii) Direct Numerical Simulation for the long term. Both are conceptually appealing but not easy to implement in practice. However, innovative approaches for integrating EFD and CFD will pay handsome dividends if they result in a highly effective, truly predictive capability to meet the needs of flight vehicle development projects.

References

[1] DoD Aeronautical Facilities Assessment, March 1997.

[2] Wilson, C.M., "F-22 Aerodynamics – Prediction vs. Flight," *Lockheed Martin Aeronautics Company, Marietta, Georgia, Presented at the NASA/DOD Workshop on Aerodynamic Flight Predictions, Williamsburg, VA, November 19-21, 2002.*

[3] Chapman, D.R., Mark, H., and Pirtle, M.W., "Computers vs. Wind Tunnels for Aerodynamic Flow Simulations," AIAA Astronautics & Aeronautics, April 1975.

[4] Bangert, L.H., Johnston, C.E., and Schoop, M.J., "CFD Applications in F-22 Design," *AIAA Paper 93-3055*, July 1993.

[5] Wooden, P.A., and Azevedo, J.J., "Use of CFD in Developing JSF F-35 Outer Mold Lines," *AIAA-2006-3663, 24th Applied Aerodynamics Conference, 2006*

[6] Mehta, U.B., "Guide to Credible Computer Simulations of Fluid Flows," Journal of Propulsion and Power, Vol. 12, No. 5, Sep-Oct 1996, pp 940-948.

[7] Wooden, P.A., Smith, B.R. and Azevedo, J.J., "CFD Predictions of Wing Pressure Distributions on the F-35 at Angles-of-Attack for Transonic Maneuvers," *AIAA-2007-4433, 25th Applied Aerodynamics Conference, 2007.*

[8] Cunningham, A.M., Jr., Anderson, W.D., Patel, S.R., and Black, C.L., "Lockheed Martin Aeronautics Perspective on Aircraft Buffet Prediction and Analysis," Symposium on Flow-Induced Unsteady Loads and Impact on Military Applications, Applied Vehicle Technology Panel (AVT), NATO, Budapest, Hungary, 25-28 April 2005.

[9] Smith, B. R., "The *k-kl* Turbulence Model and Wall Layer Model For Compressible," *AIAA Paper 1999-0365*, June 1999.

[10] Bradshaw, P., "Turbulent Secondary Flows," *Annual Review of Fluid Mechanics*, 19, 1987, pp. 53-74

A Combined Study on Shock Diffraction

Mark Kenneth Quinn
Konstantinos Kontis

Aero-Physics Laboratory
University of Manchester
George Begg Building
Sackville Street
Manchester
UK
M13 9PL
mark.quinn-2@postgrad.manchester.ac.uk

Abstract

Shock wave diffraction is a complex process which has been studied at great length but has never been fully understood. The diffraction process creates numerous complex wave structures, a shear layer and a strong vortex. The structure of this shear layer has been the subject of numerous studies. Some simulations have shown this shear layer to be unstable, observing that it develops Kelvin-Helmholtz-style instabilities. Simulation performed in this work show a strong grid dependency. The diffraction process is widely regarded as self-similar in time; however, these instabilities have never been seen experimentally at small time scales. The high speed and small scale of the phenomena present make them extremely challenging to visualise using any experimental method. The aim of this work is to provide a complete picture of the phenomena that occur when a Mach 1.46 shock diffracts around a 172 degree corner while presenting the experimental techniques which are most suited to this type of flow.

Key words: shock tube, shock diffraction, CFD, PIV, shadowgraph

Introduction

When a travelling normal shock wave encounters an increase in area, it diffracts into the area increase. Skews [1] showed how the shock wave diffracts around different angles. He showed that past a critical angle of $75°$, the flow remains unchanged. As the shock wave diffracts around the corner, a contact surface is created. This surface separates the gas that has passed through the normal shock from that which has passed through the curved shock. If the induced flow cannot navigate the sharp corner, separation occurs leading to a shear layer which is swept into the strong vortex generated [2].

Figure 1 shows the flow features behind a weak shock diffracting around a sharp corner. For incident shock Mach numbers lower than $M_i = 1.8$, the flow features resemble those seen in Figure 1. Different regions of the flow are numbered (0-3') depending on which features they have been affected by. Flow that has been affected by the planar incident shock, I, is separated from the flow exposed to the curved shock by the contact surface, CS. The shear layer, SL, created as the flow cannot navigate the sharp corner, rolls up into the strong vortex, V. As the shock Mach number increases, the expansion wave train, ET, grows to become one large area of supersonic flow, culminating in a terminating shock.
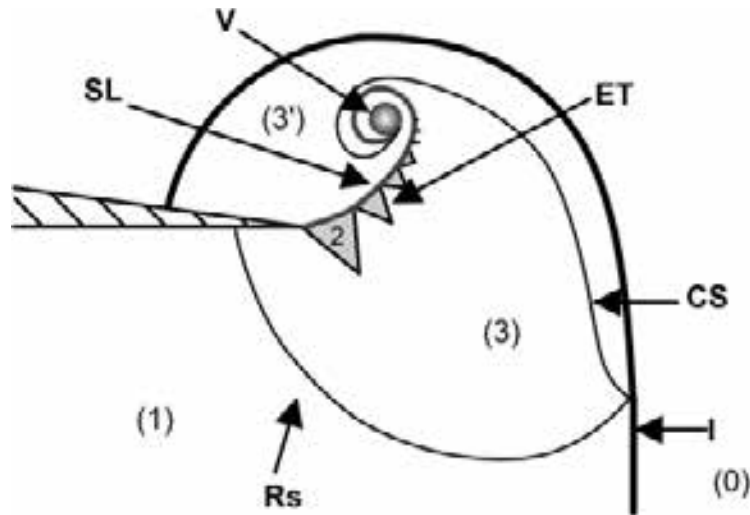
Figure 1. Weak shock diffraction Mi≈1.4

During the 18th International Symposium on Shock Waves, a special poster session was held to compare numerical codes from various researchers on the problem of shock diffraction [3]. The numerical results all showed the same strong features similar to those described above. Some of the codes showed that the shear layer was unstable and began to develop Kelvin-Helmholtz style instabilities. A later investigation into the problem by Sun and Takayama [4] found that solving the Euler equations gave an unstable shear layer, while solving the Navier-Stokes equation gave an undisturbed shear layer. As experimental evidence supporting the existence of the K-H instabilities was lacking, the authors assumed that the phenomenon was non-physical and attempted to suppress it by introducing more numerical diffusion into the simulations. Other researchers have found the shear layer in question to be stable or unstable, depending on the numerical resolution and exact formulation of the simulation [5-6].

Skews et al. [7-8] did manage to experimentally resolve some instabilities in the shear layer albeit at a significantly longer timescale than is required in simulations. This led them to conclude that the shear layer evolution process is not self-similar in time, as these instabilities have never been seen at small scales. The authors proposed that the upstream boundary layer characteristics could be a defining factor in the formation of the instabilities. However, inviscid simulations, notably by De & Thangadurai [5], captured the instabilities very clearly using inviscid simulations, leading to the doubts about the significance of the incoming boundary in the formation of this instability. Clearly this is an unsolved problem and is therefore deserving of further investigation. In this paper we will show simulations and experiments of a M_i=1.46 shock wave diffracting around a 172 degree corner.

Numerical Simulations

Numerical simulations were performed using the commercial CFD code Fluent as part of Ansys 13. A grid dependency study and solver discretisation study were both performed in order to determine the effect of numerics on the results. The grid is initialized at atmospheric pressure everywhere, with pressure outlet conditions at edges of the test sections including a sponge layer to avoid wave reflections. The driver section is then patched at the required pressure to generate the desired speed of shock wave based on inviscid theory.

Figure 2 shows the simulation of a whole shock tube (M_i=1.55) using 1st, 2nd, and 3rd order discretisation of both space and time and a comparison with inviscid theory. There appears to be little advantage to using a 3rd order solver, as the performance is almost identical in the region of shocks. The non-physical oscillations seen in the region of the diaphragm cast doubt about the robustness of the 3rd order solvers available in this code and their ability to deal with the wide range of phenomena present. For this reason, both 2nd order space and time discretisation was chosen.
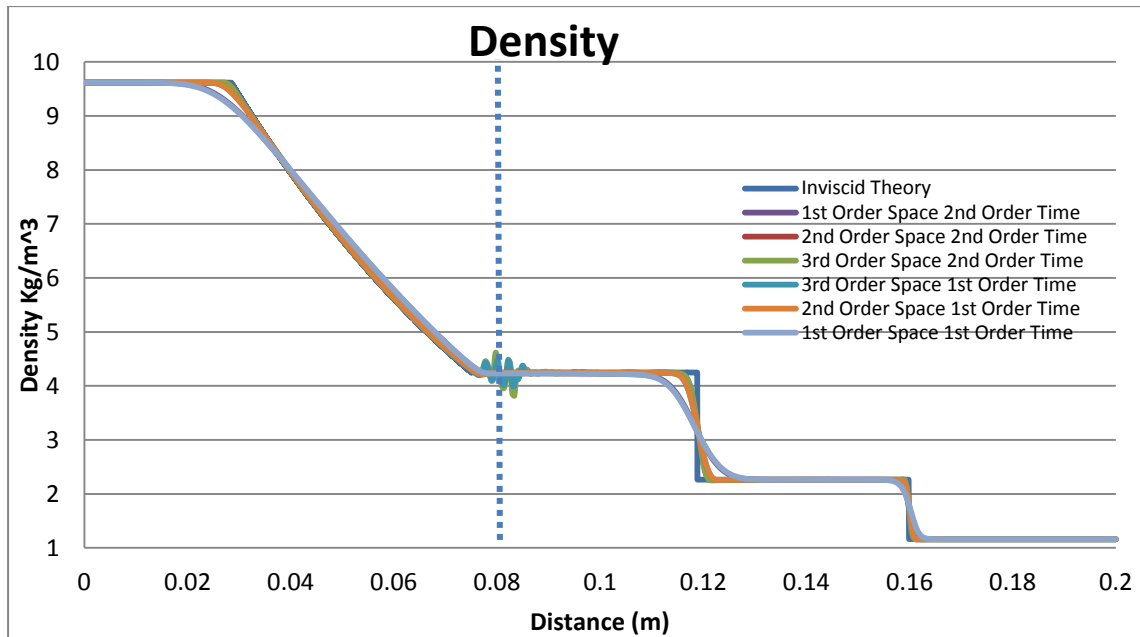
Figure 2. Mi=1.55 Shock Scheme comparison

Problems of this nature often require an adaptive grid to resolve shocks sharply. A comparison of different levels of adaption found that the critical grid size in order to resolve shear layer instabilities is ≈25x25µm. A grid coarser than this fails to resolve instabilities on the shear layer. However, this level of refinement does come at a significant computational cost.

The final simulation used an inviscid, density-based solver which was 2nd order discretised in both space and time. The ASUM+ flux vector splitting scheme was chosen as it is known to perform well when resolving shocks [5]. An initial uniform regular structured grid consisting of quadrilateral 0.4x0.4mm elements was then adapted 4 times per time-step based on the pressure gradient, giving a minimum Δx=25µm. This led to a maximum grid size of 250~300 K cells. An example of the grid is shown in Figure 3. The CFL number was kept at 0.2, as it was found that numbers larger than this gave non-physical oscillations in the region of strong shocks. This very strict CFL criterion suggests that Fluent is a highly non-diffusive code and, if controlled properly, is well suited to problems of this nature.

The simulation took approximately 2 weeks to complete on an Intel core I7 desktop PC with 8GB of RAM running Windows 7 (64 bit). The baseline mesh was generated using Gambit. Post-processing was performed using Tecplot360, allowing for the generation of numerical schlieren and shadowgraph for comparison with experimental results.
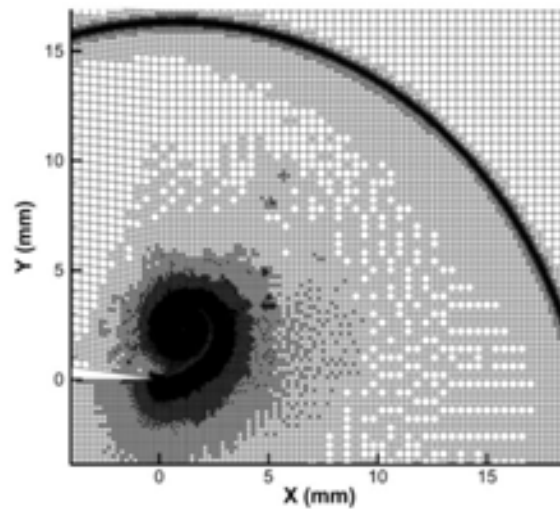
Figure 3. Example grid showing 4 levels of adaption

Experimental Setup

The experiments shown here were carried out in the University of Manchester Aero-Physics Laboratory using the square shock tube. This mechanical rupture style shock tube has a 24.8x24.8mm cross section square tube with a 700mm driver section and a 1700mm driven section. The height of the test section is 55.2mm. A schematic of the test section, which is made of 10mm Perspex, is shown in Figure 4. The geometry tested had a knife- edge tip and a wedge angle of 8°. Driver section pressure measurements and acquisition triggering were performed using two Kulite XT-190M transducers connected to a NI USB-6251 16 bit M series Multifunction DAQ operated by LabView 2011. A Kulite was placed flush to the driven section wall, 1m from the test section. This transducer was connected to an amplifier, hardware delay generator and finally a signal generator to trigger the acquisition.
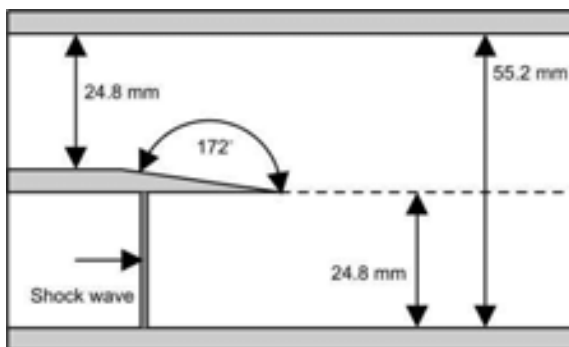
Figure 4. Schematic of test section
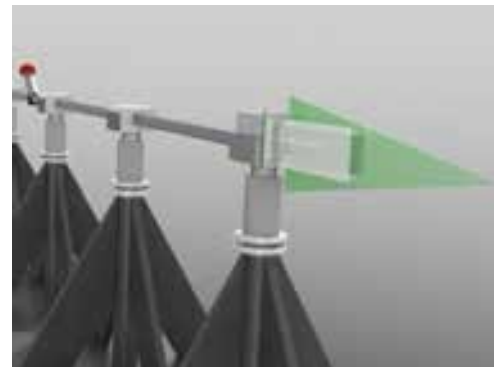
Figure 5. Illustration of the shock tube with the PIV laser sheet

Schlieren

Density-based optical measurements were made using a Z-style Toepler schlieren system with a removable knife-edge in order to convert to shadowgraph if required. Continuous illumination came from an in-house constructed, 300W Xenon short arc lamp. Collimated light produced by this lamp was condensed by a hemispherical lens to the slit. Two 8 inch, f=4.5 parabolic mirrors at 3° inclination directed the beam in the standard Z-style to a combination of +1 and +2 diopter macro lenses which focused the beam sharply on the

imaging device. Images were recorded using the Shimadzu HPV-1 at 250Kfps with an exposure time of 2μs. The full-field image shows an area of 67.5 x 56.3 mm while the close-up images show 40.8 x 34.0 mm.

The images recorded were processed using ImageJ. All of the images recorded were divided by a reference image (before the arrival of the shock) in order to remove non-uniform illumination and artifacts on the windows. The image histograms were then scaled to make the flow features more visible. This does have the effect of introducing bright areas around dark regions, although this is easily visible in the images and does not detract from the results.

The experimental shock speed was calculated by taking a slice from each image in the video recorded and stacking them up. This process, known as reslicing, creates an effective x-t diagram where both the distance and time scales are known. The x-t diagram can only be used if the shock wave is planar. Abate and Shyy described this as a *critical* shock [9].

Particle Image Velocimetry

Particle image velocimetry has been applied to problems relating to shock wave diffraction, such as compressible vortex ring propagation [10], but there have been limited applications on moving shock wave interactions. This is primarily due to the available laser repletion rate. This means that any PIV experiments have to be performed in a *spark* fashion, i.e. only acquiring one pair of images per run and then increasing the delay time. Using PIV in this fashion is extremely difficult and time-consuming, as the flow needs to be seeded every run and only one set of data can be extracted.

The PIV system used here consists of the LaVision FlowMaster with an Imager pro X 2M camera and a Litron Nano-L-200-15 PIV Nd:YAG laser. This system allows a very small δt between images, one of the limiting factors in previous studies [11]. For this experiment, $\delta t = 0.55$μs. The laser sheet was aimed vertically down the shock tube centreline (see Figure 5), with the camera normal to the laser sheet. Al_2O_3 nanoparticles were injected into the test section using a SciTech Consultants PS-10 powder seeder. The average particle size was estimated to be 0.5μm. The relaxation time was estimated to be 3.6μs using the theory given by Melling [12], with a correction for slip factor and mean free path length. Solid nanoparticles are currently the best particles for use in a flow of this type, where relaxation length and time are the most important factors for credible results. The interrogation window size was 32 x 32 pixels. Raw PIV images were used for laser sheet visualisation, as they highlighted some flow characteristics that were ambiguous in other tests**.**

Results

This section will present the results of each experiment and compare them to the numerical simulations performed.

Numerical Simulations

As mentioned previously, the numerical simulations performed showed a strong grid dependency, especially in the region of the shear layer. As can be seen in Figure 6, the shear layer, expansion fans and the contact are all poorly resolved without strong grid adaption. It should be noted that all the numerical schlieren presented in this section is non-directional. Experiments were performed using a horizontal knife-edge, giving measurements in the vertical direction. If the numerical schlieren image is calculated, based on the y density gradient, normal shock waves are invisible due to the effective zero exposure time. Therefore, for the ease of understanding, density gradient magnitudes are presented (this is akin to a small circular cut-off instead of a knife-edge).

Figure 7 shows numerical schlieren at six of the time steps that were captured experimentally. Figure 7 a) and b) show the beginning of the diffraction process and show the large scale features expected. The reflected sound wave and the contact surface are both clearly resolved, and there appears to be an expansion fan at the apex of the knife-edge geometry. The reflected sound wave propagates upstream (below the knife-edge) at a slower speed than the diffracted shock (above the knife-edge), due to the velocity induced by the incident shock wave. However, it is not clear what is happening around the shear layer due to the strong gradients nearby. At 56μs after impact (Figure 7 c), the shear layer is clearly unstable and is exhibiting the initial stages of the Kelvin-

Helmholtz instability. The instability can first be seen at 40μs after the impact of the shock wave. In the subsequent figures, the diffracted shock wave can be seen reflecting off the upper wall of the test section and propagating back towards the vortex. During this time the velocity induced by the vortex has the effect of slowing the shock wave and causing it to deviate from the regular curvature it exhibits in the early part of the process. It is interesting to note that the train of shocks and expansion fans that are expected on the underside of the shear layer are underpredicted in the simulations. The initial two lambda structures can be seen, but subsequent structures are not resolved [1, 13]. This is likely to be due to the dynamic adaption of the grid as tests on uniform grids (albeit coarser) have been shown to resolve these features successfully.
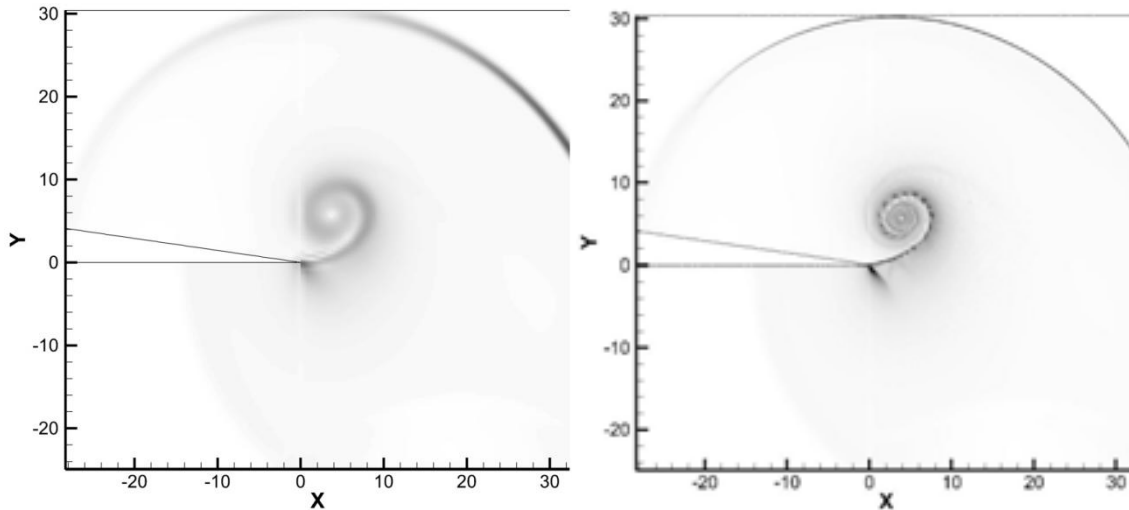
Figure 6.Comparison of baseline (left) and refined (right) mesh at the same time step

Figure 8 shows the numerical velocity vector plots at the corresponding time steps to Figure 7. The velocity vectors have been interpolated on to a uniform grid with the same resolution as the PIV system described previously. This gives 400 x 300 individual velocity vectors. The diffracting shock wave shape can clearly be seen in Figure 8 a-d). As expected, the shock wave is a different strength along all of its curvature, meaning that the induced velocity is lower at larger angles of diffraction (as the shock tends towards a sound wave). As the diffracted shock reflects off the upper surface, it begins to stagnate the flow and deflect it outwards. This leads to the reflecting shock front being visible in the velocity vector plots. The velocity vector plots show the influence of the expansion around the corner clearly as the flow is accelerated to a maximum value of 531 m/s in Figure 8 f). However, this value is localised to one cell, and the expansion region has a larger region of flow with a velocity of 480~490 m/s. It is extremely difficult to discern any instabilities along the shear layer at this resolution.
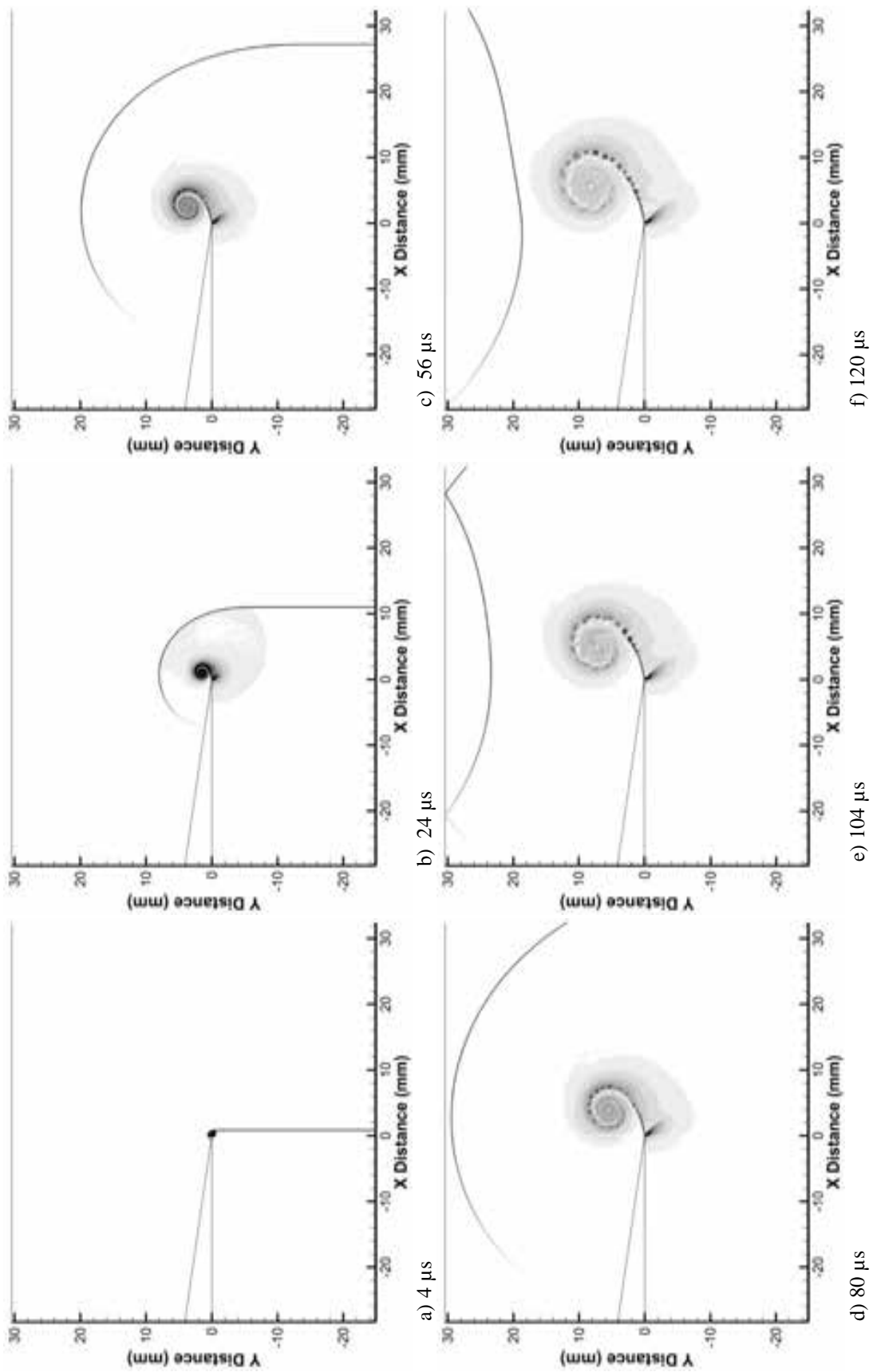
a) 4 µs   b) 24 µs   c) 56 µs

d) 80 µs   e) 104 µs   f) 120 µs

Figure 7. Simulated density gradient magnitude plots at different time steps

a) 4 µs

b) 24 µs

c) 56 µs

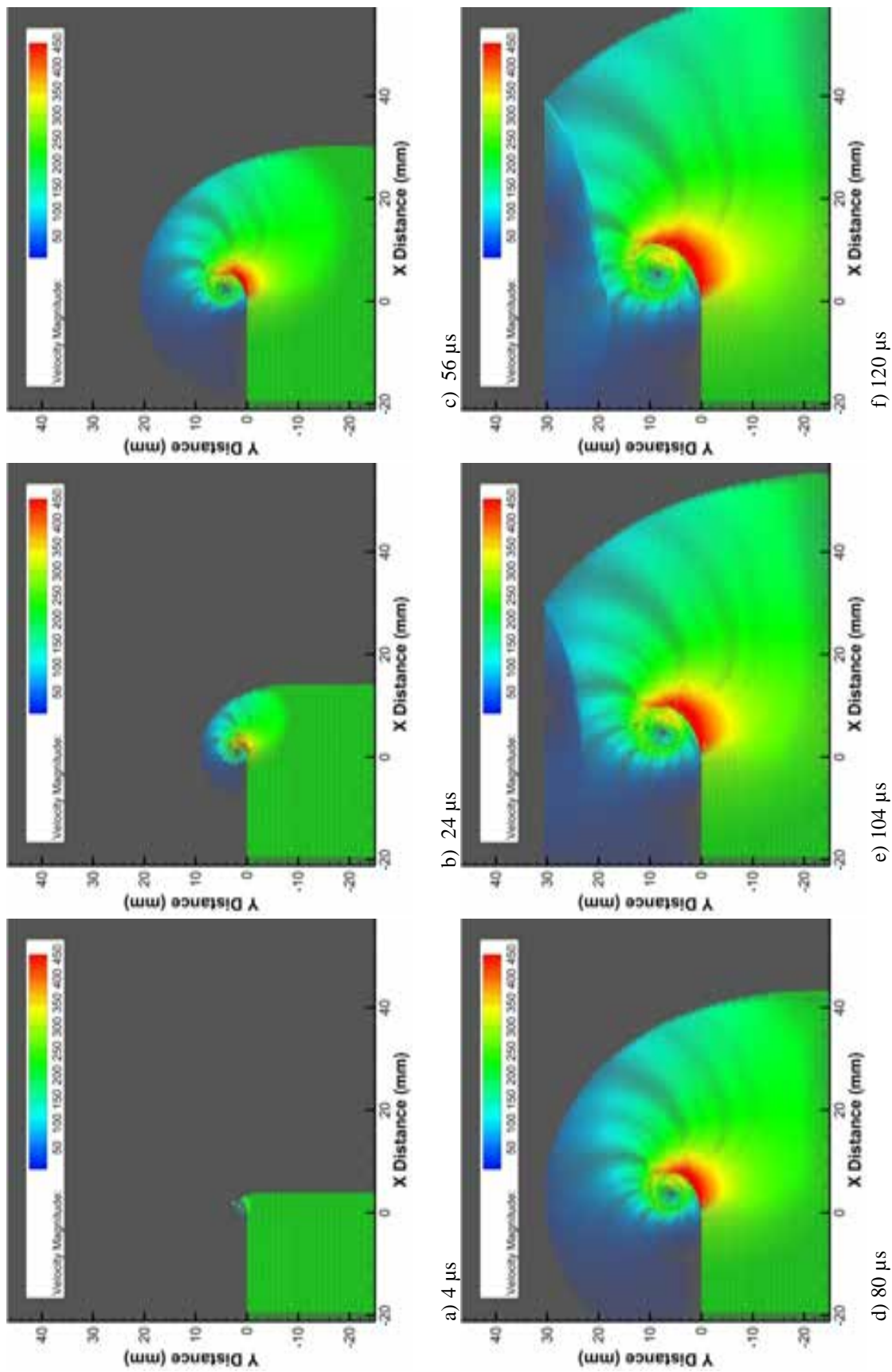d) 80 µs

e) 104 µs

f) 120 µs

Figure 8. Simulated velocity vector plots at different time steps

Experimental Schlieren

Figure 9, Figure 10, Figure 11 and Figure 12 show experimental schlieren images of different time steps at two different zooms. The close-up images (Figure 10 and Figure 12) both appear to have more noise on them than the full-field images. This is down to the finite amount of light available during the experiments. As the camera is zoomed in, less light falls on the same chip area, meaning that less of the dynamic range of the camera is utilised. The histograms of the two datasets have been adjusted for ease of understanding and comparison. Even though the incident shock wave is travelling in the x-direction and the schlieren system should only be sensitive to density gradients in the y-direction, the shock is still visible. This is due to the finite exposure time of the high-speed schlieren (2μs). In this time the shock has moved approximately 1mm.

The early stages of the shock diffraction process are shown in Figure 9 and Figure 10. In the full-field images (Figure 9) the density gradients are so strong around the main vortex core that the image is overranged in this area. Despite this, the large-scale features are resolved well. The shock shape, contact surface, reflected sound wave and vortex are clearly visible.

Underneath the shear layer it is difficult to see any flow features due to the overranging present. However, in Figure 10 c, there appears to be a structure of lambda shocks that have been seen by previous researchers [1, 13]. As the flow develops in Figure 11 and Figure 12, overranging becomes less of a problem as the density gradients are spread out, meaning that more features become visible. In both the full-field and close-up images, the lambda structures present underneath the shear layer are visible. In Figure 12 c, five distinct lambda structures can be seen with a further two *intensity changes* which are too small to distinguish clearly. These lambda structures were not resolved by the numerical schlieren but are clearly visible in the experimental results.

It is difficult to see in still images (it is much clearer in the high-speed video), but the shear layer has instabilities on it that can be individually resolved. These are most visible in Figure 11 and Figure 12 c. High-speed video results show that these instabilities are present at times as early as 80μs after the shock wave has begun to diffract. The close-up schlieren images (Figure 10 and Figure 12) show the instabilities more clearly than the full-field images. This is significantly longer than the inviscid simulation predicted. The presence of viscosity in the flow may slow down the formation process of these vortices.

In the final images of Figure 11 and Figure 12, the reflected sound wave and reflected shock wave are both influenced by the presence of the expansion region and the vortex respectively. The effect on the curvature of these waves is comparable with the numerical simulations.

Overranging is almost unavoidable in an experiment such as this one due to the large density gradients present. This makes the instabilities on the shear layer extremely difficult to find experimentally, as they are small changes in density obscured in a flow-field full of large changes in density. A real and practical schlieren system can only have a finite sensitivity over a finite range. As schlieren is only sensitive to the first spatial derivative of density, it is prone to being overranged by strong phenomena. Shadowgraph is sensitive to the double spatial derivative of density, meaning that it is less likely to be overranged and is probably the most suitable density-based technique for a flow of this type. There is a trade-off between sensitivity and blur with shadowgraph which was discussed by Biss et al. [14]. This trade-off means that it is difficult to set the sensitivity of a shadowgraph system to be sufficient to capture these instabilities without compromising the spatial resolution of the system so much that they are unclear. This has been achieved by tuning the circle-of-confusion of the system and the depth-of-field so that a good compromise between blur and sensitivity can be achieved [15].
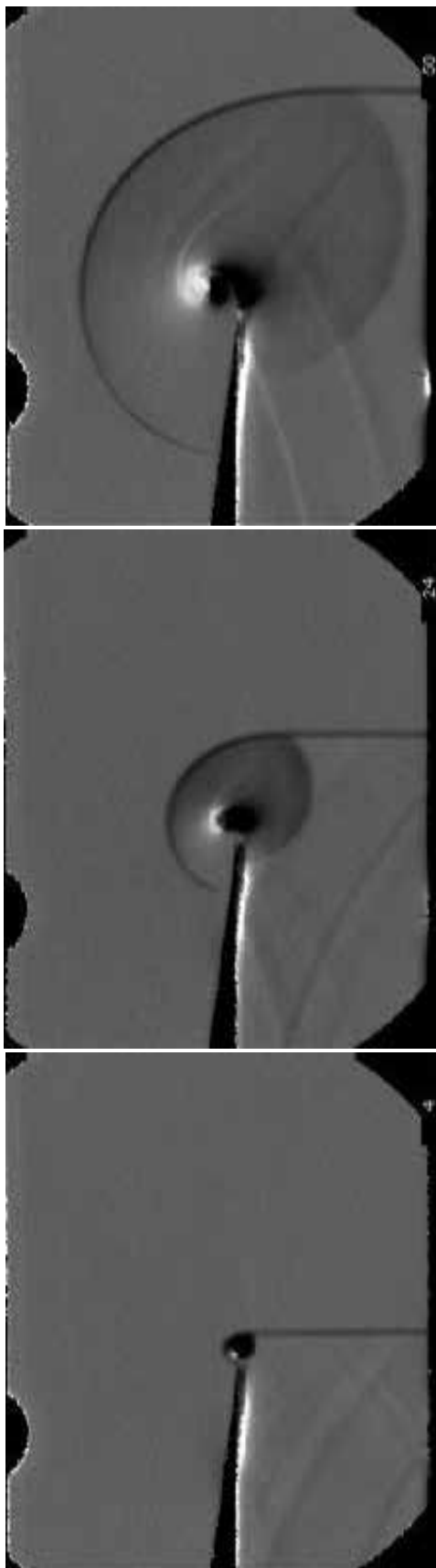
Figure 9. Schlieren montage of full-field images at 4, 24 and 56 µs after shock impingement

Figure 10. Schlieren montage of close-up images at 4, 24 and 56 µs after shock impingement
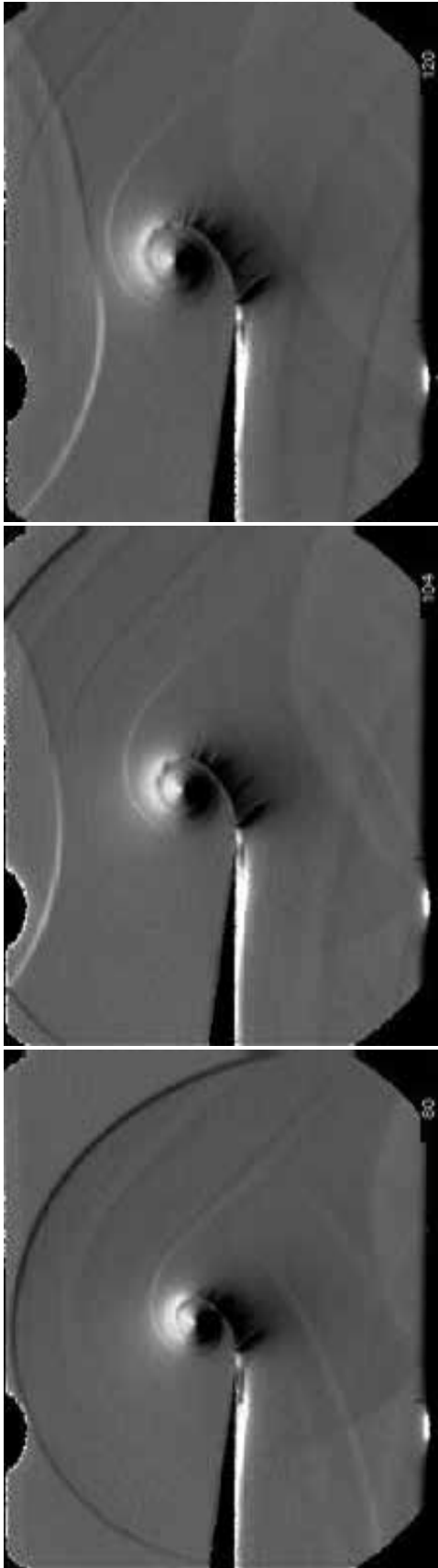
Figure 11. Schlieren montage of full-field images at 80, 104 and 120 μs after shock impingement

Figure 12. Schlieren montage of close-up images at 80, 104 and 120 μs after shock impingement
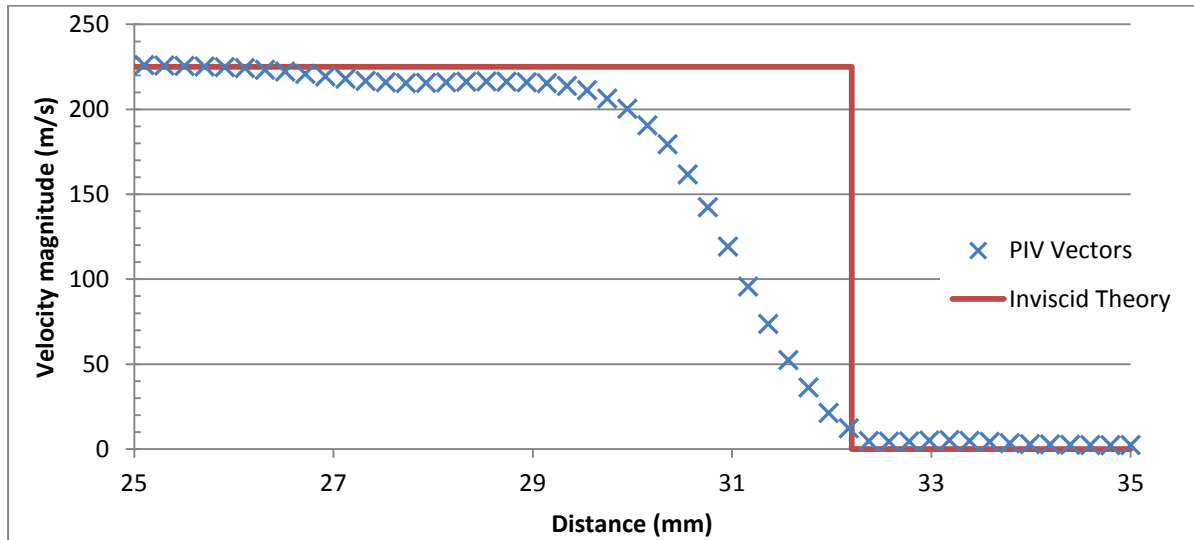
Particle Image Velocimetry

Figure 13. Shock front measurements from PIV

The PIV experiments that were conducted allowed us to use not only the vector map created, but also the raw images as a form of laser sheet visualisation. Achieving uniform seeding in PIV is a challenge in itself, but combining that with a very strong vortex means that there will inevitably be some holes in the vector. The two places where this problem is especially significant are inside the main vortex core and underneath the shear layer in the expansion region. Figure 13 shows the comparison between inviscid theory and PIV measurements of the incident shock wave. The planar incident shock front is resolved by the PIV measurements but is spread across 2.8mm (up to 95% induced velocity). This compares well with the shock spread estimated using Melling's theory [12] modified for moving shock waves, which gives 2.3mm.

The velocity vector plots presented in Figure 14 are a grid of 400x300 vectors at the same resolution as the numerical simulations shown in Figure 8. Despite the challenges mentioned above, there is excellent agreement between the numerical and experimental velocity vector plots. The curvature of the shock front is captured well and the influence of the reflected sound wave is also noticeable, as the flow now has a y-component in that region. The expansion region is shown to be accelerating the flow to supersonic speeds and there is no sign of the effect of the lambda structures seen in the experimental schlieren results. The absolute magnitude of the velocity is approximately 20m/s lower than the simulations in the expansion region. This is to be expected, as PIV will naturally underpredict the magnitude of a change in velocity, whether it be an increase or a decrease. As the diffracted shock wave reflects off the top wall of the test section, the flow is decelerated and begins to spread out, agreeing well with the simulations. The exact location of the reflected shock front is difficult to see in these images due to their small scale, but it is visible at higher zooms. Even if uniform seeding were possible around the vortex region, the grid resolution of the PIV measurements is too low to accurately resolve the instabilities seen on the shear layer.

The raw PIV images can be used as laser sheet visualisation to give a qualitative description of some of the flow features. Figure 15 shows one image from the pair of images used to create the vector plots seen in Figure 14, at each time step. From looking at Figure 15, we can see that the seeding density is not uniform everywhere in the domain. Despite this, there are some seeder particles in regions where there appear to be none, which have allowed the cross correlation algorithm in the PIV software to calculate velocity vectors. The most noticeable thing about these images is how well the shear layer appears to entrain seeder particles. As the nanoparticles have inertia, they are ejected from the vortex core of the main vortex. The particles are also ejected from the vortex cores of the K-H instabilities on the shear layer, creating an outline of them. Figure 15 d, e and f show the outline of the K-H instabilities found on the shear layer. This technique resolves the instabilities more clearly than any other experimental technique.
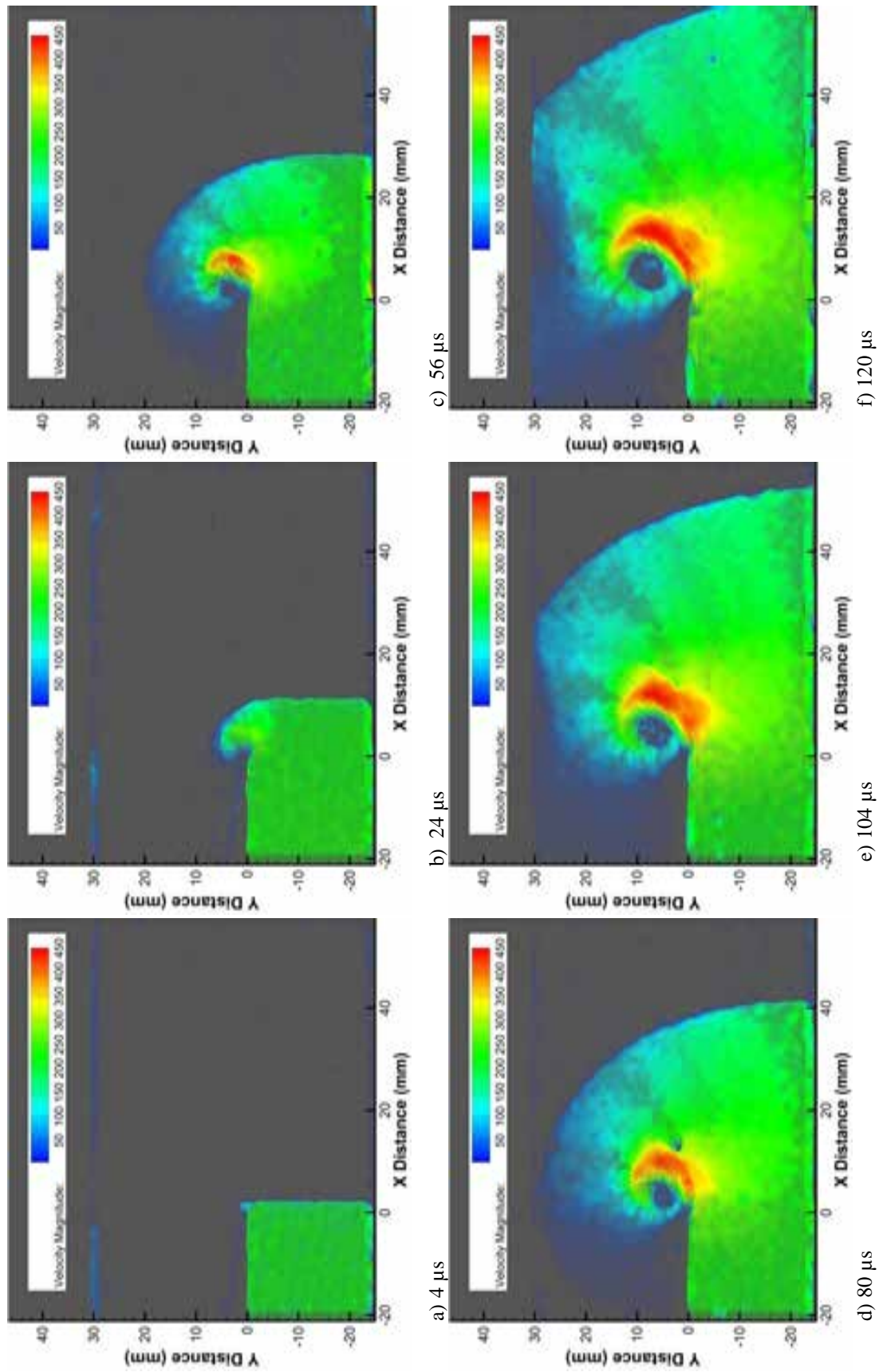
c) 56 μs

f) 120 μs

b) 24 μs

e) 104 μs

a) 4 μs

d) 80 μs

Figure 14. PIV velocity vector plots at different time steps

c) 56 μs

f) 120 μs

b) 24 μs

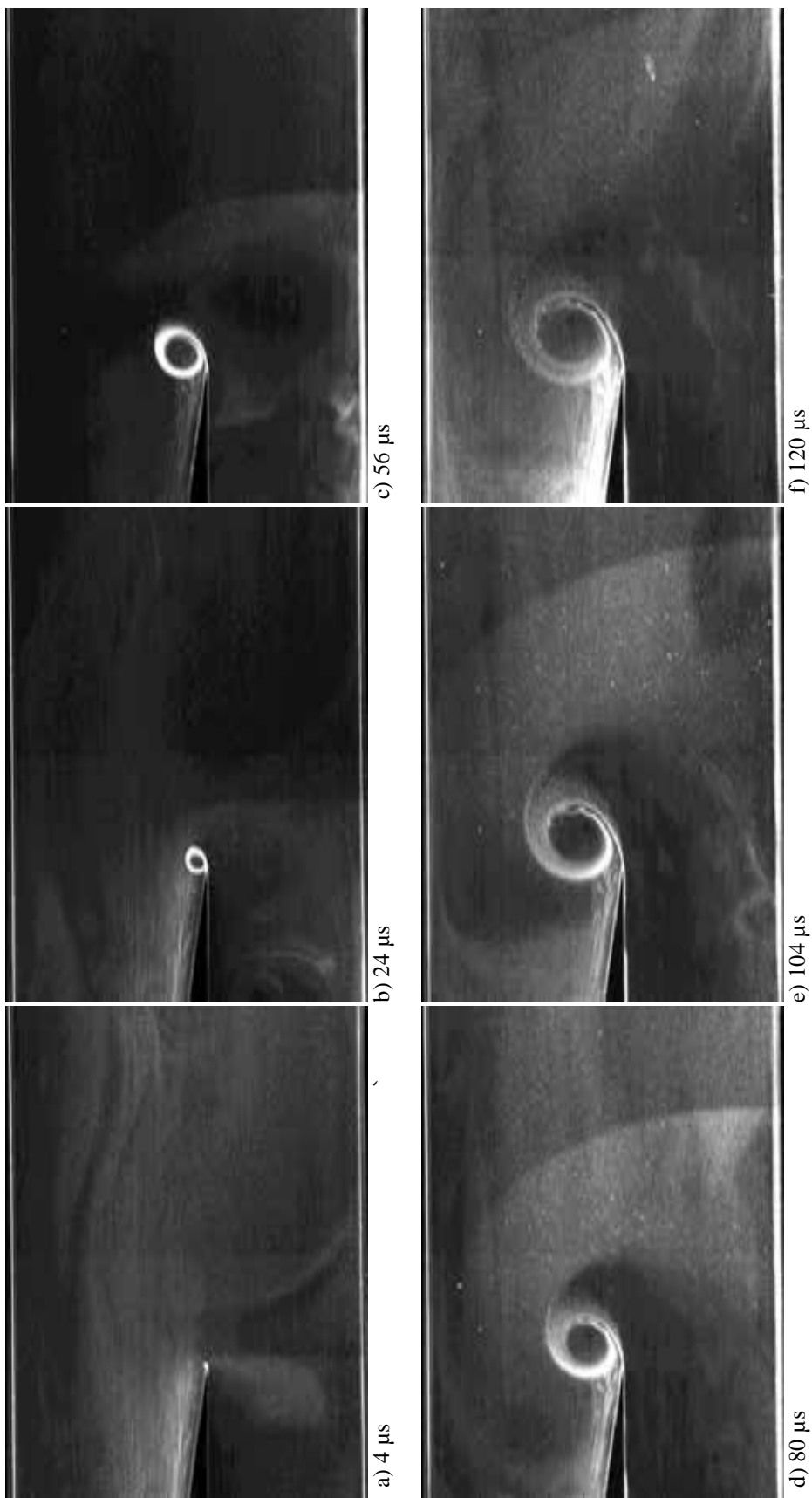e) 104 μs

a) 4 μs

d) 80 μs

Figure 15. Laser sheet visualization from Raw PIV images at different time steps

Conclusion

Shock wave diffraction of a M_i=1.46 shock wave has been investigated using simulations and a variety of experimental techniques. The numerical simulations, performed by a commercial CFD package, show a wide range of flow features. However, some of the flow features were only present if the grid was fine enough to resolve them; in particular, the K-H instabilities on the shear layer. Despite the fine grid resolution, some flow features were underpredicted. The lambda wave structures underneath the shear layer are very poorly resolved in the simulations; this appears to be dependent on the grid adaption scheme used. Numerical schlieren and velocity vector plots have been generated for direct comparison with the experiments performed.

High-speed schlieren measurements have been performed using the Shimadzu HPV-1 camera. These images, taken at a large magnification, provided a good spatial and temporal resolution. Both are essential for a complete understanding of such a transient flow. The experimental schlieren results have shown a large number of lambda wave structures underneath the shear layer which have not been resolved in simulations or using any other experimental technique. The schlieren images (particularly at the highest zoom) appear to show instabilities on the shear layer, but these images are compelling enough evidence to say that all of the flow features are resolved correctly. PIV measurements have been performed in a spark fashion in order to gain velocity vector plots for comparison with CFD. The PIV vectors resolve the shock front adequately but tend to underpredict changes in velocity such as those found in the expansion region under the shear layer. PIV measurements are extremely tricky in the vicinity of strong vortices, as particles are ejected from the vortex core. This is an unavoidable problem, unless one can find particles with zero inertia. However, the inertia characteristics of the particles outline any vortices in the flow-field, and using raw PIV images as laser sheet visualisation allows us to see more convincing evidence of the presence of K-H instabilities on the shear layer.

From this work we can see that CFD can resolved the majority of the flow features (if the grid is fine enough); however, there are some that it fails to resolve. The same is true of schlieren and PIV. When used independently, these techniques give a good understanding of the flow but not a complete picture. When these methods are combined, all of the flow features can be resolved, giving us a complete understanding.

References

[1]   B. W. Skews, "The Perturbed Region Behind a Diffracting Shock Wave," *Journal of Fluid Mechanics,* vol. 29, pp. 705-719, 1967.

[2]   M. Sun and K. Takayama, "Vorticity Production in Shock Diffraction," *Journal of Fluid Mechanics,* vol. 478, pp. 237-256, 2003.

[3]   K. Takayama and Y. Inoue, "Shock Wave Diffraction over a 90 degree Sharp Corner," *Shock Waves,* vol. 1, pp. 301-312, 1991.

[4]   M. Sun and K. Takayama, "A Note on Numerical Simulation of Vortical Structures in Shock Diffraction," *Shock Waves,* vol. 13, pp. 25-32, 2003.

[5]   S. De and M. Thangadurai, "Numerical Simulation of Shock Tube Generated Vortex Effect of Numerics," *International Journal of Computational Fluid Dynamics,* vol. 25, pp. 345-354, 2011.

[6]   T. I. Tseng and R. J. Yang, "Numerical Simulation of Vorticity Production in Shock Diffraction," *AIAA Journal,* vol. 44, pp. 1040-1047, 2006.

[7]   B. W. Skews*, et al.*, "Shear Layer Evolution in shock Wave Diffraction," in *28th International Symposium on Shock Waves*, Manchester, UK, 2011.

[8]   B. Skews*, et al.*, "Shear layer behavior resulting from shock wave diffraction," *Experiments in Fluids,* vol. 52, pp. 417-424, 2012.

[9]   G. Abate and W. Shyy, "Dynamic Structure of Confined Shocks Undergoing Sudden Expansion," *Progress in Aerospaces Sciences,* vol. 38, 2002.

[10]   R. Mariani and K. Kontis, "Experimental studies on coaxial vortex loops," *Physics of Fluids,* vol. 22, p. 126102, 2010.

[11]   M. K. Quinn*, et al.*, "Experimental Studies of Shock Wave Diffraction," in *28th International Symposium on Shock Waves*, Manchester, UK, 2011.

[12]   A. Melling, "Tracer Particles and Seeding for Particle Image Velocimetry," *Measurement Science and Technology,* vol. 8, pp. 1406-1416, 1997.

[13]   M. Sun and K. Takayama, "The Formation of a Secondary Wave Behind a Shock Wave Diffracting at a Convex Corner," *Shock Waves,* vol. 7, pp. 287-295, 1997.

[14]   M. M. Biss*, et al.*, "High-speed digital shadowgraphy of shock waves from explosions and gunshots," in *26th International Symposium on Shock Waves*, Gottingen, Germany, 2007.

[15]   M. K. Quinn and K. Kontis, "Experiments and Simulations of Weak Shock Wave Diffraction Phenomena," presented at the 20th International Shock Interaction Symposium, Stockholm, Sweden, 2012.

Wind Tunnel and CFD Studies on Production of Prebiotic Materials in Hypersonic Flow around Extraterrestrial Entry Object

Kojiro Suzuki*
Yasumasa Watanabe**

* Department of Advanced Energy, Graduate School of Frontier Sciences
The University of Tokyo
Kashiwa, 277-8561
Japan
kjsuzuki@k.u-tokyo.ac.jp
** Department of Aeronautics and Astronautics, Graduate School of Engineering
The University of Tokyo
Bunkyo, 113-8656
Japan
watanabe@daedalus.k.u-tokyo.ac.jp

Abstract

To investigate the possibility of prebiotic materials formation in high temperature shock layer around an ablating icy object entering the early earth's CO_2/N_2 atmosphere, the cooperative research of the CFD and EFD has been conducted. The thermo-chemical nonequilibrium Navier-Stokes analysis shows that HCN is efficiently produced in the stagnation region and transported into the atmosphere by the wake flow. To simulate such process experimentally in the hypersonic air flow of the wind tunnel, the experimental model composed of the ablative nose part made from water ice and dry ice to supply the C and H elements and the after-body having the electric discharge circuit in it to supply the energy necessary for chemical reactions has been designed, based on the CFD results. We observed the emission from CN in the wind tunnel, and better understanding about the phenomena is expected by comparison with the CFD analysis.

Key words: atmospheric entry, hypersonic flow, chemical reaction, ablation, ice, wind tunnel, CFD

Introduction

Frequent entries of extraterrestrial objects into the early earth's atmosphere are expected to have supplied the materials and energy necessary for forming the present earth [1]. Various chemical products in the high temperature shock layer flow over the ablating surface of an entry object were distributed into the atmosphere through the wake flow. In the present study, we consider the atmospheric entry of an icy object, because the water is one of the most common materials in the universe and it seems reasonable that such entry objects were mainly composed of the water ice. The Navier-Stokes analyses with the thermo-chemical nonequilibrium of the C-H-O-N 28 species show that Hydrogen Cyanide (HCN), which is one of the most important prebiotic materials, is efficiently produced near the surface in the stagnation region of an icy object entering the early earth's CO_2/N_2 atmosphere with the ablation injection of H_2O, and is transported into the atmosphere behind the object in almost frozen chemistry [2]. HCN is known to be significantly related to the production of amino acids. For example, adenine $C_5H_5N_5$, which is one of the bases of DNA [1], can be formed from 5 HCN's. If HCN had been efficiently produced in the high-temperature shock layer flow over ablating icy objects and supplied to the atmosphere through their wake flows, HCN from the hypersonic flow may have augmented the formation of biomolecules on the early earth.

To observe the behavior of an ice piece in hypersonic flow, the experimental studies have been conducted by the authors' research group at the hypersonic and high-enthalpy wind tunnel of Graduate School of Frontier Sciences, the University of Tokyo [3,4]. It was clearly seen that the ablation process with the phase change among vapor, water and ice at the surface plays an essential role in the phenomena of an icy object in hypersonic flow. When we put a spherical piece of water ice into the hypersonic flow at Mach number 7, the ice is melting in the stagnation region due to the severe aerodynamic heating and the surface recession significantly occurs there. On the other hand, in the shoulder region of the ice piece, the flow temperature rapidly decreases due to the strong expansion. Consequently, the vapor and/or liquid of water coming from the melting icy surface in the stagnation region are re-frozen into columns of solid ice there. The stack of such icy columns forms a complicated icy structure, which looks like the brim of a hat. As a result, the maximum diameter of the ice piece, as well as the drag force acting on it, is increasing with the exposure time in the flow until the fragmentation of icy columns due to the aerodynamic load. A typical image of such brim-like structure of ice is shown in the insert at the upper left corner of Fig. 1.

In the above process of the brim-like structure formation, a question arises: Which phase of water is transported from the stagnation region to the shoulder region, vapor (gas) or liquid? To answer to this question, we consider the phase diagram on the temperature-pressure plot shown in Fig. 1. In the experiment, the maximum available stagnation pressure (P0) and temperature (T0) are 0.95 MPa and 1000 K, respectively. The local pressure can vary from the order of 0.1 kPa (freestream condition level) to the order of 10 kPa (stagnation-point level), and the local temperature can vary from 70 K to 1000 K as indicated by a tinted area in the figure. As for the ablation process, the variation of the pressure and temperature on the surface is essential. To estimate the surface temperature of the ice piece, the use of the infrared (IR) camera is useful, because the water efficiently absorbs IR light and the black body model is applicable for water ice. A typical IR camera image is shown as an insert at the upper right corner of Fig. 1. We found that the surface temperature is kept in the range of 273-283 K during the exposure in the hypersonic flow thanks to the latent heat of the ablation. For measurement of the surface pressure over an ablating object, however, the efficient experimental technique is not available. To estimate the surface pressure, the CFD analysis of the Navier-Stokes equations is conducted for the body shape, which is determined from an instantaneous image of an ice piece in the flow as shown in the insert at the lower right corner of Fig. 1 [5]. In this case, the surface pressure is estimated to vary from 1kPa to 15 kPa. Finally we can indicate the variation of the temperature and pressure on the surface of the ablating ice piece in the flow of the hypersonic wind tunnel on the phase diagram as shown in Fig. 1. Under the assumption of the thermodynamic equilibrium, it is expected that the liquid water is transported over the surface from the stagnation region to the shoulder region. This may be a good example, in which the cooperation of CFD (Computational Fluid Dynamics) and EFD (Experimental Fluid Dynamics) can reveal the unknown mechanism of complicated phenomena.

The cooperation of CFD and EFD is also expected to play an important role in consideration of the chemical reaction process around an icy object entering the early earth's atmosphere. The hypersonic wind tunnel is a very powerful tool to simulate and observe the shape change process due to ablation. As seen in the above, the process is too complicated to be simulated by the self-consistent CFD analysis, where both the shape change due to the ablation and the flow field around the body are simultaneously solved in a coupled manner. However, the ability of the wind tunnel facility to simulate the chemical reaction process around an icy entry object is quite limited. The impulse-type flow facility, such as a high-enthalpy shock tunnel, can produce gas flow at temperature high enough to excite the chemical reactions, but the test duration is too short to obtain the ablation around the body, which occurs in the time scale of seconds. On the other hand, the long duration facility like a blow-down-type wind tunnel can supply hypersonic flow for the test time long enough to observe the ablation process as shown in Fig. 1. However, the stagnation temperature is not high enough to excite the chemical reactions. In the present study, we have tried to use the hypersonic wind tunnel to simulate the chemical reactions around an icy entry body as well as its shape change due to ablation. To excite the chemical reactions in the flow of the hypersonic wind tunnel at the stagnation temperature less than 1000 K, the energy is locally added by the electric discharge. To develop such sophisticated experimental technique and to understand the obtained results, the cooperative approach of CFD and EFD is indispensable. In addition, the CFD analysis is necessary to predict the actual phenomena around an icy object at atmospheric entry from the phenomena observed in the hypersonic wind tunnel experiment.

The major objectives in the present study are 1) To consider the possible chemical reaction process of the HCN formation around an icy object entering the early earth's atmosphere by the chemical nionequilibrium CFD

analysis, 2) To predict the chemical reaction phenomena around an ice piece in the hypersonic wind tunnel flow with local energy addition by the electric discharge, 3) To design the experimental model based on the CFD results, and 4) To assess the usefulness of such experimental technique to simulate the chemical reactions in relation to the formation of the prebiotic materials around an icy entry object by the comparison between the CFD and EFD results.
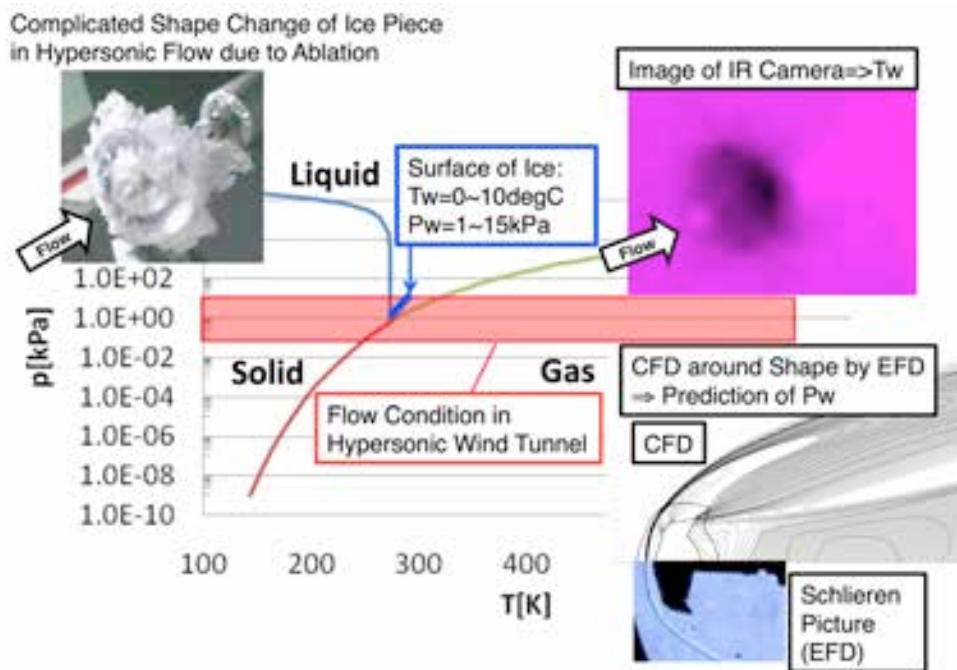

Fig. 1 Phase Diagram of Water and Ablation Process of Ice Piece in Hypersonic Wind Tunnel Flow

Chemical Reaction Process of Prebiotic Materials Formation around Icy Object

In this chapter, the chemical process of the production of HCN around an icy object entering the early earth's atmosphere and the results of the numerical analysis solving the Navier-Stokes equations with the nonequilibrium chemistry are briefly summarized based on Ref. [2].

The atmosphere of the early earth is thought to be similar to that of Mars of today and mainly composed of CO_2 and N_2. The chemical species to be considered for the hypersonic flow in the early earth's atmosphere with the ablation injection of H_2O from the icy surface of an extraterrestrial entry object will be almost the same as those to be considered for the hypersonic flow in the air (N_2 and O_2) with the gas injection from the CFRP ablator of the re-entry vehicle. Consequently, the chemical reaction model for the analysis of the ablator can be also used for the present study with small modification. The chemical reactions considered here consist of those of the 11-air-species (N_2, O_2, N, O, NO, NO^+, e^-, N^+, O^+, N_2^+, O_2^+) model, the reactions related to the carbon-containing species (C, C_2, C_3, CO_2, CO, CN, CO^+, C^+) and those of the carbon-nitrogen-oxygen-hydrogen species (H, H_2, HCN, HCO, C_2H_2, C_2H, CH, H_2O, OH). The detail is given in Ref. [2]. The thermal nonequilibrium is also considered with the two-temperature model of the translational-rotational temperature (T) and the vibrational-electronic-elctron temperature (T_v). The hybrid form of the conservative and nonconservative form equations for the axi-symmetric Navier-Stokes equation with the thermal and chemical nonequilibirum are numerically solved by using the symmetric TVD scheme for the convective terms. The non-conservative form equations are used for the nonequilibirum quantities, that is, the vibrational temperature and the mass fractions of the chemical species, because there is no discontinuity across the shock wave for these quantities.

In the present study, the ablation injection at the surface must be considered. Assuming that the surface of ice is non-catalytic, the mass fraction of the i-th species is determined by Eq. (1) that describes the mass conservation at the surface:

$$-D\frac{\partial C_i}{\partial n} + \rho\, C_i\, v_w = J_i \,, \tag{1}$$

where C_i, D, ρ, v_w and J_i are the mass fraction of the i-th species, the diffusion coefficient, the density of gas mixture, the injection velocity and the ablation injection rate of the i-th species, respectively. The outward normal velocity at the wall is calculated as:

$$v_w = (\sum_i J_i)/\rho_w \cdot \tag{2}$$

The process of the HCN production is schematically illustrated in Fig. 2. In the present model, HCN is produced only by the reaction of CN and H_2. CN is supplied by the reactions involving the species in the freestream. H_2 is supplied by the reactions from H_2O. Consequently, HCN is expected to be produced in the vicinity of the wall in the forebody region, where the flow temperature is high enough to excite the chemical reactions. For HCN produced in the stagnation region to remain in the downstream region including the wake flow, the frozen chemistry must be sustained both in the shoulder region and in the wake region.

Figure 3 shows the typical results of the mass fraction of HCN around an icy entry object. The velocity and altitude are 8 km/s and 60 km, respectively. The atmospheric properties of the early Earth are assumed to be the same as those at present except the freestream composition as CO_2:N_2=0.93:0.07 by mass. The nose radius is 0.2m. The wall temperature is 273 K and the ablation injection rate of H_2O is uniform only on the forebody surface at 0.05 kg/m²s. The upper half in the figure is the result of the laminar flow calculation, and the lower half is the result of the turbulent wake with the empirical mixing length model [6] and the turbulent Lewis number of 1.0. The computation is done on the 101X101 grid. Considering the pattern of the contour lines in Fig. 3, the main source of HCN exists in the vicinity of the surface in the stagnation region, and HCN spreads downstream by the advection and diffusion. To evaluate the extent of HCN production, the HCN production efficiency is defined as the ratio of the mass flux of HCN flowing out of the computational domain to the total ablation injection rate over the surface. In this case, the HCN production efficiency is 1.7X10⁻⁴, which means the loss of an icy entry object of volume 1 m³ results in the HCN production in the order of 0.1 kg. This number is not negligible. In Fig. 3, we assume a spherical icy object. As seen in the hypersonic wind tunnel experiments (Fig. 1), however, the shape after ablation is quite complicated, though the initial shape is sphere. To investigate the effect of the instantaneous shape of the ablating icy object on the chemical reaction, the CFD analysis is conducted for the forebody with the non-smooth shape as shown in Fig. 4. The freestream and ablation injection conditions are the same as in Fig.3. The result shows that the HCN production efficiency is hardly affected by the shape of the body.
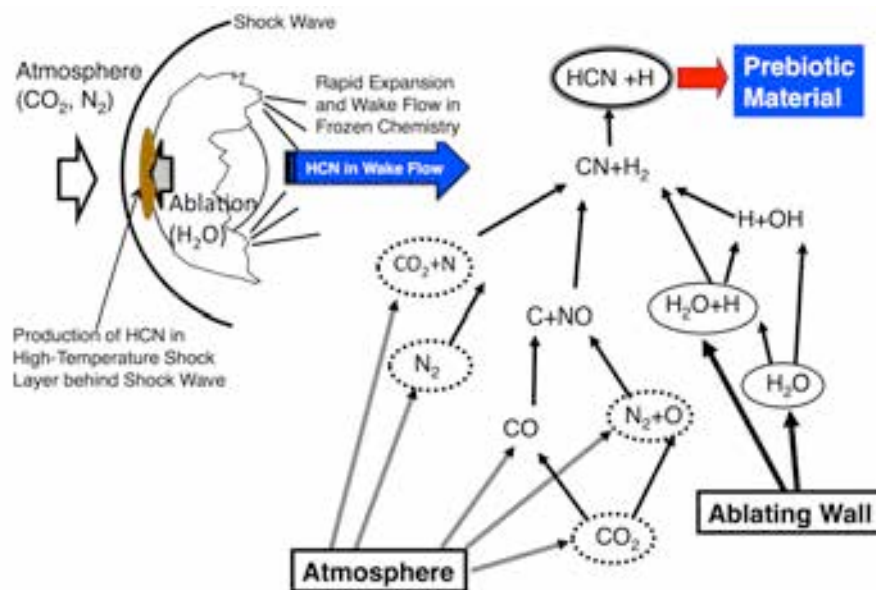

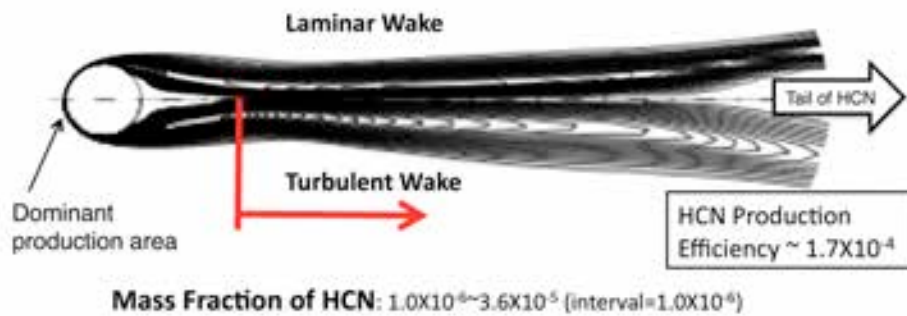**Fig. 2 Chemical Reaction Process of HCN Production in the Present Analysis Model**

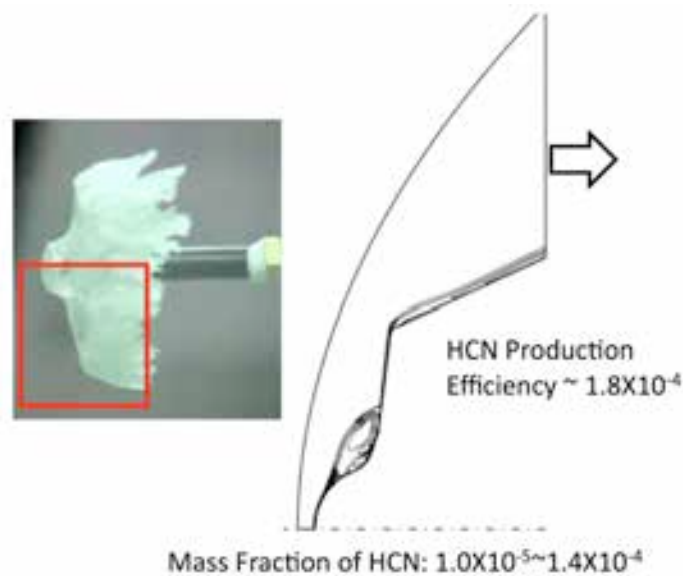**Fig. 3 Typical CFD Result on HCN Production**

Fig. 4 CFD Results of HCN Production over Icy Body with Non-smooth Shape

Design of Experimental Model

Based on the results of the CFD analyses, the reasonable setup of the experimental apparatus is discussed in this chapter. The experiments are carried out at the hypersonic and high enthalpy wind tunnel in Kashiwa campus, the University of Tokyo [7]. The maximum available stagnation temperature (T0) and pressure (P0) are about 1000 K and 0.95 MPa, respectively. The diameter of the nozzle exit is 200 mm, and the uniform flow at Mach number 7.0-7.1 is obtained in the region with 120 mm diameter around the nozzle axis. In the case of a spherical model, the maximum diameter is limited to about 40 mm due to the blockage of the flow. When the hot shut-off valve opens, the flow starts, and the model is injected into the flow after the quasi-steady flow condition has been settled. Due to the nature of the pebble-bed-type heater installed in this facility, the stagnation temperature still continues to increase gradually at slow rate of 1 K/s. The maximum available test time is about 60 s after the hot shut-off valve opens.

The extent of the chemical nonequilibirum is evaluated well by the binary scaling parameter, which is defined as the product of the freestream density and the reference length [8]. In the present cases, the reference length is the diameter of an icy object. Figure 5 shows the variations of the binary scaling parameter with the altitude for various diameters. The range of the binary scaling parameter available in the wind tunnel is also indicated by the tinted area in the figure. The experimental flow condition here is equivalent to the atmospheric flight of an entry object with 0.1-1 m diameter at 50-70 km altitude, where the significant thermo-chemical nonequilibrium is expected.

To discuss the appropriate location of the energy addition by the electric discharge, the CFD analyses explained in the previous chapter have been made, assuming the laminar axi-symmetric flow. In the case of the early earth's atmosphere, the freestream composition is the mixture of CO_2 and N_2. In the wind tunnel experiment, however, the air (N_2 and O_2) is only available as the freestream composition. To simulate the production of HCN, some mechanism to supply the carbon and hydrogen elements must be intendedly installed. To supply C and H into the flow, we use the ablation of the experimental model. The shape of the experimental model is a hemispherical cylinder. The hemispherical nose is made from the mixture of dry ice and water ice. When the model is injected in to the hypersonic flow, the ablation occurs in the nose part and the carbon and hydrogen elements are automatically supplied into the flow of N_2 and O_2 by ablation. Consequently, the chemical reactions involving C, H, O, N elements including the production of HCN become possible. The after-body is made from non-ablative ceramic material and works as the model support having the circuit of the electric discharge in it. Because the effect of the nose shape on the production of HCN is not so significant as seen in Fig. 4, a simple hemispherical shape is selected for the nose of the model.

First, we assume the electric discharge in the stagnation region, where the flow is slow and various chemical reactions are expected to be excited. The 161X171 grid for the CFD study is shown in Fig. 6. Figures 7 and 8 show the result of the CFD analysis. The freestream Mach number, P0 and T0 are 7.0, 0.95 MPa and 1000 K, respectively. The energy addition by the electric discharge is described by the source term in the equation of the viblational temperature. After the energy of the electric discharge is absorbed in the vibrational mode, the translational temperature will be raised by the translational-vibrational energy exchange. The uniform energy addition is assumed in the very thin region with 5 mm diameter around the model axis and the thickness of 1 mm from the surface, because the Joule heating of the electric discharge is expected to be confined in the sheath region. In this case, the total heat input is 500 W, which is available by the power source used in the experiment, and the density of the energy addition is 7×10^9 W/m^3. The uniform ablation injection is assumed at 0.1 kg/m^2s over the hemispherical nose. The mixture ratio is CO_2:H_2O=1:1 by mass. No ablation occurs in the region of the energy addition, because the electrodes are placed there. The distributions of the translational and vibrational temperatures are shown in Fig. 7. The maximum vibrational temperature is estimated as about 8800 K in the stagnation region. That is high enough to excite the chemical reactions of C, H, O and N. On the other hand, the translational temperature is much smaller than the vibrational temperature. Figure 8 shows the distribution of the mass fraction of HCN. In this case, the production of HCN is negligible, because the ablation injection occurs in the downstream of the energy addition, and the C and H elements are supplied to the region of high vibrational temperature only by the diffusion. Consequently, the stagnation region is not appropriate for the place of the electric discharge.

Based on the above discussion, the design of the experimental model is determined as shown in Fig. 9. The body is composed of two parts: The nose part is made from the mixture of water ice and dry ice in the hemispherical mold. The rear part is made from ceramic. The electric discharge circuit is designed based on our previous study on the plasma discharge on a flat plate [9, 10]. On the side surface, the electrodes are installed as shown in the figure, and are connected to the power supply system. For stable electric discharge, the cathode is set upstream of the anode. The electric power system is a combination of the high power supply (max. 500V, max. 6A) and the high voltage one (max. 1kV, max. 200 mA). To stabilize the plasma discharge, the high voltage power supply is switched on to ignite the plasma discharge again, when the plasma becomes weak and the current drops. After the model is injected into the hypersonic flow, the ablation occurs over the surface of the nose part, and CO_2 and H_2O are injected into the flow. The ablation injection rate is estimated from the surface recession rate, which can be determined from the temporal variation of the nose shape captured by the video camera.
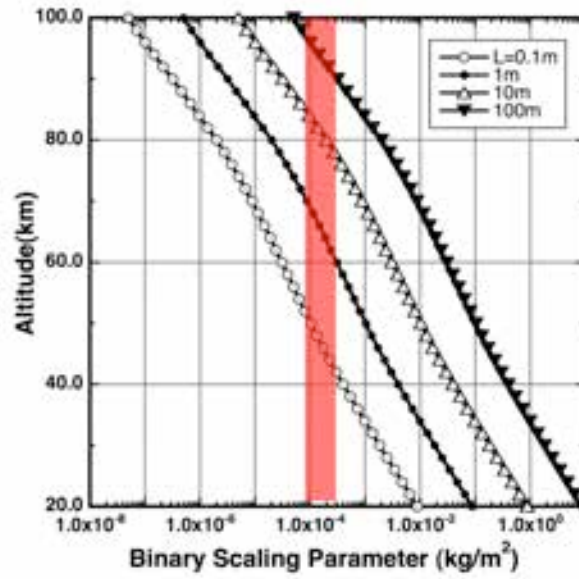
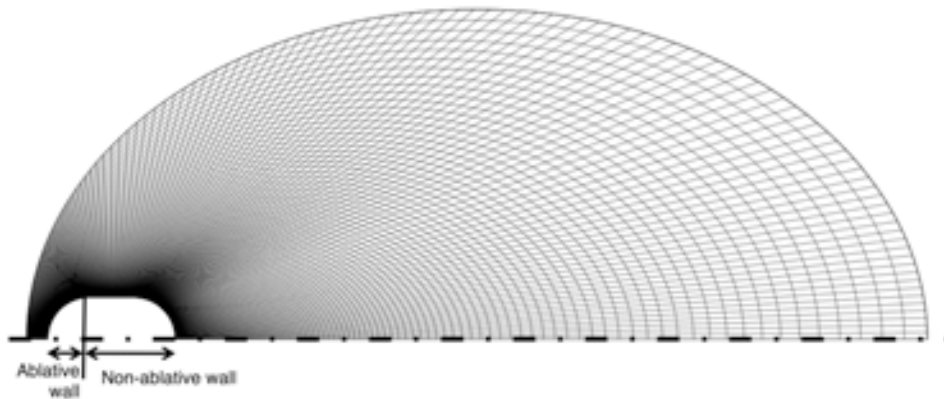**Fig. 5 Binary Scaling Parameter at Entry Flight and at Wind Tunnel Experiment**

Fig. 6 Computational Grid for CFD Analysis
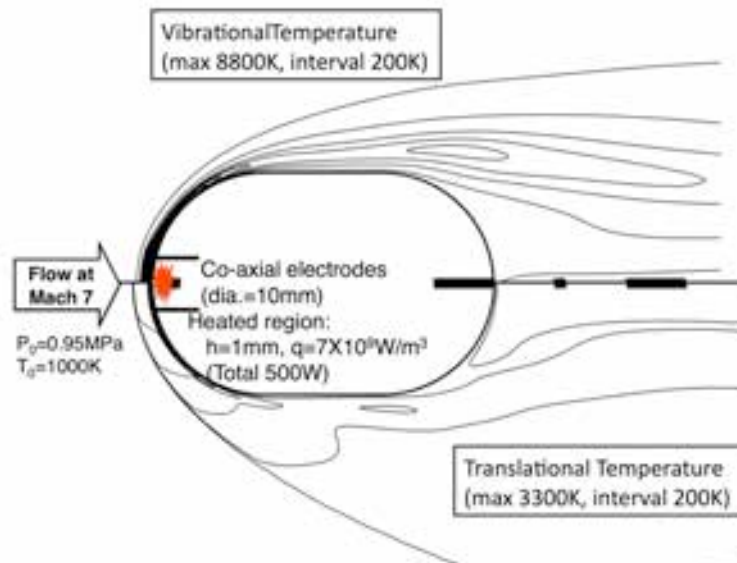

Fig. 7 Translational and Vibrational Temperatures by CFD in Case of Electric Discharge in Stagnation Region
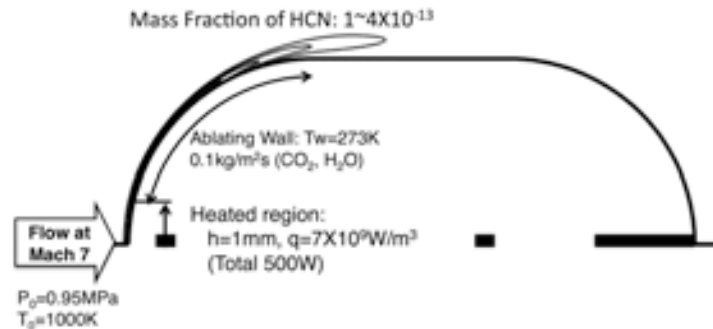
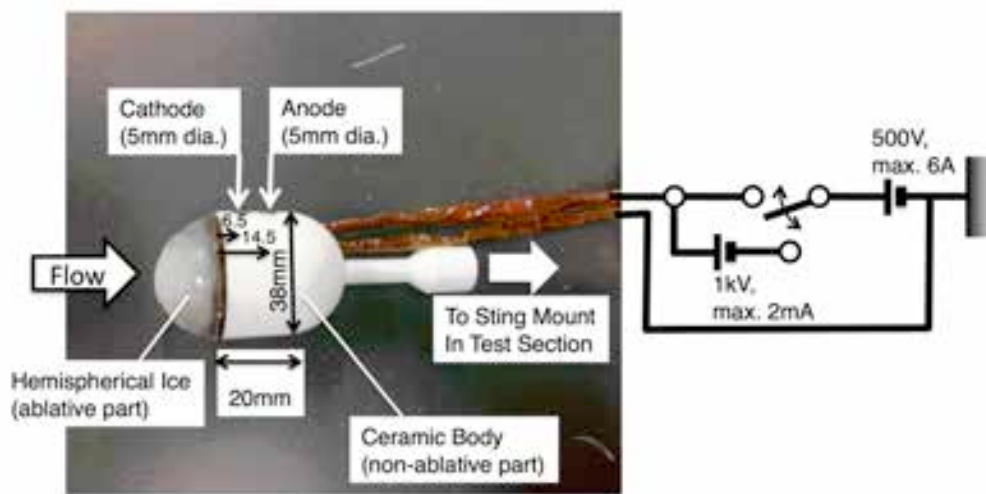**Fig. 8 Mass Fraction of HCN by CFD in Case of Electric Discharge in Stagnation Region**

Fig. 9 Experimental Model with Electric Discharge on Side Surface

Results and Discussion

Using the experimental model shown in Fig. 9, the hypersonic wind tunnel experiment was carried out. Figure 10 shows the snapshots of the normal video and schlieren video. Strong light emission is seen around the location of the electric discharge. P0 and T0 of the flow are 950 kPa and 600-650 K, respectively. The input power is about 100 W. When the stable discharge has been established, the voltage between the cathode and anode drops to 10-20 V. The nose part is made from the mixture of water ice and dry ice. From the recession rate of the nose surface taken by the video camera, the ablation injection rates of H_2O and CO_2 are roughly estimated as 0.05 kg/m^2s and 0.05 kg/m^2s, respectively. It should be noted that the shock wave shape in the schlieren image seems almost symmetric with respect to the centerline, though the discharge occurs only on the upper side. In this case, the energy addition by the electric discharge hardly affects the formation of the shock wave.

To deepen our understanding on the phenomena seen in Fig. 10, especially from a viewpoint of the chemical reactions, the thermo-chemical nonequilibirum CFD analysis has been conducted. Though the phenomena in the experiment are three-dimensional due to the arrangement of the electrodes, we assume the axi-symmetric flow as the preliminary analysis. The pressure distribution of the CFD result is shown in Fig. 11. The zone of energy addition is set on the cylindrical part of the body. The input power density is uniform at $3X10^9 W/m^3$. This is equivalent to the heat input of 100 W in a region of 3mm width, 1mm height and 10 mm length. It is confirmed by the CFD that the shock wave shape is hardly affected by the energy addition. Figure 12 shows the distributions of the translational temperature and vibrational temperature. The vibrational energy of the flow is excited up to 12500 K in the vicinity of the electric discharge. The translational temperature is also raised up to 4000 K by the translational-vibrational energy exchange there. These values are in the same order as in the stagnation region at the actual atmospheric entry flight. Various chemical reactions are expected in the discharge

region in the similar way to the stagnation region of the entry object. Figure 13 shows the distributions of the mass fractions of CN and HCN. Though their quantities are quite small, the CFD result indicates that these species will be formed over the region of the electric discharge and remain in the downstream flow.

From a viewpoint of the possibility of the prebiotic materials formation in high temperature shock layer flows, the presence of HCN should be directly confirmed in the wind tunnel flow. Unfortunately, HCN does not have the light emission of the wavelength in the visible range. In the present study, we observe the light emission of CN, because CN is a reactant of the production of HCN as shown in Fig. 2. The image through the band pass filter of 382-398 nm, which includes the wavelength of the light emission of CN, is shown in an insert of Fig. 14. The presence of the luminous spot indicates the formation of CN there, and, as a result, suggests the formation of HCN in the hypersonic flow. In general, the intensity of the emission becomes stronger in the region at higher vibrational temperature and larger number density of the species. Roughly speaking, the intensity of the emission from CN will be in proportion to $I=T^{m}T_{v}^{n}\rho_{CN}$. The contour lines of I from the CFD result are shown in the lower half of Fig. 14. The exponent m and n are set as 0 and 4, respectively. A similar pattern is obtained in comparison with the experimental image through the band pass filter. Consequently, the presence of CN in the flow is also supported by the CFD. Of course, the present discussion is based on very rough model for the phenomena. For further consideration, more precise heat input model for the electric discharge, detailed computational radiation emission analysis based on the line-by-line method, consideration of the three-dimensionality of the phenomena and so on are necessary.
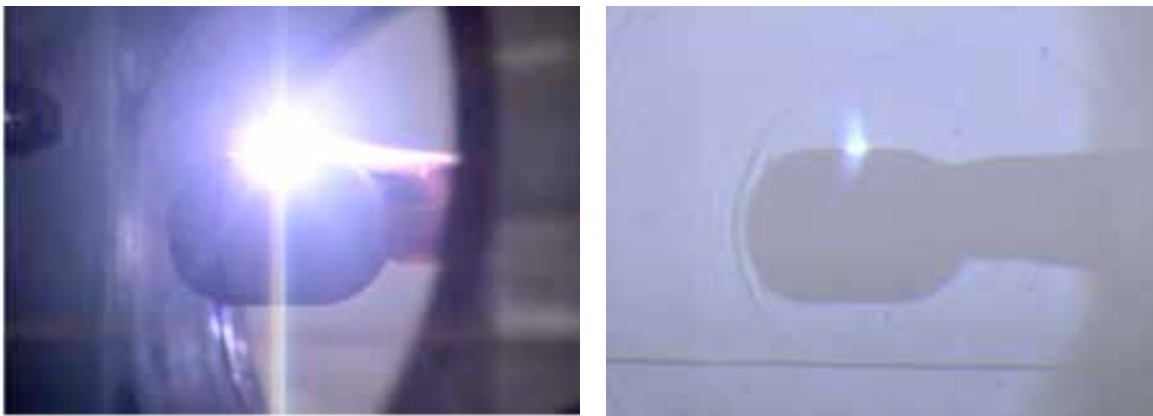
Fig. 10 Snapshots of Normal Video (left) and Schlieren Video (right) of Model in Hypersonic Flow with Electric Discharge
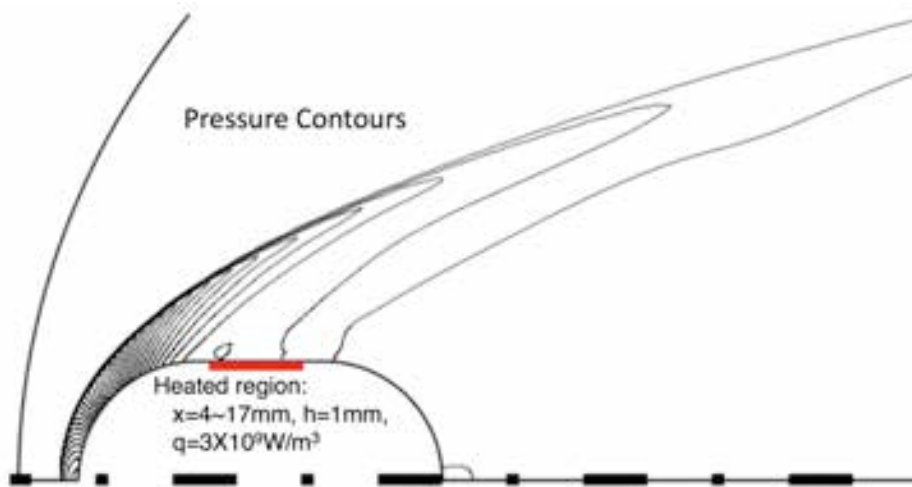

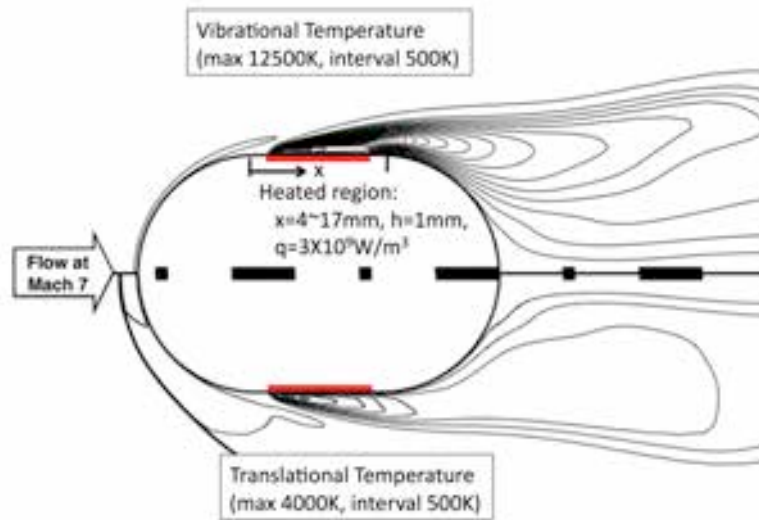**Fig. 11 Pressure Distribution by CFD for Experimental Condition**

Vibrational Temperature
(max 12500K, interval 500K)

Heated region:
x=4~17mm, h=1mm,
q=3X10⁹W/m³

Flow at
Mach 7

Translational Temperature
(max 4000K, interval 500K)

Fig. 12 Translational and Vibrational Temperatures by CFD for Experimental Condition

Mass Fraction of CN: 1~6X10⁻⁹

Mass Fraction of HCN: 0.1~1.8X10⁻¹⁰
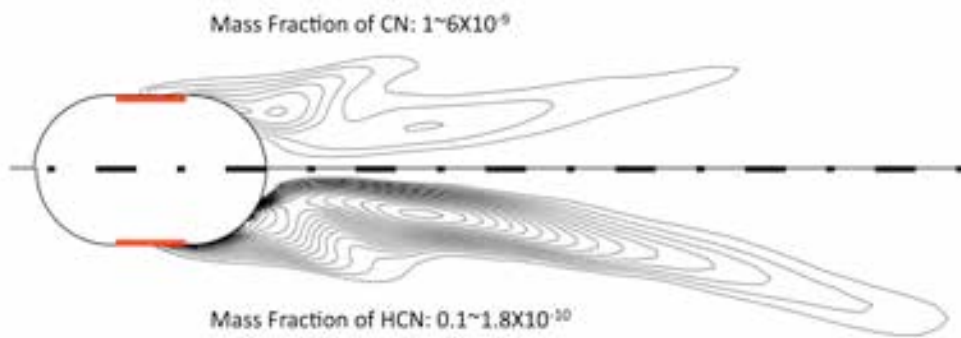
Fig. 13 Mass Fraction of HCN and CN by CFD for Experimental Condition

EFD

Schlieren Picture

Shock Wave

Air (N_2, O_2)

Flow at
Mach 7

P_0=0.95MPa
T_0=1000K

■ Heat Addition 3X10⁹ W/m³

■ Ablating Wall: Tw=273K
0.1kg/m²s (CO_2, H_2O)

⇐ Insert:
Filter (382-398nm)

anode
cathode

CFD

$Emission\ I \sim n_{CN} T_V^4$
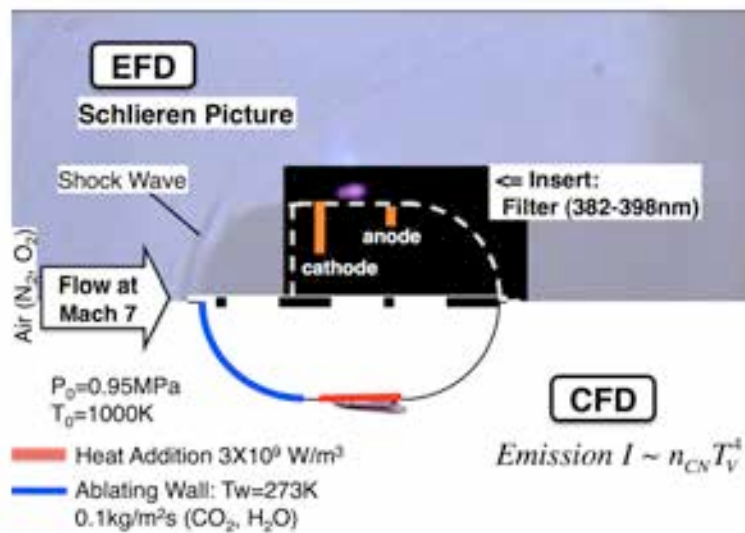
Fig. 14 Comparison between Experimental Picture of CN Emission and Estimation by CFD

Concluding Remarks

Frequent entries of extraterrestrial objects into the early earth's atmosphere are expected to have supplied the materials and energy necessary for forming the present earth. Various chemical products in the high temperature

shock layer flow over the ablating surface of an entry object were distributed into the atmosphere through the wake flow. The Navier-Stokes analyses with the thermo-chemical nonequilibrium of the C-H-O-N 28 species show: 1) HCN, which is one of the most important prebiotic materials, is efficiently produced near the surface in the stagnation region of an icy object entering the early earth's CO_2/N_2 atmosphere with the ablation injection of H_2O, and 2) HCN is transported into the atmosphere by the wake flow behind the object with almost frozen chemistry. To simulate experimentally such process in the hypersonic wind tunnel with relatively low stagnation temperature, the energy addition technique by the electric discharge is proposed. The C and H elements are supplied by the ablation injection at the body surface made from the mixture of water ice and dry ice. The experimental model consists of two parts: ablative nose part to supply the C and H elements and the non-ablative after-body, in which the circuit of the electric discharge is installed in it to supply the energy necessary for chemical reactions. To predict the chemical reaction phenomena around the model in the flow of the hypersonic wind tunnel, the thermo-chemical nonequilibrium CFD analysis has been conducted. Based on the CFD results, the location of the electrodes for the electric discharge is determined to be in the downstream of the ablative nose part. The light emission of CN is experimentally observed through the band pass filter. A similar spatial distribution of the emission of CN is reproduced in the CFD result. Consequently, the cooperative approach of the EFD and CFD will deepen our understanding on the chemical process around an extraterrestrial objects entering the earth's atmosphere in the period of the heavy bombardment $4\text{-}3.8 \times 10^9$ years ago.

Acknowledgments

References

[1] I. Gilmour and M. A. Sephton (ed.), *An Introduction to Astrobiology*, Cambridge Univ. Press, Cambridge, 2003.

[2] K. Suzuki: Thermochemical Nonequilibrium Flow Analysis for Atmospheric Entry of Icy Objects, AIAA-2011-3756, 42nd AIAA Thermophysics Conference, Honolulu, June 2011.

[3] K. Suzuki and O. Imamura: Hypersonic Wind Tunnel Experiments on Icy Body and Their Potential Contribution to Astrobiology, *International Review of Aerospace Engineering*, Vol. 3, No. 2, pp. 115-124, 2010.

[4] K. Suzuki, O. Imamura and T. Okunuki: Visualization of Ablation and Spallation of Icy Object in Hypersonic Flow at Mach Number 7, *Visualization of Mechanical Processes*, Vol. 1, Issue 3, 2011, DOI: 10.1615/VisMechProc.v1.i3.100

[5] K. Suzuki, O. Imamura, M. Kanamori and M. Yuda: Numerical Analysis on Hypersonic Flow around Icy Body, Japan-Korea CFD Workshop 2009, Sendai, Dec. 2009.

[6] D. H. Rudy and D. M. Bushnell: A Rational Approach to the Use of Prandtl's Mixing Length Model in Free Turbulent Shear Flow Calculations, *Free Turbulent Shear Flows*, Vol. 1, NASA SP-321, 1972.

[7] Kashiwa Wind Tunnel Working Group.: UT-Kashiwa Hypersonic and High-Temperature Wind Tunnel, URL: http://daedalus.k.u-tokyo.ac.jp/wt/wt_index.htm [cited Sept. 3, 2012].

[8] J. D. Anderson, Jr.: *Hypersonic and High Temperature Gas Dynamics*, McGraw-Hill, 1989.

[9] Y. Watanabe, O. Imamura and K. Suzuki: Effects of Plasma Discharge on Hypersonic Flow over Flat Plate, AIAA-2010-4761, 2010.

[10] Y. Watanabe and K. Suzuki: Effect of Impulsive Plasma Discharge in Hypersonic Boundary Layer over Flat Plate, AIAA-2011-3736, 2011.

Experimental and Numerical Study on Shock Layer Radiation for Planetary Entry Flights

Gouji Yamada, Shota Ago, Yuto Kubo, Takashi Matsuno, Hiromitsu Kawazoe
Department of Mechanical and Aerospace Engineering, Tottori University
4-101 Koyama-Minami, Tottori, 680-8552, Japan
E-mail: yamada@mech.tottori-u.ac.jp

Abstract

In this study, shock layer radiation is investigated by experimental and numerical approach. Radiation profiles of N_2, N_2^+, and N are observed in two test conditions of initial pressure and velocity by time-resolved emission spectroscopy. Flow properties behind shock front are computed by the CFD code with two-temperature thermochemical model. The results are used as inputs for the radiation analysis code "SPRADIAN 2" to derive the radiation profiles behind shock front along the line of sight. Comparison between experiments and calculations shows that the decline of calculated radiation intensity is slower than that of measured one. Therefore, the present calculation fails to reproduce the measured radiation profile. This is considered to be due to the fact that the two-temperature model seems to lose its accuracy in the intermediate hypersonic flow regime. Further investigations are necessary to improve the accuracy of the two-temperature model.

Key words: shock tube, shock layer radiation, thermochemical nonequilibrium, spectroscopy, planetary entry

Nomenclature

C	: reaction rate constant, $m^3/(mol \cdot s)$
k_f	: forward reaction rate coefficient, cm^{-3} $mole^{-1}s^{-1}$
M	: unspecified third body
n	: temperature exponent on reaction-rate coefficient
P_0	: ambient pressure ahead of the shock wave, Pa
T_a	: geometric average temperature, $\sqrt{TT_v}$, K
T_d	: characteristic temperature, K
T_t	: translational - rotational temperature, K
T_v	: vibrational - electron - electronic excitation temperature, K
T_x	: unspecified temperature (T_t, T_a, or T_v), K
t	: time from shock front, μs
V	: shock velocity, km/s
X	: distance from shock front, mm

Introduction

Thermochemical nonequilibrium process in the shock layer around hypersonic vehicles is important for the development of the vehicles because it plays an important role in determining aerodynamic characteristics and heating rates of the vehicles. Assessments of entry flight environments have been conducted by the numerical simulation based on computational fluid dynamics (CFD) with thermochemical model. The result relies on the accuracy of the model applied in the simulation. In past studies, some thermochemical models were developed and applied for the assessments of flight environments [1-4]. However, the accuracy of these models is limited due to the lack of experimental data. To improve the model accuracy, the validation of the models is necessary by experimental investigations. One of the authors conducted shock-tube experiments to validate the two-temperature kinetic model developed by Park [5-6]. In these studies, the spatial distribution of emission spectra was measured by the time-frozen spectroscopy. The temperatures of chemical species in the shock layer are

deduced from the measured spectra and compared with the temperatures calculated by the two-temperature model. The results showed the measured temperatures disagreed with the calculated temperatures immediately behind shock waves. In these studies, validations were conducted in terms of the temperatures and the discrepancy of the model assumption was made clear. Chemical processes in the shock layer are important to assess the entry flight environments. However, the accuracy of the reaction rate coefficients used in the thermochemical model is questionable because the reaction rate coefficients were deduced from the comparison with limited experimental data. Temporal profiles of shock layer radiation depend on the chemical process in the shock layer. Therefore, investigations of shock layer radiation are useful to validate the reaction rate coefficients.

The purpose of the present study is to investigate shock layer radiation by experimental and numerical approach. In this study, time-resolved radiation measurements are conducted using the hypersonic shock tube at the Tottori University. Temporal radiation profiles of N_2, N_2^+, and N are measured in two different conditions of initial pressure and velocity. Flow properties behind shock front are calculated by the CFD code with the two-temperature model. The flow properties are used as inputs for radiation analysis code "SPRADIAN 2" and the calculated radiation profiles is obtained by radiation calculations. Comparisons between experiments and calculations are conducted to validate the reaction rate coefficient used in the CFD code.

Shock-Tube Measurement

A. Shock-tube facility

Experimental investigations have been carried out using the hypersonic shock tube developed at the Tottori University. A schematic drawing of the shock tube is shown in Fig.1. The shock tube is composed of a high pressure reservoir, a compression tube, a low pressure tube, vacuum tank, and a free piston driving in the compression tube. The shock-tube facility is located on movable mounts and connected to the vacuum tank by the shock absorbing mechanism to protect the facility from the impact produced by the piston operations. This facility works according to the Stalker principle. The free piston driven by high-pressure nitrogen adiabatically compresses the helium used as a driver gas. When the pressure in the helium reaches a critical value, a steel diaphragm bursts and a shock wave is formed in the low pressure tube where the test gas is filled. The low pressure tube with 44 mm square cross-section is made of aluminum alloy to reduce emissions from impurities. The test section with four quartz windows are located 2300 mm downstream from the diaphragm. The compression tube and low pressure tubes are evacuated to the pressure of 5.0 Pa using oil rotary and root pumps before the filling of a test gas. The facility can generate shock velocities ranging from 4.0 to 7.0 km/s with test gases of air, N_2, CO_2, and CO_2 - N_2 mixture, covering the planetary entry flight conditions.
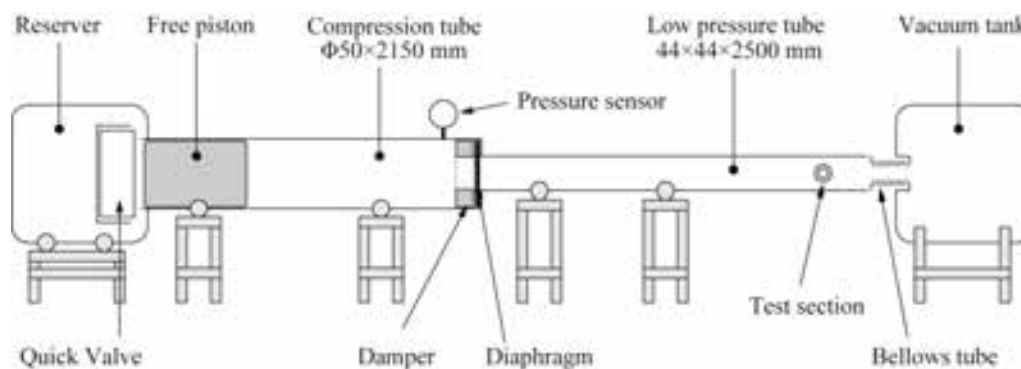

Fig.1 A schematic drawing of the hypersonic shock tube

B. Optical instrumentation

A schematic drawing of the optical instrumentation at the test section is shown in Fig.2. The shock velocity at the test section is measured by the double-laser schlieren measurement system [7]. Two laser beams are aligned along the flow direction in line to pass through the test section perpendicularly to the axis of the shock-tube flow. The optical path is adjusted by flat mirrors to reach separate avalanche photodiodes (APD). Deflection of the beams as a result of a density gradient at the shock front causes a change in the output signals of avalanche photodiodes. The shock velocity at the test section can be obtained from the beam distance and the time difference of the output signals.

Time-resolved emission spectroscopy is conducted to measure the radiation emitted from the shock layer. This technique provides information on the evolution of the radiation as a function of time. A monochromator (JASCO, CT-25C) is used with a 1200 g/mm grating and the entrance slit is fixed at 50μm. A quartz convex lens is used to focus the radiation on the entrance slit of the monochromator. To record the radiation, a photomultiplier tube (PMT) (Hamamatsu, R928) is placed behind the exit slit of the monochromator. The spectral response of the PMT ranges from 185 to 900 nm and its peak sensitivity is at 400 nm. The rise time of the PMT is 2.2 ns. The exit slit is variable depending on the measured wavelength range. The signal produced by the PMT is recorded by a digital oscilloscope (Agilent Technologies, DSOX2024A). An avalanche photodiode is placed on the other side of the monochromator to measure the total radiation intensity and its signal is used to trigger the oscilloscope at the instant of the shock arrival.
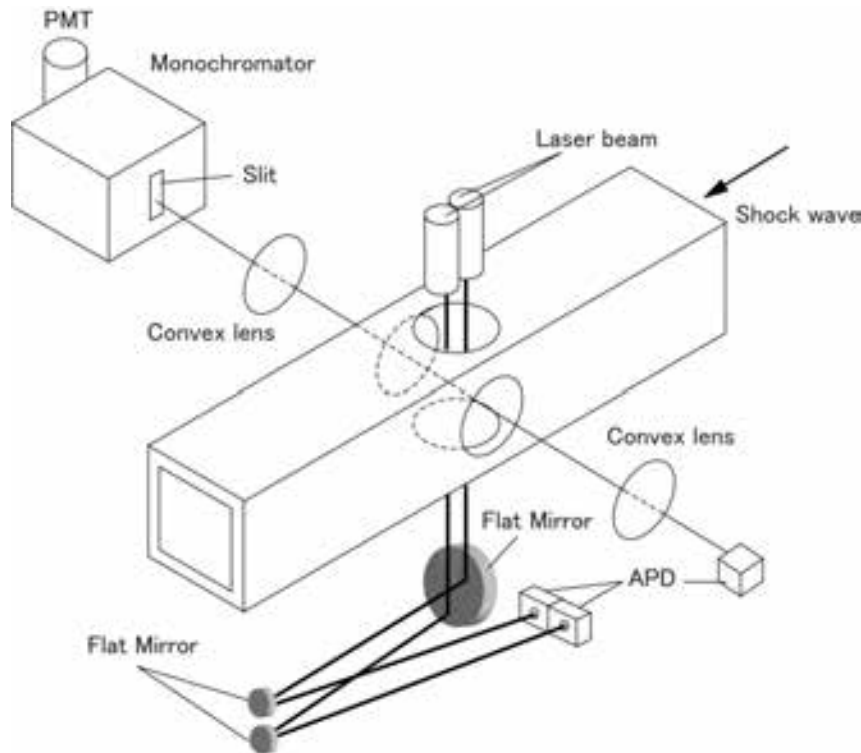
Fig.2 A schematic drawing of the optical instrumentation

C. Test conditions
Experiments are carried out using pure N_2 as a test gas simulating the Earth atmosphere. Air is not used in this study because the physical processes are more difficult than those in N_2. Test conditions are shown in Table 2. Two initial pressure /shock velocity conditions are studied: p = 100 Pa and v = 5.5 km/s (case1), p = 500 Pa, v = 4.68 km/s (case2). For these conditions, N_2 (2+) (1,0) band head, N_2^+ (1-) (0, 0) band head , and N 3p $4S^0$ - 3s ^4P triplet are monitored using the monochromator configurations listed in Table 3.

Table 1 Test conditions

Case	Pressure, Pa	Shock velocity, km/s	Test gas
1	100	5.50	N_2
2	500	4.68	N_2

Table 2 Monochromator configulations

Configuration	Grating density, g/mm	Center wavelength, nm	Wavelength span, nm	Features targeted
1	1200	316	2	N_2 (2+) (1,0)
2	1200	391	4	N_2^+ (1-) (0,0)
3	1200	744	6	N 3p $4S^0$ - 3s ^4P

Numerical Simulation

Numerical simulations are carried out to reproduce the measured temporal profile of the shock layer radiation. The flow properties in the shock layer are obtained using the CFD code which solves the one-dimensional Navier-Stokes equations with thermochemical model. The two-temperature model developed by Park is employed for the thermochemical nonequilibrium in the code. Chemical species considered are N_2, N, N_2^+, N^+, and e^-. Following Park [8], a set of six reactions related to nitrogen is taken into account. The reactions and the corresponding rate coefficients are shown in Table 3. In the present calculation, a shock wave is generated by impinging a hypersonic flow to a wall instead of solving the shock tube problem. This method is suitable to investigate the thermochemical nonequilibrium phenomena behind the shock front because the effect of expansion waves can be reduced. Figure 3 shows the computational region used for the calculation: 300 grid points corresponding to a grid spacing of 167 μm. After the hypersonic flow impinges the wall, a shock wave is generated and then the computation starts. The generated shock wave propagates leftward and calculations are conducted until the shock wave arrives at 5mm. The governing equations are integrated by a cell-centered finite volume scheme. The inviscid fluxes are evaluated by the AUSM-DV scheme [9] whose spatial accuracy is extended to second-order using the MUSCL approach [10] with the minmod limiter. The viscous fluxes are evaluated by central differencing. Time integration is performed with a CFL number of 0.1, which is combined with the diagonal point implicit method [11] for maintaining the stability of the source term.

The flow properties (temperatures and densities) calculated by the CFD code are used as input parameters for the radiation analysis code SPRADIAN 2 [12] to derive temporal profiles of the radiation along the line of sight. In the SPRADIAN2, the spectral emission and absorption coefficients are obtained at the given thermochemical conditions using a line-by-line technique. The radiation intensity is obtained by integrating the radiative transfer equation across the test section of the shock tube. The resulting intensity values are integrated over the wavelength intervals corresponding to the observation.

Table 3 Chemical reactions and the reaction rate coefficient

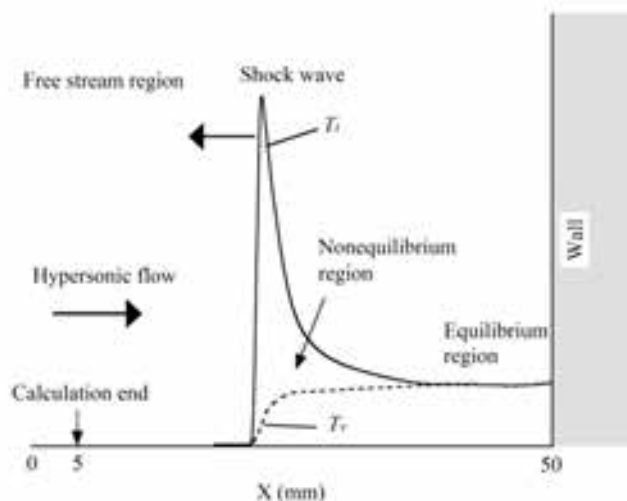|	Reactions	M	C	n	T_d	T_x	Source
	Dissociation reaction						
1	$N_2 + M \rightarrow 2N + M$	N_2, N_2^+	7.0^{15}	-1.60	113200	T_a	Ref.[4]
2	$N_2 + M \rightarrow 2N + M$	N, N^+	3.0^{16}	-1.60	113200	T_a	Ref.[4]
3	$N_2 + e^- \rightarrow 2N + e^-$		3.0^{18}	-1.60	113200	T_v	Ref.[18]
	Associative ionization						
4	$N + N \rightarrow N_2^+ + e^-$		4.4^1	1.50	67500	T_t	Ref.[4]
	Electron impact ionization						
5	$N + e^- \rightarrow N^+ + e^-$		2.5^{28}	-3.82	168600	T_v	Ref.[4]
	Charge exchange reaction						
6	$N_2 + N^+ \rightarrow N_2^+ + N$		1.0^6	0.50	12200	T_t	Ref.[4]

Fig.3 Computational region

Results and Discussion

Figure 4 shows the calculated flow properties for the case 1. The vibrational-electron-electronic temperature, T_v is significantly lower than the translational-rotational temperature, T_t immediately behind shock front. In this region, T_v is raised through the collisional processes. The equilibration between T_t and T_v are accomplished in the region after 20 μs. Dissociation of N_2 is significant and the molar fraction of N almost reaches 0.2, but ionization is fairly weak at the calculated condition. Figure 5 shows the calculated radiation spectrum using the flow properties in Fig. 4. The radiation intensity in the ultraviolet (UV) region is higher than that in visible (VIS) and near infrared light (NIR) regions. The spectrum in UV region is dominated by N_2 (2+) and N_2^+(1-) band systems. The spectrum in VIS and NIR regions are dominated by N_2 (1+) band system and atomic line of N. Figure 6 shows the detail spectra in the UV and VIS regions, respectively. In the UV region, many band head of N_2 (2+) and N_2^+ (1+) can be identified. Band heads of N_2 (2+) (1,0) at 315.9 nm and N_2^+(0,0) at 391 nm are measured in this study because the band heads are unobstructed and are free from other band systems. In the VIS region, there are many band heads of N_2 (1+). However, their band heads are not clear. Atomic lines of N 3p $4S^0$ - 3s ^{4}P triplet are seen at around 750 nm. The atomic spectrum of N is measured in this study.

The measured temporal profiles of radiation intensity are shown in Figs 7, and 8 for two cases. In these figures, the calculated temporal profiles of radiation intensity are shown as dashed lines. The measured and calculated radiation intensities are normalized by the maximum value for comparison. The rapid increase of the radiation is seen immediately behind shock front. The rapid increase of the radiation is called radiation overshoot [13]. This is caused by the nonequilibrium radiation from the excited species. After the peak, the radiation intensity decreases slowly and plateaus. The measured radiation profiles are different from the calculated radiation profiles in all figures. Especially, the decline of the measured radiation intensity is much slower than the calculated one. This difference is considered to be caused by the boundary-layer growth on the inner wall of the shock tube [14]. In the boundary layer, the test gas is adiabatically compressed and the temperature and densities are increased, resulting in the rise in radiation intensity. Therefore, the decline of the measured radiation intensity becomes slower than the calculated one. Disagreement becomes more significant in case 2, where shock velocity is slower than that in case 1. The two-temperature model was validated and its accuracy was demonstrated in flight conditions at around 6 km/s [8, 15]. Past studies showed that the two-temperature model failed to reproduce the measured shock standoff distances in the intermediate hypersonic flow regime from 2.5 to 4.5 km/s [16, 17]. In this flow regime, the two-temperature model seems to lose its accuracy. In the present study, the two-temperature model is validated by radiation measurements in the conditions closer to the intermediate hypersonic flow regime. Therefore, the present calculation fails to reproduce the measured radiation profiles. Further investigations are necessary to improve the accuracy of the two-temperature model in the intermediate hypersonic flow regime.

Conclusion

Shock layer radiation is investigated by shock tube measurements and CFD simulations coupled with radiation calculations. The temporal radiation profiles of N_2, N_2^+ and N are measured by the time-resolved spectroscopy and compared with the numerical calculations. The measured radiation profiles disagree with the calculated one. Disagreement is more significant in case 2, where shock velocity is slower than that in case 1. The present calculation fails to reproduce the measured radiation profile. This is because that the two-temperature model seems to lose its accuracy in the present test conditions. Modification of the model is necessary by further investigations.

Acknowledgment

(a) Temperatures   (b) Species mole ftactions
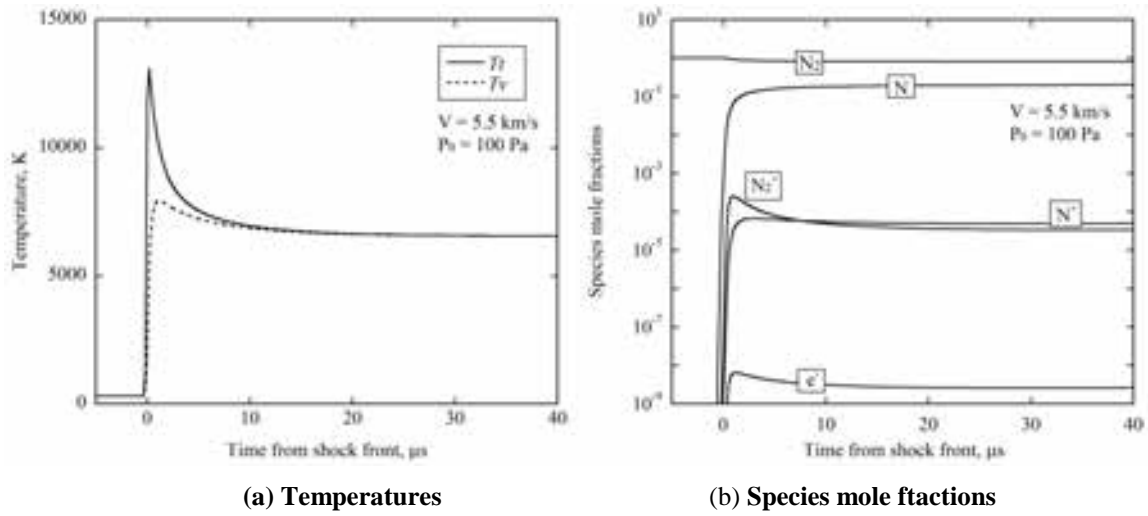
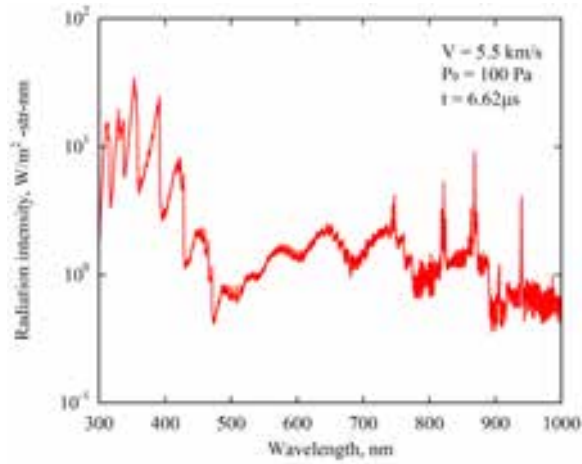**Fig.4 calculated flow properties behind shock front for case1**

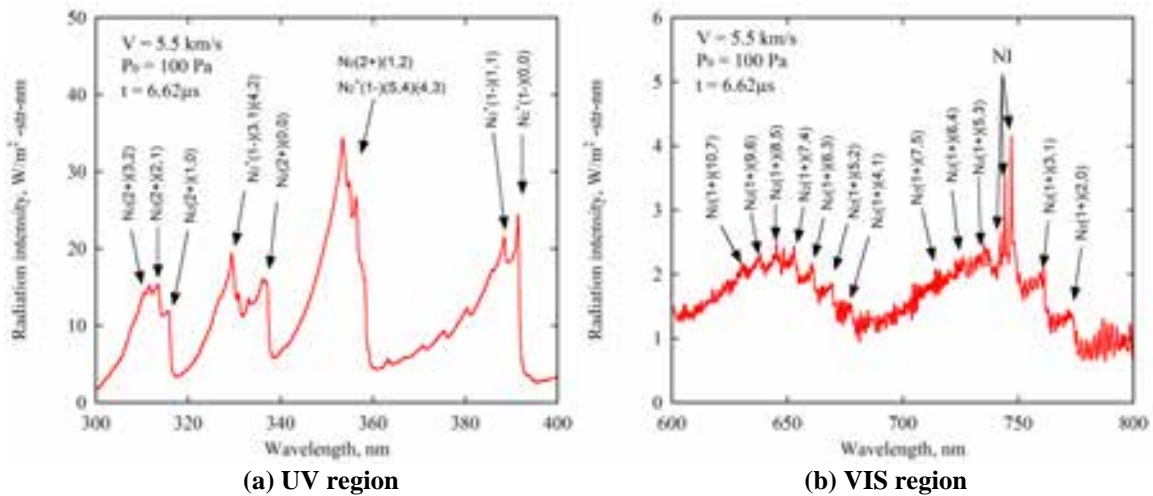**Fig.5 Calculated emission spectrum for case1**

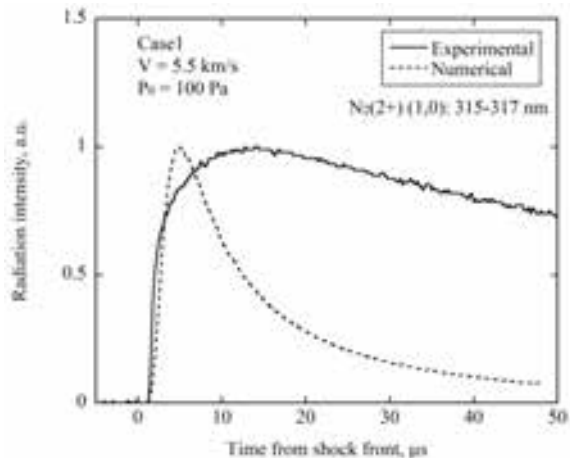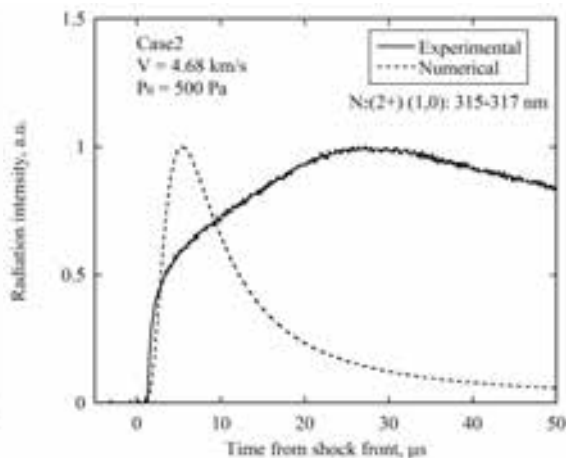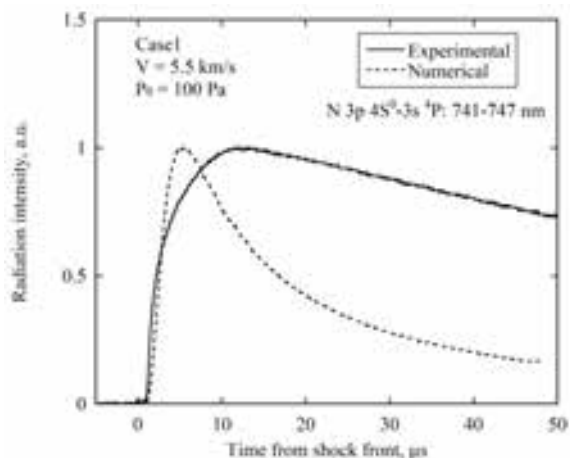
(a) UV region   (b) VIS region

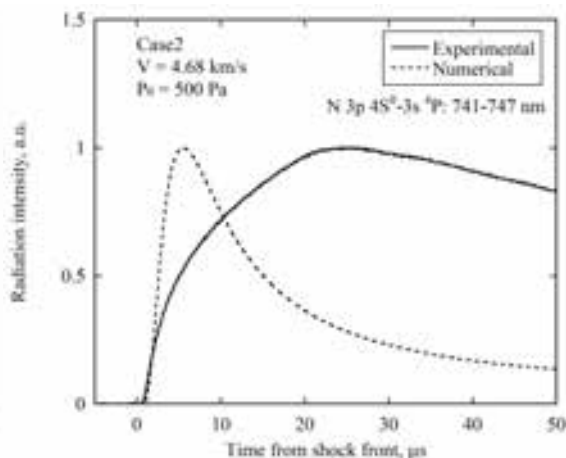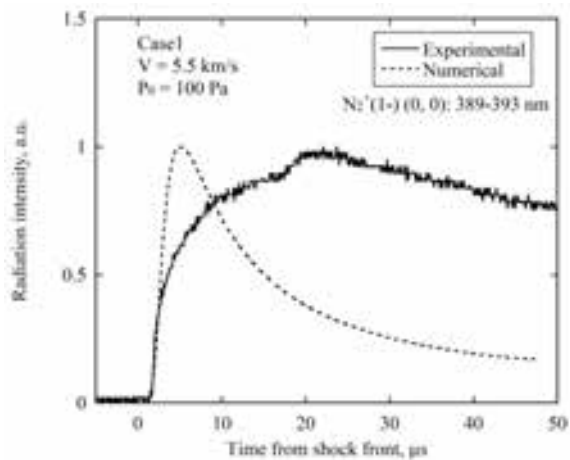**Fig.6 Calculated UV and VIS spectra for case 1**
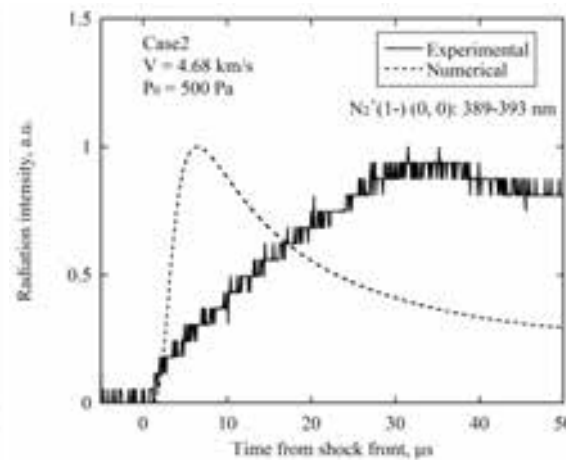
a) N_2 (2+) (1,0)

a) N_2 (2+) (1,0)

b) N 3p $4S^0$ - 3s ^{4}P

b) N 3p $4S^0$ - 3s ^{4}P

c) N_2^+ (1-) (0, 0)

c) N_2^+ (1-) (0, 0)

Fig.7 Comparison result for case1

Fig.8 Comparison result for case2

References

[1] Park, C.: Nonequilibrium Hypersonic Aerothermodynamics, John Wiley & Sons, New York, 1990.

[2] Gnoffo, P. A., Gupta, R. N., and Shinn, J. L.: Conservation Equations and Physical Models for Hypersonic Air Flows in Thermal and Chemical Nonequilibrium, *NASA TP-2867*, 1989.

[3] Gupta, R. N., Yos, J. M., Thompson, R. A., and Lee, K. P.: A Review of Reaction rates and Thermodynamic and Transport Properties for the 11-Species Air Model for Chemical and Thermal Nonequilibrium Calculations to 30000 K, *NASA TM-101528*, 1989.

[4] Park, C.: Review of Chemical-Kinetic Problems of Future NASA Missions, I: Earth Entries, *Journal of Thermophysics and Heat Transfer*, Vol. 7, No. 3, pp. 385-398, 1993.

[5] Yamada, G., TAKAYANAGI, H., SUZUKI, T. and FUJITA, K.: Shock Layer Radiation Analysis using a Hypervelocity Shock Tube (HVST), *Transactions of the Japan Society for Aeronautical and Space Sciences* Vol. 55, pp.37-43, 2012.

[6] Yamada, G., TAKAYANAGI, H., SUZUKI, T. and FUJITA, K.: Analysis of Shock Layer Radiation from the Vacuum-Ultraviolet to Near-Infrared Regions, *Transactions of the Japan Society for Aeronautical and Space Sciences* Vol. 55, pp.60-67, 2012.

[7] Yamada, G., SUZUKI, T., TAKAYANAGI, H. and FUJITA, K.: Development of Shock Tube for Ground Testing Reentry Aerothermodynamics, *Transactions of the Japan Society for Aeronautical and Space Sciences* Vol. 54, pp.51-61, 2011.

[8] Park, C.: Assessment of a Two-Temperature Kinetic Model for Dissociating and Weakly Ionizing Nitrogen, *Journal of Thermophysics and Heat Transfer*, Vol. 2, pp. 8-16, 1988.

[9] Wada, Y. and Liu, M. S.: A Flux Splitting Scheme with High-resolution and Robustness for Discontinuities, *AIAA Paper* 94-0083, 1994.

[10] Anderson, W. K., Thomad, J. L., and van Leer, B.: Computation of Finite Volume Flux Vector Splitting for the Euler Equations, *AIAA Journal*, Vol. 24, pp. 1453-1460, 1986.

[11] Everhardt, S. and Imlay, S.: Diagonal Implicit Scheme for Computing Flows with Finite Rate Chemistry, Journal of Thermophysics and Heat Transfer, Vol. 6, , pp. 208-216, 1992.

[12] Fujita, K., Mizuno, M., Ishida, K., Ito, T., Spectroscopic Flow Evaluation in Inductively Coupled Plasma Wind Tunnel, Journal of Thermophysics and Heat Transfer, Vol.22, pp. 685-694, 2008.

[13] Willson, J.: Ionization Rate of Air behind High-Speed Shock Waves, The physics of Fluids, Vol. 9, No. 10, 1966.

[14] Park, C.: Assessment of a Two-Temperature Kinetic Model for Ionizing Air, Journal of Thermophysics and Heat Transfer, Vol. 3, pp. 233-244, 1989.

[15] Sharma, P. S, and Gillespie, W.: Nonequilibrium and Equilibrium Shock Front Radiation Measurements, Journal of Thermophysics and Heat Transfer, Vol. 5, pp. 257-265, 1991.

[16] Furudate M., Nonaka, S., and Sawada, K.: Behavior of Two-Temperature Model in Intermediate Hypersonic Regime, Journal of Thermophysics and Heat Transfer, Vol. 13, pp. 424-430.

[17] Furudate M., Nonaka, S., and Sawada, K.: Calculation of Shock Shapes over Sharp Cone in Intermediate Hypersonic Airflow, Journal of Thermophysics and Heat Transfer, Vol. 13, pp. 424-430.

[18] Park, C., Jaffe, C., and Partridge, H.: Chemical-Kinetic Parameters of Hyperbolic Earth Entry, Journal of Thermophysics and *Heat Transfer*, Vol. 15, pp. 76-89, 2001.

Numerical Study on Anomalous Heating over Apollo CM Test Model in Free-Piston Shock Tunnel HIEST

Tomoaki Ishihara[*]
Yousuke Ogino[†]
Naofumi Ohnishi[‡]
Keisuke Sawada[§]
Hideyuki Tanno[¶]

[*†‡] Tohoku University, 6-6-01 Aramaki-Aza-Aoba, Aoba-ku, Sendai, Miyagi, 980-8579, Japan
  [*]ishihara@cfd.mech.tohoku.ac.jp, [†]yogi@cfd.mech.tohoku.ac.jp, [‡]ohnishi@rhd.mech.tohoku.ac.jp,
  [§]sawada@cfd.mech.tohokuac.jp
[¶] Japan Aerospace Exploration Agency, Kakuda Space Center, 1 Koganezawa, Kimigaya, Kakuda, Miyagi,
  981-1525, Japan
  tanno.hideyuki@jaxa.jp

Abstract

Aeroheating measurements on the Apollo CM test model placed in the free-piston shock tunnel HIEST was conducted. Although the convective heat flux distributions along wall surface normalized by a product of Stanton number and the square root of the Reynolds number should fall on a single curve for laminar flow case, the measured data for high enthalpy conditions resulted in significantly larger than one for low enthalpy conditions. In the HIEST experiment, stagnation heat fluxes on small probes were also measured. We could find that the anomalous heating phenomena are not shown for small test model but for large one that is called the scaling effect of anomalous heating phenomena. Similar tendencies were also observed at other shock tunnels: NASA Ames 42-Inch Shock Tunnel, Caltec T5, and CUBRC LENS. The cause for those anomalous heating phenomena is yet unknown. Anomalous heating poses a critical issue over the existing design method of thermal protection system for entry capsules. To clarify the cause of it, we numerically investigate these two factors: The radiative heat transfer in the shock layer and the radiation heating from the driver gas. From the results of our computations, radiative heating from shock layer was negligibly small. While, obtained total heat flux considering radiative heating from driver gas agreed well with measured heat flux. Scaling effect of the anomalous heating phenomena was also explained by accounting for the radiation from the driver gas. Therefore, we can say that the radiative heating from the driver gas may be the cause of those phenomena.

Key words: hypersonic flow, aerodynamic heating, shock tunnel

Introduction

NASA decided the retirement of space shuttles in July, 2011 due to enormous maintenance costs and safety defects, and announced Multi-Purpose Crew Vehicle (MPCV) concept as the next-generation manned space vehicle. MPCV is an Apollo-like space capsule which aims human explorations of the moon and Mars. Space capsules such as MPCV are now paid attention to, in the future, will play the principal role. When such a space capsule enters into the atmosphere of a planet, a strong shock wave is formed around the capsule, and it is exposed to severe aerodynamic heating in the shock layer. To protect the capsule from such heating environment, appropriate thermal protection system must be equipped. Therefore, it is critical to predict the heat fluxes accurately for the design of space capsules.

The free-piston shock tunnel, HIEST shown in Fig. 1, can produce test flow at stagnation pressure up to 150 MPa and at stagnation enthalpy up to 25 MJ/kg. Recently, aerodynamic heating on the Apollo command-module AS-202 test model illustrated in Fig. 2 placed in HIEST was measured by Tanno et al. [1, 2] The model was 6.4% scaled AS-202 command model made of SUS 304 stainless steel and had a diameter of 250 mm. To measure heat flux around the model, 84 miniature co-axial thermocouples were mounted on the forebody. Table 1 summarizes the upstream conditions of the test section determined by an axi-symmetric nozzle code [3]. The heat flux data were normalized by a product of Stanton number and the square-root of the Reynolds number in order to compare the HIEST heat flux data with the results obtained in other tunnel facilities and flight test. Measured heat flux with calculated one by thermochemical nonequilibrium calculation are summarized along the centerline of the model for AOA 30 deg. as shown in Fig. 3. The convective heat flux distributions along wall surface normalized by $St \times (Re_{\infty,D})^{1/2}$ should fall on a single curve for laminar flow case. We can confirm that calculated one normalized by $St \times (Re_{\infty,D})^{1/2}$ are almost same for all the cases. On the other hand, the measured data for high enthalpy condition resulted in larger than those for low enthalpy condition and measured values are considerably higher than calculated convective ones for all conditions. Such anomalous heating phenomena obviously pose a critical issue over the existing design method of thermal protection system for entry capsules.

Additionally, in HIEST experiment, stagnation heat fluxes on small probes also measured [4]. Figure 4-(a) and (b) show the configurations of the probes which have the base radius $\Phi = 20$ and $\Phi = 50$ mm, respectively. The $\Phi20$ probe has the nose radius $R = 10$ or $R = 50$ mm. The $\Phi50$ probe has $R = 100$ mm. Figure 5 shows the normalized stagnation heat flux for each probe with the results of Apollo CM test model ($\Phi = 250$ mm, $R = 300$ mm). The heat flux measured in HIEST is normalized by calculated convective heat flux at stagnation point. Freestream parameters are summarized in Tab. 2. For $\Phi20R10$ and $\Phi20R10$ probes, we can see that the values are from 1.0 to 1.3. While, for $\Phi50R100$ probe and Apollo CM test model, the values are over 1.4. This means that there are large discrepancies between measured heat flux and calculated convective one. The anomalous heating phenomena are not shown for small test model but for large one.

Anomalous heating phenomena were also observed at other shock tunnels; NASA Ames 42-Inch Shock Tunnel [5], Caltec T5 [6, 7, 8], CUBRC LENS I [9, 10]. From these literatures, large discrepancies between calculated convective heat flux by LAURA [11, 12] or DPLR [13, 14] codes and measured heat flux by each shock tunnel were confirmed. For instance, in Ref. [6], the effect of turbulence heat transport was investigated to examine the cause of those discrepancies. Comparison of T5 data with the calculated heating rate by DPLR accounting for turbulence was performed. As a result, measured profiles were not explained by only turbulence transport.

As the cause of anomalous heating phenomena, we focus on radiative heating from driver gas. In HIEST experiments, the driver gas is compressed by a heavy piston, then the pressure and temperature in the compression tube rise up. When diaphragms rupture, remarkable luminosities are observed, therefore, the intense radiation from the driver gas can be the cause for anomalous heating. Since the driver gas is compressed in other shock tunnels as with HIEST, this phenomena can occur not only in HIEST but also in other shock tunnels. In this study, we compute the flowfield over the forebody of the Apollo CM test model and evaluate the convective and radiative heat fluxes on the model surface. The heat flux on small probes are also calculated to examine the scaling effect of anomalous heating. In order to clarify the cause of anomalous heating, we examine the radiative heating both from the shock layer and the driver gas.
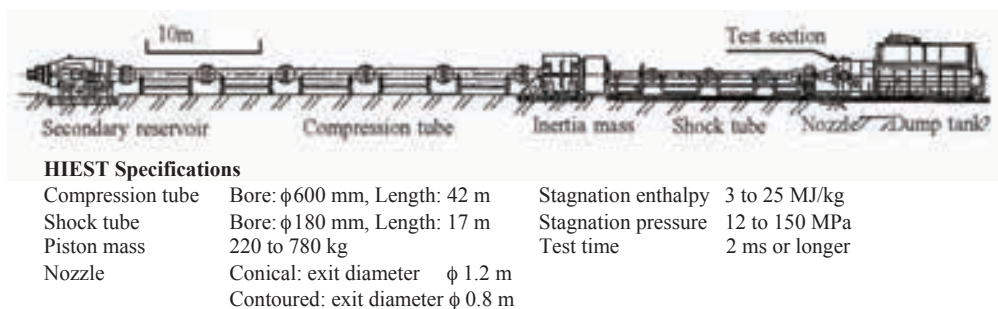

HIEST Specifications

Compression tube	Bore: ϕ600 mm, Length: 42 m	Stagnation enthalpy	3 to 25 MJ/kg
Shock tube	Bore: ϕ180 mm, Length: 17 m	Stagnation pressure	12 to 150 MPa
Piston mass	220 to 780 kg	Test time	2 ms or longer
Nozzle	Conical: exit diameter ϕ 1.2 m		
	Contoured: exit diameter ϕ 0.8 m		

Figure 1. Free-piston shock tunnel HIEST [1].

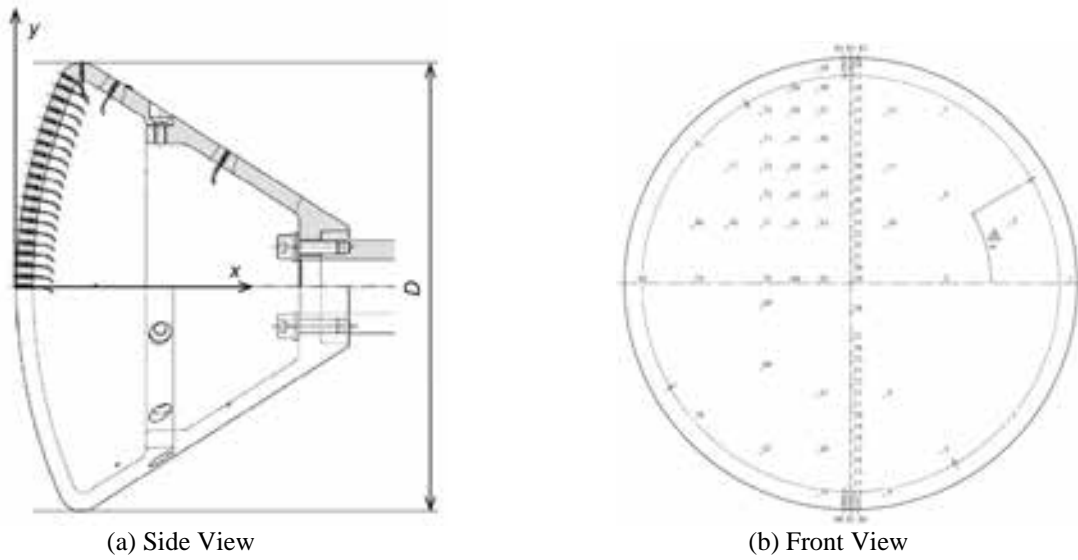(a) Side View   (b) Front View

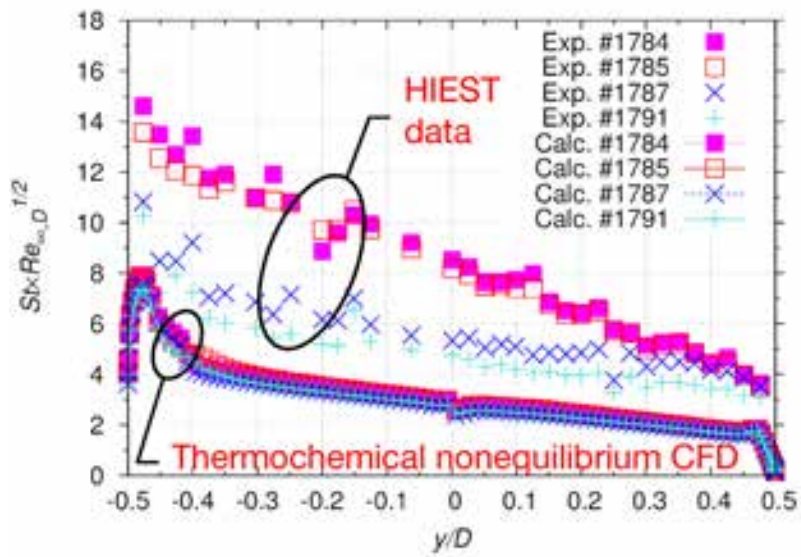**Figure 2. Apollo CM test model [1].**

Figure 3. Measured heat flux distribution along the centerline of the model.

Table 1. Freestream parameters of Apollo CM test campaign at HIEST calculated by JAXA in-house code.

Shot #	H_0 [MJ/kg]	P_0 [MPa]	$T_{t\infty}$ [K]	$T_{v\infty}$ [K]	ρ_∞ [kg/m^3]	V_∞ [m/s]	M_∞	Re_∞ $\times 10^6$[1/m]
1784	19.554	57.401	2035.2	2038.2	0.01457	5507.3	5.909	1.167
1785	21.059	55.060	2143.0	2146.8	0.01315	5690.2	5.885	1.050
1787	8.094	49.700	841.7	849.5	0.02643	3729.1	6.496	2.595
1791	6.759	30.750	649.7	668.1	0.01919	3420.8	6.739	2.060
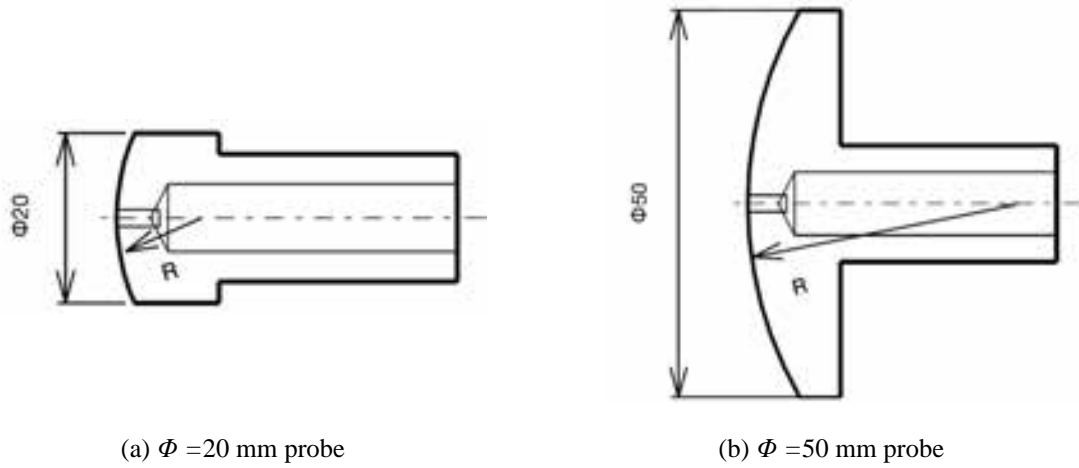
(a) Φ =20 mm probe   (b) Φ =50 mm probe

Figure 4. Schematic of small probes.
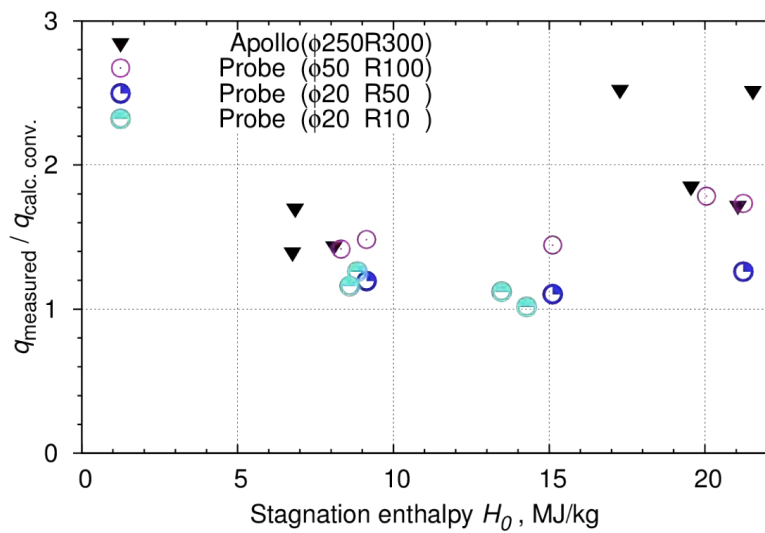
Figure 5. Scaling effect of the anomalous heating phenomena.

Table 2. Freestream parameters of small probes campaign in HIEST calculated by JAXA in-house code.

Shot #	Test gas	Test model [mm]	H_0 [MJ/kg]	P_0 [MPa]	$T_{t\infty}$ [K]	$T_{v\infty}$ [K]	ρ_∞ [kg/m³]	V_∞ [m/s]	M_∞	Re_∞ ×10⁶ [1/m]
1886	Air	$\Phi20R10$	13.471	47.906	1455.9	1461.8	0.01633	4665.8	6.108	1.443
1887	Air	$\Phi20R10$	11.326	49.102	1242.8	1249.3	0.01942	4327.5	6.190	1.762
1888	N₂	$\Phi20R10$	14.276	48.996	1243.7	3169.2	0.01467	4934.5	7.021	1.407
1889	Air	$\Phi20R10$	8.596	54.634	908.7	915.8	0.02717	3835.8	6.440	2.640
1890	N₂	$\Phi20R10$	8.845	55.530	614.8	2581.9	0.02293	3950.1	7.867	2.733
1891	Air	$\Phi50$	8.318	52.841	869.9	877.3	0.02702	3778.5	6.479	2.663
1893	Air	$\Phi50$	20.048	42.506	1946.4	1952.3	0.01050	5551.9	6.013	0.920
1894	N₂	$\Phi20R50, \Phi50$	21.232	43.941	2261.4	3563.4	0.01026	5785.3	6.036	0.867
1895	N₂	$\Phi20R50, \Phi50$	15.112	48.230	1359.8	3231.9	0.01397	5055.6	6.882	1.306
1896	N₂	$\Phi20R50, \Phi50$	9.140	57.726	643.5	2606.8	0.02324	4014.4	7.824	2.728

Numerical Methods

The numerical method is based on the cell-center finite volume discretization. For calculation of flowfield over Apollo CM test model, we solve the three-dimensional Navier-Stokes equations accounting for thermochemical nonequilibrium in the shock layer. On the other hand, for small probes, we solve the axi-symmetric ones. We employ Park's two-temperature thermochemical model [15] in which five chemical species (O, N, NO, N_2, O_2) are considered. The convective numerical flux is calculated by SLAU [16]. We employ MUSCL approach [17] for attaining a second order spatial accuracy. In the time integration, we use the LU-SGS implicit method [18] and Euler explicit method, for computation of flowfield over Apollo CM test model and small probes, respectively. To improve the stability in the integration of source terms, the diagonal point implicit method [19] is utilized.

The radiative transfer equation is solved one-dimensionally in the direction normal to the wall [20]. The absorption coefficients are calculated using the multi-band model [21]. O, N, NO, O_2, and N_2 are considered as contributors to radiation. Absorption coefficients of each contributor are evaluated at 10,000 wavelength points. They are constructed for the wavelength region from 750 to 15,000 Å. In this numerical work, radiative heat transfer calculation is uncoupled with flowfield.

Numerical Conditions

Freestream conditions for aeroheating measurements on Apollo CM test model and small probes equal to experimental value in Tab. 1 and 2, respectively. We compute the four typical conditions: Shot # 1785, 1791, 1889, 1891. Mass fractions of freestream calculated by NENZF [22] are listed in Tab. 3 and 4. We assume that wall boundary condition is isothermal and fully-catalytic wall.

We generate grids adapted to the shock wave front to estimate heat flux appropriately [23]. A typical example of the computational grid for Apollo CM test model, shown in Fig. 6, has 51 points in the wall normal direction and in the direction along the wall and 65 points in circumferential direction. Figure 7 shows grids for $\Phi 20R50$ and $\Phi 50R100$ probes. Since we are interested in the only stagnation heat flux, the configuration of afterbody is simplified. There are 51 grid points in the wall normal direction and 101 points in the direction along the wall. The distance between the first layer and the wall surface, that means grid resolution for temperature boundary layer, is determined from grid convergence property of convective heat flux.

Table 3. Mass fraction of freestream in Apollo CM test campaign.

Shot #	$C_{O\infty}$	$C_{N\infty}$	$C_{NO\infty}$	$C_{O_2\infty}$	$C_{N_2\infty}$
1785	1.308×10^{-1}	4.514×10^{-6}	3.600×10^{-2}	8.326×10^{-2}	7.500×10^{-1}
1791	2.397×10^{-3}	4.399×10^{-12}	5.931×10^{-2}	2.009×10^{-1}	7.373×10^{-1}

Table 4. Mass fraction of freestream in small probes campaign.

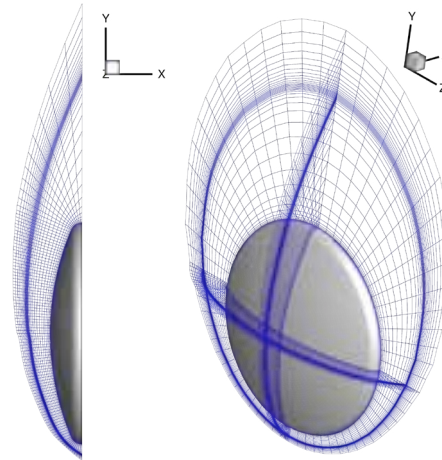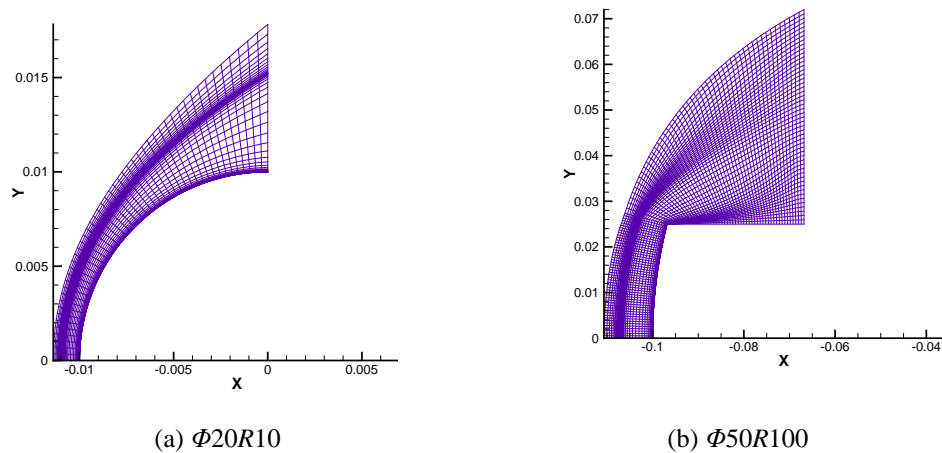| Shot #	$C_{O\infty}$	$C_{N\infty}$	$C_{NO\infty}$	$C_{O_2\infty}$	$C_{N_2\infty}$
1889	4.785×10^{-3}	5.819×10^{-12}	6.054×10^{-2}	1.979×10^{-1}	7.368×10^{-1}
1891	4.139×10^{-3}	4.738×10^{-12}	6.038×10^{-2}	1.986×10^{-1}	7.368×10^{-1}

Figure 6. Solution-adaptive grids for Apollo CM test model.

(a) $\Phi20R10$ (b) $\Phi50R100$

Figure 7. Solution-adaptive grids for small probes.

Results and Discussion

Effects of Radiative Heat Flux

When the radiative heating from driver gas is considered, we simply regard the driver gas as a black body, and set the Plank function B_λ as a boundary of the radiative heat transfer equation in the shock layer. Since the driver gas temperature was not able to measure due to experimental constraints, we assume a certain driver gas temperature T_{est} at which calculated heat flux agree well with experimental one.

Figure 8 shows normalized total heat flux including radiative heating from driver gas for Shot # 1791 (low enthalpy condition) and Shot # 1785 (high enthalpy condition). Asterisk-shaped symbols show the baseline convective heat flux profile. While, open-square symbols show the sum of the convective heat flux and radiative heat flux from the shock layer. Total heat fluxes including radiation from driver gas are indicated cross-shaped symbols. Radiative heat flux from the shock layer is negligibly small both for conditions. For Shot # 1791, as shown in Fig. 8-(a), we could obtain a good agreement with HIEST heat flux data, if we assume the temperature of the driver gas T_{est} to be 2,700 K. For Shot # 1785, as shown in Fig. 8-(b), we obtain a reasonable agreement with HIEST heat flux data, if we assume the temperature of the driver gas T_{est} to be 4,500 K. One can find that

the radiation from driver gas greatly contributes to radiative heat flux to the wall surface. Since the temperature in shock layer is about 10,000 K at most even for higher enthalpy condition, then absorption coefficients are relatively small. Therefore, the radiative heating from driver gas is hardly absorbed in the shock layer and directly heats the test model.

Validation of the estimated temperature of the driver gas

We validate the driver gas temperature T_{est} at which we could obtain good agreement with measured data. In the HIEST experiment, it is hard to measure the driver gas temperature directly because of experimental configuration. We estimate the experimental temperature of driver gas assuming adiabatic compression given by following expression,

$$T_{exp} = \left(\frac{P_{rup}}{P_{init}} \right)^{\frac{\gamma-1}{\gamma}} \times T_{init} \ , \tag{1}$$

where P_{init} and T_{init} mean the pressure and temperature before compression, respectively. We set $P_{init} = 1,013$ hPa, and $T_{init} = 300$ K. P_{rup} which indicates the measured pressure when the first diaphragm ruptured is 85 MPa and 37 MPa for Shot # 1791 and Shot # 1785, respectively. Since driver gas is composed of He and Ar, we set $\gamma = 5/3$. Then, the temperature of the driver gas T_{exp} is 3,200 K and 4,400 K, respectively. For Shot # 1785, the T_{est} seems a reasonable assumption. While, for Shot # 1791, there are discrepancies between T_{est} and T_{exp}.

We estimated experimental driver gas temperature T_{exp} at which the first diaphragm ruptures. However, T_{exp} may change from the value at which the first diaphragm ruptures, since there is a time delay before measuring heat flux. Thus, we need to calculate flowfield in compression tube, shock tube and nozzle for accurate estimation of the experimental driver gas temperature T_{exp}. In addition, since spectroscopic measurement is carried out before too long, we will investigate the radiation from driver gas in more detail.

Scaling Effect of Anomalous Heating Phenomena

Figure 9 shows the total heat flux distribution including radiative heating from the driver gas on $\Phi 20R10$ probe for Shot # 1886 and $\Phi 50R100$ probe for Shot # 1893. The stagnation enthalpy both for shots is comparable. Horizontal axis shows the distance from stagnation point. We assumed the driver gas temperature $T_{est} = 3,000$ K. In the case of $\Phi 20R10$ probe, we can find that convective heat flux is significantly larger than radiative heat flux. Since the ratio of radiative heat flux to convective heat flux is small, the anomalous heating phenomena are not shown notably. While, in the case of $\Phi 50R100$ probe, since the ratio of radiative heat flux to convective heat flux is not small, the anomalous heating phenomena are observed. Therefore, scaling effect of the anomalous heating phenomena is also explained by accounting for the radiation from the driver gas.

(a) Shot # 1791 (driver gas temperature: 2,700 K)   (b) Shot # 1785 (driver gas temperature: 4,500 K)
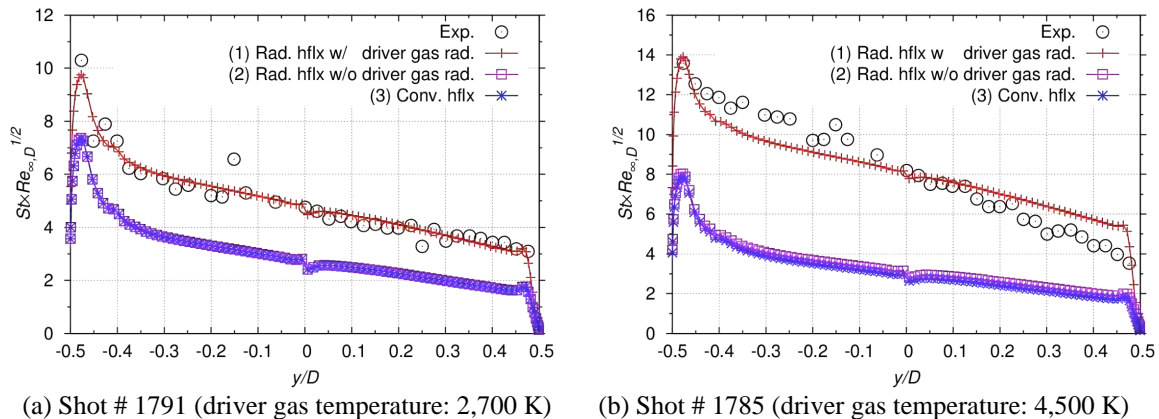
Figure 8. Normalized total heat flux including radiative heating from driver gas at AOA 30 deg.

(a) $\Phi 20 R 10$ probe for Shot # 1889   (b) $\Phi 50 R 100$ probe for Shot # 1891
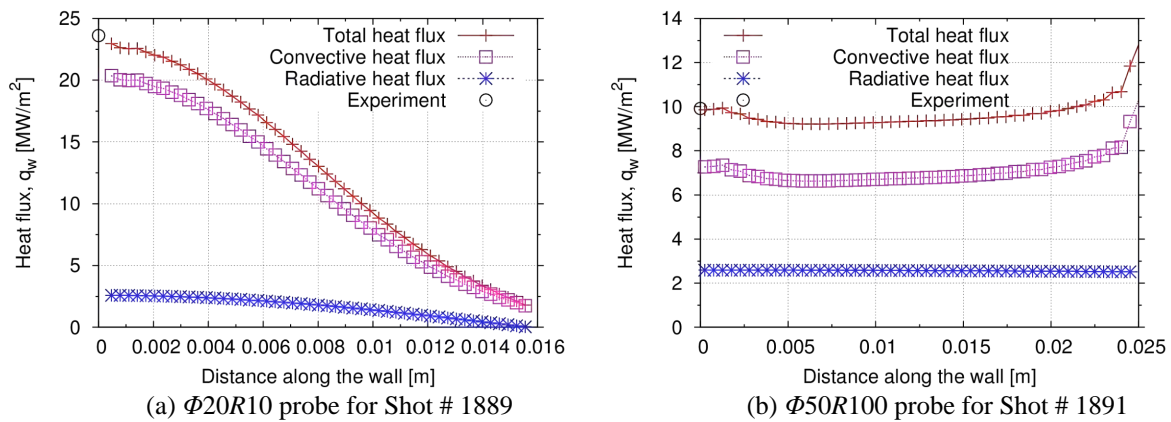
Figure 9. Total heat flux including radiative heating from the driver gas on small probes.

Summary

In this study, we computed heat fluxes for the forebody of Apollo CM test model to clarify the cause of the anomalous heating phenomena measured in HIEST experiments. We examined radiative heating both from the shock layer and the driver gas. It was found that HIEST heat flux data could be reproduced if radiative heating from the driver gas was included, with the temperature of the driver gas properly chosen. On the other hand, radiative heating from the shock layer was negligibly small.

We also examined the scaling effect of the anomalous heating phenomena. For probes, which had small radius, convective heat flux was significantly larger than radiative heat flux. Since the ratio of radiative heat flux to convective one was small, the anomalous heating phenomena were not shown notably. While, for probes which had large radius, the ratio of radiative heat flux to convective one was not small, such phenomena were shown. Scaling effect of the anomalous heating phenomena was also explained by accounting for the radiation from the driver gas.

Therefore, it is quite likely that anomalous heating phenomena seen in measured heat flux data are caused by radiative heating from the driver gas, although the further validation of driver gas temperature is needed. The anomalous heating phenomena in other shock tunnels also can be caused by the radiative heating from driver gas.

References

[1] Tanno, H., Kodera, M., Komuro, T., Sato, K., Takahashi, M., and Itoh, K., "Aeroheating Measurements on a Reentry Capsule Model in Free-Piston Shock Tunnel HIEST," AIAA Paper 2010-1181, 2010.

[2] Tanno, H., Komuro, T., Sato, K., Itoh, K., Yamada, T., Sato, N., and Nakano, E., "Heat Flux Measurement of Apollo Capsule Model in the Free-piston Shock Tunnel HIEST," AIAA Paper 2009-7304, 2009.

[3] Takahashi, M., Kodera, M., Itoh, K., Sato, K., and Tanno, H., "Influence of Thermal Non-equilibrium on Nozzle Flow Condition of High Enthalpy Shock Tunnel HIEST," AIAA Paper 2009-7267, 2009.

[4] Tanno, H., Komuro, T., Sato, K., Itoh, Ishihara, T., Ogino, Y., and Sawada, K. "Stagnation Heat Flux of Blunt Models in a High-Enthalpy Wind Tunnel," Conference proceedings of Symposium on SHOCK WAVES 1A1-2, 2012.

[5] Stewart, D. A. and Chen, Y. K., "Hypersonic Convective Heat Transfer over 140-deg Blunt Cones in Different Gases," *Journal of Spacecraft and Rockets*, Vol.31, No. 5, pp.735-743, 1994.

[6] Eric, M., Stuart, L., and Hans, G., "Apollo-Shaped Capsule Boundary Layer Transition at High-Entahlpy in T5," AIAA Paper 2010-446, 2010.

[7] Wright, M. J., Olejniczak, J., Brown, J. L., Hornung, H. G., and Edquist, K. T., "Modeling of Shock Tunnel Aeroheating Data on the Mars Science Laboratory Aeroshell," *Journal of Thermophysics and Heat Transfer,* Vol. 20, No. 4, pp.641-651, 2006.

[8] Olenjniczak, J., Wright, M. J., Laurence, S., Hornung, H. G., and Edquist, K. T., "Computational Modeling of T5 Laminar and Turbulent Heating Data on Blunt Cones, Part I: Titan Applications," AIAA Paper 2005-0176, 2005.

[9] Hollis, B. R., Liechty, D. S., Wright, M. J., Holden, M. S., Wadhams, T. P., MacLean, M., and Dyakonov, A., "Transition Onset and Turbulent Heating Measurements for the Mars Science Laboratory Entry Vehicle," AIAA Paper 2005-1437, 2005.

[10] MacLean, M., Wadhams, T., Holden, M., and Hollis, B. R., "Investigation of Blunt Bodies with CO2 Test Gas Including Catalytic Effects," AIAA Paper 2005-4693, 2005.

[11] Gnoffo, P. A., "An Upwind Biased, Point-Implicit Relaxation Algorithm for Viscous, Compressible Perfect-Gas Flows," NASA TP-2953, 1990.

[12] Mazaheri, Alireza, Gnoffo, P. A., Johnson, C. O., and Kleb,W., "LAURA Users Manual: 5.3-28528," NASA TM-2010-216386, 2010.

[13] Wright, M. J., Candler, G. V., and Bose, D., "Data-Parallel Line Relaxation Method for the Navier-Stokes Equations," *AIAA Journal*, Vol. 36, No.9, pp.1603-1609, 1998.

[14] Wright, M. J., White, T., and Mangini, N., "Data Parallel Line Relaxation (DPLR) Code User Manual Acadia-Version 4.01.1," NASA-TM-209-215388, 2009.

[15] Park, C., *Nonequilibrium Hypersonic Aerothermodynamics*, John Wiley and Sons Inc., New York, 1989.

[16] Kitamura, K. and Shima, E., "A New Pressure Flux for AUSM-Family Schemes for Hypersonic Heating Computations," AIAA Paper 2011-3056, 2011.

[17] Van Leer, B., "Towards the Ultimate Conservation Difference Scheme. V. A Second-Order Sequel to Godunov's Method," *Journal of Computational Physics*, Vol. 32, No. 1, pp.101-136, 1979.

[18] Yoon, S. and Jameson, A., "An Lu-ssor Scheme for the Euler and Navier-Stokes Equations," AIAA Paper 87-600, 1987.

[19] Eberhartdt, S. and Imlay, S., "Diagonal Implicit Scheme for Computing Flows with Finite Rate Chemistry," *Journal of Thermophysics and* Heat Transfer, Vol. 6, No. 2, pp. 208-216, 1992.

[20] Vincenti, W. G. and Kruger, C. H., *Introduction of Physical Gas Dynamics*, John Wiley and Sons Inc., New York, 1967.

[21] Park, C. and Milos, F. S., "Computational Equations for Radiating and Ablating Shock Layers," AIAA Paper 90-0356, 1990.

[22] Lordi, J. A., Mates, R. E., and Mossele, J. R., "Computer Program for Numerical Solution of Nonequilibrium Expansions of Reacting Gas Mixtures," NASA CR-472, 1966.

[23] Candler, G. V. and Nompelis, I., "Computation Fluid Dynamics for Atmospheric Entry," Von Karman Institute for Fluid Dynamics Lecture Series, RTO-EN-AVT-162, 2009.

Visualization of Unsteady Behavior of Shock Waves around Supersonic Intake installed in Shock Tunnel

Naruaki TANAKA
Toshiharu MIZUKAKI

Department of Aeronautics and Astronautics, Graduate School
Tokai University
4-1-1 Kitakaname, Hiratsuka-shi, Kanagawa, 259-1292
Japan
1bmjm021@mail.tokai-u.jp

Abstract

This paper describes unsteady behavior of shock waves around supersonic intake at Mach 2.5. The experiment carried out by small shock tunnel. Flow visualization was conducted with shadowgraph method and pressure-sensitive paint (PSP). A fast response anodized aluminum pressure-sensitive paint (AA-PSP) was used in the experiment. And to confirm the valid of experimental results, numerical calculation were performed by compressible Navier-Stokes equations with Weighted Average Flux (WAF) method and Adaptive Mesh Refinement (AMR). From the results of shock wave structures and pressure distribution, we confirmed shock waves behavior around the supersonic intake model at subcritical state. It considers occurring buzz.

Key words: supersonic intake, buzz, shock tunnel, flow visualization, pressure-sensitive paint

Introduction

A ramjet engine is considered as an engine of a next generation supersonic plane and a space plane. A ramjet engine is an air breathing engine, which compresses air by shock waves, which occurs at supersonic flight. Therefore, a supersonic intake is an important component for engine efficiency.
To keep the stable combustion of a ramjet engine, a supersonic intake should capture enough air and should be a certain level of pressure recovery [1]. When shock wave oscillation (buzz) occurs at a supersonic intake, ideal air mass flow and ideal pressure recovery are difficult to obtain. At worst, buzz leads to structural damages of a ramjet engine [2]. Unknown portion remains in the mechanism of buzz generation. Therefore, it is important to confirm the flow structure and flow characteristics around a supersonic intake, to clarify buzz mechanism.
The purpose of this study is to confirm unsteady behavior of shock waves around the supersonic intake by shock wave structures and pressure distribution. The experiment is carried out by small shock tunnel. Also shock wave structures are obtained by shadowgraph method, and pressure distribution is obtained by a fast response anodized aluminum pressure-sensitive paint (AA-PSP). The experiment results are evaluated with the numerical results calculated with the compressible Navier-Stokes equation.

Experimental Setup

Shock Tunnel
Figure 1 shows a schematic diagram of the small shock tunnel used in this experiment.
The length of high pressure tube is 1000 mm, low pressure tube is 3000 mm, test section is 310 mm and the dump tank is 800 mm. The bore of high pressure tube is 50 mm, the bore of dump tank is 195 mm and the cross section of low pressure tube is 30 mm × 40 mm. Also, reduce enlarging back pressure, an extra dump tank (1000 mm height) is added. High pressure tube and low pressure tube are separated by polyethylene

terephthalate diaphragm (TORAY INDUSTRIS, INC., Lumirror). A needle is set at high pressure tube, which is puncturing a diaphragm. A nitrogen cylinder is connected to the high pressure tube and a vacuum pump is connected to the dump tank. Two pressure ports (PT1 and PT3) are set at the low pressure tube. Fast response piezoelectric pressure transducers (PCB PIEZOTRONNICS INC., 113A20 series) are installed in each pressure ports. Output voltage resulting from pressure transducers are recorded by a digital oscilloscope (Yokogawa Electric Corporation, DL-750). From each pressure results, we measure shock wave arrival time and calculate shock Mach number.

Figure 2 shows a schematic diagram of the test section used in this experiment. The test section has two dimensional Laval nozzle (design Mach number 2.5).
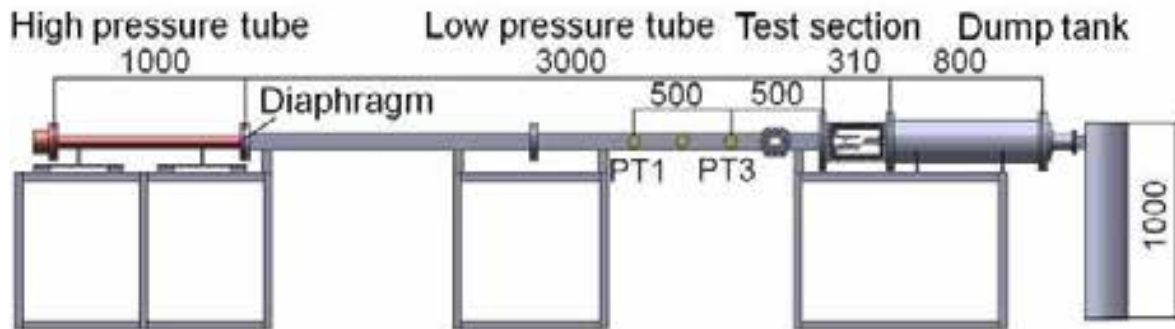
Fig. 1. Shock Tunnel. (unit: mm)
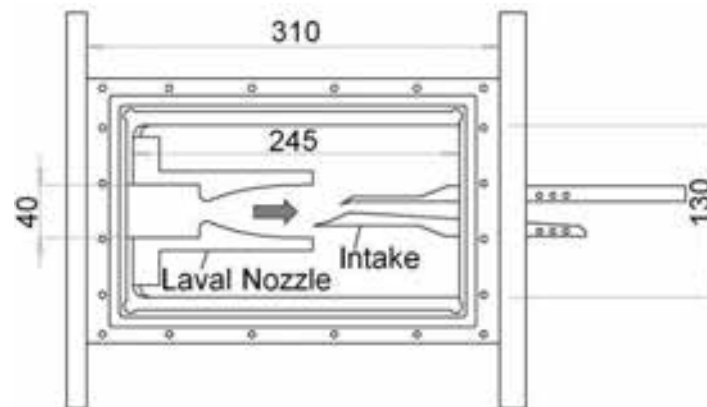
Fig. 2. Test Section. (unit: mm)

Supersonic Intake Model

Figure 3 shows the external supersonic intake model (design Mach number 2.4) used this experiment. The intake model is consisted of a double-wedge ramp, cowl, subsonic diffuser, and a plug. The plug is set at rear of the intake model and is able to adjust a position of the intake model. The plug, which is able to change back pressure by moving back and forward.
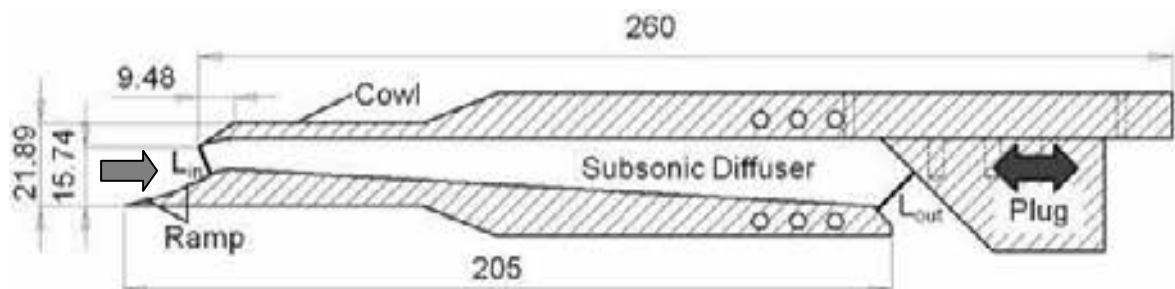
Fig. 3. Supersonic Intake model. (unit: mm)

Measurement Technique
Shadowgraph Method

Figure 4 is schematic diagram of shadowgraph system. Flow visualization is conducted by through digital delay circuit (SUGAWARA Laboratories Inc., FG-310), that trigger signal is from piezoelectric pressure transducers PT1. Flow visualization images are acquired by a digital high speed camera (Vision Research Inc., Phantom V7.1) and a digital still camera (Nikon Corporation, D200; Maximum effective pixels 3872 × 2592 pixels). Metal halide fiber optic illuminator (Dolan-Jenner Industries, MH100) is used for high speed camera light source. Xenon flash lamp (SUGAWARA Laboratories Inc., NP1-A; Flash duration 180 μs) is used for digital still camera light source.
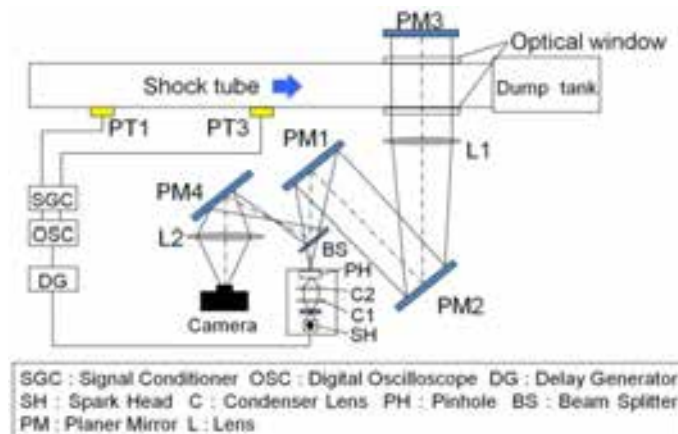
Fig. 4. Schematic diagram of shadowgraph system.

Pressure-Sensitive Paint

The pressure-sensitive paint (PSP) is the molecular sensor, which used oxygen quenching from the organic molecule luminescence. General polymer PSP is insufficient time response for high speed unsteady phenomenon measurement (e.g., measuring buzz). Therefore, a fast response anodized aluminum pressure-sensitive paint (AA-PSP) is used in the experiment [3] [4] [5]. The AA-PSP gives short response, which is suitable for high-speed unstable phenomenon measurement. The AA-PSP is produced anodized coating on aluminum material, and adsorbs the dye on its coating. The AA-PSP has more than 10 kHz time response. In this experiment, dye is Bathophenanthroline Ruthenium ([Ru(ph2-phen)3]Cl2). Figure 5 is Schematic diagram of AA-PSP structure.
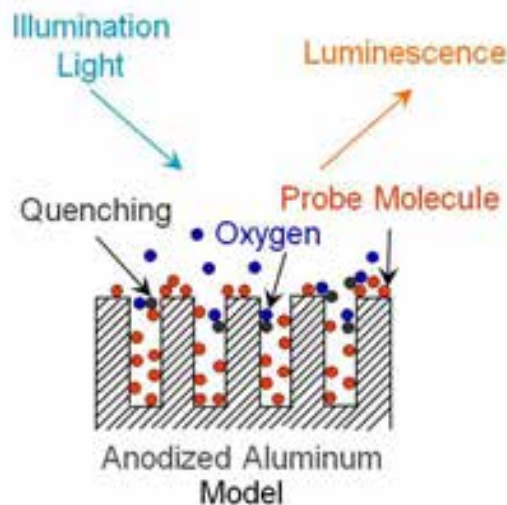
Fig. 5. Schematic diagram of AA-PSP structure.

Figure 6 shows schematic diagram of PSP system. The Ar+ laser (Coherent Inc., Innova 70; Wavelength 488.0 nm) is as the illumination light source. Pressure-sensitive paint images is obtained by a digital high speed camera (Vision Research Inc., Phantom V7.1) and the luminescence filter (HOYA CORPORATION, O-58), which is transmitted only 580 nm or more. The aluminum board (A-5052) which coated the AA-PSP is installed in test section of the supersonic intake model side wall.
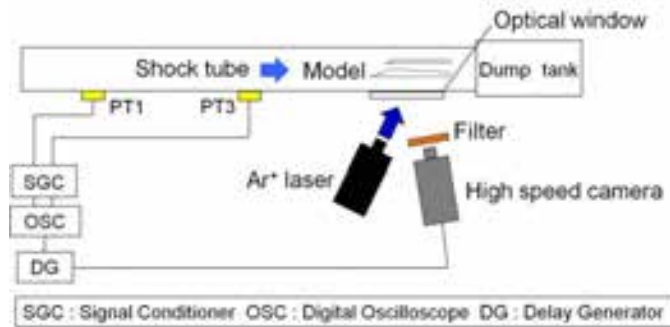
Fig. 6. Schematic diagram of PSP system.

Experimental Condition

Table 1 shows experiment condition in this research. Experiments are carried out on three pattern back pressures. Back pressure is adjusted by the plug is moving back and forward, and changing the ratio of the intake exit L_{out} to the intake entrance L_{in}. But at pattern (a), the plug is not installed.
Table 2 shows shock tunnel condition in this experiment. Test flow is about Mach 2.5.

Table. 1. Experimental conditions.

	L_{in} [mm]	L_{out} [mm]	L_{out} / L_{in}
(a)	8.09	—	—
(b)	8.09	8.09	1.00
(c)	8.09	4.05	0.501

Table. 2. Shock tunnel conditions.

	(a) (b)	(c)
Driver Gas	N_2	N_2
Driven Gas	Air	Air
P_1	10 [kPa]	10 [kPa]
P_4	2000 [kPa]	500 [kPa]
P_4/P_1	200	50
Ms	2.45	2.07
Me	2.54	2.50

P_1: Low pressure room

P_4: High pressure room

Numerical Calculation

Numerical calculations are performed by compressible Navier-Stokes equations with Weighted Average Flux (WAF) and Adaptive Mesh Refinement (AMR) [6] [7].

Boundary condition is isothermal wall, Prandtl number is $Pr = 0.733$, and Reynolds number is $Re = 7.71 \times 10^4$. Reynolds number's diameter is decided by low pressure tube's cross-section height. Another numerical calculation condition is the same as experimental condition.

Figure 7 is schematic diagram of computational domain in this calculation. Its left edge is in flow boundary condition and right edge is out flow boundary condition. Also, a shock wave is generated from the position shown in Fig. 7.
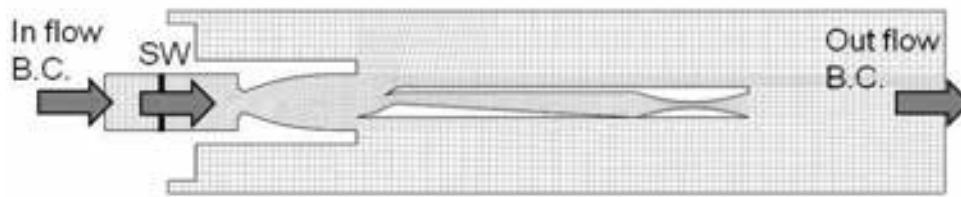
Fig. 7. Computational domain.

Results

Shadowgraph Method
Plug Position Variation

Figure 8 is flow visualization images around supersonic intake by shadowgraph method. These images are acquired by a digital high speed camera.

From pattern (a) result, two oblique shock waves can be confirmed at two ramps. These are concentrated on around the cowl lip. Also, two oblique shock waves can be confirmed in the subsonic diffuser. It can be determined; flow speed in the diffuser is supersonic. Therefore, the supersonic intake is supercritical state.

From pattern (b) result, two oblique shock waves can be confirmed at two ramps. These are concentrated at the cowl lip. Also, a normal shock wave can be confirmed on the cowl lip, and shock waves cannot be confirmed at the diffuser. This is because the plug is adjusted and air is compressed properly. Therefore, it can be determined flow speed in the diffuser is subsonic, and the supersonic intake is critical state.

From pattern (c) result, two oblique shock waves can be confirmed at two ramps. Also, a normal shock wave can be confirmed on left of the cowl lip. This is because the intake back pressure is increased by the plug adjustment, and shock waves are pushed. And, two oblique shock waves can be confirmed in the diffuser. This is because behind the normal shock wave flow is accelerated at until flow goes into the diffuser. Therefore, it can be determined; the supersonic intake is subcritical state.
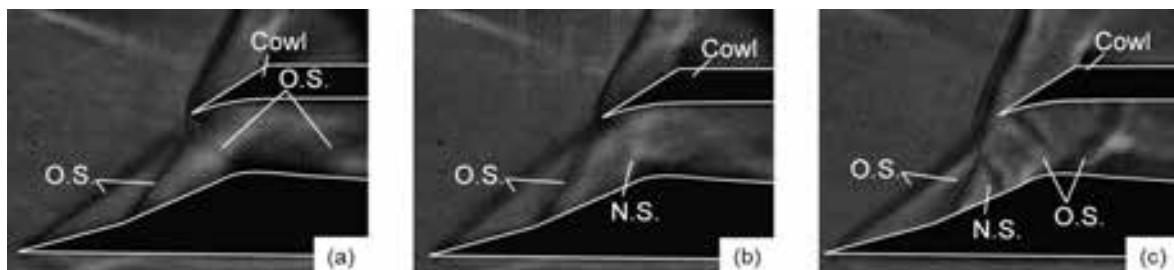
N.S. : Normal Shock Wave   O.S. : Oblique Shock Wave
Fig. 8. Visualization Image Results (plug position variation).

Time Variation

Figure 9 is flow visualization images around supersonic intake by shadowgraph method. These images are taken at time change in subcritical state. The acquiring is conducted by a digital still camera. The state of Fig. 8 (c) is set to 0 μs, and a shadowgraph image is taken in 500 μs and 1000 μs.
From results of Fig. 9, a normal shock wave that behind oblique shock waves can be confirmed moving to left at ramps. Also, at 500 μs and 1000 μs, we cannot confirm oblique shock waves at the diffuser. This is because air is leaking from the cowl lip, and air does not flow in the diffuser. Therefore, from results of Fig. 9, moving shock waves to left is considered occurring shock wave oscillations (buzz).
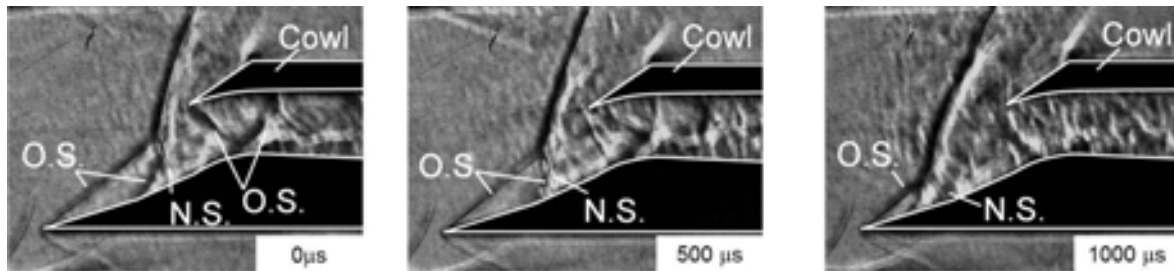
N.S. : Normal Shock Wave   O.S. : Oblique Shock Wave
Fig. 9. Visualization Image Results (time variation).

Pressure-Sensitive Paint

Figure 10 are PSP images (top) and numerical results (bottom) at supercritical state (left row) and subcritical state (right row). These results are shown pressure distribution.
From the PSP result of supercritical state, we can be confirmed high pressure area at ramps. This is because two oblique shock waves occur at ramps. Therefore, air is compressed and pressure is increasing. Also, we can be confirmed high pressure area at around the cowl lip. These results are same as numerical results.
From the PSP result of subcritical state, we can be confirmed high pressure area at left of the cowl lip. This is because shock waves occur at left of the cowl lip. From the numerical result, we can be confirmed same result.
Figure 11 are PSP images at subcritical state. These images are taken at time change in subcritical state. The state of Fig. 10 of subcritical state is set to 0 μs, and a PSP image is taken in 500 μs and 1000 μs.
From the PSP result, we can be confirmed high pressure area at left of the cowl lip and high pressure area is moving to left on the ramps. This is because shock waves move to left by shock wave oscillation. It can be confirmed shadowgraph images (Fig. 9). Therefore, we can be confirmed buzz by pressure-sensitive paint.
But, all PSP image results are not sharpness by noise. This is because, the brightness of the taken images are not enough. Therefore, we should obtain more luminance by AA-PSP luminescence.

PSP image   **PSP image**

Numerical result image   **Numerical result image**
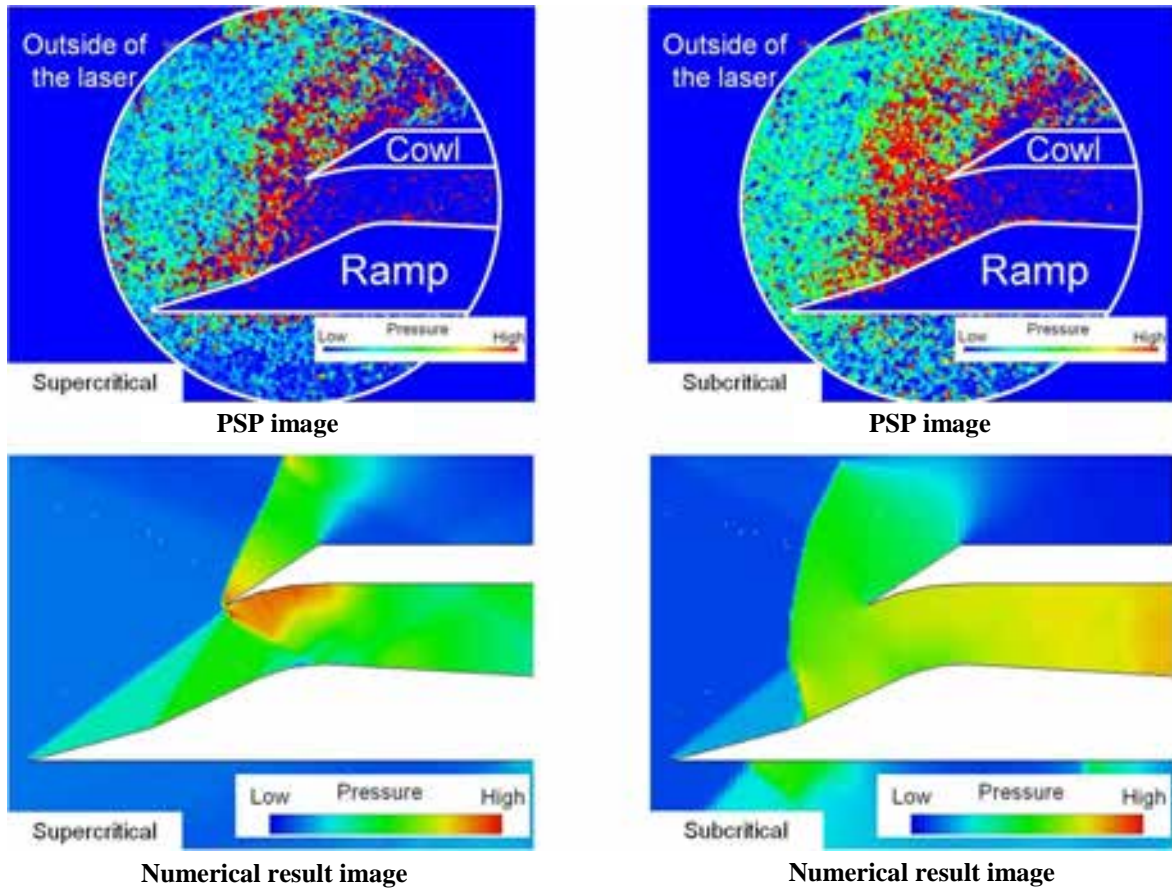
Fig. 10. PSP Image Results and Numerical results.
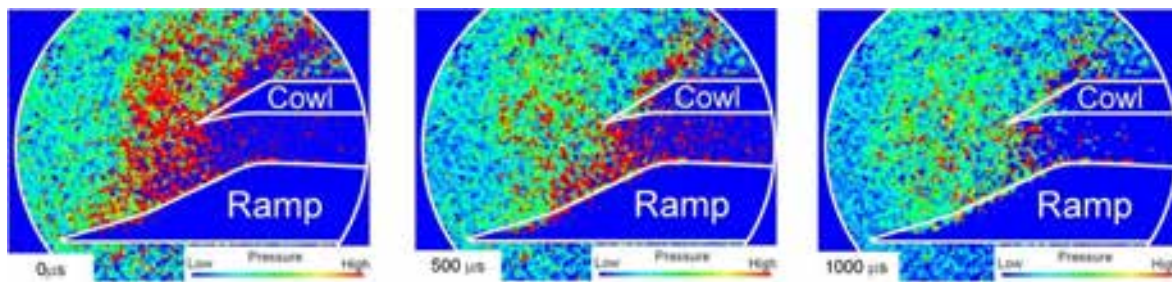
Fig. 11. PSP Image Results (time variation).

Conclusions

In this research, we visualized shock wave structures around the external supersonic intake model. Flow visualization was conducted by shadowgraph method and PSP. Also, PSP experiment results were evaluated with the numerical results. The results indicate below.

- We confirmed supercritical state, critical state and subcritical state by experiment.

- Shock wave behaviors can be confirmed at subcritical state by shadowgraph method. It considers occurring buzz.

- We obtained intake side wall surface pressure distribution and to confirmed shock wave behavior by PSP image results.

- Almost pressure distribution of PSP results are same as numerical pressure distribution results.

- From the PSP results, we should obtain more luminance by AA-PSP luminescence, to obtain more sharp results.

Acknowledgment

References

[1] J. Seddon and E. L. Goldsmith. *Intake Aerodynamics.* 2nd Edition, AIAA Education Series, 1999.

[2] T. Asanuma, T. Obokata and T. Nagashima.: Experimental Study on Supersonic Air Intake Buzz. *Institute of Space and Aeronautical Science, University of Tokyo Report*, 9(2_C), pp 499-542, 1973.

[3] K. Asai, H. Kanda, C. T. Cunningham, R. Erausquin and J. Sullivan.: Surface Pressure Measurement in a cryogenic wind tunnel by using luminescent coating. *ICIASF 97*, Record, pp 105-114, 1997.

[4] H. Sakaue, J. P. Sullivan, K. Asai., Y. Iijima and T. Kunimasu.: Anodized Aluminum Pressure Sensitive Paint in a Cryogenic Wind Tunnel. *ISA Proceedings of the 45th International Instrumentation Symposium*, pp 345-354, 1999.

[5] K. Nakakita and K. Asai.: Pressure-Sensitive Paint Application to a Wing-Body Model in a Hypersonic Shock Tunnel. *22nd AIAA Aerodynamics Measurement Technology and Ground Testing Conference*, 2002.

[6] E. F. Toro.: *Riemann Solvers and Numerical Methods for Fluid Dynamics.* 2nd Edition, Springer, 1999.

[7] A. Abe.: *Experimental and numerical studies of shock wave attenuation over bodies with complex configurations.* Tohoku University Graduate School of Engineering Ph.D. Dissertation, 2002.

Experimental investigation of initial shear-layer effect on the pressure oscillation in supersonic cavity flows

Takaya Ozaki
Shinji Maruyama
Hatsuki Kakuno
Taro Handa

Department of Energy and Environmental Engineering
Kyushu University
Kasuga City, Fukuoka 816-8580
Japan
2ES11160M@s.kyushu-u.ac.jp

Abstract

In the present study, features of oscillatory supersonic flows over a rectangular cavity are measured by changing the initial shear-layer property for the purpose of validating the numerical flow simulation perfomed as future work. In the experiments, two inlet flows having the same Mach number of 1.7 and different initial shear-layer properties are tested. The pressure oscillation is measured at the bottom wall of the cavity by use of the semiconductor-type pressure transducer by changing the length-to-depth ratio of the cavity at each condition. The instantaneous flow fields are also visualized by the schlieren method with a high-speed camera. As a result, it is found that the dominant oscillation frequency and the strength in pressure oscillation depend strongly not only on the length-to-depth ratio but also on the initial shear-layer property.

Key words: cavity flow, supersonic flow, flow oscillation, mixing enhancement

Introduction

Since the 1950s, a lot of investigations have been performed in order to understand the complicated flow structure of a supersonic flow over a rectangular cavity [1-6]. This flow is known to oscillate at certain predominant frequencies due to the feedback mechanism that involves shear layer instability and pressure wave propagation in the cavity. Such oscillations are possibly utilized to enhance supersonic mixing in the scramjet engine combustor [7-11] and chemical oxygen and iodine laser (COIL) [12].

In utilizing the cavity-induced pressure oscillation in the mixing enhancement, it is desirable that the flow keeps oscillating when the flow encounters a change in inlet conditions. If the flow encounters an inlet condition at which the flow oscillation becomes weakened, the flow should be controlled so as to keep oscillating, which might be achieved by adjusting the cavity depth. It is, therefore, important to predict the conditions at which the flow oscillates moderately. It is also important to understand the physical mechanism by which the oscillation is amplified or attenuated. In order to attain these, we have to rely on the computational fluid dynamics (CFD) because a lot of inlet conditions can be attempted in the numerical simulation more easily than in the experiment. In addition, the detailed flow behaviors by which the oscillation is amplified or attenuated may be found out in the numerical simulation. In contrast to such usefulness of CFD, the computational results should be checked carefully by the experimental results. However, it is difficult to validate the CFD results due to lack of experimental data.

The caivty-induced flow oscillation is expecded to sensitive to several parameters, such as inlet Mach number, Reynolds number, cavity length and depth, initial shear-layer property, and so on. The effect of inlet Mach

number was investigated experimentally by Zhang and Edwards [5], who tested two inlet Mach numbers of 1.5 and 2.5 changing the cavity length L from $L = 15$ mm to $L = 135$ mm at the constant cavity-depth D (= 15 mm). According to their results, the flow at the Mach number of 1.5 osccilates more strongly than that at at the Mach number of 2.5 over all the tested L/D's.

Chandra and Chacravathy [6] measured the dominant oscillation frequenies by changing L and D at an inlet Mach number of 1.5. Their results reveal that the oscillation frequency is quite sensitive not only to L but also to D. Such a variation in frequency with respect to L/D is explained reasonably well by the oscillation model proposed by Handa and Masuda [7].

Upon reviewing the above studies, a question about supersonic cavity flows emerges. That is, how does the initial shear-layer property affect the characteristic of the cavity-induced flow oscillation? In order to answer this question, in the present study we test two inlet conditions with the same Mach number and the different initial shear-layer properties. In the experiments, the pressure oscillation is measured by changing the length-to-depth ratio of the cavity for both inlet conditions. The flow fields are also visualized by the schlieren method with a high-speed camera.

Experimental method

The experiments are carried out using a suction-type supersonic wind tunnel operated by dry nitrogen with atmospheric pressure and temperature. Before a tunnel run, the nitrogen is stored in the balloon that is connected to the stagnation chamber through a tube. This gas has a water content of less than 5ppm, and condensation in the duct is avoided by using this gas.

In order to investigate the effect of the initial shear-layer, two test ducts are designed as shown in Figures 1(a) and (b). Two symmetric contoured nozzles are designed using the method of characteristics. These are connected to the two test ducts, respectively. The Mach numbers at the nozzle exit are designed to be 1.7 and 2.0 for cases 1 (Fig. 1(a)) and 2 (Fig. 1(b)) respectively. However, the inlet Mach numbers can be set to the almost same value for both cases by making the distance from the nozzle exit to the leading edge of the cavity for case 2 longer than that for case 1. The inlet Mach numbers calculated from the static pressure measured at the location 6.0 mm upstream of the leading edge are 1.68 and 1.74 for case 1 and 2, respectively.

Both test ducts have the same rectangular cross-section whose height and width are 10.5 mm and 28.0 mm, respectively. The cavity length L is 14.0 mm and the cavity depth is adjustable. In the present experiments, the cavity depth is ranged from 4.7 mm to 28.0 mm ($L/D = 0.5 - 3.0$). Both test ducts have a section with a 10° divergence angle downstream of the cavity in order to avoid unstarting in the wind tunnel due to the boundary layer growth. The coordinate systems used to analyze the results are defined in Figs. 1(a) and (b), where x and y are the streamwise and height coordinates, respectively. The pressure and temperature in the stagnation chamber are maintained at 101 kPa and 301 K respectively. The free-stream Reynolds number based on the duct height is 1.48×10^5.

The temporal variation of the static pressure is measured with a semiconductor-type pressure transducer (Kulite, XCQ-062-25SG). This transducer is mounted on the bottom wall of the cavity and is located 7.0 mm downstream of the front wall of the cavity and this is placed on the central plane of the duct. The temporal pressure signals are recorded by a digital oscilloscope (IWATSU DS-9121) at 1000k samples per second for a total of 16384 samples.

The oscillatory flow fields are visualized by the schlieren method. In the optical setup, two concave mirrors with focal lengths of 200 cm are used to collimate the light passing through the test section. The flow field is imaged through a single lens with a focal length of 100 cm and a diameter of 5 cm. Imaging scale is estimated to be ~0.6 for the present schlieren system. A camera with a fast frame rate (NAC Image Technology, ULTRA Cam HS-106E) is used to capture the schlieren images. The frame rate is set to 600,000 frames per second. The exposure time is set to 0.3 μs. One pixel on a digitized image corresponds to the physical size of 87.5 μm × 87.5 μm. The distance that the pressure wave propagates during the exposure time is estimated to be ~0.1 mm. This value indicates that the temporal resolution is high enough to capture the pressure waves in the flow field. The number of images captured per experimental run is 120. The light source is a xenon lump (Nissin
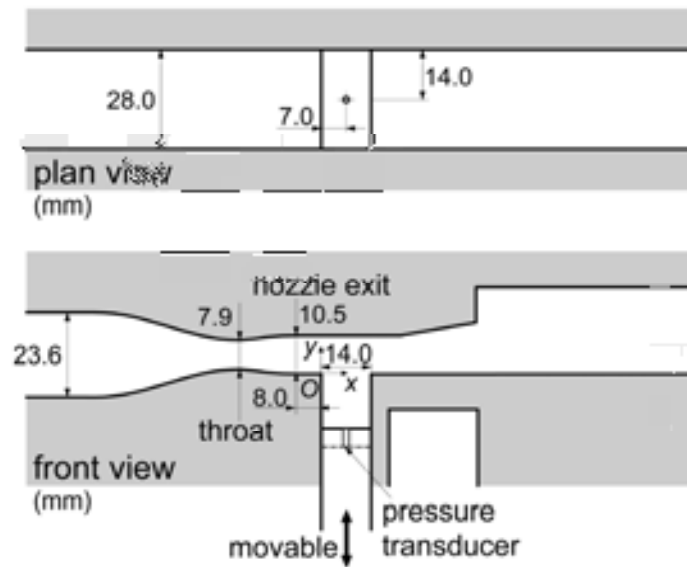
(a) case 1
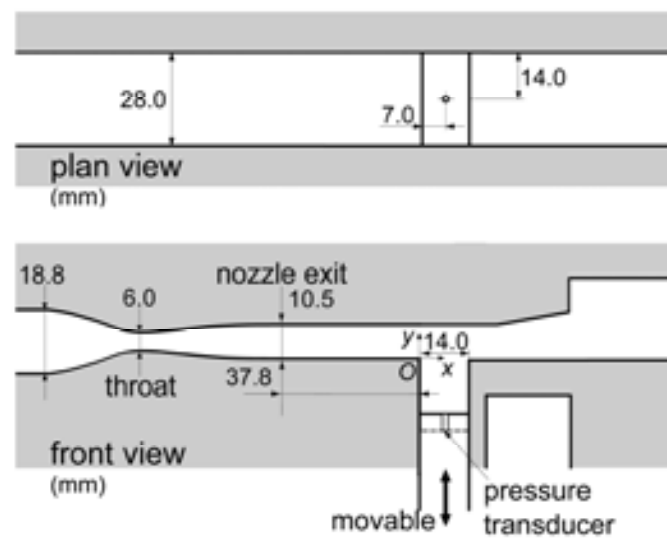
(b) case 2
Fig. 1 Test ducts

Electronic SAX-100H). The flash duration of this lump is ~1ms, and the light emission becomes stable 150 μs after the lump starts to flash. The capture of images, therefore, is started 150 μs after the flash.

In order to measure the density profiles across the initial shear layer, another schlieren visualization is performed. In this visualization, a continuous light source (tungsten lump) is used with the same concave mirrors and lens as those used in the high-speed visualization. A charge coupled device (CCD) camera (Tokyo Electronic Industry, CS8310) is used to capture the schlieren images. The exposure time is set to 1/60 sec. One pixel on the digitized image captured in this camera corresponds to the physical size of 22.2 μm × 22.2 μm.

A density profile across the shear-layer is obtained by integrating the contrast of the digitized schlieren image along a *y*-direction from a point in the external flow to a point inside the cavity at which the flow is assumed to be stagnated. The density in the external flow is calculated from the time-averaged static pressure on the side

(a) case 1   (b) case 2
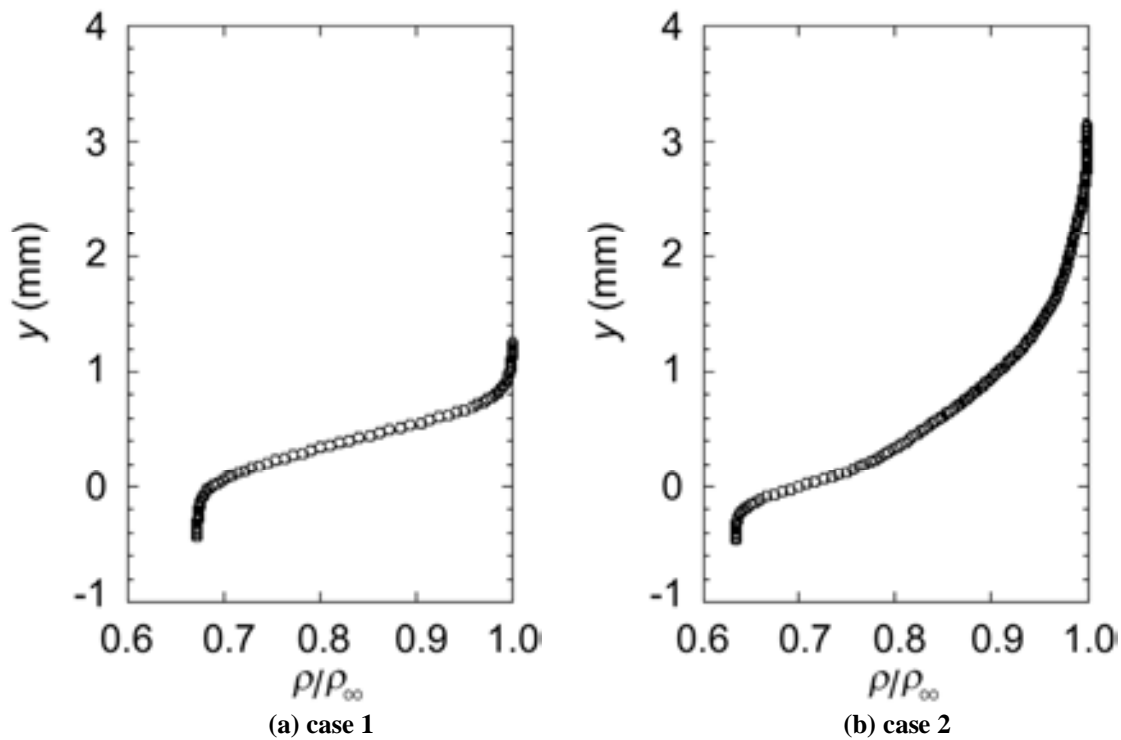
Fig. 2 Density profiles across the shear layer at *x*=1.0mm

(a) *L/D*=0.95   (b) *L/D*=1.2
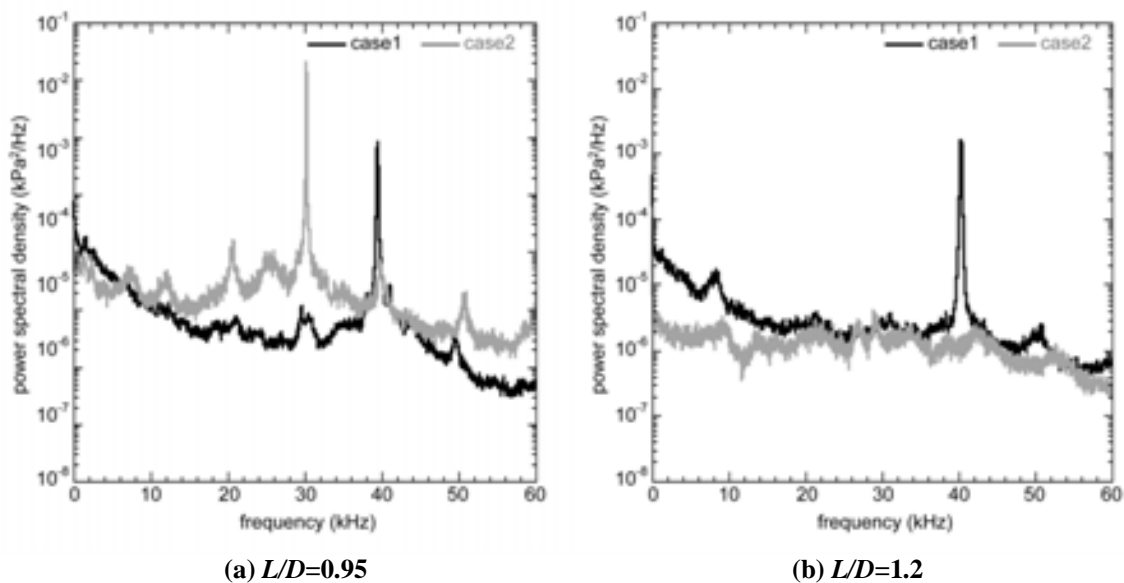
Fig.3 Power spectral density distributions

wall, the stagnation pressure and temperature in the prenum chamber. The density inside the cavity is calculated by assuming that the free-stream is stagnated adiabatically. The resulting density profiles at $x = 1.0$ mm are shown in Fig. 2. It is clear from this figure that the shear-layer for case 2 is thicker than that for case 1.
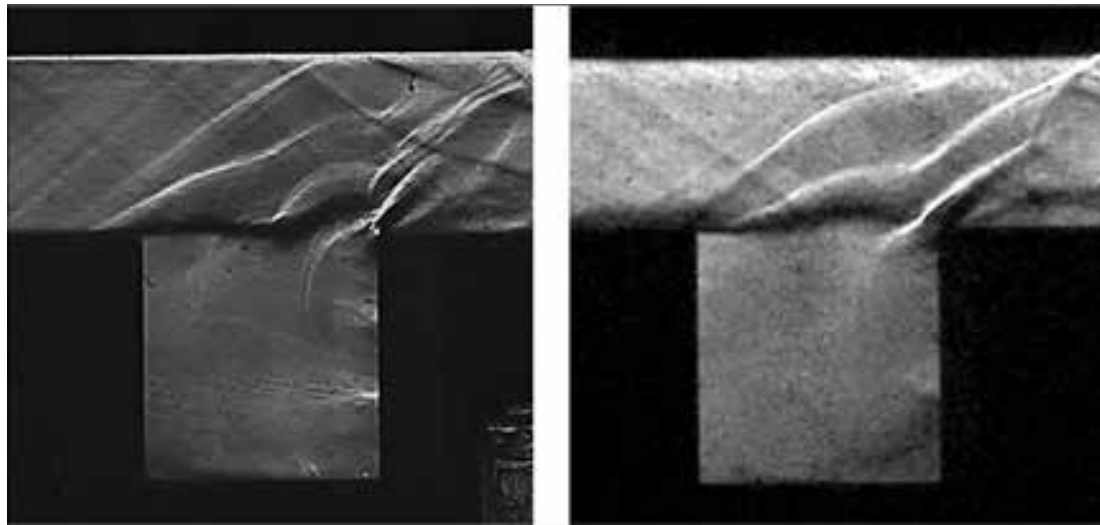
(a) case 1   (b) case 2

Fig. 4 Instantaneous schlieren images (*L/D*=0.95)
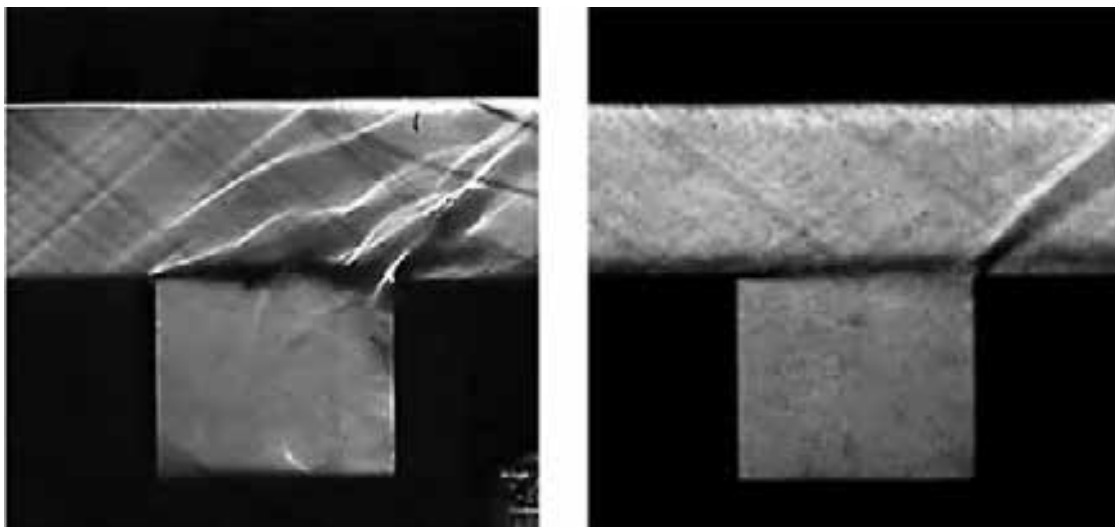
(a) case 1   (b) case 2

Fig. 5 Instantaneous schlieren images (*L/D*=1.2)

Results and Discussion

The power spectral density is calculated from the pressure signal measured on the bottom floor of the cavity for each *L/D*. The representative results are shown in Figs. 3(a) (*L/D* = 0.95) and (b) (*L/D* = 1.2). In Fig. 3(a), a sharp peak is observed for both cases 1 and 2. It is clear from these sharp spectral peaks that self-sustained oscillation occurs at *L/D* = 0.95 for both cases. However, the dominant frequencies are different between two cases at *L/D* = 0.95 (Fig. 3(a)). This implies that the initial shear-layer property strongly affects the dominant oscillation frequency. The flow oscillation is also recognized in the instantaneous schlieren images of Fig. 4. The pressure waves generated as a result of the oscillation are clearly observed above the cavity for both cases. The pressure waves are also seen clearly inside the cavity for case 1 (Fig. 4(a)), whereas not clearly seen for
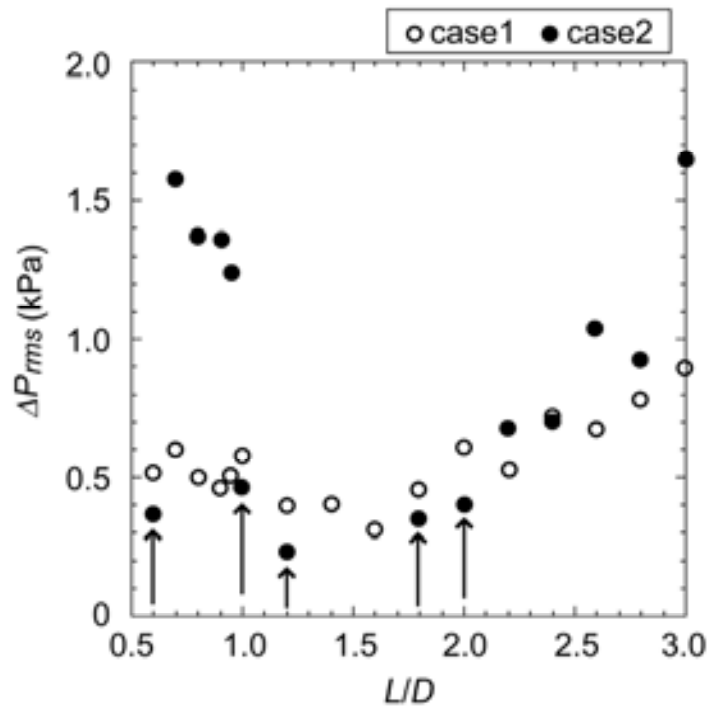
Fig.6 Plot of Δp_{rms} vs. L/D

case 2 (Fig. 4(b)). It is supposed that a three-dimensional flow might be formed inside the cavity for case 2. As a result of this three-dimensional flow, the pressure waves might have three-dimensional shapes. Therefore, it is concluded that the initial shear-layer property affects the three-dimensionality of the flow inside the cavity.

In Fig. 3(b) (L/D = 1.2), a sharp spectal peak is also seen only for case 1, whereas no remarkable peak is seen for case 2; i.e., the flow is quite steady for case 2. Such a steady flow is recognized in the instantaneous schlieren image of Fig. 5(b). No remarkable traveling pressure-waves are observed in this image. On the other hand, the pressure waves similar to those observed in Figs. 4(a) and (b) are also observed in Fig. 5(a). It is clear from the results for L/D = 1.2 that the initial shear-layer property affects the strength in flow oscillation because inlet flow parameters except initial the shear-layer profiles are the same between case 1 and 2.

The root-mean-square of the pressure fluctuation Δp_{rms} is calculated at each flow condition. The results are shown in Fig. 6. There are no data at L/D=1.4 and 1.6 for case 2 because unstarting occurs in the wind tunnel. It is found from the results that Δp_{rms} is strongly affected not only by the initial shear layer property but also by the length-to-depth ratio of the cavity. The results also reveal that there are several values of L/D at which a pressure oscillation for case 2 becomes much stronger than that for case 1, especially in deep-cavity flows, whereas, that there are also several values of L/D at which a flow is quite stable for case 2 (denoted by upward arrows). At present, we have no clear explanation for these phenomena. We have to rely on the computational fluid dynamics in order to clarify the reason why the flow is so selective in its oscillation even if the cavity length and inlet Mach number remain constant.

Conclusion

In the present study, features of oscillatory supersonic flows over a rectangular cavity are measured changing the initial shear-layer property for the purpose of validating the numerical flow simulation perfomed as future work. Two inlet flows having the same Mach number and different initial shear-layer properties are tested. The measurement results reveal that the initial shear-layer property strongly affects the dominant oscillation frequency and the strength in pressure oscillation especially in deep-cavity flows. At present, we have no clear

reason why the dominant oscillation frequency becomes different between two flows produced under the same condition except the initial shear-layer properties, and why the flow selects, depending on the cavity depth, either an oscillatory state or a very quiet state even if the cavity length and inlet Mach-number remain constant. In order to clarify these reasons, the numerical flow simulation have to be performed and the resulting computational flow-fields have to be analyzed in detail.

References

[1] K. Krishnamurty. : Acoustic Radiation from Two Dimensional Rectangular Cutouts in Aerodynamic Surfaces. *NACA Technical Note*, 3487, 1955.

[2] J. E. Rossiter. : Wind-Tunnel Experiments on the Flow over Rectangular Cavities at Subsonic and Transonic Speeds. *ARC R&M* 3438, 1964.

[3] H. H. Heller, D. G. Holmes, and E. E. Covert. : Flow Induced Pressure Oscillations in Shallow Cavities. *Journal of Sound and Vibration*, Vol. 18, pp. 545-553, 1971.

[4] D. Rockwell, and E. Naudascher. : Review – Self Sustaining Oscillations of Flow Past Cavities. *Journal of Fluids Engineering*, Vol. 100, pp.152-165, 1978.

[5] X. Zhang and J. A. Edwards. : An Investigation of Supersonic Oscillatiory Cavity Flows Driven by Thick Shear Layers. *Aeronautical Journal*, Vol. 94, pp. 355-364, 1990.

[6] B. U. Chandra and S.R. Chakravathy. : Experimental Investigation of Cavity-Induced Acoustic Oscillations in Confined Supersonic Flow. *Journal of Fluids Engineering*, Vol. 127, pp.761-769, 2005.

[7] T. Handa and M. Masuda. : On the Jump in the Frequency of Acoustic Oscillations in Supersonic Flows over Rectangular Cavity. *Physics of Fluids*, Vol. 21, 026102, 2009.

[8] K. H. Yu and K. C. Schadow. : Cavity-Actuated Supersonic Mixing and Combustion Control. *Combustion and Flame*, Vol. 99, pp. 295-301, 1994.

[9] N. Sato, A. Imamura, S. Shiba, S. Takahashi, M. Tsue, and M. Kano. : Advanced Mixing Control in Supersonic Airstream with a Wall-Mounted Cavity. *Journal of Propulsion and Power*, Vol.15, pp.358-360, 1999.

[10] J. M. Seiner, S. M. Dash, D. C. Kenzakowski : Historical Survey on Enhanced Mixing in Scramjet Engine. *Journal of Propulsion and Power*, Vol.17, pp.1273-1286, 2001.

[11] V. A. Nenmeni, K. Yu. : Cavity-Induced Mixing Enhancement in Confined Supersonic Flows. *AIAA Paper* 2002-1010, 2002.

[12] C. Noren, P. Vorobieff, C. R. Truman, and T. J. Madden : Mixing in a Supersonic COIL Laser: Influence of Trip Jets. *Experiments in Fluids*, Vol. 50, pp. 443-455, 2011.

Aerodynamic Characteristics of a Delta Wing with Arc Camber for Mars Exploration

Takao Unoguchi,[1] Shogo Aoyama,[1] Hiroshi Suemura,[1] Gouji Yamada,[1] Takashi Matsuno[1] Shigeru Obayashi[2] and Hiromitsu Kawazoe[1]

[1] Tottori University, 4-101 Koyama-Minami, Tottori, 680-8552, Japan
[2] Tohoku University, Katahira 2-1-1, Sendai, 980-8577, Japan
Email address:M11T1005B@edu.tottori-u.ac.jp

Abstract

In this research, we propose a delta wing with an arc camber to explore the Mars in flight at low Reynolds number of 1.0×10^4 order. The research focuses on L/D of a cambered delta wing to get a wide cross range for the Mars exploration by computational analysis and aerodynamic force measurements using a newly developed three-component force balance. The CFD results show that L/D of the delta wing with an arc camber is much better than the no-camber delta wing at a low angle of attack. Especially, the wing with the camber rate of 5% gives the best performance. The validation results by the EFD approach supports the CFD analysis.

Key words: Delta wing, Arc camber, Aerodynamics, Mars exploration, Three-component force balance

1. Introduction

Mars exploration by an airplane is expected as one of prospective methods, because it will enable to explore wide area of the Mars compared with a method by a land rover vehicle [1-3]. Such the airplane needs a wing suitable for the flight at a low Reynolds number in the Mars atmosphere. On the other hand, considering a high speed flight at a high altitude and performance of a wide cross range, a delta wing with a high ratio of lift to drag should be one of the candidates. Furthermore, a light, simple, and structurally strong wing is favorable for the carry to the Mars and the certain operation.

Supposing a Mars airplane which flies from high to low altitude in various speed, we have proposed a delta wing with a variable swept back angle of the leading edge. Furthermore, focusing on a low altitude flight at low speed in the Mars, a delta wing, the camber of which is changeable, has been also suggested to get a suitable performance of the ratio of lift to drag to the flight just above the Mars surface. In this paper, a delta wing with thin thickness and an arc-shape chord was investigated by the numerical and the experimental studies in the condition of a low Reynolds number [4-5]. Analysis by the computational fluid dynamics was carried out to study the characteristics of a thin delta wing with arc camber in such a low Reynolds number as the order of 1.0×10^4. Especially, we want to know what rate of the camber gives the maximum L/D. On the other hand, the experimental study was undertaken to make sure the prediction of the numerical analysis.

2. Prediction by the CFD Approach
2.1 Numerical Procedure

The plane shape of the thin delta wing of the research is shown in Fig.1, which has the swept-back angle of 60 degrees and the root chord length of 260 mm. The delta wing shown in Fig.1(a) has an arc-shape chord. The ratio of the maximum camber of the delta wing to the root chord, which is called as a camber ratio in the research, was changed from 0 to 15%. The aerodynamic performances of such the arc-shape cambered delta wings with a camber ratio were expected by numerical simulations based on the computational fluid dynamics (CFD). The higher the lift-drag ratio (L/D) becomes, the wider the cross range is. The delta wing in Fig.1(b) is a flat-plate type which was also investigated in the both of the numerical and the experimental approaches as a base delta wing. The CFD condition and the camber ratio for the CFD analysis are indicated in Tables 1 and 2.

The airflow around a delta wing were simulated for the various cases listed in Table 2 by the STAR-CCM+ code which is capable of generating grids and post processing the results. Figure 2 shows the computational grids for the case of the camber ratio of 5%. Incompressible Navier-Stokes equation without a turbulence model was used for these simulations.

(a) Cambered delta wing   (b) Flat delta wing
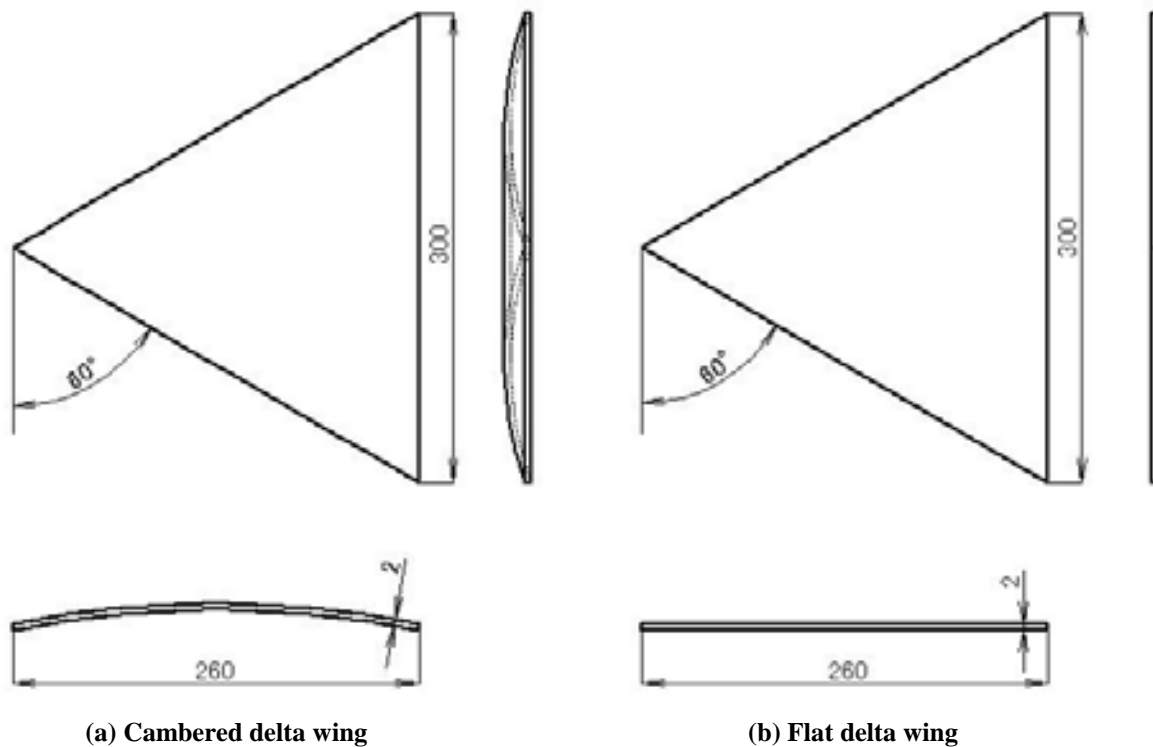
Fig.1 Delta wing geometry

Table 1 CFD condition for Mars atmosphere

Atmospheric condition	component	CO_2 100%
	density	0.0155 [kg/m^3]
	velocity	34 [m/s]
	pressure	700 [Pa]
	viscosity	1.36×10-5 [Pa·S]
	Reynolds number	$1.0×10^4$
Number of numerical cells		500,000 for the half span (Fig.2)

Table 2 Camber ratio in CFD approach

camber ratio	camber [mm]	root chord [mm]	Re
0%	0	260	1.0×10^4
0.5%	1.3	260	1.0×10^4
1%	2.6	260	1.0×10^4
3%	7.8	260	1.0×10^4
5%	13	260	1.0×10^4
7%	18.2	260	1.0×10^4
10%	26	260	1.0×10^4
15%	39	260	1.0×10^4
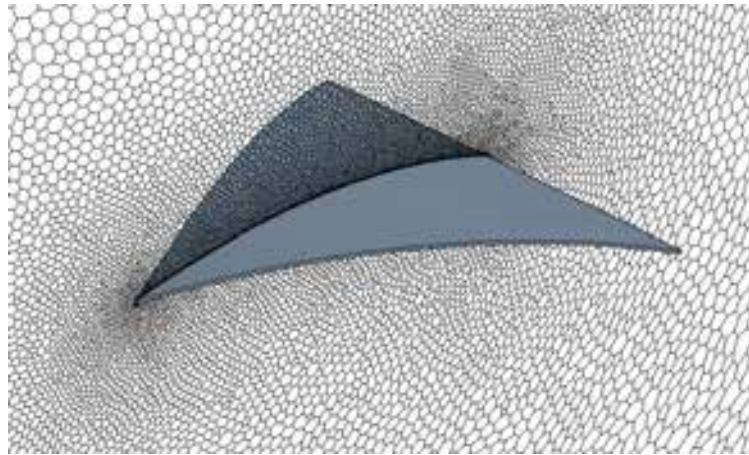
Fig.2 Volume mesh condition around the delta wing (camber ratio of 5%)

2.2 CFD Results

Figure 3 shows the L/D versus a camber ratio of the delta wings in the case of the Reynolds number of 1.0×10^4. The delta wing with an arc camber obtained higher performance than the flat delta wing at a low angle of attack. Especially, the delta wing with the camber ratio of nearby 5% gives the best performance compared to the other cambered wings at the all of the attack angle, namely 0, 5, and 10 degrees.

Figure 4 shows the longitudinal three components of aerodynamic force and moment (C_L, C_D, C_M) and L/D versus an angle of attack for the representative camber ratios of 0, 3, 5, and 7 %. It was found from the results that the delta wing with a large camber obtained high lift because of its effect similar to a flap. However, drag increases more rapidly than lift at an attack angle over 5 degrees. Therefore, the L/D of a large cambered delta wing decreases at a high angle of attack as shown in Fig.4(d). These results show that an optimum camber ratio exists to obtain a maximum L/D and it becomes about 5% in this study. Moreover, the change of L/D is very small at the attack angle between 0 and 5 degrees.

The results mentioned above are based on only the CFD analysis and it is, therefore, necessary to validate them by the experimental fluid dynamics (EFD) approach. However, experimental measurements of aerodynamic force and moment using a force balance should be very difficult for small lift and drag due to a low Reynolds number [6-9]. For the difficulties we newly designed and made a compact force balance to measure them. In the next chapter the force balance will be mentioned shortly and the validation to the CFD results by the EFD approach with the force balance will be described.
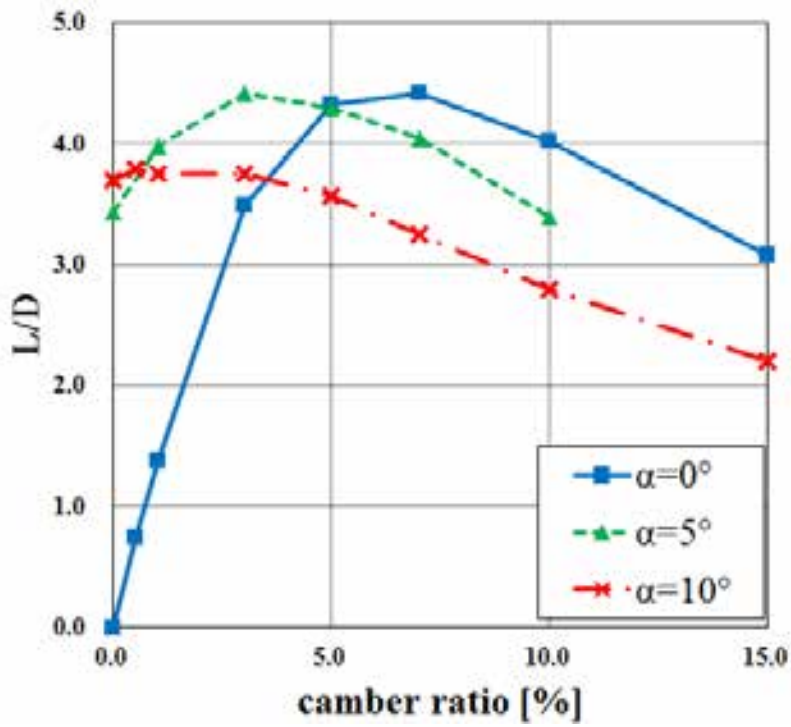
Fig.3 L/D characteristics with a camber ratio

(a) Lift

(b) Drag

(c) Pitching moment

(d) L/D
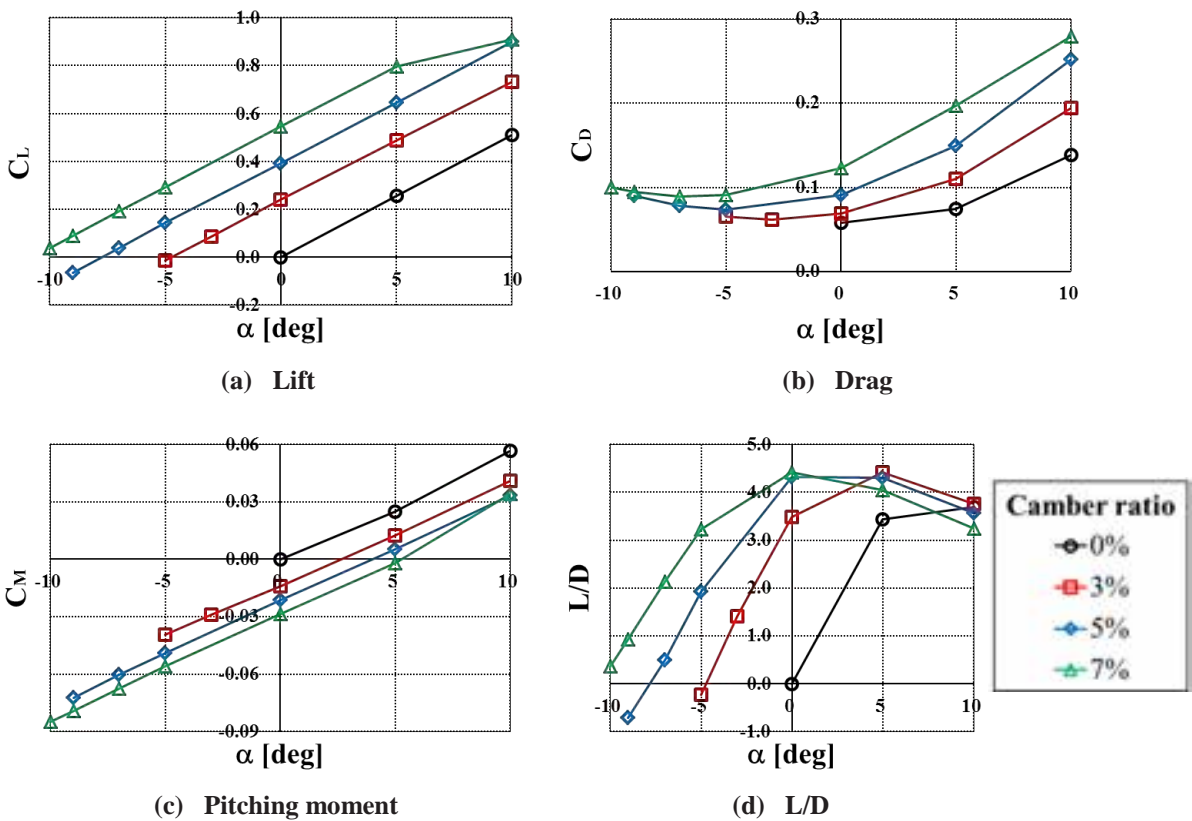
Fig.4 Aerodynamic characteristics of the cambered delta wings ($Re = 1.0 \times 10^4$)

3. Validation by the EFD Approach
3.1 Compact Force Balance

In the case of the low Reynolds number of 1.0×10^4 with the size of the delta wing shown in Fig.1, lift, drag and pitching moment were estimated no more than 0.15 N, 0.04 N, and 1.6×10^{-3} Nm respectively. A new type of force balance was then designed for the measurement as shown in Fig.5 and was made as shown in Fig.6. The ring part of the force balance has the diameter of 21 mm with the thickness of 0.5 mm and the width of 10 mm. Strains at the locations of the symbols F(y) and F(z) in Fig.5 corresponds to drag and lift in the research.

Measurements of aerodynamic force and moment were carried out at the low-speed wind tunnel of Tottori University as shown in Fig.7. The wind tunnel has the test section of 0.6 m × 0.6 m. Two delta wing models with an arc camber and no camber were made for the EFD validation measurements, the camber ratio of which is 5%. The no camber model was made of a flat plate with the thickness of 2 mm. These models made of aluminum. The geometrical data of these delta wings are the half size of the CFD research, that is the root chord of 130 mm. Table 3 shows the experimental conditions. Because lift and drag in the condition of the low Reynolds number, 1.0×10^4, became so small to detect by the newly developed force balance, the speed of the wind flow was increased from 1.2 m/s of for the Reynolds number of 1.0×10^4 to 6 m/s and 10 m/s corresponding to the Reynolds number of 5.0×10^4 and 8.2×10^4 respectively. These are the case name, EXP01 and EXP02, in Table 3, and analysis by the CFD simulation was also carried out for the case of the Reynolds number of 5.0×10^4 in the case of the root chord of 130 mm as shown in Table 3.

unit: mm
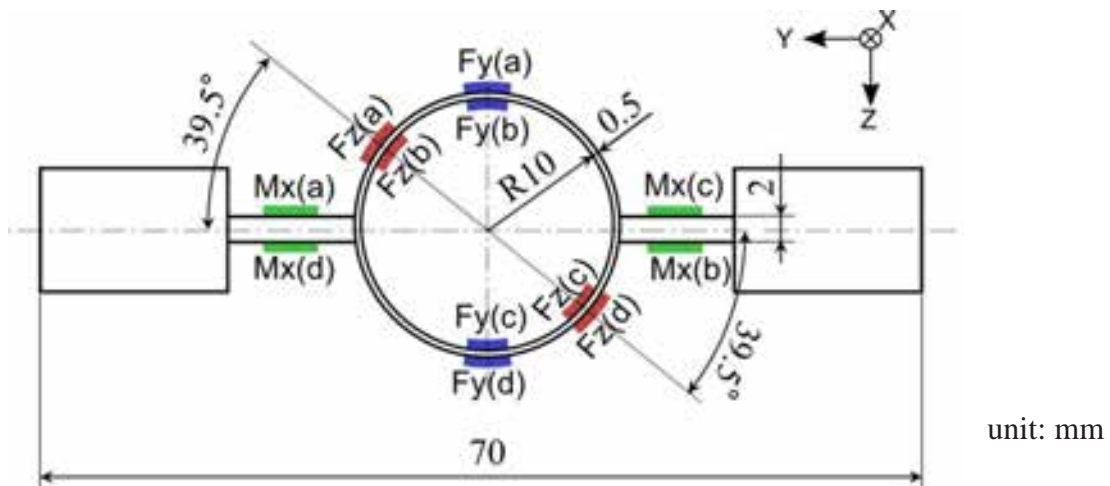
Fig.5 Schematic diagram of the three-component force balance
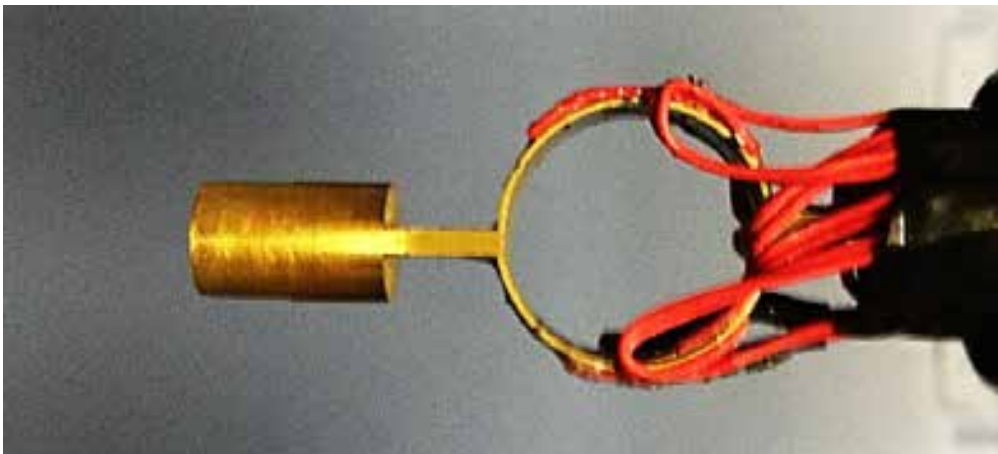
Fig.6 Developed three-component force balance
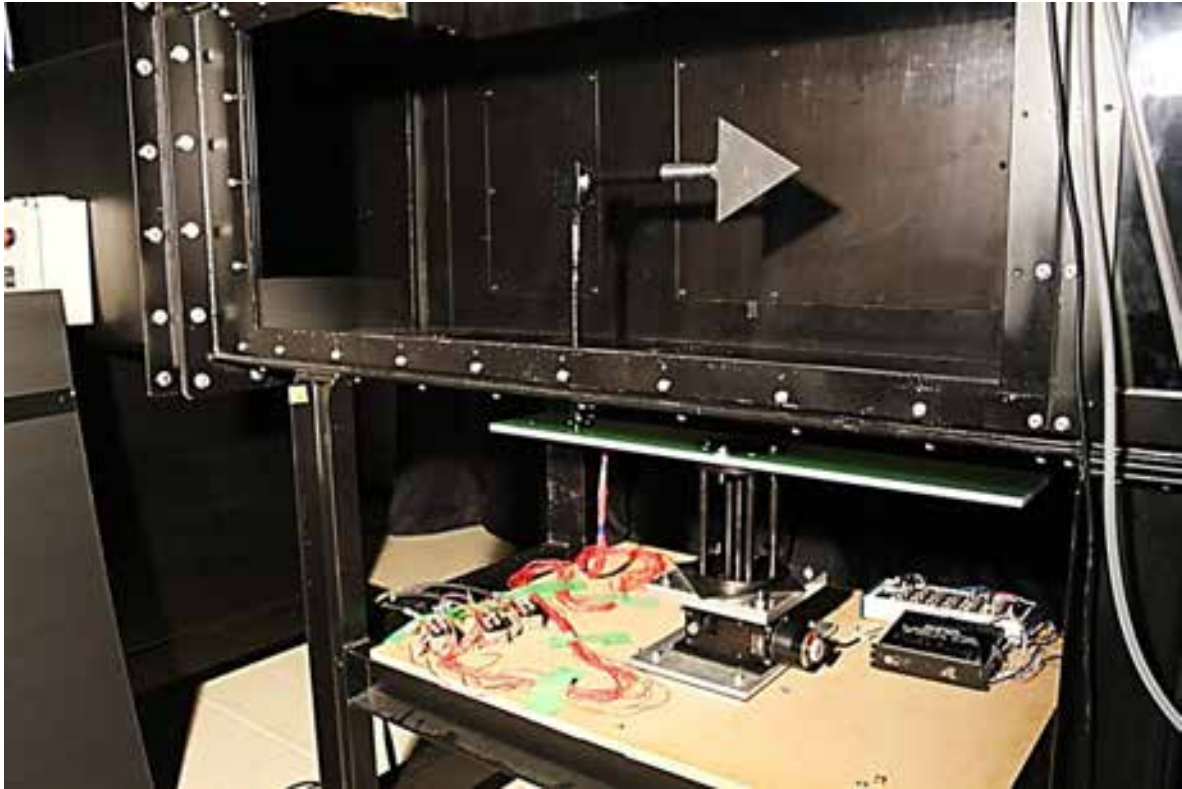
Fig.7 Experimental setup in the test section of the wind tunnel

Table 3 Experimental conditions

case	model	camber [mm]	root chord [mm]	flow velocity [m/s]	Re
EXP01	flat	0	130	10	8.2×10^4
	5% cambered	6.5		10	
EXP02	flat	0	130	6	5.0×10^4
	5% cambered	6.5		6	
CFD	flat	0	130	6	5.0×10^4
	5% cambered	6.5		6	

3.2 EFD Results

Aerodynamic characteristics of the arc camber and the flat delta wings are shown in Fig.8 comparing with the CFD results indicated by the solid and the dotted lines. First, from the results of the lift characteristics of Fig.8(a), it was found that the cambered delta wing gives higher lift than the flat delta wing because of its flap effect as same as the CFD results. The quantitative difference between them, namely about 4%, are almost the same in the EFD and the CFD results similar to those of Fig.4(a). Furthermore, considering the results of the EXP01 and EXP02 which is for the cases of the Reynolds number of 8.2×10^4 and 5.0×10^4, the CFD results of Fig.4(a) for the Reynolds number of 1.0×10^4 can be considered to be quantitatively reasonable values. However, the slopes of the C_L-α by the CFD approach become a little bit gentle compared with the EFD ones. The reason might be due to the assumption of laminar flow in the CFD approach even for vortical flows coming from the leading edge of the delta wing.

(a) C_L-α curve

(b) C_D-α curve
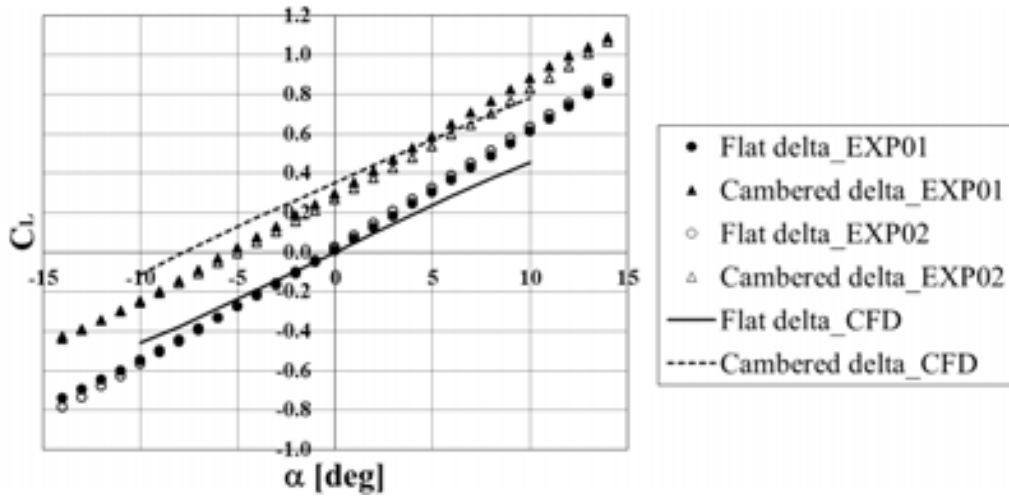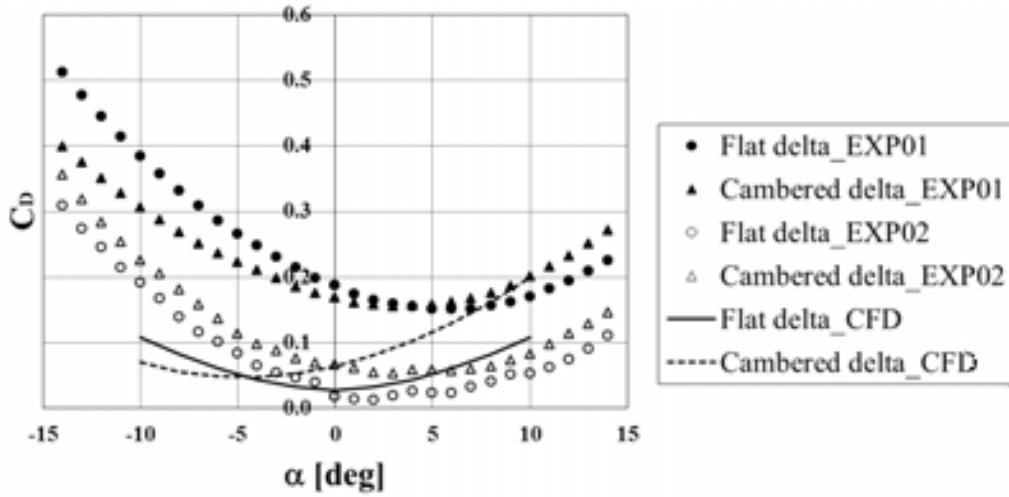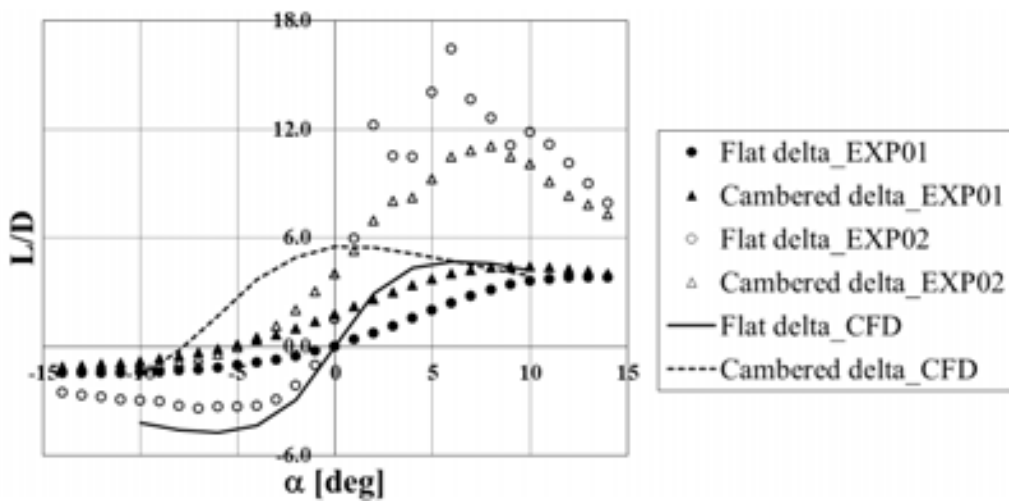
(c) L/D-α curve

Fig.8 Aerodynamic characteristics of the arc camber and the flat delta wings compared with the CFD results
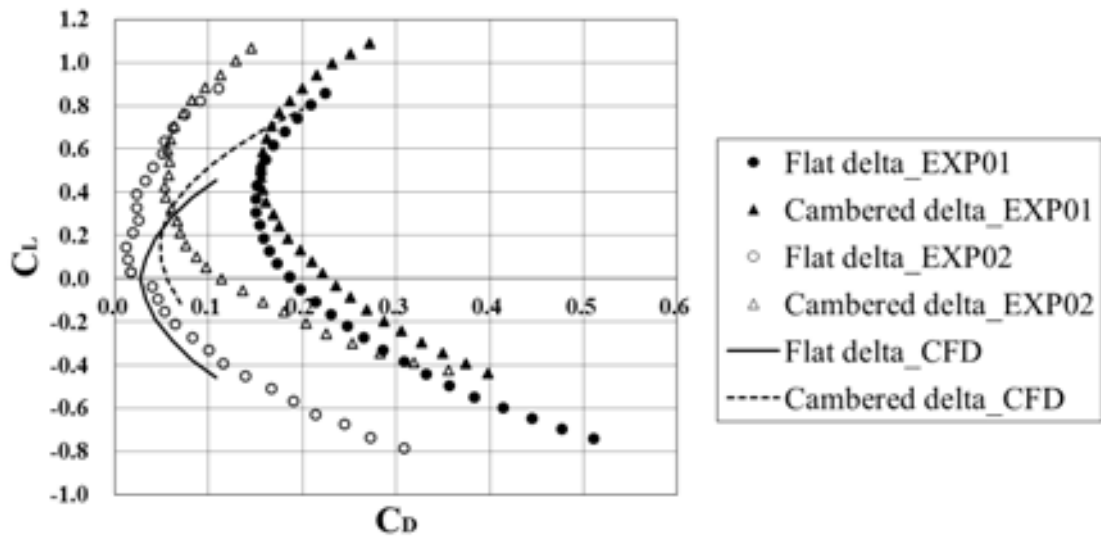
Fig.9 Drag polar curves

Second, the angle of attack to give a minimum C_D for the arc camber delta wing was smaller than the flat delta wing, which should be a cambered effect as shown in Fig.7(b). For example, the minimum C_D of the flat delta in the EXP01 condition is at the attack angle of 6 degrees. On the other hand, the minimum C_D of the arc camber delta wing appears at the attack angle of 3 degrees. These effect also appears in the CFD results in Fig.8(b) as well as in Figs.4(b) and 8(b) for the EXP01. From these results, the CFD analysis can reproduce an actual phenomena quantitatively but involves such an quantitative difference that an attack angle giving a minimum C_D shifts to the smaller side than the both conditions of EXP01 and EXP02.

Third, the L/D of the arc camber delta wing is larger than the flat delta wing except an attack angle over one degree of the EXP02 as shown in Fig.8(c). These effects also appear in the CFD results of Figs.4(d) and 8(c) for the condition of EXP01. The reason for the different result of the EXP02 should be due to the fairly low drag of the flat delta wing at the attack angle over 0 degree in Fig.8(b). It is different from the EXP01 case. It will be one of the future subjects.

With the regard to the difference between the CFD and the EFD results, followings are the summary. The slope of C_L-α is gradual in the CFD approach. The attack angle giving a minimum C_D for the CFD case is smaller than the EFD result and the C_D of the EXP02 becomes larger for the all angles of attack as shown in Fig.8(b). The L/D of the flat delta wing in the EXP02 is much larger than the arc camber delta wing in Fig.8(c). We could consider the reason as follows. It might come from the interference between the wing and the sting with the force balance in the EFD approach. Furthermore, the CFD approach might not simulate correctly the vortical airflows of the delta wing, especially an leading edge separation vortex and such the behavior as vortex breakdown, because the CFD adopts the Navier-Stokes equation without turbulent flow.

Finally, Figure 9 shows the drag polar curves given by C_L and C_D in Fig.8. It suggests that an arc camber delta wing is definitely proper for the flight which needs such the relatively high lift as $C_L \geq 0.5$.

4. Conclusion

A delta wing with an arc camber has been proposed for such a low Reynolds number flight as a flight above the Mars surface and the characteristics were investigated by both the CFD and the EFD approaches. The optimum camber ratio for the flight in the Reynolds number of 1.0×10^4 was studied by the CFD and the resultant validation was inspected by the EFD. As the results, the followings were made sure.
(1)   An optimum camber ratio exists according to a flight condition.
(2)   The camber ratio of 5% is the best for the delta wing in the research.
(3)   The camber acts as a flap and gives a high performance in the flight which needs the high lift such as C_L over 0.5.
(4)   The CFD results represent the flow field around the arc camber delta wing qualitatively and some results, although, do not coincide to the EFD results quantitatively.
(5)   The reason for the difference might be from the CFD procedure, for example without considering a turbulent flow.

References

[1] Akira Oyama and Kozo Fujii, A Study of Airfoil Design for Future Mars Airplane, AIAA Paper, No.2006-1484, 2006.

[2] Taku Nonomura, Ryoji Kojima, Hiroaki Fukumoto, Akira Oyama and Kozo Fujii, Comparative Study of Aerodynamic Characteristics of Rectangular and Delta Wings under a Low Reynolds Number Condition, Proceedings of 42nd Fluid Dynamics Conference/Aerospace Numerical Simulation Symposium 2010, pp.161-166, 2010. (in Japanese)

[3] Taku Nonomura, Ryoji Kojima, Masayuki Anyoji, Akira Oyama and Kozo Fujii, Aerodynamic Characteristics of Ishii Airfoil (Re=23,000) using LES, J. JSASS-2011-2033, 2011. (in Japanese)

[4] Alain Pelletier and Thomas J. Mueller, Low Reynolds Number Aerodynamics of Low-Aspect-Ratio, Thin/Flat/Cambered-Plate Wings, Jounal of AIRCRAFT, Vol.37, No.5, pp.825-832, September-October 2000.

[5] Makoto Mizoguchi and Yutaka Yamaguchi, Aerodynamic Characteristics of Rectangular Flat Plate Wings in Low Reynolds Number Flows, J. JSASS, Vol.60, No.3, pp.121-127,2012. (in Japanese)

[6] Tomohisa Ohtake, Yusuke Nakae and Tatsuo Motohashi, Nonlinearity of the Aerodynamic Characterristics of NACA0012 Aerofoil at Low Reynolds Numbers, J. JSASS, Vol.55, No.644, pp.439-445, 2007. (in Japanese)

[7] Asei Tezuka, Yasuto Sunada and Kenichi Rinoie, Aerodynamic Characteristics of 4% Cambered-Plate and NACA0012 Airfoil at the Reynolds Numbers Region for Micro Air Vehicles, J. JSASS, Vol.57, No.665, pp.258-265, 2009. (in Japanese)

[8] Tomohisa Ohtake, Yusuke Nakae, Akinori Muramatsu and Tatsuo Motohashi, Flow Field Phenomena Contains Laminar Separation and Separation Bubble on NACA0012 Airfoil at Low Reynolds Number, Proceedings of 42nd Fluid Dynamics Conference/Aerospace Numerical Simulation Symposium 2010, pp.283-286, 2010. (in Japanese)

[9] Yusuke Nakae, Tomohisa Ohtake, Akinori Muramatsu and Tatsuo Motohashi, Three Dimensionalization of the Flow Field around a NACA0012 Airfoil at Low Reynolds Number, J. JSASS, Vol.59, No.692, pp.244-251, 2011. (in Japanese)

CFD Calculation of Airfoil Characteristics for Performance Prediction of Vertical Axis Wind Turbine

Naoko INOUE
Kana TANAKA
Yutaka HARA
Takahiro SUMI

Department of Mechanical and Aerospace Engineering, Graduate School of Engineering
Tottori University
Koyama-Cho, Tottori, 680-8552
Japan
M11T8003C@edu.tottori-u.ac.jp

Abstract

Blade element momentum (BEM) theory is useful for the design of wind turbines because of its moderate calculation costs, but highly accurate airfoil aerodynamic data are essential in order to make reliable predictions of wind turbine performance. Such data are particularly needed for the design of vertical-axis wind turbines, which operate under a wide range of angles of attack and various Reynolds numbers. The ultimate objective of this study is to establish an aerodynamic characteristics database for various airfoils using computational fluid dynamics (CFD). This report represents the first stage of the study. Two-dimensional CFD was employed to estimate data for a symmetric airfoil for which data is already available in order to examine how accurate this method will be. The aerodynamic data obtained by CFD were employed as actual inputs for a calculation of wind turbine characteristics using BEM theory.

Key words: aerodynamic characteristics, wind turbine, CFD, BEM

1. Introduction

The topic of renewable energy has received much attention domestically and around the world, and both large and small wind turbines have been the subject of vigorous research and development as wind energy systems. Currently, 3-bladed propeller horizontal axis wind turbines are the most common type, but recently, the idea has been proposed that large floating vertical axis wind turbines (VAWTs) may provide cost savings in off-shore installations[1]; there are also many studies of small versions of VAWTs[2, 3]. Blade element momentum (BEM) theory[4] is useful for the design of WTs as its calculation costs are low, but highly accurate aerodynamic data are necessary in order to make very reliable predictions of WT performance[5]. A particularly notable factor is that the angle of attack of the airfoil of a VAWT varies widely with operating conditions, and data on the variation of aerodynamic characteristics with Reynolds number (Re) must be known in order to make calculations under differing operating conditions. Most publicly available airfoil data are intended for aircraft, however; only for a quite limited set of airfoils do data include high angles of attack, up to stall (preferably, from $-180°$ to $+180°$) and a wide range of Re.

In this study, the aerodynamic forces acting on airfoils were estimated using computational fluid dynamics (CFD) for a wide range of angle of attack (α) and Re, with the ultimate goal of creating an aerodynamic characteristics database for a variety of airfoils. This report describes the first stage of this effort, in which CFD was employed on a symmetric NACA0018 section, for which previously existing data are available. An investigation was made of the range of accurate aerodynamic data that can be obtained at a relatively low calculation cost. The aerodynamic data obtained by CFD were employed as actual inputs for a calculation of WT characteristics according to the BEM theory, and these were compared with experimental results.

2. Calculation Method
2-1 Conditions for Calculation

STAR-CCM+ ver. 6.06, a general purpose CFD code, was used in this research to calculate the aerodynamic characteristics (lift coefficient C_l and drag coefficient C_d) of the airfoil. Two-dimensional steady-state

computations were carried out using a Reynolds-Averaged Navier-Stokes (RANS) model in order to minimize the computation time for each condition and to obtain results for a large number of conditions. The single-equation Spalart-Allmaras model was employed to simulate the turbulent flow model. The airfoil was a 1 m chord NACA0018 section and calculations were carried out with α values from 0º to 180° and Re values of 1.0×10^4, 2.0×10^4, 4.0×10^4, 8.0×10^4, 1.6×10^5, 3.6×10^5, 7.0×10^5, 1.0×10^6, 2.0×10^6, 5.0×10^6 and 1.0×10^7. The calculations were performed at 2º increments for $0º \leq \alpha \leq 30º$ and at 10º increments for $30º \leq \alpha \leq 180º$. Table 1 provides a summary of the calculation conditions.

2-2 Computational Mesh

The region for these calculations was a circular volume (Region 1) whose radius was 20 times the airfoil chord (Figure 1(a)). A fine polyhedral mesh was defined near and in the wake region of the airfoil (Region 2: mesh spacing about 3% that of the far boundary; see Figure 1(b)). A prism layer mesh was employed in the vicinity of the airfoil surface (see Figure 1(c)). It was assumed that a uniform flow in the horizontal direction entered from the left far semicircle boundary of Figure 1(a) and that there was zero pressure gradient at the right far semicircle boundary. The orientation of the airfoil placed in the center of the calculation region was varied to set the value of α. Table 2 summarizes the meshing conditions.

Table 1 Conditions of calculation

Airfoil	NACA 0018 (c=1[m])
Turbulent model	Spalart-Allmaras model
Fluid	Compressible ideal gas Temperature: 293[K] (at far field)
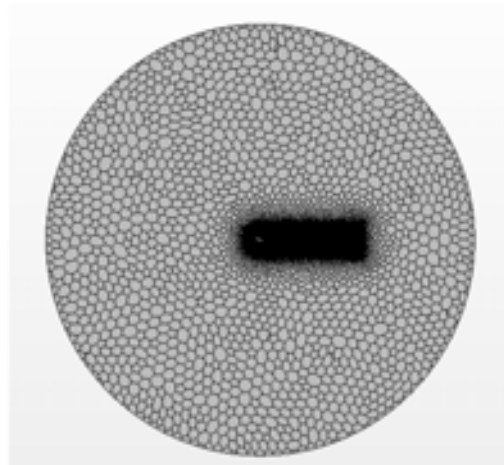
(a) Overall view of computational domain (region1+2)
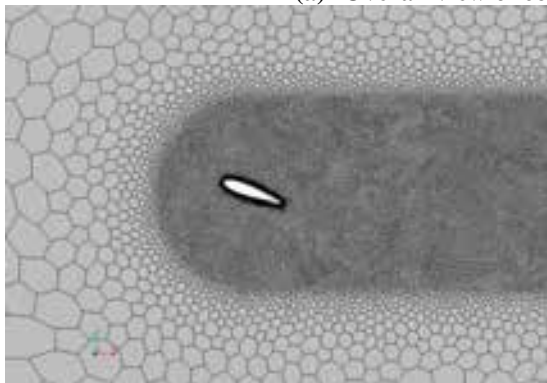
(b) Close-up view of computational mesh near region 2
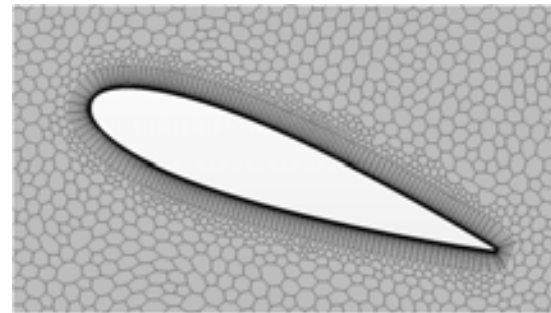
(c) Close-up view of computational mesh near airfoil surface

Fig. 1 Details of computational mesh

Table 2 Conditions of computational mesh

The minimum mesh width of a surface area perpendicular direction	4×10^{-5}[m]
The range of a prism layer mesh	0.05[m] (direction perpendicular to a field)
The number of layers of a prism layer mesh	30
The total number of nodes	About 65000
The total number of cell	About 35000

2-3 Post-processing

These calculations assumed steady state conditions even for flow fields with separation, which are unsteady by nature. In such cases, the aerodynamic coefficients do not converge, and the solutions oscillated at a constant amplitude. When no convergent solution was obtained in this study, the arithmetic mean of the final 1000 steps of the calculation with a steady oscillation amplitude was taken when a constant amplitude had been obtained a sufficient number of times and was employed for each aerodynamic coefficient at the given calculation conditions.

3. Results of Calculations and Observations

Figure 2 shows the calculated aerodynamic characteristics of the airfoil over a wide range of α (0º - 180°) at Re $= 2 \times 10^4$. Figure 3 focuses on the low-α region of 0º - 30º at the same Re. Figures 4 and 5 provide the same results with Re of 2.0×10^6 and 1.0×10^7 over the same low-α region. The solid lines in Figures 2 through 5 represent the values published in the literature for comparison. At Re $= 1.0 \times 10^4 - 1.6 \times 10^5$ and $0º \leq \alpha \leq 30º$, the data of Kumar et al.[6] were chosen for CFD modeling of the laminar-turbulent flow transition. The data of Sheldahl et al.[7], based on observed values and extrapolation of numerical values, were used for other α ranges and Re conditions.

The C_l values over the wide range of α presented in Figure 2(a) are fairly close to the values given in the literature, but the C_d values in Figure 2(b) differ significantly from the published values at around α=90º. This was typical of the findings at all Re.

Considering Figure 3(a) and Figure 4(a), up to stall, C_l is nearly identical to the published values, but tends to be higher than those values throughout the post-stall region. The causes of this may be that the present method did not consider the laminar-turbulent flow transition, and in addition, since it was a 2-dimensional computation, it neglected the dissipation of vortices. The values of C_d are also higher than the published values throughout the α range in Figure 3(b) and in the pre-stall range in Figure 4(b).

Comparing the calculated values for C_l and C_d at the higher Re value of 1.0×10^7 (Figure 5), again, we find that they both differ significantly from the values in the literature. This suggests that the mesh in this calculation did not provide sufficient resolution.

(a) C_l (b) C_d
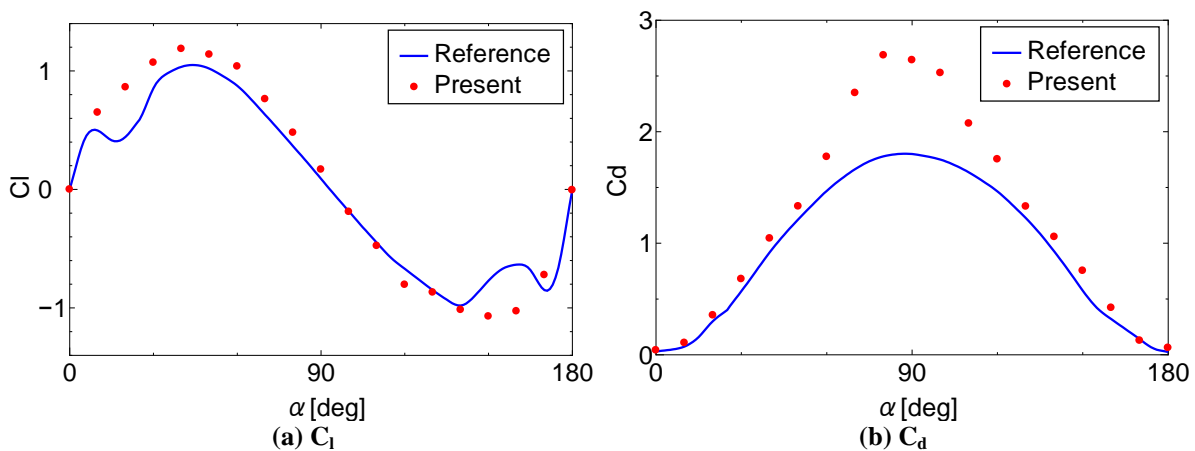
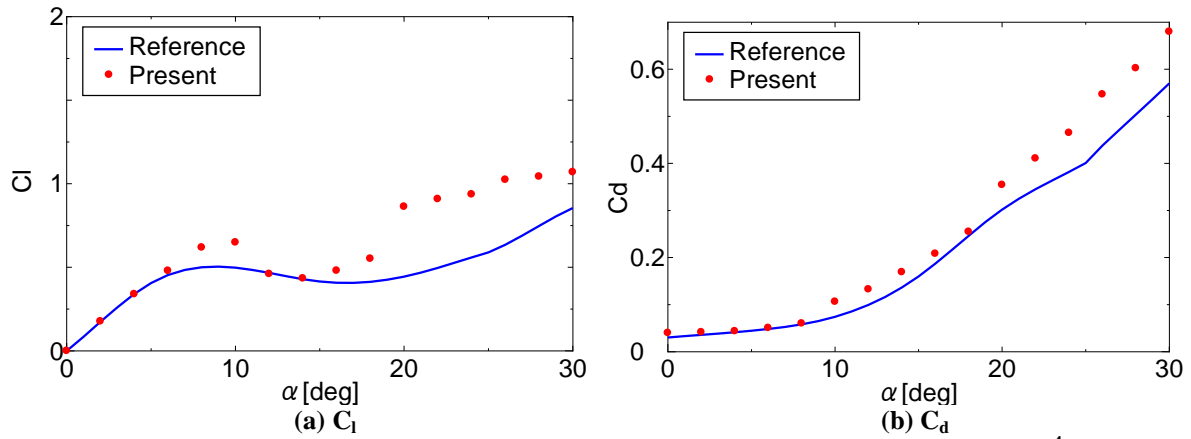**Fig. 2 Aerodynamic characteristics of airfoil (Re=2×10^4)**

(a) C_l **(b) C_d**

Fig. 3 Aerodynamic characteristics of airfoil in low angles of attack (Re=2×10⁴)

(a) C_l **(b) C_d**
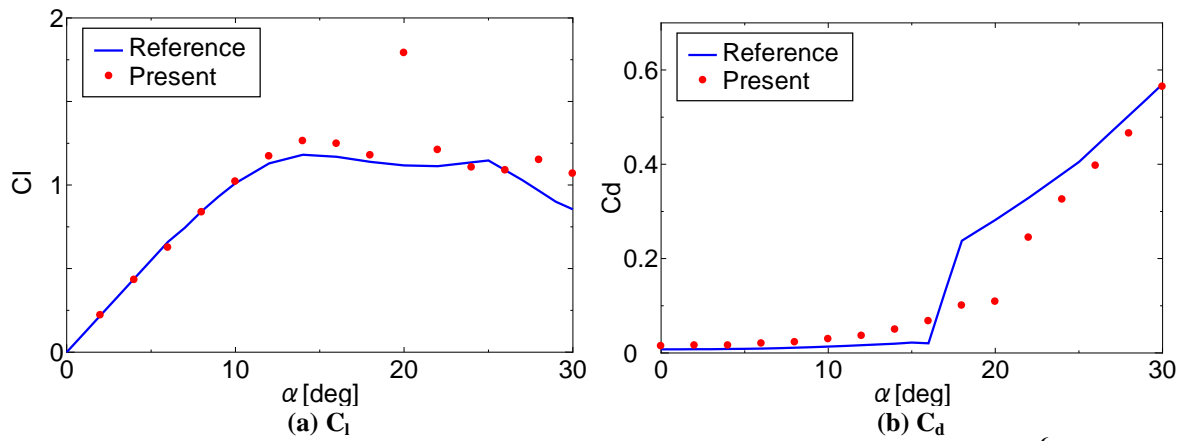
Fig. 4 Aerodynamic characteristics of airfoil in low angles of attack (Re=2×10⁶)
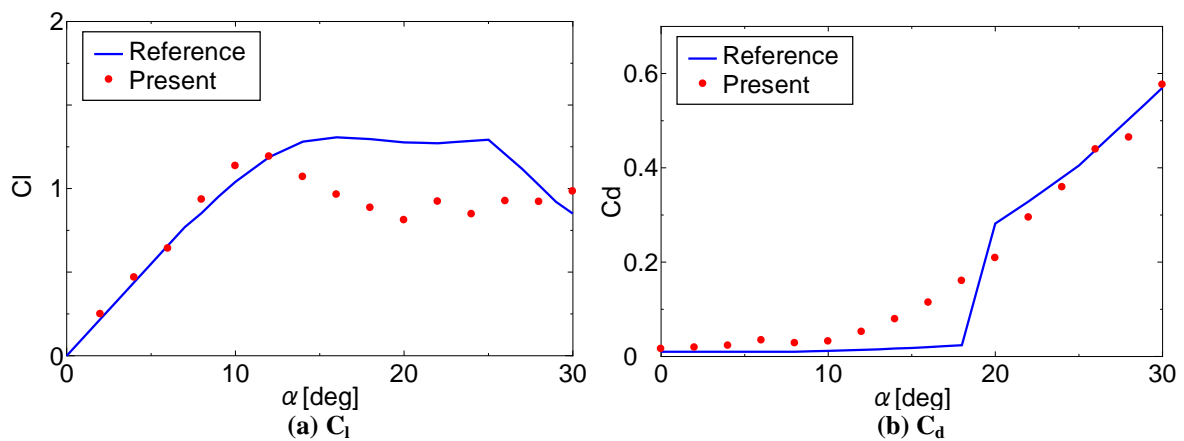

(a) C_l **(b) C_d**

Fig. 5 Aerodynamic characteristics of airfoil in low angles of attack (Re=1×10⁷)

The aerodynamic data obtained in these calculations were converted to data at 1-degree increments using spline interpolation and those results were used to calculate the lift-drag ratio (C_l/C_d). Those ratios are provided in Figure 6 for all the specified Re (11 values) over the α range of 0º − 30º. Figure 7 provides the same ratios given in the literature. We see in Figure 6 that up to Re = 1.6×10^5, the ratios obtained in these calculations have peaks with relatively smooth slopes where C_l/C_d gradually increases with Re. At Re = 3.6×10^5 and above, however, C_l/C_d is considerably lower than indicated in the literature (Figure 7), and the α dependence of this ratio shows unnatural "bumpiness".
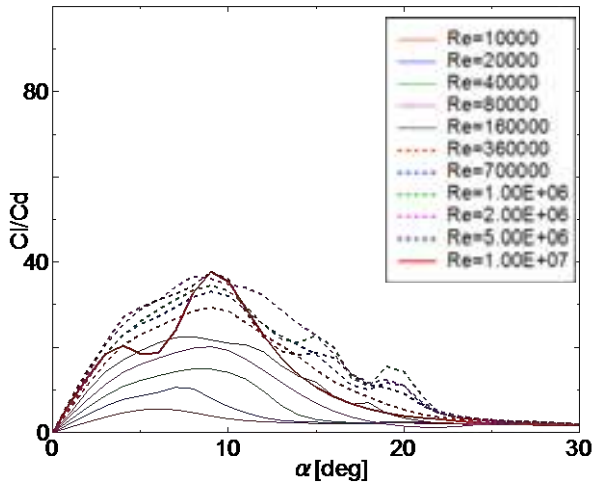
Fig. 6 The lift drag ratio obtained by the present calculation
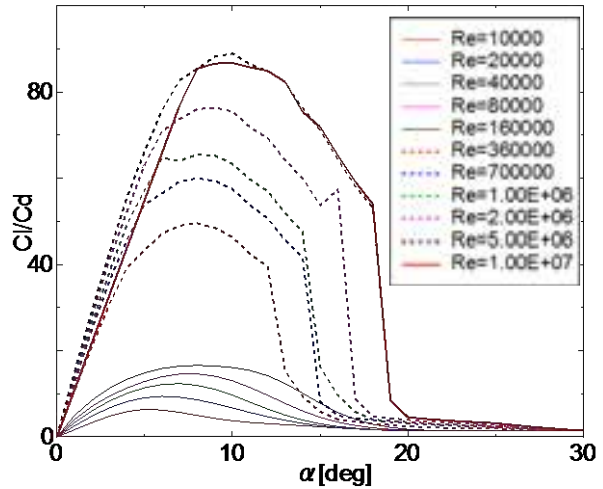
Fig. 7 The lift drag ratio obtained by the reference data [6, 7]

4. Application for Predicting Characteristics of Vertical-Axis Wind Turbine

The aerodynamic coefficients (C_l, C_d) obtained in this study were employed as the input data to estimate the performance of a VAWT using BEM theory. The double multiple streamtube theory was employed here as a flow-field model with the modified Gormont model (assuming $A_M = 1000$) to account for dynamic stall[4]. Figure 8 presents the calculated results and experimental findings versus tip speed ratio λ for a large Darrieus wind turbine (the Sandia 17 m machine)[8] and Figure 9 presents those for a small 0.6 m diameter experimental straight-bladed VAWT[3]. Both graphs use the following symbology for the input data: red lines to show the present calculation results based on the aerodynamic data, pink lines for the results based on the published values of Sheldahl *et al.*, and green lines for calculations using the data of Kumar *et al.* partially replaced by the data of Kumar *et al.* (the solid lines in Figure 2 – Figure 5). These warn clearly that there are problems in the aerodynamic data found in this study for high Re (Figure 8); nonetheless, the results at low Re (Figure 9) tend to more closely approach the experimentally found values compared to those in the literature.
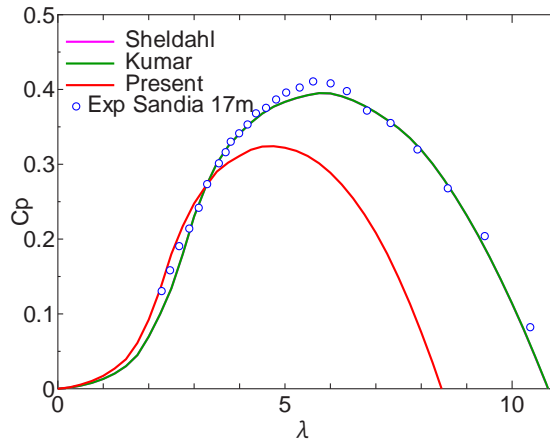
Fig. 8 Power coefficient of a large Darius wind turbine (SANDIA 17m , 50.6 rpm; Re ≈2×10^6 at λ=6)
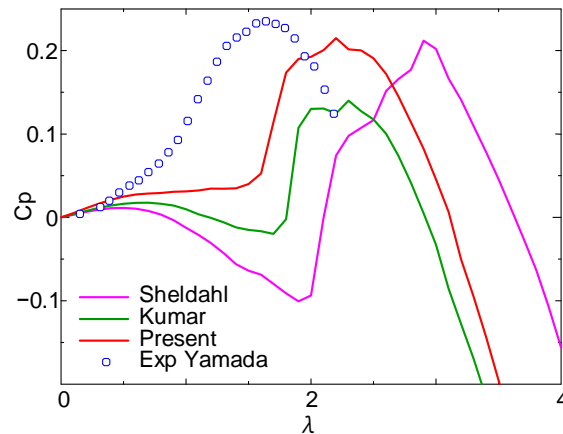
Fig. 9 Power coefficient of a micro wind turbine
(Straight-bladed VAWT, D=0.6m, V=6m/s; Re $\approx 1 \times 10^5$ at λ=2)

5. Conclusions

This study revealed that aerodynamic data for an airfoil can be calculated at relatively low cost with some degree of accuracy at low Reynolds numbers of 1.0 ⚡ 10^4 – 1.6 ⚡ 10^5, in 2-dimensional steady-state computations. Nevertheless, in order to increase the accuracy under wider calculation conditions, we will examine methods for improving the mesh resolution, and incorporating unsteady calculations, 3-dimensional calculations and turbulence models.

Acknowledgements

References

[1] Akimoto, H., Tanaka, K., Uzawa, K., Floating axis wind turbines for offshore power generation – a conceptual study, *Environmental Research Letters*, Vol.6, No.4, (2011), 044017.

[2] Yutaka, H., Proposal of Low Center-of-Gravity Vertical Axis Wind Turbine and Performance Prediction with Blade Element Momentum Theory, *Wind Energy*, 35-2, (2011), pp.134-139.

[3] Yamada, S., Tamura, T., Mochizuki, S., Effects of Wing Section on Mean Characteristics and Temporal Torque Variation for a Small Straight-Bladed Vertical Axis Wind Turbine, *J. Fluid Science and Technology*, Vol.6, No.6, (2011), pp.875-886.

[4] Paraschivoiu, I., Wind Turbine Design with Emphasis on Darrieus Concept, Polytechnic International Press, (2002).

[5] Hansen, M. O. L., Madsen, H. A., Review Paper on Wind Turbine Aerodynamics, *J. Fluids Engineering*, 133-11, (2011), 114001-1.

[6] Kumar, V., Paraschivoiu, M., Paraschivoiu, I., Low Reynolds Number Vertical Axis Wind Turbine for Mars, *Wind Engineering*, Vol.34, No.4, (2010), pp.461-476.

[7] Sheldahl, R. E., Klimas, P. C., Aerodynamic Characteristics of Seven Symmetrical Airfoil Sections Through 180-Degree Angle of Attack for Use in Aerodynamic Analysis of Vertical Axis Wind Turbines, *Sandia Report*, (1981), SAND80-2114.

[8] Wilson, R. E., Walker, S. N., Fixed - Wake Analysis of the Darrieus Rotor, *Sandia Report*, (1981), SAND81-7026.

Multi-objective Optimization of Airfoil of
Mars Exploration Aircraft using Evolutionary Algorithm

Gaku Sasaki
Tomoaki Tatsukawa
Taku Nonomura
Koichi Yonemoto
Akira Oyama
Takaaki Matsumoto
Tomohiro Narumi

Kyushu Institute of Technology
1-1 Sensui Tobata Kita-kyushu Fukuoka
Japan
k344133g@tobata.isc.kyutech.ac.jp

Abstract

The airfoils of Mars exploration aircraft are designed by genetic algorithm and evaluated by computational fluid dynamics. The objectives of optimization are maximization of lift coefficient and minimization of drag coefficient at the angle of attack of 3 degrees. Reynolds number is carefully set to 2.3×10^4, which is the cruising condition of the aircraft. The present computation is utilized supercomputers FX-1 in Institute of Space and Aeronautical Science (ISAS) / Japan Aerospace Exploration Agency (JAXA).

The results show that two types of airfoil excel in aerodynamic performance. One airfoil with two large cambers which generate separation bubbles at upper surface has large lift coefficient. The other one with a strong camber in the front of under surface has small drag coefficient and fairy large lift coefficient. Most airfoils on Pareto front have thin thickness under 10% of cord. The present optimization indicates the first step of multi-objective design optimization for practical airfoil design for Mars exploration aircraft.

Key words: Optimization, Low Reynolds number flow, Airfoil design

Introduction

Mars exploration aircraft is now being researched by a working group of JAXA/ISAS an Aerospace Exploration Agency/Institute of Space and Astronautical Sciences) and university researchers for the near future multi-objective planet exploration mission called MELOS (Mars Exploration with Lander-Orbiter Synergy). The aircraft type explorer has the advantages in current and previous Martian surface survey; wider area exploration than a rover and closer image capturing than an orbiting satellite [1].

The order of Mars flight Reynolds number is about the range from 10^4 to 10^5 due to ultra low Martian atmospheric density which is an about one-hundredth part of that of the earth. Many researchers have reported that the aerodynamic characteristics on the low Reynolds number flow around airfoil are quite different from that of commercial aircrafts in the earth, which caused by laminar separations and unsteady vortices on airfoil upper surface. Because of this, conventional airfoils of earth aircrafts cannot satisfy the required performance to fly on Mars [2][3][4].

Therefore, the purpose of this study is to find the optimal airfoil in low Reynolds number condition as the first step to design the optimal airfoil for Mars exploration aircraft. The airfoil is designed by genetic algorithm and evaluated by computational fluid dynamics (CFD).

Airfoil Shape Parameterization

The first step of airfoil shape design optimization is the parameterization of airfoil shape. In this study, nine control points and B-spline curves are used for the parameterization (Fig.1). In order to express leading and trailing edges of airfoil, three control points are pegged. The movable points have the x and z coordinated values, which are design parameters. Table 1 shows the upper and lower bounds of control points. Designing airfoil with B-spline curves enables various expression of airfoil shape with small number of design parameters.

Table.1 The Range of Control Points

Design parameter	Upper bound	Lower bound
x1	0.999	0.66
x2	0.66	0.33
x3	0.33	0.001
x4	0.33	0.001
x5	0.66	0.33
x6	0.999	0.66
y1	0.2	-0.2
y2	0.2	-0.2
y3	0.2	-0.2
y4	0.4	-0.05
y5	0.4	-0.05
y6	0.4	-0.05
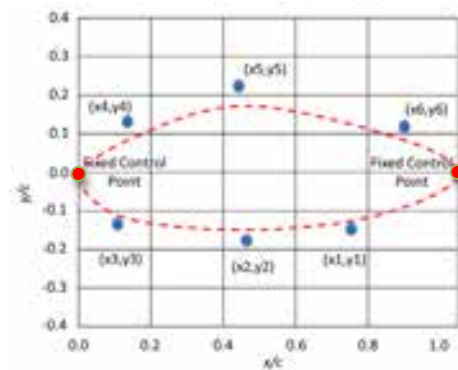
Fig.1 Design Airfoil

Genetic Algorithm

Genetic Algorisms (GA) simulates the mechanism of natural evolution where biological populations which consist of multiple individuals evolves over generations to adapt to an certain environment by genetic operators such as selection and reproduction, and consequently can bear the best individual adapting to the environment (Fig.2) [5].

In recent years, GA has been applied to various design optimization problems because it has some advantages. First, GA can be applied to any design optimization problem. Second, GA can solve optimization problems without any special knowledge of the problems if only the objective and constraint functions are given mathematically. Third, GA can avoid local optimal solutions and find the global optimal solution independently of initial values of solution because GA deals with multiple solutions simultaneously during the optimization process.

In this study, Non-dominated Sorting Genetic Algorithms II (NSGA-II) [6][7] was used. NSGA-II has an outstanding feature that emphasizes population members which are placed a distance from a set of supplied or predefined reference points. That means NSGA-II has advantages for globally search and acquirement Pareto front than any genetic algorithm (Fig.3). Pareto front is some elements that are at least as good on every variable. Blended crossover (BLX-0.7) is used for recombination, and mutation takes place at a probability of 10%. The population size is 20 and the maximum number of generations is set to 20. The initial population is generated randomly over the entire design space. The objective functions of the design optimization problem are maximization of the lift coefficient and minimization of drag coefficient.
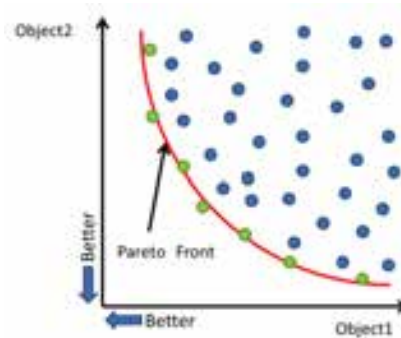
Fig.2 Flow Chart of Genetic Algorithm   **Fig.3 Plato Front**

Aerodynamic evaluation

Mach number is 0.2 and Reynolds number is 2.3×10^4. The two-dimensional compressible Favre Averaged Navier-Stokes equations are solved for the aerodynamic airfoil shape design optimization. In addition, all flow fields are assumed as laminar flow without turbulence. Angle of attack is 3 degrees.

For each design candidates in the optimal process, the grid generator by algebraic method creates C-typed grid: 497 grid points in chordwise direction, 101 grid points in normal direction.

In addition, in order to judge whether the optimal airfoil has superior aerodynamic performance compared with ready-made airfoil, the Ishii airfoil is also evaluated (Fig.4). Ishii airfoil has a good aerodynamic performance at the low Reynolds number condition from the past experimental studies [2][8][9].

Fig.4 Ishii Airfoil

Results

The plots in figure 5 present non-dominated solutions and dominated solutions with NSGA-II and CFD. The number of non-dominated solutions is 36. In addition, there are 26 airfoils that the lift-drag ratio larger than Ishii airfoil. This figure also indicates that there are two groups with the boundary that lift coefficient is roughly 0.75 in the obtained non-dominated solutions; low drag design region and high lift design region compared with Ishii airfoil (Fig.5).
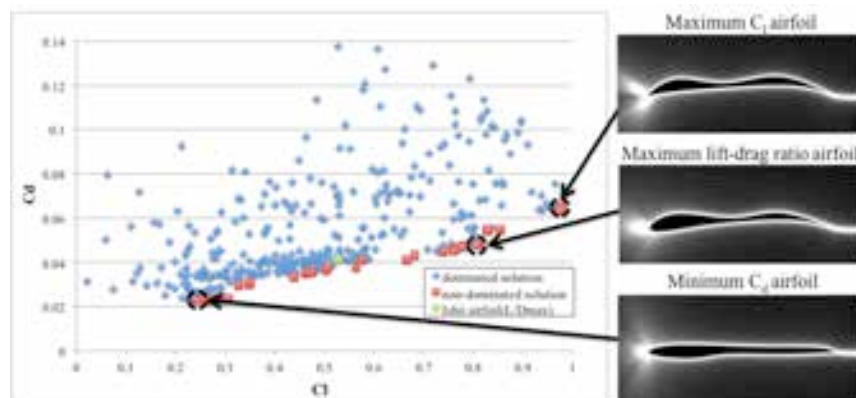
Fig. 5 Distribution of Non-Dominated and Dominated Solutions by NSGA-II

Figure 6 presents the average flow field and surface pressure distributions of typical airfoil in high lift design region. These airfoils have two large convex to generate separation bubbles at upper surface. This is the reason why these airfoils can generate high negative pressure on upper surface. In addition, they have a particular shape like a circular arc airfoil at lower surface and like a flap at trailing edge. The shape produces high positive pressure [10][11]. Table 2 shows aerodynamic characteristics of Ishii airfoil and the some optimized airfoils at the present design condition. The aerodynamic characteristics of Ishii airfoil are calculated by the same computational fluid dynamics as the optimization. The optimized airfoil that has the maximum lift-drag ratio has 30% larger lift-drag ratio than that of Ishii airfoil.

i) Maximum lift-drag ratio airfoil
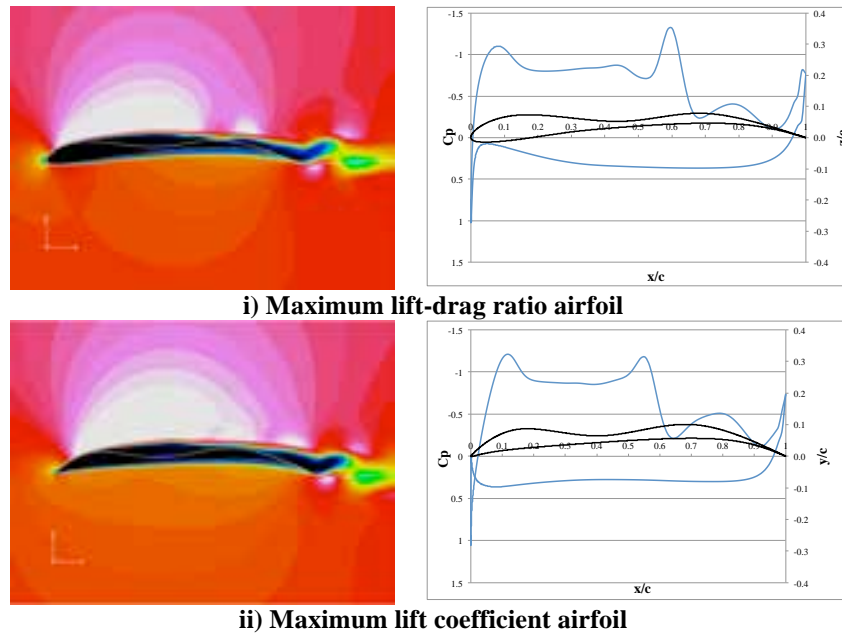
ii) Maximum lift coefficient airfoil
Fig. 6 Average Flow Field and Surface Pressure Distributions

Table.2

Airfoil	Lift coefficient	Drag coefficient	Lift-drag ratio
Ishii airfoil at maximum lift-drag ratio	0.527	0.042	12.90
Maximum lift coefficient airfoil	0.976	0.065	15.11
Minimum drag coefficient airfoil	0.241	0.023	10.51
Maximum lift-drag ratio airfoil	0.808	0.048	16.88

Almost all of optimum airfoils in small drag design region have characteristic shape like the minimum drag coefficient airfoil (Fig. 7). One of the feature is flat shape on upper surface to moderate laminar separation. This phenomenon brings a good aerodynamic effect in low Reynolds condition [2][9][11].
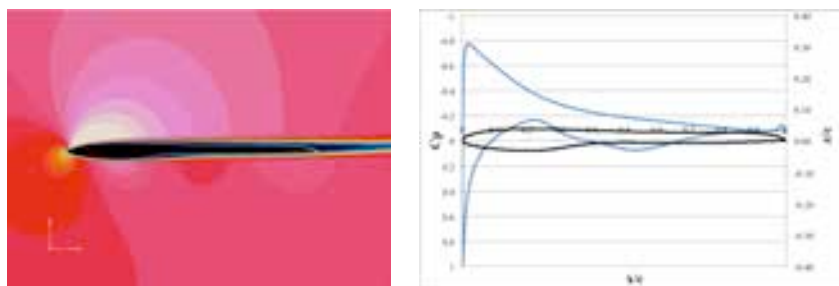
Fig. 7 Average Flow Field and Surface Pressure Distributions
of The Minimum Drag Coefficient Airfoil

The other feature is strong camber in the front of under surface. As shown in figure 8, at the point of the strong camber, the pressure of lower surface changes from negative pressure to positive pressure. This phenomenon is also observed the Ishii airfoil [2][8].

Conclusions

This study shows that aerodynamic design optimization of an airfoil in low Reynolds number flow by using a genetic algorithm is effective measure. This is a preliminary research of the optimization of Mars exploration aircraft airfoil so that the optimization was done only the condition of three degrees angle of attack. The population of each generation was only 20; however, some important findings were obtained. 1) There are many airfoils on Pareto front, but some of them can be grouped. 2) Some solutions can be superior to a ready-made airfoil. In the future, the optimization will be conducted for various angles of attack, which will include cruising, ascending, descending and so on.

References

[1] A. Oyama.: Conceptual design of Mars airplane for MELOS," 54th Space Science Technology Conf., 3F01, 2010.

[2] S. Shigeoka et al.: Variable-pressure Wind Tunnel Test on Low Reynolds Number Aerodynamic Characteristics of Three-dimensional Wings, 8th Int. Conf. on Flow Dynamics, 2011.

[3] F. W. Schmitz.: Aerodynamics of the model airplane part1 airfoil measurements, p. 203, 1967.

[4] E. V. Laitone.: Wind tunnel tests of wings at reynolds numbers below 70000. Experiments in Fluids, Vol. 23, pp. 405–409, 1997.

[5] Goldberg, et al.: Genetic Algorithms in Search, Optimization and machine Learning, Addison Wesley, 1989

[6] Deb. K.: Multi-Objective Optimization Using Evolutionary Algorithms. Wiley, Chichester, 2001

[7] Deb. K, et al.: A fast and elitist multiobjective genetic algorithm: NSGA-II. IEEE Transactions on Evolutionary Computation, pp.182–197, 2002.

[8] M.Anyoji, et al.: Aerodynamic Characteristics of Ishii Airfoil at Low Reynolds Numbers, 8th Int. Conf. on Flow Dynamics, 2011.

[9] K. Asai et al, :Low Reynolds-Number Airfoil Testing in a Mars Wind Tunnel, 54th Symposium on Space Science and Technology, Sizuoka, November 17-19, 2010.

[10] E.V. Laitone.: Aerodynamic lift at Reynolds numbers below 7×10^4, AIAA Journal, p. 2, 1996.

[11] F. W. Schmitz.: the aerodynamics of small reynolds numbers. NASA technical memorandum, p. 51, 1980.

Bow-Shock Instability around an Edged Ballistic Object in a Low-Gamma Gas

Yosuke Sato[1]
Kanako Yasue[2]
Takamasa Kikuchi[3]
Kiyonobu Ohtani[4]
Naofumi Ohnishi[5]

[1]Department of Aerospace Engineering, Tohoku University
Sendai, 980-8579
Japan
yosato@rhd.mech.tohoku.ac.jp
[2]Aerospace Research and Development Directorate
Japan Aerospace Exploration Agency
Chofu, 182-8522
Japan
yasue@chofu.jaxa.jp
[3]Institute of Fluid Science, Tohoku University
Sendai, 980-8577
Japan
kikuchi@edge.ifs.tohoku.ac.jp
[4]Institute of Fluid Science, Tohoku University
Sendai, 980-8577
Japan
ohtani@edge.ifs.tohoku.ac.jp
[5]Department of Aerospace Engineering, Tohoku University
Sendai, 980-8579
Japan
ohnishi@rhd.mech.tohoku.ac.jp

Abstract

Bow-shock instability observed in a low γ flow was investigated by three-dimensional numerical simulation with a circular cone. We designed experiments based on the numerical results in order to validate our numerical results and demonstrate that bow shock wave is unstable in a low γ gas with the edged body. The experimental results show that bow shock becomes unsteady and unstable in the proposed condition, and our numerical prediction was validated.

Key words: bow-shock instability, discontinuous Galerkin method, ballistic range.

Introduction

Some problems caused by shock waves in a supersonic flight, such as wave drag, heat load, and sonic boom, prevent from realizing affordable supersonic transports, although many attempts have been made to conquer them. In order to propose a new shock wave application, which is different from existing methods based on steady shock waves, we have focused on an instability of bow shock wave. Actively using this instability, the shock wave itself may be weakened; therefore, wave drag, heat load, and sonic boom are also reduced all

together. Moreover, understanding dynamics of the detached shock wave is very important for evaluating heat flux for a re-entry vehicle.

In some experiments using a ballistic range, the results suggest that the bow shock wave may be unstable in low-γ gas[1, 2, 3], as shown in Fig. 1[1, 2]. From experimental results of Baryshnikov et al., it was concluded that the instability occurs depending on Mach number, ambient gas pressure, and curvature of a blunt body. They also mentioned that a cause of the instability is chemical reaction in the shock layer. However, since it is difficult to analyze the flowfield behind the shock wave in the experiments, the mechanism of the instability has not yet been revealed. So, it is expected that computational fluid dynamics (CFD) enables a detailed analysis of the instability and clarifying the cause of it.

On the other hand, in CFD with a strong shock wave, most of shock-capturing schemes become unstable when the shock wave is parallel to computational grids; this is so-called carbuncle phenomenon[4]. The carbuncle phenomenon also occurs depending on various factors such as flow conditions, computational grids, and flux function schemes. Therefore, an appropriate computational condition is required to extract the physical instability by keeping off the carbuncle phenomenon. Even now, however, a main factor of this numerical instability is not revealed, in spite of numerical and theoretical studies. Therefore, in analysis of shock-wave instabilities, we must assess the carbuncle phenomenon for the obtained results in a careful way.

We have conducted three-dimensional computations with Discontinuous Galerkin (DG) method[5] on unstructured grids in order to explore mechanism of the bow-shock instability which was observed in Freon by ballistic experiments more than thirty years ago. We have examined robustness of Riemann solvers against the carbuncle phenomenon in the condition we want[6] and employed a AUSM family scheme in the present paper. Moreover, through analysis with semi-ellipsoids of large aspect ratios, we obtained computational grids which seem to cause less numerical instability. With the above knowledge, we investigated dependency of the instability on body shapes[7]. As a result, our numerical simulations show that the instability appears around an edged object such as base of cone or cylinder with neither chemical reaction nor viscous effect when specific heat ratio of main stream is lower than the critical one. This instability is likely to be physical one, but the existence of the carbuncle phenomenon does not enable us to conclude that the numerical results are really caused by physical origins.

Therefore, we have designed experiments with ballistic range in a condition based on our numerical results, such as body shape, freestream Mach number, and specific heat ratio. The experimental results will validate our numerical simulations and may consequently suggest a better experimental design by a suitable numerical modeling like hypersonic effects which can describe the realistic bow-shock instability in the laboratory.
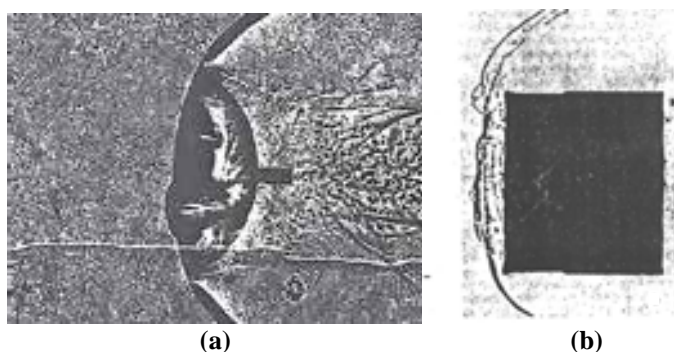

(a)   (b)

Fig. 1 Experimentally observed unstable bow shock waves[1, 2].

Numerical Simulation

The experimentally observed instability is three-dimensional phenomenon, and the body shape may have a significant role on inducing the instability. Therefore, we use three-dimensional unstructured grids which have geometrical flexibility and are easy to change its configuration according to the body shape. Euler equations are solved by the DG method which is a kind of finite-element method and can achieve relatively high order of accuracy even on the unstructured grids. In this study, the spatial accuracy of the DG method is second-order, and we employ SLAU[8] method as a numerical flux function. For the time integration, two-stage TVD Runge-Kutta method[9] is used. We do not consider any chemistry behind the shock wave. As computational conditions, Mainstream Mach number changes from 1.0 to 10.0, ratio of specific heat varies from 1.0 to 1.4 with zero angle of attack. Moreover, CFL number is commonly set to 0.3, and prismatic computational cells were used in our simulations.

Experiment

Experiments were conducted with a ballistic range at the Institute of Fluid Science (IFS), Tohoku University in the single stage powder gun mode[10]. It consists of a powder chamber, acceleration tube with 15 mm in diameter and 3.0 m in length, and a test section with 1.66 m in diameter and 12 m in length. We set a test chamber (60 mm $\times$ 145 mm $\times$ 1500 mm) in the test section, and usage of a test gas can be greatly reduced by filling the gas only in the chamber with diaphragms. Schematics of the chamber part is shown in Fig. 2. High purity of the test gas is acquired by vacuuming the chamber before filling the gas. This optical setup for shadowgraph method is used with continuous light source (metal halide lamp, LS-M210, SUMITA, 210 W).
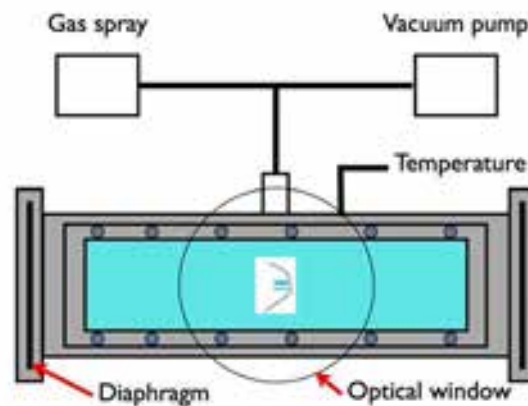
Fig. 2 Schematics of test chamber.

Results and Discussion

Dependency of Bow-Shock Instability on Body Shapes

Mach number distributions in subsonic region around a circular cone and circular cylinder are shown in Fig. [3] when γ is 1.01. Although the shock fronts become steady in both cases, a deformation of the shock front is observed with the circular cone. The asymmetric disturbances in the distributions are found for both cases. Additionally, the features of the shock deformation ahead of the circular cone resemble the ones obtained by the past experiments (Fig. 1 (a)). So, the observed instability may result from a physical origin.

(a)   (b)
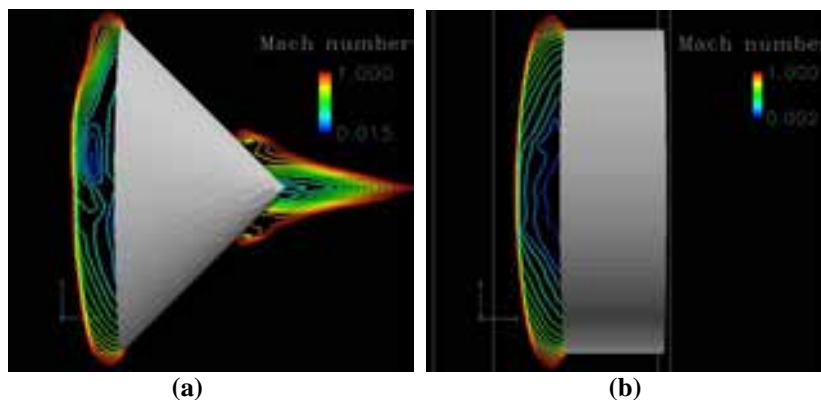
Fig. 3 Mach number distribution in subsonic region around (a) circular cone and (b) circular cylinder.

Assessment of carbuncle phenomenon

As mentioned above, it is known that a computed shock wave tends to unstable with strong shock wave. If the results with our simulation are numerical instability caused by numerical error, however, the wavelength of the

shock deformations should depend on the computational grids. So, we checked grid dependency of the obtained results. Three different grids were used, and the numbers of the cells are 375,436, 1,488,852, and 2,009,070, respectively. Figure 4 shows pressure distributions with these grid systems. Note that the freestream condition is $M = 3.9$, $\gamma = 1.05$. In all cases, comparable wavelength is predominant in the shock deformations, so this instability should be physical one. Since the scale of the wavelength is close to the cone radius, a characteristic length for the body may have an effect on determining it.

(a)   **(b)**   **(c)**
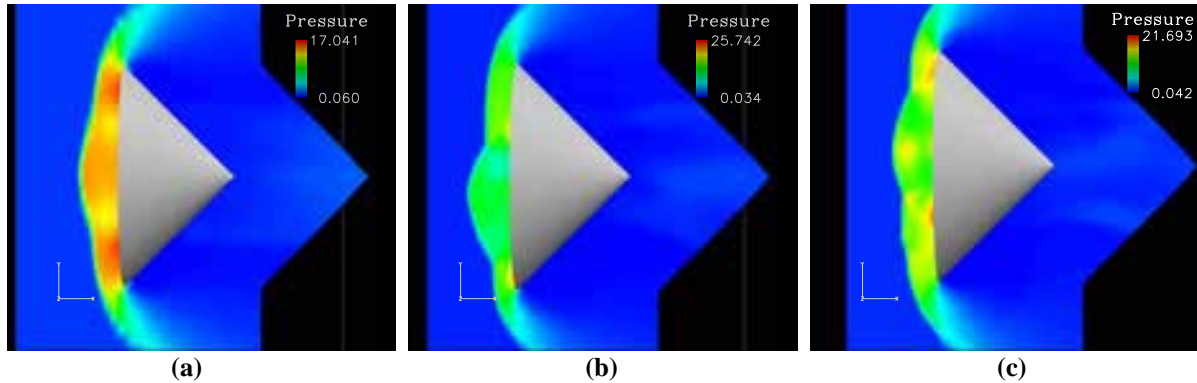
Fig. 4 Grid dependency of instability around (a) 375,436 cells, (b) 1,488,852 cells and (c) 2,009,070 cells.

Stability diagram in $\gamma - M$ plane

Figure 5 shows numerical results for parameters of γ and *M*. Blue symbols indicate the bow shock are unstable, and red stable. With the circular cone, a critical line for unstable bow is found in γ–*M* plane. Generally, shock stand-off distance becomes small when γ is low and *M* is high. The narrow shock layer may make it unstable by an interaction between the shock front and vortices generated in the shock layer. The critical Mach number greatly changes at $\gamma = 1.2$. This suggests that not only the shock thickness but also vortex generation induced by large density ratio across the shock wave may affect this instability.
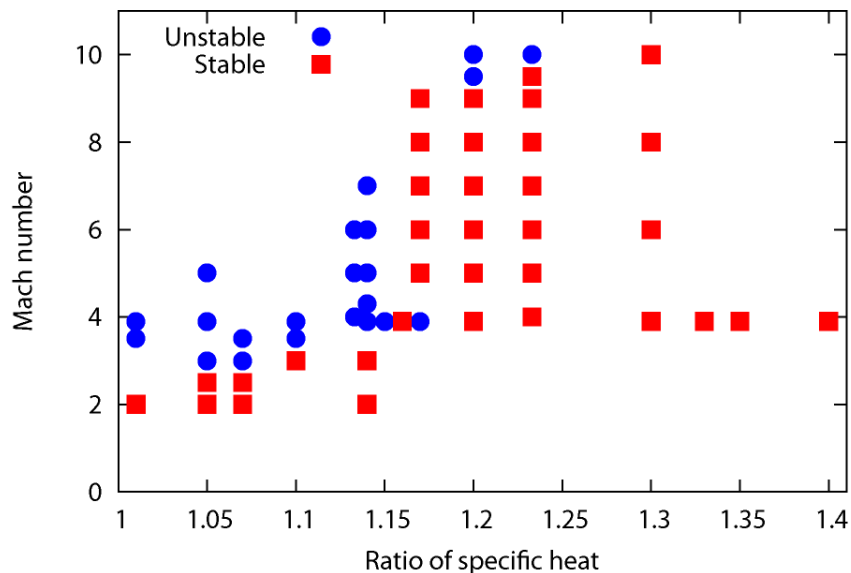
Fig. 5 Stability diagram in $\gamma - M$ plane.

Experimental Condition Based on Numerical Results

As a test gas, we use HFC-134a (CH_2FCF_3) which is generally used as a refrigerant gas. Specific heat ratio of this gas is 1.23, so the flight Mach number is set to 10 from Fig. 5. Because this gas is polyatomic, sound speed in it is relatively small and about 180 m/s at room temperature and atmospheric pressure. Therefore, injection

speed of the projectile is about 1.8 km/s when Mach is 10, and we can conduct an experiment in this condition using the ballistic range facility at IFS, Tohoku University. Note that HFC-134a is unbarnable and non-corrosive. Ozone depletion potential is also zero. Thus there is no need for special consideration under the experiment and for post-processing of the gas. Computed density distribution for the assumed condition is shown in Fig. 6. Deformation is found at the shock front, and this scale deformation can be observed by the resolution of the experiment.
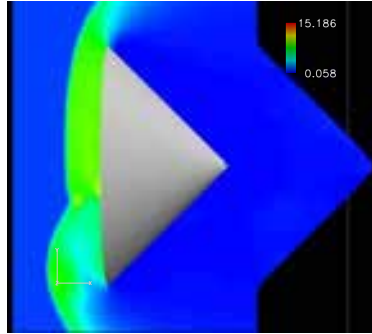
Fig. 6 Density distribution for the assumed condition.

Projectile

Figure 7 depicts a projectile used in the experiment. From the numerical assessment for body shape, we found that flowfield around the edge part of the cone is important for this instability[11]. Therefore, we use a projectile whose front part is cone with 45 degree edge like the simulation, and rear part is a cylinder of $\phi = 15$ mm which fits experimental device. The weight is about 4 g. We have confirmed that the deformation arises at the shock front even with different rear shapes by numerical simulations. Additionally, From the Mach number distribution in Fig. 3, it is obvious that the shape of the rear part does not affect flowfields in front of it. The front part is made of duralumin for withstanding severe heating due to hypersonic speed, and the rear part is polycarbonate.
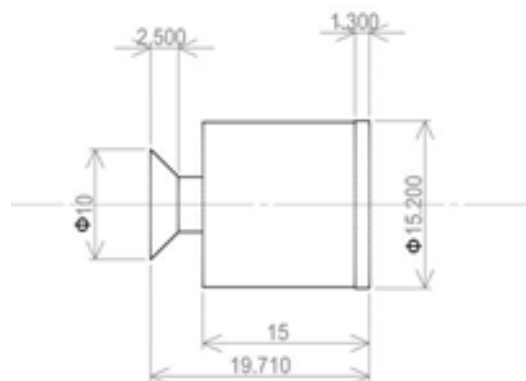
Fig. 7 Projectile shape.

Experimental results

Figure 8 depicts sequential shadowgraph images of the experiment. The projectile speed was estimated about 1.8 m/s ($M = 10.5$), and the angle of attack is zero. Time variation and deformation of the shock front ahead of the body is observed, which suggests the bow shock be unsteady and unstable in this condition. Note that the bow shock has a three-dimensional structure, so the front part of the body is not seen in these images. The shape of the shock front is deferent from numerical results. Some factors may affect this discrepancy. First, the flight Mach number is not the same as numerical simulation, and M does affect the shape of the shock front. Secondly, real gas effect such as dissociation due to severe temperature increase in a hypersonic shock may affect. The shock layer temperature reaches about 3,000 K; thus this effect may not be neglected. Moreover, other causes

are arguable, and more detailed analysis and simulations are needed. However, a principal objective of this experiment that validates the instability of bow shock wave was achieved. These results suggest that a main factor of bow-shock instability is likely pure hydrodynamic effect, although real gas effects could not be neglected in the real problem.
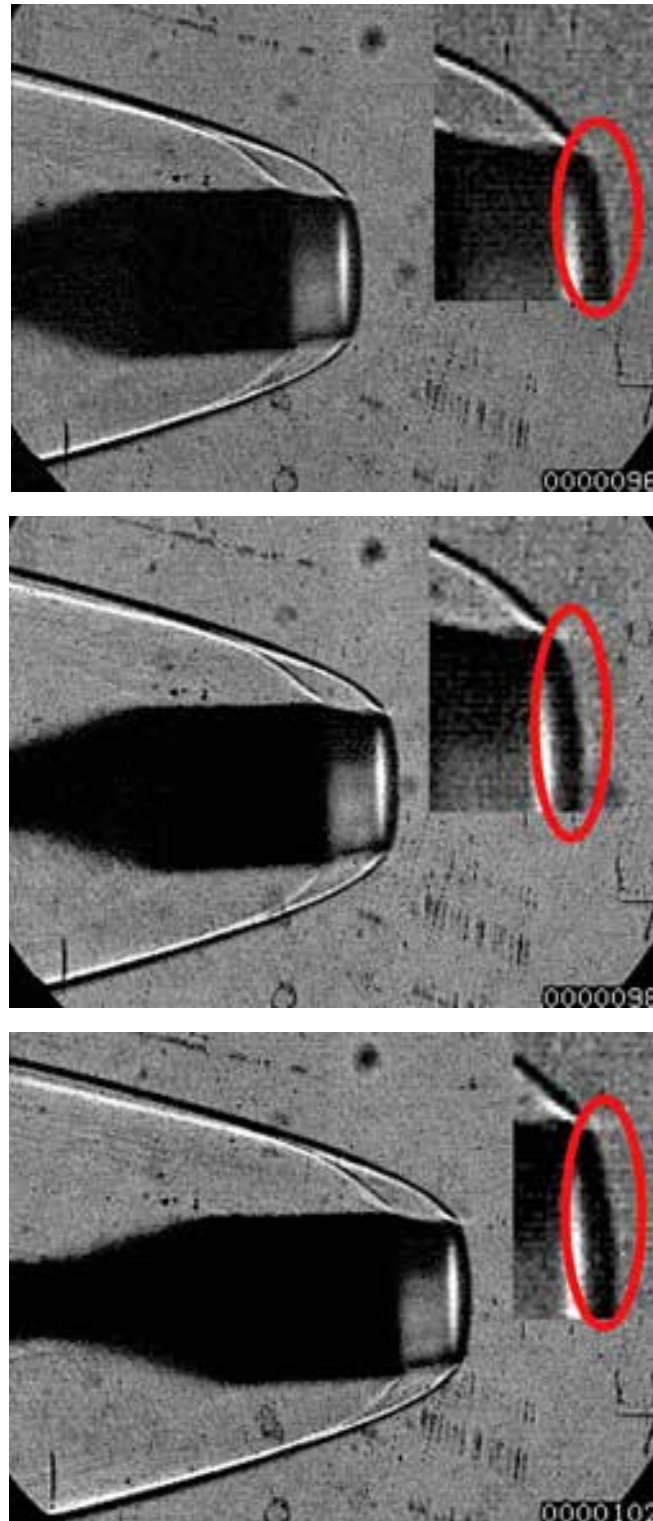

Fig. 8 Shadowgraph images of the bow shock around the projectile in the test gas. (a) $t = 0\,\mu$s, **(b)** $t = 2\,\mu$s, **and (c)** $t = 6\,\mu$s.

Conclusions

Three-dimensional numerical simulations were conducted with DG finite-element method on unstructured grids, and bow-shock instability was reproduced with a circular cone in a low γ flow. Based on the numerical results, we designed an experiment to observe the instability in the laboratory in order to validate our results. The experimental results depicted that the bow shock wave in the condition can be unsteady and unstable. Therefore, our numerical results with Euler equations were validated to some extent, although the shock shape was different from the calculation. There are some factors for this discrepancy, such as real gas effect due to hypersonic speed and time variation of projectile speed or posture. However, the numerical and the experimental results suggest that the bow shock can become unstable by purely hydrodynamic effect. We will conduct further experiments and more detailed analysis by our numerical simulation validated in this experiment.

Acknowledgements

References

[1] A. S. Baryshnikov, A. P. Bedin, V. G. Maslennikov and G. I. Mishin, Stability of a bow shock. *Sov. Tech. Phys. Lett*, **5**, 113-114 (1979).

[2] A. S Baryshnikov, Baroclinic turbulence of dissociating gas as a reason for instability of bow shock wave. *Phys. Scr.*, **T132**, 014007 (2008).

[3] H. G. Hornung and P. Lemieux, Shock layer instability near the Newtonian limit of hypervelocity flows. *Physics of Fluids*, **13**, 8 (2001)

[4] J. Quirk, A contribution to the great Riemann solver debate. *International Journal for Numerical Methods in Fluids*, **18**, 555 (1994).

[5] B. Cockburn and C.-W. Shu, The Runge-Kutta discontinuous Galerkin method for conservation laws V: Multimensional systems. *Journal of Computational Physics*, **141**, 199 (1998).

[6] Y. Sato, Y. Suzuki, K. Yasue and N. Ohnishi, Three-dimensional simulation of bow-shock instability using discontinuous Galerkin method. *Proceedings of the 28th International Symposium on Shock Waves*, **1**, 1027, Springer (2011).

[7] Y. Sato, K. Yasue and N. Ohnishi, Bow-shock instability with edged body in low-γ flow. *AIAA Paper*, 2012-2708 (2012).

[8] E. Shima and K. Kitamura, On New Simple Low-Dissipation Scheme of AUSM-Family for All Speeds. *AIAA Paper*, 2009-136 (2009).

[9] S. Gottlieb and C.-W. Shu, Total Variation Diminishing Runge-Kutta Schemes. *Mathematics of Computation*, **67**, 73 (1998).

[10] D. Numata, Experimental study on hypervelocity impact phenomena at low temperatures with ballistic range, *Doctor thesis, Tohoku University* (2008)

[11] Y. Sato, K. Yasue and N. Ohnishi, Numerical simulation of Bow-shock instability around circular cone. *Proceedings of 20th International Shock Interaction Symposium*, 157 (2012).

A Study on Pressure Variation of a Rotor Blade Tip using PSP

Kidong Kim
Kijung Kwon

Aircraft System Engineering Dept.
University of Science and Technology (UST)
217 Gajeong-ro, Yuseong-gu, Daejeon
South Korea
kdkim4@gmail.com,

Aerodynamics Team
Korea Aerospace Research Institute (KARI)
169-84 Gwahangno, Yuseong-gu, Daejeon
South Korea
kjkwon@kari.re.kr

Abstract

The present study was performed to verify the accuracy of measuring the upper surface pressure on a rotor blade tip using recently developed fast-response Pressure Sensitive Paint (PSP). Conventionally, *in situ* calibration was used to increase the accuracy of PSP measurement. However, it is very difficult to install the pressure measurement instruments such as a pressure tap on a rotor blade. Correction coefficient from CFD results was applied to this PSP experiment instead of *in situ* calibration. The experiment was performed using the small-scale rotor test stand in hovering condition. Blade had a NACA 0012 airfoil, and Rotational tip speed was about 87 m/s. Blade collective pitch was adjusted three different angle conditions (5°, 8°, 12°). The corrected PSP data was compared with well-known experimental pressure coefficients to examine the possibility of PSP application for pressure measurement on a rotor blade tip.

Key words: PSP, rotor blade, blade tip pressure, single-shot, lifetime

Introduction

In order to understand aerodynamic and acoustic characteristics of a rotorcraft, it has been necessary to examine the pressure variation on a rotor blade. The way for investigation of pressure distribution on a rotor blade has been used to experimental measurement techniques or numerical calculation methods. In case of the conventional pressure measurement techniques, pressure taps and pressure transducers have been installed on a rotor blade. However, it had several problems. At first, it has been very difficult to install the pressure sensors on the narrow rotor blade, and also had balancing problems. Moreover, rotating rotor blade has generated vibration and deformation, so they might disrupt pressure measurement. Hence, computational fluid dynamics (CFD) has attempted to predict rotor performance instead of experimental measurement technique due to those problems as well as high cost. CFD has been based on theoretical governing equations of fluid dynamics. Even though CFD have solved many complicated and challenging problems in the field of aerodynamics, experimentally measured data was also applied to aerodynamic study for an accurate analysis. For the reason above, the present study was demonstrated to measure the pressure variation on a rotor blade tip using fast-response Pressure Sensitive Paint (PSP), and CFD data was used to correct PSP results.

PSP has been developed as an advanced pressure measurement technique. In 1935, H. Kautsky and H. Hirsch discovered the oxygen quenching of luminescence for the first time. The principles of PSP are based on the oxygen quenching [1]. After first discovered, many researchers such as Bell et al. [2] and Liu et al. [3] have tried to apply the principles to the field of aerodynamics. Various PSP techniques and technologies are developed in order to improve accuracy of PSP [4]. For the steady pressure measurement, intensity-based technique has been studied to acquire luminescent intensity on a model surface. For the unsteady pressure measurement, lifetime-based technique and fast-response PSP were developed by many researchers [5, 6, 7].

Reviews of unsteady and fast-response PSP developments were described by Gregory et al. [8, 9] and Asahi et al. [10]. Both techniques were qualitatively demonstrated by Wong et al. [11], where outer the 15% of each blade was painted with PSP. Recently, Kumar et al [12] and Juliano et al [13] carried out the surface pressure measurement on a rotating surface using single-shot, lifetime-based fast-response PSP technique.

Previous researches focused on measurement techniques and paint developments such as fast-response PSP. The objective of a present study is to apply those techniques to a small-scale rotor blade so that examine surface pressure variation and verify the possibility of PSP application for pressure measurement of a rotor blade tip using recently developed single-shot, lifetime-based fast-response PSP.

Single-shot, lifetime-based fast-response PSP technique

Principle of PSP
As previously mentioned, the principle of PSP is based on the oxygen quenching. Shortly describes the basic principle of PSP, the luminescent probe is imbedded in a polymer binder form as shown in Figure 1. The luminescent molecular absorbs energy from light source of the proper wavelength, it emits different luminescent intensity depending on concentration of oxygen on a model surface. According to Henry's law, the concentration of oxygen in a PSP polymer is proportional to the partial pressure of oxygen in gas above the polymer [1].
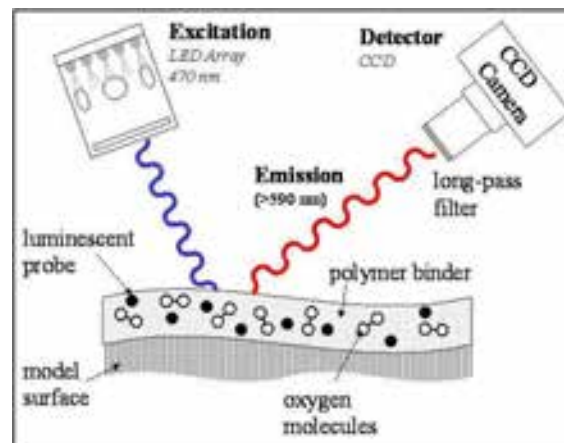
Figure 1: Basic components of a PSP system [14]

Once luminescent intensity is detected by a CCD camera, it can easily calculate surface pressure on a model using Stern-Volmer equation (1). Stern-Volmer equation describes relationship between the luminescent intensity from PSP and oxygen concentration:

$$\frac{I_{ref}}{I} = A(T) + B(T)\frac{P}{P_{ref}} \tag{1}$$

where P is pressure at a test(wind-on) condition, I is luminescent intensity at a test(wind-on) condition, P_{ref} is pressure at a reference(wind-off) condition, I_{ref} is luminescent intensity at a reference(wind-off) condition, and A(T), B(T) are calibration coefficients depending on temperature. The reference is basically taken at a vacuum condition. However, it is very difficult to measure at the vacuum condition. Hence, the reference is usually taken at the ambient air condition instead of the vacuum condition. The reason why the reference is needed that used to eliminate the effects of non-uniform illumination and uneven paint coating.

Lifetime-based technique
There are two methods for capturing PSP images. One is an intensity-based technique, and the other is a lifetime-based technique. In order to measure unsteady or rotating surface pressure, lifetime-based technique is the best way to get correct images, because intensity-based technique gives time averaged data. The theoretical

background of lifetime-based technique is based on the luminescence decay lifetime. As shown in Figure 2, the luminescence is insensitive to pressure when the luminescence is excited by light source. After the light disappears, the luminescence is relaxing from its excited state. At the time, the luminescence decay lifetime is inversely proportional to the concentration of oxygen. If the oxygen concentration is high on a model surface, the luminescence decay time will be short. On the other hand, if the oxygen concentration is low, the luminescence decay time will be short. In other words, the captured image can use reference data (gate 1) while light is on. The sensitive data (gate 2) can be obtained by capturing the luminescence intensity of decay lifetime. From Stern-Volmer equation, luminescence intensity I can be replaced with gate 1 and gate 2. Hence, Stern-Volmer equation is expressed in terms of gate 1 and gate 2 (2):

$$\frac{(Gate_2 / Gate_1)_{ref}}{(Gate_2 / Gate_1)} = A(T) + B(T)\frac{P}{P_{ref}} \qquad (2)$$

The pressure at the test condition can be estimated using revised Stern-Volmer equation (2).
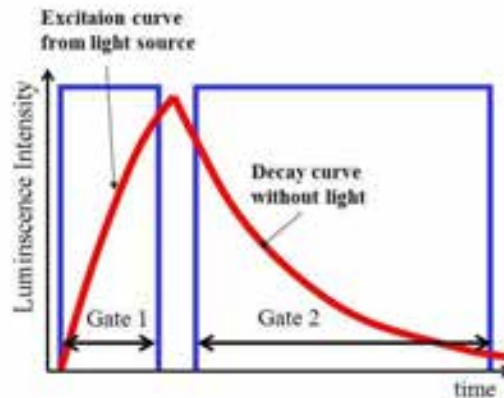
Figure 2: PSP Lifetime curve

Single-shot technique using pulsed Nd:YAG laser
CCD camera and light source are essentially required for PSP measurement. As a light source, pulsed LED arrays or flash lamp with band-pass filter have been conventionally used. In case of unsteady pressure measurement using PSP, lifetime-based technique is required because pressure is quickly changed in unsteady conditions. The lifetime of luminescence is the order of microsecond. Therefore, light should be able to emit powerful energy to paint during microsecond. Figure 3 shows comparison of LED arrays and Nd:YAG laser as a light source. The intensity image was taken only once. If images added together into one image to increase intensity during rotor PSP experiment, the image might not be exactly combined due to deformation of rotor blade during rotation. The results from obtained images showed that the pulsed laser could acquire stronger intensity images than LED arrays. Hence, the pulsed Nd:YAG laser which has 532 nm wavelength is eligible to use as a excitation source for lifetime-based PSP.
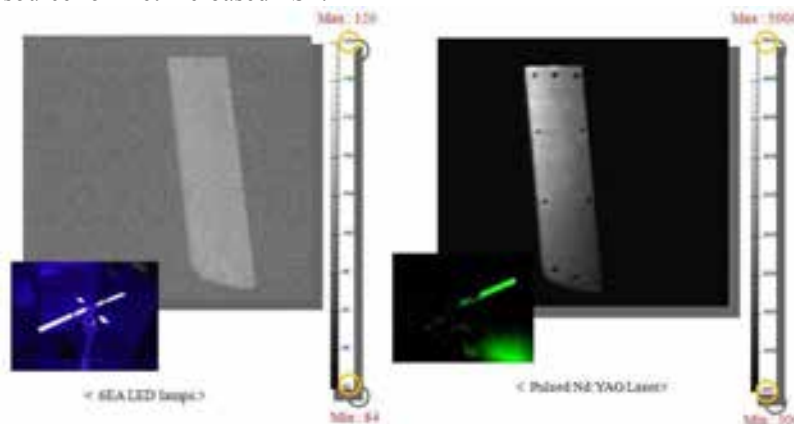

Figure 3: Comparison of LED arrays and laser

Fast-response PSP

There are many pressure sensitive paints depending on luminescent probe and binder form. The paints have different characteristics. Conventional polymer-based PSPs are not appropriate for using unsteady pressure measurement because the response time of PSPs is as slow as seconds. It is related to the rate of oxygen diffusion (τ_{diff}) of the paint. The oxygen diffusion is proportional to the binder thickness (h) and inversely proportional to the mass oxygen diffusivity (D_m) of the paint (3):

$$\tau_{diff} \propto \frac{h^2}{D_m} \qquad (3)$$

Therefore, the response time of PSP can be improved by either decreasing the binder thickness or increasing the mass oxygen diffusivity of the paint. Decreasing the binder thickness would imply lesser luminescence emission. Thus, porous binders have been developed for increasing the mass oxygen diffusivity of the paint. Figure 4 shows comparison of conventional binder and porous binder. The PSP which used for the present experiment was developed by Innovative Scientific Solution Inc, (ISSI). The paint was commonly called fast-response PSP since the response time was up to 20 kHz. The PSP was composed of acrylic polymer and ceramics, so it also called polymer/ceramic PSP.
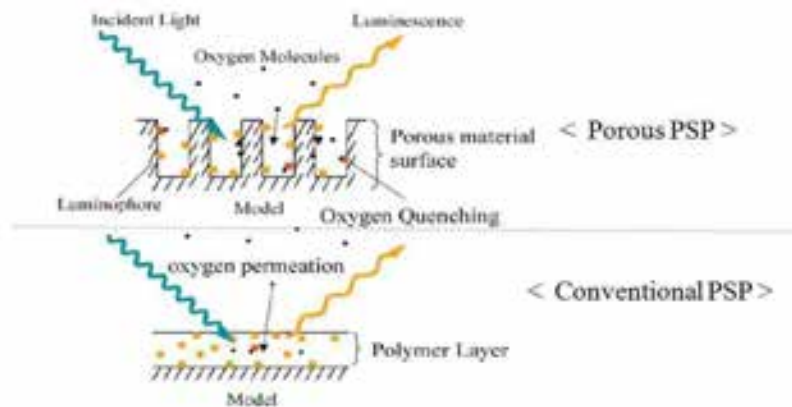
Figure 4: Comparison of conventional binder and porous binder [17]

Experimental set-up

The present PSP experiment was conducted using small-scale rotor test stand in the Korea Aerospace Research Institute (KARI). The main body was a commercial RC helicopter, and it had two rotor blades. The rotor blades were especially produced for the PSP experiment. The blades were made of NACA 0012 airfoil section (Figure 5) with a rectangular planform using composite materials. The blade length was 340 mm and its chord was 40 mm. The outer 30% (from tip to 120 mm) of the blade was coated with a fast-response PSP (Figure 6) in order to examine pressure variation on a rotor blade tip area. After coated with the PSP, registration markers for image alignment were located on the painted blade. The rotating speed of the blade was 2080 rpm (tip speed=12 m/s) in the test condition. The images were obtained by changing collective pitch angle of blade. The collective pitch angles of blade were respectively adjusted to 5°, 8°, and 12° in hovering condition. Suppose the forward flight direction was azimuth 180°, the camera shutter was open when the blade was located at 270° azimuth angle. More specific rotor parameters are shown in Table 1.

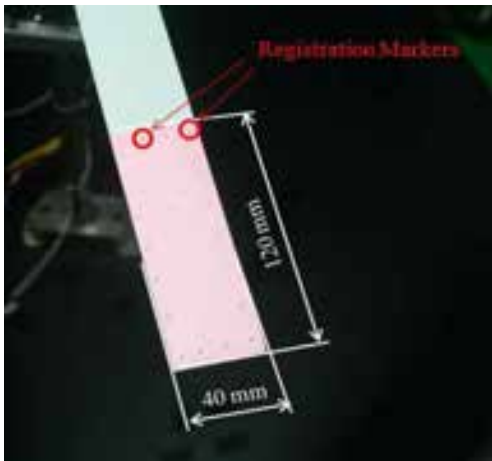

Figure 5: Airfoil section geometry (NACA 0012)

Figure 6: Registration markers

Table 1: Rotor parameters

Blade Length (mm)	340
Blade Chord (mm)	40
PSP Painted Length (mm)	120
Rotor Radius (mm)	400
Rotational Speed (rpm)	2080
Tip Speed (m/s)	87.12
Tip Mach Number	0.2562

As previously described, pulsed Nd:YAG laser was used to emit powerful energy to PSP coated rotor blade. The images were acquired using CCD camera which was a PCO2000. It has high resolution (2048 x 2048 pixels) and the digitizer operates at 14-bit resolution. PCO2000 has been typically used for Particle Image Velocimetry (PIV). The camera was operated using double exposure mode so that allows for the acquisition of two images such as gate 1 and gate 2. Only gate 1 exposure time could adjust in double exposure mode. AF 24-85 mm Nikon zoom-lens was mounted to the CCD camera, and a long-pass optical filter was equipped in front of the camera lens to capture only paint intensities. Figure 7 shows schematic of the PSP experimental set up. All images were recorded by CamWare software.

To control the camera shutter and laser pulse, micro photo sensor was installed bottom of the main rotor shaft. It provided a once-per-revolution signal while rotor was spinning. Figure 8 shows timing diagram for the present experiment. The Q-switch delay time decides laser intensity. Laser Q-switch was adjusted 185 µs in order to emit proper energy. Gate 1 exposure time selected 190 µs to equalize the gate 1 and gate 2 intensities within 20%.
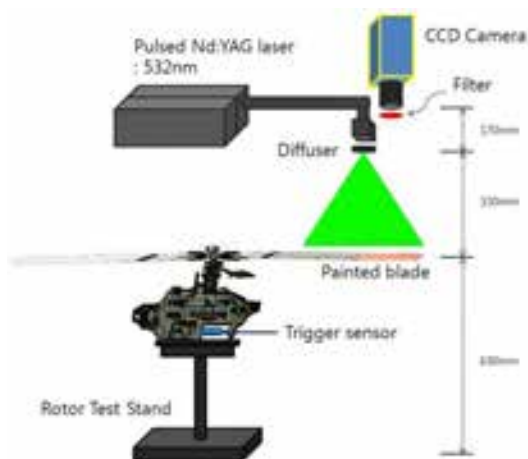
Figure 7: Schematic of the PSP experiment
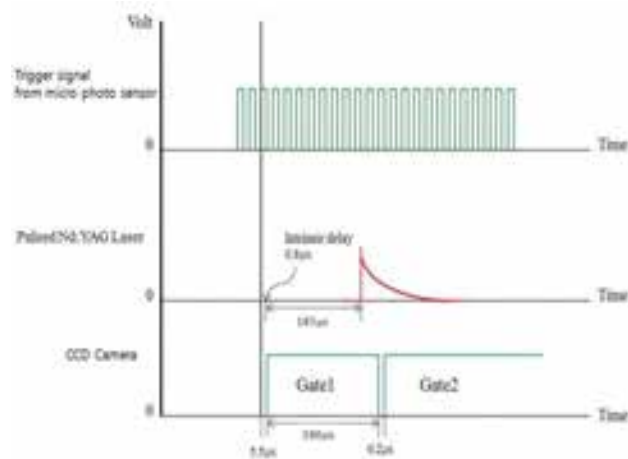
Figure 8: Timing diagram

A priori calibration was undertaken to know relation between luminescence intensity and oxygen concentration, and also estimated temperature coefficients A(T) and B(T). *A priori* calibration was similar to the test condition in temperature. Ambient temperature was about 26 ºC and atmospheric pressure was about 100,400 ~ 101,000 Pa during the experiment. Moreover, temperature did not significantly change while the PSP experiment was proceeding (±0.2 ºC). Background images were also acquired to eliminate unexpected luminescence such as monitor, camera dark noise, etc.

PSP Results

Figure 9 shows surface pressure distributions on a rotor blade tip at three collective pitch angle conditions. The bottom color-bar indicates the pressure ratio, where the reference condition is atmospheric pressure. As theoretically known, the low pressure region is observed near the leading edge and increase toward the trailing edge at all three collective pitch angles. The upper surface pressure decreases with increasing the collective pitch angle, as expected. The high pressure region was observed near the blade tip as a result of the blade tip-vortex. Also, there are a high pressure lines at the trailing edges at all conditions. When applying single-shot, lifetime-based PSP technique to measure surface pressure on a rotor blade, gate 2 exposure time could not control. Moreover, the acquisition time of the gate 2 was much longer than gate 1. Thus, acquired gate 2 images had motion blur. The motion blur results in nonphysical pressure on the trailing edges of the blades.
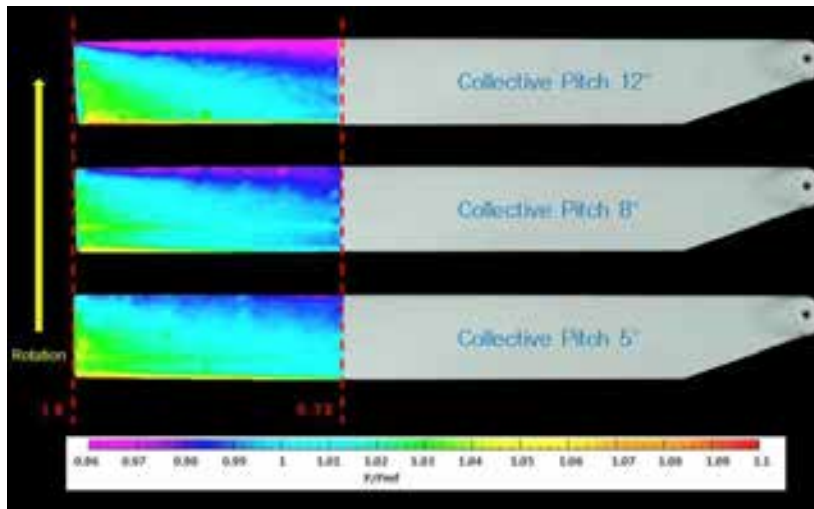
Figure 9: The results of pressure variation depending on collective pitch angles

In case of the collective pitch 5° and 8°, there are high pressure region near x/c = 0.65 and it continuously appears to the horizontal direction. When images captured using CCD camera, the dual converter mode was on. In that case, the intensity image was slightly different between left side and right side owing to the effect of the dual converter mode. The effects could not be corrected via post-image processing. For the reason, the pressure data was eliminated from x/c = 0.65 to the trailing edge. Figure 10 indicates pressure coefficient curve depending on collective pitch angles at r/R = 0.96. Basically, the pressure coefficients of upper surface are minus values. However, the PSP results show several plus pressure coefficients. Typically, *in situ* calibration has been used to correct this problem. Unfortunately, it is very difficult to install the pressure taps on a rotor blade for *in situ* calibration. Hence, the PSP results were complemented by CFD results.
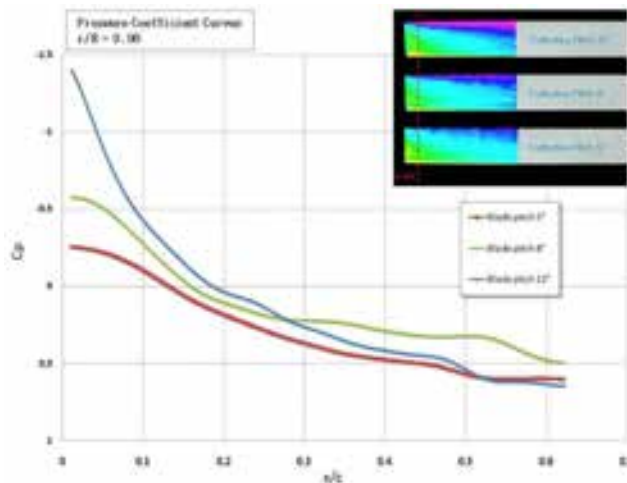

Figure 10: Chordwise pressure coefficient for three collective angles at r/R = 0.96

CFD application

Three-dimensional viscous flow field around a lifting helicopter rotor in hover was calculated by using an unstructured mesh methodology by H.J. Kang [15]. Calculations are made for the experiment hovering rotor of Caradonna and Tung [16].Therefore, the calculation model has two-blades, untwisted, rigid rotor, and blades are made of a NACA 0012 airfoil section. The experimental conditions of the present PSP experiment are also based on Caradonna and Tung's experiment [16]. Therefore, Both CFD and PSP experiment are designed at very similar conditions. Only difference is that CFD results was computed in the case of M_{tip}=0.439 at collective pitch 8°. By comparing the case of M_{tip}=0.225 with M_{tip}=0.439 using Caradonna and Tung's experiment [16], there were no significant difference of pressure coefficient depending on tip speed because both cases were low speed conditions. The correction coefficient was estimated from CFD results at collective pitch 8°. Figure 11, Figure 12, and Figure 13 shows corrected pressure coefficients of PSP experiment, and also compare with well-known experimental pressure coefficients [16]. All pressure coefficients which measured using PSP show lower Cp without correction. After the PSP results were corrected using CFD results, and then the pressure coefficients of PSP coincide well with the Caradonna and Tung's pressure measurement.
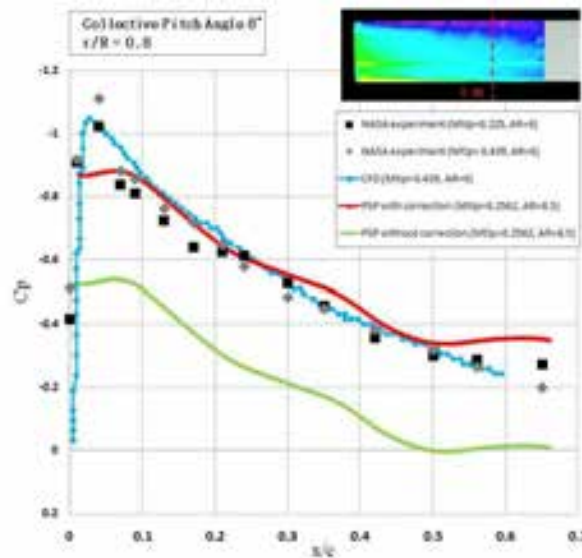

Figure 11: Corrected PSP Cp and Comparison with NASA experiment [16] at r/R=0.8 and pitch=8°

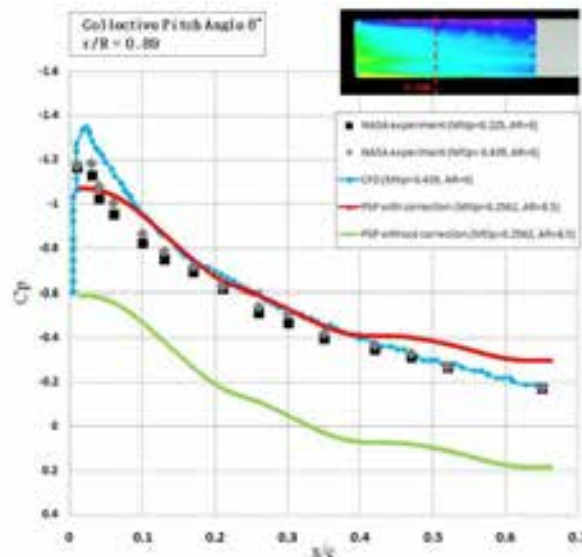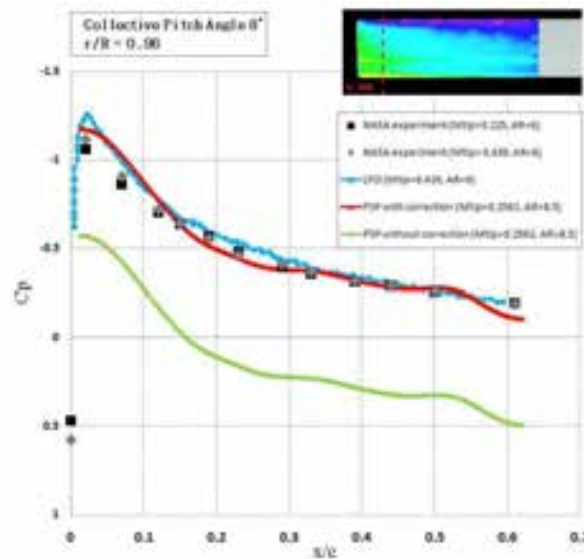**Figure 12: Corrected PSP Cp and Comparison with NASA experiment [16] at r/R=0.89 and pitch=8°**

Figure 13: Corrected PSP Cp and Comparison with NASA experiment [16] at r/R=0.96 and pitch=8°

Conclusion

The present study has attempted to establish the possibility of PSP application for pressure measurement of a rotor blade tip using single-shot, lifetime-based fast-response PSP. The results of the present study showed global surface pressure fields on a rotor blade tip in hovering condition, and well measured pressure distributions, qualitatively. In order to obtain exact pressure coefficient of a rotor blade surface, *in situ* calibration is required to increase accuracy. The present study suggested and tried to apply correction coefficient from CFD results instead of *in situ* calibration. As shown in the results, corrected pressure coefficient of PSP experiment was almost identical with well-known pressure coefficient on a rotor blade at similar conditions. Even though several problems still exist, single-shot, lifetime-based fast-response PSP technique has potential to provide accurate pressure on a rotor blade tip.

References

[1] T. Liu and J. P. Sullivan.: Pressure and temperature sensitive paints. *Springer, New York,* 2005.

[2] T. Liu.: B. T. Campbell.: S. P. Burns.: J. P. Sullivan.: Temperature-and Pressure-Sensitive Luminescent Paints in Aerodynamics. *Applied Mechanics Reviews,* Vol. 50, No.4, pp.227-246, 1997

[3] J. H. Bell.: E. T. Schairer.: L. A. Hand and R. D. Mehta.: Surface Pressure measurements using luminescent coatings. *Annual Review of Fluid Mechanics*, Vol. 33, pp.155-206, 2001.

[4] T. Liu.: M. Guille and J.P. Sullivan.: Accuracy of Pressure Sensitive Paint. *AIAA Journal,* Vol. 39, No. 1, 2001

[5] R. H. Engler and C. Klein.: DLR PSP System: Intensity and Lifetime measurements. *Instrumentation in Aerospace Simulation Facilities, 17th International Congress on ICIASF 1997,* pp.46-56.

[6] K. Mitsuo.: K. Asai.: A. Rakahashi and H. Mizushima.: Advanced lifetime PSP imaging system for pressure and temperature field measurement. *Measurement Science and Technology,* Vol. 17, No. 6, pp.1282-1291, 2006.

[7]   A. N. Watkins.: J. D. Jordan.: B. D. Leighty.: J. L. Ingram and D.M. Oglesby.: Development of next generation lifetime PSP imaging systems. *Instrumentation in Aerospace Simulation Facilities, 20th International Congress on ICIASF '03*, pp. 372-382, 2003.

[8]   J. W. Gregory.: Porous pressure-sensitive paint for measurement of unsteady pressures in turbomachinery. *42nd AIAA Aerospace Sciences Meeting and Exhibit, Reno, NV, AIAA 2004-0294, January*, 2004.

[9]   J. W. Gergory.: K. Asai.: M kameda.: T. Liu and J.P. Sullivan.: A review of pressure-sensitive paint for high-speed and unsteady aerodynamics. *Proceedings of the Institution of Mechanical Engineers, Part G, Journal of Aerospace Engineering*, Vol. 222, No.2, pp 249-290.

[10] K, Asai.: K. Nakakita.: M. Kameda.: K. Teduka.: Recent topics in fast-responding pressure-sensitive paint technology at national aerospace laboratory. *Instrumentation in Aerospace Simulation Facilities, 19th International Congress on ICIASF 2001, Cleveland, OH,* pp. 25-36, *August,* 2001,.

[11] O. D. Wong.: A. Neal Watkins and JoAnne L. Ingram.: Pressure sensitive paint measurements on 15% scale rotor blades in hover. *35th AIAA Fluid Dynamics Conference and Exhibit, San Francisco, CA, AIAA 2005-5008*, *June,* 2005.

[12] P. Kumar.: Development of a single-shot lifetime PSP measurement technique for rotating surfaces. *M.S. Thesis, The Ohio State University, Columbus, OH,* 2010.

[13] T. J. Juliano.: P. Kumar.: D. Peng.: J. W. Gregory.: J. Crafton and S. Fonov.: Single-shot, lifetime-based pressure-sensitive paint for rotating blades. *Measurement Science and Technology,* Vol. 22, No.8, 2011.

[14] L. Goss.: G. Jones.: J. Crafton.: S. Fonov.: V. Fonov.: Temperature Compensation for Lifetime-Based Pressure Sensitive Paint Systems. *Instrumentation in Aerospace Simulation Facilities, 21st International Congress on ICIASF 2005, Sendai, Japan*, pp.283-292, 2005.

[15] H.J. Kang and O.J.Kwon.: Unstructured Mesh Navier-Stokes Calculations of the Flow Field of a Helicopter Rotor in Hover. *Journal of The American Helicopter Society,* Vol. 47, No. 2, pp.90-99,2002

[16] F. X. Caradonna, and C. Tung.: Experimental and Analytical Studies of a Model Helicopter Rotor in Hover. *NASA-TM-81232*

[17] H. Sakaue.: Porous pressure sensitive paints for aerodynamic applications. *MS Thesis, School of Aeronautics and Astronautics, Purdue University, West Lafayette, IN,* 1999.

[18] J. P. Hubner.: J. D. Abbitt and B. F. Carroll.: Pressure measurements on rotating machinery using lifetime imaging of pressure sensitive paint. *32nd AIAA/ASME/SAE/ASEE Joint Propulsion Conference and Exhibit, Lake Buena Vista, FL, 1-3 July,* pp.1-9, 1996.

[19] Y. Sakamura.: T. Suzuki.: M. Matsumoto.: G. Masuya and Y. Ikeda.: Optical measurements of high-frequency pressure fluctuations using a pressure-sensitive paint and Cassegrain optics. *Journal of Measurement Science and Technology,* Vol. 13, No.10, pp. 1591-1598, October, 2002.

[20] M. Kameda.: T. Tabei.: K. Nakakita.: H. Sakaue and K. Asai.: Imaging measurement of unsteady pressure fluctuation on a delta wing by an anodized aluminum PSP. *Measurement Science and Technology*, Vol. 16, No12, 2005.

Assessment of Some Experimental and Processing Factors for Background Oriented Schlieren Measurements

Ardian B. Gojani
Shigeru Obayashi

Institute of Fluid Science
Tohoku University
2-1-1 Katahira, Aoba, Sendai 980-8577
Japan
gojani@edge.ifs.tohoku.ac.jp

Abstract

An outline of background oriented schlieren (BOS) and its application to two types of flow is given. Extraction of quantitative data from the images depend on a number of factors, which are influenced from instrumentation and experimental adjustments, as well as from the image analysis and post-processing. These effects are investigated,

Key words: flow visualization, background oriented schlieren, sensitivity, error analysis.

Introduction

The problem we would like to address is the extraction of quantitative data from flow visualization, in particular from background oriented schlieren (BOS) technique. The technique was proposed and its fundamentals outlined in references [1] and [2], and a broad assessment is given in [3]. In BOS, a flow is made visible by comparing images of the flow in two different states, with each state being defined by a different distribution of flow properties. Since there exists a direct relationship between fluid flow properties and the fluid's refractive index, for gases explicitly expressed by the Gladstone-Dale equation, as a result, light rays will bend (refract) into two different directions, yielding a distorted image of the field of view.

Since its beginnings, flow visualization has mainly been concerned with qualitative description of the flow [4], while quantitative measurements were carried only in some limiting cases, mainly for two reasons:
  1. quantitative measurements were impossible, e. g. shadowgraphy records the illumination change due to the second derivative of the density, which is impossible to be double integrated and give density values, or
  2. quantitative measurements were too difficult and/or inaccurate compared to other techniques, e. g. interferometry.

The development of digital image processing and analysis has made possible new investigations into quantitative flow visualization. An outcome of these investigations is BOS, which makes use of a combination of standard photography and of cross-correlation methods of image analysis, as developed for laser speckle photography and particle image velocimetry.

In general, any type of background that shows locally illumination value differences may be used as a field of view for BOS visualization. For example, in references [5], the natural landscape full of features, mainly grass and trees, has been used as the field of view. A variant of BOS that makes use of backgrounds with specific features, prepared according to the requirements of the experiment, sometimes is referred as synthetic schlieren [6].

The present paper will argue that BOS can be used for quantitative measurements of the flow field, and, in line with [7] and [8], will investigate the accuracy of the technique as applied to synthetic images. Also, experimental results for two types of flows will be presented, showing the potential and limitations of the technique.

BOS technique

The principle of BOS lays in the difference between two images of the same pattern imaged through a test fluid: a reference image is taken without and a measurement image with a disturbance in the fluid that is to be evaluated, as illustrated in Fig. 1. The figure shows a side view of a BOS arrangement with the imaged background pattern B, the test section T (phase object with refractive index gradient $\partial n(\mathbf{r})/\partial y$), the objective lens L, and image plan, coplanar with the recording sensor, I. The angle of deflection due to the gradient of refractive index $n(\mathbf{r})$ is ε. Distances a, w, d between different sections of the BOS system, as well as the object and image distances s_o and s_i, respectively, are also noted. The recorded dot shift in the image plane is dy_i and its apparent shift in the background is dy_o. The full line along the optical axis is the light ray when a reference image is being taken, while the dashed line shows the ray during the measurement imaging in the presence of a fluid disturbance. The disturbance, e. g. a shock or a heat wave, causes local changes of density, resulting in changes of the refractive index. Hence, an imaging light beam passing through the disturbance will deflect and the angle of deflection is encoded in the difference between the measurement and the reference image. The equation that tracks the position of the ray is

$$\frac{d}{ds}\left(n(\mathbf{r})\, d\, \frac{\mathbf{r}}{ds} \right) = \nabla\, n(\mathbf{r}) \quad , \tag{1}$$

where $\mathbf{r}(s)$ is the position vector representing the position of any point in the ray, $n=n(\mathbf{r})$ is the refractive index of the medium through which the ray passes, and ds is the infinitesimal arc length. From Eq. (1), considering plane $x=0$, and assuming paraxial approximation along optical axis z and negligible ray deviations – but, non-negligible change of ray's curvature, the angle of deflection along direction y is

$$\varepsilon_y = \int_a^{a+w} \frac{1}{n} \frac{\partial n}{\partial y}\, dz \quad , \tag{2}$$

with a and $a+w$ the entry and exit points in the phase object. This angle, and subsequently the refractive index, can be extracted, for example, by cross-correlation or ray tracing algorithms, enabling the deduction of the fluid's density from the relationship between the density and the refractive index. This relationship is given by the Gladstone-Dale relation

$$n - 1 = K\rho \quad , \tag{3}$$

where K is a constant of the medium and $\rho = \rho(\mathbf{r})$ is the density. Combination of Eqs. (1) and (3) gives the density field of the disturbance.

A BOS measurement consists of two stages: image recording and image evaluation. Image recording constitutes the choice of the background pattern, the recording system, i. e. cameras and lightning, and their arrangement. The background is characterized by two numbers: dot size and dot density, which are determined based on the pixel size and pixel count of the camera sensor. BOS' light capturing unit is an image sensor (CCD or CMOS based camera), characterized by its pixel count N_{px} and size Δ_{px}. Since the phenomena for which BOS is used are transient, the recording system needs to be fast enough to freeze the motion of the fluid under investigation. In general, sensors with large pixel count and pixel size take images with better quality, but the increase of these two parameters means that the field of view also needs to be large. Given a sensor with a certain pixel count and size, or alternatively a fixed field of view corresponding to the test section, the imaged dimensions of the fluid under study can be adjusted mainly through optical arrangement of the setup by setting distances a and d.

Image evaluation constitutes the comparison of reference and measurement image data and usually is done by using cross-correlation algorithms. The recorded images are a set of data that are divided into smaller sections, representing the interrogation windows. For an image recording done properly, the interrogation window of the reference and measurement images will have the same number of dots and with the same relative distances to each other, but shifted in reference to the absolute position. Correlation algorithms result in a peak that corresponds to the average dot shift in the image plane, with a resolution down to 0.1 pixels, achieved by
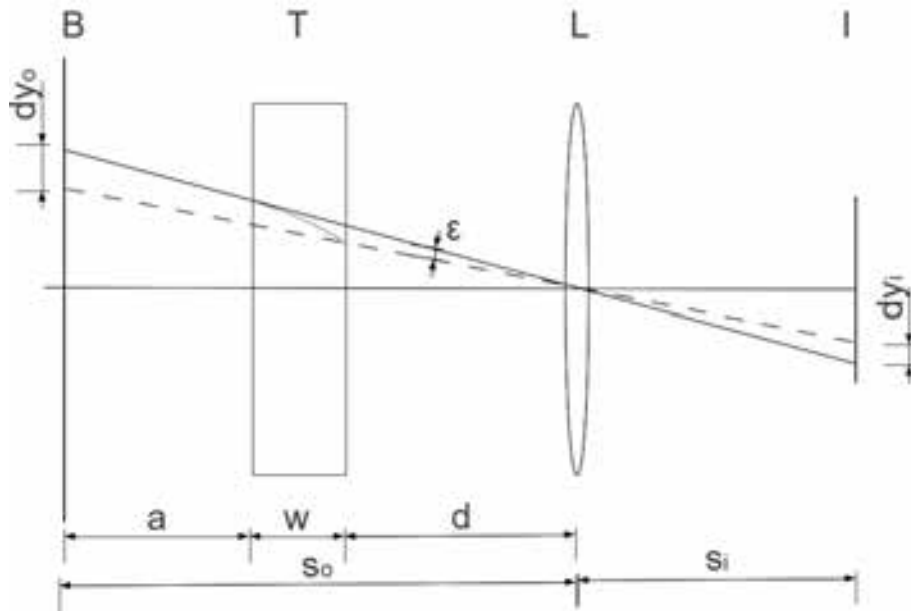
Figure 1. A meridional plane of a BOS setup: B – the background, T – the test section where the fluid flows, L – the imaging lens focused on the background, I – the image plane, coplanar with the recording sensor. The full line indicates the light ray during the imaging of the reference image, while the dashed line illustrates the deflection of the ray in the test section and shows the ray position during the measurement image.
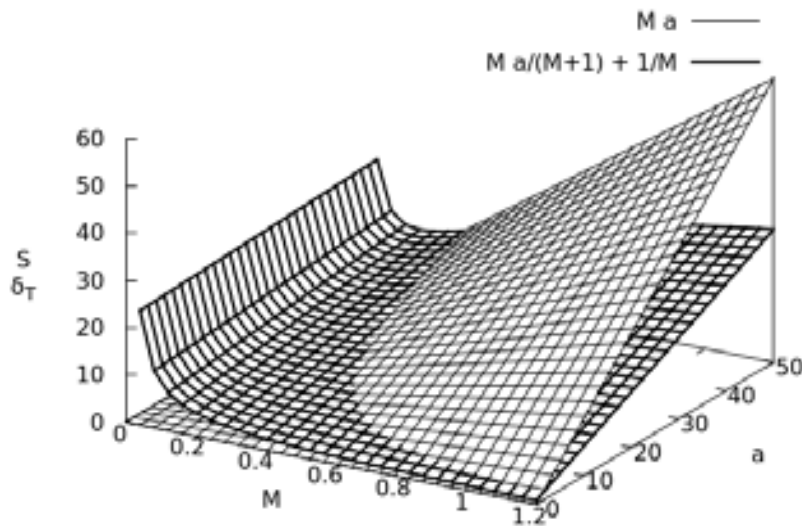

Figure 2. Surface plot of the sensitivity S (thin line, Eq. 6) and uncertainty δt (thick line, Eq. 7) of a BOS system for unit values of $f_\#$ (f-number of the lens) and Δpx (linear dimension of the pixel size). For small magnifications, uncertainty plays the determining role in adjusting the system, while for large magnifications, the system can be made quite sensitive. In practice, $f_\#$ is 5.6-32, while Δpx≈10 μm.

Gaussian interpolation. Interrogation windows usually are smaller than 1/10th of the overall image size and have at least three - four dots.

BOS is a line-of-sight integrating technique that gives the 2D projection of the density field. Its spatial and temporal resolutions depend on the optical setup and instruments used, while its sensitivity and accuracy depend - in addition to the above, - on the density gradients in the flow that is being imaged. Determination of temporal resolution of BOS is pretty easy, because it depends on the camera's exposure times. Spatial resolution, on the other hand, requires more careful analysis. Referring to Fig. 1, the smallest detectable dot shift in the image plane is dy_i, in the best case scenario equal to 0.1 px, which physically can be a fraction of a micrometer. The apparent background dot shift, defining the spatial resolution of the system, is the product of this value to the magnification of the system $M=s_o/s_i$,

$$dy_o = M\, dy_i = M\, a\, \varepsilon \quad , \tag{5}$$

The sensitivity S of a BOS setup, defined as the smallest detectable angle of deflection ε, in paraxial approximation with $s_o \gg w$, is expressed as

$$S = M\, a \quad . \tag{6}$$

Thus, the sensitivity increases by having an optical system with large magnification, achieved by using longer focal length lenses on cameras with high pixel count, as well as by setting the test section closer to the lens and the background further from it, i.e adjusting for big numerical value for a and small for d. But, since the lens is focused on the background, distance d between the test section and the lens is limited by the blur. The blur is quantified as the increase of the dot area in the image plane and can be neglected only if the blurred dot size is much smaller than the interrogation window during image evaluation process. Combination of the blur diameter and the interrogation window size defines the measurement uncertainty δ_t. Since the imaging sensor is made of a rectangular grid of pixels, each integrating the light acquired from the incident cone, a point from the background is imaged into an area corresponding to the size of the pixel Δ_{px}. Thus, the image gives a discretized picture of the field of view, a feature that provides the lower limit for the spatial resolution of the BOS system. Numerically, this value is

$$\delta_t = \frac{M}{M+1}\frac{a}{f_\#} + \frac{\Delta_{px}}{M} \quad , \tag{7}$$

where $f_\#$ is the f-number of the lens. Figure 2 shows the plot of the sensitivity S and uncertainty δ_t as functions of magnification M and distance background-flow field a for unit values of $f_\#$ and Δ_{px}.

Image quality and instrumentation

Image quality characterizes the output achieved by the image recording system (the combination of the camera and the lightning), compared to an ideal image, usually produced numerically on computer. Determination of image quality is largely a subjective matter, but it can be judged based on several general factors, such as noise, dynamic range, sharpness, and contrast and brightness ranges. BOS images present an easier task for image quality determination, because these images are random dots scattered over the field of view; hence, the structural similarities of the compared images do not play a crucial role for image quality determination. In fact, their role becomes the most important, once the recording system is decided, and are evaluated by cross-correlation.

The speed with which a fluid flows determines the shutter speed (exposure time) that the camera needs to operate with, and this proves to be one of the most demanding factors in choosing an image sensor. Shock waves in a shock tube, for example, can be imaged only with scientific grade high-speed cameras, such as Imacon DSR200 or Shimadzu HPV-1, which are capable of imaging at times shorter than 1 μs. Slow flows that can reach a pseudosteady state, such as slow cooling by natural convection, can be imaged with standard DSLR cameras. In these later cases, exposure time is not a limiting factor, because it can be large enough to reach an average value of temperature reading smaller than the measurement uncertainty, but still be orders of magnitude smaller than the temperature measurement steps. Thus, one would be free to choose a camera with a high pixel count or a large sensor size, so that the image detail is satisfactory for precise measurements. Images shown in Fig. 3 are from both types of high speed cameras and show a detail of the same background imaged through the test section of a shock tube. If one considers the sensitivity of a BOS setup based on the geometry of the layout and the size of the image sensor, Imacon camera would be preferable to Shimadzu, for two reasons: larger pixel

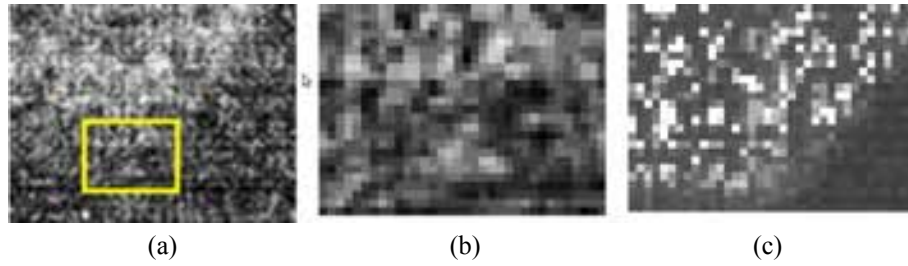(a)   (b)   (c)

Figure 3. Images (a) and (b) – the latter being the framed part of the former, - are taken with Imacon DSR200 camera, and (c) with Shimadzu HPV-1. Images (a) and (c) show the same field of view, while (b) and (c) have the same pixel count.

count (1200 × 980 pixels for Imacon vs. 312 × 260 pixels for Shimadzu), and smaller pixel size (≈ 10 μm vs. ≈ 60μm). But, despite the facts that the shown field of view is the same and that the images were taken with the same lens as well as under the same illumination, obtained images are quite different, which fundamentally comes about due to the different quantum efficiencies of the respective image sensors. A dramatic outcome of this difference is that the direct (without any processing) evaluation with cross-correlation of images captured by Imacon camera could not give any meaningful results, while images captured by Shimadzu did, as illustrated later. The difference can be explained through different response to luminance of the image sensors and the contrast values of the output file. Both cameras have a sensor with 10 bit dynamic range and give comparable dark images, but the histogram of the measurement images, shows that the Shimadzu camera produces a better contrast.

To quantify the quality of the images obtained by these cameras, we calculated the modified universal image quality index Q', as proposed by Wang and Bovik [9]. As it is well known, an image is a vector or grayscale values x_i, therefore we can determine image's average $<x>$ and standard deviation σ_x. If x is the measurement image (the image for which the quality index is being determined) and y is the ideal reference image (the background produced on computer), then the original definition of universal image quality index Q is given by

$$Q = \frac{\sigma_{xy}}{\sigma_x \sigma_y} \frac{2\bar{x}\bar{y}}{\bar{x}^2 \bar{y}^2} \frac{2\sigma_x \sigma_y}{\sigma_x^2 + \sigma_y^2} \quad , \tag{8}$$

where

$$\sigma_{xy} = \Sigma \frac{(x_i - \bar{x})(y_i - \bar{y})}{N_{px} - 1} \quad . \tag{9}$$

The universal image quality index Q is made of three terms: the first one corresponds to the correlation between images x and y, the second term gives the response to luminance, and the third term describes the contrast. The closer the image x is to the ideal y, the closer is the value of Q to 1, for each individual term, while complete discrepancy would give $Q = -1$. Since the background image is a high frequency random distribution of dots, the first term for all images is very close to 0, and the image quality index can be modified to take into account only the second and the third terms, namely

$$Q' = Q_L Q_C = \frac{2\bar{x}\bar{y}}{\bar{x}^2 \bar{y}^2} \frac{2\sigma_x \sigma_y}{\sigma_x^2 + \sigma_y^2} \quad , \tag{10}$$

where Q_L and Q_C are the values for luminance and contrast, respectively. These values for the employed cameras in the experiments described below, are given in Table 1.

Table 1. Luminance and contrast image quality indices for high speed cameras (Imacon, Shimadzu) and standard DSLR cameras (Pentax K-5).

	QL	QC
Imacon DSR200	0.18	0.07
Shimadzu HPV-1	0.62	0.54
Pentax K-5	0.99	0.71

The imaging of high speed flows, such as shock waves, is constrained by the requirement of instrumentation with superior time response, such as high speed cameras. This has the drawback that the quality of the images obtained is not so high. The imaging of natural convection was done with a Pentax K-5 DSRL camera, and, as it is expected, it performs much better, demonstrated by the high values of QL and QC. Therefore, a preliminary investigation of the cameras used for BOS can be done by determining Q' (specifically, QL and QC): a fixed value that would qualify an image as useful or not-useful for image analysis is impossible to be given, but a reasonable judgment can be given based on how close the luminance and contrast terms of Q are to 1, and the main factor effecting low image quality (luminance or contrast) can be diagnosed.

Image evaluation by cross-correlation

In quantitative evaluation of flow visualization, the measurement of several parameters is quite straight forward, e. g. a and d, from Fig. 1. Since the required end result is density field, this can be achieved by determining dyi, which, in turn, is done only through image evaluation. Several techniques for image evaluation exist, but the majority of BOS studies rely on cross-correlation, which consists on defining subsets of the measurement image, representing the interrogation window (IW), and comparing their intensity fields to all equal in size subsets in the reference image. The output of cross-correlation for a prearranged IW is a vector $\mathbf{d}$, with magnitude and direction corresponding to the shift of the correlation peak. Applying a three point Gaussian peak detection scheme, this vector can be determined with an accuracy of better than 0.1 pixel. The magnitude of $\mathbf{d}$ is the amount of pixel shift of a background pattern due to light deflection, dyi. The number of independent vectors, thus, the evaluated spatial resolution, depends on the size of IW.

There are several sources of uncertainties in flow visualization measurements, which can be divided into two main categories:
1.   those due to specifications of instruments, and
2.   those that arise from image analysis.
In practice, the dominant type of uncertainties belong to the second type, because the arrangement of the instrumentation in a BOS setup allows for adjustments of sensitivity and spatial resolution to higher levels than those achieved by image analysis.

Displacement vector obtained by image analysis is influenced by IW, background pattern size, spatial frequency of pattern structure, and gradients within IW, which are responsible for error sources such as peak locking, pattern smoothening, etc. The effect of each factor is investigated by applying a step function to a synthetic image, and evaluated with the same procedure as evaluated BOS images. Half of a 128 x 128 pixels synthetically generated reference image of randomly distributed dots is shifted for a number of pixels, giving the simulated measurement image. In other words, the image is sliced in two equal parts, with the right side (pixels in horizontal locations 64 and higher) slided for one or more pixels to the left. Then, the simulated reference and measurement images are cross-correlated by using the PIV plugin for ImageJ [10] and [11]. The effects were observed by the changes on the step function response width (SFRW), as defined in [12].

Image evaluation with different IW shows that the smaller the IW the closer the evaluated jump is to the real step function, as shown in Fig. 4. In this investigation, the simulated images had a dot the size of a pixel, and the image coverage by dots was 50%. The spread and gradual increase of the discontinuity means that there can not be an independent shift vector within the length it takes the evaluated pixel shift value to jump. Therefore, the evaluated spatial resolution for IW=32 is about 36 px, and for IW=8 it is about 10 px. Multipass evaluation with successively smaller IW did not show any improvement in the evaluation of the jump, while it gave erroneous (fluctuating) values for the amount of the pixel shift.

The preparation of the background involves determination of the dot size, frequency (in terms of the number of dots in the field of view), and coverage. While in experiments with natural backgrounds the experimenter has no control over the background features, in experiments under laboratory conditions (e. g. shock tube or wind tunnel experiments), the experimenter can prepare a background that optimizes the measurement based on the camera specifics and the field of view. Figure 5 shows the effect of the dot size in the resolution, where dot sizes δ_d equal to one and four pixels are compared after images are treated by a one pixel step function. The evaluation does not show any large effect on the resolution, but it does give different values for the pixel shift. For the case with $\delta_d = 4$ px, the effective shift of the image corresponds to a quarter of a dot, hence some pixels
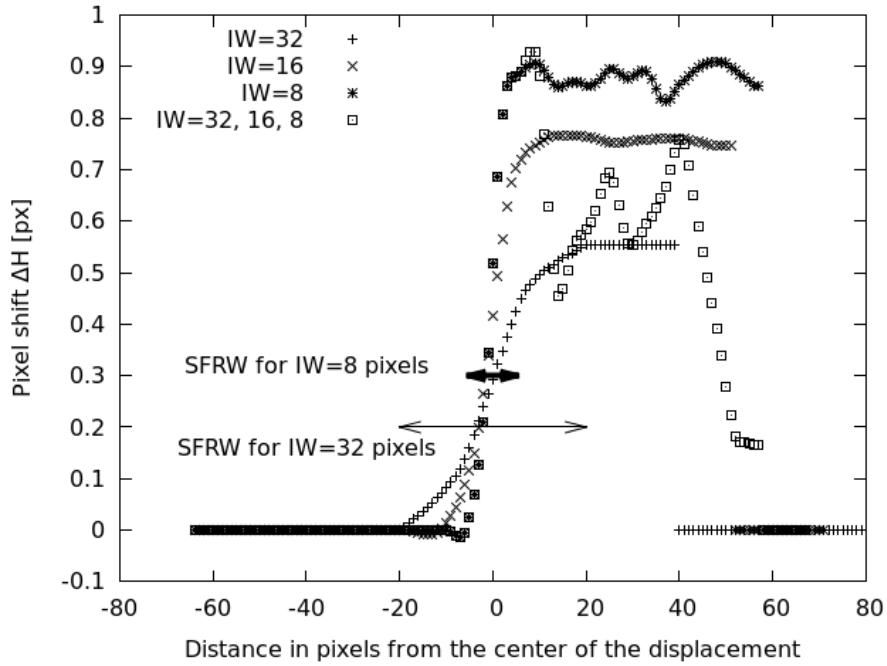
Figure 4. The resolution of the evaluation of a one pixel shift as a function of different sizes of IW. The case for IW = 32, 16, 8 pixels, shows the multipass evaluation. SFRW for extreme cases is also displayed.
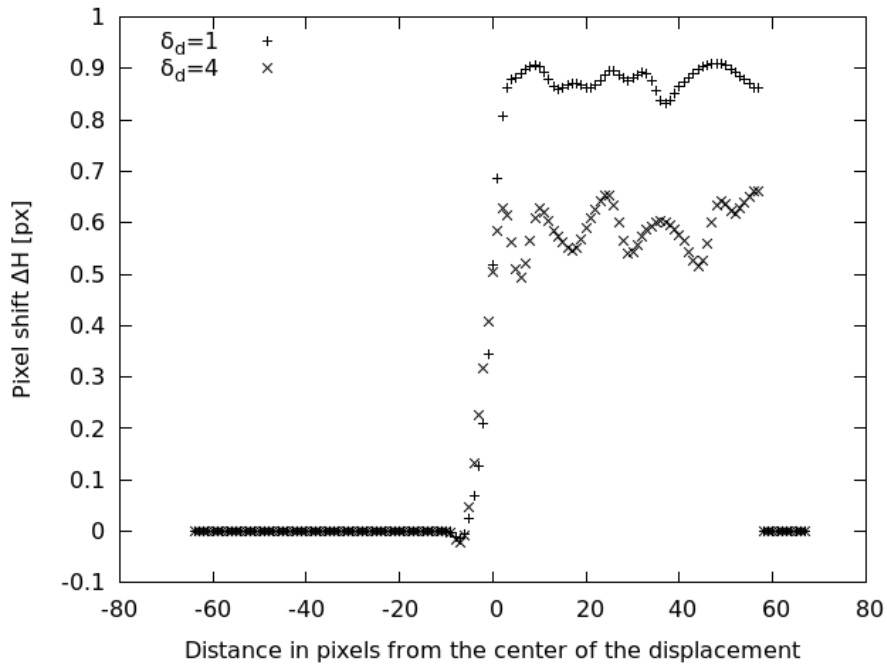

Figure 5. The effect of the dot size on pixel shift. Images with a dot size of one pixel and four pixels are shifted for a pixel and cross-correlated. The SFRW is virtually the same for both cases, but the S/N ratio and the pixel shift is different.
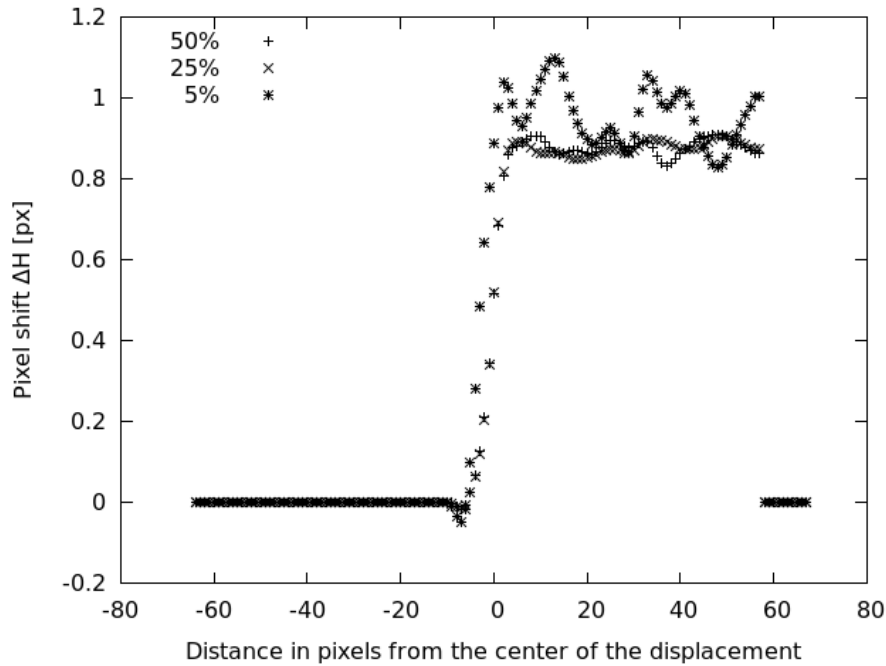
Figure 6. The effect of the coverage of the background by dots. Images covered with black dots of one pixel size are shifted for a pixel and cross-correlated. The SFRW for the images with 25% and 50% coverage are the same, while that for the image with 5% coverage is slightly (but noticeably) larger.
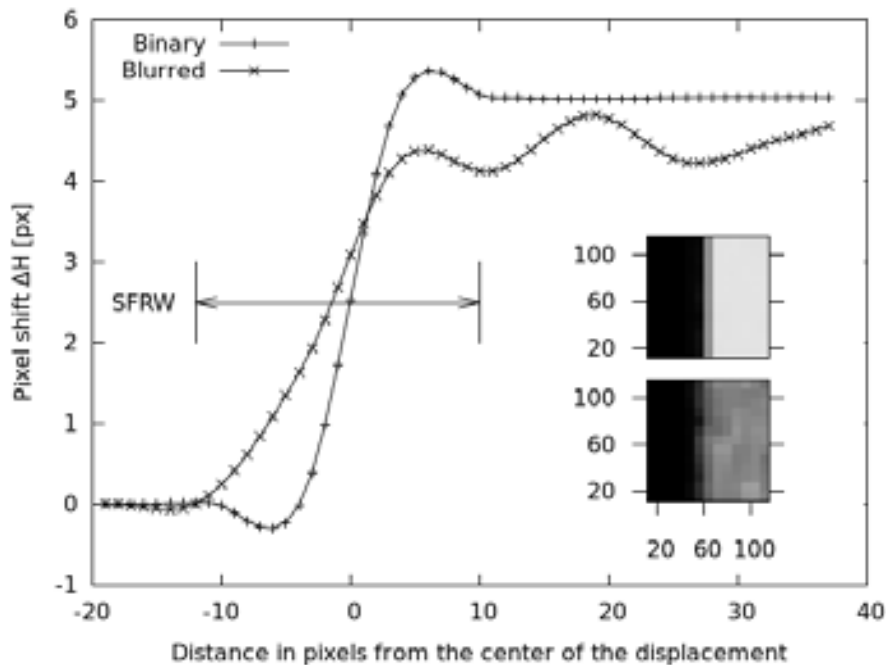
Figure 7. Pixel shift evaluation by cross-correlation (IW=16 pixels) of binary (inset, up) and Gaussian blurred (inset, down) synthetic images with dots of one pixel, shifted for 5 pixels. Tics in insets are image pixels. Again, SFRW is virtually the same for both cases, but the S/N changes for the worst in the case of blurred images.

are not recorded as shifted. This situation appears in synthetic image evaluations, because these images have a well defined binary structure. In experiments, an image of a binary background results in a grayscale image with spread histogram peaks around the binary values. This leads to more accurate results during evaluation. Figure 6 shows the effect of dot density, which is defined as the number of dots per unit area of the field of view projected in the total image area. Maximal dot density, 50%, means that half of the image is covered by dots, and the minimal density simulated (5% coverage with dots) is mainly a white featureless background. As previously, the image is treated to a one pixel shift and evaluated with IW=8 px. Virtually, there is no difference in evaluating images with dot density of higher than 20-25%, but pixel shift evaluation artifacts start showing for images with lower number of dots. This result is in agreement with the previously published requirement that an IW should have at least four to five dots, each covering 2 pixels [13]. The effect of the blur is investigated by treating the synthetic measurement image with a Gaussian blur of radius of 2 pixels. In this case, the image was shifted for five pixels and the interrogation window was 16 pixels. The effect of the blurring in SFRW is negligible, but this is not so for the determination of the amount of pixel shift. The blurring of the image has the effect of reducing this value for about 10% and introducing fluctuations in its behaviour, thus yielding a lower signal-to-noise (S/N) ratio. This effect comes about because, as compared to the binary image, the blurred image is populated by all possible grayscale values and pattern's spatial frequency is not conserved.

Experimental examples

Two examples of application of BOS to experiments will be given: one for the reflection of a shock wave from an inclined plane (wedge) in a shock tube, and one for the determination of the temperature field during the natural convective cooling.

A BOS experiment for the investigation of shock diffraction and reflection from a wedge (inclined plane) in a shock tube was conduced, with the aim of testing BOS capabilities, because the passage of a planar shock wave is a well studied and documented phenomenon, thus it can serve as a benchmark test. A photo of the experimental setup is shown in Fig. 8. The shock tube was run with air at $p_1 = 0.10$ MPa as the driven gas and nitrogen N_2 at $p_4 = 0.35$ MPa as the driver gas. The model was a stainless steel wedge with the base attached to the top of the shock tube, effectively creating an inclined plane with inclination of 49°. Shock propagation was monitored by three Kistler 603B pressure transducers (only two shown in the figure, the third one being outside of the frame), which also sent the triggering signal for the image recording system. Timing of the experiment was controlled by a combination of an oscilloscope and a pulsed delay generator. Shock Mach number for all experiments was 1.3, and since the effective field of view was 220 mm x 150 mm, a high speed camera was needed for freezing shock's motion. For this reason, two types of cameras were used:

(i) Shimadzu HPV-1 camera with 312 x 260 pixel count and time resolution of 0.5 μs, capable of taking 100 images with a maximal frame rate of 1 Mfps. The camera sensor is of the IS-CCD type, with a linear dimension of pixel's light collecting area of about 50 μm.

(ii) Imacon DRS 200 camera with 1200 x 980 pixel count and linear dimension of pixel size approximately 6.5 μm. This camera has 7 channels, each being capable of taking two images with the fastest interframe of 1 μs, thus resulting in a total of 14 images. Since all 7 channels are independent, their respective interframes can be adjusted freely. The minimal exposure time of the camera is 5 ns, which is faster than the required and used 1 μs time resolution.

The main differences between these two cameras come from their pixel count, with Imacon having a 10x better characteristic, and the pixel area, with the Shimadzu one having a 10x larger area. The background used in the shock tube experiments was a white sheet with randomly distributed square dots of 1 mm. This background was illuminated by a xenon flashlamp that has pulse duration longer than 1 ms. Although in both experiments the background was a binary image, that is with only white and black areas, the recorded image was an 8 bit grayscale digital file.

The steady temperature field was achieved by a linear tube radiative heater with diameter of 10 mm, length of 150 mm (corresponding to w in Fig. 1), and power of 100 W, placed perpendicularly to the background. Since the field did not change with time, the requirements on the temporal resolution were minimal, so a standard DSLR (Pentax K-5) camera was used. This camera has a sensor of 23.6 mm x 15.8 mm and pixel count of 4928 x 3264 pixels, hence a linear pixel size of ~ 5 μm. The objective lens had a focal length of 300 mm and experiments were done with aperture of f/32. Small apertures were used in order to obtain longer depths of field. Illumination was achieved by back-lighting the printed background with a xenon flashlamp, and the camera exposure times were from 1/180 s. Several types of backgrounds were generated by printing a random dot
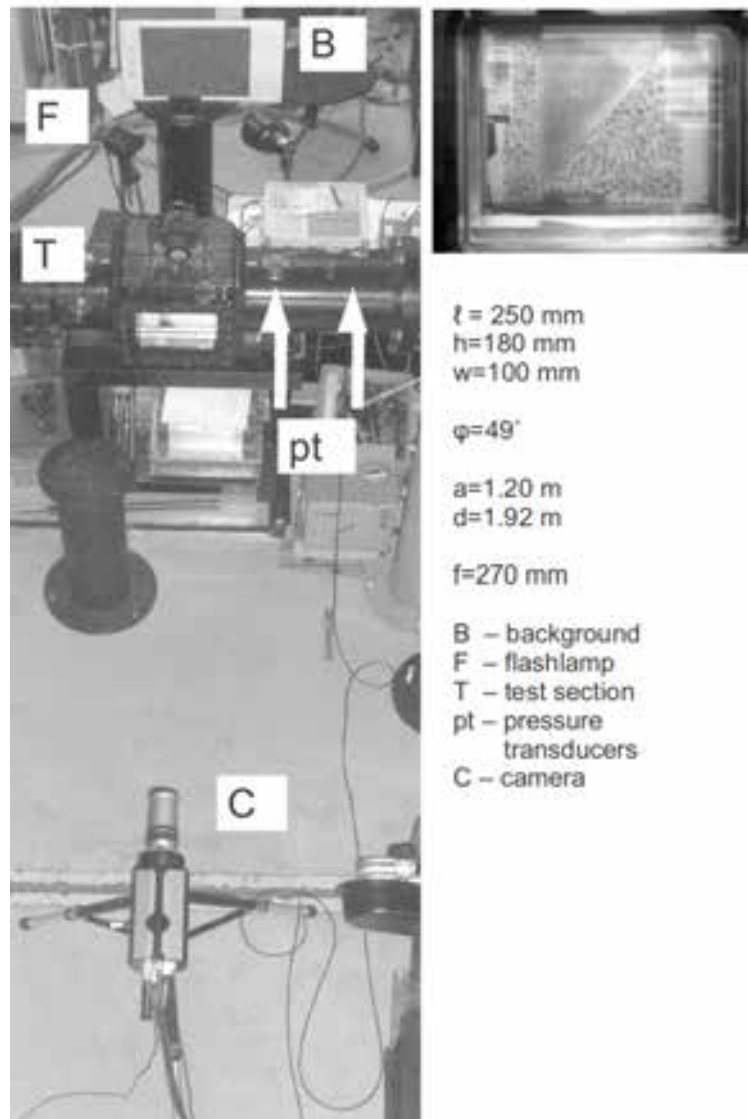
Figure 8. A photo of the experimental setup for the shock reflection experiment, diagnosed by BOS. The inset shows the view of the background from the perspective of the camera C.

pattern in an A4 paper. Setup distances were adjusted to achieve an optical magnification of the system $M =0.1$, with 30 px imaging 1 mm of the field of view. The temperature was simultaneously monitored by 8 thermocouples with temperature resolution of 0.1 K.

The results of these measurements are shown in Figs. 9 and 10. Figure 9 shows the magnitude map of the pixel displacement vector shift. The interrogation window for this evaluation was 8 px, thus giving a resolution of 10 px. Since the optical magnification was 0.1, the measurement uncertainty then is 5 mm. As already stated when the role of the interrogation window was discussed, its large results in the spill of the pixel shifts inside the wedge. Nevertheless, some clear features of the phenomena are observed, such as the shock wave and its reflection, and probably the acoustic region after the reflection.

While these results for density gradient measurement behind a shock wave in a shock tube are very coarse, mainly due to the low pixel count of the high speed camera, the results of BOS applied to natural convection show fine detail, as given in the inset of Fig. 10. Comparison of temperature evolution by BOS, thermocouple
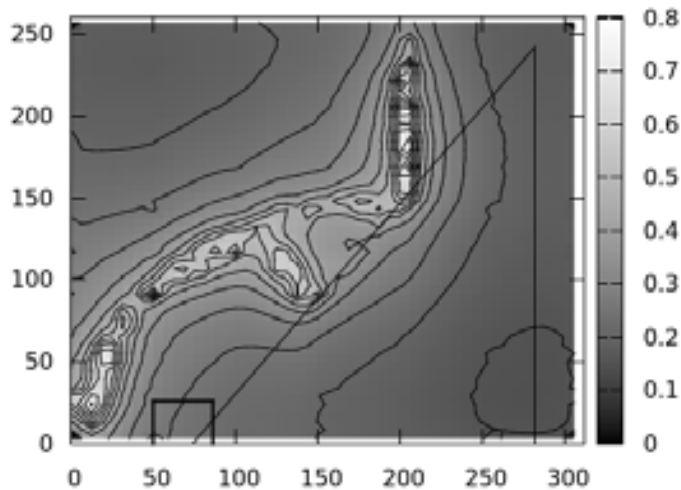
Figure 9. Background oriented schlieren result for the shck reflection from a wedge (black full lines), shown as a magnitude map of vector shift, with pixel locations in coordinates and pixel shift amount in the magnitude bar. The small rectangle starting at pixel (50,0) is the part of the image given in Fig. 3.
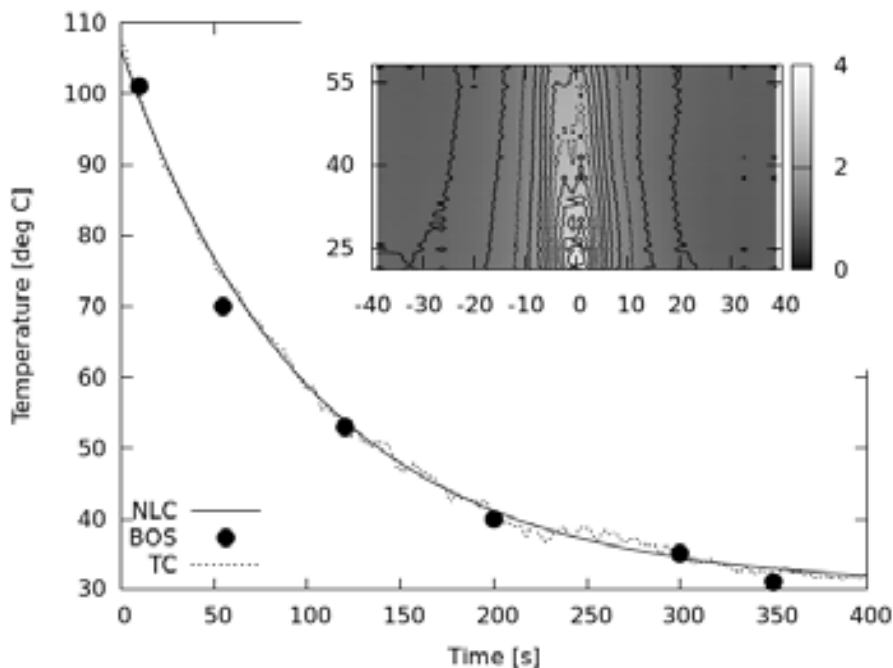
Figure 10. Quantitative BOS result for cooling by natural convection, and the comparison of BOS data to thermocouple (TC) readings and Newton's law of cooling (NLC). Coordinates in the inset give the distance from the center of the heat source, in mm, and the magnitude bar gives the pixel shift.

readings, and according to Newton's law of cooling shows a satisfactory agreement. BOS imaging was done with an extra large pixel count camera (16 megapixels), which had several benefits: a dot covered 8 x 8 px, the dots had five distinct grayscale values, IW was 16 x 16 px. For the sake of computational speed, the image was reduced in size 4 times per direction, giving two pixels per dot. The dot density was 50% and the magnification of the setup was 0.15, with 30 px covering 1 mm of the field of view. Hence, the measurement uncertainty of the BOS technique was estimated to be similar to that of the thermocouples (0.1 K).

Conclusions

The development of background oriented schlieren (BOS) technique is advanced by assessing several factors that influence the extraction of quantitative data, be it in the experimental or image evaluation stage. Introduction of the image quality index is beneficial for simple determination of the instrumentation that would yield desirable and useful images, or for possible diagnostics of the faulty arrangements (illumination or contrast). Investigation of the geometrical arrangement of the instruments used for BOS visualization reveal that arbitrary sensitivity and resolution can be achieved, but, these specifications, though, are later deteriorated by image evaluation. Uncertainties related to the point of measurement are influenced by the interrogation window, defining the spatial resolution of the measurement, while image blurring influences the determination of the pixel shift. BOS technique was applied to two types of flows, with variable success.

Acknoledgment

References

[1] G. E. A. Meier: Computerized background-oriented schlieren. *Exp. Fluids*, Vol. 33, pp. 181-187, 2002.

[2] H. Richard and M. Raffel: Principle and applications of the background oriented schlieren (BOS) method.*Meas. Sci. Technol.*, Vol. 12, pp. 1576-1585, 2001.

[3] E. Goldhahn and J. Seume: The background oriented schlieren technique: sensitivity, accuracy, resolution and application to a three-dimensional density field. *Exp. Fluids*, Vol. 43, pp. 241-249, 2007.

[4] S. Tavoularis. *Measurements in Fluid Mechanics*. Cambridge University Press, p. 221, 2005.

[5] M. J. Hargather and G. S. Settles: Natural-background-oriented schlieren imaging. *Exp. Fluids*, Vol. 48, pp. 59-68, 2010.

[6] S. B. Dalziel, G. O. Hughes and B. R. Sutherland: Whole-field density measurement by 'synthetic schlieren'.*Exp. Fluids*, Vol. 28, pp. 322-335, 2000.

[7] O. A. Yevtikhiyeva, N. M. Skornyakova and A. V. Udalov: An investigation of the error of the background schlieren method. *Measurement Techniques*, Vol. 52, pp. 1300-1305, 2009.

[8] N. A. Vinnichenko, I. A. Znamenskaya, F. N. Glazyrin and A. V. Udarov: Study of background oriented schlieren method accuracy by means of synthetic images analysis. *Proc.* 22*nd Inter. Symp. Transport Phenomena.* Delft, The Netherlands, 2011.

[9] Z. Wang and A. C. Bovik: A universal image quality index. *IEEE Signal Proc. Lett.* , Vol. 9, pp. 81–84, 2002.

[10] Q. Tseng, E. Duchemin-Pelletier, A. Deshiere, M. Balland, H. Guillou, O. Filhol, and M. Thry: Spatial organization of the extracellular matrix regulates cell-cell junction positioning. *PNAS* Vol. 109, pp. 1506–1511, 2012.

[11] M. D. Abramoff, P. J. Magalhaes and S. J. Ram: Image Processing with ImageJ. *Biophotonics International* Vol. 11, pp. 36–42, 2004.

[12] C. J. Kähler, S. Scharnowski, and C. Cierpka: On the resolution limit of digital particle a image velocimetry. *Exp. Fluids* Vol. 52, pp. 1629–1639, 2012.

[13] M. Raffel, C. E. Willert, and J. Kompenhans: *Particle image velocimetry: a practical guide.* Springer, p. 167, 1998.

Dynamic Wind-Tunnel Testing of a Delta Wing Using a Multi-Degree-of-Freedom Robotic Manipulator

*Tatsuya HARA,
*Daiju NUMATA
*Keisuke ASAI
*Takafumi ITO
*Xin JIANG

*Graduate School of Engineering, Tohoku University
6-6-01 Aramaki-Aza-Aoba Aoba-ku, Sendai
980-8579
Japan
hara.tatuya@aero.mech.tohoku.ac.jp

Abstract

The purpose of this study is to measure the unsteady force acting on a slender delta wing in two degree-of-freedom (DoF) motion. A serial-type robot manipulator was used to oscillate the model in two modes; one is roll-yaw coupled lateral motion and the other is pitch-heave coupled longitudinal motion. Unsteady forces and moments were measured by a six-component balance and the effects of oscillation frequency and amplitude were evaluated. In the 2-DoF roll-yaw coupled mode, hysteresis loop was noted at high angles of attack and changes of rolling moment are delayed as compared with the 1-DoF case. In the pitch-heave coupled experiment, it was found that the effect of pitch rate on unsteady force is negligible at the frequency and amplitude ranges covered in this experiment.

Key words: Dynamic Wind-Tunnel Testing, Multi-Degree-of-Freedom, Robotic Manipulator, Delta Wing, Vortex Breakdown

Introduction

The conventional linear theory based on stability derivatives might not be valid for the flight region at high angles of attack where the flow on the vehicle is highly separated and exhibits nonlinear (and/or unsteady) aerodynamic characteristics[1-4]. In addition, in such extreme flight conditions, the motion of aircraft is inherently multi-directional so each degree-of-freedom cannot be treated separately. This means that dynamics of those vehicles has to be treated as multi-degree-of-freedom problems such as roll-yaw and pitch-heave combined motions.

Recently, the studies on multiple-degrees of freedom motion has been becoming possible using robotic devices like the link mechanism at Tottori University [5] and the Model Positioning Mechanism (MPM) at DLR [6].

In this study, a multi-degree-of-freedom dynamic wind-tunnel testing has been conducted to evaluate dynamic behaviors of a delta wing model at high angles of attack [7,8]. To accomplish arbitrary multi-DOF model motion, a serial-type robotic manipulator has been introduced. A slender delta wing model was tested in two different 2-DoF modes: one is roll-yaw-coupled lateral motion and the other is pitch-heave coupled longitudinal motion.

In this experiment, unsteady force and moment were measured by a six-component balance and effects of oscillation frequency and amplitude were studied. From the results, the relationship between high-angle of attack characteristics of the slender delta wing and unsteady flow field in 2-DoF motions is discussed.

Description of Experiment

Robotic Manipulator

An intelligent serial-type robot manipulator (PA-10, Mitsubishi Heavy Industries, Ltd.) was used (Fig. 1). This manipulator consists of seven actuators that can be operated independently. Maximum angular speed is 2π rad/sec for a motor at the tip and 1 rad/sec for the other motors.
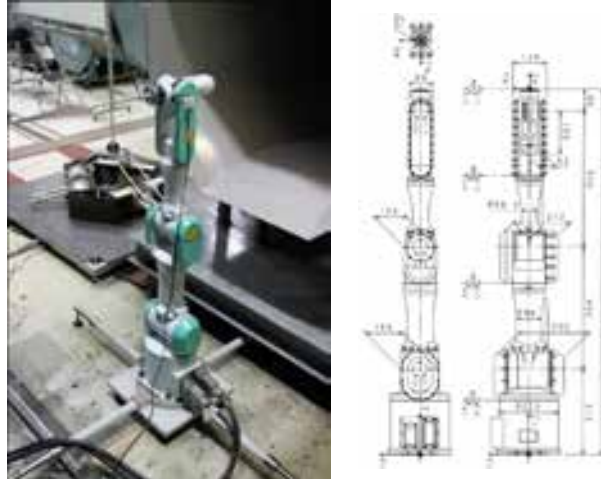

Fig. 1 Robotic manipulator

Test Model

The model used in this study is a simple flat-plate model with the sweep angle of 80 degrees. The length (*c*) is 300 mm and the thickness (*h*) is 2 mm. The leading-edge is sharp and truncated at 45 deg. The model was mounted on the tip of the manipulator. (Fig. 2)

| (a) roll and yaw | (b) pitch and heave |
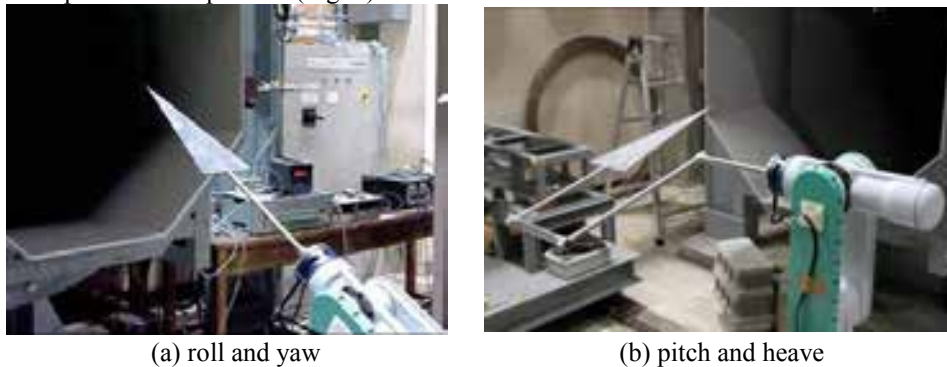
Fig. 2 Set-up for 2-DOF experiments

Wind Tunnel

Experiments were conducted in the Low-Turbulence Wind Tunnel at Institute of Fluid Science (IFS), Tohoku University. This is a closed circuit wind-tunnel with the open-type test section with the cross distance of 0.8 m. Additionally, flow visualization tests on the delta wing were conducted in the IFS's blown-type low-speed tunnel at IFS having a nozzle with 0.8-m square cross section.

Test condition

In the roll-yaw experiment, the amplitude of rolling motion has been changed from 5 to 30 degrees while the yawing amplitude has been changed from 2.5 to 10 degrees. The oscillating frequency has been changed from zero to 1 Hz. This corresponds to the non-dimensional frequency ($k=fc/U_\infty$) range up to 0.01 for the free-

stream velocity of 30 m/sec and the model length c of 0.3 m. A phase angle between the roll and yaw motion was set at π/2 to simulate Dutch-roll like motion (Fig. 3). The angle of attack was changed from zero to 40 deg.

The pitch-heave experiment was conducted at the center angles of attack α_0 at 30 and 38 deg. The amplitude of effective angle of attack α_{eff} and that of pitch rate q were fixed at 3 deg. The oscillating frequency was set either at 0.6 and 0.9 Hz that correspond to the non-dimensional frequency (k=fc/U_∞) of 0.024 and 0.036, respectively, for the free-stream velocity   of 7.5 m/sec and the model length c of 0.3 m. The phase angle between the pitch and heave motions was set at π/2 to produce pure pitching motion (Fig. 4).

Aerodynamic forces and moments were measured using a six-component load cell (IFS-90M31A50-150, Nitta Corp.) installed on the tip of the manipulator. The tare due to inertia of the model was measured under no-wind condition and subtracted from the measurement under wind-on condition to extract pure aerodynamic effects. To reduce the noise, the same measurement was repeated over 40 times. The obtained data were then ensemble averaged and filtered by a low-pass filter with the cut-off frequency at 15 Hz for roll-yaw experiment and at 3 Hz for pitch-heave experiment.

In the flow visualization experiment, the cross section of the leading-edge separation vortices was illuminated by a thin sheet of laser light produced by a 5 W Argon laser. A smoke generator was used to produce smoke. The laser sheet was set to illuminate the model at x/c = 0.5 and 1.0 and images of vortex were recorded by a digital camera (IOS 7D, Canon Corp.) at 30 fps. In this experiment, the free-stream velocity was set at 2 m/s to prevent a diffusion of the smoke. It is noted that the vortex breakdown over slender, sharp-edged, delta wings are insensitive to Reynolds number [9].
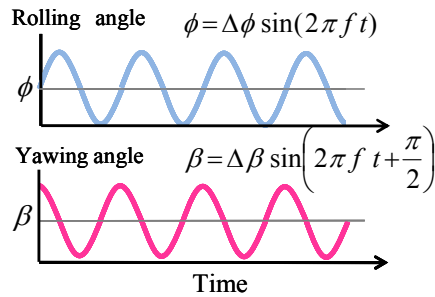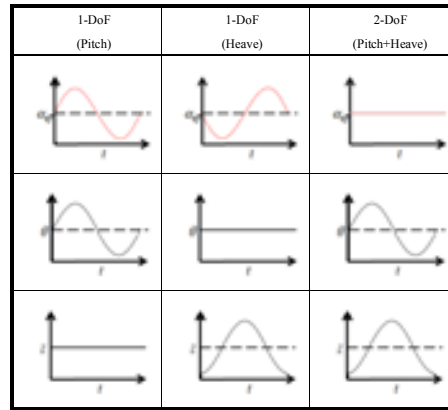

Fig. 3 Roll-yaw coupled mode

Fig. 4 Pitch-heave coupled mode

Results and Discussion

Roll and yaw coupled motion

Aerodynamic behavior of delta wings are determined by behavior of the leading-edge vortices [1, 10-13]. Figure 5 shows the observed boundaries of vortex symmetry/ asymmetry and burst for a delta wing [10]. Two specific boundaries are noted to distinguish vortex behaviors. These boundaries are determined by the effective angle of attack α_{eff} and the effective sweep angle Λ_{eff} given by the following equations;

$$\alpha_{eff} = \tan^{-1}(\tan\alpha\cos\phi)\cos\beta \qquad (1)$$

$$\Lambda_{eff} = 90 \pm \beta - (\theta \pm \tan^{-1}(\tan\alpha\sin\phi)) \qquad (2)$$

where ϕ is roll angle, β is side slip angle, and θ is pitch angle of the model.

Figure 6 shows the rolling moment for angles of attack from 15 to 40 deg. For comparison, the rolling moment in pure rolling motion (meaning 1-DOF motion) is shown as dashed line. As shown in Fig. 6, strong hysteretic characteristics appear at angles of attack higher than 35 degree.

Figure 7 shows a plot of roll damping coefficient given by

$$C_{\ell_p} = \frac{\partial C_\ell}{\partial \dfrac{pb}{2U_\infty}} = \frac{\partial C_\ell}{\partial p}\frac{2U_\infty}{b} \qquad (3)$$

As shown in Fig. 7, the rolling motion is damped as the roll angle approaches to maximum amplitude. This damping effect becomes much smaller in the 2-DOF case. In the 2-DoF cases, the rolling moment forms a counter-clockwise loop at low angles of attack that is attributed to the dihedral effects of sweep angle (stabilizing effect). At angles of attack higher than 35 deg, the rolling moment starts to form a clockwise loop in the range of small roll angle that will cause dynamic instability. In these conditions, energy is supplied from the free stream to the rolling wing.

The similar trend can be seen in Fig. 8 that shows the effects of yawing amplitude on rolling moment It is noted that the instability increases with increasing yawing amplitude.

Figure 9 shows the effects of roll amplitude on rolling moment. It is noted that there is no indication of unsteadiness for $\Delta\varphi$ =5 deg and 10 deg, suggesting that a quasi-steady aerodynamic model is effective for oscillations with small amplitudes. For larger amplitudes, however, unsteady and nonlinear aerodynamic effects become dominant.

Figure 10 shows time variation of C_{roll} over one oscillation cycle. Plots of C_{roll}-ϕ relationship are also shown for comparison purpose. It is seen that there is time lag between the 2-DoF and 1-DoF cases for the leading-edge separation vortices to follow the moving wing surface. It is noted that, at α = 35 degree, the onset of vortex breakdown is delayed by an effect of yawing motion. This observation is also supported by the flow visualization experiments (Fig. 11). In the case of 2-DoF motion, detachment of the leading-edge vortices is delayed on the wing moving upward while the breakdown of the leading-edge vortices is delayed on the wing moving downward. For the 1-DoF oscillation, it takes $\Delta t/T = 0.46$ for the vortex to recover from the breakdown. On the other hand, for the 2-DoF oscillation, it takes only $\Delta t/T = 0.35$. This means that the yawing motion has an effect to delay vortex breakdown and promote its recovery.

 Figure 12 shows the effects of DOF on the temporal locations of vortex breakdown and recovery in one oscillation cycle. It is noted that behaviors of the leading-edge vortices are about the same between the 1-DoF and 2-DoF cases, when expressed in terms of effective angle of attack α_{eff} and effective sweep angle Λ_{eff} (Eqs. 1 and 2). These results suggest that the criteria based on α_{eff} and Λ_{eff} are valid even when the model is moving in 2-DoF mode.
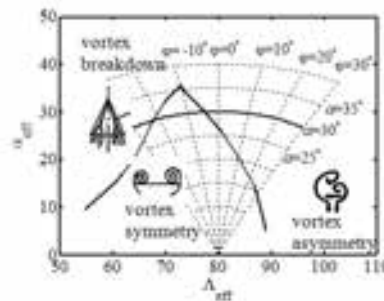

Fig. 5 Leading-edge vortex boundary for delta wings as a function of effective AoA and effective sweep angle
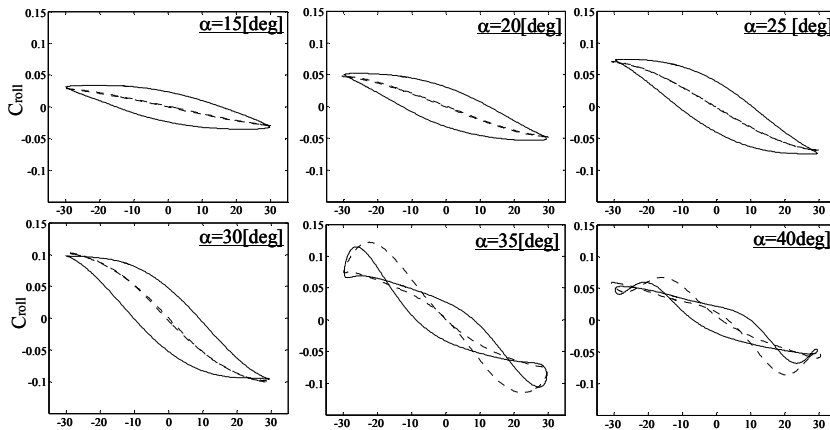

Fig. 6 Rolling moment in roll-yaw coupled motion for α from 15 to 40 deg
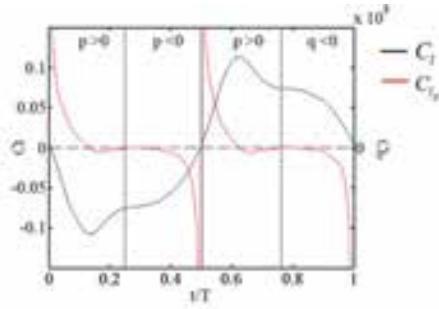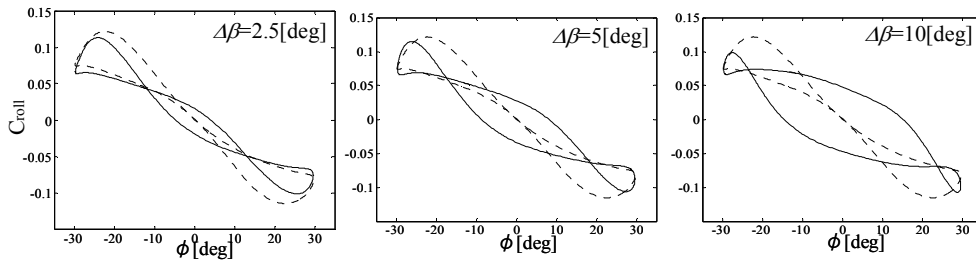
Fig. 7 Roll-dumpling coefficient

Fig. 8 Effects of yaw amplitude on rolling moment in roll-yaw coupled motion,
α = 35 deg, $\Delta\beta$ = 5 deg , k = 0.01 (f = 1 Hz), dashed lines indicate the data for $\Delta\beta$ = 0 deg.
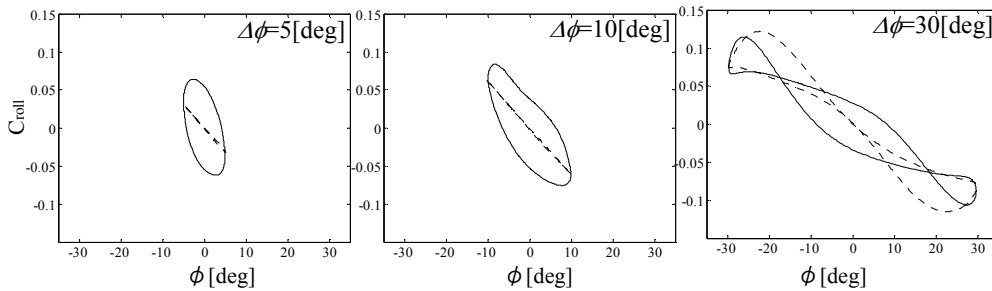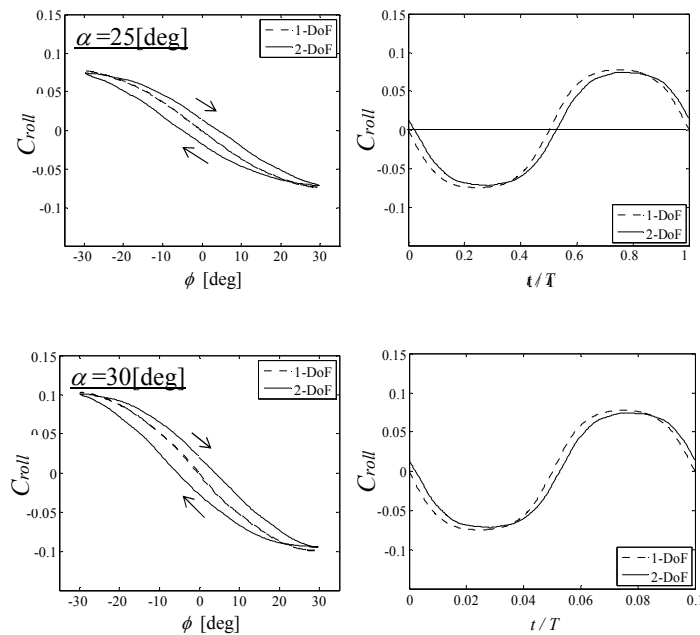

Fig. 9 Effects of roll amplitude on rolling moment in roll-yaw coupled motion,
α = 35 deg, $\Delta\varphi$ = 30 deg, k = 0.01 (f = 1 Hz), dashed lines indicate the data for $\Delta\beta$ = 0 deg.
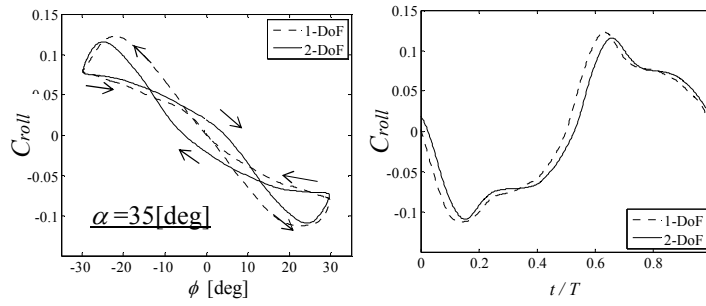

(continued)

Fig. 10 Comparison of rolling-moment in 1-DoF and 2-DoF cases for α from 25 to 35 deg, Δφ = 30 deg, k = 0.01 (f = 1 Hz), dashed lines indicate the data for 1-DoF.
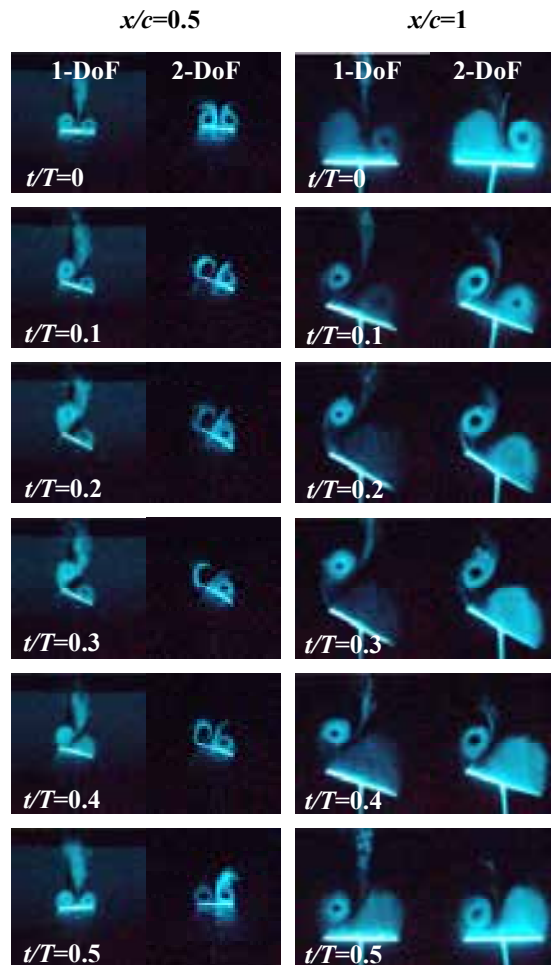
Fig. 11 Laser-light-sheet visualization of leading-edge vortices; a comparison between 1-DoF and 2-DoF cases
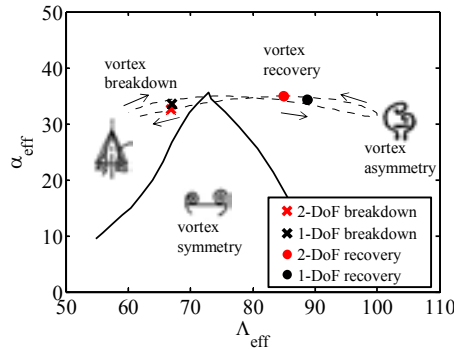
Fig. 12 Effect of yawing motion on breakdown and recovery of leading-edge vortices

Pitch and heave coupled motion

Unsteady delta-wing research has shown the normal force coefficients in pitching to overshoot or undershoot the static values. These unsteady phenomena are caused by the effect of pitch rate on breakdown of leading-edge vortices.

Figure 13 shows the static normal-force coefficients obtained when the model is pitched in the upward and downward directions. Hysteretic behavior is noted at angles of attack higher than 35 deg, suggesting an occurrence of vortex breakdown.

Considering dynamic pitching motion, the normal force coefficient acting on the model can be expressed by the following equation;

$$C_N = C_{N_0} + C_{N_\alpha}\alpha + C_{N_{\dot\alpha}}\dot\alpha + C_{N_q}q \tag{4}$$

In simple pitch oscillation ($\theta = \Delta\theta\sin(2\pi f \cdot t)$), both $\dot\alpha$ and pitch rate q are changed with time. On the other hand, in simple heaving motion ($z = \Delta z \cdot \sin(2\pi f \cdot t)$) with a fixed pitch angle, a pure effect of the effective angle of attack can be obtained. A pure effect of pitch rate can be obtained by conducting a pitch-heave coupled oscillation.

Figure 14 compares the dynamic normal coefficients for pitching, heaving, and 2-DoF coupled motions for non-dimensional frequency of 0.024. It is seen that, in the case of $\alpha_0 = 30$ deg, the dynamic data does not show any hysteretic behavior, meaning there is no unsteady effect. On the other hand, for $\alpha_0 = 38$ deg, dynamic hysteresis loop appears in pure pitching and heaving cases. Note here that hysteresis loop does not exist for 2-DoF tests, indicating that the effect of pitch rate on unsteady normal force is negligible at the frequency and amplitude range realized in this experiment. The same statement is valid for the case of $k = 0.036$.
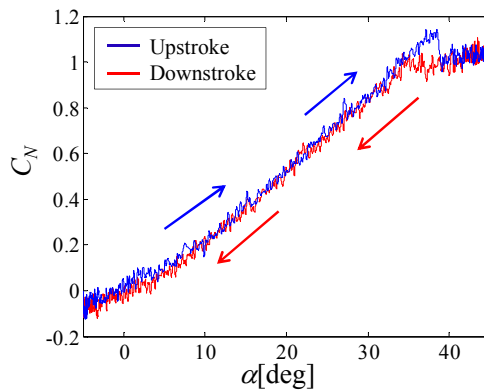

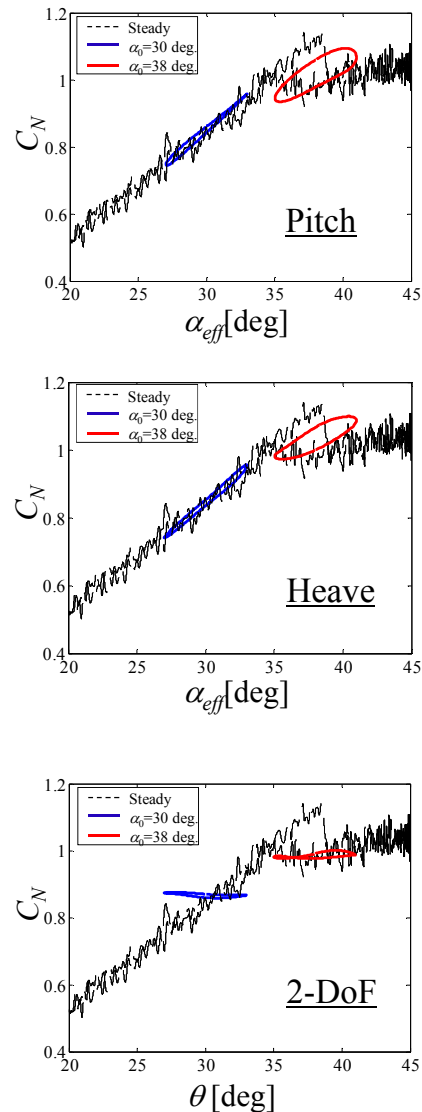**Fig. 13 Static normal force as a function of angle of attack**

Fig. 14 Static normal force as a function of angle of attack

Concluding Remarks

   In the present study, a slender delta wing model with sweep angle of 80 degree was tested in two different 2-DoF modes.

   From the results in the roll-yaw experiment, it was found that the yawing motion has an effect to delay an onset of vortex breakdown, resulting in the time lag in unsteady rolling moment. On the other hand, from the pitch-yaw experiment, it was found that the effect of pitch rate on unsteady normal force is negligible in the frequency and amplitude range covered in this experiment.

   To express behavior of a maneuvering delta wing at high angles of attack in more realistic manner, the unsteady effects have to be considered in modelling aerodynamic terms in the equation of motion. As demonstrated in the present study, multi-DoF robotic manipulators could be a useful device for dynamic wind-tunnel testing. However, a serial arm-type robotic manipulator has an inherent limitation of performance and speed that prevents us from evaluating the effects of oscillating frequencies and amplitudes over a wide range. A manipulator with parallel-link mechanism such as MPM and HEXA has much faster frequency performance and can be a solution to the present problem of serial robots.

Acknowledgement

References

[1] Nelson R C, et al, "The unsteady aerodynamics of slender wing and aircraft undergoing large amplitude maneuvers", Progress in Aerospace Sciences Vol. 39, pp. 185-248 (2003)

[2] Greenwell D I, "A review of unsteady aerodynamic modelling for flight dynamics of manoeuvrable aircraft," AIAA Atmospheric Flight Mechanics Conference and Exhibit, Rhode Island, USA, AIAA-2004-5276 (2004)

[3] Huang X Z, et al., "Introduction and Experimental Aspects of The NATO RTO Task Group AVT-080: Study of Vortex Breakdown Over Slender Wings", European Congress on Computational Methods in Applied Sciences and Engineering ECCOMAS (2004)

[4] Cummings R M, et al, "An Integrated Computational/ Experimental Approach to UCAV Stability & Control Estimation: Overview of NATO RTO AVT-161", the 28th AIAA Applied Aerodynamics Conference, Chicago, IL, USA, AIAA-2010-4392 (2010)

[5] Kawazoe H, et al, "Ground Effect on the Dynamic Characteristics of a Wing-rock Delta Wing," the 34th AIAA Fluid Dynamics Conference and Exhibit, Portland, Oregon, USA, AIAA-2004-2352 (2004)

[6] Bergmann A, et al, "Experimental and numerical research on the aerodynamics of unsteady moving aircraft," Progress in Aerospace Sciences Vol. 44, pp.121-197 (2008)

[7] Abe   H, "2-DoF Dynamic Wind-tunnel Testing of a Rolling Delta-wing Using a Robotic Manipulator," Master Thesis, Department of Aerospace Engineering, Tohoku University, March 2012 (2012)

[8] Takayama   D, "2-DoF Dynamic Wind-tunnel Testing of a Pitching Delta-wing Using a Robotic Manipulator," Graduation Thesis, Tohoku University, March 2012 (2012)

[9] Lambert C and Gursul I, "Insensitivity of Unsteady Vortex Interactions to Reynolds Number," AIAA Journal, vol. 38, no. 5, pp. 937-939 (2000)

[10] Polhamus E C, "Predictions of Vortex Lift Characteristics by a Leading-Edge Suction Analogy", J. Aircraft, Vol. 8, p.193-1990 (1971)

[11] Shimbo Y and Sato J, "Unsteady Aerodynamic Forces on Rolling Delta Wings at High Angle of Attack," Trans. of the Japan Society for Aeronautical and Space Sciences, Vol. 37, No. 429 (1989)

[12] Kwak D Y, Sunada Y, Sato J, "Experimental Research on Unsteady Aerodynamics of Rolling Delta Wings," Trans. of the Japan Society for Aeronautical and Space Sciences, Vol. 45, No. 419 (1997)

Integration between Measurements and Particle Simulations for Hypersonic Rarefied Flows

Takashi Ozawa
Toshiyuki Suzuki
Kazuhisa Fujita

Aerospace Research and Development Directorate
Japan Aerospace Exploration Agency
Chofu, Tokyo 182-8522
JAPAN
ozawa.takashi@jaxa.jp

Abstract

The hypersonic rarefied wind tunnel has lately been developed at JAXA. The characteristics of hypersonic rarefied flows have been investigated experimentally and numerically in this work. Using a sphere pendulous model, the test flow has been probed by measuring its displacement due to the aerodynamic force. In addition, a spatial variation of total pressure of the test flow has also been measured by using total pressure tubes. The flow field from a conical nozzle to a test section was simulated by computational fluid dynamics/direct simulation Monte Carlo loosely coupled computations, and the flow fields were deduced by integrating experimental and numerical results. Consequently, a 25-mm hypersonic rarefied core flow was obtained using a 45-degree conical nozzle with a Mach number greater than 10 and a Knudsen number greater than 0.1.

Key words: HRWT, rarefied gas, aerodynamics, DSMC, hypersonic

Introduction

In order to develop atmospheric reentry systems and planetary entry probes, it is crucial to evaluate the aerodynamic performance of aerospace vehicles in hypersonic flow regime accurately. In the mean time, the Super Low Altitude Test Satellite (SLATS) [1], an engineering test satellite, is under development at Japan Aerospace Exploration Agency (JAXA) so as to improve the resolution for ground observations and reduce the cost for optical systems. The SLATS is operated on the sun-synchronous orbit (SSO) to keep the electric power available for the electric propulsion system, and the target altitude is in a super low earth orbit between 180 and 300 km, where the satellite speed needs to be recovered in order to maintain the satellite altitude. Thus, the assessment of rarefied aerodynamic forces acting on the satellite is important for the SLATS mission. In general, the maximum errors of 10 % and 5 % for force and moment coefficients, respectively, are demanded in these missions.

Thus far, hypersonic aerodynamic prediction has been improved by both ground tests and numerical simulations, especially in continuum flow regime. Aerodynamic forces in free-molecular flow regime can be well-predicted numerically. In transitional hypersonic flow regime, however, we generally rely on direct simulation Monte Carlo (DSMC) [2] computations to estimate rarefied aerodynamic performance for such vehicles since it is difficult and costly to realize rarefied hypersonic test flows equivalent to the flight environments in ground test facilities. State-of-the-art techniques for DSMC simulations are highly sophisticated enough to offer useful information of the rarefied aerodynamics. However, there still remain considerable demands of direct measurement of the vehicle aerodynamics and the heat transfer rate in hypersonic rarefied flows. Besides, the numerical simulations often suffer from inevitable uncertainties originating from accommodation coefficients of

molecules colliding against vehicle surfaces, which are difficult to exactly determine without experiments. Fujita *et al*. [1] investigated details of SLATS aerodynamic characteristics using an analytical method, and found that the aerodynamic coefficients considerably depend on the accommodation parameters of surface materials. Hence, the measurement of accommodation coefficients in hypersonic rarefied flows is necessary to improve the accuracy of aerodynamic prediction on the SLATS.

For these high demands in direct rarefied hypersonic aerodynamic measurements, a pilot model of the hypersonic rarefied wind tunnel (HRWT) [3] has lately been developed at JAXA. This middle-sized wind tunnel is designed to be capable of generating a nominal hypersonic rarefied flow condition; Namely, the flow condition of a Mach number M greater than 10 and a Knudsen number Kn greater than 0.1 is aimed. In order to measure the aerodynamic force in HRWT, it is important to understand characteristics of flow produced by the HRWT accurately. In this work, thus, the rarefied hypersonic flow characteristics of HRWT have been investigated experimentally and numerically. First, a measurement system using a simple pendulous sphere model or total pressure tubes has been developed to probe the hypersonic rarefied gas flows in HRWT. Second, numerical schemes have been developed to simulate the overall HRWT flows. Due to the combined condition of the continuum nozzle flow and the dilute test section, the computational fluid dynamics (CFD) and DSMC methods have been coupled to calculate the HRWT flows. Finally, an integration system between the HRWT measurement and numerical simulations has been developed to improve the understandings of the gas flow characteristics and to measure surface accommodation coefficients on a test model.
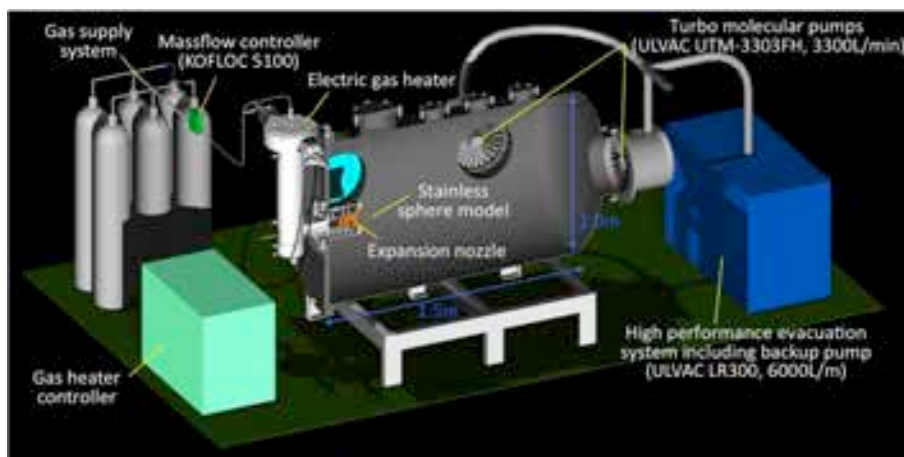

Figure 1 Schematic view of hypersonic rarefied wind tunnel (HRWT).

Experimental Apparatus

A schematic view of the HRWT is shown in Figure 1. The HRWT consists of an expansion nozzle with a large expansion ratio, a vacuum chamber as a test section, and an evacuation system with high exhaust velocity to allow a continuous operation at low ambient pressure. Nitrogen gas from a gas supply system flows into a vacuum chamber through a conical nozzle. The vacuum chamber is 1.0 m in diameter and 1.5 m in length. Three turbo molecular pumps (ULVAC UTM-3303FH, 3.3 m^3/s exhaust capacity) and a back-up dry pump (ULVAC LR300, 0.1 m^3/s exhaust capacity) are equipped in the vacuum chamber. This HRWT pumping system can maintain vacuum pressure in the test section on the order of 1 Pa at a mass flow rate of 0.08 g/s. The static pressure is monitored with a Pirani vacuum gauge (ULVAC GP-1G), a ceramic capacitance monometer (ULVAC CCMH-1A), and a metal ionization gauge (ULVAC GI-M2). These vacuum gauges are mounted on the vacuum chamber.

The HRWT is also equipped with an electric gas heater to increase the flow velocity and the static temperature of flows in the test section. Note that a discharge-less heating system has been selected for HRWT to avoid contamination in the test flow. The electric gas heater consists of a tungsten mesh heater, thermal insulators made of ZrO_2 and Al_2O_3, and a water-cooled outer structure made of stainless steel. The total temperature is monitored at a plenum chamber by using a type-K thermocouple, while a tungsten rhenium alloy wire thermocouple is used to monitor the heater temperature. In order to avoid oxidation of the tungsten mesh heater

at high temperatures, inert gases such as pure nitrogen and noble gases are only allowed to use as the working gas. This heating system is capable of heating the test gas up to approximately 800 K. The nitrogen test gas in the plenum chamber expands into the test section through a conical nozzle. The nozzle throat diameter is 1.632 mm, and the inlet and exit diameters of the nozzle are 25 and 100 mm, respectively. The inlet and outlet half-cone angles are selected to be 45 degree based on our preliminary numerical investigation. The total pressure in the plenum chamber is measured by using a capacitance manometer (ULVAC CCMT-1000D). The temperature of cooling water near the nozzle surface is measured by using a type-K thermocouple, and this temperature is assumed to be identical to the nozzle wall surface temperature in this work.

In order to probe the test flow, a stainless-steel sphere pendulous model with the diameter of 5 mm is inserted into the HRWT flow. Figure 2A shows the typical operation of the test using the sphere model. The sphere model is suspended by a stainless-steel wire to measure the radial distribution of flow properties. The wire has a diameter of 20 μm and a length of 220 mm, respectively. The wire is then connected to a traverse mount which allows triaxial adjustment of the test model position in relation to the test flow. The sphere model is initially set at 17 mm downstream from the nozzle exit and on the nozzle center line. The flexural rigidity of the wire was found negligible compared to aerodynamic forces acting on the model. In addition, total pressure tubes were designed to measure the total pressure distribution in the HRWT test section. A typical operation is shown in Fig. 2B. Two types of tube diameter are tested in this study: One is outer diameter(d_o)/inner diameter(d_i)=2.5/1.5 mm, the other is d_o/d_i=1.6/1.0 mm. Similar to the pendulous model, total pressure tubes are attached to the triaxial stage, and the two-dimensional pressure distributions can be measured. The location of sphere test model and total pressure tube is measured by an image processing technique using a megapixel CCD camera mounted on the quartz window of the test chamber. The original coordinate data is digitized by scanning the photograph, and the experimental uncertainty of the coordinate is estimated to be less than ±0.25 mm.
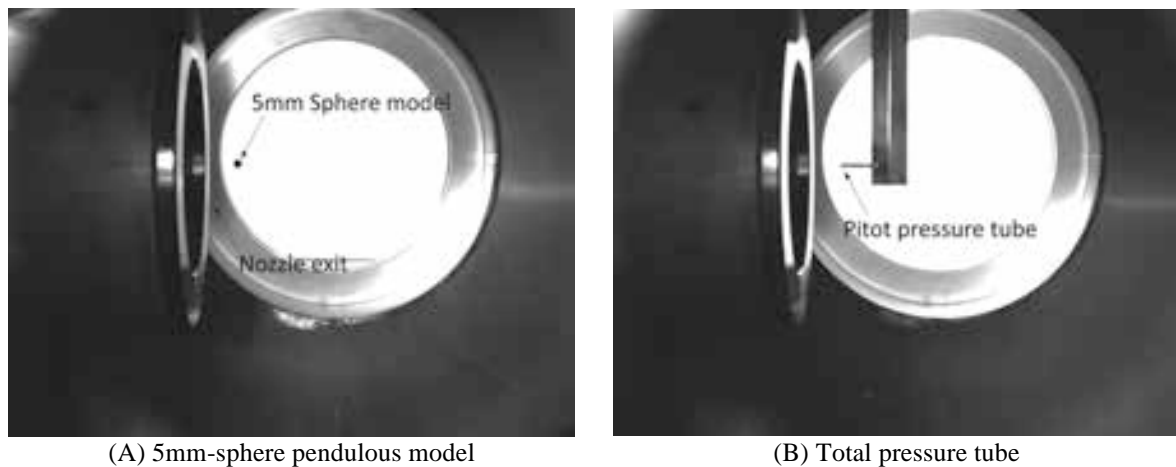

(A) 5mm-sphere pendulous model   (B) Total pressure tube

Figure 2 Aerodynamic force measurement system installed in HRWT.

Numerical Flow Modeling

Although the N_2 nozzle flow in the convergence section is so dense that the CFD is capable of calculating the flow field, the flow becomes rarefied in the divergence and test section, where continuum assumption may not be eligible. On the other hand, it is too expensive to simulate the overall section inside the nozzle using the DSMC, and thus, the CFD and DSMC methods are loosely coupled so as to perform the full nozzle flow calculations. The HWRT flow simulations have been performed for the mass flow rate of 0.08 g/s, and the stagnation pressure has been determined accordingly.

CFD calculations in this work were carried out using the JAXA's optimized nonequilibrium aerothermodynamic analysis (JONATHAN) code [4]. In the code, the convective numerical flux is formulated by the AUSM-DV scheme [5] with the second-order upwind-based MUSCL scheme [6]. To settle the strong stiffness originating from chemical reactions, the diagonal implicit scheme [7] is applied to the chemical source terms, whereas the convective and the viscous terms are integrated explicitly in time using local time steps. The collision integrals

in the JONATHAN database are mostly taken from Refs. [8]-[10]. The coefficients of viscosity, thermal conductivity, and ordinary diffusion are computed by the first-order expressions of the Chapman-Enscog theory. The further details of the JONATHAN code can be found in Ref. [11]. In this work, N_2 gas nozzle flows were simulated with respect to each condition inside the nozzle in HRWT. Although a two-temperature model and thermochemical models with several chemical reaction databases were available, neither vibrational excitations nor chemical reactions were considered in this work. To begin with, the nozzle configuration and mesh were generated, and then the convergence-divergence nozzle flow was simulated with a specified total pressure and temperature in the reservoir to fit with the mass flow rate of 0.08 g/s. Only N_2 was considered in the simulations, and for the gas-surface interaction, a non-slip diffuse model was employed.

In this study, the Modeling Of Transitional-Ionized Flows (MOTIF) [12],[13] DSMC code is used to simulate rarefied nozzle flow. In the code, the computational time step is chosen with the one associated with molecular collisions. The no time counter (NTC) scheme [2] is employed for modeling the molecular collision frequency, and the variable hard sphere (VHS) model [2] is used for modeling the collision cross section between particles. The Borgnakke-Larsen (BL) model with temperature-dependent rotational and vibrational relaxation numbers is used for modeling rotation-translation (R-T) and vibration-translation (V-T) energy transfers between neutral species. The Millikan and White (MW) form of the relaxation time are used for V-T rates, and Parker's rates for the R-T rates. For modeling chemical reactions the total collision energy (TCE) model is used, and for modeling electronic excitation transitions, either the quantum-kinetic (Q-K) model or cross section (CS) model is utilized in the code. For the gas-surface interaction modeling, both the Maxwell reflection model and Cercignani-Lampis-Lord (CLL) reflection model are employed. In the Maxwell model, the Maxwell accommodation factor of the surface decides the ratio of a diffuse reflection to a specular reflection. The CLL model assumes no coupling between the normal and tangential components of the velocity during the reflection process. Therefore, three accommodation parameters for normal and tangential velocity and energy fractions are required in this model.

In this work, 3D DSMC calculations were carried out for 100 % N_2 nozzle flows using the MOTIF code. Although the nozzle flow was assumed to be chemically frozen, R-T and V-T energy transfers were considered. Only N_2 species was considered in the flow, and the VHS parameters can be found in Refs. [2] and [14]. The gas-surface interaction was modeled using the Maxwell model, and a diffuse condition with total energy and momentum accommodation with the measured surface temperature was used for the nozzle surface. The time step, cell size, computational domain, and total number of simulated molecules were investigated to obtain results that are independent of these DSMC numerical parameters. Macroparameter sampling is started after a time period that is sufficient to reach the steady state and the total number of time steps used in the sampling is approximately 25,000. The DSMC computational domain extends from approximately 18 mm downstream from the nozzle throat to 150 mm downstream from the nozzle exit. The DSMC inflow boundary condition is given by the converged solution obtained by CFD computation, while the equilibrium condition at the measured ambient pressure is assumed at the outer boundary condition.

In order to consider the effect of flow disturbances due to a test model and calculate the drag on the model from the microscopic viewpoint, it is necessary to integrate the model with DSMC calculations to compute the model displacement more accurately. In DSMC, the force on the model is calculated from the summation of particle momentum transfer during the sampling time as

$$\mathbf{F} = \sum_p [(m\mathbf{v}_p^{pre} - m\mathbf{v}_p^{post})F_{num,p}]/\Delta t. \tag{1}$$

The particle information is accumulated over the sampling time and the force are the average value over the sampling time to reduce the statistical noise. The displacement of the test model is calculated by using the force obtained in Eq. (1) as

$$\theta = \tan^{-1}\left(\frac{F_x}{m_s g - F_z}\right), \tag{2}$$

$$\Delta x = L\sin\theta, \ \Delta z = L(1-\cos\theta), \tag{3}$$

where m_s and L are the mass of the sphere model and the length of the wire sustaining the sphere model, respectively.

In the course of the present DSMC calculation, the sphere model is initially set at 17 mm from the nozzle exit along the centerline in accordance with the HRWT measurement. Once the flow reaches the steady state, the aerodynamic forces acting on the sphere model and the displacement are calculated by using Eqs. (1)-(3). The

sphere model is then moved to a new balanced position, and the DSMC calculation is again carried out. The aerodynamic forces and the displacement are calculated every 3,000 time steps. This iteration is repeated until the amount of displacement becomes less than 10 % of the representative length of the test model (0.25 mm). Note that the test model is placed on the x-z plane in order to maintain the symmetric condition about the transversal (y) direction. The sphere model diameter d_s and the wire length L is set to 5 mm and 220 mm in accordance with the HRWT measurement. In the DSMC code, both the Maxwell reflection model and the CLL reflection model [15] are employed for the test model. The accommodation parameters can be investigated for the dependence on the material, surface temperature, surface roughness, and so forth. In this work, the gas-surface interaction was modeled using the Maxwell model, and two extreme boundary conditions are applied: One is a diffuse condition with total energy and momentum accommodation with a surface temperature of 290 K, and another is a specular condition.

Results and Discussions

From our previous work, it was found that for the accurate estimation of the test model displacement, it is necessary to integrate the test model with the DSMC flow field calculation because the flow disturbance due to the test model is not negligible. Flow-sphere integrated DSMC calculations have been carried out, and the effect of the test model integration has been investigated. Figure 3 shows comparison of Mach number contours between the cases with and without the sphere model. A uniform core flow (M > 10) with a diameter of 25 mm is generated in the test section, and the effect of a sphere model can be seen approximately 10 mm upstream of the sphere. The flow is dramatically decelerated near the model. The core flow speed is approximately 940 m/s without heating, and the displacement is approximately 16 mm. The flow speed decreases around the sphere model, and the sphere model integration in DSMC improved the displacement prediction by 15 % at a maximum.
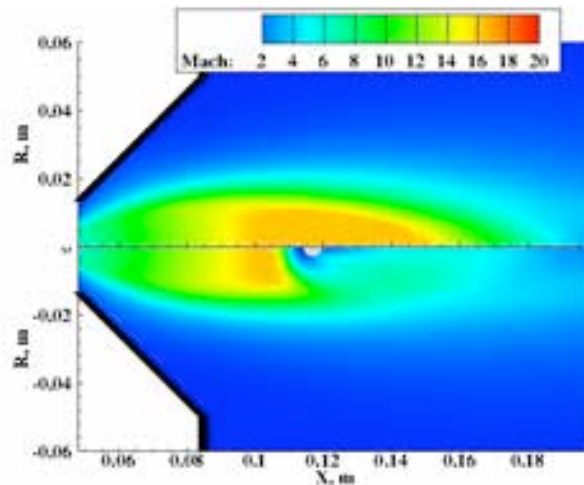

Figure 3 Comparison of Mach number contours between cases with and without a sphere model.

The sphere model displacements due to the aerodynamic forces were investigated along the radial direction. Figure 4 shows comparison of the sphere model displacement between the calculated and measured results for (a) non-heated case (T_0=290 K) and (b) heated case (T_0=750 K) at the mass flow rate of 0.08 g/s. For the calculation, the results are shown for the diffuse and the specular cases. From the measured results, it can be seen that although significant radial change exists in the outer region of the test flow, the displacement of the model is almost constant in the 25 mm core region. From the comparison between Fig. 4A and 4B, one can see that the amount of displacement for the heated case becomes larger than that of the non-heated case. This result is attributed to the increase of flow velocity in the test section with increasing the stagnation temperature. For the heated case, the core velocity is increased by approximately 500 m/s from the non-heated case and becomes faster than 1,200 m/s. From the calculated results shown in Fig. 4A, one can see that the displacement for the diffuse condition becomes larger than that for the specular condition for all radial position. Almost the same situation can be seen in Fig. 4B. This trend can be explained as follows: In the present study, the surface temperature of sphere model is assumed to be 290 K. For the diffuse condition, N_2 molecule striking on the sphere model surface completely accommodates with the model surface temperature of 290 K. For this case, the average speed of reflected molecule for diffuse condition is mostly smaller than that for specular condition. As a

result, the number density of N_2 molecule for the diffuse case becomes higher than that for specular one, resulting in higher dynamic pressure acting on the model for the diffuse case. For these reasons, the model displacement becomes higher with the diffuse wall compared to that with the specular wall.
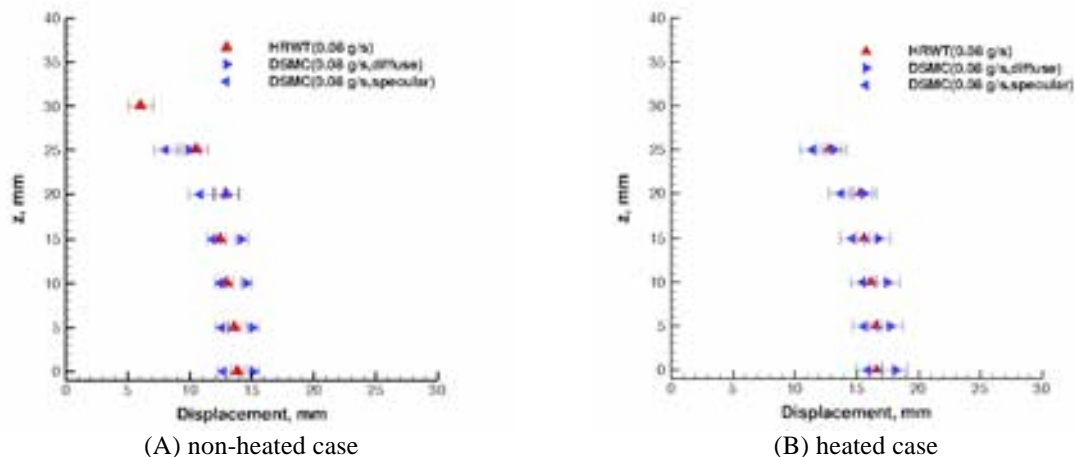

(A) non-heated case   (B) heated case

Figure 4 Comparison of sphere model displacement between calculation and measurement at 17 mm downstream from the nozzle exit.

From the comparison between the calculation and the measurement in Fig. 4, good agreement can be seen between the measured and computed results because the measured displacement is located between the DSMC specular and diffuse calculations. Base on this result, it is believed that the present numerical method can reproduce the characteristics of the HRWT flows within the uncertainty originating from the accommodation factor of molecules colliding against the sphere model. Note that slight discrepancy can be seen in the outer region of the core flow in Fig. 4A. The increase in the measured displacement near $z = 20$ mm is caused by the interaction among the core flow development, boundary layer development, and the background pressure, which is approximately 1.4 Pa. In the DSMC computations, this phenomenon is slightly under-estimated. One possible reason for this may come from the difference in the boundary layer thickness between the calculation and the measurement. In general, the nozzle wall surface might be rough compared with an ideal wall surface assumed in the DSMC calculation. In order to examine the hypothesis about the boundary layer thickness, the DSMC calculation was further performed by changing the boundary layer thickness artificially [16]. From this investigation, it was confirmed that the thickness of boundary layer becomes larger and the core flow diameter becomes smaller with increasing the surface temperature of the nozzle. It was also found that the dynamic pressure around the flow center becomes higher when the boundary layer becomes thicker. Correspondingly, the flow field around the sphere model was re-calculated by correcting the boundary layer thickness, and the sphere model displacement was re-estimated. The agreement between the calculation and the measurement was improved, and the measured displacement became between the DSMC specular and diffuse results. Note that no evidential result for condensation to liquid state was obtained in the cases under consideration, even though the flow temperature is believed to be below dew point temperature especially for the non-heated case. This trend is believed to occur because the Knudsen number remains at the order of 0.1 due to the low density of test flow. In order to avoid this peculiar discussion, the gas heater system will be improved so that the test flow temperature in the test chamber could be higher than the dew point temperature in the future.

The total pressure distributions in the test section were investigated by using the total pressure tubes. Using the total pressure tube of 2.5 mm outer diameter, total pressure distributions were measured with an interval of 5 mm for cases (A) and (B). In Fig. Figure 5, the measured total pressure distributions are compared with the computed dynamic pressure. The obtained results are shown in Fig. 5A for the non-heated case (A) and in Fig. 5B for the heated case (B). For case (A), a trend of pressure increase in the interaction region between the core flow and the background gas can be seen clearly in both the measured and computed results. This trend is decreased for the 750 K case. From the measured results shown in Fig. 5, it can be seen that the total pressure near the nozzle exit for case (B) becomes higher than that for case (A). This feature is due to the increase of the flow velocity with increasing the stagnation temperature. In Fig. 5, calculated dynamic pressure distributions around the nozzle exit are also shown for the purpose of comparison. In order to compare the calculated results with experimental data directly, total pressure needs to be calculated from the numerical results so that the

calculated total pressure can be viewed as the pressure that would be obtained if a total pressure tube were put into the computed flow field. Following the study in Refs. [17] and [18], the total pressure is calculated by taking account of the effect of rarefaction as follows:

(1)Total pressure behind a shock wave is first calculated by using the calculated static pressure with the Rayleigh pitot tube equation [19] as

$$p_{02}/p_1 = \left[\frac{(\gamma+1)^2 M^2}{2(2\gamma M^2 - \gamma + 1)}\right]^{\frac{\gamma}{\gamma-1}} \frac{2\gamma M^2 - \gamma + 1}{\gamma + 1}. \tag{4}$$

(2)The measured total pressure, p_{0m}, is finally obtained by taking account of the effect of rarefaction as

$$\log_{10}(p_{0m}/p_{02}) = a - b\log_{10}(\mathrm{Re}_2), \tag{5}$$

where the probe Reynolds number behind a shock wave is calculated using the actual diameter of the pressure tube (d_p) as

$$\mathrm{Re}_2 = \rho_2 u_2 d_p / \mu_2. \tag{6}$$

Because the experimental condition and the tube diameter in this study are different from those in the work of Boyd *et al*. [17], the degree of rarefaction of the present study seems to be different from those conditions. For this reason, the constant parameters in Eq. (5) are determined independently in this study. The parameters used in this study are summarized in Table 1.

Table 1 Parameters used in Eq. (5)

Parameters	290 K	750 K
a	0.3	0.05
b	0.5	0.5

The computed total pressure are compared with the measured one in Fig. 6A for case (A), and in Fig. 6B for case (B). In Fig. 6, two pressure tube results for the d_o of 2.5 mm and 1.6 mm, respectively, are presented. It can be seen in the figure that the differences in tube outer diameter between 2.5 and 1.6 mm are clearly seen in both computed and measured results. The overall agreement between computed and measured results are considerably good except for a slight difference for case (A) with the 1.6-mm outer diameter tube. The difference may be attributed to the slight increase in the stagnation pressure during the measurement.

From the experimental and numerical results about the sphere model and the total pressure tube, it is considered that the present numerical method can reproduce the major characteristics of the test flows in HWRT. The flow Mach number and the Knudsen number for mass flow rate of 0.08 g/s are estimated by numerical results, and the obtained results are presented in Fig. 7. As shown in Fig. 7, the core flow diameter is estimated to be roughly 25 mm. For case (A), although the flow Mach number is higher than 10, the Knudsen number remains below 0.1. On the other hand, the flow Mach number of 16 and the Knudsen number of 0.2 are achieved for case (B).
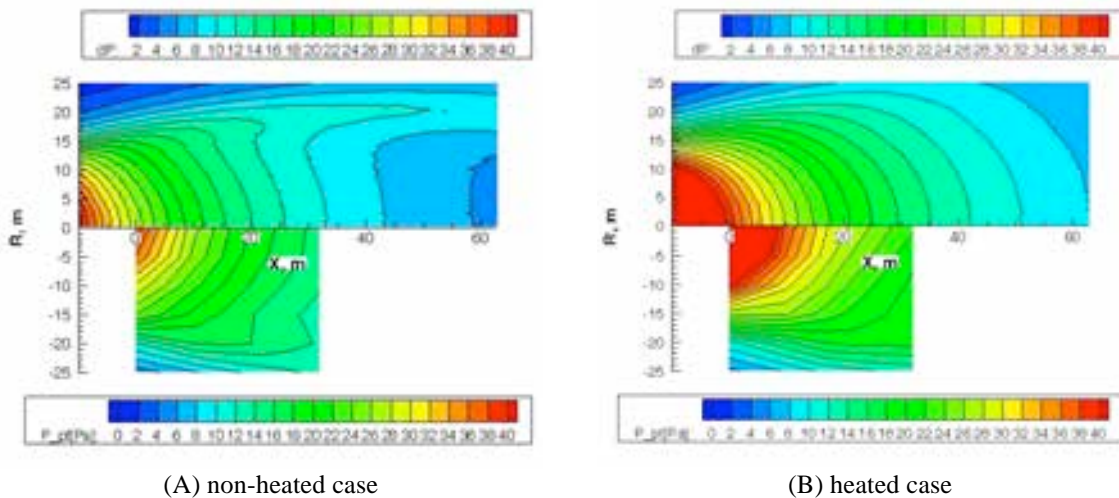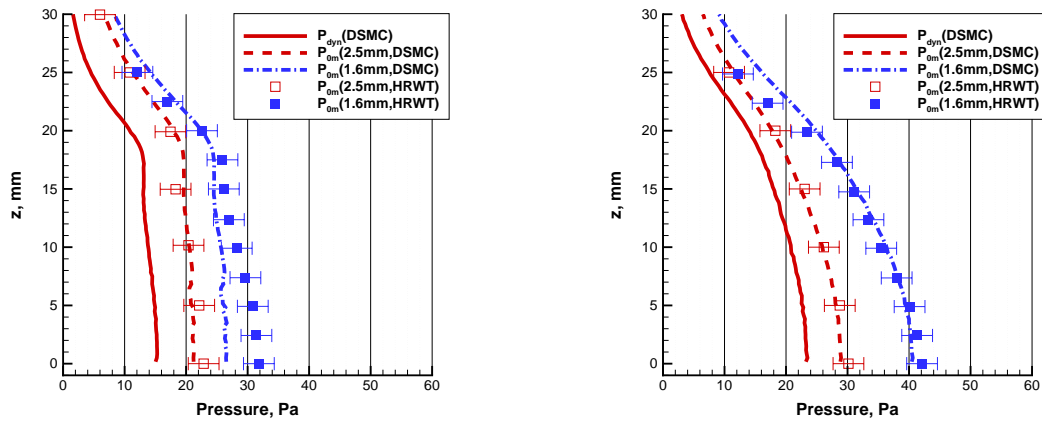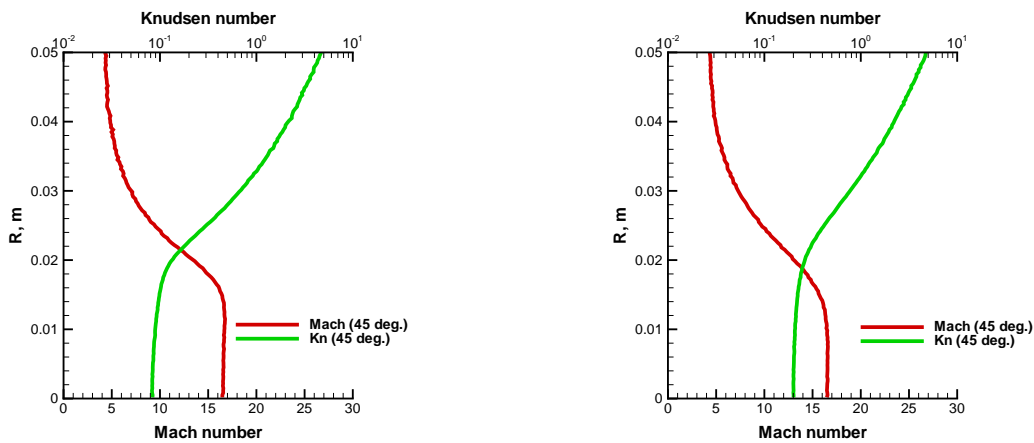

(A) non-heated case   (B) heated case

Figure 5 Comparison of computed dynamic pressure (top) and measured total pressure (bottom).

(A) non-heated case   (B) heated case

Figure 6 Comparison of computed and measured total pressure profiles along radial direction at 17 mm downstream from the nozzle exit.

(A) non-heated case   (B) heated case

Figure 7 Mach number and Knudsen number distributions along the radial direction at 17 mm downstream from the nozzle exit.

Conclusions

Flow characteristics of HRWT have been investigated by using the pendulous sphere model and the total pressure tubes. Using the CFD/DSMC numerical approach integrating with the HRWT test model, we analyzed the major characteristics of the test flows in HRWT. It was found that the test flows are well-represented by the numerical approach, and the heating effect increases the Knudsen number in the test section. With the heater activated, the free stream Mach number greater than 10 and Knudsen number of 0.1 are achieved in the 25mm-core flow region.

References

[1]   K. Fujita and A. Noda, Rarefied Aerodynamics of a Super Low Altitude Test Satellite, AIAA Paper 2009-3606, 2009.

[2]   G. A. Bird, Molecular Gas Dynamics and the Direct Simulation of Gas Flows, Clarendon, Oxford, England, U.K., 1994.

[3]   K. Fujita, T. Suzuki, T. Ozawa, Development of a Pilot Model of Hypersonic Rarefied Wind-Tunnel, in 27th International Symposium on Rarefied Gas Dynamics, AIP Conference Proceedings, Vol. 1333, pp. 407-412, 2010.

[4]   K. Fujita, S. Matsuyama, and T. Suzuki, Prediction of Forebody and Aftbody Heat Transfer Rate for Mars Aerocapture Demonstrator, AIAA Paper 2012-3001, 2012.

[5]   Y. Wada and M. S. Liou, A Flux Splitting Scheme with High-Resolution and Robustness for Discontinuities, AIAA paper 1994-0083, 1994.

[6]   B. van Lee, Toward the Ultimate Conservative Difference Scheme. 5, A Second-Order Sequel to Godonov's Method, Journal of Computational Physics, Vol. 23, No. 1, pp. 101–136, 1979.

[7]   S. Eberhardt and S. Imlay, Diagonal Implicit Scheme for Computing Flows with Finite Rate Chemistry, ournal of Thermophysics and Heat Transfer, Vol. 6, No. 2, pp. 208–216, 1992.

[8]   C. Park, R. L. Jaffe and H. Partridge, Chemical-Kinetic Parameters of Hyperbolic Earth Entry," Journal of Thermophysics and Heat Transfer, Vol. 15, No. 1, pp. 76–90, 2001.

[9]   M. Capitelli, C. Gorse, S. Longo and D. Giordano, Collision Integrals of High-Temperature Air Species, Journal of Thermophysics and Heat Transfer, Vol. 14, No. 2, pp. 259–268, 2000.

[10] E. Levin and M. J. Wright, Collision Integrals for Ion-Neutral Interactions of Nitrogen and Oxygen, Journal of Thermophysics and Heat Transfer, Vol. 18, No. 1, pp. 143–147, 2004.

[11] K. Fujita, T. Sumi, T. Yamada and N. Ishii, Heating Environments of a Venus Entry Capsule in a Trail Baloon Mission, Journal of Thermophysics and Heat Transfer, Vol. 20, No. 3, pp. 507–516, 2006.

[12] T. Ozawa, T. Suzuki, H. Takayanagi and K. Fujita, Investigation of Martian-Dust Drag and Heat Transfer for Mars Sample Return Mission, Journal of Thermophysics and Heat Transfer, Vol. 25, No. 3, pp. 341–353, 2011.

[13] T. Ozawa, T. Suzuki, H. Takayanagi and K. Fujita, Analysis of Non-Continuum Hypersonic Flows for the Hayabusa Reentry, AIAA Paper 2011-3311, 2011.

[14] G. C. Maitland, Critical Reassessment of Viscosities of 11 Common Gases, Journal of Chemical and Engineering Data, Vol. 17, No. 2, pp. 150–156, 1972.

[15] M. O. Hedahl and R. G. Wilmoth, Comparison of the Maxwell and CLL Gas/Surface Interaction Models Using DSMC, NASA TM-110205, 1995.

[16] T. Suzuki, T. Ozawa and K. Fujita, Experimental and Numerical Study of Flow Diagnostics in Hypersonic Rarefied Wind Tunnel in JAXA, AIAA Paper 2012-0370, 2012.

[17] I. D. Boyd, P. F. Penko, D. L. Meissner and K. J. DeWitt, Experimental and Numerical Investigations of Low-Density Nozzle and Plume Flows of Nitrogen, AIAA Journal, Vol. 30, No. 10, pp. 2453–2461, 1992.

[18] W. B. Stephenson, Use of the Pitot Tube in Very Low Density Flows, AEDC-TR-81-11, Arnold, AFS, TN, 1981.

[19] A. H. Shapiro, The Dynamics and Thermodynamics of Compressible Fluid Flow, Ronald Press, New York, 1953.

Experimental Data Reconstruction Using CFD Results Based on Proper Orthogonal Decomposition

Kanako Yasue
Shigeru Kuchi-Ishi
Shigeya Watanabe

Japan Aerospace Exploration Agency
Tokyo 182-8579
Japan
yasue@chofu.jaxa.jp

Abstract

An experimental fluid dynamics (EFD)/computational fluid dynamics (CFD) integration technique using proper orthogonal decomposition (POD) is developed for reconstructing a flow field of measurement data with equal information as CFD analysis. First, POD modes are extracted from several CFD data sets (snapshots) using a snapshot POD method. Then the entire flow field of measured data can be reconstructed using a "gappy" POD method. In this study, the entire flow field over a DLR-F6 FX2B wind tunnel model is reconstructed from only the measured pressure coefficient (Cp) data of pressure ports. Use of pressure-sensitive paint (PSP) data is also examined, and the accuracy of reconstructed results is examined. We show that a flow field can be reconstructed from pressure port data or from PSP data with satisfactory accuracy.

Keywords: EFD/CFD integration method, proper orthogonal decomposition.

Introduction

In developing aerospace vehicles, wind tunnel tests and computational fluid dynamics (CFD) are widely used for predicting aerodynamic characteristics under actual flight conditions. Both tools, however, have some discrepancy with flight conditions. For example, setting free-stream conditions to mimic flight conditions is usually difficult in wind tunnel tests. The existence of wind tunnel walls and support systems is peculiar to wind tunnel tests. Also, CFD modeling cannot exactly simulate real flight. While many researchers have been working to improve both techniques, it is necessary to combine the advantages of wind tunnel tests and CFD to achieve more highly accurate predictions of aerodynamic characteristics.

In wind tunnel tests and experimental fluid dynamics (EFD), recent measurement techniques ensure that data have high reliability. Moreover, pressure sensitive paint (PSP) and particle image velocimetry (PIV) have made possible the acquisition of surface and spatial data, in addition to point data. However, obtainable variables and regions are still restricted, and data are sometimes partially lost due to instrumental or settings issues. It is therefore difficult to get a complete view of a flow field, even when data sets are measured with a high degree of accuracy. Since CFD can contain a wide variety of physical quantities, it is useful for understanding flow fields in detail. CFD has uncertainty in computational models, however, especially for complicated flow-fields like turbulent flows. Accordingly, CFD results must be validated. The ability to obtain precise measured data with an equivalent amount of information as CFD by applying some kind of integration of EFD and CFD would lead to highly accurate predictions of aerodynamic characteristics. We believe that proper orthogonal decomposition (POD) [1] can play a role in realizing this.

POD extracts dominant components (or modes) from large-scale data sets. It is also known as principle component analysis in the statistical literature [1], or as a Karhunen-Loève expansion in pattern recognition [2, 3], and is widely used in various fields. In fluid dynamics, POD is employed in many applications, such as the extraction of coherent structure in turbulence [4], aeroacoustics [5, 6], fluid control [7, 8], data assimilation [9], and aerodynamic design optimization [10]. The snapshot POD method introduced by Sirovich [4] is usually applied, especially for large-scale problems. In this POD process, data can be represented as a linear combination of POD modes (bases) and expansion coefficients. A set of instantaneous flow solutions ("snapshots") is used to compute a set of POD modes. POD is also applied to the reconstruction of the incomplete ("gappy") data set. In that case, a gappy POD method, developed by Everson and Sirovich, is usually employed for reconstructing marred images [11]. In this technique, an incomplete data set can be reconstructed by solving a small linear system, once a set of POD modes is given.

In this research, we aim to reconstruct a flow field that has the same information level as the CFD from limited measurement data by applying an EFD/CFD integration technique based on the snapshot POD and the gappy POD. The POD modes are first extracted from several snapshots of CFD solutions using the snapshot POD method. Then the entire flow field of measured data can be reconstructed for various variables by obtaining the expansion coefficients using the POD modes, and limited experimental data sets can be reconstructed by applying the gappy POD method. In this paper, the reconstruction process using the POD approach is first outlined, and then, several test cases for reconstructing the flow field from measured pressure port data or PSP data are shown.

Data Reconstruction Method Using Proper Orthogonal Decomposition

The flow field data can be orthogonally decomposed using the POD as a linear combination of POD modes and expansion coefficients, and written as follows:

$$q_i = \sum_{i=1}^{m} a_i \phi_i \tag{1}$$

where ϕ_i and a_i represent a POD mode and an expansion coefficient, respectively. Therefore, the flow field of a measured data set can be reconstructed if the POD modes and the expansion coefficients are determined.

In this POD approach, the POD modes are extracted from a number of CFD solutions that are pre-computed in several free-stream conditions. Given m snapshots, a set of snapshots is written in matrix form as

$$\mathbf{Q} = \begin{bmatrix} q_1 & q_2 & \cdots & q_m \end{bmatrix} \tag{2}$$

q_i is the CFD solution vector:

$$q = \begin{pmatrix} \rho_i(1)\cdots\rho_i(n) & u_i(1)\cdots u_i(n) & v_i(n)\cdots v_i(n) & w_i(1)\cdots w_i(n) & p_i(1)\cdots p_i(n) \end{pmatrix}^{\mathrm{T}} \tag{3}$$

where ρ is the fluid density; u, v, and w are the Cartesian velocity components; p is the pressure; and n is the number of cells or nodes. It is well known that the POD modes can be computed by solving the eigenvalue problem

$$\mathbf{R}\phi_i = \lambda_i \phi_i \qquad (i = 1, 2, \cdots, m) \tag{4}$$

where $\mathbf{R}$ denotes the covariance matrix, written as

$$\mathbf{R} = \mathbf{Q}\mathbf{Q}^{\mathrm{T}} \tag{5}$$

and λ is the eigenvalue. Note that λ represents the energy contributions of the corresponding POD modes, and is defined as

$$\lambda_1 > \lambda_2 > \cdots > \lambda_m > 0 \tag{6}$$

However the size of the covariance matrix $\mathbf{R}$ is $5n \times 5n$ in this case, so its computational costs would be huge. In the snapshot POD method, therefore, the POD modes are constructed by solving a small eigenvalue problem for covariance matrix $\mathbf{R}'$:

$$\mathbf{R}'\psi_i = \lambda_i \psi_i \qquad (i = 1, 2, \cdots, m) \tag{7}$$

The small covariance matrix $\mathbf{R}'$ is written as

$$\mathbf{R}' = \mathbf{Q}^{\mathrm{T}}\mathbf{Q} \tag{8}$$

where ψ_i is the eigenvalue of matrix $\mathbf{R}'$. The size of this matrix $\mathbf{R}'$ is $m \times m$, and m is usually small compared with the number of cells or nodes of a CFD solution. Finally, the POD modes can be obtained using ψ_i as in the following equation:

$$\phi_i = \frac{\mathbf{Q}\psi_i}{\sqrt{\lambda_i}}. \tag{9}$$

In this study, all POD modes are used because the number of snapshots is very small. However, it is not necessary to use all POD modes to reconstruct the data.

Once the POD modes are determined, the expansion coefficients can be computed from the limited experimental data sets by using the gappy POD method. Let g be the reconstructed vector that we want to obtain, and consider that the measured data is a part of g with the following mask vector,

$$m = \begin{cases} 1 & \text{if existing exp. data} \\ 0 & \text{if not existing exp. data} \end{cases}. \tag{10}$$

Then the measured data can be also decomposed using the POD approach as

$$\tilde{g}_i = \sum_{i=1}^{m} b_i \tilde{\phi}_i, \tag{11}$$

where $\tilde{g}$ denotes the measured data set, $\tilde{\phi}_i$ the POD mode corresponding to $\tilde{g}$, b_i the expansion coefficient, and $\tilde{n}$ the number of measurement data. Here the measured data $\tilde{g}$ and the POD mode ϕ_i are already known, so we can determine the expansion coefficient by applying the least-squares method to minimize the evaluation function J as,

$$J = \| \sum_{i=1}^{m} b_i \tilde{\phi}_i - \tilde{g} \| \rightarrow \min. \tag{12}$$

This leads to a simple linear system as follows:

$$\tilde{\Phi}^{\mathrm{T}} \tilde{\Phi} \mathbf{B} = \tilde{\Phi}^{\mathrm{T}} \tilde{g}, \tag{13}$$

where

$$\tilde{\Phi} = \begin{bmatrix} \tilde{\phi}_1 & \cdots & \tilde{\phi}_m \end{bmatrix}, \tag{14}$$

and

$$\mathbf{B} = \begin{bmatrix} b_1 & \cdots & b_m \end{bmatrix}^{\mathrm{T}}. \tag{15}$$

Finally, the flow field for the measured data set can be reconstructed by the following equation:

$$g_i = \sum_{i=1}^{m} b_i \phi_i. \tag{16}$$

Results and Discussion
Data reconstruction from measured pressure port data over DLR-F6 FX2B wind tunnel model

We first attempt this approach to reconstruct an entire flow field over a DLR-F6 FX2B model [12, 13] from measured pressure coefficient (Cp) data of pressure ports and several CFD results. The experimental data were measured at the JAXA 2 m $\times$ 2 m transonic wind tunnel facility. There are 137 pressure ports located at a total of five cross-sectional surfaces of the left wing (Fig 1). Table 1 shows the free-stream conditions of the experimental data. The Mach number of this measurement data is set to be 0.75, the Reynolds number is 1.5 million, and the angle of attack is 1.5 deg. In this case, seven snapshots, which are the Reynolds-averaged Navier-Stokes solutions computed by a CFD solver FaSTAR [14] together with an automatic unstructured mesh generator HexaGrid [15], are prepared for extracting POD modes. Table 1 also lists free-stream conditions for the snapshots. Note that the free-stream conditions of the experimental data are not included in the CFD results. Total number of cells for each snapshot is about 15 million.

Figure 2 shows the obtained three-dimensional pressure distributions. Using this POD approach, a three-dimensional flow field that is consistent with the experimental data and has same amount of information as a CFD solution can be obtained from limited experimental data sets. The CPU time required to obtain this flow

field was about 2 min using the JAXA supercomputer system (JSS). Since it takes more than 10 h for CFD computation using 40 JSS processing elements, it is advantageous that this POD approach provides the same amount of information as CFD in a much shorter time. Figure 3 shows the Cp profiles at η = 0.150, 0.331, 0.514, 0.638, and 0.847 with those obtained from CFD analysis under the experimental conditions for comparison. As can be seen, the results of this POD approach show much better agreement with the experimental data than do the CFD results.

To confirm that the reconstructed flow field can follow experimental trends other than pressure port sections, the obtained surface Cp distributions are compared with those obtained by PSP [15], which were measured under the same conditions as the pressure port data. Figures 4 and 5 respectively show the Cp contours on the upper surface and the Cp profiles at several spanwise locations. As can be seen, the shock positions of the results obtained by POD are closer to the experimental data than those obtained by CFD computation. This indicates that one can obtain the entire flow field close to the experiment from a limited amount of pressure port data and CFD solutions using this POD approach. As shown in Fig. 5(c), the Cp profiles located from x/c = 0 to x/c = 0.2 are not improved compared with CFD results. This is because the number of snapshots is insufficient to reconstruct this flow field.

Table 1: Free-stream conditions for the experimental data and the CFD results (snapshots)

	Mach number	Reynolds number $\times 10^6$	Angle of attack [deg]
Experiment	0.75	1.5	1.538
Snapshot 1 (CFD)	0.75	1.5	-3.0
Snapshot 2 (CFD)	0.75	1.5	-2.0
Snapshot 3 (CFD)	0.75	1.5	-1.0
Snapshot 4 (CFD)	0.75	1.5	0.0
Snapshot 5 (CFD)	0.75	1.5	1.0
Snapshot 6 (CFD)	0.75	1.5	2.0
Snapshot 7 (CFD)	0.75	1.5	3.0
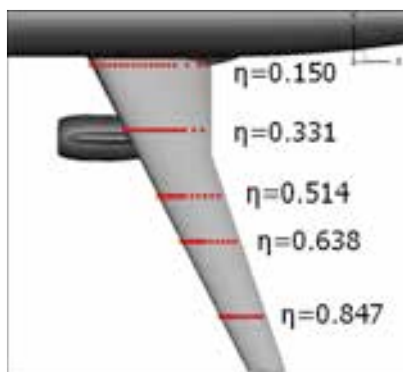
Fig. 1 Positions of pressure ports.

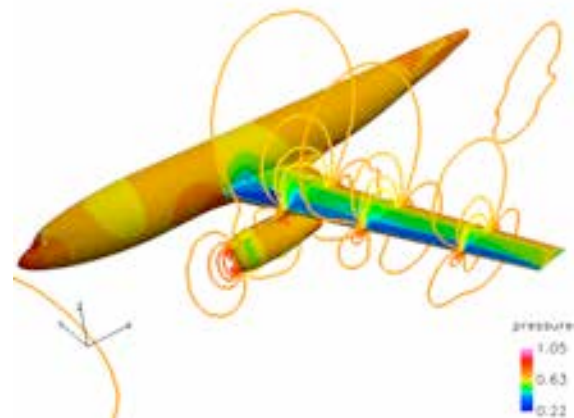**Fig. 2 Obtained three-dimensional pressure distributions around the DLR-F6 FX2B wind tunnel model.**

(a)   (b)   (c)
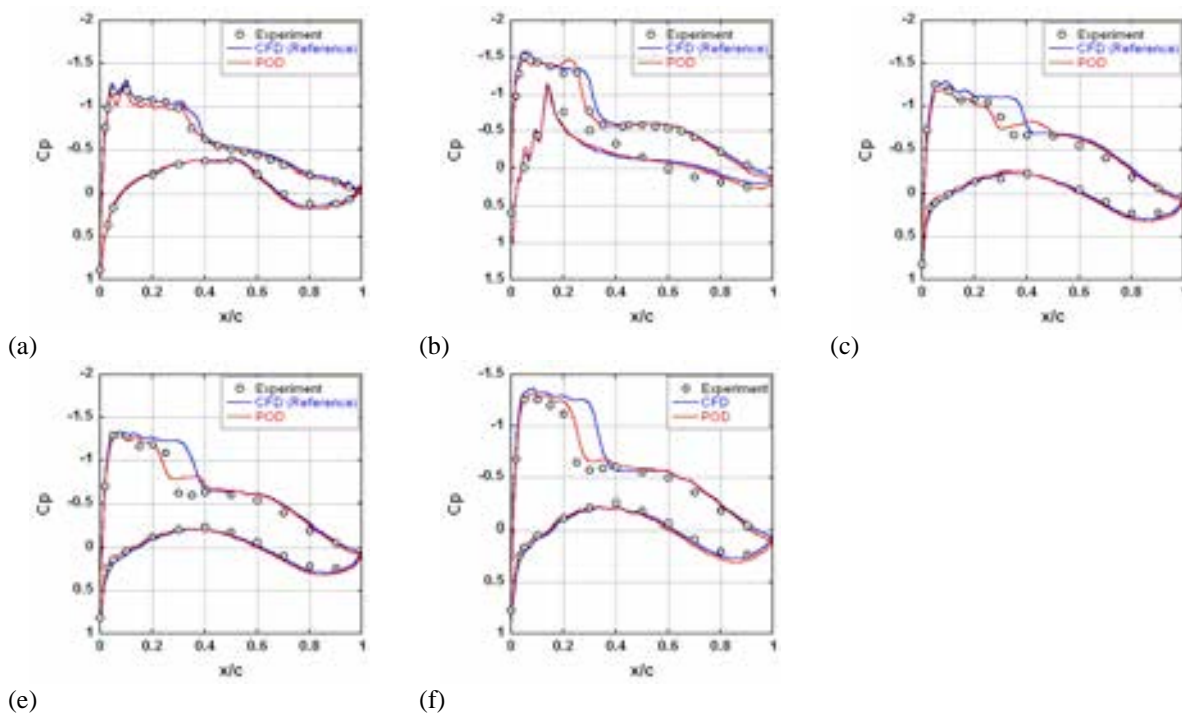

(e)   (f)

Fig. 3 Cp distributions obtained by the POD approach and distributions from experiment and CFD for (a) $\eta = 0.150$, (b) $\eta = 0.331$, (c) $\eta = 0.514$, (d) $\eta = 0.638$, and (e) $\eta = 0.847$.
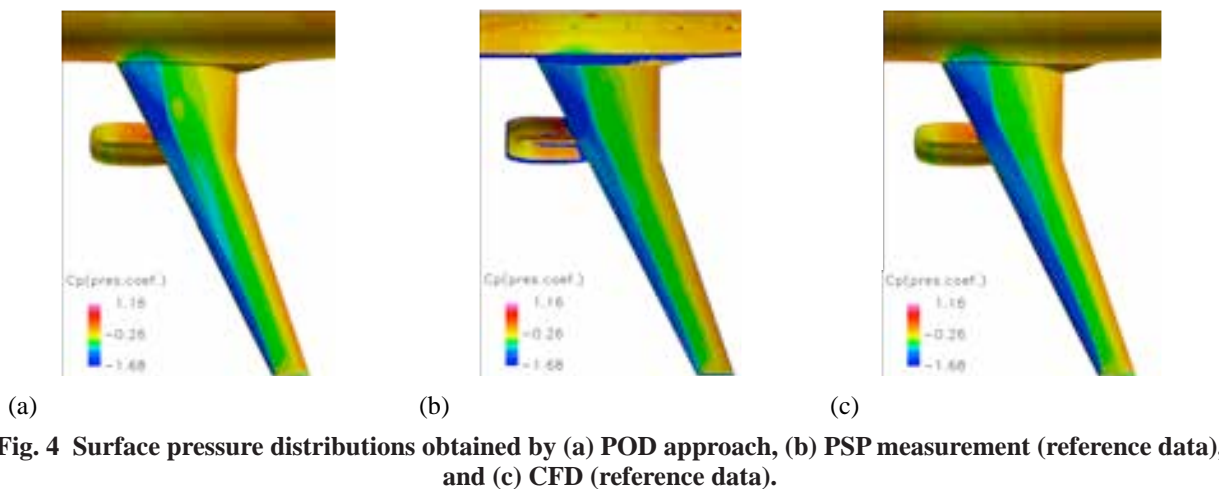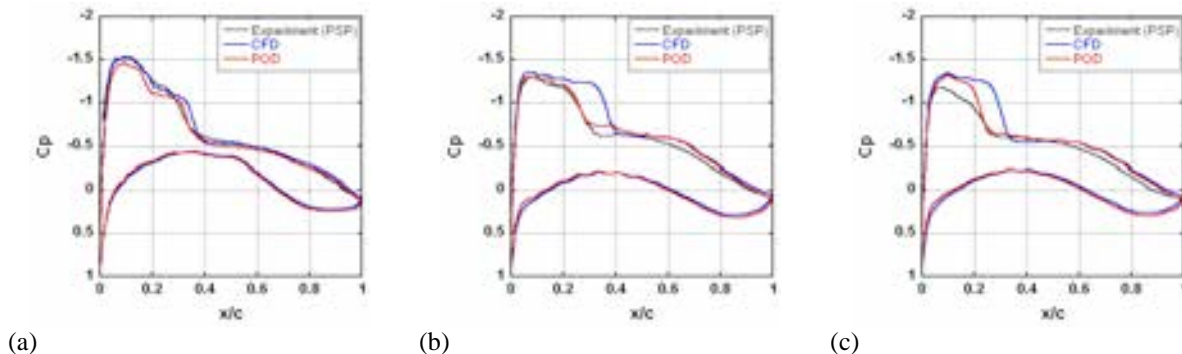

(a)   (b)   (c)

Fig. 4 Surface pressure distributions obtained by (a) POD approach, (b) PSP measurement (reference data), and (c) CFD (reference data).

(a)   (b)   (c)

Fig. 5 Cp distributions obtained by the POD approach and Cp distributions from PSP data and CFD for (a) $\eta = 0.400$, (b) $\eta = 0.700$, and (c) $\eta = 0.900$.

Reconstruction of PSP data measured with the DLR-F6 FX2B wind tunnel model

We next extend this approach to reconstruct an entire flow field from measured PSP data and several CFD results. The PSP data, which has the Cp distribution over the upper surface shown in Fig. 6, were measured at the JAXA 2 m × 2 m transonic wind tunnel facility [16]. The free-stream conditions of the experimental data are the same as in the previous subsection. The snapshots prepared for this case are also same as in the previous subsection.

The obtained Cp profiles at several spanwise locations are shown in Fig. 7 with those of the PSP data and the CFD results. We can see that the flow field is successfully obtained from the PSP data. In the PSP measurement, measurement error could occur due to the lighting setup or painting setup as shown near x/c = 0 at the η = 0.847 spanwise location in Fig. 7(f). The obtained results using the POD approach, however, provide reasonable profiles without the effect of this measurement error.
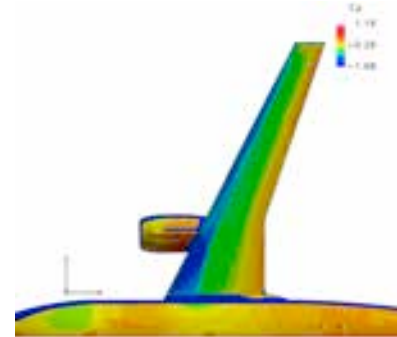
Fig. 6 The Cp contours obtained by PSP measurement.

Concluding Remarks

An EFD/CFD integration approach utilizing snapshot POD and gappy POD was successfully developed for obtaining the three-dimensional flow field from a limited experimental data set and several CFD solutions. We first attempted this POD approach to reconstruct the flow field over a DLR-F6 FX2B wind tunnel model from its pressure port data and seven CFD solutions. The results showed that the entire flow field can be reconstructed with satisfactory accuracy from a very small amount of measurement data and CFD solutions. Moreover, this POD approach can obtain a flow field that has equal information with the CFD result, in a much shorter time than is required for CFD calculation. In some locations, however, the results farther from the experimental data for the POD approach compared with CFD, because the number of prepared snapshots is insufficient. Thus, the necessary number of snapshots or the snapshot parameters should be examined to improve the results. We next extended this approach to PSP data over the DLR-F6 FX2B model. A reasonable flow field can be obtained, even though measurement error is included in the PSP data.

The results of several test cases indicate that the POD-based EFD/CFD integration approach can be an effective tool for complementing experimental data or predicting entire flow fields, if there are several existing CFD solutions. In future research we will investigate improvements in the accuracy of the present method by a careful understanding and treatment of the obtained POD modes and expansion coefficients.

Acknowledgements

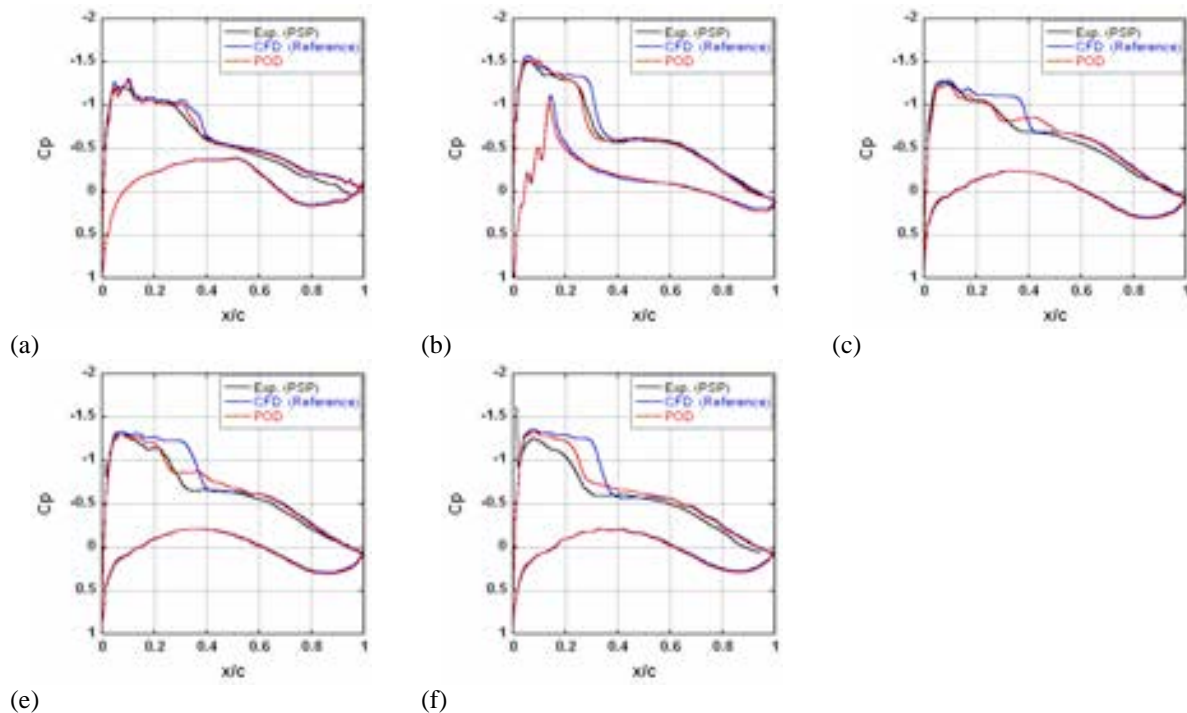**Fig. 7 Cp distributions obtained by the POD approach and distributions from the experimental data and CFD for (a) η = 0.150, (b) η = 0.331, (c) η = 0.514, (d) η = 0.638, and (e) η = 0.847.**

References

[1] N. Ahmed and M. H. Goldstein, "Orthogonal Transforms for Digital Signal Processing," Springer-Verlag, N. Y., (1975).
[2] R. B. Ash and M. F. Gardner, "Topics in Stochastic Processes," Academic Press, New York, (1975).
[3] K. Fukunaga, "Introduction to Statistical Pattern Recognition," Academic Press, New York, (1972).
[4] L. Sirovich, "Turbulence and the dynamics of coherent structures Part I, " *Q. Appl. Math.,* XLV(3) (1987), pp. 561-571.
[5] C. E. Tinney, L. S. Ukeiley and M. N. Glauser, "Low-dimentional Characteristics of a Transonic Jet. Part 1. Proper Orthogonal Decomposition," *J. Fluid Mech.,* 612(2008), pp.107-141.
[6] J. B. Freund and T. Colonius, "Turbulence and Sound-field POD Analysis of a Turbulent Jet," *Int'l J. Aeroacoustics*, 8(2009), pp.337-354.
[7] R. King, "Active Flow Control II," Springer, (2010).
[8] R. D. Joslin, and D. N. Miller, "Fundamentals and Applications of Modern Flow Control," AIAA Progress in Astronautics ad Aeronautics, 231(2009).
[9] X. Ma, G. E. Karniadakis, H. Park and M. Gharib, "DPIV-driven Flow Simulation: A New Computational Paradigm," Proc. R. Soc. Lond. A, 459(2003), pp.547-565.
[10] T. Bui-Thanh and M. Damodaran, "Aerodynamic Data Reconstruction and Inverse Design Using Proper Orthogonal; Decomposition, "*AIAA J.*, 42(8) (2004), pp. 1505-1516.
[11] R. Everson and L. Sirovich, "Karhunen-Loeve Procedure for Gappy Data," *J. Opt. Soc. Am. A*, 12(8) (1995), pp.1657-1664.
[12] "2nd AIAA Drag Prediction Workshop," http://aaac.larc.nasa.gov/tsab/cfdlarc/aiaa-dpw/Workshop2/workshop2.html.
[13] "3rd AIAA Drag Prediction Workshop," http://aaac.larc.nasa.gov/tsab/cfdlarc/aiaa-dpw/Workshop3/.
[14] A.Hashimoto, K. Murakami and T. Aoyama, "JAXA Digital/Analog Hybrid Wind Tunnel: Development of Digital Wind Tunnel, " *JAXA-SP-09-003*, (2010).
[15] A. Hashimoto, K. Murakami, T. Aoyama and P. Lahur, "Lift and Drag Prediction Using Automatic Hexahedra Grid Generation Method, "*AIAA paper 2009-1365*, (2009).
[16] K. Nakakita, M. Kurita K. Mitsuo and S. Watanabe, "Practical Pressure-Sensitive Paint Measurement System for Industrial Wind Tunnels at JAXA," *Meas. Sci. Tech.*, 17(2005), pp.359-366.

Drag and Lift Estimation from 3-D Velocity Field Data Measured by Multi-Plane Stereo PIV

Hiroyuki Kato
Kisa Matsushima
Makoto Ueno
Shunsuke Koike
Shigeya Watanabe

Japan Aerospace Exploration Agency
Chofu, Tokyo 182-8522
 Japan
kato.hiroyuki@jaxa.jp

Abstract

For airplane design, it is crucial to have tools that can accurately predict airplane drag and lift. Usually drag and lift prediction methods are force measurement using wind tunnel balance. Unfortunately, balance data do not provide information contribution of airplane to components to drag and lift for more precise and competitive airplane design. To obtain such information, a wake integration method for use drag and lift estimation was developed for use in wake survey data analysis. Wake survey data is commonly measured by multi-hole pressure probes. But pressure probe measurement requires considerable time, so that it is difficult to apply many conditions in wind tunnel testing. On the other hand, PIV measurement possesses the ability to acquire velocity distribution data at relatively short times. However, PIV measurement does not provide pressure data directly. Therefore, the pressure estimation technique is developed to enhance the value of PIV data. The technique conducts computational fluid dynamics (CFD) computation to estimate pressure field using multi-plane stereo PIV velocity data. Finally, drag and lift profiles are predicted by the wake integration method using velocity data measured by PIV and pressure data estimated by CFD.

Key words: Wind Tunnel Testing, Flow Measurements, Wake, PIV

Introduction

In general, the aerodynamic forces exerted on a wind tunnel test model are obtained using an aerodynamic force balance, which measures the integrals of pressure and friction on the model's surface and gives a near-field representation of the aerodynamic forces. Wake integration method is an attractive tool both for wind tunnel testing and CFD analysis, mainly because it can render the spanwise distribution of drag and lift visible quantitatively, and this knowledge of the aerodynamic force distribution is useful for drag source identification. Additionally, it can decompose drag into induced drag and profile drag components. Drag decomposition gives insight into the flow physics necessary for design improvement. But pressure probe measurement requires considerable time, so that it is difficult to apply many conditions in wind tunnel testing. On the other hand, PIV measurement possesses the ability to acquire velocity distribution data at relatively short times. However, PIV measurement does not provide pressure data directly. Therefore, the pressure estimation technique is developed to enhance the value of PIV data. The technique conducts computational fluid dynamics (CFD) computation to estimate pressure field using PIV velocity data. Finally, drag and lift profiles are predicted by the wake integration method using velocity data measured by PIV and pressure data estimated by CFD. In the verification procedures, this technique were performed of the PIV data of the NACA0012 rectangle wing model in wind tunnel testing, and the drag and lift forces estimated by PIV data directly compared with measured balance data.

Drag and Lift Prediction Method

The Poisson equation for pressure (equation (1)) is the basic equation for the computation. The equation is derived fro the divergence form of three-dimensional incompressible Navier-Stokes equations. It is assumed that velocity gradient in the freestream direction is 0 and a flow is steady. Then the two dimensional equation is obtained. All terms of the equation are discretized using the 2nd-oder central difference method. General coordinates transformation is done for wide applicability of the system. The discretized Poisson equation for pressure which is a simultaneous linear equation system is solved numerically by SOR (successive-over-relaxation) method [2].

$$\frac{\partial^2 p}{\partial y^2} + \frac{\partial^2 p}{\partial z^2} = -\left\{\left(\frac{\partial v}{\partial y}\right)^2 + 2\frac{\partial v}{\partial z}\frac{\partial w}{\partial y} + \left(\frac{\partial w}{\partial z}\right)^2 + v\frac{\partial D}{\partial y} + w\frac{\partial D}{\partial z}\right\} + \frac{1}{Re}\left(\frac{\partial^2 D}{\partial y^2} + \frac{\partial^2 D}{\partial z^2}\right)$$

$$\left(D = \frac{\partial v}{\partial y} + \frac{\partial w}{\partial z}\right) \tag{1}$$

The aerodynamic forces are expressed as the balance of momentum over a control volume around the model. Although the classical far-field method requires the integration of physical properties over the entire surface of the control volume, Betz succeeded in confining the integral to the inside the model's wake for two-dimensional wind tunnel drag measurement, and the theory was extended to three-dimensional wind tunnel testing by Maskell. Maskell's method was epoch-making as it required planar traversing measurement only within the wake of a wind tunnel model to acquire aerodynamic drag and lift forces (Figure 1).
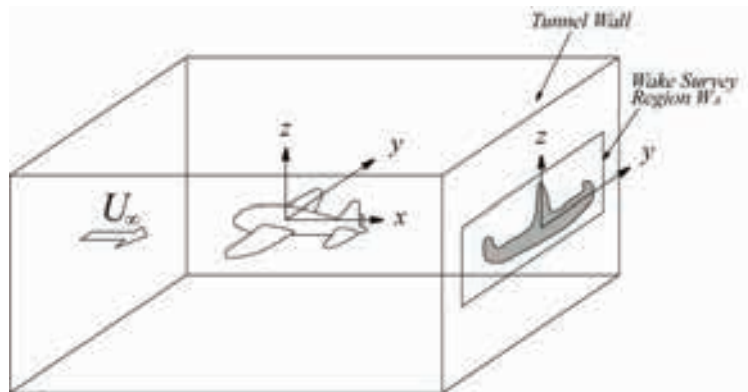

Figure 1 Image of wake integral control volume.

The wake integral method is described by Kusunose[1] in detail. The drag coefficient (CD) is written as

$$CD = CDP + CDI + CDP2 + O\,(\Delta 3) \tag{2}$$

CDP, CDI, CDP2 are profile drag coefficient, induced drag coefficient, 2nd order profile drag coefficient, respectively. And profile drag coefficient (CDP) is as follows

$$CDP = \frac{\iint_{WA} P_\infty \frac{\Delta s}{R}\,dydz}{\frac{1}{2}\rho_\infty U_\infty^2 S} \tag{3}$$

Denominator in right-hand side is dynamic pressure, and S control volume surface area. P_∞, ρ_∞, U_∞ are static pressure, density, velocity of freestream, respectively, and Δs is perturbation entropy, R is gas constant. WA is integral area over the model wake region. Induced drag (CDI) is as follows

$$CDI = \frac{\iint_{WA} \psi \xi \, dydz}{\frac{1}{2}\rho_\infty U_\infty^2 S} \qquad (4)$$

ξ is x-component of vorticity vector, and ψ, ϕ two-dimensional stream function, and are as follows

$$v = \frac{\partial \psi}{\partial z} + \frac{\partial \phi}{\partial y}, \quad w = -\frac{\partial \psi}{\partial y} + \frac{\partial \phi}{\partial z} \qquad (5)$$

2nd order profile drag is as follows

$$CDP2 = \frac{\iint_{WA} \frac{P_\infty}{2}\left(\frac{\Delta s}{R}\right)^2 dydz}{\frac{1}{2}\rho_\infty U_\infty^2 S} \qquad (6)$$

Lift coefficient is as follows

$$CL = \frac{\rho_\infty U_\infty \iint_{WA} y\xi \, dydz - \rho_\infty U_\infty^2 \left(1-M_\infty^2\right)\iint_{WA} \frac{w}{U_\infty}\frac{\Delta u}{U_\infty}\, ds + M_\infty^2 \frac{\gamma P_\infty}{R}\iint_{WA} \frac{w}{U_\infty}\Delta s\, ds}{\frac{1}{2}\rho_\infty U_\infty^2 S} \qquad (7)$$

Wind Tunnel Testing

A conventional low-speed wind tunnel with a 2m x 2m test section was used for the present PIV test. A photograph of the wind tunnel model is shown in figure 2. The model is a NACA0012 rectangular wing (chord = 200 mm, span = 1,000 mm). The test was conducted at a freestream velocity U_∞ of 30.0m/s. Angle of attack (α) was set in a range between 0º and 8º.
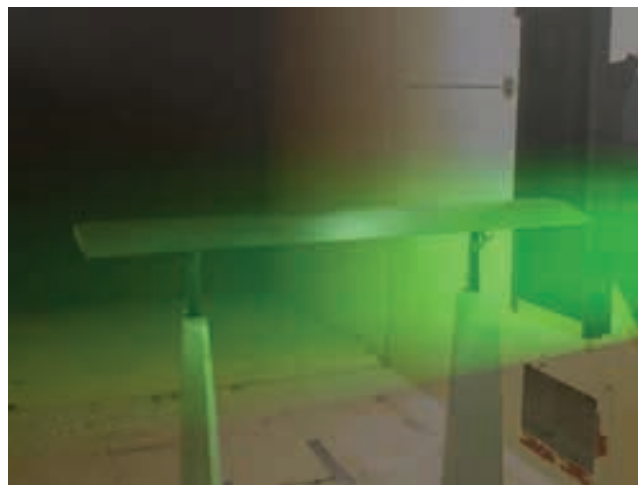
Figure 2 The wind tunnel test model of NACA0012 rectangle wing.

A stereoscopic (3-C) PIV system which has been developed for the JAXA wind tunnels was employed for the present test. In the PIV measurement, the laser light sheet was located perpendicular to the freestream (figure 3).
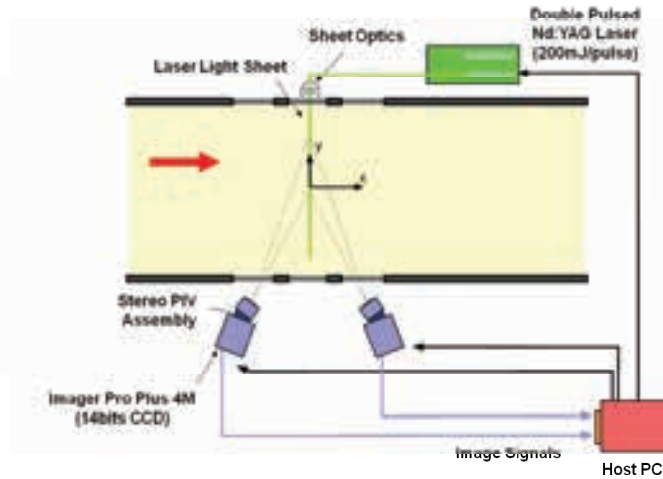

Figure 3 Schematic of Stereo PIV setting.

A stereoscopic (3-C) PIV system which has been developed for the JAXA wind tunnels [3] was employed for the present test. In this measurement, stereoscopic PIV with two cameras with different view angles were performed. Figure 3 shows stereoscopic PIV configuration. In some cases, we employed to measure three components of velocity. In vector processing, we applied several steps of velocity vector validation. After the validation, ensemble instantaneous data at an identical test condition are averaged. Oil droplets with a diameter of around 1μm were used as the seed particles. In the stereoscopic PIV measurement, the sheet was located perpendicular to the free stream. Interrogation spot size is 32 x 32 pixels with 50% overlap. Time separation Δt was set from 45 to 55 μs step by 0.2 μs in order to reduce bias error due to difference of Δt.
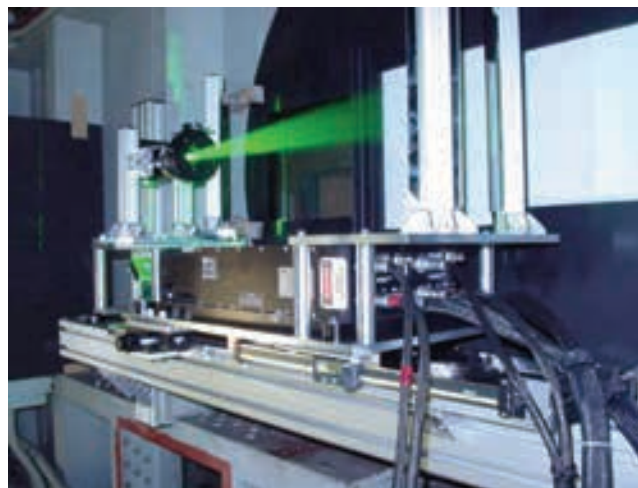
Figure 4 Laser light sheet optics.

Experimental Results

Figure 5 shows three components of velocity distribution measured in the wind-tunnel testing. Color contour shows a velocity component of the freestream direction (u).
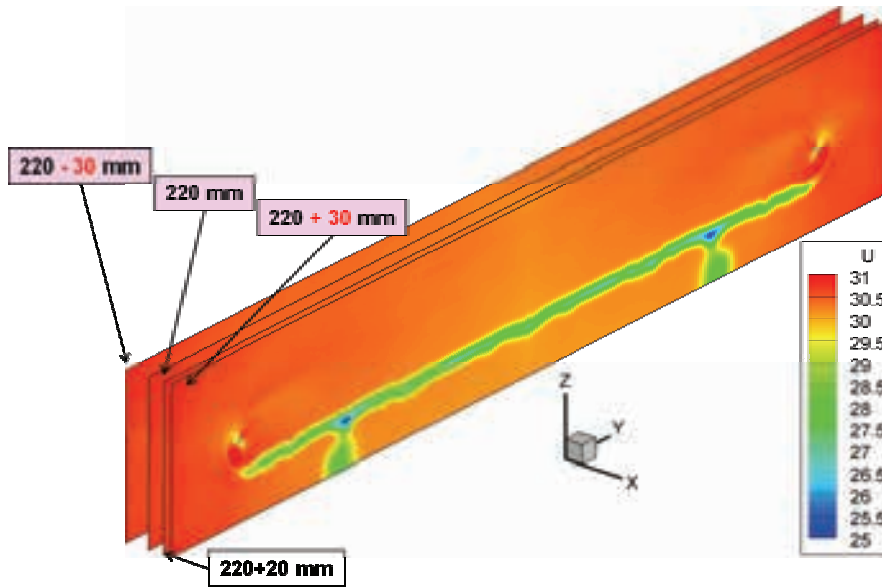
Figure 5 multi-plane stereo PIV results (U=30m/s, AoA=8deg).

Figure 6 shows pressure distributions estimated from three velocity components by CFD method. In the case of attack of angle 8 degree, it is qualitatively good results that there are low pressure region near a wing tip vortex.
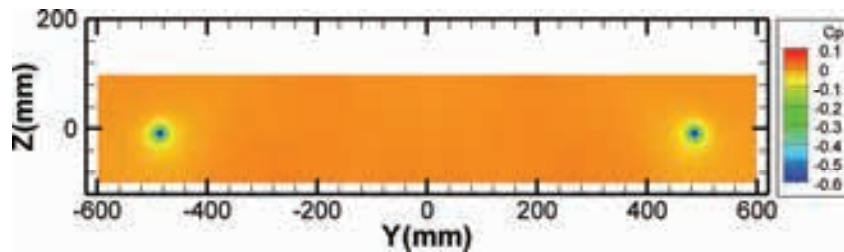

Figure 6 multi-plane stereo PIV results (U=30m/s, AoA=8deg).

Figure 7 and 8 show profile drag distribution (cdp) and induced drag distribution (cdi), respectively. These results are calculated from three velocity components and pressure distribution at wake region by wake integration method. The computational code developed and validated by Ueno et. al[4] was used applied wake integration method.
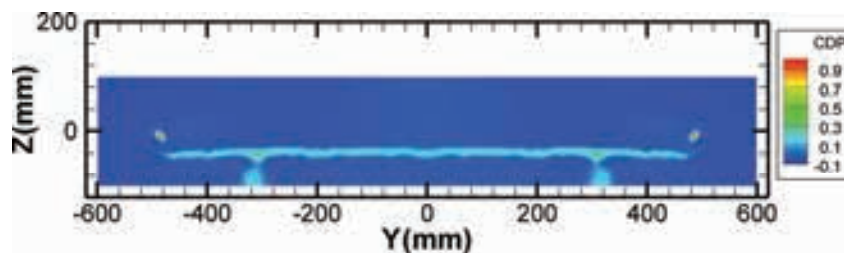
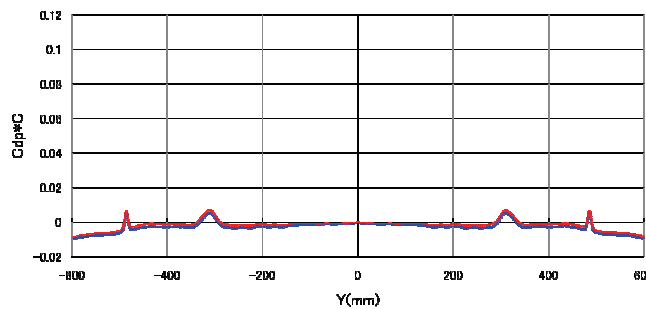**Figure 7 multi-plane stereo PIV results (U=30m/s, AoA=8deg).**
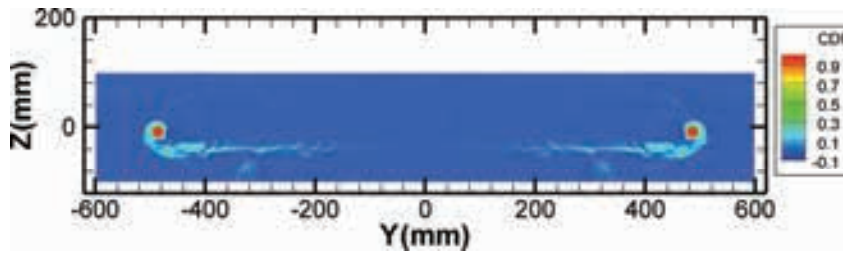
Figure 8 multi-plane stereo PIV results (U=30m/s, AoA=8deg).

In the profile drag distribution, there are large drag components at the model and model supports. On the other hand, in the induced drag distribution, thre are peaks of profile drag near the tip vortex at attack of angle 8 degree.

Figure 9, 10 and 11 show profile drag, induced drag and lift distributions in spanwise direction, respectively. Also in the spanwise distributions, profile and induced drag denote the same tendency of the distributions in the wake plane. In the lift distribution, it is fairly good results that there is a peak at center of the wing span.

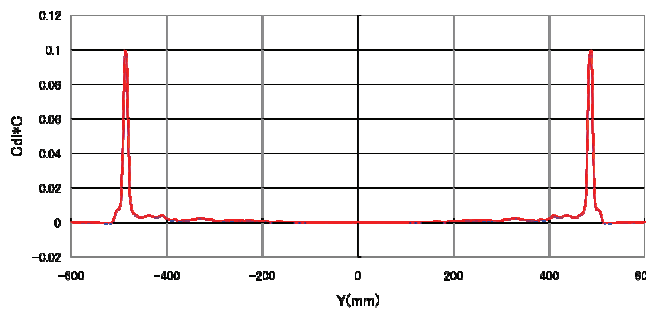**Figure 9 multi-plane stereo PIV results (U=30m/s, AoA=8deg).**

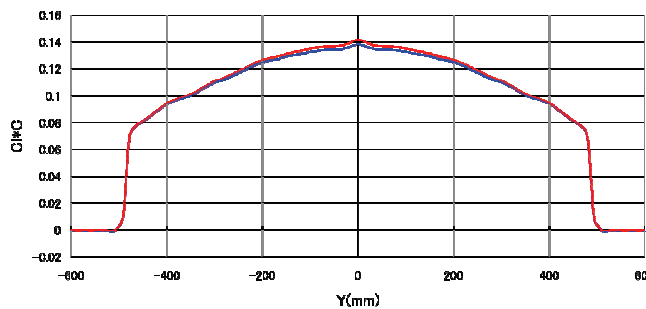**Figure10 multi-plane stereo PIV results (U=30m/s, AoA=8deg).**

Figure 11 multi-plane stereo PIV results (U=30m/s, AoA=8deg).

Conclusions

Pressure distribution is estimated from three velocity components at wake plane measured by stereo PIV system by CFD technique. It is development that the technique is applicable to wake integration method by means of velocity distribution measured by PIV and pressure distribution estimated by CFD

The wind tunnel testing was carried out in order to validate this technique. NACA0012 rectangle wing model was used in the wind tunnel testing. In the result, the drag estimated by PIV data is 0.01 differences from balance data due to the model supports. On the other hand, he lift estimated by PIV data is fairly good agreement with balance data, while the difference between PIV and balance is from 0.01 to 0.03. Also, the profile and induced drag estimation is qualitatively good results about wake plane distributions and spanwise distributions. Finally, It is demonstrated that profile and induced drag and lift force can be estimated by only PIV data.

Acknowledgments

The authors are indebted to Junichi Akatsuka and Akiko Hidaka, Wind Tunnel Technology Center, JAXA. The authors are also indebted to the members of Low-Speed Wind Tunnel Section, Wind Tunnel Technology Center, JAXA for their support to the wind tunnel experiments and the data processing.

References

[1] Kusunose, K.: A Wake Integration method for Airplane Drag Prediction, Tohoku University Pres., 2005.

[2] Aso, T., Matsushima, K. Nakahashi, K.: CFD Pressure Estimation using PIV Data. Proceedings of 2006 KSAS-JSASS Joint International Symposium,,159-163, 2006.

[3] Watanabe, S.; Kato, H.: Stereo PIV Applications to Large-Scale Low-Speed Wind Tunnels, AIAA Paper 2003-0919, 2003.

[4] Ueno, M. Akatsuka, J. and Hidaka, A.: Drag Decomposition Analysis of CFD Data of the DLR-F6 Model, AIAA Paper2008-6903, 2008.

Hosted by:

Japan Aerospace Exploration Agency (JAXA)
http://www.jaxa.jp/index_e.html

Tohoku University
http://www.tohoku.ac.jp/english/

in corporation with

Japan Society for Aeronautical and Space Sciences (JSASS)
http://www.jsass.or.jp/webe/

Japan Society of Fluid Mechanics (JSFM)
http://www.nagare.or.jp/en/index.html

Japan Society for Industrial and Applied Mathematics (JSIAM)
http://www.jsiam.org/publication/jsiam-english.html

Japan Society of Mechanical Engineers (JSME)
http://www.jsme.or.jp/English/

Visualization Society of Japan (VSJ)
http://www.visualization.jp/

Society of Automotive Engineers of Japan (JSAE)
http://www.jsae.or.jp/index_e.php

Acknowledgement